ORNL/FMP-91/2

U.S. Department of Energy

FOSSIL ENERGY ADVANCED RESEARCH AND TECHNOLOGY DEVELOPMENT MATERIALS PROGRAM

Semiannual Progress Report for the Period Ending September 30, 1991

Fossil Energy Materials Program Office

OAK RIDGE NATIONAL LABORATORY
MANAGED BY MARTIN MARIETTA ENERGY SYSTEMS, INC.
FOR THE U.S. DEPARTMENT OF ENERGY

Fossil Energy Program

ORNL/FMP-91/2

FOSSIL ENERGY ADVANCED RESEARCH AND TECHNOLOGY DEVELOPMENT (AR&TD) MATERIALS PROGRAM SEMIANNUAL PROGRESS REPORT FOR THE PERIOD ENDING SEPTEMBER 30, 1991

Compiled by
R. R. Judkins
N. C. Cole

ORNL/FMP--91/2

DE92 016504

Contributions by

Argonne National Laboratory
Battelle Columbus Laboratories
Colorado School of Mines
Foster Wheeler Development Corporation
Georgia Institute of Technology
Idaho National Engineering Laboratory
Lawrence Berkeley Laboratory
Los Alamos National Laboratory
National Institute of Standards and Technology
North Carolina A&T State University
Oak Ridge K-25 Site
Oak Ridge National Laboratory
Ohio State University
Pacific Northwest Laboratory
Rensselaer Polytechnic Institute
Sandia National Laboratories
University of Cincinnati
University of Notre Dame
University of Tennessee
Virginia Polytechnic Institute and State University
Westinghouse Hanford Company

Date Published: April 1992

Compiled for
Department of Energy
Fossil Energy Office of Technical Coordination
and
Oak Ridge Field Office
Budget Activity AA 15 10 10 0

by

Oak Ridge National Laboratory
Oak Ridge, Tennessee 37831-6285
managed by
MARTIN MARIETTA ENERGY SYSTEMS, INC.
for the
U.S. DEPARTMENT OF ENERGY
under Contract DE-AC05-84OR21400

PREVIOUS REPORTS IN THIS SERIES

ORNL/FMP-81/1	AR&TD Fossil Energy Materials Program Quarterly Progress Report for Period Ending December 31, 1980.
ORNL/FMP-81/2	AR&TD Fossil Energy Materials Program Quarterly Progress Report for Period Ending March 31, 1981.
ORNL/FMP-81/3	AR&TD Fossil Energy Materials Program Quarterly Progress Report for Period Ending June 30, 1981.
ORNL/FMP-81/4	AR&TD Fossil Energy Materials Program Quarterly Progress Report for Period Ending September 30, 1981.
ORNL/FMP-82/1	AR&TD Fossil Energy Materials Program Quarterly Progress Report for Period Ending December 31, 1981.
ORNL/FMP-82/2	AR&TD Fossil Energy Materials Program Quarterly Progress Report for Period Ending March 31, 1982.
ORNL/FMP-82/3	AR&TD Fossil Energy Materials Program Quarterly Progress Report for Period Ending June 30, 1982.
ORNL/FMP-82/4	AR&TD Fossil Energy Materials Program Quarterly Progress Report for Period Ending September 30, 1982.
ORNL/FMP-83/1	AR&TD Fossil Energy Materials Program Quarterly Progress Report for Period Ending December 31, 1982.
ORNL/FMP-83/2	AR&TD Fossil Energy Materials Program Quarterly Progress Report for Period Ending March 31, 1983.
ORNL/FMP-83/3	AR&TD Fossil Energy Materials Program Quarterly Progress Report for Period Ending June 30, 1983.
ORNL/FMP-83/4	AR&TD Fossil Energy Materials Program Quarterly Progress Report for Period Ending September 30, 1983.
ORNL/FMP-84/1	AR&TD Fossil Energy Materials Program Quarterly Progress Report for Period Ending December 31, 1983.
ORNL/FMP-84/2	AR&TD Fossil Energy Materials Program Quarterly Progress Report for Period Ending March 31, 1984.
ORNL/FMP-84/3	AR&FD Fossil Energy Materials Program Quarterly Progress Report for Period Ending June 30, 1984.
ORNL/FMP-84/4	AR&TD Fossil Energy Materials Program Quarterly Progress Report for Period Ending September 30, 1984.

ORNL/FMP-85/1	AR&TD Fossil Energy Materials Program Quarterly Progress Report for Period Ending December 31, 1984.
ORNL/FMP-85/2	AR&TD Fossil Energy Materials Program Quarterly Progress Report for Period Ending March 31, 1985.
ORNL/FMP-85/3	AR&TD Fossil Energy Materials Program Quarterly Progress Report for Period Ending June 30, 1985.
ORNL/FMP-85/4	AR&TD Fossil Energy Materials Program Quarterly Progress Report for Period Ending September 30, 1985.
ORNL/FMP-86/1	AR&TD Fossil Energy Materials Program Quarterly Progress Report for Period Ending December 31, 1985.
ORNL/FMP-86/2	AR&TD Fossil Energy Materials Program Quarterly Progress Report for Period Ending March 31, 1986.
ORNL/FMP-86/3	AR&TD Fossil Energy Materials Program Quarterly Progress Report for Period Ending June 30, 1986.
ORNL/FMP-86/4	AR&TD Fossil Energy Materials Program Quarterly Progress Report for Period Ending September 30, 1986.
ORNL/FMP-87/1	AR&TD Fossil Energy Materials Program Semiannual Progress Report for Period Ending March 31, 1987.
ORNL/FMP-87/2	AR&TD Fossil Energy Materials Program Semiannual Progress Report for Period Ending September 30, 1987.
ORNL/FMP-88/1	AR&TD Fossil Energy Materials Program Semiannual Progress Report for Period Ending March 31, 1988.
ORNL/FMP-88/2	AR&TD Fossil Energy Materials Program Semiannual Progress Report for Period Ending September 30, 1988.
ORNL/FMP-89/1	AR&TD Fossil Energy Materials Program Semiannual Progress Report for Period Ending March 31, 1989.
ORNL/FMP-89/2	Fossil Energy AR&TD Materials Program Semiannual Progress Report for Period Ending September 30, 1989.
ORNL/FMP-90/1	Proceedings of the Fourth Annual Conference on Fossil Energy Materials, AR&TD Materials Program and ASM International (August 1990).
ORNL/FMP-90/2	Fossil Energy AR&TD Materials Program Semiannual Progress Report for Period Ending September 30, 1990

ORNL/FMP-91/1

Proceedings of the Fifth Annual Conference on Fossil Energy Materials, AR&TD Materials Program and ASM International (September 1991).

TABLE OF CONTENTS

*The acronym preceding the title of the contribution designates the responsible contractor and the program work element. See Table 1 of Part I for further information.

PART I - INTRODUCTION

INTRODUCTION

N. C. Cole and R. R. Judkins

Oak Ridge National Laboratory
Oak Ridge, Tennessee 37831

The objective of the Fossil Energy Advanced Research and Technology Development (AR&TD) Materials Program is to conduct research and development on materials for fossil energy applications with a focus on the longer-term and generic needs of the various fossil fuel technologies. The Program includes research aimed toward a better understanding of materials behavior in fossil energy environments and the development of new materials capable of substantial enhancement of plant operations and reliability.

The management of the Program has been decentralized to the DOE Oak Ridge Field Office (OR) and the Oak Ridge National laboratory (ORNL) as technical support contractor. The organizational relationships among DOE Headquarters, OR, and ORNL are illustrated in Fig. 1. A substantial portion of the work on the AR&TD Materials Program is performed by participating subcontractor organizations. The performing institution and principal investigator for each project are shown in Table 1.

This combined semiannual progress report of activities on the Program is in accordance with a work breakdown structure in which projects are organized according to materials research areas. These areas are (1) Ceramics, (2) New Alloys, (3) Corrosion and Erosion Research, and (4) Technology Development and Transfer. A schematic summary of this organization is provided in Fig. 2.

These Fossil Energy AR&TD Materials Program semiannual progress reports are intended to aid in the dissemination of information developed on the Program. Highlights of projects that are part of this program are provided in the bimonthly DOE newsletter, *Materials and Components in Fossil Energy Applications*, published by Battelle Columbus Laboratories.

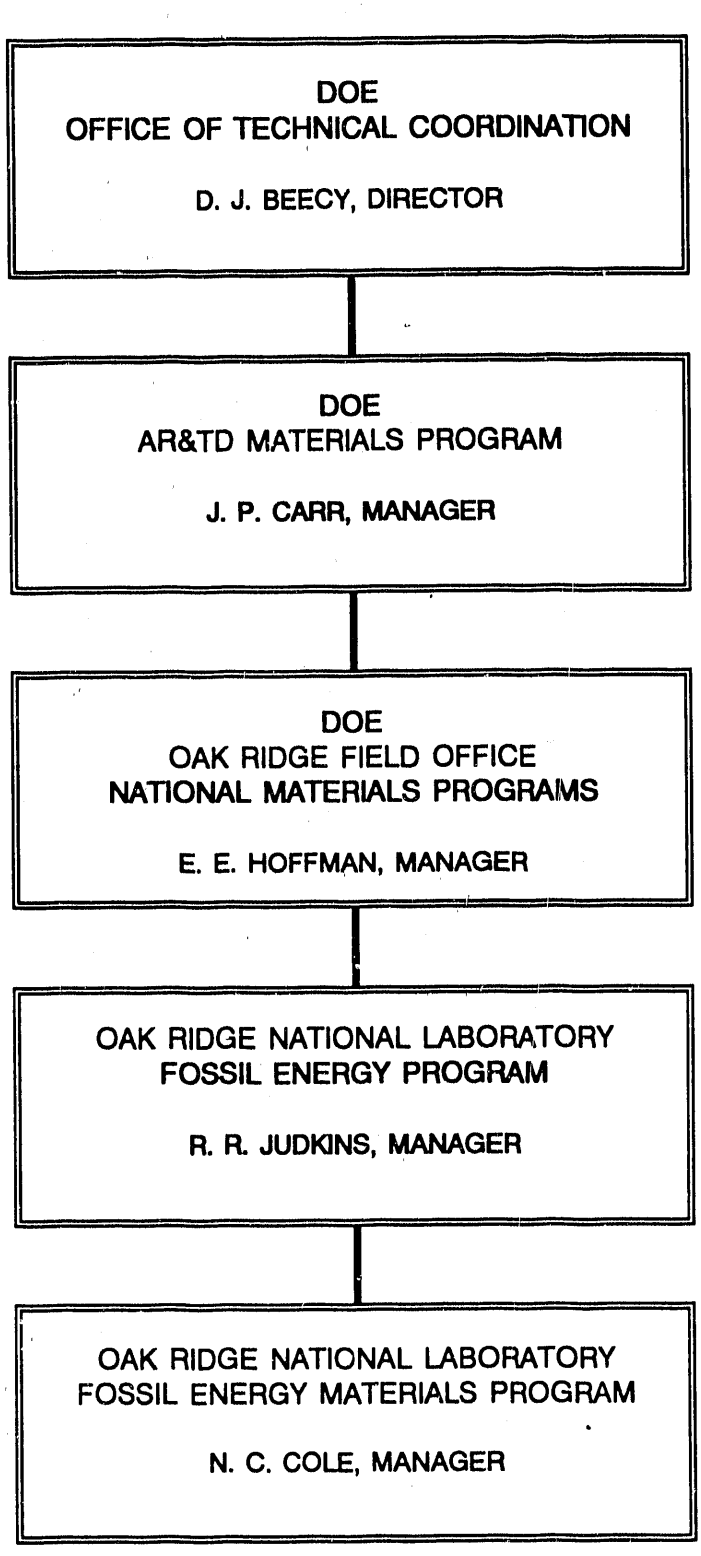

Fig. 1. Organizational relationships among DOE Headquarters, DOE Oak Ridge Field Office, and Oak Ridge National Laboratory for the AR&TD Materials Program.

Table 1. Projects of the AR&TD Materials Program

Project Work Breakdown Structure Element and Title	Performing Institution	Principal Investigator
Ceramics		
ANL-1: Development of Nondestructive Evaluation Methods for and Effects of Flaws on the Fracture Behavior of Structural Ceramics	Argonne National Laboratory	W. A. Ellingson
GT-1(A): Modeling of Fibrous Preforms for CVD Infiltration	Georgia Tech Research Institute	T. L. Starr
GT-1: Development of Advanced Fiber-Reinforced Ceramics	Georgia Tech Research Institute	T. L. Starr
INEL-1(A): Nondestructive Evaluation of Advanced Ceramic Composite Materials	Idaho National Engineering Laboratory	L. A. Lott
INEL-1(B): Joining of Silicon Carbide Ceramics and Composites	Idaho National Engineering Laboratory	B. H. Rabin
NIST-1: Structural Reliability and Damage Tolerance of Ceramic Composites	National Institute of Standards and Technology	E. R. Fuller
NCAT-1: Mechanical Properties Testing of Ceramic Fiber-Ceramic Matrix Composites	North Carolina A&T State University	J. Sankar
ORGDP-1: Development of Ceramic Membranes for Gas Separation	Oak Ridge K-25 Site	D. E. Fain
ORNL-1(A): Fabrication of Fiber-Reinforced Composites by Chemical Infiltration and Deposition	Oak Ridge National Laboratory	D. P. Stinton
ORNL-1(C): Interfaces and Mechanical Properties of Continuous Fiber-Reinforced Ceramic Composites	Oak Ridge National Laboratory	R. A. Lowden
ORNL-1(D): Microwave Sintering of Ceramics for Fuel Cells	Oak Ridge National Laboratory	M. A. Janney
PNL-1: Advanced Materials and Electrochemical Processes in High-Temperature Solid Electrolytes	Pacific Northwest Laboratory	J. L. Bates
SNL-1: Ceramic Catalyst Materials: Hydrous Metal Oxide Ion-Exchange Supports for Direct Coal Liquefaction	Sandia National Laboratories	D. H. Doughty
VPI-1: Investigation of Properties and Performance of Ceramic Composite Components	Virginia Polytechnic Institute and State University	K. L. Reifsnider
New Alloys		
B&W-2: Evaluation of the Fabricability of Advanced Austenitic Alloys	Babcock & Wilcox Research	M. J. Topolski
CSM-2: Grain Growth Kinetics of Iron Aluminide Alloy FA-129	Colorado School of Mines	G. R. Edwards
INEL-2: The Influence of Thermomechanical Processing on Microstructure and Mechanical Properties of Fe_3Al Alloys	Idaho National Engineering Laboratory	R. N. Wright
ORNL-2(B): Investigation of Austenitic Alloys for Advanced Heat Recovery and Hot-Gas Cleanup Systems	Oak Ridge National Laboratory	R. W. Swindeman
ORNL-2(F): Development of Iron Aluminides	Oak Ridge National Laboratory	C. G. McKamey
OSU-2: Pack Cementation Diffusion Coatings for Iron-Base Alloys: Codeposition of Chromium and Silicon	Ohio State University	R. A. Rapp
RPI-2: Investigation of Moisture-Induced Embrittlement of Iron Aluminides	Rensselaer Polytechnic Institute	N. S. Stoloff
UTN-2: Investigation of Joining Techniques for Advanced Austenitic Alloys	University of Tennessee	C. D. Lundin
WHC-2: Electro-Spark Deposited Coatings for Protection of Materials in Sulfidizing Atmospheres	Westinghouse Hanford Company	R. N. Johnson

Table 1. Projects of the AR&TD Materials Program (continued)

Project Work Breakdown Structure Element and Title	Performing Institution	Principal Investigator
Corrosion and Erosion Research		
ANL-3: Corrosion and Mechanical Properties of Alloys in FBC and Mixed-Gas Environments	Argonne National Laboratory	K. Natesan
LBL-3: Wastage of Steels in the Erosion-Corrosion (E-C) Environments of Fluidized Bed Combustors	Lawrence Berkeley Laboratory	A. V. Levy
NIST-3: Mechanisms of Galling and Abrasive Wear	National Institute of Standards and Technology	L. K. Ives
ORNL-2(A): Environmental Effects on Iron Aluminides	Oak Ridge National Laboratory	J. H. DeVan
ORNL-3(B): Responses of Metallic and Oxide Surfaces to Deformation	Oak Ridge National Laboratory	J. R. Keiser
UCIN-3: Study of Particle Rebound Characteristics and Material Erosion at High Temperatures	University of Cincinnati	W. Tabakoff
UND-3: A Study of Erosive Particle Rebound Parameters	University of Notre Dame	T. H. Kosel
UTN-3: Corrosion of Iron Aluminides in Acidic, Basic, and Chloride Solutions	University of Tennessee	R. A. Buchanan
Technology Development and Transfer		
BCL-4: *Materials and Components in Fossil Energy Applications* Newsletter	Battelle-Columbus Laboratories	I. G. Wright
CARB-4: Engineering-Scale Development of the Vapor-Liquid-Solid (VLS) Process for the Production of Silicon Carbide Whiskers	The Carborundum Company	J. J. Kim
LANL-4: Vapor-Liquid-Solid SiC Whisker Process Development	Los Alamos National Laboratory	J. D. Katz
ORNL-4(B): Coal Conversion and Utilization Plant Support Services	Oak Ridge National Laboratory	J. R. Keiser

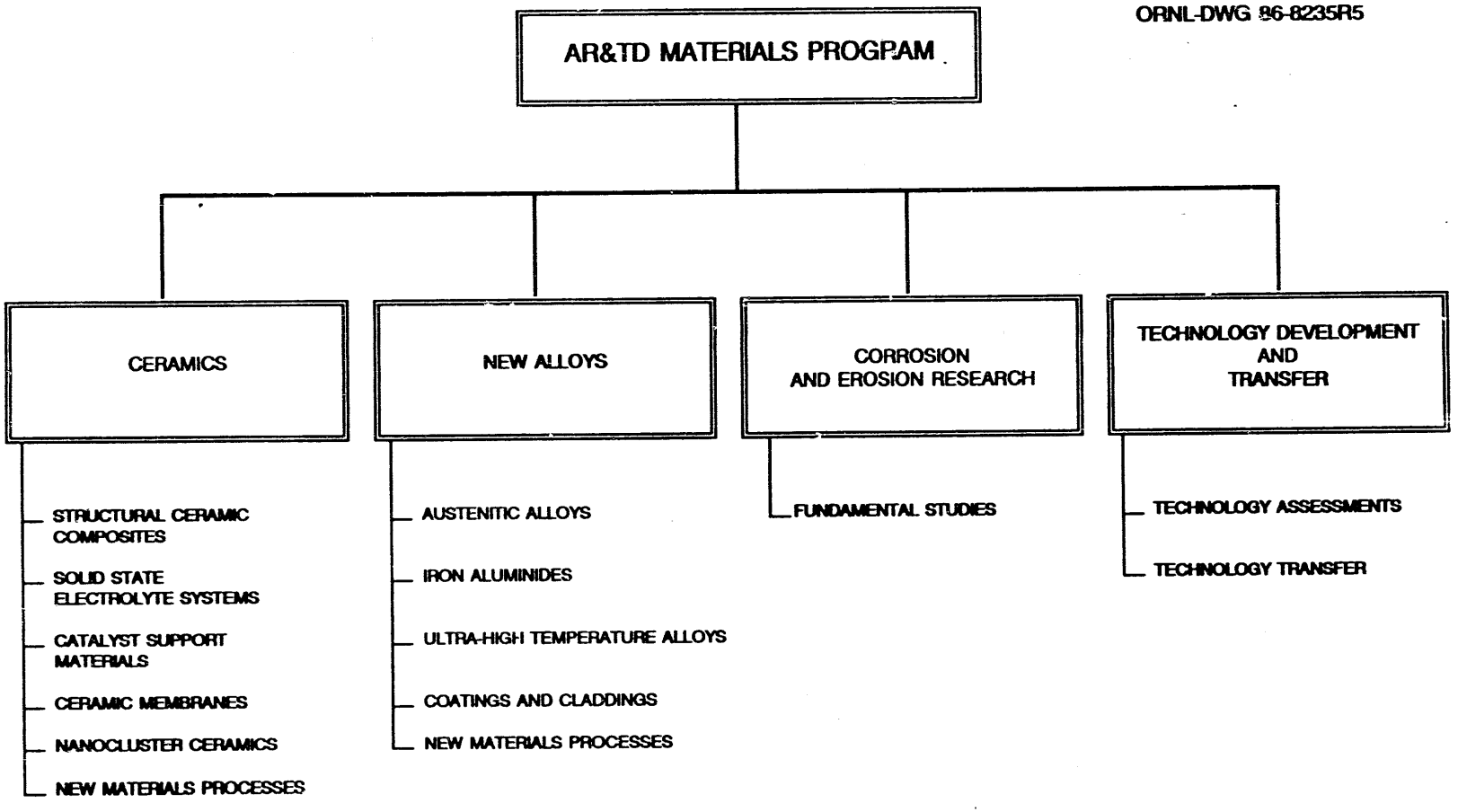

Fig. 2. Organization of research activities on the AR&TD Materials Program.

PART II - CERAMICS

ANL-1 - DEVELOPMENT OF NONDESTRUCTIVE EVALUATION METHODS FOR AND EFFECTS OF FLAWS ON THE FRACTURE BEHAVIOR OF STRUCTURAL CERAMICS

W. A. Ellingson, J. P. Singh, D. Singh, R. Sayre, S. H. Sheen,
S. L. Dieckman, W. P. Lawrence, and T. Hentea*

Argonne National Laboratory
Materials and Components Technology Division
Argonne, IL 60439

INTRODUCTION

The purpose of this program is to (1) develop nondestructive characterization (NDC) methods and protocols that can be used to characterize structural ceramics (with emphasis on ceramic/ceramic composites), as well as detect flaws in early stages of processing and in the final densified state and (2) correlate the characteristics of flaws with mechanical properties of ceramic materials to obtain an understanding of the effects various flaws and processing parameters have on fracture behavior. The NDC techniques being developed include (1) three-dimensional X-ray microcomputed tomography, (2) nuclear magnetic resonance (imaging and spectroscopy), (3) bulk body and surface acoustics with advanced signal processing, and (4) low-kV X-ray radiography (contact, projection, and real-time) with digital image processing. Fracture studies focus on both green and dense ceramic/ceramic composites, with emphasis on Si_3N_4–matrix composites with SiC or Si_3N_4 whiskers. Limited effort this past fiscal year has been devoted to continuous-fiber CVI composites, but next fiscal year will almost exclusively focus on continuous fiber composites.

---

*Purdue University–Calumet, Hammond, IN.

DISCUSSION OF CURRENT ACTIVITIES

Development of Nondestructive Evaluation

Application of Three-Dimensional Microfocus X-ray Imaging to Ceramic-Matrix Composites

Si_3N_4(w)/Si_3N_4 cold pressed composites. The work which we had reported on earlier relative to detection of whisker concentration by X-ray microfocus computed tomography was continued this period. We examined cold pressed MOR bars of Si_3N_4 whisker based Si_3N_4. The whisker content varied from 0 to 25 vol. %. At each whisker content, 3 MOR bars were produced. The data given for these bars relative to density as a function of volume concentration of whiskers is given in Fig. 1. This is a somewhat surprising relationship between density and volume concentration of whiskers as all prior data sets suggested that the maximum green density was reached with 10-15 vol. % whiskers. These measured data (by archimedes) also do not agree with the X-ray CT measured data. In order to obtain X-ray CT data, to correlate to the archimedes data, we averaged the X-ray CT images for all cross-sections (25 cross section per MOR bars). Thus we have a volumetric average gray scale (from X-ray CT data) versus the archimedes measured density. The plot showing the relationship between the X-ray CT measured gray scale (related to density) and measured density is shown in Fig. 2. We also tried again to correlate X-ray CT data with volume concentration of whiskers. These data are shown in Fig. 3. This is consistent with earlier data which shows that maximum gray scale (density) is achieved at 10–15 vol. % whiskers. This again calls into question the reliability of the measured density data and this discrepancy needs to be studied.

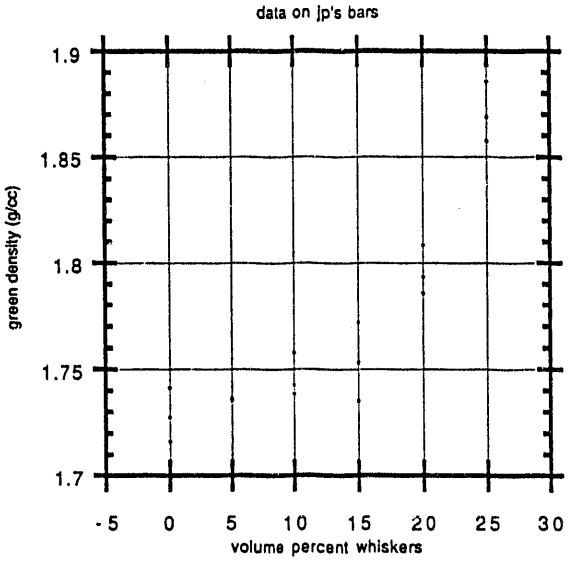

Fig. 1. Measured green density of cold-pressed $Si_3N_4(w)/Si_3N_4$ as a function of volume percent whiskers

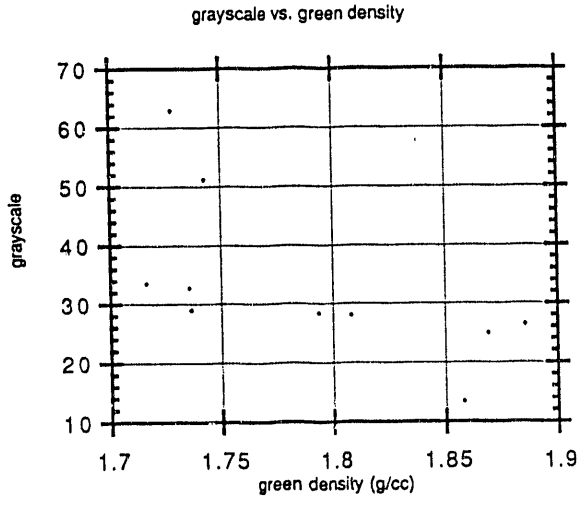

Fig. 2. Microfocus X-ray computed tomography data (image gray scale) as a function of measured density for cold pressed $Si_3N_4(w)/Si_3N_4$

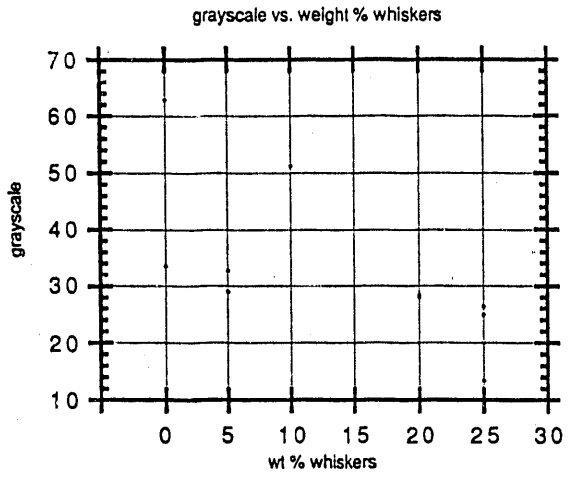

Fig. 3. Microfocus X-ray computed tomography data (image gray-scale) as a function of volume % whiskers for cold-pressed $Si_3N_4(w)/Si_3N_4$

Microfocus X-ray CT system development. We have noted in earlier reports that in order to achieve higher spatial resolution, especially on complex shaped parts, that a method needed to be developed which would allow only a pre-determined volume to be reconstructed and not be forced to reconstruct the entire object. This is sometimes called Region-of-Interest (ROI) tomography[1] or also called "local tomography".[2] There have been several attempts at this by others[1,2] but none have applied this to 3D (cone-beam) tomography.

In order to develop and evaluate new ROI codes we have been investigating two different codes to simulated data sets for ROI code development. These two codes were developed by guest scientists[3,4] and are being revised and developed at ANL for application. These two codes are capable of generating quite different data sets. The Sivers code can generate ellipsoids of different major/minor axis ratios and at different orientation. The Rizo code can generate up to 20 spheres at any position and in a nested configuration.

We have had some problems in developing these codes for simulated data set generation. However, we were able to overcome these this period and will show examples of the results.

Case I: Sivers Data Simulation

Figure 4 shows a schematic diagram of the data simulated. We chose to simulate a 26 mm radius sphere with two internal ellipsoids. One ellipsoid was located in the top right center of the sphere with its major axis parallel to the X-axis. As the density of the sphere was set at a relative value of 0.15, the density of the ellipsoid was set at —0.15 such that the reconstructed density would be 0 to simulate a void. The second ellipsoid was centered below the sphere center but with an axis inclined 30° above the horizontal. The density assigned to this ellipsoid was also 0.15 which resulted in the reconstructed density being equal to 2 times the original sphere density. We simulated 131 projections, and used a 256 x 256 reconstruction matrix. We know that this will result in an aliasing in the images. But this was acceptable for these tests. We reconstructed 3 cross sections each with a 2.85 mm

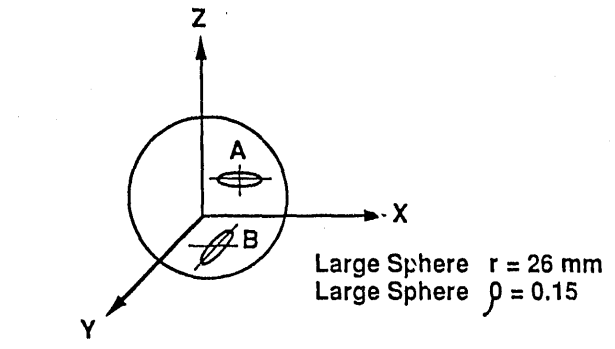

A Ellipsoid	B Ellipsoid
Center at:	Center at:
X = 3 mm	X = 0
Y = 0	Y = 0
Z = 5 mm	Z = -5 mm
Size:	Size:
rx = 3 mm	rx = 2 mm
ry = 2 mm	ry = 4 mm
rz = 1 mm	rz = 2 mm
Density = - 0.15	Density = + 0.15
Angle = 0 °	Angle = 15 °

Fig. 4. Schematic diagram showing data simulation geometries for Sivers simulation

thickness. The resulting images, (printed with an available laser printer) are shown in Fig. 5. Figure 5a is a cross section which does not contain either of the ellipsoids; Fig. 5b is through the simulated void ellipsoid and Fig. 5c is through the double density ellipsoid simulated with an inclined axis. Note that aliasing in present as expected in each image. Note also however, that appropriate densities are noted, i.e., void in white and double density is much darker as shown.

Case II: Rizo data simulation

In this case, we were attempting to avoid inherent problems with circular artifacts which seem to be more prevalent is these simulated data. Figure 6 shows a schematic diagram of the setup used to simulate the data. The source to detect or distance was set at 500 mm and source to specimen was set at 250 mm. The sphere was set to be of 8 mm radius. We reconstructed the data using 60 projections and used a 64 X 64 matrix. Again we recognize that this will result in aliasing. We reconstructed 5 consecutive tomograms with 1 mm slice thickness. The first set of reconstructions see Fig. 7, were taken at the mid plane section and the second set (see Fig. 8) was taken such that the first tomogram reconstructed the top of the sphere. We will continue to work on these data simulation sets so that we can be more general in our simulated data for testing the ROI code.

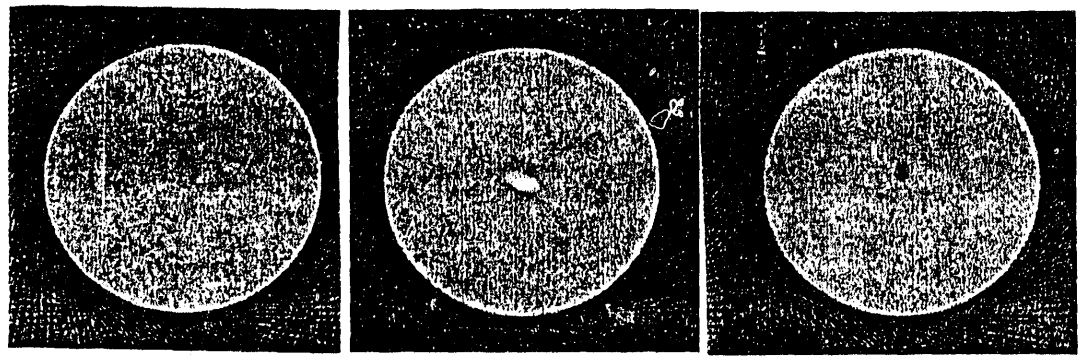

(a) (b) (c)

Fig. 5. Reconstructed images from Sivers data simulation: (a) cross section through sphere, (b) through simulated ellipsoid void, and (c) through simulatedinclined ellipsoid with double density

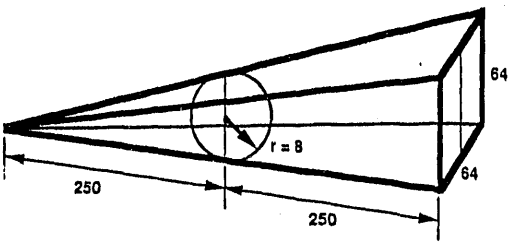

Fig. 6. Schematic diagram of Rizo simulation data configuration

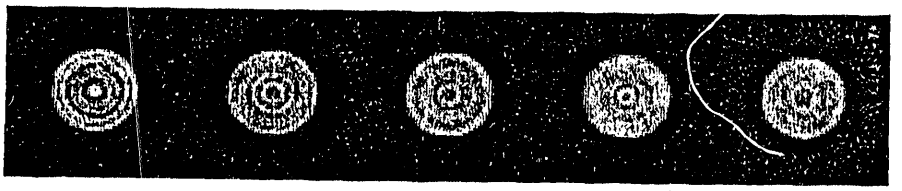

Fig. 7. Reconstructed images using Rizo simulation data sets with reconstruction near the center planes

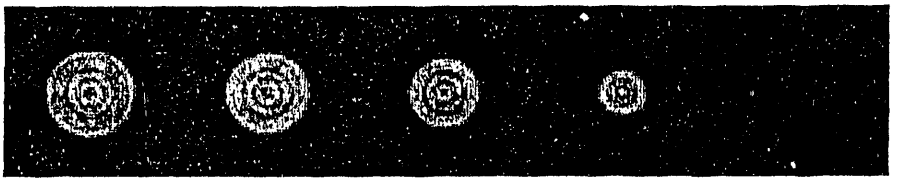

Fig. 8. Reconstructed images using Rizo simulation data sets with reconstructions starting from top of sphere

Nuclear Magnetic Resonance Spectroscopy of Ceramic Composites

Multi-nuclear (^{1}H, ^{13}C, and ^{29}Si) NMR spectroscopic studies are being designed to investigate (a) the composition of bulk ceramic materials; (b) the surface chemistry of these materials; (c) the chemistry of the ceramic interfacial regions; (d) and the chemistry of the whisker and fiber coatings. The ultimately goal of this work is to develop and demonstrate spectroscopic techniques capable of probing the nature of the micro-chemical environments of the ceramic surfaces and the bulk/fiber interfaces, and to correlate results obtained using these techniques with the microstructural and mechanical properties of the composite specimens.

NMR spectroscopy is currently quite capable of quantifying the chemical composition of bulk ceramic materials. For example, using ^{29}Si NMR "Magic-Angle" spinning (MAS), it has been demonstrated that NMR can quantify crystal type in Si_3N_4 (i.e. α, β, and amorphous materials) materials, as well as determine surface coatings such as silica concentration, and oxynitrides concentration. Note that NMR has a distinct and significant advantage over X-ray crystallographic methods in its ability to quantify the amorphous materials. When dealing with materials with mixed polytypes, such as SiC, NMR is capable of quantifying the individual polytypes. Additionally, ^{13}C NMR can be used to characterize and quantify carboniferous coatings on whisker and fibers. These analysis can all be performed as a function of specimen preparation (i.e. mixing conditions, sintering conditions, and atmospheric constituents).

In this pursuit, initial ^{29}Si NMR experiments were performed on a bulk Si_3N_4 sample. Preliminary experimental results obtained at a magnetic field strength of 7.1 T indicated extremely long spin-lattice (T_1) relaxation rates (approximately 2 h) for the these materials. T_1 decay rates essentially determine the ability to obtain signal in a given length of time. While the delays are lengthy, it is possible to perform the experiments at this magnetic field strength. Additionally NMR experiments attempted on this material at a magnetic field strength of 2.3 T. At this field strength the T_1 decay rates are shorter suggesting that the data should be more readily obtainable. However, a large ^{29}Si background signal from the NMR probe precluded the use of the 2.3 T NMR system at the present time. Initial ^{13}C

experiments were also performed on a SiC/Al_2O_3 (10/90 wt%) mixture to establish the experimental sensitivity at 2.3 T. While the T_1 delays are also lengthy, the results indicate that sufficient sensitivity for natural abundance ^{13}C exists to accurately characterize the SiC polytypes at this field strength and dilution. Spectroscopic studies of commercially available ceramic materials and on available chemically ceramics with modified surfaces will continue. Additionally, experiments aimed at the modification of the ceramic surfaces for spectroscopic sensitivity enhancement will be performed.

Ultrasonic NDE Techniques for Structural Ceramics

We have developed a new acousto-ultrasonic NDE method for the determination of fiber orientations in a composite laminate. The method uses two 0.5 MHz P-wave transducers mounted on the same surface of a composite laminate. One transducer serves as a transmitter and the other acts as a receiver. Figure 9 shows the experimental setup for the measurement. A measurement involves transmitting ultrasonic pulses perpendicularly into a laminate and monitoring the received signals at the receiver placed at a fixed distance away from the transmitter. The received signals were analyzed for their spectra and times-of-flight (TOF) which were used to correlate with fiber orientation and mechanical properties of the composite sample. Table 1 gives the dimensions of the specimens examined. Acousto-ultrasound is generated in the specimens when wavelengths are less than the plate thickness. One significant observation from the measurements is that the received signal in a composite laminate shows two groups of waves, attributing to propagations through different media, fibers and epoxy matrix. An example of such a real time signal is given in Fig. 10. We also found that the TOF of the received signal depends on the fiber orientation. Figures 11 and 12 show the inverse of TOF as a function of transducer orientation for two types of laminates. The orientations of fibers are clearly detected. The same technique will be applied to structural ceramics.

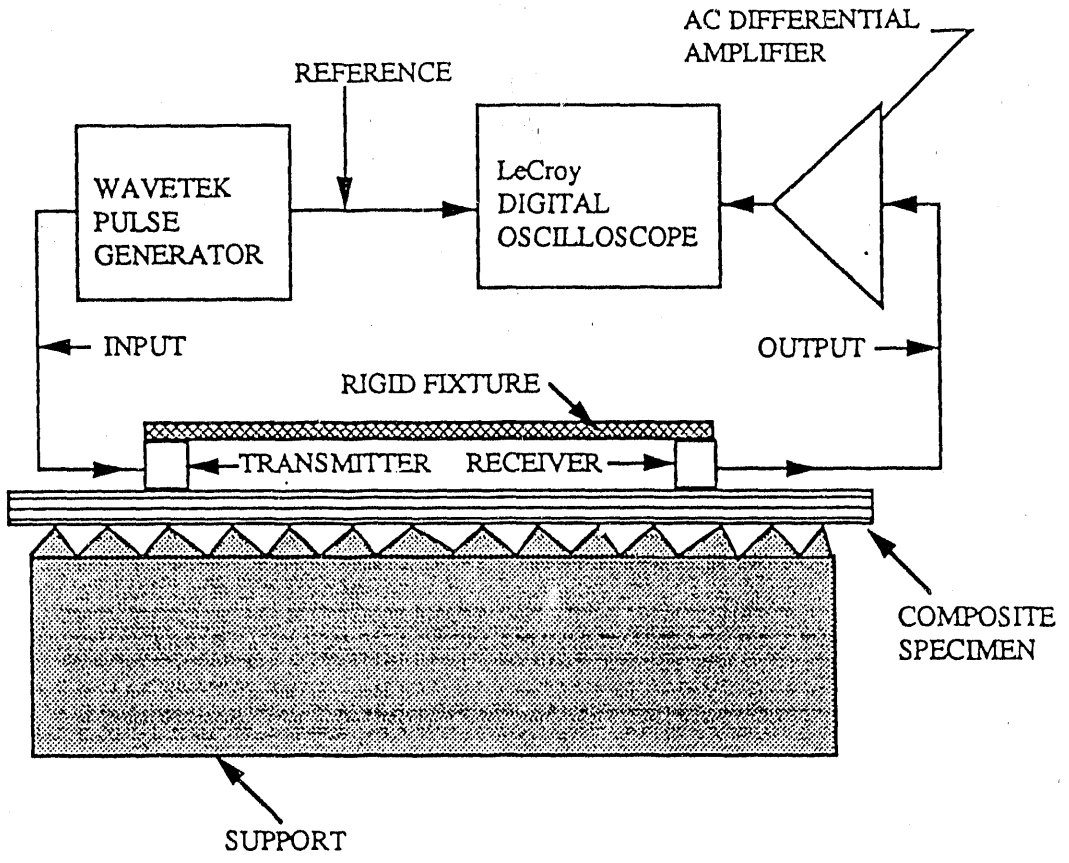

Fig. 9. Acousto-ultrasonic experimental setup

Table 1. Dimensions of the composite specimens examined

MATERIAL	LAMINATION (degree)	THICKNESS (in)	LENGTH (in)	WIDTH (in)
PLEXIGLASS	-	0.456	12.78	6.31
KEVLAR/EPOXY	0	0.113	2.00	2.00
GLASS/POLYESTER	0	0.092	17.91	9.53
GLASS/POLYESTER	[0/90]S	0.092	17.91	9.53

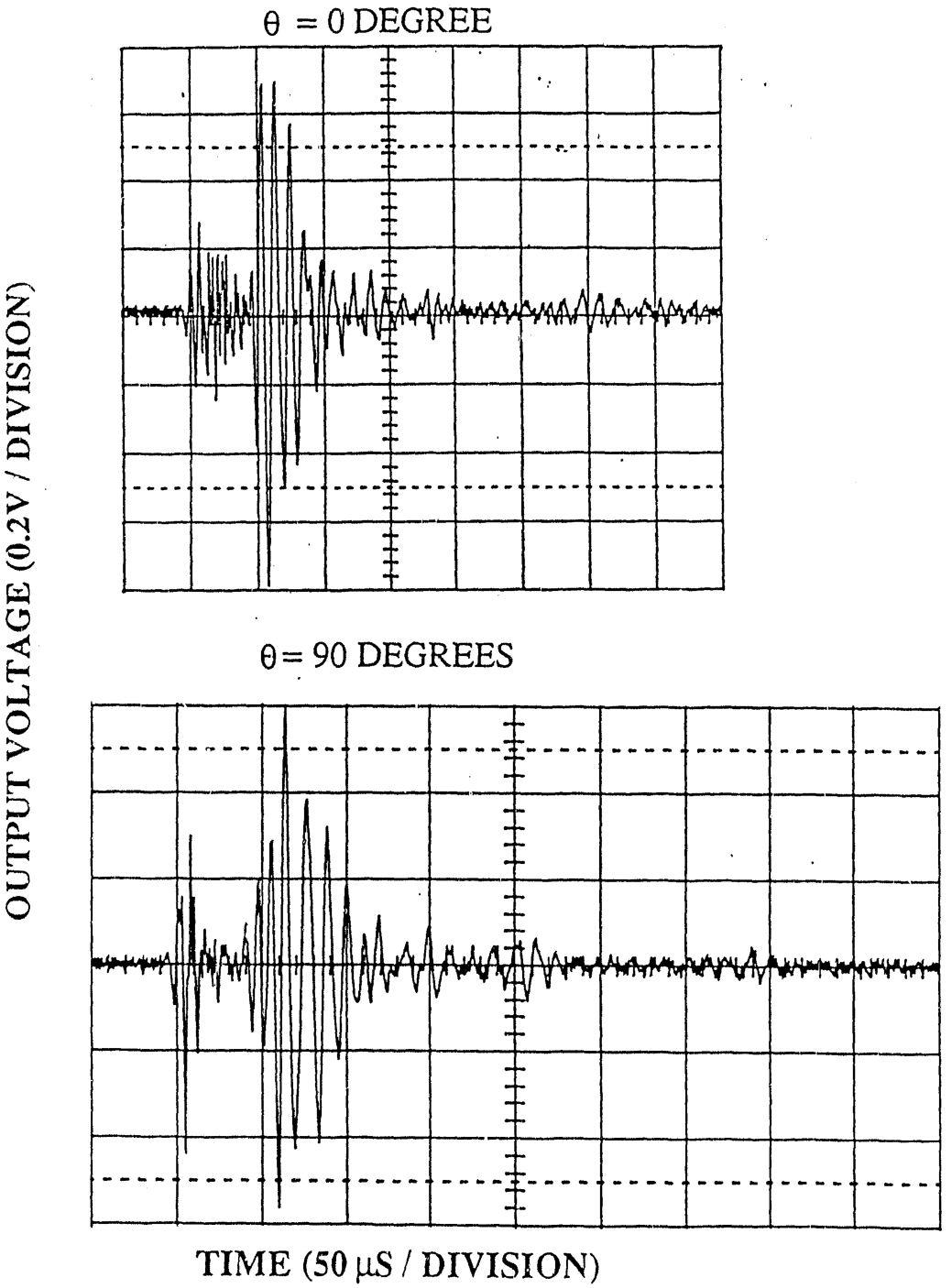

Fig. 10. Waveforms of the received ultrasonic signals. Specimen: E-glass/polyester symmetric cross-ply laminate, DTR = 6", propagation angle θ = 0 and 90 degrees

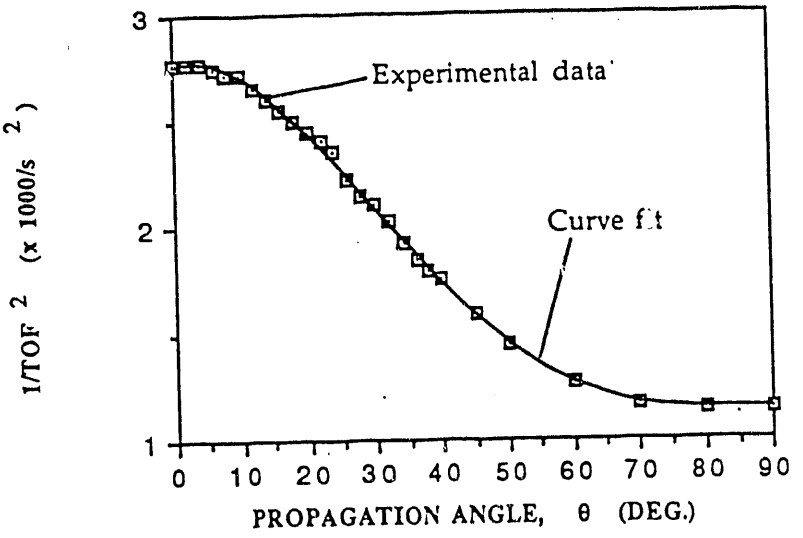

Fig. 11. [0] E-glass/polyester lamina, DTR = 3"

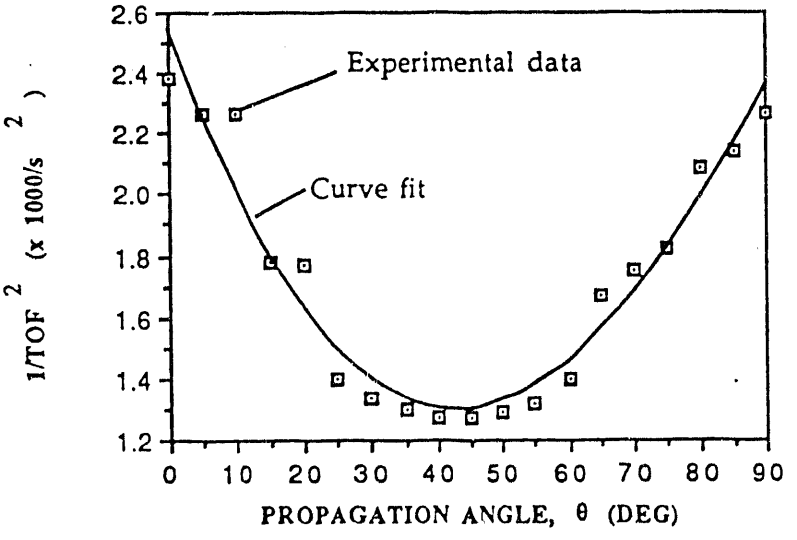

Fig. 12. [0/90] symmetric E-glass/polyester laminate, DTR = 3"

Effects of Flaws on Fracture Behavior

The purpose of this part of Task ANL–1 is to characterize the fracture behavior of structural ceramics and composites and to correlate fracture behavior with critical flaws. For whisker composites, Si_3N_4 and its composites are fabricated and microstructure and mechanical properties are evaluated. The critical flaws are located by fractography and their sizes are correlated with mechanical properties. The fractographic observations are compared with nondestructive evaluation (NDE) data for the location of potential critical flaws to provide useful information for developing NDE procedures. For continuous fiber composites, effect of processing on the flaw generation in continuous SiC fiber–reinforced SiC matrix composites are evaluated and correlated with mechanical properties.

During this reporting period, fracture–NDE work has continued on both whisker and continuous fiber reinforced ceramic matrix composites. Specifically, effort has concentrated in three areas: (1) specimen preparation (powder preparation, cold pressing, bisque–firing and hot isostatic pressing for whisker composites); (2) flexural strength and flaw size distribution measurement and fractographic evaluation of the fracture surface to locate critical flaws in both whisker and continuous fiber reinforced ceramic matrix composites; and (3) correlation of flaw size distribution in green and corresponding densified specimens for whisker reinforced composites.

The powders of monolithic Si_3N_4 (~0.3 μm) and its composites with 15 vol.% Si_3N_4 whiskers (0.6 μm in diameter and 45 μm in length) were prepared by a conventional ceramic powder processing route[5]. MgO was used as sintering aid and polyethylene glycol was used as binder. Rectangular bar specimens of Si_3N_4 and composites were uniaxially cold pressed at ~25000 psi in a steel die. Subsequently, these specimens were bisque–fired in a pure nitrogen atmosphere at 650°C for 2 hours to burn–out the binder. A set of 60 specimens each of 0 and 15 vol.% Si_3N_4 whisker-reinforced Si_3N_4 matrix composite were prepared in our laboratory. Subsequently, half of each set of specimens were hot isostatically pressed (HIPed) at Allied–Signal Aerospace Company, Garrett Processing Division, California.

Average density of green (cold pressed and bisque–fired) monolithic and composite specimens, measured using geometrical method, were 1.8 and 1.93 g/cc, respectively. Monolithic and composite bar specimens received after HIPing had a density of 3.075 and 3.102 g/cc, respectively, measured using Archimedes' method. Phase content of HIPed specimens were determined by X–ray diffraction using CuKa radiation. Monolithic specimens had close to 80% of β phase and rest α, whereas, in composite specimens it was 100% β. Modulus of elasticity, measured by ultrasonic technique, gave values of 322 GPa and 316 GPa for monolithic and composite specimens, respectively.

Flexural strength of green and HIPed specimens was measured using a four–point bend test set–up. HIPed specimens were carefully ground to a standard surface finish of 600 grit. Edges of the tensile face were chamfered to avoid any stress concentrations at the sharp corners. All tests were conducted at ambient conditions on a universal testing machine with a typical loading rate of 1.27 mm/min. Figures 13 a&b show the Weibull strength distribution plots obtained for green monolithic Si_3N_4 and its composite with 15 vol% whisker reinforcements. The average strength for green monolithic Si_3N_4 and its composites were 3.9 MPa and 4.1 MPa, respectively. The Weibull moduli were evaluated from the slopes of the strength versus probability of failure (F) plots on a logarithmic scale. The values for Weibull modulus were 6.5 and 6.9. Figures 14 a & b show similar Weibull plots for the HIPed monolithic and composite specimens. The average strengths of the HIPed monolithic and composite specimens were 838 MPa and 540 MPa and the Weibull moduli were 5.1 and 4.9, respectively.

In four–point–bend flexural testing, tensile face is subjected to the largest stresses, therefore, it is expected that failure causing critical flaw will be a surface and/or subsurface flaw located near the tensile face. This was confirmed by observation of the locations of critical flaws on the fracture surfaces using scanning electron microscopy (SEM). Figure 15 shows a SEM micrograph of monolithic specimen showing the location of the critical flaw at or near the tensile surface. The strength data indicate little or no difference in the Weibull modulus for green and the corresponding HIPed specimens. This suggests that the subsurface/surface flaw

population controlling the strength distribution of green Si_3N_4 and composite specimens does not change during densification (HIPing) process.

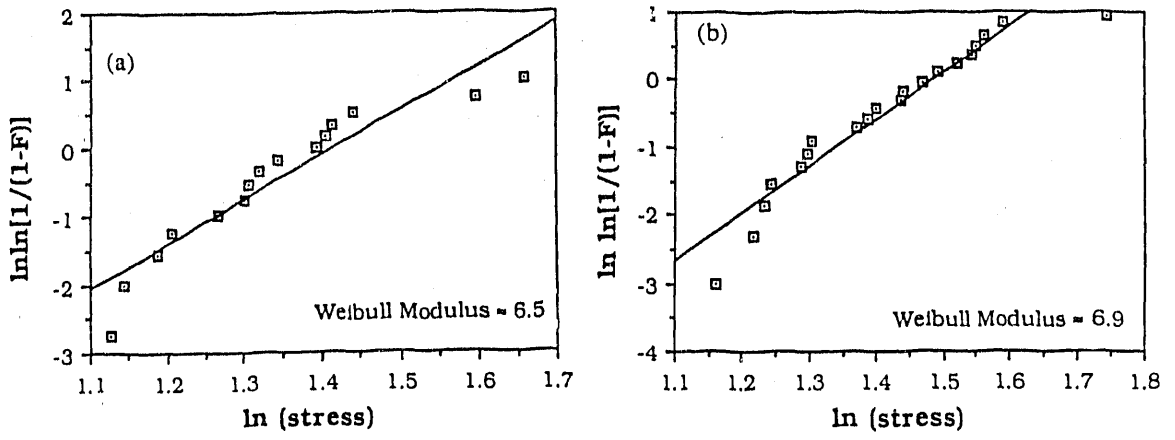

Fig. 13. Weibull Plots of Green Specimens: (a) Monolithic (b) Composite (15 vol% whisker)

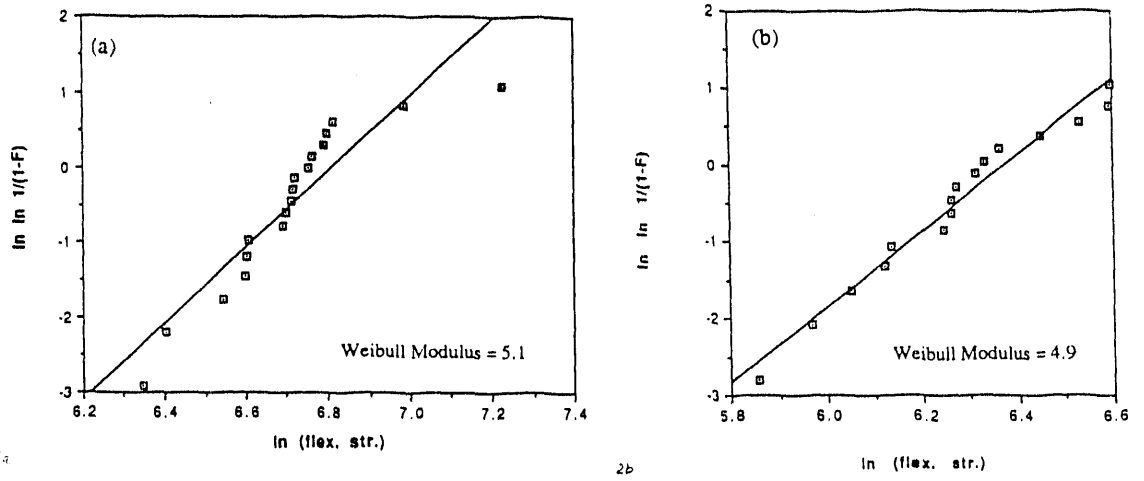

Fig. 14. Weibull Plots of HIPed Specimens: (a) Monolithic (b) Composite (15 vol% whisker)

REFERENCES

1. Reimers, P., Kettschau, A., and Goebbels, J., "Region-of-Interest (ROI) Mode in Industrial Computed Tomography," in NDT International Vol. 23, No. 5, Oct. 1990 pp. 255-261.

2. Faridani, A., Keinert, F., Natterer, F., Ritman, E.L., "Local and Global Tomography," in Mathematical Foundation of Computed Tomography, Applied Optics, 1985, pp. 241-255.

3. Rizo, P. private communication.

4. Sivers, E. A., private communication.

5. C.Y. Chu and J.P. Singh, "Mechanical Properties and Microstructure of Si3N4–Whisker–Reinforced Matrix Composites," Proceedings of 14th Annual Conference on Composites and Advanced Ceramics, Cocoa Beach, FL, Jan. 14–17 (1990).

GT-1(A)-MODELING OF FIBROUS PREFORMS FOR CVD INFILTRATION

T. L. Starr and A. W. Smith

Materials Science and Technology Laboratory
Georgia Tech Research Institute
Atlanta, Georgia 30332

INTRODUCTION

Chemical vapor infiltration (CVI) has demonstrated considerable promise as a technique for fabrication of fiber reinforced ceramic composites. An analytical model provides insight into the CVI process, helps identify key processing parameters and guides experimental process optimization efforts. A three-dimensional model, GTCVI, has been developed to simulate the densification process with a cloth lay-up preform. This model can be used to support scale-up of the CVI process for larger, more complex structural components.

DISCUSSION OF CURRENT ACTIVITIES

Efforts this period include modification of the deposition kinetics portion of the model to match recent CVD experiments at ORNL and comparison of model density profiles to experimental results from a series of interrupted CVI runs.

Deposition Kinetics

A key part of any CVI simulation model is the deposition kinetics expression. Past modeling efforts have invariably used a simple first-order rate law[1,2,3]. Although this expression is the easiest to incorporate into a process model, the primary motivation for this assumption has been the absence of experimental rate studies, under conditions similar to those used in CVI processing, that indicate a more complex rate law. Indeed, the one rate study that most directly matched

CVI process conditions produced an apparent first-order rate law[4]. Since this work involved only one reactor geometry and one gas flow rate, extension to other deposition systems must be made with care.

More recently, experiments at ORNL over a range of flow rates and gas compositions indicate a more complex deposition rate relationship that includes a strong inhibition effect due to the accumulation of HCl, a by-product of the reaction[5]. This yields the rate expression,

$$R_l = \frac{k_r P_r}{1 + K_p P_p}$$

where R_l is the linear deposition rate, P_r and P_p are partial pressures of reactant (MTS) and product (HCl), k_r and K_p are rate constants given by Arrhenius expressions,

$$k_r = A_r \exp(-E_r/RT)$$
$$K_p = A_p \exp(-E_p/RT)$$

where A_r, A_p, E_r and E_p are constants determined from CVD experiments, R is the gas constant and T is the absolute temperature. For conditions where $K_p P_p \ll 1$, i.e. little depletion of the reactant gas, the rate law is still nearly first-order in the reactant partial pressure. However, for $K_p P_p \gg 1$, i.e. significant depletion, the rate is proportional to the ratio of the reactant and product partial pressures.

For low values of depletion, i.e. little HCl produced, the ORNL rate is substantially higher than the Brennfleck[4] rate. However, as the percent depletion increases, the rate can be lower or higher depending on the percent depletion and the temperature.

In order to incorporate this rate expression in the CVI model it is necessary to calculate the concentration of HCl at each volume element in the preform. Adding this additional concentration parameter to the model involves only a few additional lines of computer code. The inflow boundary concentration of HCl is set to zero and the production rate of HCl at any volume element is based on the assumption that three moles of HCl are produced for each mole of SiC deposited. As before, steady-state solutions are obtained sequentially and iteratively for each process parameter -- temperature, pressure and the two concentrations.

Intermediate Density Profiles

The most demanding test of a CVI model is comparison of the predicted and experimental densities at specific points in the preform at a series of times prior to full densification. The only set of experimental data suitable for this comparison involves four CVI runs at ORNL[6]. One run was continued until full densification. The other three runs, using identical temperatures and gas flow rates, were interrupted at intermediate times. Density profiles for each resulting composite were determined by slicing the disks into regular pieces and then weighing and measuring these.

Using the 2-D version of GTCVI with cylindrical coordinates we model this series of runs using a 6x15 analytical grid as shown in Figure 1. Boundary conditions for temperature, flow rate and reagent concentration are set to match experimental conditions used. Model results for back-pressure (Figure 2) are in good agreement with experiment although the model value rises a little more rapidly than experiment at the very end of the run. More importantly, local densities at intermediate times (Figures 3-6) also show good agreement with corresponding experimental results.

This good agreement with experiment is based on a particular microstructure model, as described previously[7], with adjustments to the model parameters so as to match experimental densification and back-pressure measurements. While these parameter values are not arbitrary their correspondence to physical microstructure features still must be demonstrated. This is an important step toward applying this model to CVI of larger, more complex shapes and different fiber architectures.

REFERENCES

1. J.Y. Rossignol, F. Langlais and R. Naslain, "A Tentative Modelization of Titanium Carbide CVI Within the Pore Network of Two-dimensional Carbon-Carbon Composite Preforms," in Proc. Ninth Int. Conf. on Chemical Vapor Deposition, Electrochemical Society, Pennington, NJ (1984).

2. S.M. Gupte and J.A. Tsamopoulos, "Forced-Flow Chemical Vapor Infiltration of Porous Ceramic Materials," J. Electrochem. Soc. 137 (11) 3675-82 (1990).

3. S.V. Sotirchos and M.M. Tomadakis, "Modelling Transport, Reaction, and Pore Structure Evolution During Densification of Cellular or Fibrous Structures," in Proc. Eleventh Int. Conf. on Chemical Vapor Deposition, Electrochemical Society, Pennington, NJ (1990).

4. K. Brennfleck, E. Fitzer, B. Schoch and M. Dietrich, "CVD of SiC Interlayers and Their Interaction with Carbon Fibers and with Multi-layered NbN Coatings," in Proc. Ninth Int. Conf. on Chemical Vapor Deposition, Electrochemical Society, Pennington, NJ, pp. 649-662 (1984).

5. B.W. Sheldon and T.M. Bessman, Oak Ridge National Laboratory, private communication, July 1991.

6. Y.G. Roman and T.M. Bessman, Oak Ridge National Laboratory, private communication, September 1990.

7. T. L. Starr, in AR&TD Fossil Energy, Energy Materials Program Semi-annual Progress Report for the period ending September 30, 1990, Oak Ridge National Laboratory report ORNL/FMP-90/2.

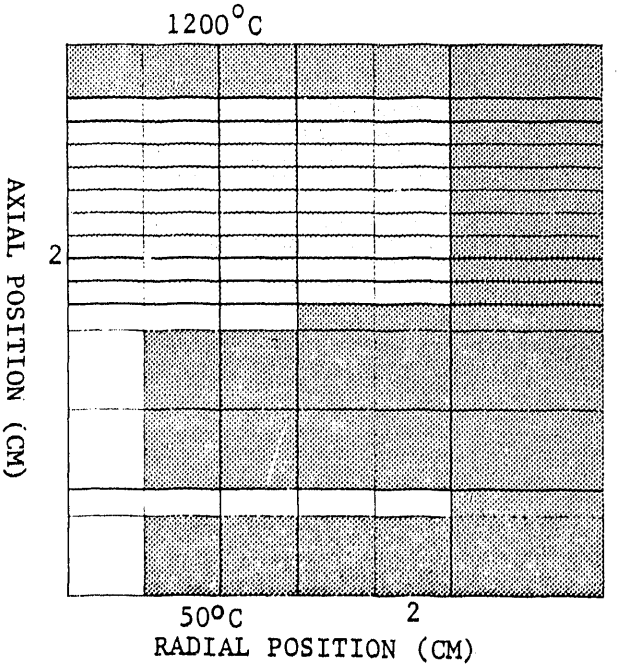

Figure 1. Analytical model of ORNL 2" CVI reactor uses 6x15 element grid. Boundary conditions are set to match experimental process parameters.

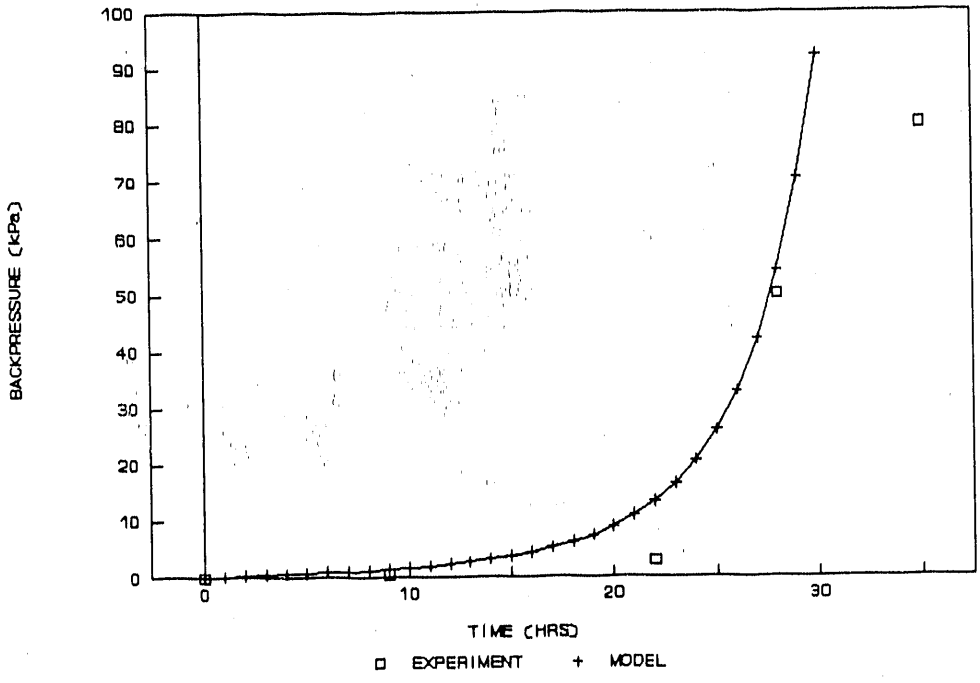

Figure 2. Model prediction for backpressure shows good match to experimental measurements except that model pressure rises too sharply near the end of the run.

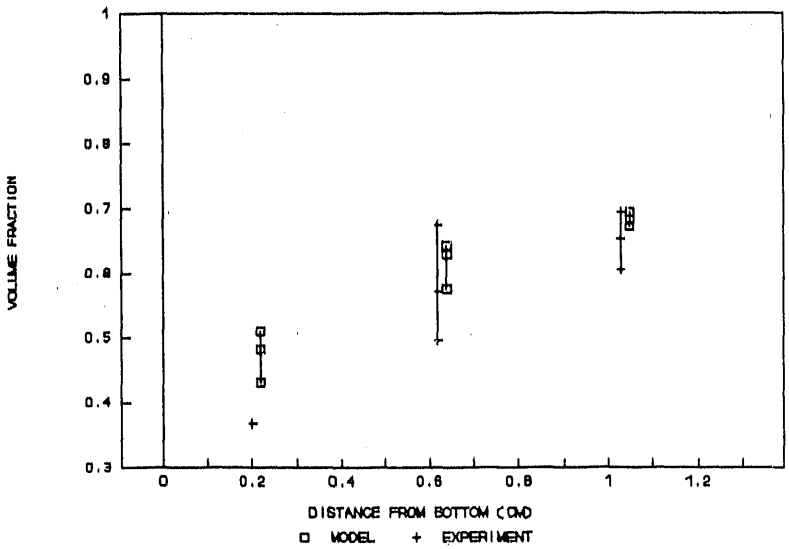

Figure 3. Model predicted density matches experiment at bottom, middle and top of preform after nine hours of processing. Range of values plotted corresponds to variation in density from the center to the edge of the disk.

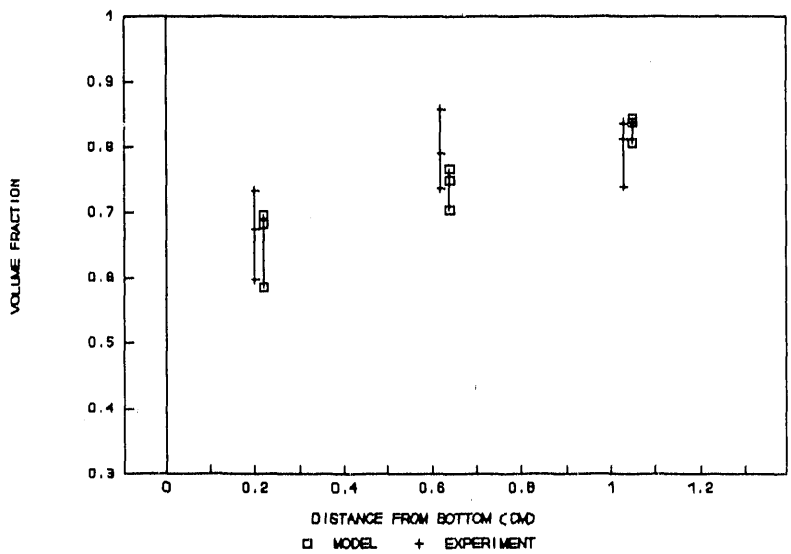

Figure 4. Model predicted density matches experiment at bottom, middle and top of preform after 22 hours of processing.

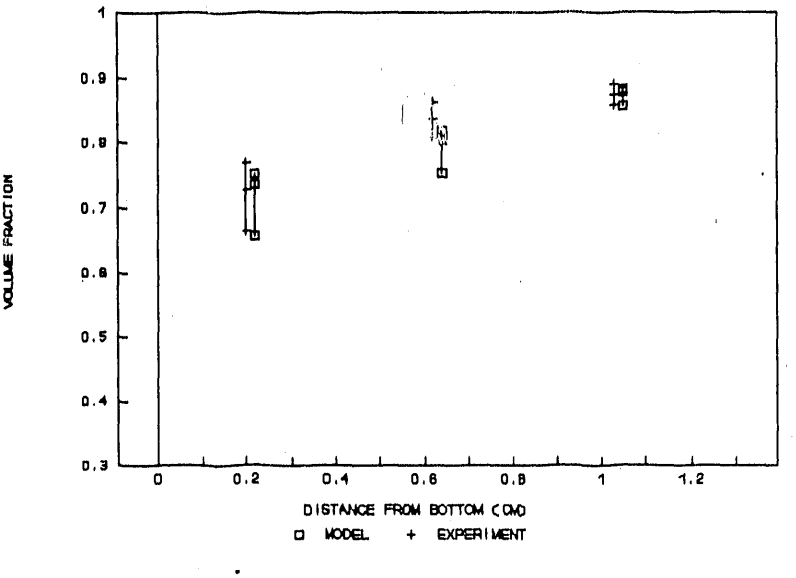

Figure 5. Model predicted density matches experiment at bottom, middle and top of preform after 28 hours of processing.

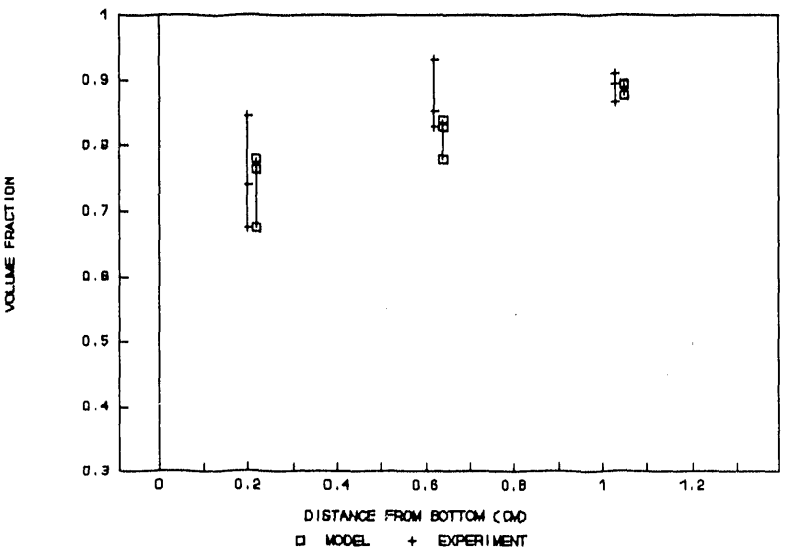

Figure 6. Model predicted density matches experiment at bottom, middle and top of preform at end of processing (31 hours for model, 35 hours for experiment).

GT-1— DEVELOPMENT OF ADVANCED FIBER REINFORCED CERAMICS

T. L. Starr and D. L. Mohr

Materials Science and Technology Laboratory
Georgia Tech Research Institute
Atlanta, Georgia 30332

INTRODUCTION

Ceramic composites continue to offer great promise for increasing the efficiency of fossil fuel utilization. Fabricability is an important factor in such applications, particularly for the relatively large and complex shapes used for fossil energy conversion systems. The objective of this program is to develop a near-net-shape fabrication method for silicon nitride ceramic composites using lay-up techniques and reaction sintering. Two factors limit the mechanical performance of such composites, the density and distribution of matrix material, and the bonding between fiber and matrix. Fabrication techniques are needed that will produce a uniform matrix microstructure and provide better distribution of load to the reinforcing fibers. In addition, a fiber coating is needed that is stable in the reaction sintering environment and provides good debonding between the fiber and matrix during crack propagation.

DISCUSSION OF CURRENT ACTIVITIES

Our work over this period has included development of tape fabrication methods and application of duplex coatings to Nicalon fiber.

Tape Fabrication Methods

Since previous attempts to impregnate woven cloths with silicon have resulted in poor penetration of powder between filaments, we have redirected our efforts toward a fabrication process consisting of

impregnation and winding of fiber tow to form a unidirectional tape, and subsequently cutting and stacking this tape to form the "green" composite. Our apparatus for performing the first step of this process includes a trough of silicon powder dispersion with rollers to guide and spread the fiber, and a commercial filament winding machine (Figure 1). The trough portion of this apparatus (Figure 2) contains a dispersion of attritor-milled silicon powder in an organic liquid with a small amount of binder. Convex-shaped rollers below the liquid surface spread the tow while it is immersed, encouraging good penetration between filaments. The impregnated tow is then wound onto a hexagonal mandrel. After drying flat, rectangular sheets are cut and stacked to form the composite.

A critical requirement for successful implementation of this fabrication method is obtaining the proper amount and distribution of silicon powder during the winding operation. The "correct" amount of powder uptake can be estimated from considering the desired final composite. For a composite consisting of 50% by volume of Nicalon fiber and a matrix of reaction sintered silicon nitride with 15% residual porosity, the fiber should show a weight gain of 65%. A weight gain greater than this would lead to low volume fraction fiber in the final composite. A smaller weight gain, however, can be adjusted by adding powder during the lay-up process. Parameters that influence the amount and distribution of powder include composition of the dispersion, tension on the tow during immersion and winding, and winding speed.

Our initial winding experiment used one composition of dispersion (30 wt% solids in ethanol) and several winding speeds. Results indicate that winding speed does not have much impact on weight gain, which varied between 32-35% over the available speeds. Microscopic examination of the dried, impregnated tow show good penetration between filaments (Figure 3). Future experiments will utilize a higher concentration of solid in the dispersion to get a higher weight gain.

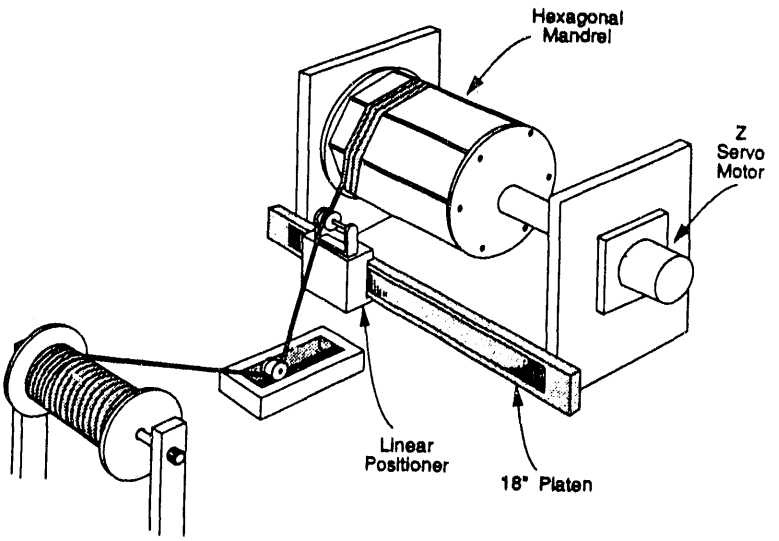

Figure 1. Schematic shows fiber impregantion/tape winding apparatus. Layers cut from flat sides of hexagonal mandrel are stacked to form composite.

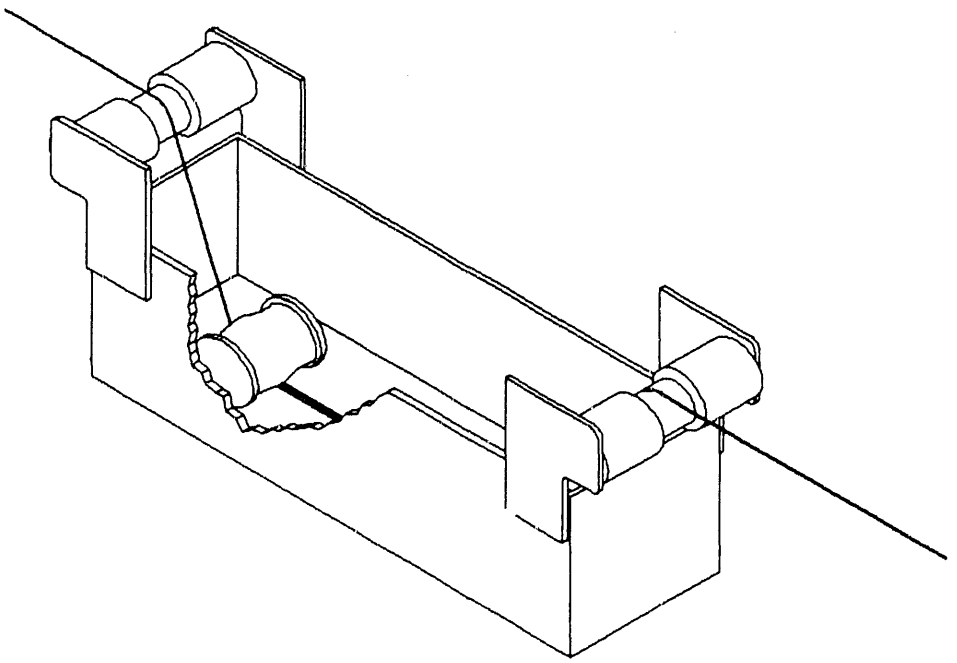

Figure 2. Rollers guide fiber through trough containing dispersion of silicon powder. Convex rollers in bottom spread tow while immersed to encourage good penetration between filaments.

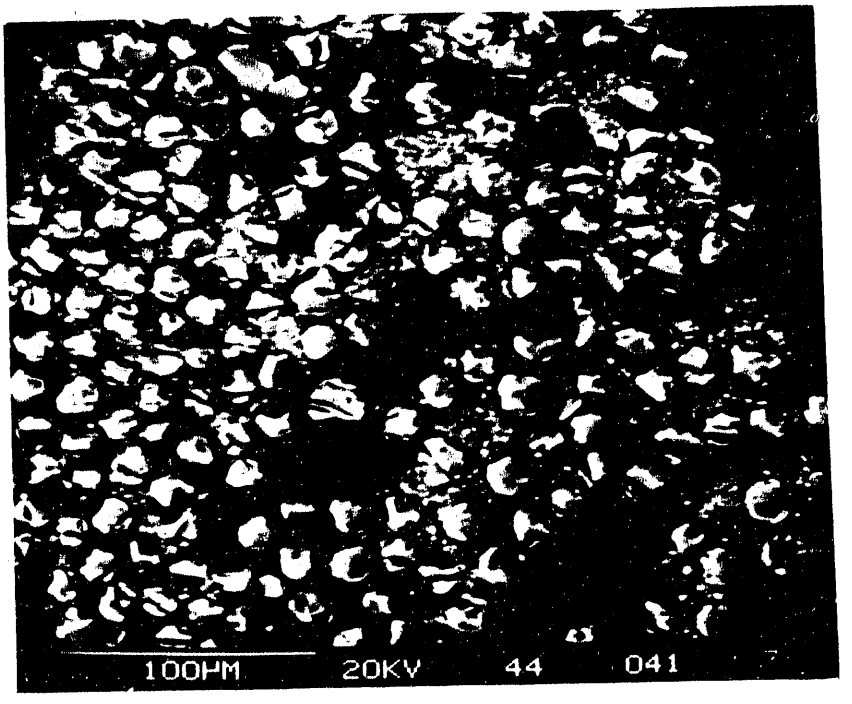

Figure 3. Micrograph of silicon powder impreganted tow shows good infiltration between filaments.

Fiber Coating

A fiber coating may play several roles in application to ceramic composites. These include protecting the fiber during composite fabrication and use, and providing a suitably weak interface between the fiber and matrix. While carbon coating has proven successful for protecting Nicalon fiber during CVI processing[1] it has not been effective under our nitriding conditions[2]. Further, while carbon does provide suitable interface control for the composite, the coating is susceptible to oxidation under many application environments.

In order to overcome these problems we plan to apply a duplex coating to Nicalon fiber prior to composite fabrication. This coating will consist of a layer of pyrocarbon followed by a layer of silicon carbide. The carbon layer will provide interface control while the silicon carbide will enhance fiber protection under processing and use environments.

Our initial experiments have utilized batch coating in a CVD furnace. Carbon was deposited from propylene while silicon carbide deposition used methyltrichlorosilane (MTS). A series of runs are in progress to define proper deposition conditions and times for each coating, with a goal of 0.1-0.3 microns thickness for each layer. Once these processing conditions are determined, several hundred feet of fiber will be coated using our continuous fiber coater.

REFERENCES

1. R. A. Lowden and D. P. Stinton, "The Influence of the Fiber-Matrix Bond on the Mechanical Behavior of Nicalon/SiC Composites," ORNL/TM-10667, Oak Ridge National Laboratory, Oak Ridge, TN (December 1987).

2. G.B Freeman, T.L. Starr, J.N. Harris, R.E. Kirchain and D.L. Mohr, "Characterization of the Fiber-Matrix Interfaces in SiC-Si_3N_4 Ceramic Composite System", Proc. of the First International Conference on Heat-Resistant Materials, ASM International, Materials Park, Ohio (1991)

INEL-1(A) - NONDESTRUCTIVE EVALUATION OF ADVANCED CERAMIC COMPOSITE MATERIALS

L. A. Lott, and D. C. Kunerth

Idaho National Engineering Laboratory
EG&G Idaho, Inc.
P. O. Box 1625
Idaho Falls, ID 83415-2209

INTRODUCTION

Advanced ceramic composites are currently of great interest for high-temperature structural applications, because they exhibit significantly higher fracture toughness than do monolithic ceramics. The fiber-matrix interface bond has a significant role in determining the fracture toughness of the material. Phenomena such as interface debonding, fiber slip, or pull-out, will improve material toughness by increasing the energy required to propagate a crack.[1] However, a bond that is too strong permits a crack to propagate directly through a fiber-matrix interface without being significantly impeded, resulting in brittle fracture. In a bond that is too weak, the toughening mechanisms are not significant. As a result, special processes are required in the manufacture of these materials to achieve optimum fiber-matrix bonding.[2] Effective NDE techniques capable of characterizing the fiber-matrix interface are needed to maintain control of the manufacturing process and to ensure the quality of fabricated components. This is the last report of this study and summarizes the investigation of acousto-ultrasonics (AU) to characterize the fiber-matrix interface of a SiC continuous fiber reinforced, SiC matrix composite.

DISCUSSION OF CURRENT ACTIVITIES

Material Samples

Composite specimens were supplied by Oak Ridge National Laboratory (ORNL) for this investigation. The material consisted of a SiC matrix with a continuous fiber reinforcement of 2-d weave Nicalon (Nippon Carbon Co., Tokyo, Japan) cloth layered in a 30-60-90 pattern. A chemical vapor infiltration (CVI) process was employed to form the matrix. The specimens were in the form of right circular cylinders 45 mm in diameter and 11.5 mm high, with 40 vol% fiber and 85% of theoretical density.

Specimens with strong, intermediate, and weak interface bond strengths were fabricated. A weak interface bond was produced by coating the Nicalon fibers with a 0.5 μm layer of carbon prior to infiltration. Following infiltration, the specimen was heat treated (850°C) for two hours in flowing oxygen to oxidize the carbon interlayer. This resulted in essentially no bonding or friction at the interface. An intermediate bond strength was produced by also coating the fibers with a 0.05 μm carbon layer, but no heat treatment was performed. A strong interface bond resulted, when neither a fiber precoat nor subsequent heat treatment was used. A silica layer that forms on the surface of the uncoated Nicalon fibers during initial heating during the CVI process bonds strongly to both the fiber and the deposited matrix. The relationship between fabrication parameters and interfacial frictional stress has been confirmed for such specimens.[3]

Acousto-Ultrasonic Response

Experimental System

The acousto-ultrasonic (AU) technique was developed by Vary and coworkers[4] to characterize the mechanical properties of materials. The name of the technique stems from the fact that it is basically a hybrid between ultrasonics and acoustic emission. Two piezoelectric transducers are placed on the same side of a material sample as shown

in Figure 1. An excitation pulse to one transducer generates acoustic waves in the sample that are received by the other transducer, amplified, and recorded in a manner similar to conventional transmit-receive ultrasonics. The difference is that, instead of detecting a well-defined acoustic pulse traveling between the transducers, as is the case with conventional ultrasonics, a complicated superposition of wave modes and sample reverberations that resembles an acoustic emission signal is generated and detected.

The AU measurement system used for this work employed Valpey-Fisher "pinducers," which are high-sensitivity, small-diameter (2.4 mm) piezoelectric transducers. These transducers were chosen primarily for their small size, which makes them ideal for point measurements. They were also chosen because they minimize perturbations to the vibration modes of the sample.

Data Analysis Methods

Method of Moments. In this method[5], the time signal from the receiving transducer is first transformed to the frequency domain using the Fast-Fourier Transform (FFT). Various moments of the frequency spectrum are then taken about the amplitude axis. For discrete data, the nth moment can be expressed as

$$M_n = \sum_i W_i f_i^n \Delta f,$$

where W_i is the power spectral density at frequency f_i, and Δf is the frequency increment. $A1 = M_0$ is the area under the power spectral density curve and thus is directly proportional to the energy of the signal. It is a measure of the ability of the sample to transmit acoustic energy. $A2 = M_1/M_0$ represents the centroid of the power spectral density curve, or the center frequency of the signal relative to its energy content. Comparison of A2 between samples reveals differences in absorption of acoustic energy as a function of frequency.

Diffuse Field Decay Analysis. A measure of the internal absorption can also be obtained by the diffuse field decay rate

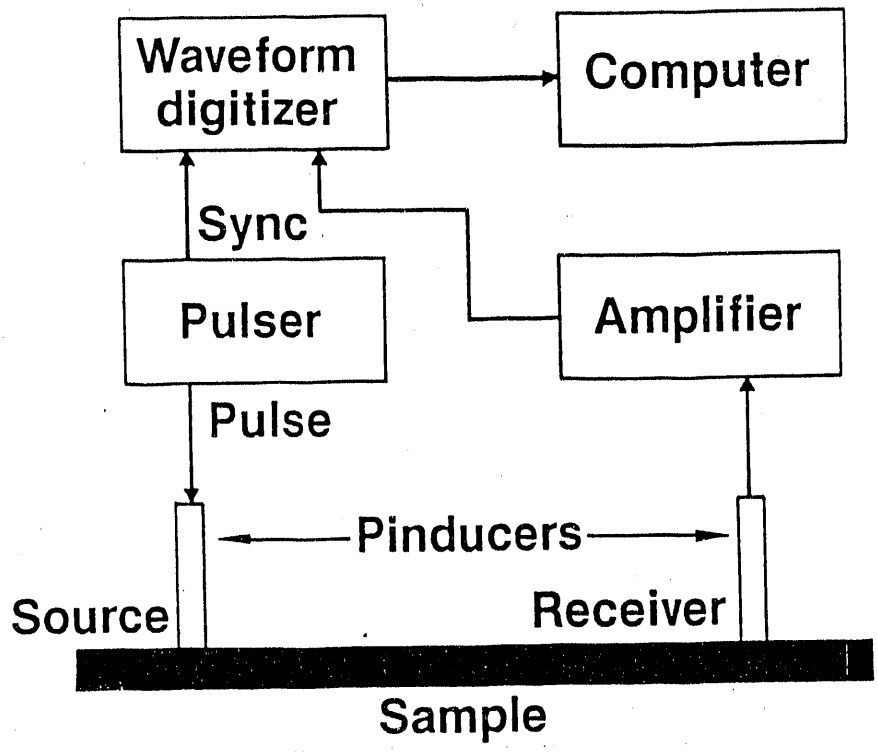

Fig. 1 - Diagram of experimental setup for acousto-ultrasonic measurements.

method.[6] This analysis is based upon the premise that a diffuse ultrasonic field in an isolated sample will decay due only to absorption mechanisms, when the contributions of damping by air, transducers, and fixturing are minimal. The damping is measured through determination of the volume-averaged decay rate of the ultrasonic field as a function of frequency and time. A greater decay rate indicates a greater amount of internal damping or energy absorption through internal friction. Determination of the decay rate is accomplished by dividing the recorded waveform into a number of time windows for which Fourier transforms are performed. The resulting spectra are then broken into frequency bins and the mean square spectral amplitude is calculated for each bin. This provides a measure of the signal decay rate for individual frequency bins as a function of time.

Experimental Data

Acousto-ultrasonic measurements were made on one weak, three intermediate, and one strong interface bond specimens. Following excitation of the pulsing transducer, a 320 μs length of the received signal was digitized at a rate of 12.5 MHz and stored. This produced time records of 4,000 points each. The time signals were transformed to the frequency domain with a 4,096 point FFT. Because there can be significant scatter in AU data taken at different points on a single specimen, measurements were taken at 10 positions on each specimen and the data were processed for each position.

Figure 2 shows typical recorded time signals for the strong bond sample and the weak bond sample. There is an obvious qualitative difference between the two signals. The total energy contained in the signal response from the well-bonded sample is more than 100 times

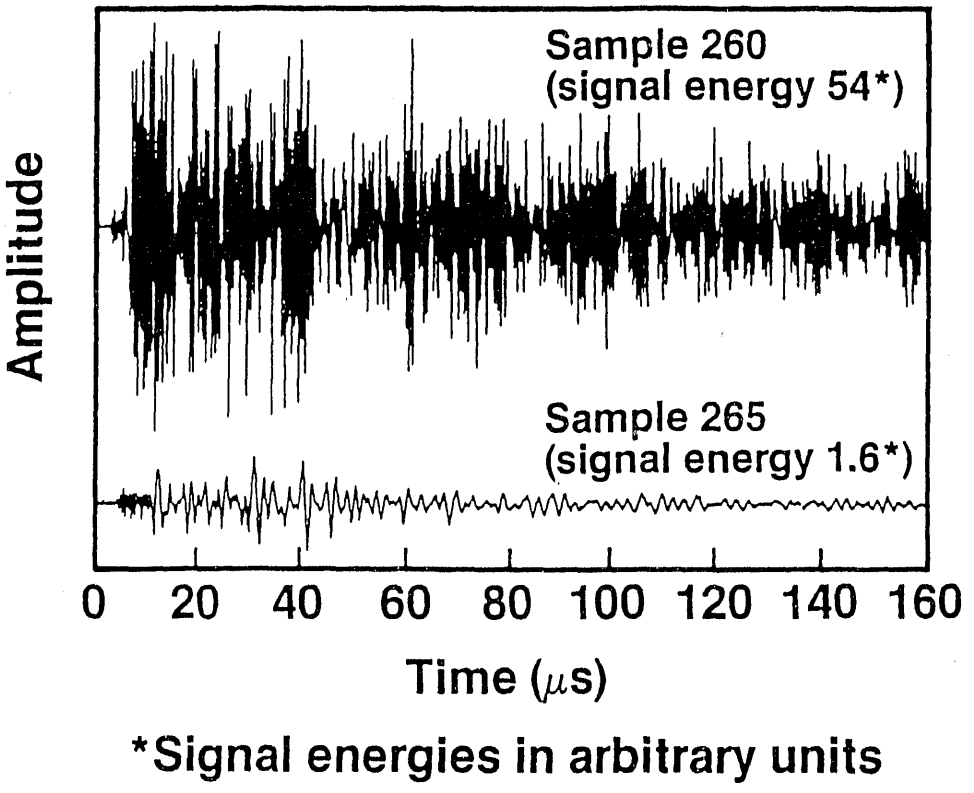

Fig. 2 - Typical AU signals for samples having strong (Sample 260) and weak (Sample 265) interface bonds.

greater than that of the poorly-bonded sample. Based on measurements made on other samples of this material, acoustic property differences of this magnitude would be expected only for material samples having significantly different porosity content. However, since the densities of these samples are approximately the same, the different AU responses are attributed to the differences in fiber-matrix bonding.

Significant differences are also seen in the frequency spectra shown in Figure 3. The spectrum for the weak bond sample shows a marked decrease in high frequency content, indicating a greater absorption of acoustic energy than the strongly bonded sample. This should correspond to a lower value of A2 and a higher diffuse field decay rate for the weak bond sample.

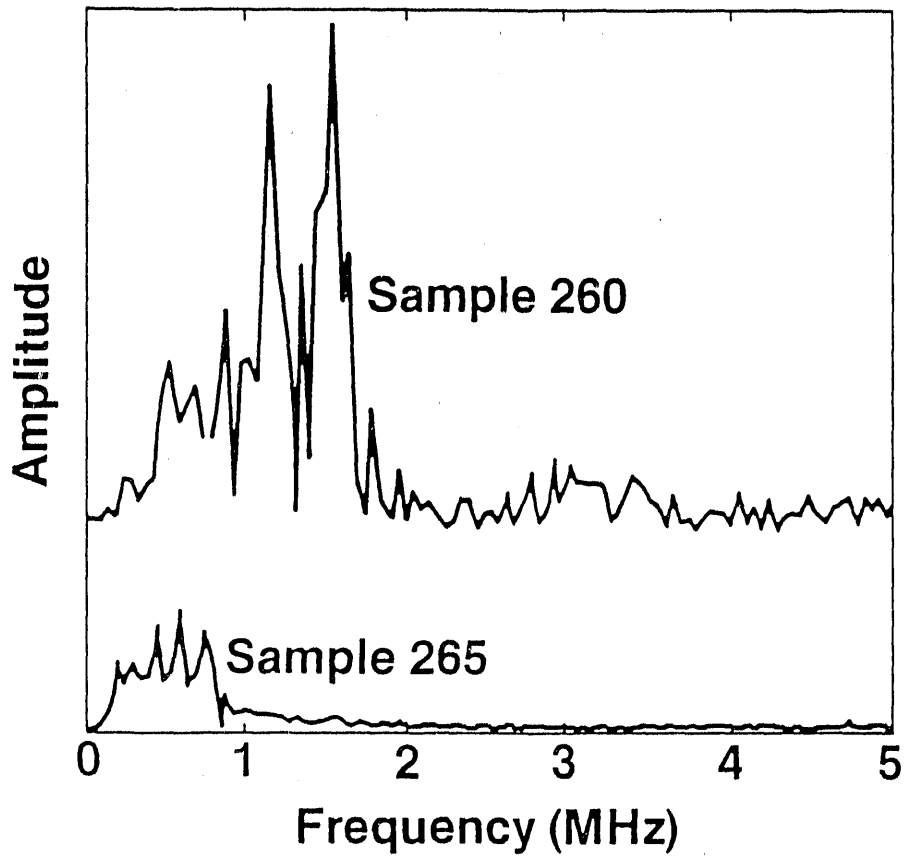

Fig. 3 - Frequency spectra of signals of Fig. 2.

Diffuse Field Decay Rate Analysis

Diffuse field decay rate analyses were performed on the AU signals for the interface bond specimens. To process the data, 16 μs time windows and 0.5 MHz frequency bins were used. To avoid initial field transients, the first 48 μs of the recorded AU waveforms were not used. The results are shown in Figure 4, in which the averaged time decay rates of each specimen are plotted against frequency. A clear discrimination is observed between different bond strengths; at any given frequency, except at the very low frequency range, the composite specimens exhibit increasing absorption of vibrational energy with decreasing bond strength. The decay rates also increase directly with increasing frequency.

To illustrate the relationship between the AU results and the material properties, the interfacial shear stress and flexure strength measured by ORNL[3] for specimens fabricated under identical conditions as the specimens used in this study are plotted in Figure 5 vs. the AU

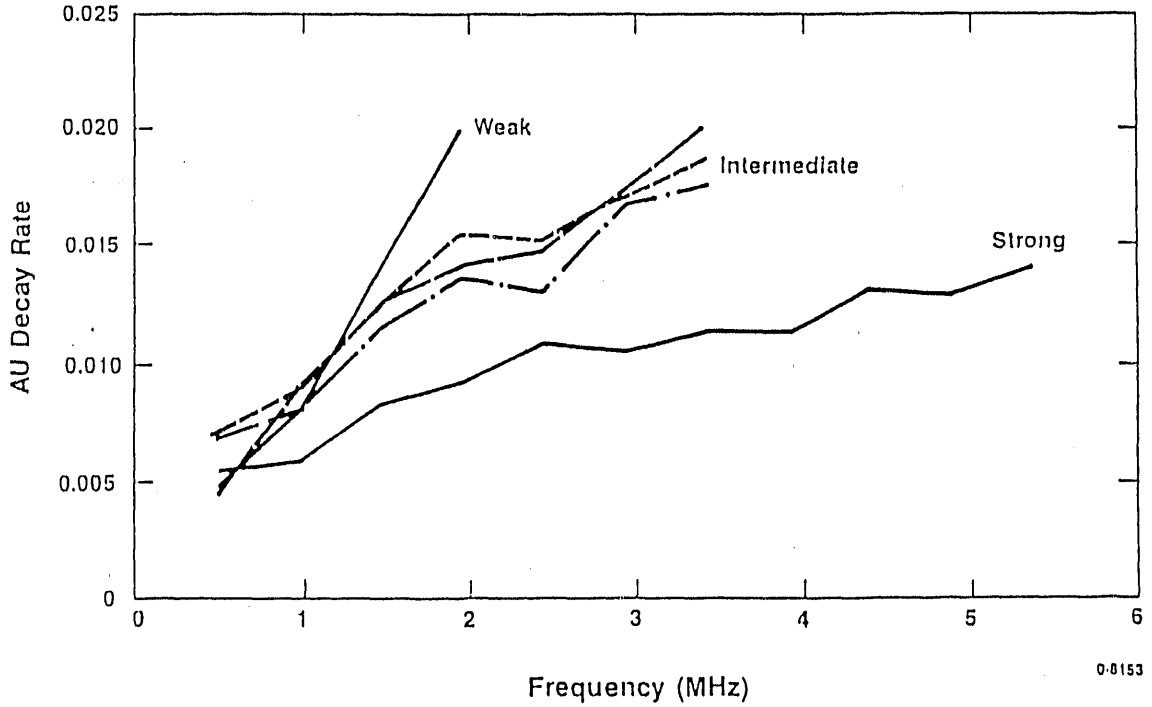

Fig. 4 - Diffuse field decay rate analysis of AU data for interface bond specimens. Decay rate vs. frequency.

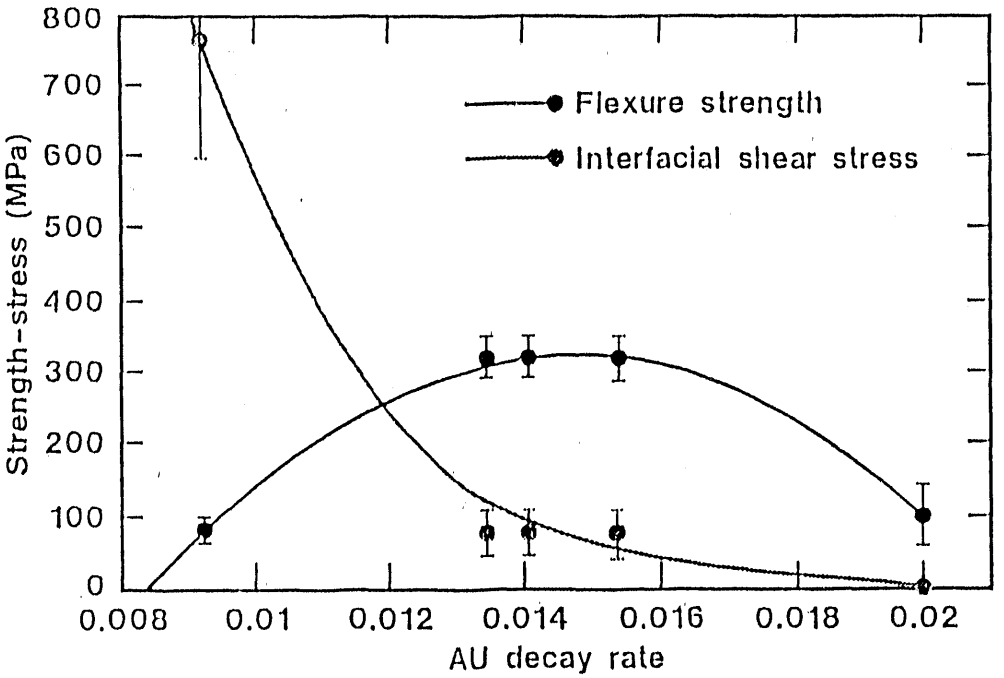

Fig. 5 - Diffuse field decay rate analysis of AU data for interface bond specimens. Flexure strength and interfacial strength vs. 2 MHz decay rate.

decay rates at 2 MHz frequency. The error bars for interfacial shear stress and flexure strength are those reported by ORNL. The lines connecting the data points represent least squares fits of the data to second order polynomials and have no other physical significance. The interfacial shear strength measurement technique used by ORNL involves a microhardness indentor to apply a force to the end of a fiber imbedded in the matrix. Interfacial shear stresses are determined from the applied load and the observed displacement of the fiber relative to the matrix. Although the interfacial shear stress was not measured on the actual samples for which the AU measurements were made, the figure does show the general relationships involved.

Analysis by Method of Moments

The AU data were also analyzed by the method of moments. The results are summarized in Figures 6 and 7. The ORNL interfacial shear

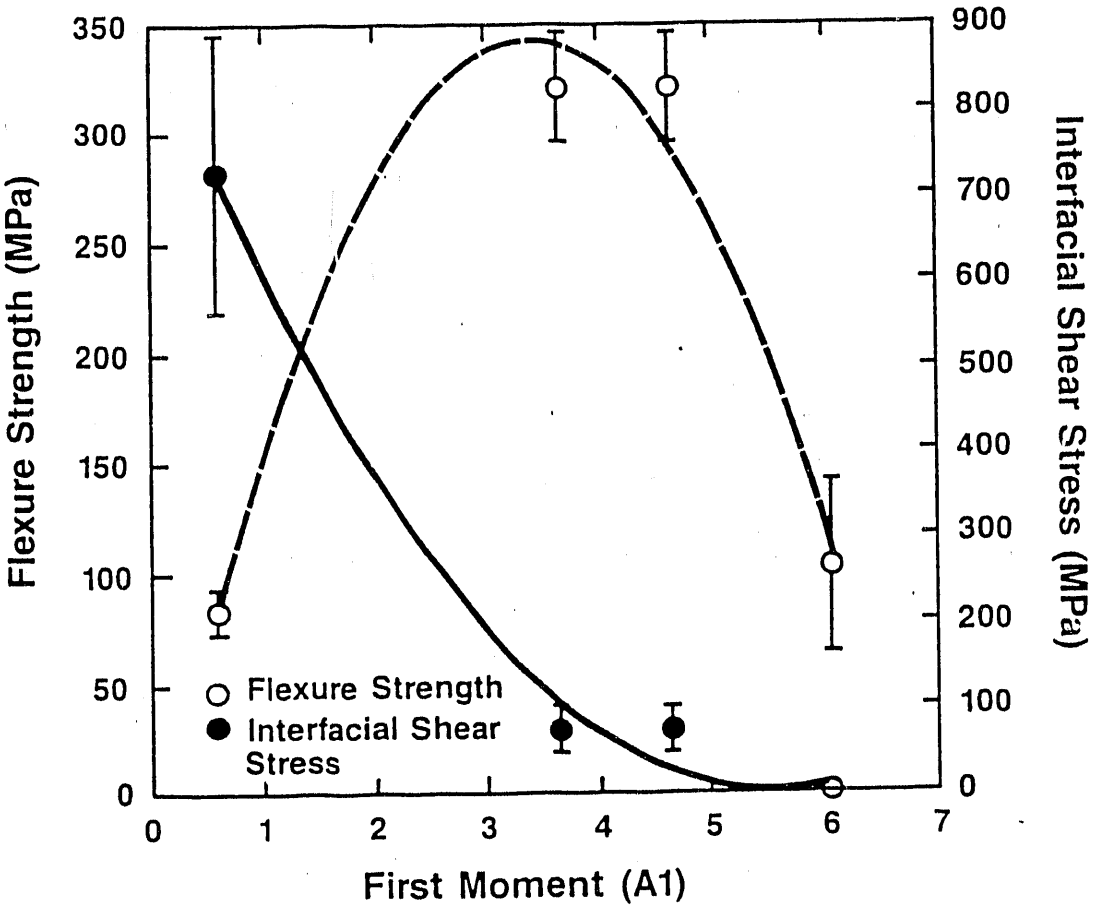

Fig. 6 - Flexure and interfacial shear stress vs. 1st moment of AU signal.

stress and flexure strength values are plotted as functions of A1 and A2. The differences in the first and second moments of the power spectral density of AU signals are attributed to differences in fiber-matrix interface conditions, as the specimens are otherwise identical. This agrees with the results obtained by the diffuse field decay analysis method.

Summary and Conclusions

This study has demonstrated the feasibility of acousto-ultrasonic measurements of internal damping for discriminating between differences in fiber-matrix interface conditions in otherwise identical samples.

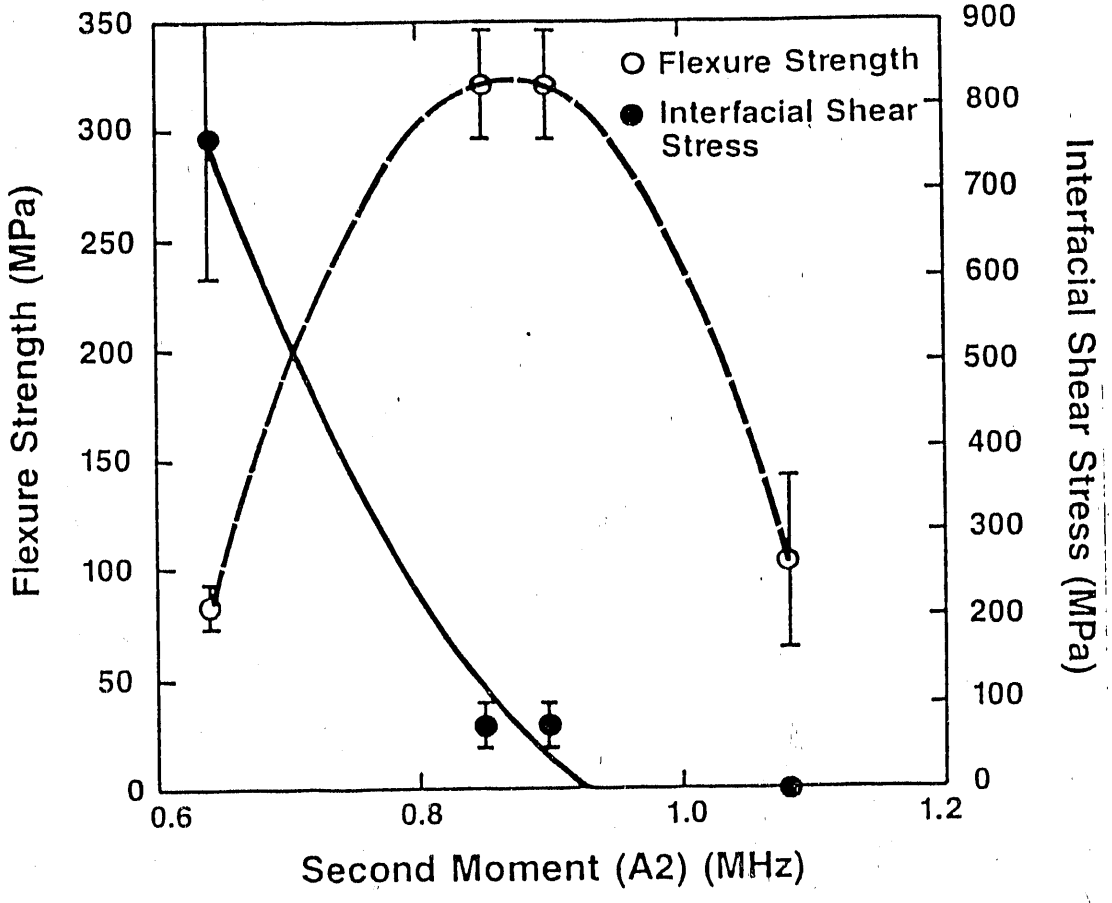

Fig. 7 - Flexure and interfacial shear stress vs. 2nd moment of AU signal.

It is important to note that the technique is possible with noncontacting laser-based sensors, enabling measurements to be performed on components at high temperatures or in other hostile environments. This means that the techniques have great potential for in situ process monitoring techniques for composite quality control during fabrication and to ensure the quality and integrity of composite materials and components while in service.

Future work should include measurements on larger sample bases to firmly establish correlations between fiber-matrix interface conditions and measured acoustic and ultrasonic properties. Attention should also be given to effects of component size and shape on measurement and analysis techniques. Finally, additional research needs to be

completed on the mechanisms of laser-ultrasonic generation and on detection of ceramic matrix components.

REFERENCES

1. R. A. Lowden, D. P. Stinton, and T. M. Besmann, "Characterization of Fiber-Matrix Interfaces in Ceramic Composites," Whisker and Fiber-Toughened Ceramics, ASM Conference Proceedings, 1988, pp. 253-264.

2. A. J. Caputo, D. P. Stinton, R. A. Lowden, and T. M. Besmann, "Fiber-Reinforced SiC Composites with Improved Mechanical Properties," Am. Ceram. Soc. Bull., 66(2), 1987, pp. 368-372.

3. R. A. Lowden, "Characterization and Control of the Fiber-Matrix Interface in Ceramic Matrix Composites," ORNL/TM-11039, March 1989.

4. A. Vary and K. J. Bowles, "An Ultrasonic-Acoustic Technique for Nondestructive Evaluation of Fiber Composite Quality," Polymer Engineering and Science, 19, 1979, pp. 373-377.

5. M. T. Kiernan and J. C. Duke, Jr., "PC Analysis of an Acousto-Ultrasonic Signal," Materials Evaluation, Vol. 46, p. 1344-1352, September 1988.

6. R. L. Weaver, "Diffuse Field Decay Rates For Material Characterization," Solid Mechanics Research for Quantitative Nondestructive Evaluation, edited by J. D. Achenbach and Y. Rajapaskie, Martinus Nijhoff Publishers, 1987, p. 425.

INEL-1(B) - JOINING OF SILICON CARBIDE CERAMICS AND COMPOSITES

B. H. Rabin and G. A. Moore

Idaho National Engineering Laboratory
P.O. Box 1625
Idaho Falls, ID 83415-2218

INTRODUCTION

Silicon carbide (SiC) matrix composites produced by chemical vapor infiltration techniques are under development for use in elevated temperature structural applications[1-3]. These composites typically contain ~40 vol.% of fiber reinforcement, and are infiltrated to ~85% of theoretical density with silicon carbide. In order to fully realize the advantages of these materials in fossil energy systems, practical joining techniques must be developed. Successful joining methods will permit the design and fabrication of large components and complex shapes, and will allow integration of component parts into existing systems.

Joining of SiC matrix composites is comparable to joining of dense SiC; however, the presence of the fiber reinforcement introduces additional concerns. The type of fiber, as well as any fiber/matrix interfacial coating, must also be considered when developing a joining process. For example, in the case of SiC/SiC composites containing Nicalon fibers, losses in component strength result from prolonged exposure to processing or service temperatures above ~1200°C[4]. Nicalon fiber degradation occurs at these temperatures, and in the presence of oxidizing atmospheres, the carbon-rich interfacial coating required for toughening is also degraded. Thus, for this material the upper use temperature, as well as the highest processing temperature allowable for joining, is limited to ~1200°C. Property reduction can be minimized by coating the components with an external protective layer of SiC[4], or by using other fibers, not yet readily available, that are more resistant to thermal degradation. It is expected that continued research and development will produce SiC matrix composites for use at temperatures at or above 1400°C. Applicable joining methods must therefore avoid property degradation of the composite caused by excessive processing temperatures, and must also provide joints that can withstand these expected use temperatures.

Dense SiC has been joined using a variety of techniques; these have been listed in a previous report[5]. Considering the applicability of these methods for composite joining, metallic brazing techniques are ruled out because of the intended service temperatures. Direct

diffusion bonding, hot pressing with various interlayer materials, and vitreous brazing require temperatures exceeding ~1650°C and would therefore result in composite property degradation. Of the previously studied techniques, only metallic bonding with reactive metals such as titanium shows promise for composite joining[6,7].

Prior work on this project identified a new joining technique applicable to SiC matrix composites that involves simultaneous *in situ* reaction synthesis and bonding[5,8]. The technique was demonstrated for dense SiC and SiC/SiC composites using combustion reactions in the Ti-C-Ni system that were initiated below 1200°C in a hot press. A TiC-Ni joint interlayer was formed, and bonding was attributed to an interfacial reaction between the TiC-Ni and SiC. Room temperature joint strengths measured in four-point bending exceeded 100 MPa. The Ti-C-Ni system was initially chosen to demonstrate this new joining method; however, concerns have been identified regarding the maximum use temperature and sulfidation resistance of TiC-Ni joints. Thus, in addition to the continuing studies on the Ti-C-Ni system, recent efforts have also considered alternative joining systems.

DISCUSSION OF CURRENT ACTIVITIES

The research effort during this report period has focussed on (1) continued studies of the Ti-C-Ni joining system, and (2) identification and evaluation of alternative joining systems.

Joining with Ti-C-Ni Combustion Reactions

Studies involving joining with Ti-C-Ni combustion reactions have continued with emphasis on further characterization of joint microstructures, and optimization of the joint composition and processing variables. In prior work it was shown that during the joining process, the TiC-Ni chemically reacted with the SiC to form a microscopically rough interface rich in TiC. It was also shown through x-ray dot mapping that a significant concentration of Ti and Si existed in the Ni-rich phase. Figure 1 shows an x-ray diffraction scan taken from the fracture surface of a joint produced using a Ti-C-Ni mixture. In bulk pellets produced by combustion synthesis of Ti-C-Ni mixtures only the TiC and Ni phases were present. In contrast, Figure 1 indicates the reaction product formed by *in situ* reaction within the SiC joint shows the presence of TiC, the phase $Ni_{16}Ti_6Si_7$, and very little metallic Ni. Thus, during the joining process, dissolution of SiC at the joint interface allowed enough Si to diffuse into the Ni melt to result in formation of the silicide. The reason for the increased Ti concentration within the

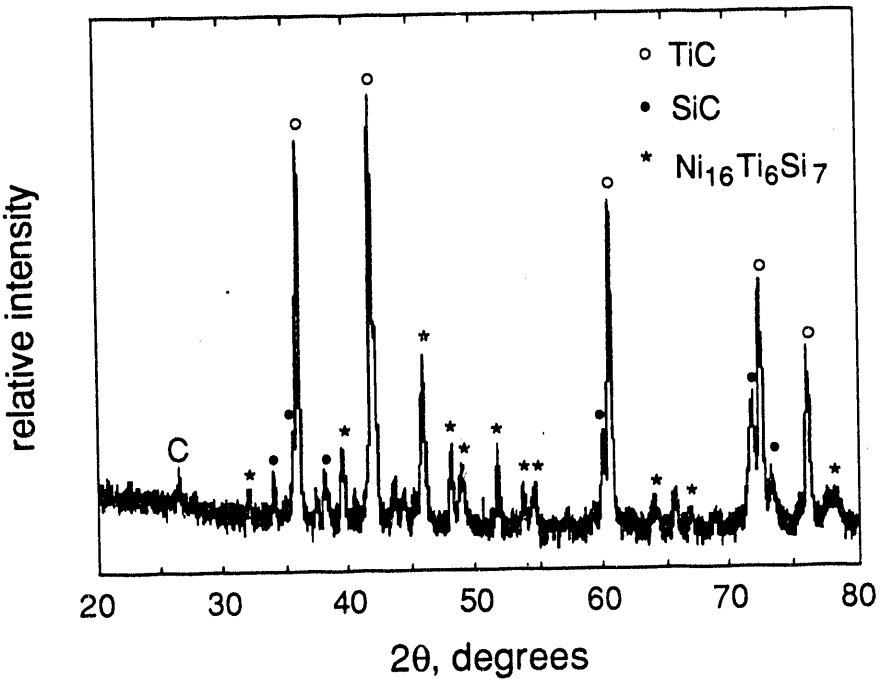

Figure 1. X-ray diffraction scan obtained from the fracture surface of a SiC to SiC joint produced by *in situ* reaction of a Ti-C-Ni powder mixture.

Ni-rich phase in the *in situ* reacted material compared to the bulk reacted material is uncertain. Nevertheless, the presence of $Ni_{16}Ti_6Si_7$ in the joint is significant. As a silicide, this material is expected to exhibit superior oxidation and sulfidation resistance compared to pure Ni. In addition, the mechanical properties of the joint interlayer material are expected to be different from those of TiC-Ni materials formed by combustion synthesis of bulk Ti-C-Ni pellets.

There have been continuing problems with the quality and reproducibility of joints produced using Ti-C-Ni mixtures, mainly as a result of large porosity defects that frequently resulted in low joint strengths. Porosity in combustion synthesized materials often originates from the large volume change associated with the reaction, as well as the evolution of gases during rapid exothermic heating[9]. In the current studies, the large density difference of the starting powders, the application of binder assisted processing, and the use of extremely fine, agglomerated carbon powder were also potential sources of porosity. A variety of studies were therefore conducted to determine the origin of the porosity. The studies examined the effects of several variables on overall joint quality, including carbon particle size (0.02 μm acetylene black vs 1.0 μm graphite), Ni content (5 to 25 wt.%), amount of binder (3 to 36 wt.%), method of forming joint interlayer (tape casting, die pressing, slurry painting), and joining temperature.

The results of these studies indicated that most of the porosity could be attributed to the volume change and gas evolution associated with combustion synthesis; the other variables examined had a lesser influence on the amount of porosity observed. The volume change for the reaction was estimated to be ~25%, and since the starting powder mixtures had porosity levels on the order of 40%, a volume shrinkage of approximately 65% was required to completely densify the material. This amount of shrinkage is difficult to achieve during the reaction, even when external pressure is applied, because of the short time at elevated temperature. It was also determined that gas evolution likely contributed to pore formation, since significant weight losses were observed by thermogravimetric analysis during the reaction. The amount of gas evolution can be reduced by outgassing the powders prior to reaction[10], although it cannot be eliminated.

The following additional observations were made regarding other variables examined. The type of carbon powder had a significant influence on the quality of the microstructure, as demonstrated in Figure 2. The fine 0.02 μm acetylene black resulted in a more fully reacted and uniform microstructure, in contrast to the coarse 1.0 μm graphite powder that resulted in large areas of unreacted graphite. Other researchers have achieved good combustion synthesis results using coarse graphite powders[11], although samples were typically considerably larger than those used in the joining studies, and combustion temperatures were probably significantly higher. The effect of nickel content is illustrated in Figure 3, which shows micrographs of joints prepared with 7.5, 15, and 25 wt.% Ni. Improved densification and homogeneity were achieved with higher Ni contents as a result of the greater liquid volume during reaction. More extensive reaction at the SiC interface was also observed, indicating the important role played by Ni in the bonding mechanism. The method of preparing the thin layer of powder reactants did not appear to significantly influence the final porosity; however, tape casting proved most useful for producing thin layers having controlled thickness and uniform green density. Variations in binder content had little effect on the final porosity observed in joints. Finally, higher joining temperatures were found to be beneficial for improving the density of joints. Prior joining studies were conducted at ≤1300°C. In contrast, the recent results indicate that temperatures greater than ~1350°C are necessary to allow post-reaction densification mechanisms to operate. It is anticipated that the observations discussed above can be used to improve the quality and reproducibility of joints produced using Ti-C-Ni mixtures. Higher nickel contents and joining temperatures are expected to be beneficial.

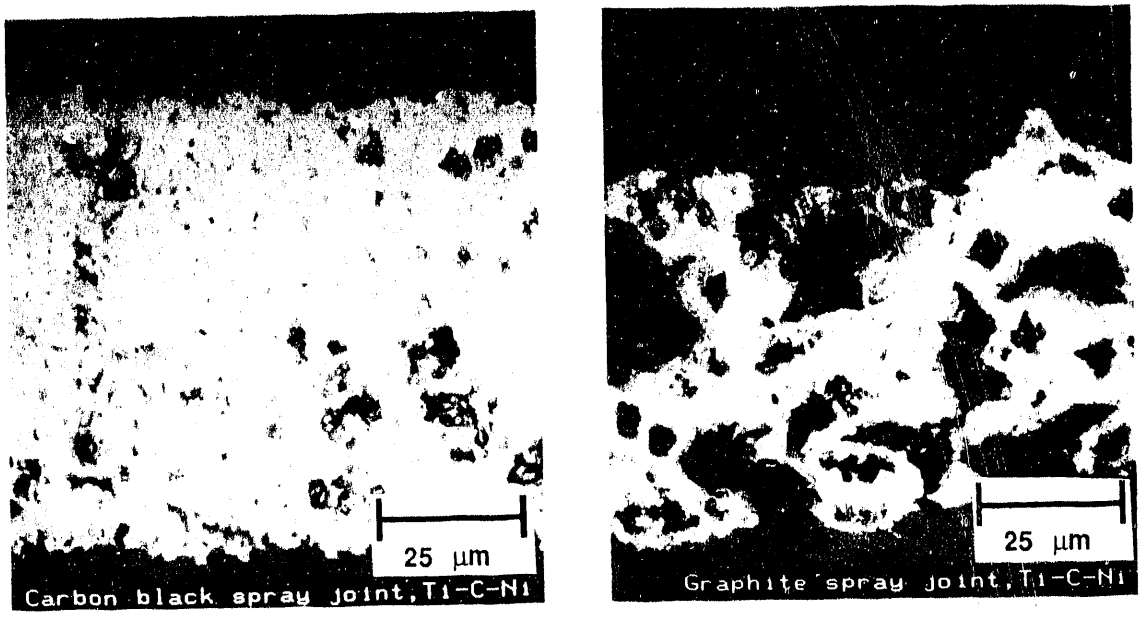

(a) (b)

Figure 2. Optical micrographs of SiC to SiC joints produced using *in situ* reaction of Ti-C-Ni powder mixtures prepared with (a) 0.02 μm acetylene black, and (b) 1.0 μm graphite.

Alternative Joining Systems

Studies have been initiated to develop alternative joining materials and methods. One system of interest is the $MoSi_2$-SiC system. Composite materials in this system have been shown to exhibit good toughness and excellent oxidation resistance[12]. For these materials, two types of joining methods are being considered. One method involves using combustion reactions, similar to prior work on the Ti-C-Ni system. In addition, a liquid infiltration/reaction bonding technique is being investigated. If successful, this technique will be more practical than the previous method in that infiltration requires no external pressure to achieve densification, and therefore a hot press would not be required.

Although combustion synthesis of $MoSi_2$ has been studied[13,14], production of $MoSi_2$-SiC composites by this method has not previously been reported. Initial studies have shown that $MoSi_2$-SiC powder mixtures can be produced by reaction of Mo-Si-C elemental powders. As shown by DTA in Figure 4, an exothermic reaction can be initiated by furnace heating a Mo-Si-C compact. The composition of the compact was adjusted to result in approximately a 50-50 vol.%

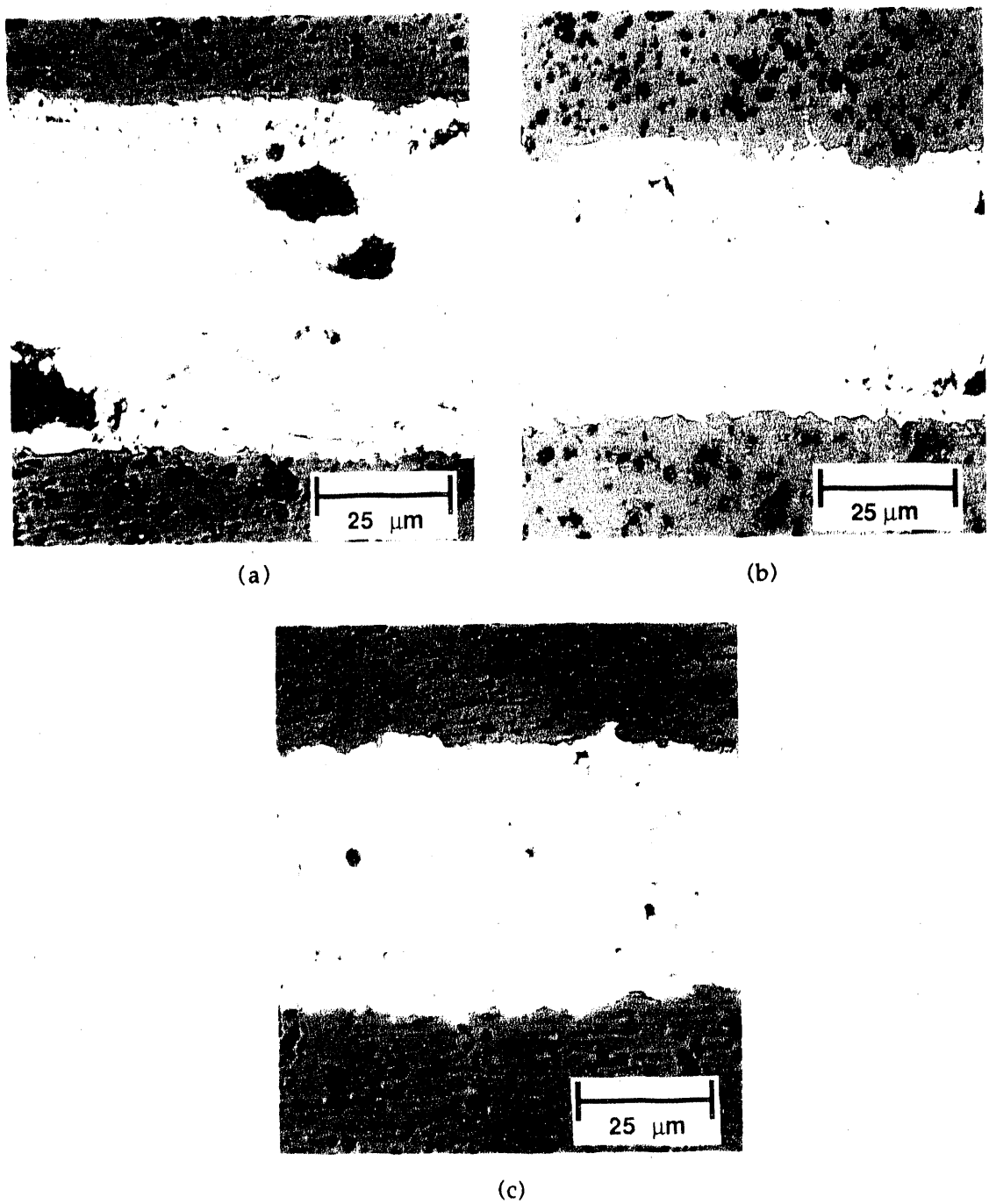

Figure 3. Optical micrographs of SiC to SiC joints produced by *in situ* reaction of Ti-C-Ni powder mixtures prepared using (a) 7.5 wt.% Ni, (b) 15 wt.% Ni, and (c) 25 wt.% Ni.

mixture of $MoSi_2$ and SiC after reaction. The product of the reaction was a friable, porous mass that was subsequently ground into powder and analyzed using x-ray diffraction. Figure 5 shows

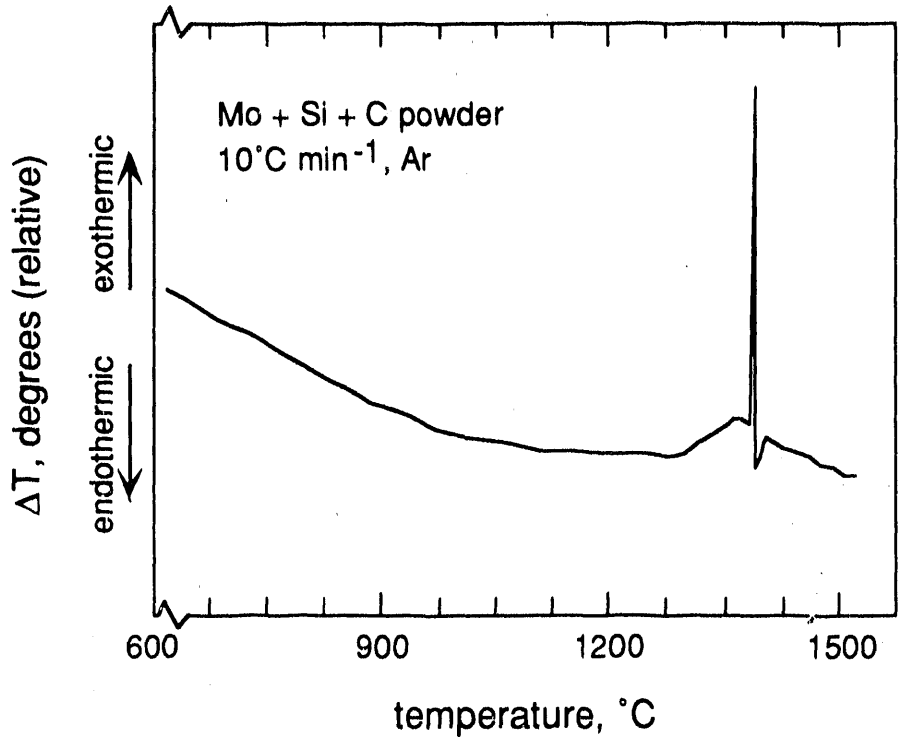

Figure 4. DTA scan conducted on a mixture of Mo-Si-C powders.

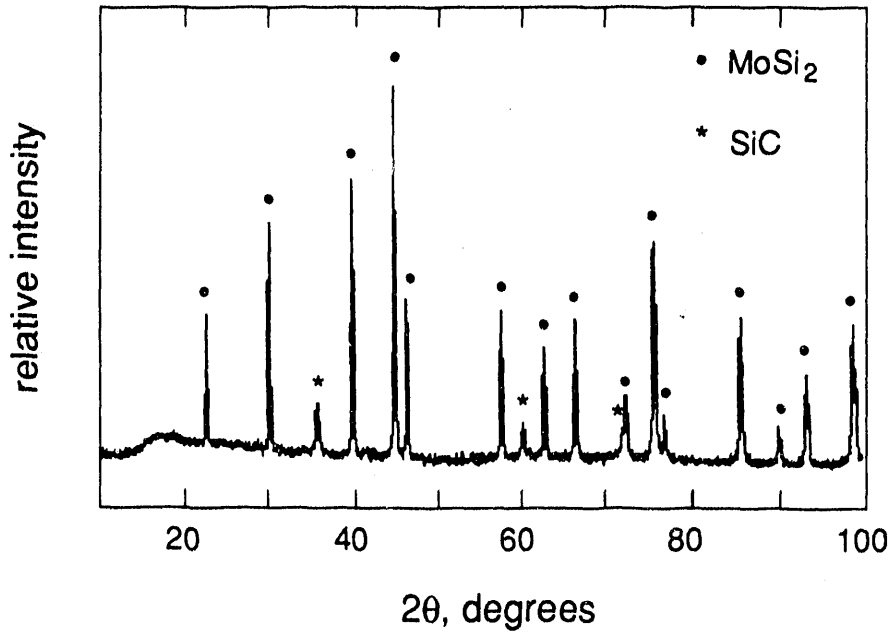

Figure 5. X-ray diffraction results for a reacted mixture of Mo-Si-C powders.

the results indicating the reaction had gone to completion and that only $MoSi_2$ and SiC were present. The morphology of the powder is shown in Figure 6. A bimodal particle size distribution was clearly evident. Energy dispersive x-ray analysis indicated the angular shaped, larger ~1-3 μm diameter particles were $MoSi_2$. The aggolmerated submicron particles were SiC. Further work is required to assess the densification behavior of these powders. One possible approach would involve simultaneous synthesis, densification, and joint bonding through the application of external pressure, as was accomplished in the Ti-C-Ni system. Alternati' ly, the powder could be milled to produce a high surface area, sinterable powder which could be densified within the joint in a separate step.

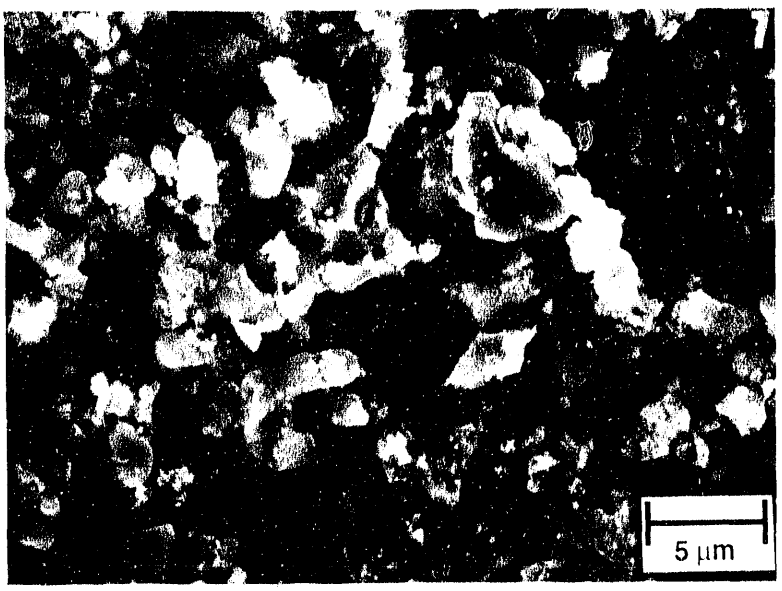

Figure 6. Scanning electron micrograph showing the morphology of the powder produced by combustion synthesis of Mo-Si-C powder compacts. The 1-3 μm angular particles are $MoSi_2$, and the agglomerated submicron particles are SiC.

Joining of SiC by infiltrating the joint region with molten Si to produce a reaction bonded silicon carbide (RBSC) joint interlayer has previously been demonstrated[15,16]. RBSC exhibits excellent oxidation resistance and good strength. The process is relatively simple to carry out, and offers considerable control over the resultant joint microstructure. Infiltration takes place at approximately 1450°C, above the melting point of Si. Work is now underway to optimize this joining method.

Typically, RBSC contains about 10-15 vol.% free Si, which causes strength to decrease rapidly above ~1400°C. Researchers have recently demonstrated that by using a Si melt

alloyed with Mo, it is possible to produce a reaction bonded $MoSi_2$-SiC composite containing no free Si that exhibits superior high temperature properties[17]. Efforts are now underway to investigate the use of the alloyed melt infiltration approach for fabrication of SiC joints that could be used above 1400°C.

REFERENCES

1. D. P. Stinton, A. J. Caputo and R. A. Lowden, "Synthesis of Fiber-Reinforced SiC Composites by Chemical Vapor Infiltration," *Amer. Ceram. Soc. Bull.*, 65(2), pp. 347-350, 1986.

2. A. J. Caputo, et al., "Fiber-Reinforced SiC Composites with Improved Mechanical Properties," *Amer. Ceram. Soc. Bull.*, 66(2), pp. 368-372, 1987.

3. D. P. Stinton, T. M. Besmann, and R. A. Lowden, "Advanced Ceramics by Chemical Vapor Deposition Techniques," *Amer. Ceram. Soc. Bull.*, 67(2), PP. 350-355, 1988.

4. D. P. Stinton, R. A. Lowden and R. H. Krabill, "Mechanical Property Characterization of Fiber-Reinforced SiC Matrix Composites, ORNL/TN-11524, Oak Ridge National Laboratory, Oak Ridge, TN, April, 1990.

5. B. H. Rabin, "Joining of Fiber-Reinforced Silicon Carbide Composites," Proc. Fifth Annual Conf. on Fossil Energy Materials, Oak Ridge, TN, May, 1991, in press.

6. S. Morozumi, et al., "Bonding Mechanism Between Silicon Carbide and Thin Foils of Reactive Metals," *J. Mater. Sci.*, vol. 20, pp.3976-3982, 1985.

7. B. Gottselig, et al., "Contribution to the Joining Technique of SiC-Ceramic Using Metallic Interlayers," Juel-2288, Berichte der Kernforschungsanlage, Institut fur Reaktorwerkstoffe, Julich, GmbH, July, 1989.

8. B. H. Rabin, "Joining of SiC/SiC Composites and Dense SiC Using Combustion Reactions in the Ti-C-Ni System," *J. Amer. Ceram. Soc.*, in press, 1991.

9. R. W. Rice and W. J. McDonough, "Intrinsic Volume Changes of Self-Propagating Synthesis," *J. Amer. Ceram. Soc.*, 68(5), pp. C-122-C-123, 1985.

10. L. J. Kecskes and A. Niiler, "Impurities in the Combustion Synthesis of Titanium Carbide", *J. Am. Ceram. Soc.*, 72[4], 655-661, 1989.

11. S. D. Dunmead, et al., "Kinetics of Combustion Synthesis in the Ti-C and Ti-C-Ni Systems," *J. Amer. Ceram. Soc.*, 72(12), pp. 2318-2324, 1989.

12. F. D. Gac and J. J. Petrovic, "Feasibility of a Composite of SiC Whiskers in an $MoSi_2$ Matrix," *J. Amer. Ceram. Soc.* , 68(8), pp. C-200 - C-201, 1985.

13. S. Zhang and Z. A. Munir, "Synthesis of Molybdenum Silicides by the Self-Propagating Combustion Method," *J. Mater. Sci.*, 26, pp. 3685-3688, 1991.

14. S. C. Deevi, "Self-Propagating High-Temperature Synthesis of Molybdenum Disilicide," *J. Mater. Sci.*, 26, pp. 3343-3353, 1991.

15. T. Iseki and H. Suzuki, "Joining of Dense Silicon Carbide," Proc. First Int. Symp. on Ceramic Components for Engine, S. Somiya, et al. (eds.), D. Reidel Publishing Co., Boston, MA, pp. 603-611, 1984.

16. B. H. Rabin, "Joining of Fiber-Reinforced Silicon Carbide Composites," Proc. Fourth Annual Conf. on Fossil Energy Materials, ORNL/FMP-90/1, Oak Ridge, TN, pp. 85-95, August, 1990.

17. R. P. Messner and Y-M. Chiang, "Liquid-Phase Reaction Bonding of Silicon Carbide Using Alloyed Silicon-Molybdenum Melts," *J. Amer. Ceram. Soc.*, 73(5), pp. 1193-1200, 1990.

NIST-1 - STRUCTURAL RELIABILITY AND DAMAGE TOLERANCE OF CERAMIC COMPOSITES

E. R. Fuller, Jr.

Ceramics Division
Materials Science and Engineering Laboratory
National Institute of Standards and Technology
Gaithersburg, MD 20899

INTRODUCTION

The achievement of higher efficiency heat engines and heat recovery systems requires the availability of high-temperature, high-performance structural materials. Structural ceramics, and more recently, ceramic matrix composites have received particular attention for these applications due to their high strength and excellent resistance to corrosion, erosion and thermal shock. Even with these positive attributes, improved reliability and extended lifetime under service conditions are necessary for structural ceramics and ceramic composites to gain wide industrial acceptance. This reliability is only achieved with improved knowledge of in-service damage modes and failure mechanisms, and the processing knowledge to improve this performance by microstructural modifications. The inherent problems are mechanical and chemical in nature and are enhanced by the high temperatures, reactive environments, and extreme thermal gradients and thermal cycling, to which these materials are subjected.

With an objective of improved performance for heat engine/heat recovery applications, the NIST program addresses these problems through a determination and characterization of major toughening mechanisms in ceramic composites, examining both model crack-fiber systems and "real" composites. A key aspect of the program is a determination of the critical processing factors which influence microstructure and interfacial behavior in these materials, and which thereby influence these toughening mechanisms. Activities of the program are designed to develop key data, associated test methods and companion predictive models. The status of the work is detailed below.

DISCUSSION OF CURRENT ACTIVITIES

IN SITU OBSERVATIONS OF TOUGHENING PROCESSES IN ALUMINA REINFORCED WITH SILICON CARBIDE WHISKERS

Summary

An in situ study was made of crack interfaces in composites of alumina reinforced with silicon carbide whiskers. Both qualitative observations of the whisker bridging micromechanisms and quantitative measurements of the crack profile are made to assess the specific role of the whiskers on the toughness-curve (T-curve or R-curve). At small crack-wall separations the whiskers act as elastic restraints to the point of rupture. In some cases the whiskers remain in frictional contact with the alumina matrix over large pullout distances, more than 1 μm, corresponding to a bridging zone approaching 1 mm. The results are discussed in relation to existing models of whisker reinforcement and published long-crack T-curve data. [Key words: toughness, bridging, composites, cracks, pullout, deflection.]

Introduction

The incorporation of silicon carbide whiskers ($\approx$ 1 μm diam) into alumina can lead to considerable toughening.[1-8] A typical composite shows a monotonic toughness increase (toughness T-curve, or crack-resistance R-curve) relative to $\approx$ 2.5 MPa$\cdot$m$^{1/2}$ for the base alumina; maximum reported toughness values are 5 to 9 MPa$\cdot$m$^{1/2}$ (refs. 8 to 11), depending on the properties and volume fraction of whiskers. It is generally accepted that the T-curve mechanisms involve some form of crack-interface bridging.[8] However, the precise nature of these mechanisms remain an issue of much debate. Many argue, e.g., from near-tip observations using transmission electron microscopy,[4,7] that the bridging primarily entails debonding and subsequent elastic deformation of the whiskers to abrupt rupture immediately (within 20 μm) behind the advancing crack tip. Those observations have been used as the basis for most micromechanics modelling.[8] Few efforts have been made to reconcile such small-scale bridging zones with long-crack T-curve data (typical

crack extension range ≈ 100 μm to 1 mm),[9-11] e.g., by invoking an artificially enhanced "tail" in the fiber-matrix constitutive stress-displacement function (associated with a distribution in whisker strengths) or secondary bridging from the alumina grains in a coarse-grained matrix.[12,13]

In this report we describe the results of some in situ experiments on crack growth in fine-grained alumina matrix materials reinforced with silicon carbide whiskers. The fine grain size minimizes potential bridging from the alumina grains themselves,[12,13] so that we may investigate more clearly the micromechanisms of whisker toughening. Observations of whisker bridging sites under load enable identification of these micromechanisms and, together with measurements of crack-opening displacements over the crack interface, indicate that the bridging which contributes to the toughness can indeed occur over substantial distances, i.e., up to 1 mm, behind the crack tip. The results reveal the following features in the whisker toughening process: (1) a considerably greater role of extended whisker pullout than hitherto proposed; (2) identification of the T-curve baseline with the matrix (grain boundary) toughness; (3) enhancement of the bridge formation processes from internal residual stresses.

Experiment

Two composites of SiC whiskers* and Al_2O_3 powder† were hot pressed as 50 mm diam disks at 1700°C for 1 hr at a pressure of 42 MPa. Composite A was fabricated with 20 vol% whiskers 0.3 to 0.6 μm diam and 5-15 μm length, composite B with 30 vol% whiskers 1.1 μm diam and 50 μm length. The resultant composites achieved a density > 99% with a random distribution of whiskers (except for slight alignment perpendicular to the hot-pressing direction) in matrices of grain size 1 to 2 μm.

The disks were surface-ground to 1 mm thickness and one surface of each was polished with diamond paste to 1 μm finish. Compact-tension specimens with a notch of length 7 mm and tip radius 150 μm were sawn from

* Tokai SiC whiskers: TWS 100 (0.3 to 0.6 μm diam, 5-15 μm length) and TWS 400 (1.1 μm diam, 50 μm length) from Tokai Carbon Ltd., Japan.

† Reynolds high-purity alumina grade RC-HP DBM with 0.05% MgO, mean particle size 0.5 μm, surface area 7.6 m^2/g from Reynolds Metals Co., Chemical Division, Richmond, VA.

the disks.[14] A tapered cut was made ahead of the notch from the back (unpolished) surface to produce a chevron guide ≈ 2 mm in length.[14] This latter was to provide extra stability in the ensuing crack extension. A Vickers indentation flaw (load 50 N) placed immediately ahead of the notch tip in the polished surface was then subjected to a preliminary load cycle to induce pop-in. The notch was finally re-sawn through the indentation, leaving a starter pre-crack ≈ 100 μm long.

The specimens were mounted into a fixture for in situ experiments in the scanning electron microscope (SEM)[15] with the polished side facing the electron beam for direct observation of the crack trace. Loads applied externally to the SEM enabled the crack to be propagated stably (if sometimes discontinuously) for distances up to ≈ 1 mm within the chevron. Individual bridging sites were monitored during the crack growth. Crack-opening displacements (COD) were measured behind the crack tip, to determine the bridged interface profiles.[14]

After running the crack through the chevron the specimens were withdrawn and re-sawn for repeat experiments.

Results

Crack Propagation and Whisker Bridge Evolution. Specific examples of whisker bridging sites monitored in the SEM are shown in Figs. 1 and 2. Generally, the fracture followed an intergranular path in the alumina matrix, with markedly abrupt deflections along or around the whiskers, although not always exactly along the whisker/matrix interfaces. These abrupt deflections appeared to be a most effective precursor to bridge formation. A majority of the whisker bridges ruptured at a distance < 100 μm behind the crack tip, but some remained active over much greater distances. No detached microcracking at whisker-matrix interfaces more than a few grain diameters from the primary crack plane was observed.

Immediately behind the crack tip the walls begin to separate but the whiskers remain mechanically connected across the interface. Fig. 1a shows one such whisker ≈ 10 μm behind the tip, i.e., in the range ordinarily considered appropriate for "elastic" bridges.[4,7] Many of the whiskers observed in our materials did disengage from the matrix within

this range, with little indication of pullout. However, the particular whisker in

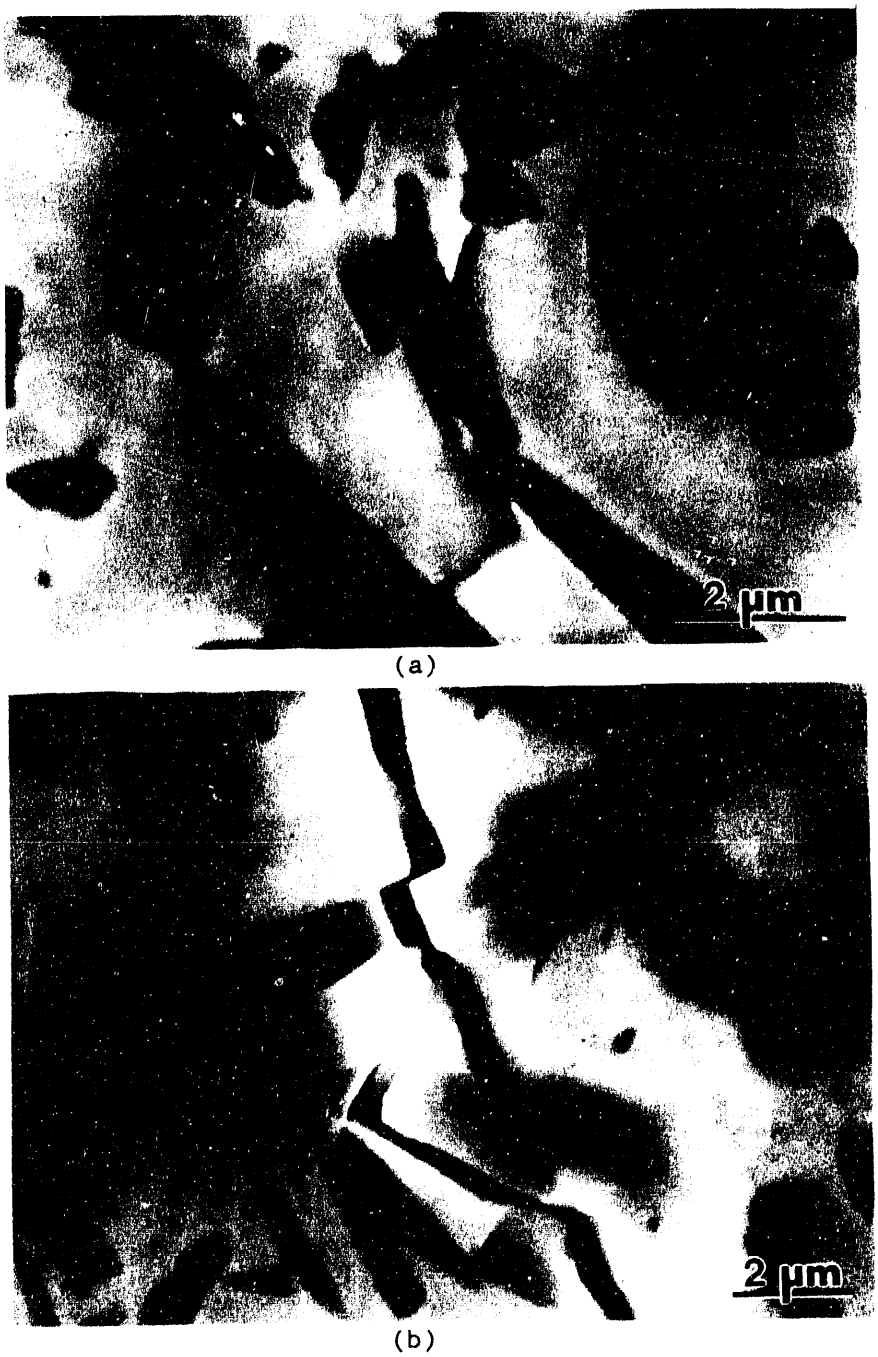

Fig. 1. In situ SEM micrographs of bridging SiC whiskers in Al_2O_3, material B (crack direction downward). (a) Elastic bridge (central whisker) 10 μm behind crack tip. Note strong deflections at this bridge, not exactly along the whisker-matrix interface. (b) Mechanically interlocked whisker 350 μm behind the crack tip. Note adjoining microfracture in surrounding matrix at bridge site.

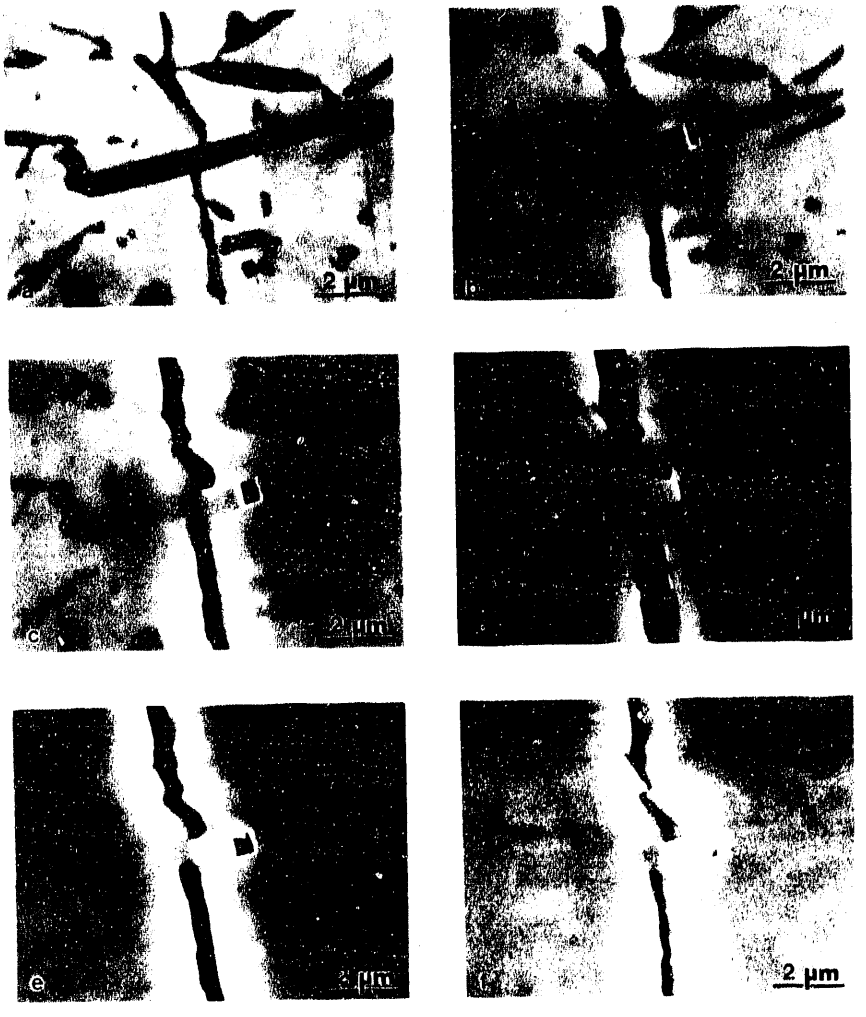

Fig. 2. In situ SEM sequence showing evolution of bridge whisker pullout, material A (crack direction downward). Distance x behind crack tip and force P on compact tension load points:
(a) x = 100 μm, P = 167 N; (b) x = 110 μm, P = 209 N;
(c) x = 330 μm, P = 213 N; (d) x = 830 μm, P = 233 N;
(e) x = 830 μm, P = 101 N; (f) x = 830 μm, P = 0 N.

Fig. 1a remained intact prior to abrupt rupture until the tip had progressed ≈ 120 μm beyond the site, corresponding to a COD ≈ 300 nm. Other bridges showed even longer range effects. Fig. 1b shows one such site where the debonding and stress build up was sufficient to cause secondary, off-plane matrix fragmentation around the embedded whisker ≈ 350 μm behind the crack tip. This implies a long tail to the bridging stress-separation function.

An even more striking example of a whisker with long-range interaction across the interface is shown in the sequence of Fig. 2. In this case the whisker is located only ≈ 70 μm from the mouth of the extending crack (i.e., from the notch tip). The whisker ruptures well away from the crack plane, and pulls out in apparently sustained frictional contact with the matrix over this distance during monotonic loading through (a)-(c). The whisker is slightly inclined to the separation plane, and so is subjected to increasing bending stresses during its pullout. At disengagement in (d) it is ≈ 830 μm behind the crack tip, corresponding to a COD ≈ 1 μm. The now unconstrained whisker rotates at its free end; so that, on unloading through (e)-(f), the whisker does not re-enter its "socket" without some misfit, leaving the "closed" crack interface in a residual state of internal wedge loading.

Crack-Opening Displacement (COD). The COD measurements at the loaded crack interfaces allow us to construct the K-field plots in Fig. 3. We start with the Irwin relation for COD in terms of the stress-intensity factor K and coordinate x behind the crack tip[14]

$$u(x) = (8x/\pi)^{1/2}(1 - \nu^2)K/E \qquad (1)$$

with Young's modulus E ≈ 400 GPa and Poisson's ratio ν ≈ 0.25. This relation may reasonably be expected to hold in the region $x \leq \Delta c << c_0$ (recall crack extension Δc ≈ 1 mm and notch length c_0 ≈ 7 mm in our experiments) if the crack walls were stress free (i.e., zero bridging). In reality, the bridging K-field acts to restrain the crack walls from opening as wide as Eq. 1 predicts.

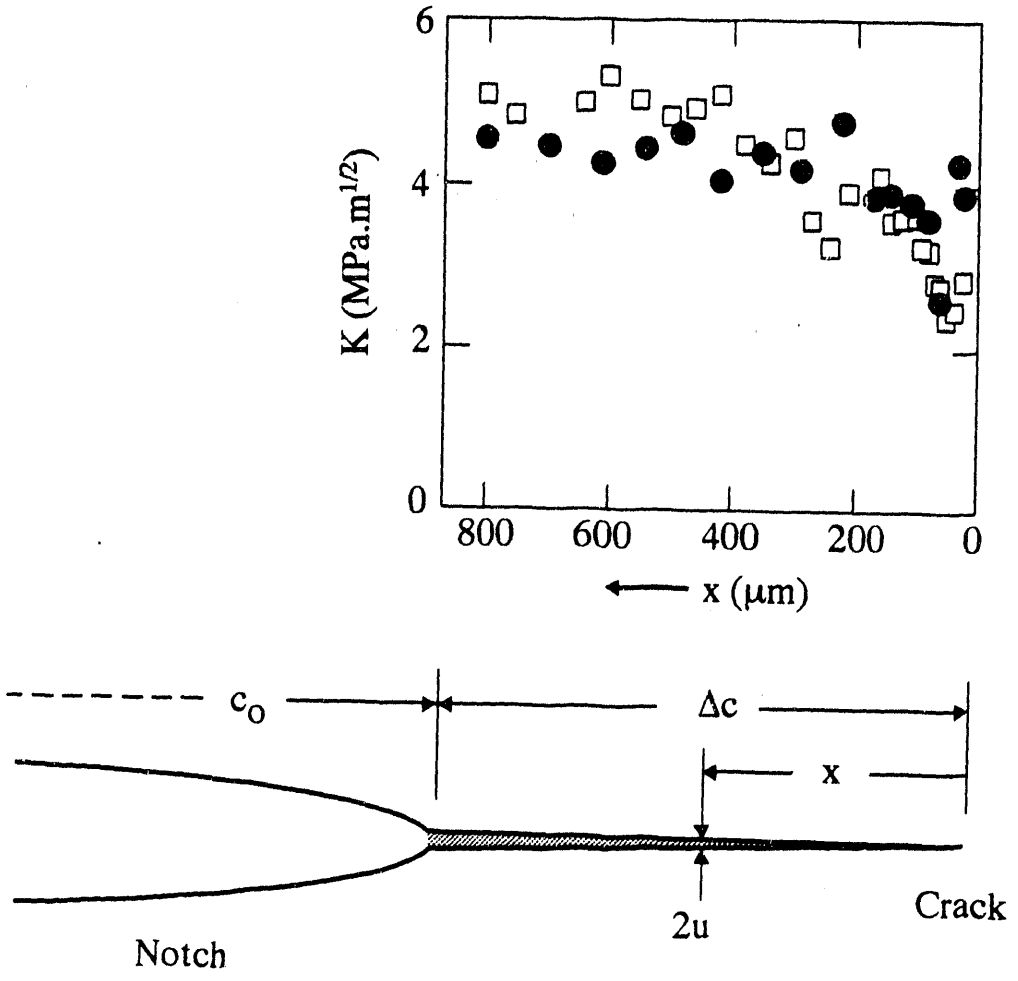

Fig 3. K-field evaluated from crack-opening displacements along crack interface in silicon carbide whisker-reinforced alumina, material A (closed symbols) and B (open symbols). Cracks remain bridged (hatched region in schematic) in propagation through $\Delta c \approx 1000$ μm through chevron from notch of length c_0 = 7 mm. Data points are K-field evaluations from inverted form of Irwin relation, Eq. 1.

The K[u(x)] data points shown in Fig. 3 are accordingly obtained by inversion of Eq. 1. The data in this figure indicates the K-field an "Irwinian" observer would measure on traversing the crack plane from crack tip ($x = 0$) to mouth ($x = \Delta c$). At $x = \Delta c$, $K = 5.1$ MPa·m$^{1/2}$ is an approximate (under-)estimate of the unshielded, applied stress-intensity factor, corresponding to the limiting toughness at the long-crack plateau of the T-curve. At the extrapolated limit $x \to 0$, $K = 2.5$ MPa·m$^{1/2}$ represents the shielded, crack-tip stress-intensity factor, and is close to the intrinsic grain boundary toughness of the matrix alumina. This extrapolated value lies well below the minimum ≈ 5 MPa·m$^{1/2}$ measured by more conventional T-curve methods.[8-11] We note that the K-field is slightly greater for material B, i.e., the material with the higher density of coarser fibers. We also note that the K-field increases up to $x \approx 500$ μm, indicating a broad bridging zone and a corresponding long-range T-curve.[14,‡]

Discussion

The present *in situ* observations enable us to identify more closely the bridging micromechanics of silicon carbide whisker reinforcement in an alumina matrix, and to ascertain the range of the bridging zone.

For the bridging micromechanics, we see evidence for the short-range elastic component proposed in most analytical models.[8] Local matrix stress is transferred to the progressively debonding whisker, until abrupt rupture (whisker or matrix or both) in the near-crack plane. This rupture occurs most frequently at distances $x < 100$ μm from the crack tip in our materials, with attendant energy dissipation by acoustic waves. However, in many instances such as in Fig. 1 the rupture point is located much further behind the crack tip than previously supposed.

However, even these unusually strong elastic bridges cannot account for the crack extension range of 1 mm or so apparent in the reported T-curve measurements.[8-11] Additionally, as may be deduced from indentation-

‡ A complete, self-consistent analysis of the profile over the bridging zone is a complex numerical procedure,[16] requiring (among other things) knowledge of the complete bridging stress-separation function.

measure of the lower limit of the T-curve than do conventional fracture mechanics techniques. These latter are restricted by the scale of the pop-in starter cracks (typically 100 μm) used in the crack extension measurements. Here, extrapolation of our data to the crack tip ($x = 0$) in fig. 3 yields $K \approx 2.5$ MPa$\cdot$m$^{1/2}$, corresponding to the grain boundary toughness, whereas the more conventional fracture mechanics methods are generally unable to obtain data below $K \approx 5$ MPa$\cdot$m$^{1/2}$ (refs. 8 to 11).

Finally, we may recall our observations in Sect. 3A of markedly abrupt crack deflections in the proximity of whiskers. Such behavior may be attributed either to weak interphase boundaries or to strong local internal stresses. Recall again, however, that the deflections do not always occur exactly along the whisker/matrix interfaces (Fig. 1a). Direct measurements of internal stresses in our composites using neutron diffraction techniques reveal substantial thermal expansion mismatch stresses in the alumina ($\approx$ +200 MPa in composite A and +430 MPa in composite B) and silicon carbide ($\approx$ -1330 MPa in composite A and -1050 MPa in composite B).[22] We conclude that residual stresses play an important role not only in the energetics, but also in the formation, of bridging, by enhancing crack deflection.

ACKNOWLEDGMENTS

This work was conducted in collaboration with Jürgen Rödel, Materials Science and Engineering Department, Lehigh University, and Brian R. Lawn, NIST, who were funded by the U.S. Air Force Office of Scientific Research. We also acknowledge and thank Ralph F. Krause, Jr. for hot pressing the samples and James F. Kelly for assistance with the SEM imaging.

REFERENCES

1. P.F. Becher and G.C. Wei, "Toughening Behavior in SiC-Whisker Reinforced Alumina," J. Am. Ceram. Soc. 67 [12] C267-C269 (1984).
2. J. Homeny, W.L. Vaughn and M.K. Ferber, "Processing and Mechanical Properties of SiC-Whisker-Al_2O_3-Matrix Composites," Ceram. Bull. 66 [2] 333-38 (1987).
3. J. Homeny and W.L. Vaughn, "Whisker-Reinforced Ceramic Matrix

Mat. Res. Soc. Bull. 7 [7] 66-71 (1987).
4. P.F. Becher, C-H. Hsueh, P. Angelini and T.N. Tiegs, "Toughening Behavior in Whisker-Reinforced Ceramic Matrix Composites," J. Am. Ceram. Soc. 71 [12] 1050-61 (1988).
5. P.F. Becher, "Recent Advances in Whisker-Reinforced Ceramics," Ann. Rev. Mater. Sci. 20 179-95 (1990).
6. J. Homeny, W.L. Vaughn and M.K. Ferber, "Silicon Carbide Whisker/Alumina Matrix Composites: Effect of Whisker Surface Treatment on Fracture Toughness," J. Am. Ceram. Soc. 73 [2] 394-402 (1990).
7. G.H. Campbell, M. Rühle, B.J. Dalgleish and A.G. Evans, "Whisker Toughening: A Comparison Between Aluminum Oxide and Silicon Nitride Toughened with Silicon Carbide," J. Am. Ceram. Soc. 73 [3] 521-30 (1990).
8. P.F. Becher, "Microstructural Design of Toughened Ceramics", J. Am. Ceram. Soc. 74 [2] 255-69 (1991).
9. R.F. Krause, E.R. Fuller and J.F. Rhodes, "Fracture Resistance Behavior of Silicon Carbide Whisker-Reinforced Alumina Composites with Different Porosities," J. Am. Ceram. Soc. 73 [3] 559-66 (1990).
10. J. Homeny and W.L. Vaughn, "R-Curve Behavior in a Silicon Carbide Whisker/Alumina Matrix Composite," J. Am. Ceram. Soc. 73 [7] 2060-62 (1990).
11. S.V. Nair, "Crack-Wake Debonding and Toughness in Fiber- or Whisker-Reinforced Brittle-Matrix Composites," J. Am. Ceram. Soc. 73 [10] 2839-47 (1990).
12. P.L. Swanson, C.J. Fairbanks, B.R. Lawn, Y-W Mai and B.J. Hockey, "Crack-Interface Grain Bridging as a Fracture Resistance Mechanism in Ceramics: I. Experimental Study on Alumina," J. Am Ceram. Soc. 70 [4] 279-89 (1987).
13. P.F.Becher, E.R. Fuller, Jr., and P. Angelini, "Matrix-Grain-Bridging Contributions to the Toughness of Whisker-Reinforcrd Ceramics," J. Am. Ceram. Soc., (1991), in press.
14. J. Rödel, J.F. Kelly, and B.R. Lawn, "In Situ Measurements of Bridged Crack Interfaces in the SEM", J. Am. Ceram. Soc. 73 [11] 3313-18 (1990).
15. J. Rödel, J.F. Kelly, M.R. Stoudt and S.J. Bennison, "A Loading Device for Fracture Testing of Compact Tension Specimens in the SEM," Scanning Microscopy 5 [1] 29-35 (1991).
16. B.N. Cox and D.B. Marshall, "Determination of Crack Bridging Forces," Int. J. Fract., in press.
17. P. Chantikul, S.J. Bennison and B.R. Lawn, "Role of Grain Size in the Strength and R-Curve Properties of Alumina," J. Am. Ceram. Soc. 73 [8] 2419-27 (1990).
18. J. Bowling and G.W. Groves, "The Debonding and Pullout of Ductile Wires from a Brittle Matrix," J. Mat. Sci. 14 [2] 431-42 (1979).
19. V.C. Li, Y. Wang and S. Backer, "Effect of Inclining Angle, Bundling and Surface Treatment on Synthetic Fibre Pull-Out From a Cement Matrix," Composites 21 [2] 132-40 (1990).
20. R.O. Ritchie, "Mechanisms of Fatigue Crack Propagation in Metals, Ceramics and Composites: Role of Crack Tip Shielding," Mat. Sci. Eng. A103 [2] 15-28 (1988).

21. S. Lathabai, J. Rödel and B.R. Lawn, "Cyclic Fatigue from Frictional Degradation at Bridging Grains in Alumina," J. Am. Ceram. Soc. 74 [6] 1340-48 (1991).
22. H. Prask, C. Choi, E.R. Fuller, R.F. Krause, A. Krawitz and J. Richardson, "Micro-Stresses in Ceramic Composites," Annual Report, NIST Reactor Radiation Division, 1990.

NCAT-1- MECHANICAL PROPERTIES TESTING OF CERAMIC FIBER - CERAMIC MATRIX COMPOSITES

J. Sankar, A. D. Kelkar, and R. Vaidyanathan

Department of Mechanical Engineering
North Carolina A & T State University
Greensboro, North Carolina 27411

INTRODUCTION

Ceramic fiber-ceramic matrix composites fabricated by chemical vapor infiltration (CVI) are currently being developed as practical engineering materials because of their potential high toughness, especially at elevated temperatures. With continuing development through efforts such as in the present research, ceramic composites should find use in turbine and automobile engine components, recuperators, heat exchangers, and other high temperature applications.

Two methods of infiltration have been used to manufacture these ceramic matrix composites, namely, isothermal chemical vapor infiltration (ICVI) and forced chemical vapor infiltration (FCVI). The isothermal infiltration method has been developed by Societe Europeanne de Propulsion (SEP) and is currently licensed to Du Pont, USA. The forced infiltration method has been developed at the Oak Ridge National Laboratory (ORNL) which combines a thermal gradient and forced flow approach. The details of the above two processes and procedures have been discussed in detail elsewhere[1,2]. The advantage of the FCVI process over the ICVI process is that it results in significantly reduced infiltration times[1]. The aim of the present research is to collaborate with the ORNL staff to establish and expand the currently available mechanical property data base for these systems.

In this program, SiC fiber reinforced SiC matrix system developed through both the FCVI and ICVI methods will be investigated. FCVI samples will be supplied by the ORNL while the ICVI samples will be supplied by DuPont. The effect of the reinforcement and the interfacial bond of the composite on the tensile strength, thermal shock resistance, oxidation resistance, and tensile strength during cyclic loading, at temperatures up to 1000 ^{0}C, shall be investigated in the proposed work.

The effort comprises of the following tasks:

NCAT1-1 - Tensile strength - The objective of this task is to determine the uniaxial tensile strength and strain behavior of SiC fiber-SiC matrix composite at room temperature and at 1000 ^{0}C.

NCAT1-2 - Cyclic loading - The response of the SiC fiber-SiC matrix composite to cyclic loading is of considerable interest. The cyclic loading shall consist of loading the sample to about 10 % of the anticipated total load at failure and removing the load, reloading the sample to about 20 % of failure load etc. until failure. A tensile curve shall be determined in cyclic loading.

NCAT1-3- Thermal shock resistance - Fiber reinforced composites are exposed thermal shock during service. Therefore, the response of the material to this characteristic shall be determined.

NCAT1-4- Oxidation resistance - Fiber reinforced composites are exposed to extended service in oxidizing atmospheres. Therefore, the response of the material to oxidation shall be determined.

DISCUSSION OF CURRENT ACTIVITIES

The tensile strength characterization under NCAT1-1, NCAT1-2, NCAT1-3 and NCAT1-4 continued during the reporting period. The room temperature tensile testing part of NCAT1-1 was also completed during this period. The work concentrated during this quarterly were :

1. Room temperature uniaxial tensile testing.
2. Room temperature uniaxial tensile testing after exposure to thermal shock and oxidizing atmospheres.
3. Room temperature cyclic tensile loading tests.
4. Preparation of specimens for transmission electron microscopy (TEM).
5. Development of an analytical model using Plain-Weave Classical Laminate Theory (PWCLT) for the prediction of the mechanical properties of ceramic matrix composites.

Room temperature uniaxial tensile testing

During the reporting period, Forced CVI and Isothermal CVI SiC/SiC specimens were tested in uniaxial tension at room temperature. Two different lay ups were tested in each

type. $(0/30/60)_{repeated}$ and $(0/45/45/0)_{repeated}$ layups (supplied by the Oak Ridge National Laboratory) were tested in the FCVI case, while $(0/90)_{repeated}$ and $(0/45/90)_{symmetric}$ layups (supplied by Du Pont) were tested in the ICVI case. To facilitate a comparison with the values of tensile strength available in literature as well as between the individual layups, the tensile strength of all the specimens are given in Figure 1. The room temperature tensile strength and strain values are given in Tables 1 through 4. The results indicate that strength and strain exhibited by the forced CVI specimens were higher than the tensile strength and strain exhibited by the Isothermal CVI specimens. The $(0/30/60)_{repeated}$ FCVI specimens exhibited a tensile strength between 167 and 193 MPa (average = 181 MPa) and a strain of 0.7 %. The $(0/45/45/0)_{repeated}$ FCVI specimens showed a tensile strength between 130 and 207 MPa (average = 181 MPa) with a tensile strain of 0.96 % (average). In the case of ICVI materials, the $(0/90)_{repeated}$ specimens exhibited an average strength of 147 MPa, while the $(0/45/90)_{symmetric}$ specimens showed an average strength of 171 MPa and strain of 0.26%.

Typical stress strain curves for the FCVI and ICVI materials are given in Figures 2 and 3 respectively. It may be observed that the stress-strain behavior of the FCVI and ICVI materials are quite different. The FCVI materials exhibit much more nonlinear behavior (Figure 2) than the ICVI materials. In addition, the stress-strain behavior pattern exhibited by ICVI materials (Figure 3) shows some typical step pattern. Scanning electron microscopy of the fracture surfaces are currently underway to understand and correlate the stress-strain behavior to the fracture processes.

Room temperature uniaxial tensile testing after exposure to thermal shock and oxidizing atmospheres

Initial room temperature tension test results for FCVI and ICVI materials after exposure to thermal shock and oxidizing atmospheres are given in Tables 5 and 6. From the initial results, it may be observed that the tensile strength after thermal shock as well as exposure to oxidizing atmospheres did not degrade the tensile properties but rather, improved the total strain before failure.It appears therefore, that the toughness of this material improves after exposure to thermal shock and oxidizing atmospheres, which is a desirable improvement in the properties of this material.

Thermal shock was applied by heating the specimens to 1000 ^{0}C, holding for uniform temperature, and quenching to about 100 ^{0}C in about a minute using flowing air. Ten (10) such cycles of thermal shock were applied to each specimen. Exposure to oxidizing

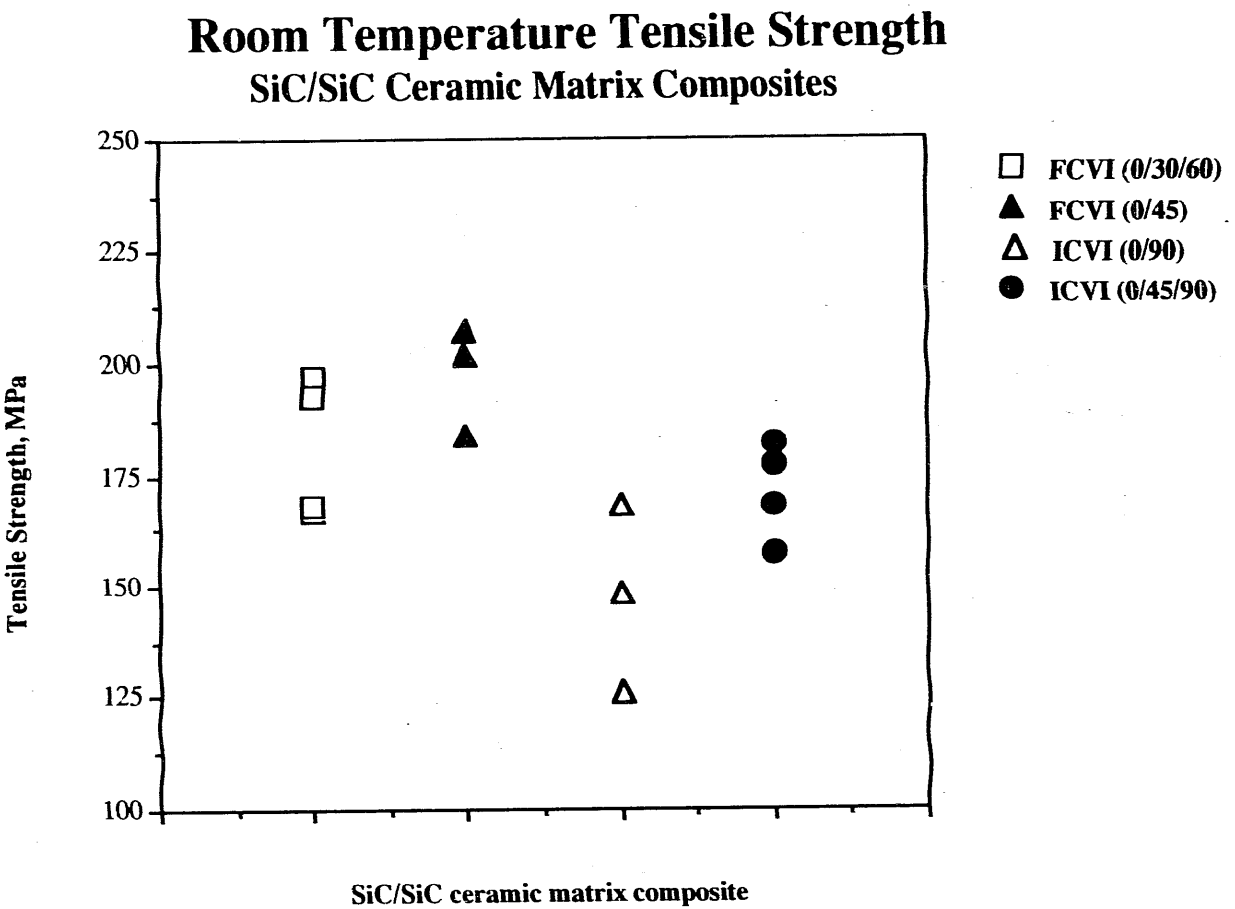

Figure 1. Room Temperature tensile data, SiC/SiC system

Table 1. Tension Test Results for FCVI SiC/SiC ceramic matrix composites at RT; $(0/30/60)_{repeated}$ layup

No.	Tensile Strength MPa (ksi)	Tensile Strain Inch/Inch	Remarks
1	167 (24.22)	Not measured	*
2	168(24.37)	Not measured	*
3	197(28.57)	Not measured	*
4	193(27.99)	0.00748	**; 420-6

Average Strength = 181 MPa (26.25 ksi)

* Specimens tested with ordinary mechanical wedge grips
** Specimens tested with wedge grips attached to self-aligning grip

Table 2. Tension Test Results for FCVI SiC/SiC ceramic matrix composites at RT; $(0/45)_{repeated}$ layup

No.	Tensile Strength MPa (ksi)	Tensile Strain Inch/Inch	Remarks
1	129.8(18.83)	0.0109	**; 411-2B
2	183.6(26.63)	0.00709	**; 411-3T
3	201.6(29.24)	Not measured	**; 411-2T
4	207(30.02)	0.01	***

Average Strength = 181 MPa (26.25 ksi); Average Strain = 0.0096

** Specimens tested with wedge grips attached to self aligning grip
*** Specimen tested by ATS Corporation

Table 3. Tension Test Results for ICVI SiC/SiC ceramic matrix composites at RT; $(0/90)_{repeated}$ layup

No.	Tensile Strength MPa (ksi)	Tensile Strain Inch/Inch	Remarks
1	126(18.27)	Not measured	**; Coupon 2
2	168(24.37)	Not measured	**; Coupon 4
3	Not measured	Not measured	Coupon 5; Specimen broke in handling
4	148(21.46)	Not measured	Coupon 7

Average Strength = 147 MPa (21.37 ksi)

** Specimens tested with wedge grips attached to self aligning grip

Table 4. Tension Test Results for ICVI SiC/SiC ceramic matrix composites at RT; $(0/45/90)_{repeated}$ layup

No.	Tensile Strength MPa (ksi)	Tensile Strain Inch/Inch	Remarks
1	181.8(26.37)	0.00228	**; Coupon 1
2	168.1(24.38)	Not measured	**; Coupon 2
3	157.5(22.84)	0.0032	**; Coupon 3
4	177.3(25.71)	0.00225	**; Coupon 4

Average Strength = 171 MPa (24.80 ksi); Average Strain = 0.0026

** Specimens tested with wedge grips attached to self aligning grip

Table 5. Tension Test Results for CVI SiC/SiC ceramic matrix composites at RT after Thermal shock

No.	Tensile Strength MPa (ksi)	Tensile Strain Inch/Inch	Remarks
FCVI (0/30/60)	199.61(28.95)	0.0148	**; 420-4
FCVI (0/45)	179.66(26.06)	0.0144	**; 411-4T
ICVI (0/90)	155.21(22.51)	0.0035	**; Coupon 8
ICVI (0/45/90)	110.84(16.08)	0.0023	**; Coupon 2

** Specimens tested with wedge grips attached to self aligning grip

Table 6. Tension Test Results for CVI SiC/SiC ceramic matrix composites at RT after exposure to oxidizing atmosphere for 100 hours

No.	Tensile Strength MPa (ksi)	Tensile Strain Inch/Inch	Remarks
FCVI (0/30/60)	204.83(29.71)	0.0090	**
FCVI (0/45)	110(15.95)	0.0006	**
ICVI (0/90)	139.61(20.25)	0.002834	**
ICVI (0/45/90)	105.36(15.28)	0.00266	**

** Specimens tested with wedge grips attached to self aligning grip

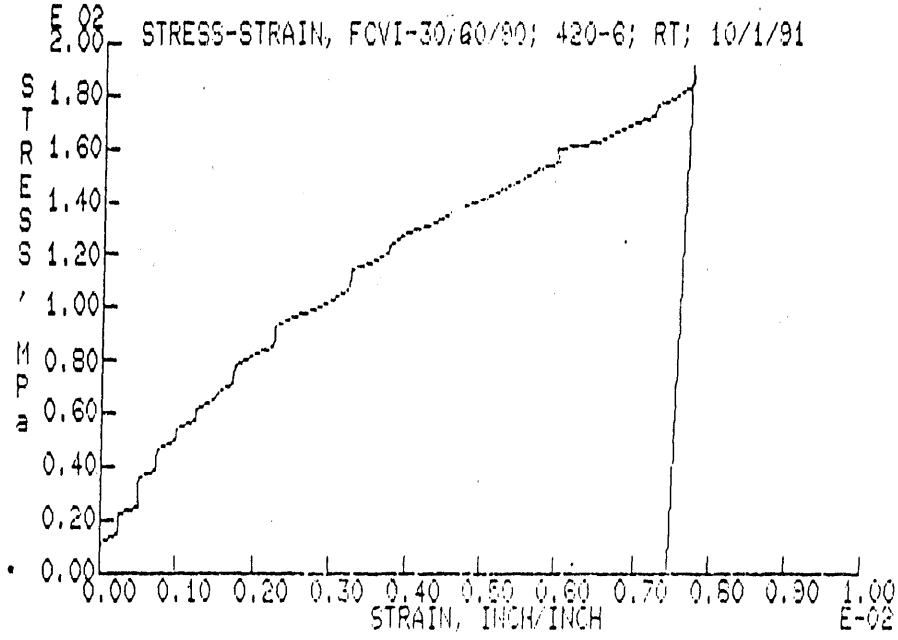

Figure 2. A typical stress strain curve for a (0/30/60)repeat layup FCVI material

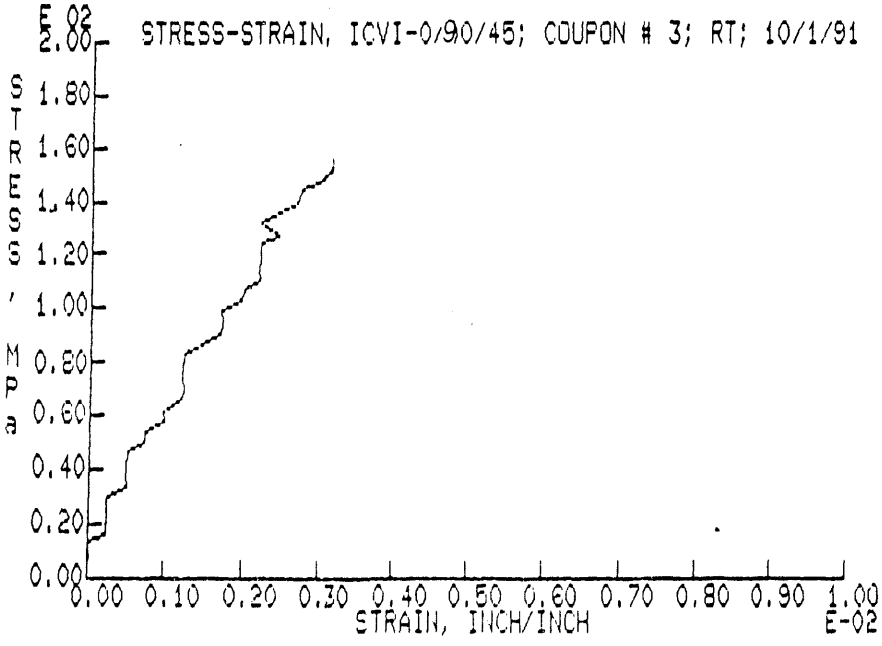

Figure 3. A typical stress strain curve for a (0/45/90)symmetric layup ICVI material

atmosphere was achieved by heating the specimens to 1000 ^{0}C, and holding for 100 hours. Typical room temperature stress-strain curves for the two types of FCVI materials after thermal shock are given in Figures 4 and 5. Comparing these with Figure 2, it can be observed that while the strength level is maintained, both the non linearity as well as the strain to failure increased. Similar behavior was also observed in the ICVI materials after thermal shock treatment.

Room temperature cyclic tensile loading tests

Cyclic tensile loading tests were also performed on one(1) specimen of each layups. Due to constraints placed on the total number of data points that could be acquired during the entire test by the current computer program and system, the obtained plots of stress-strain data could not provide any meaningful information. However, the tensile strength values obtained in these tests are correct and these are shown in Table 7. The computer program has already been modified to acquire the test data with the necessary sensitivity and tests are expected to be conducted soon. Initial test data showed that there was an improvement in the tensile strength after the cyclic tensile loading.

Preparation of specimens for transmission electron microscopy

Specimens are currently being prepared for the TEM analysis using the methods outlined in Stinton et al[3]. The TEM specimens are being prepared with the help of Ms. Karren More of ORNL by R. Vaidyanathan using ORNL dimpler and other facilities. Three specimens have been prepared so far. Future specimens will be prepared at North Carolina A & T. A proposal is also being prepared currently to use the User Center at the High Temperature Materials Laboratory at ORNL for TEM usage.

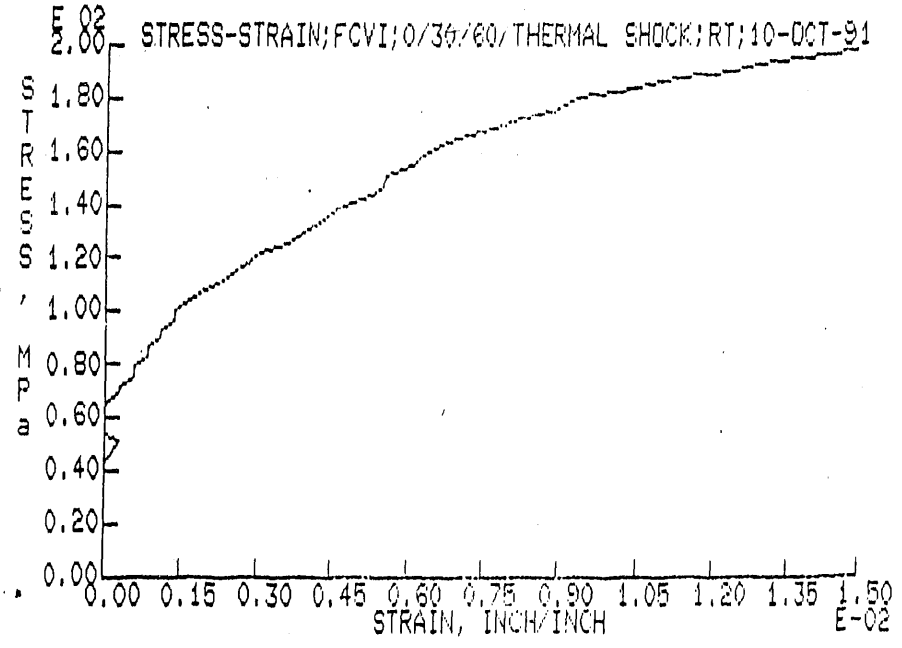

Figure 4. A typical stress strain curve for a (0/30/60)repeat layup FCVI material after thermal shock

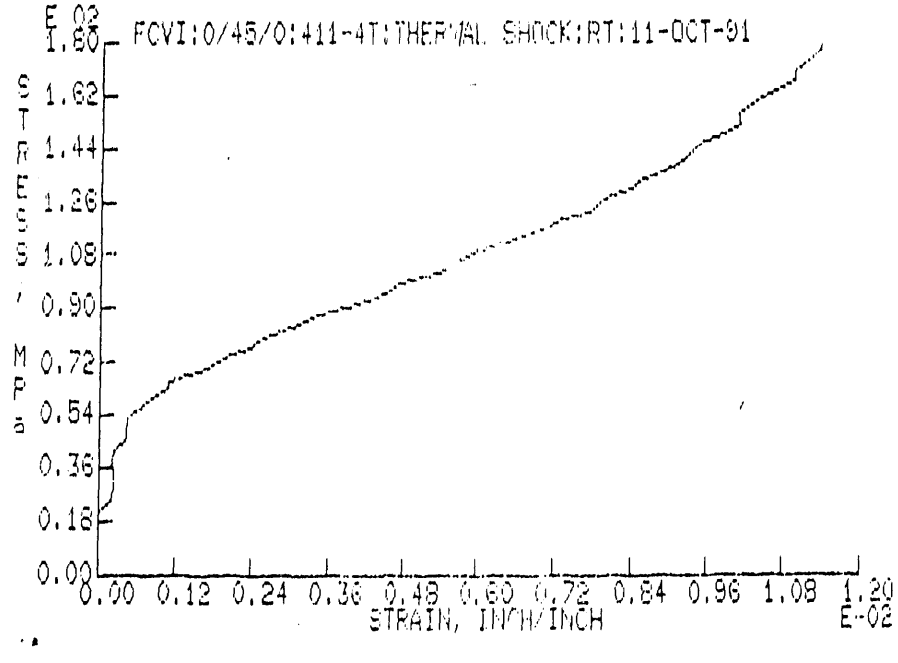

Figure 5. A typical stress strain curve for a (0/45)repeat layup FCVI material after thermal shock

Table 7. Cyclic Tension Test Results for CVI SiC/SiC ceramic matrix composites at RT*

No.	Tensile Strength MPa (ksi)	Tensile Strain Inch/Inch	Remarks
FCVI (0/30/60)	213.47(30.96)	Not measured	**
FCVI (0/45)	204.15(29.61)	Not measured	**
ICVI (0/90)	145.04(21.04)	Not measured	**
ICVI (0/45/90)	Not measured	Not measured	**

* Data acquisition procedure being modified to acquire stress and strain data at short intervals.

** Specimens tested with wedge grips attached to self aligning grip

Analytical Modeling

The aim of the analytical modeling study was to develop a model for the prediction of mechanical properties such as Young's Modulus, Poisson's ratio, and shear moduli for ceramic matrix composites, similar to polymeric matrix composites. The major objectives were :

a) To develop an analytical model to determine the mechanical properties of a single plain weave fabric composite;

b) To predict the mechanical properties of composite laminate fabricated by stacking single plain weave plies at various orientations;

c) To test the analytical model for graphite/epoxy woven composite with known experimental results; and,

d) To extend the model for woven SiC/SiC ceramic matrix composites with known experimental results.

The plain weave interlacing pattern used in these composites is shown in Figure 6. Figure 7 shows the unit cell representation of the plain weave pattern. Each unit cell has two Fill Tows (horizontal sets of fibers) and two Warp Tows (vertical sets of fibers). The x and y directions are along the midplane of the unit cell. The two thickness is assumed to be h_t, while the ply thickness is assumed to be 2h. The height of the matrix on the top and bottom of the unit cell therefore is = $(h- h_t)$.

The unit cell may be divided into three regions each, along the x and y directions. There are two regions with a length of a_0 each, where the properties of the unit cell are constant, while in the region with a length of a_u, the properties of the unit cell are assumed to be changing sinusoidally. The length a_u is called the undulation length.

From the knowledge of the individual constituent properties of the fibers and the matrix, an off-axis stiffness matrix (Q_{ij}) is obtained. By integrating Q_{ij} along the height, a reduced inplane, coupling, and bending stiffness matrix ($Qbar_{ij}$) for the unit cell is obtained. This reduced stiffness matrix is further integrated along a volume element to provide the inplane (A_{ij}), bending (D_{ij}), and coupling (B_{ij}) stiffness matrices for the unit cell. The details of the computation and derivations are given in reference 4.

The constituent material properties for Graphite/Epoxy and SiC/SiC systems are given in Table 8. The properties of the Graphite/Epoxy system were used to test the analytical model and the SiC/SiC system properties were used to extend the model to ceramic matrix composites (CMC). Since all the constituent material properties for the SiC/SiC system were not available, it was assumed that both the fibers as well as the matrix were isotropic. In real situations, this may not always be true.

A computer program PWCLT written in FORTRAN was used for calculating the properties of a single lamina of the fabric composite. The input/output format for using this program is essentially simple, and is given in Table 9. The results obtained for the Graphite/Epoxy system are given in Table 10. Two different packing densities were tested for the Graphite/Epoxy case : $p_d = 0.8$, and $p_d = 0.74$. It might be observed that the longitudinal and transverse modulii obtained using PWCLT are very close to the experimental values reported by NASA-Langley for the Graphite/Epoxy system. However, the Poisson's ratio reported and calculated by the PWCLT program varied by about 50 %. This discrepancy may be due to the fact that experimental evaluation of Poisson's ratio is extremely difficult and may lead to erroneous values. Experimental values for shear modulus for Graphite/Epoxy were not available during the course of this study.

The program PWCLT was then tested for the case of the SiC/SiC system. The results are shown in Table 11. The modulii as well as the Poisson's ratio obtained with the program PWCLT are very close to the experimental values reported in the literature. However, there is a considerable difference in the shear modulus reported and the shear modulus predicted by PWCLT. This may be due to the assumption made about the isotropic nature of the fiber and the matrix. However, the program PWCLT can accurately predict the mechanical properties provided accurate constituent property values are available.

The calculation of the mechanical properties of fabric ceramic matrix composites only requires the accurate knowledge of the constituent material properties for the fiber and the matrix. It does not require the development of a Finite element code and complex algorithms. The salient features of the PWCLT algorithm includes the input of fiber and matrix properties through a file. The program can be executed interactively and the desired properties can be obtained in real time. Once the properties of a single plain weave are known, then the classical laminate theory can be used to predict the mechanical properties of a laminate fabricated by stacking single plain weave plies at various orientations. The effect of packing density and different fiber volume fractions may also be calculated using this model. Experimental studies to correlate failure behavior and theories can help in the prediction of strength.

PRESENTATIONS AND PUBLICATIONS

1. Sankar, J., Kelkar, A. D., Vaidyanathan, R., "Mechanical Properties and Testing of Ceramic Fiber-Ceramic Matrix Composites", presented at the Poster session at the Fifth Annual Conference on Fossil Energy Materials, Oak Ridge, Tennessee, May 1991,

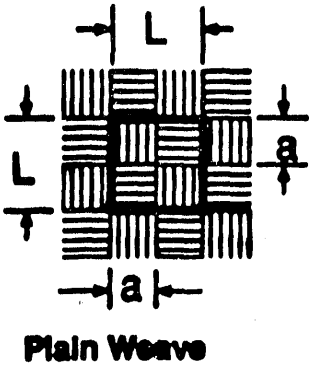

Figure 6. Plain weave interlacing pattern used in fabric composites

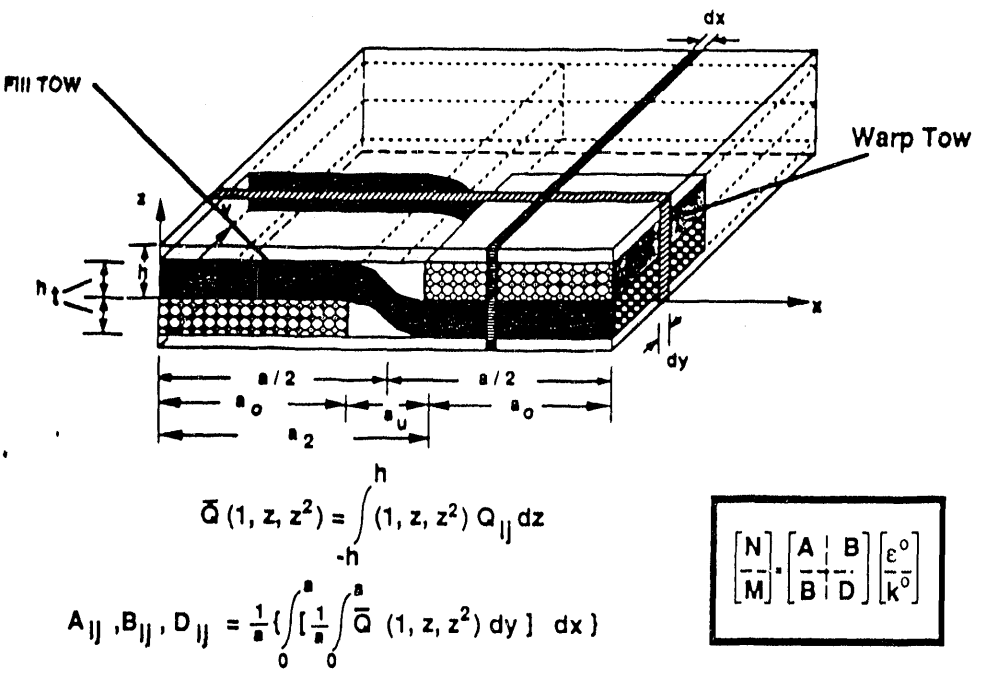

Figure 7. Unit cell representation of the plain weave pattern

Table 8. Constituent Material Properties for Graphite/Epoxy and SiC/SiC systems

Graphite/Epoxy	SiC/SiC
Fiber Properties	Fiber Properties
E_{11} = 22.0 Msi	E = 58 Msi
$E_{22} = E_{33}$ = 2.0 Msi	ν = 0.20
$\nu_{12} = \nu_{23}$ = 0.25	G = 24.1 Msi
ν_{23} = 0.40	
$G_{12} = G_{13} = G_{23}$ = 1.0 Msi	
Matrix Properties	Matrix Properties
E = 0.5 Msi	E = 13.3 Msi
ν = 0.35	ν = 0.15 (Assumed Value)
G = 0.185 Msi	G = 5.78 Msi

Table 9. Input/Output format for program PWCLT

INPUT

Unit cell sizes
a (Unit cell size), h (half ply height), h_t (tow height), V_f (fiber volume fraction), p_d (packing density), No. of materials

Fiber Properties
E_{11}, E_{22}, E_{33}, ν_{12}, ν_{13}, ν_{23}, G_{12}, G_{13}, G_{23}, Fiber orientation

Matrix Properties
E_{11}, E_{22}, E_{33}, ν_{12}, ν_{13}, ν_{23}, G_{12}, G_{13}, G_{23}

OUTPUT

Undulation length, Warp and Fill fiber volumes, Total unit cell volume, stiffness matrices, E_x, E_y, ν_{xy}, and G_{xy}

Table 10. Comparison of PWCLT model results with experimental results for Graphite/Epoxy Fabric Composite

	Plain Weave CLT (Vf = 0.64)		NASA Langley Experimental Values[5] (V_f = 0.64)
	p_d = 0.8, a_u = 0.0111 (N.C.A & T State Univ.)[5]	p_d = 0.74, a_u = 0.0075	
E_x, 10^6 psi	8.56	9.528	9.13
E_x, 10^6 psi	8.56	9.528	8.83
ν_{xy}	0.0516	0.0489	0.11
G_{xy}, 10^6 psi	0.837	0.890	-

Table 11. Comparison of PWCLT model results with experimental results for SiC/SiC Composite

	Plain Weave CLT (Vf = 0.46) p_d = 0.85, a_u = 1.8353, a = 4.0 (N.C.A & T State Univ.)	Experimental Values[6,7] (V_f = 0.4-0.5) Drexel Univ[6]	Du Pont[7]
E_x, 10^6 psi	37.5	34.8	33.0
E_x, 10^6 psi	37.5	34.8	33.0
ν_{xy}	0.19	0.19	0.18
G_{xy}, 10^6 psi	15.69	3.20	

published in Proceedings of the Fifth Annual Conference on Fossil Energy Materials, pp. 85-95, US DoE Fossil Energy Advanced Research and Technology Development and ASM International, (1991).

2. Kelkar, A. D., Sankar, J., Raju, I. S., and Vaidyanathan, R., "Analysis of Ceramic Matrix Composites using a Plain Weave Classical Laminate Theory", presented at the First Canadian International Composites Conference, Montreal, Canada, September 1991, to be published as part of Proceedings by Elsevier.

REFERENCES

1. A. J. Caputo, D. P. Stinton, R. A. Lowden and T. M. Besmann, "Fiber-reinforced SiC composites with Improved mechanical properties", *Am. Cer. Soc. Bull.*, **66**[2], pp. 368-72 (1987).

2. W. J. Lackey, and T. L. Starr, "Fabrication of Fiber-reinforced ceramic composites by chemical vapor infiltration: Processing, structure, and properties", pp. 397-450, in Fiber reinforced ceramic composites, edited by K. S. Mazdiyasni, Noyes Publications, NJ, USA (1990).

3. Stinton, D. P., Hembree, D. M., More, K. L., Sheldon, B. W., and Besmann, T. M., "Characterization of Ceramic Matrix Composites fabricated by chemical vapor infiltration", pp. 273-280 in Chemical Vapor Deposition of Refractory Metals and Ceramics, Materials Research Society Symposium Volume No. **168** edited by Besmann, T. M., and Gallois, B. M., Materials Research Society, Pittsburgh, PA, (1990).

4. Kelkar, A. D., Sankar, J., Raju, I. S., and Vaidyanathan, R., "Analysis of Ceramic Matrix Composites using a Plain Weave Classical Laminate Theory", presented at the First Canadian International Composites Conference, Montreal, Canada, September 1991, to be published as part of Proceedings by Elsevier.

5. Raju, I. S., Craft, W. J., and Avva, V. S., "Thermal Expansion Coefficients of woven fabric composites", Proceedings of the Advances in Structural testing, analysis and design (ICSTAD) conference, Vol. **1**, pp. 3-10, Bangalore, India, (July 1990).

6. Ko, F. K., "Preform Fiber Architecture for Ceramic Matrix Composites", *Am. Cer. Soc. Bull.*, **68**[2], pp. 401-414, (1989).

7. Preliminary engineering data on SiC/SiC composites, Du Pont De Nemours and Co. Inc.

ORGDP-1 - DEVELOPMENT OF CERAMIC MEMBRANES FOR GAS SEPARATION

D. E. Fain
G. E. Roettger
D. E. White
K. D. Adcock

Oak Ridge K-25 Site
P. O. Box 2003
Oak Ridge, TN 37831-7271

INTRODUCTION

There is much interest today in developing ceramic membranes having very small pores that would separate gas molecules on the basis of molecular size. This approach to separating gases is usually referred to as molecular screening or molecular sieving. Such ceramic membranes could potentially achieve very high separation factors and could be used for separating gases at high temperatures and in corrosive environments, i.e., in applications that could not be tolerated by polymeric membranes. Ceramic membranes could thus be used in a number of new applications that are outside the range of currently available membranes.

Development work being carried out at the Oak Ridge K-25 Site (K-25) for the current project has an initial goal of producing a ceramic membrane that will effectively separate hydrogen from gasified coal at temperatures of 1000°F or higher and at a feed pressure of 600 psi. This project utilizes experience and capabilities that are available at K-25 to design, develop, fabricate, and characterize inorganic membranes.

The specific objectives of this project for FY 1991 are shown below.

1. Issue report documenting FY 1990 membrane development work.
2. Complete upgrading of membrane fabrication equipment needed for preparation of smaller pore size membranes.
3. Demonstrate method for sealing ceramic membranes to metal to permit membranes to be tested at high temperature.
4. Demonstrate treatment procedure that will reduce membrane pore size to 3 to 5 angstroms (A).
5. Further develop theoretical model for gas transport to include effects of temperature.

DISCUSSION OF CURRENT ACTIVITIES

The following section of this report reviews membrane development activities during the second half of FY 1991. The discussion is of a general nature because some details of the membrane fabrication technology are presently classified as Confidential-Restricted Data. Efforts to finalize a declassification agreement that would permit the technology to be used for industrial applications are continuing.

Membrane Development

One of the primary goals of development efforts during the second half of FY 1991 was to reduce the pore size of K-25-produced ceramic membranes. Membranes having mean pore radii as small as 6.7A had been produced previously.[1] A mathematical model for gas transport through inorganic membranes, described in a recent report, indicated that a mean pore radius of 3A or smaller would be required to achieve high separation factors from molecular screening.[2]

Equipment Upgrading

To provide capabilities needed to fabricate membranes having smaller pores, work was completed during the second half of FY 1991 to permit operation of a much improved membrane fabrication system. A safety analysis was documented and approved for the system, and some compliance deficiencies in the laboratory facility (identified during plant-wide audits) were all resolved. Initial operation of the improved system has been achieved, which will impact results during the next report period.

Pore Size Reduction

Continued progress was made in developing procedures for preparing membranes with small pore size. At the present state of development, experimental alumina membranes have been produced and characterized that have mean pore radii as small as 5A as measured by the Dynamic Pore Size (DPS) test. The procedure being developed appears to offer good potential for reducing pore size further.

Pore Size Determination

At present, the lower limit of the DPS system is a measurement of the flow between a pore radius of 0 and 10A, for an incremental average of 5A. Thus, for membranes in which all the flow

through the membrane occurs between 0 and 10A, the average pore radius is assumed to be 5A, although it could be any value between about 2 and 10A. Preparations are currently being made to evaluate a modified test cycle (using inert carrier gases having a range of molecular sizes) that may permit the evaluation of the mean pore radius in that increment. An alternative approach for monitoring future development efforts to prepare membranes with smaller pore radii (3A or less) would be to measure pure gas flows with high precision using several inert gases having a wide range of molecular sizes. Preparations have been made to evaluate this approach as well as the modified DPS test cycle noted above. Unknown transport mechanisms that are different for these different gases could complicate this evaluation.

Separation Factors from Pure Gas Flow Measurements

Pure gas flow measurements have been obtained on recent alumina membranes having mean pore radii as small as 5A as measured by the DPS test. The flow measurements were made at room temperature using helium, nitrogen, and carbon dioxide as test gases. Separation factors for the gas pairs were calculated from the ratios of the pure gas specific flows. These calculated separation factors continued to agree well with values predicted by the current gas transport model for mean pore radii down to 5A. For example, the separation factors calculated from the pure gas flow data for the gas pair helium/carbon dioxide are plotted as a function of membrane pore size in Fig. 1 and compared with the calculations from the gas transport model. The data follow closely the trends predicted by the model. For the helium/carbon dioxide gas pair, the model predicts that the separation factor at room temperature will decrease as the pore size is reduced from about 12A to about 3A (due to surface flow effects). Below about 3A, the model predicts that the separation factor will increase very rapidly to very high values due to molecular screening effects.

Ceramic to Metal Seals

Another important objective of this project was to develop a method for sealing the ceramic membranes to metal components to permit the membranes to be tested at temperatures up to 1000°F. Past tests demonstrated that 446 stainless steel end pieces could be joined to the ends of the porous alumina tubes using an active metal brazing technique, but subsequent thermal cycling of the brazed assemblies often resulted in crack formation in the ceramic.[1] These results indicated a need to reduce stresses on the ceramic resulting from thermal expansion mismatch between the metal and ceramic components.

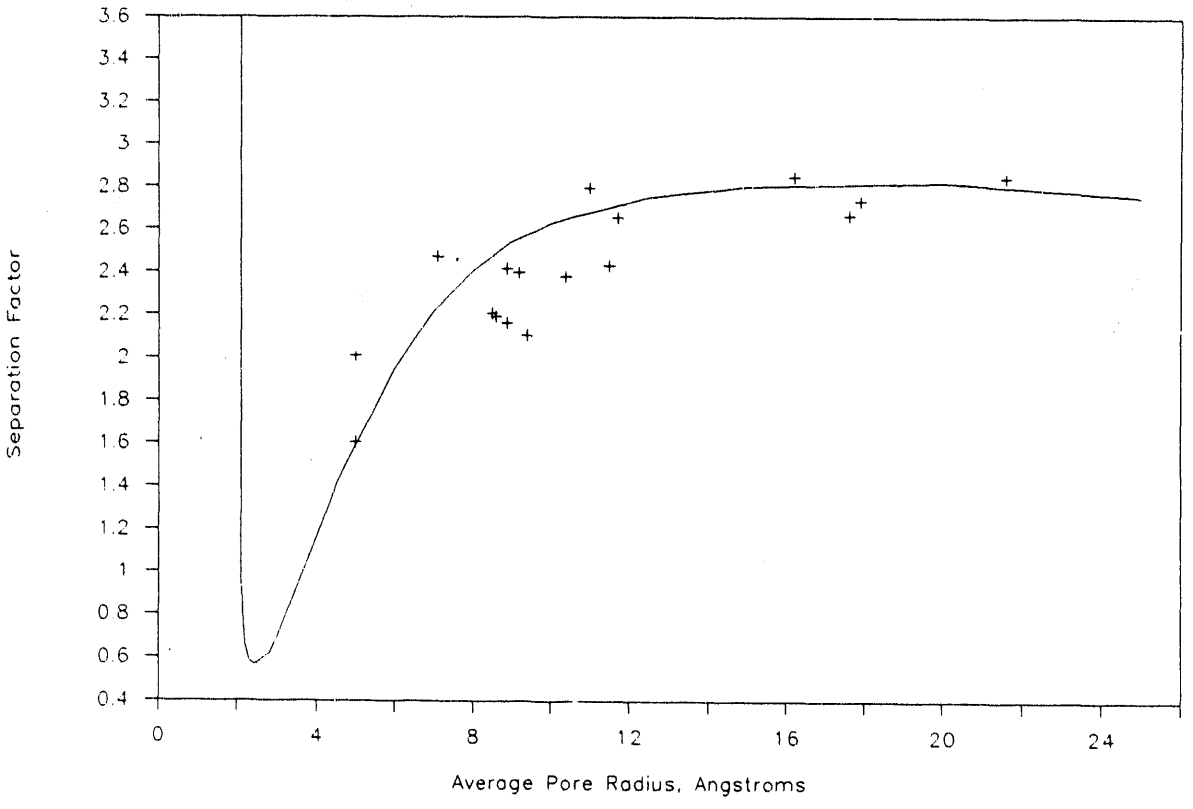

Fig. 1. Comparison of separation factors calculated from He and CO_2 pure gas flow data with calculations from the transport model.

To minimize stresses on the alumina membrane, a ring of niobium (which has a thermal expansion coefficient similar to alumina) was joined to the alumina tube and a stainless steel ferrule was joined to the niobium ring. An active metal brazing technique was used to join the three components in one brazing cycle. Test assemblies that were fabricated in this manner showed no evidence of damage to the ceramic following thermal cycling to 1000°F and back to room temperature.

This technique for sealing ceramic membranes to metal was applied to provide initial membrane assemblies for high temperature testing in the Oak Ridge National Laboratory (ORNL) flow test system. These assemblies were designed to match the size and flow rate capabilities of the ORNI test system. Each assembly included a section of ceramic membrane with niobium rings joined to both ends and stainless steel tubing joined to the niobium rings. Active metal brazing was employed to join all of the components in a single brazing cycle. Ongoing testing of these assemblies should provide flow data at temperatures up to 1000°F.

Gas Transport Model

Further development of the gas transport model to include the effects of temperature has been postponed until adequate flow data can be measured on membranes at elevated temperatures. Such data will be necessary to adequately interpret the transport modes to be included and to reliably evaluate the temperature dependence of the transport coefficients. However, a qualitative description can be given of the general trends that should be observed with a gas mixture and as pressure and temperature increase. Separation factors calculated for a mixture of helium and carbon dioxide based on the predicted pure gas flows for each gas are shown plotted against membrane pore size in Fig. 2. As the pore size decreases, surface flow of carbon dioxide increases and, therefore, the separation factor decreases. There is little or no surface flow of helium. The effective pore diameter for transport is the difference between the pore diameter and the diameter of the gas molecule. Since the carbon dioxide molecule is larger than the helium molecule, the diffusion coefficient and the effective area of the membrane decrease more rapidly (with decreasing pore size) for carbon dioxide than for helium. Therefore, at some very small pore size, the separation factor increases and a minimum in separation factor results. When the pore size becomes smaller than a carbon dioxide molecule but still larger than a helium molecule, only helium will be transported through the membrane and the separation factor becomes infinite.

As the pressure is increased, the adsorption of the carbon dioxide on the walls of the membrane increases. This adsorption decreases the effective pore size of the membrane and, thus, decreases the diffusion coefficient of the gas, decreases the effective area of the membrane and reduces the transport of carbon dioxide. For pure gases, there is not a corresponding decrease in the helium transport, since there is not much adsorption of helium. This effect results in higher apparent separation factors at higher pressures when the calculation is based on pure individual gas flows.

The model calculation based on individual pure gas flows is the proper comparison to make when the experimental separation factors are based on calculations from pure gas flow measurements. However, it should be recognized that these calculated results are not necessarily what should be expected for the actual separation factors for measurements with a gas mixture. The case for a gas mixture will be discussed below.

The situation is different for increasing temperature. As the temperature increases, the adsorption of gases on the walls of the membrane will decrease and the surface flow will eventually decrease. Then the transport should approach the ideal diffusion of finite size, hard

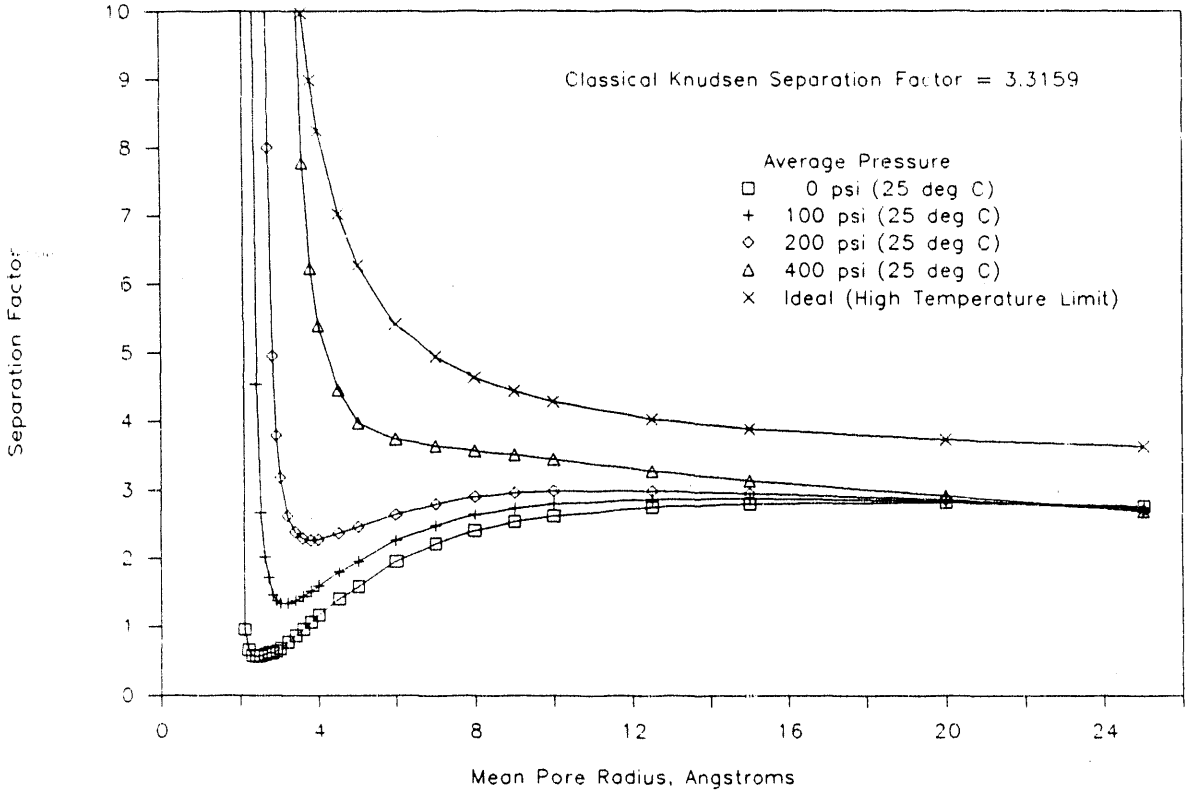

Fig. 2. Transport model calculations for He-CO_2 separation factors for various pressures at room temperature and at the ideal high temperature limit.

sphere molecules as indicated by the gas transport model. The separation factor for ideal diffusion of finite sized, hard sphere molecules in small pores is shown in Fig. 2 as the ideal high temperature limit. This particular curve is important because it shows that while the current measurements that have been made at room temperature indicate separation factors that are not particularly encouraging, it is expected that the separation factors should be much higher at higher temperatures. For example, this curve indicates that the currently achieved mean pore radius of about 5A should provide a separation factor of about 6.5 for helium/carbon dioxide if operated at a sufficiently high temperature. Correspondingly, a membrane with a mean pore radius of 3A should have a high temperature separation factor of about 17, a mean pore radius of 2.5A should have a separation factor of about 50, and a mean pore radius of 2A should be essentially infinite.

A similar plot is shown in Fig. 3, except that the transport is calculated for a mixture. In the case of a mixture, the adsorption of gas on the walls of the membrane will affect the transport of both gases rather than just the gas being adsorbed. This is the major source of the difference in the curves in Figs. 2 and 3. It should be noted that no momentum transfer between gases is assumed and since there is no surface flow of helium, there is no interference with the surface flow of the carbon dioxide. Figure 4 is a repeat of Fig. 2 on the same scale as Fig. 3 for better

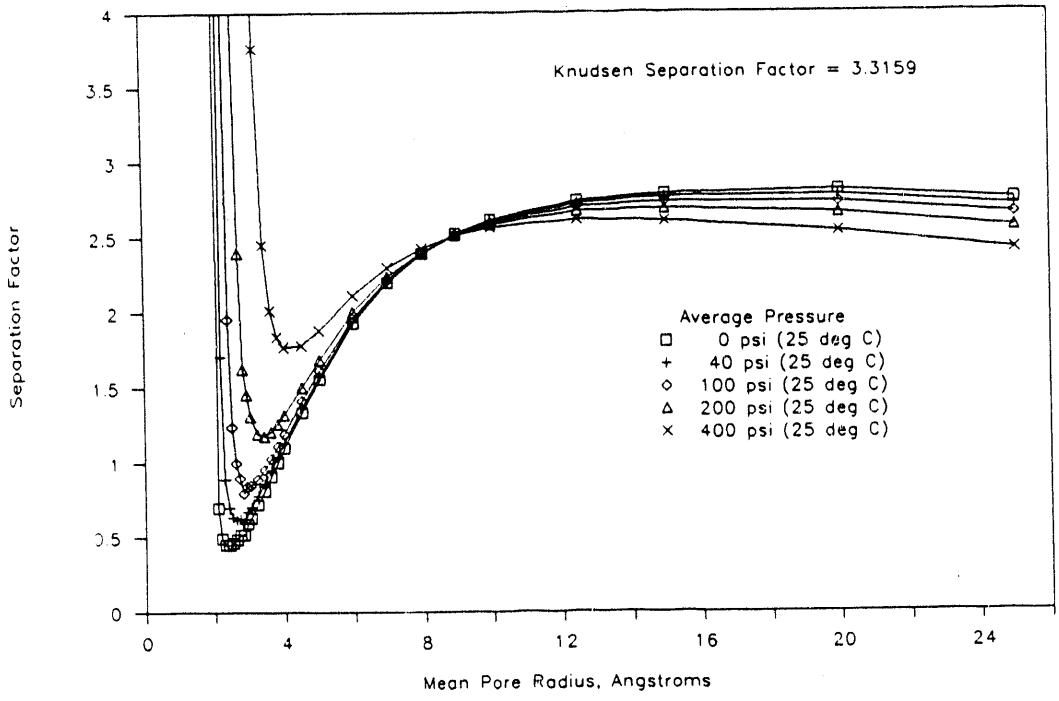

Fig. 3. He-CO_2 separation factors from gas transport model for gas mixture flows (without momentum transfer).

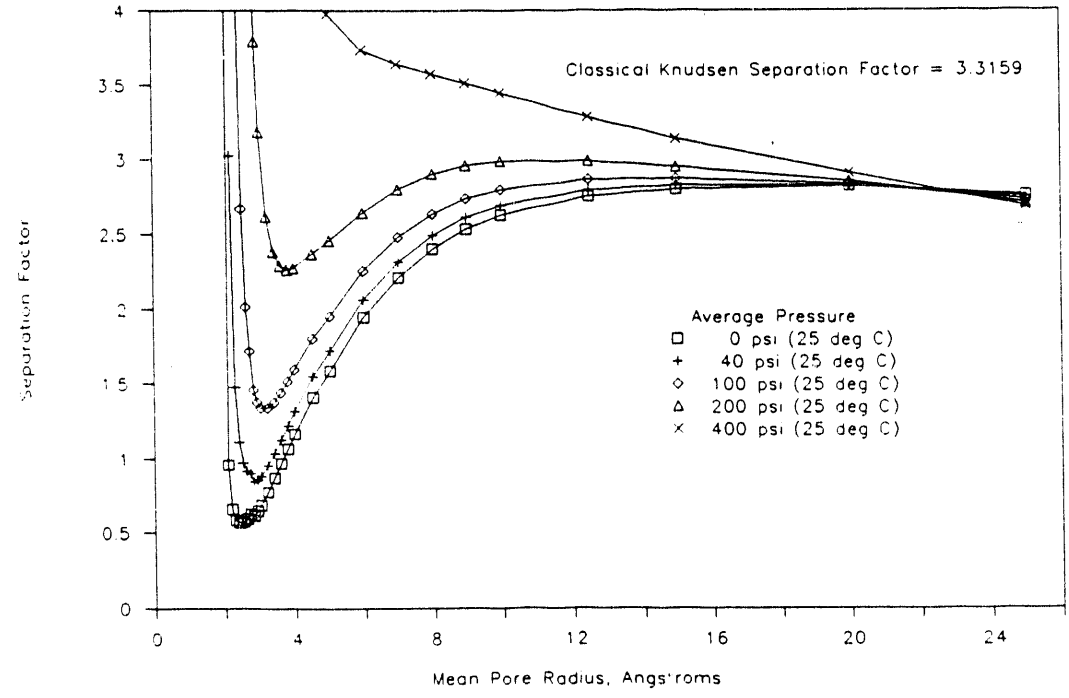

Fig. 4. He-CO_2 separation factors calculated from the gas transport model for individual pure gas flows.

comparison. The high temperature limit should be the same in both cases. Again, this indicates that the membranes currently being fabricated should have high separation factors when operated at sufficiently high temperatures. The separation factor calculated from the gas transport model for ideal diffusion of finite size, hard sphere molecules for several gas pairs is shown in Fig. 5. These may be assumed to be the separation factors that would be expected for operation at sufficiently high temperature.

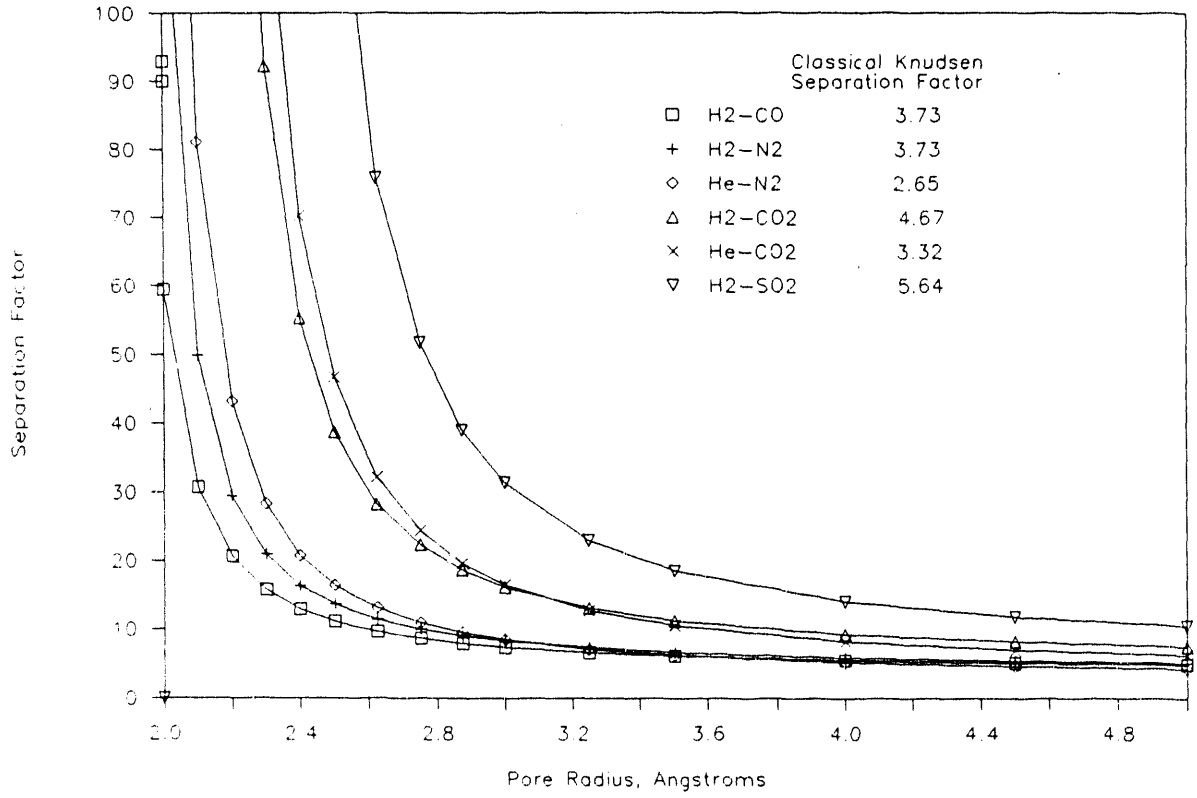

Fig. 5. Separation factors calculated for various gas pairs for ideal diffusion of finite size, hard sphere molecules.

REFERENCES

1. D. E. Fain, G. E. Roettger, D. E. White, "Development of Ceramic Membranes for High-Temperature Hydrogen Separation," in *Proceedings of the Fifth Annual Conference on Fossil Energy Materials*, ORNL/FMP-91/1, p. 55-64, Oak Ridge, Tennessee, May 14-16, 1991, Martin Marietta Energy Systems, Inc., Oak Ridge National Laboratory, Oak Ridge, Tennessee, September 1991.
2. D. E. Fain, G. E. Roettger, D. E. White, "Development of Ceramic Membranes for Gas Separation - FY 1990 Development Activities," K/QT-413, Martin Marietta Energy Systems, Inc., Oak Ridge K-25 Site, Oak Ridge, Tennessee, June 1991.

ORNL-1(A)-FABRICATION OF FIBER-REINFORCED COMPOSITES BY CHEMICAL INFILTRATION AND DEPOSITION

D. P. Stinton, R. A. Lowden, and T. M. Besmann

Oak Ridge National Laboratory
Oak Ridge, Tennessee 37831

INTRODUCTION

The purpose of this task is to develop a ceramic composite having higher than normal strength and toughness yet retaining the normal ceramic attributes of refractoriness and high resistance to abrasion and corrosion. Ceramic fiber-ceramic matrix composites are being fabricated by infiltrating fibrous structures with vapors that deposit on and between the fibers to form the matrix of the composites.

Background

Fiber composites are in the limelight as a result of exceptionally high toughness values recently achieved for glass ceramics reinforced with silicon carbide fibers. Because use of ceramics is frequently restricted by inadequate toughness, any progress toward toughening ceramics will greatly expand their potential market. However, a generic problem that must be overcome is that normal ceramic fabrication processes tend to damage fibers mechanically and chemically when the fibers are consolidated within a ceramic matrix. The purpose of this task is to form the matrix by a comparatively low-stress, low-temperature chemical vapor deposition (CVD) infiltration process that will avoid the pitfalls of conventional ceramic processing.

As reported previously, others have used CVD infiltration for fabricating ceramic composites. The vapor consolidation technique has been used to prepare fiber composites with matrices of carbon and/or such ceramics as SiC, Si_3N_4, B_4C, BN, and TiB_2.

Approach

Our goal is to demonstrate a rapid process for fabricating, via chemical vapor infiltration, a ceramic fiber-ceramic matrix composite consisting of materials of high interest to the fossil energy community. An initial assessment identified SiC fibers and matrices of Si_3N_4 and SiC as being promising. An infiltrating process utilizing a thermal gradient combined with forced flow of the reactants is being pursued.

DISCUSSION OF CURRENT ACTIVITIES

Infiltration of tubular preforms of different fiber architectures continued this period. Nicalon preforms of a tubular geometry (2.5 to 3.8 cm ID by 0.6 cm wall thickness by $\approx$ 15 cm long) were fabricated with different fiber architectures. Filament winding of fiber tows was used to fabricate components that require high hoop or radial strengths but relatively modest axial strengths. A fiber architecture of this type would be ideal for combustors or headers. Three dimensional braiding was used to fabricate components for applications such as burner tubes or heat exchangers that require high axial strengths but only modest hoop strengths. Preforms were also fabricated by wrapping layers of cloth around a mandrel so that half the fibers were in the hoop direction and half in the axial direction.

Filament wound preforms formed on graphite mandrels were prepared by the K-25 Plant in Oak Ridge. The graphite mandrels contained hundreds of holes to permit ready access of reactant gases to the fibrous preform. Preforms were produced with the fibers 10° off the hoop direction to insure adequate axial strength. Initially, space was left between fiber tows, however, large pores were aligned on top of each other. The winding technique was then modified to place adjacent tows in contact. This winding technique produced a density of about 47 vol % and prevented the formation of large pores in the preform.

Quadrax Corporation prepared 3D braided preforms on graphite mandrels for this study. The initial tubes were braided very loosely and contained only about 15 vol%

Nicalon fibers. Near the ends of the preforms, the braided fibers were bound to the graphite mandrel with graphite yarn to prevent the braid from unraveling. Infiltration of such a low density preform proved to be impossible with the forced CVI process. Therefore, researchers at Quadrax Corporation modified their process in order to fabricate tubes containing up to 40 vol % Nicalon fibers.

A process was developed to fabricate preforms for hot-gas filters that combines continuous and chopped fibers. The continuous fiber produces the strength, damage tolerance, and thermal shock resistance while the chopped fibers control the permeability and filtering efficiency of the filter surface. One further advantage of the process is that expensive Nicalon fibers can be replaced by less expensive chopped alumina or Nextel fibers. Because of the reduced cost, hybrid preforms may also find application in heat exchangers or regenerators where strength requirements are quite modest. Hybrid preforms are fabricated by fiber molding chopped fibers into the open pores of braided or filament wound substrates. Hybrid preforms have proven to be ideal for hot gas filter applications. Full size candle filters (1.5 m long by 6cm diam.) have been fabricated and are being tested at The 3M Company.

The forced chemical vapor infiltration process was recently modified so that tubular preforms could be infiltrated by creating a thermal gradient from the outside of the tube to the inside.(Fig 1) While the outside of the preform is heated, cold water is circulated through the stainless steel injector to cool the inside diameter of the fibrous preform. The gaseous reactants enter the furnace through tubing that runs within the water cooling passage. Reactants flow from the tubing in the cooling passage into a graphite gas distributor and are dispersed along the length of the preform through parallel slots in a graphite gas distributor. Reactants then proceed uniformly through holes in the graphite mandrel into the preform.

Densification of the tubular preforms occurs when hydrogen and methyltrichlorosilane (CH_3SiCl_3 or MTS) flow through the mandrel. Decomposition of the MTS and deposition of SiC occurs as the gases approach the higher temperature regions near the outer diameter of the preform. Deposition of SiC within the hot region of the preform increases the density and thermal conductivity of the material. Therefore, the deposition zone moves from the outer diameter, hotter regions toward the inner diameter, cooler regions.

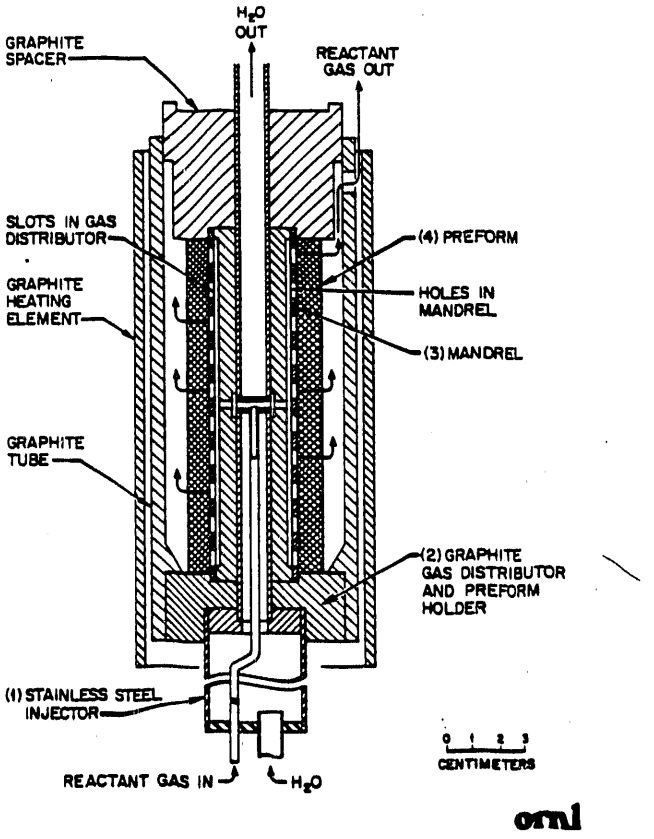

Fig. 1 Schematic of the forced CVI process used to infiltrate tubular composite.

Filament wound preforms were effectively infiltrated from the outset using this system. The high fiber content of the preform produced a sufficient backpressure within the preform to disperse the reactants along the length of the tube allowing them to flow uniformly through the walls of the preform. The hottest regions of the preform densified first, however, which forced reactants into less dense areas of the preform. The microstructure of filament wound composites demonstrate that the limited amount of porosity is distributed uniformly through the thickness.

Braided preforms were much more difficult to infiltrate than filament wound preforms. Braided preforms with a fiber content of only 15 vol% were investigated initially. The low fiber content and large gaps between fiber bundles created voids that extended through the thickness of the preform. Because of these voids, no backpressure

was created by the preform to disperse reactants along the length of the tube. Therefore, reactant gases entered the center of the preform and flowed directly through the walls so rapidly that very little SiC was deposited. Preforms that had been braided to a fiber loading of 33 vol % were also infiltrated. The porosity created by this braid was uniformly distributed, however the permeability was relatively high and reactants moved through the preform very rapidly. The high permeability of the preform failed to distribute the reactants uniformly along the length of the preform. More of the gases flowed through the center of the preform causing greater deposition near the center than near the ends of the preform. Braided preforms with still higher densities (i.e. reduced permeabilities) will be required to obtain proper infiltration.

Preforms fabricated for use as hot-gas filters or heat exchangers containing braided continuous fibers and fiber molded chopped fibers were also investigated. Since chopped fibers are much less permeable to gases than cloth, the hybrid preform created a significant backpressure that dispersed the reactants along the length of the tubular preform. Infiltration proceeded as desired. The reactants entered the preform, dispersed along the length of the preform, and flowed slowly through the walls of the preform. The uniform movement of reactants through the preform resulted in SiC being deposited in the hot outer region of the tube. After sufficient densification occurred, the infiltration proceeded to the center and inner diameter of the preform.

The characterization of tubular SiC matrix composites reinforced with Nicalon fibers has been very limited. C-ring compression testing was performed on one filament wound 3.8 cm diameter (6 mm wall thickness) tubular composite. The 16 cm long tubular composite was cut into 6mm thick C-ring specimens. Room temperature compression testing of three of these rings ranged from 777 MPa to 842 Mpa. Testing at 1000°C resulted in slightly lower strengths that ranged from 574 to 603 MPa. Composites reinforced with braided or filament wound preforms are currently being fabricated for tension/torsion testing at room and elevated temperature.

ORNL-1(C)-INTERFACES AND MECHANICAL PROPERTIES OF CONTINUOUS FIBER-REINFORCED CERAMIC COMPOSITES

R. A. Lowden

Oak Ridge National Laboratory
P. O. Box 2008
Oak Ridge, TN 37831-6063

INTRODUCTION

The purpose of this task is to examine fiber-matrix interfaces and optimize the mechanical behavior of continuous fiber-reinforced ceramic composites fabricated utilizing a forced-flow, thermal-gradient chemical vapor infiltration technique (FCVI). The strength and toughness of fiber-reinforced ceramic composites are controlled by the properties of the interface between the fiber and the matrix, thus emphasis is to be placed on developing methods to characterize the fiber-matrix interface and measure interfacial stresses in fiber-reinforced ceramic composite systems. Coating or pretreatment processes can then be utilized to tailor the fiber-matrix interface within various composite systems and to optimize the strength and toughness of the composite.

DISCUSSION OF CURRENT ACTIVITIES

Oxidation Resistant Interlayers

To date, emphasis in the development of continuous fiber-reinforced ceramic composites has been placed on processing and mechanical properties. Ceramic and glass-ceramic matrices are being reinforced with ceramic fibers and filaments, and moderate quantities of these materials are being fabricated using a variety of techniques. Although exceptional room and elevated temperature properties have been reported, only limited information has been presented regarding the stability of these composite systems in corrosive or simulated service environments. High temperature corrosion can have detrimental effects

must be addressed before final acceptance of these materials for critical components in elevated-temperature commercial applications.

It is well known that although the fibers and matrix play major roles in determining the final properties of a composite, the fiber-matrix interface has a significant influence on the fracture behavior and mechanical properties of reinforced ceramics. Typically, coatings are used to protect ceramic fibers from chemical attack during processing and to control interfacial forces. Carbon, whether intentionally deposited on the fibers prior to consolidation[1,2] or formed serendipitously during processing,[3] is the most commonly used interlayer in ceramic composites today. Carbon coatings have performed well in a variety of systems; including the Nicalon/SiC composites which have been the subject of this work. However, the poor oxidation resistance of carbonaceous materials has prompted intense scrutiny of their usefulness at elevated temperatures in oxidizing environments.

Carbon begins to oxidize at temperatures around 700 K and oxidation is rapid in air at temperatures above 1173 K. It has been shown that the oxidation of Nicalon/SiC composites with a graphitic carbon interlayer begins by attack of the carbon interface coating at exposed fiber ends.[4-6] Once the carbon is removed along the entire fiber length, the matrix and fiber oxidize to form a silica layer that eventually bonds the components together. The strong bond at the fiber-matrix interface does not permit fiber debonding and sliding, resulting in brittle behavior. Also, oxidation degrades the properties of the fiber, enhancing the embrittlement of the composite.

This poor oxidation resistance of carbon has lead to the examination of alternate coating materials or concepts for controlling the force at the fiber-matrix interface in ceramic-ceramic composites. Many factors must be considered in the selection of materials for interlayers in high-temperature composite systems. Chemical compatibility with the fibers and matrix, elevated temperature stability, and oxidation resistance are obvious requirements for an interface coating, however, the mechanical and physical properties of the coating also play an important role in determining interfacial bonding and shear stresses.

The theoretical aspects of thin films at the interface in whisker- and fiber-reinforced ceramic composites and their effects on the stresses due to thermal expansion mismatches have been examined.[7] A reduction in thermomechanical stress is suggested only when a low modulus interfacial coating is present. For many composites, the matrix has a higher thermal expansion than the fiber thus upon cooling from processing temperatures, a clamping of the fibers occurs. An interlayer must alter the compressive stresses at the interface to permit

debonding and produce low interfacial shear stress. A coating that is able to deform (ie. low modulus), can act as a buffer layer and accommodate a portion of the residual clamping stress of the matrix, thus controlling interfacial shear and frictional forces.

Few materials possess all of the properties essential for the ideal interface layer, but as described, a graphitic carbon coating has proven to perform well in numerous ceramic composite systems including fiber-reinforced glasses and ceramics and SiC whisker-toughened alumina. It appears that the presence of the carbon interlayer alters the stresses at the interface.[8,9] Graphitic carbon possesses an extremely low modulus along the c-axis. It is hypothesized that the carbon coating is able to deform and act as a buffer layer, accommodating a portion of residual clamping stresses of the matrix that occur due to thermal expansion differences between the fiber and matrix. The thickness of the carbon coating influences the clamping stress on the fiber and thus controls interfacial shear stress. Interfacial shear strength was shown to be inversely proportional to fiber coating thickness. Thicker coatings produce lower interfacial shear stresses because they are able to absorb more of the stress caused by the thermal expansion mismatch of the components.

But again, carbon oxidizes at low temperatures, and thus other materials with mechanical and physical properties similar to carbon but possessing improved oxidation resistance are being examined. Much of the work on alternate interface coatings for silicon-based composite materials has paralleled the efforts to improve the oxidation resistance of carbonaceous materials, such as structural graphite and carbon-carbon composites. These efforts have focused on the development of glass forming materials, specifically glasses with melting temperatures and viscosities lower than that of pure silica. Boron is the most frequently studied addition to silica-forming materials for service temperatures around 1273 K (1000°C).[10-15] The boron lowers the melting point of the glass that forms during oxidation. This allows the formation of a glass which will form and flow more readily at lower temperatures, offering improved protection for the composites in various relevant environments.

Hexagonal boron nitride posseses a structure and mechanical properties similar to those of graphite, however, due to the presence of boron, BN offers a distinct improvement in oxidation resistance. BN has been examined as an interface layer in this program in the past, but with the exception of a small sample of CVD coated fabric*, all previous experiences with BN-coated Nicalon were disappointing. Attempts to deposit polycrystalline-BN layers

on the fibers using CVD techniques resulted in extensive damage to the fibers and amorphous deposits produced at low temperatures decomposed at room temperature.

Favorable results were obtained from the limited supply of CVD-coated fabric and there have been reports of improved long-term oxidation resistance for BN coated fibers in analogous composite systems. This prompted the re-evaluation of BN as an interface layer. Fibrous preforms and individual fabric layers have been coated with BN using techniques similar to those used in the deposition of the carbon interface coatings. Boron trichloride and ammonia were reacted in hydrogen at 1373 K and 0.033 atm, conditions similar to those for the standard carbon interface coating. Deposition conditions were varied to alter the composition and the thickness of the interlayer. Experimental conditions were determined to deposit the appropriate interlayer composition and structure at rates similar to those for the graphitic carbon fiber coating. Although the strengths of the coated fibers were not measured, the fibers remained flexible and intact after deposition. The preforms have been densified with a SiC matrix using the FCVI process. Specimens for mechanical property testing, corrosion studies, and electron microscopy characterization are being prepared. The results of the characterization and testing will be compared to previous studies of the composites with a carbon interlayer.

Boron or borate glass additions have been used to improve the oxidation resistance of carbon and carbon-carbon composites.[13-15] A similar approach is being examined to enhance the oxidation properties of the fiber-matrix interface coating. Boron is being added to the carbon interlayer during deposition process, again employing previously established techniques. Boron trichloride and hydrogen were introduced to the argon-propylene gas mixture that is typically employed to deposit the graphitic carbon interlayer. The addition of the BCl_3 and H_2 produces boron carbide dispersions in the carbon layer. Upon oxidation, B_2O_3 galss will form and hinder further attack of the interface coating. The amount of boron in the layer is being varied. The experiments will determine the feasibility of this approach as well as the quantity of boron needed to provide adequate protection. Composites are being fabricated from the coated preforms, and both corrosion and flexure specimens are being prepared. The effects of the boron additions on the mechanical properties of the interface and composites, and the oxidation resistance of the material will be evaluated.

* Produce by Comurhex, CVD Department, Pierrolette, France.

Sol-Gel Oxide Interlayers

Chemical vapor deposition is one of numerous methods that have been employed for the deposition of thin layers on the surface of fibers. Sol-gel techniques have also proven useful for producing coatings on fibers, especially for oxide coating compositions. Nicalon fabric samples were coated with oxide layers by Dr. Jay E. Lane at Westinghouse Science and Technology Center, Pittsburgh, PA. Eight oxide compositions of two thicknesses were applied to Nicalon plain weave cloth using sol-gel techniques. The coatings included alumina, mullite, Ca-doped cordierite, alumina-magnesia-yttria, titania, zircon, zirconia, and Y-doped zirconia. The coated fabric samples were used to fabricate composites so that the effectiveness of oxide interlayers could be examined.

Nicalon fabric samples coated with the aforementioned oxide layers were incorporated into a SiC matrix employing the Forced CVI technique. Flexure specimens were prepared from the composites and tested in four-point bending. The mechanical property testing of the composites was paralleled by thermochemical evaluation of the chemical stability of the oxides as an interlayer in a non-oxide system as well as the survivability of the oxide layers during FCVI processing. The calculations required the addition of numerous compounds to the data base used by the SOLGASMIX-PV program.[16] Extensive review of the literature and of the many oxide phase diagrams was necessary to complete the information. The calculations were used to aid in determining the most promising interface coating compositions and to assess the stability of the coatings in the Nicalon/SiC system during fabrication and in service.

The thermomechanical aspects of the oxide interlayers were also considered. Following guidelines outlined by Hsueh, et al.,[7] calculations were performed to examine the effect of the oxide layers on the residual stresses in the system upon cooling from CVI processing temperatures. The axial and radial forces were examined, and the theoretical effectiveness of each material was addressed. The calculations were used to determine which oxides may potentially reduce interfacial shear stresses and ana;lyze the effect of interlayer thickness on residual stresses. The latter can be used to determine an approximate optimum thickness for each oxide composition.

SiC composites containing Nicalon fabric samples coated with alumina, titania, and

zirconia performed well in the initial room temperature flexure tests. The test results support the theoretical calculations that predicted reductions in the residual stresses at the fiber-matrix interface in the Nicalon/SiC system when using the aforementioned oxides. The decrease in residual stresses at the interface are necessary to permit fiber debonding and slip, and produce the desired gradual composite failure. Remaining pieces of coated fabric and the composites fabricated from such are being examined employing electron microscopy techniques. Coating compositions and integrity are being evaluated to facilitate the procurement of larger quantities of fabric coated the aforementioned materials. Composite specimens are to be fabricated to examine the long-term stability and corrosion resistance of Nicalon/Sic composites with oxide interlayers. Primary control of this work has been transfered to D. Matthew Walukus and will be completed under WBS Element UT-1.

Interlayer Property Effects

In previous periods, the influence of the fiber-matrix interface on the mechanical properties of Nicalon/SiC composites was investigated. Emphasis was placed on determining the relationships between interfacial forces and the flexure behavior of the composites, specifically matrix cracking stress, ultimate strength, and work of fracture, ie. toughness. Interesting correlations between interlayer thickness, interfacial forces, and mechanical properties have been observed[1,2,8,9], however, little attention has been given to the effects of the interface on the interlaminar properties of the Nicalon/SiC composites. Therefore, composite specimens with varying interfacial properties have been fabricated to examine the influence of interfacial shear stress on the interlaminar and impact properties of the materials.

As before, the thickness of the carbon layer has been varied to control the forces at the fiber-matrix interface. Shear and impact specimens have been prepared and are currently being tested. Composites with graphitic carbon coatings ranging in thickness from 0.03 to 1.25 μm were fabricated. Flexure bars were prepared from each of the composites. The specimens were cut parallel to the 0° orientation of the top layer of cloth using a diamond saw, and tensile and compression surfaces were ground parallel to the long axis of the specimen. The average dimensions of the specimens samples were 3 $\times$ 4 $\times$ 50 mm and all were measured and weighed to determine densities. Room temperature flexure strengths were measured in four-point bending using a support span of 40 mm, a loading span of 20

mm, and a crosshead speed of 0.508 mm/min. All specimens were loaded perpendicular to the layers of cloth. Load-displacement curves were recorded to examine the fracture process and were used to determine the loads for matrix fracture and ultimate strength. In general, a single matrix crack was observed in the tests and was noted as a sudden drop in the load-displacement curve and/or deviation from linearity. Flexure strengths are listed in Table 1.

Shear specimens and impact samples were also prepared from the composites. Both types of coupons were cut with the long axis parallel to the 0° orientation of the fabic lay-up. The average dimensions of the specimens for the shear and impact specimens were 10 x 20 x 3 mm and 6 x 6 x 50 mm, respectively. Again, all were weighed and measured to determine densities. Notches approximately 0.3 mm were cut across the 10 mm width at 5 mm from each end and on opposites sides of the shear specimens. Chevron notches were cut at the midpoint along the length of the impact specimens.

The shear specimens were tested at room temperature in compression with a cross head speed of 0.508 cm/min. The Chevron notch are being used to measure the work of fracture, or toughness, of the Nicalon/SiC composites with varying interfacial shear strengths. Both slow testing in three point bending, and rapid testing in impact, are being conducted, and the measurements compared. The results will be used to further optimize the mechanical properties of the Nicalon/SiC composites. Table 1 also gives the shear measurements for the samples.

Table 1. The influence of the carbon layer thickness on the properties of Nicalon/SiC composites.

Carbon Deposition Time (h)	Approximate Interlayer Thickness (μm)	Average Flexure Bar Density (g/cm^3)	Room Temp. Flexure Strength (MPa)	Room Temp. Shear Strength (MPa)
0.00	0	2.58 ± 0.09	64 ± 11	9 ± 4
0.25	0.03	2.54 ± 0.07	273 ± 30	25 ± 10
0.50	0.06	2.64 ± 0.06	402 ± 24	32 ± 4
1.00	0.13	2.59 ± 0.06	421 ± 27	29 ± 4
2.00	0.27	2.60 ± 0.08	399 ± 28	25 ± 2
4.00	0.61	2.54 ± 0.05	304 ± 30	20 ± 4
8.00	1.25	2.58 ± 0.06	271 ± 32	21 ± 3

REFERENCES

1. Lowden, R. A., *Characterization and Control of the Fiber-Matrix Interface in Ceramic Matrix Composites,* ORNL/TM-11039, Oak Ridge National Laboratory, (March 1989).

2. Lowden, R. A., and K. L. More, "The Effect of Fiber Coatings on Interfacial Shear Strength and the Mechanical Behavior of Ceramic Composites," *MRS Symposium Proceedings, Vol. 170, Tailoring Multiphase and Composite Ceramics* (March 1989).

3. Brennan, J. J., "Interfacial Characterization of Glass and Glass-Ceramic Matrix/Nicalon SiC Fiber Composites," *MRS Proceedings, Vol. 20, Tailoring Multiphase and Composite Ceramics,* ed. R. E. Tressler et al., Plenum Publishing Corporation, 549-560 (1986).

4. R. A. Lowden and R. D. James, *High Temperature Corrosion of Nicalon/SiC Composites*, ORNL/TM-11893, August 1991.

5. R. A. Lowden and R. D. James, "Effects of Oxidation and Combustion Environments on the Properties of Nicalon®/SiC Composites," *Proceedings of the Fifth Annual Conference on Fossil Energy Materials*, ed. by R. Judkins, Oak Ridge, TN, May 15-17, 1991.

6. R. D. James, R. A. Lowden, and K. L. More, "The Effects of Oxidation and Corrosion on the Properties of Nicalon®/SiC Composites," pp. 925-935 in *Ceramic Transactions*, Vol. 19, Advanced Composite Materials, ed. by Michael D. Sacks, The American Ceramic Society, Westerville, Ohio (1991).

7. Hsueh, C.-H., P. F. Becher, and P. Angelini, "Effects of Interfacial Films on Thermal Stresses in Whisker-Reinforced Ceramics," *J. Am. Ceram. Soc.* 71(11), 929-933 (1988).

8. R. A. Lowden, "Fiber Coatings and the Mechanical Properties of a Fiber-Reinforced Ceramic Composite," pp. 619-630 in *Ceramic Transactions*, Vol. 19, Advanced Composite Materials, ed. by Michael D. Sacks, The American Ceramic Society, Westerville, Ohio (1991).

9. R. A. Lowden, "Interface Effects and Fracture in Nicalon/SiC Composites," pp. 97-114 in the *Proceedings of the Fourth Annual Conference on Fossil Energy Materials*, ed. by R. Judkins, Oak Ridge, TN, May 15-17, 1990.

10. P. E. Gray, "Oxidation Inhibited Carbon-Carbon Composites," U. S. Patent Appl. 676,985, Nov. 30,1984.

11. P. E. Gray and J. E. Sheehan, "Oxidation Protected Carbon-Carbon Composite Development," *NASA Conference Publication 2445*, Metal Matrix, Carbon, and Ceramic Matrix Composites 1986, Edited by J. D. Buckley, Cocoa Beach, Florida, January 1986.

12. D. M. Shuford, "Enhancement Coatings and Process for Carbonaceous Substrates," U. S. Patent 4,471,023, September 1984.

13. P. Ehrburger, P. Baranne, and J. Lahaye, "Inhibition of the Oxidation of Carbon-Carbon Composite by Boron Oxide," *Carbon* 24(4), 495-99 (1986).

14. D. W. McKee, C. L. Spiro, and E. J. Lamby, "The Effects of Boron Additives on the Oxidation Behavior of Carbons," *Carbon* 22(6) 507-511 (1984).

15. W. D. Kingery, "Surface Tension of Some Liquid Oxides and Their Temperature Coefficients," *J. Am. Ceram. Soc.* 42 [1] 6-10 (1959).

16. T. M. Besmann, *SOLGAS-PV, a Computer Program to Calculate Equilibrium Relationships in Complex Chemical Systems*, ORNL/TM-5775, April 1977.

ORNL-1(D)-MICROWAVE SINTERING OF CERAMICS FOR FUEL CELLS

M. A. Janney and H. D. Kimrey

Oak Ridge National Laboratory
P.O. Box 2008
Oak Ridge, TN 37831-6087

INTRODUCTION

In the last semiannual report, it was shown that lanthanum chromite is easy to fire in a 2.45 GHz microwave furnace. It couples well because of its relatively low electrical resistivity ($\sim$0.1 ohm-cm at ambient temperature). However, no "microwave effect" was observed for the system studied. There was no acceleration of densification or microstructural development in the system produced by microwave firing. This was in marked contrast to the large "microwave effects" that had been observed previously in systems such as alumina and zirconia. The absence of a "microwave effect" in lanthanum chromite is attributed to the way that microwaves couple to it. In the chromite system, coupling is to the electrons, which do not participate in diffusion. In the alumina and zirconia systems, coupling is to the ionic defects in the crystal, which are directly responsible for diffusion.

An investigation of the role that ionic and electronic conductivity play in determining the "microwave effect" has been initiated. The model system that is being investigated is based on the ZrO_2-CeO_2 system. This system has two properties that make it attractive for study: (1) its total electrical conductivity can be varied over several orders of magnitude; and, (2) its conductivity can be altered from being predominantly ionic to predominantly electronic in nature. We will synthesize several different compositions in the ZrO_2-CeO_2-Y_2O_3 system. The addition of Y_2O_3 to the system provides a means to fix the level of ionic conductivity in the system by the creation of oxygen vacancies. This will allow us to work in a convenient range of conductivities to assure that we examine a wide variation in the ionic to electronic conductivity ratio. Yttria levels between 0.1 and 3 mol% and ceria levels between 10 and 15 mol% will be examined.

EXPERIMENTAL PROCEDURE

We have focused on developing the microwave experimental procedures required to repeatably fire CeO_2 - doped ZrO_2 ceramics in the microwave furnace under controlled-atmosphere conditions. Our major concerns include the proper control of the atmosphere around the sample, appropriate thermal insulation systems, and chemical compatibility of the insulation system with the samples to be microwave fired.

Numerous insulation systems have been evaluated. In all cases, a "picket fence" arrangement of SiC rods has been used because of the need for "indirect" heating of the CeO_2 - doped ZrO_2 at temperatures below ~700 C. (The usefulness of the "picket fence" in the sintering of zirconia was demonstrated previously in this project.) The most promising insulation systems are based on a three-part arrangement of the components, Fig 1.

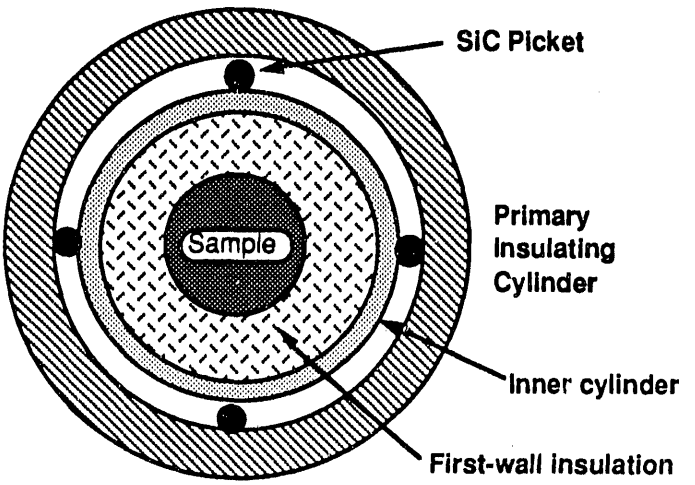

Figure 1. Schematic of "picket fence" insulation system for ZrO_2 microwave sintering.

The first wall insulation is the most important component of the insulation system. It must perform several tasks if the insulation system is to be considered successful. First, it must be chemically compatible with the CeO_2 - doped ZrO_2 samples. This eliminates the use of commercial zirconia bulk fiber, which is doped with 8 mol% Y_2O_3. During thermal processing, diffusion of the Y_2O_3 into the CeO_2 - doped ZrO_2 sample would invalidate our experiments by changing the conductivity of the sample in an uncontrolled manner. Second, the first-wall insulation must have dielectric properties similar to those of the sample. Third, it must be a good thermal insulator.

Two approaches were taken to achieve the goals outlined above. First, ZrO_2 - 12 mol% CeO_2 powder was consolidated and pre-fired to form -10 mesh granules. these were poured around the sample to form the first-wall insulation. This approach worked passably well, but some problems were encountered with sample cracking during sintering. A better first-wall insulation was made by mixing ZrO_2 -12 mol% CeO_2 powder with bulk alumina fiber insulation in a 3:1 ratio by weight. This material had better insulating properties than the granulated ZrO_2 - 12 mol% CeO_2 powder and eliminated cracking. Both of these approaches have the advantage that they provide an insulation that is with the sample and that matches the dielectric response of the sample. Also, as the composition of the sample is changed, by selective doping with yttria, the chemical composition of the insulation can be readily changed as well. Using the zirconia-alumina fiber mixture along with the "picket fence" arrangement, an initial sreies of sintering experiments was completed.

RESULTS AND DISCUSSION

Our working hypothesis is that there should be differences in the heating and sintering of CeO_2 - doped ZrO_2 fired in different atmospheres. These differences in heating exist because of the relative ratio of electronic to ionic conductivity. The firing curves shown in Figure 2 confirm that there are significant differences in the heating of CeO_2 - doped ZrO_2 fired in air and in Ar-H_2.

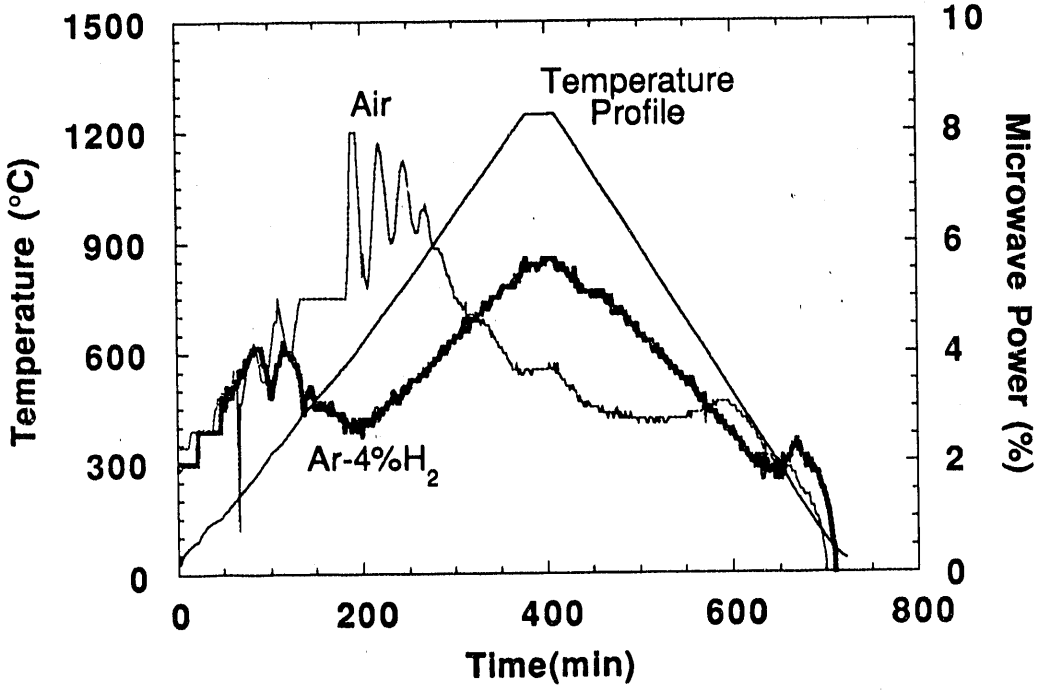

Figure 2. The microwave heating profiles for ZrO_2 - 12 mol% CeO_2 fired in air and in Ar-4%H_2 were significantly different.

The microwave power curve for the sample fired in air shows behavior that is typically observed in the firing of alumina or zirconia ceramics using the picket fence arrangement. At low termperatures, the power increases with increaseing temperature. This indicates that the microwaves are coupling to the SiC rods and are heating the zirconia indirectly by radiation and conduction. As the temperature increases, the amount of microwave power absorbed by the zirconia relative to the SiC rods increases. Eventually, all of the heating will be by direct microwave heating of the zirconia. At about 700 C, the total power starts to decrease. At this point,virtually all of the microave power is being absorbed by the zirconia sample. As the sample heats further, the efficiency with which it is heated by the microwaves increases. This increase in efficiency is caused by the increase in dielectric loss tangent of the zirconia with temperature. Above ~900 C, the power steadily drops until a plateau is reached at the sintering temperature of 1250 C. Samples fired in air were white in color after firing, indicating that the sample was fully oxidized.

The microwave power curve for the sample fired in Ar-$4H_2$ is quite different from that for firing in air. At temperatures up to ~300 C, there is a similar increase in power. However, above 300 C, the sample fired in Ar-$4H_2$ shows a decrease in power up to ~600 C. This is followed by a monotonic increase in power up to the sintering temperature of 1250 C. At temperatures below ~1000 C the Ar-$4H_2$ sample requires leess power than the air sample; in contrast, above 1000 C, it requires more power. Samples fired in Ar-4H2 were dark gray in color indicating that some of the Ce^{+4} had been reduced to Ce^{+3}.

What particular mechanisms cause the differences between the air and the Ar-$4H_2$ cases have not been determined so far. The change in color indicates that there should be significant electronic conductivity in the samples fired in Ar-4%H_2. Determination of the dielectric properties of these materials at microwave frequencies would be helpful. We will attempt to get those measurements made during the coming semi-annual period.

SUMMARY AND CONCLUSIONS

Microwave firing of ZrO_2 - 12 mol% CeO_2 in air and in Ar-4%H2 showed very different trends. Air firing followed behavior similar to that previously observed for ZrO_2 - 8 mol% Y_2O_3 and alumina. Firing in Ar-4%H_2 deviated significantly from previous experience for zirconia. The differences are thought to be because the reduced samples had higher electronic conductivity.

PNL-1 ADVANCED MATERIALS AND ELECTROCHEMICAL PROCESSES IN HIGH-TEMPERATURE SOLID ELECTROLYTES

J. L. Bates, L. A. Chick, G. D. Maupin, L. R. Pederson, W. J. Weber, and G. E. Youngblood

Pacific Northwest Laboratory[1]
Richland, Washington 99352

J. Hurst, A. E. Bell, D. W. Grainger, S. B. Rananavare, D. K. Roe, and D. H. Thompson

Oregon Graduate Institute
Beaverton, Oregon 97006-1999

INTRODUCTION

The purpose of this project is to develop advanced ceramic materials for use in solid oxide fuel cells (SOFCs) and other advanced electrochemical technologies related to the broad, clean, and efficient use of coal and other fossil fuels. Objectives of this project are to 1) identify and develop new electrically conducting materials for use as electrolytes, electrodes, bipolar connections, membranes, and catalysts in solid-state electrochemical processes; 2) develop a fundamental understanding of molecular processes associated with advanced electrochemical and catalytic systems; and 3) develop novel materials synthesis and processing methodology to improve quality, reduce cost, and/or provide the capability to produce new materials, forms, and structures.

BACKGROUND

Many new concepts for improved utilization of fossil energy relate to electrochemical processes that are useful above 600°C. Solid-state electrochemical processes utilize a dense, ionically conducting, solid electrolyte membrane coupled with highly electronically conducting electrodes intimately attached to the electrolyte. In some uses, the cells are joined together with electronically conducting interconnections. The electrochemical cells operate in the presence of DC electric currents and/or electric

---

[1] Pacific Northwest Laboratory is operated by Battelle Memorial Institute for the U.S. Department of Energy under Contract DE-AC06-76RL0 1830.

potentials. High-temperature electrochemical cells using solid electrolytes have application in fuel cells, oxygen and other gas pumps, sensors, fluid purifiers, chemical separators, and in chemical synthesis. In addition, these materials have application as catalysts in chemical reactions where the electrochemical activity can be controlled by an applied potential.

The major challenges for utilizing high-temperature electrochemical cells center around the development of improved materials, particularly solid-state electrolytes that work well in conjunction with the electrode and current interconnect components. Cell component materials are needed with the desired electrical, thermal, structural, catalytic, and electrochemical properties to enable a broader and cleaner utilization of fossil fuels, particularly coal. Synthesis and fabrication methodology to co-process different ceramic materials into a cell or stack of cells is needed. A fundamental understanding of molecular processes associated with advanced electrochemical and catalytic systems is essential, including reactions occurring at surfaces and interfaces.

A new approach to enhancing reaction kinetics is electrochemical catalysis and promotion. Many processes involving fossil fuels use catalysts to increase reaction rates to practical values. Currently, the most common catalysts are the noble metals. Increased attention is being given to electrically conducting oxides as catalysts to reduce costs and for use in oxidizing and otherwise hostile environments. Recently, it has been shown that the catalytic nature of mixed ionic/electronic oxides can be enhanced by several orders of magnitude through electrochemical modification. This approach holds high potential for improved utilization of fossil fuels.

APPROACH

The scope of this project includes materials development and electrochemical studies for SOFCs; development of advanced electrolytes; electrochemical catalysis studies; and synthesis of advanced catalysts and membrane materials. Emphasis during this reporting period has been placed on determining air sintering mechanisms of chromite interconnect materials, on studies of electrochemical processes occurring at gas/electrode/electrolyte interfaces, and on the synthesis of materials for use as catalysts and membranes.

DISCUSSION OF CURRENT ACTIVITIES

Air Sintering Mechanisms of Chromite Interconnect Materials

Chromites are used as current interconnections in SOFCs because they are chemically stable in both oxidizing and reducing atmospheres and can be formulated to yield high electrical conductivity with a thermal expansion matched to the yttria stabilized zirconia (YSZ) electrolyte. However, the chromites are difficult to sinter to near full density (closed porosity) in air at temperatures below 1550°C, as required for the co-sintering of the SOFC. Synthesis of very reactive chromite powders by the glycine/nitrate process (GNP) [1,2] has enabled studies of air-sintering mechanisms, in which some chromite compositions have been sintered to near full density in air. A previous report [3] discussed the effects of composition and sintering atmosphere on sintering of $La(Sr)CrO_3$. This report compares the effects of composition on sintering of $La_{1-x}Sr_xCrO_3$ (LSC) and $Y_{1-x}Ca_xCrO_3$ (YCC) and discusses the implications for sintering mechanisms.

Experimental

Chromite powders were prepared by glycine/nitrate combustion synthesis [1,2]. All compositions were synthesized using a stoichiometric glycine/nitrate ratio calculated to yield N_2, CO_2, and H_2O as the gaseous products of combustion [2]. For the chromites, this condition generally results in 1450°C flame temperatures and nearly complete combustion. The ash product had an average crystallite size of 20 nm, with excellent particle-to-particle homogeneity [2]. The powders were uniaxially pressed at 35 MPa and then isostatically pressed at 140 MPa. Pellets were placed on edge in an electrically heated furnace in either stagnant or 0.25 l/s flowing air. The furnace was heated at 300°/h to 1550°C, held for 8 h, and cooled at 300°/h. Sintered densities were determined by an immersion technique using ethyl alcohol and compared with theoretical densities (TD) determined by X-ray diffraction (XRD).

Effects of Alkaline Earth Concentration

Effects of dopant concentration and air flow rate on sintering of LSC were discussed previously [3]. However, the same data are reproduced here for

direct comparison with the YCC system. Sintered densities for both the LSC and the YCC systems generally increased as alkaline earth dopant level was increased (Figure 1). For $x<0.3$, higher sintered densities were obtained in flowing air than in stagnant air. For $x>0.3$, the trend was reversed for YCC, and possibly for LSC. Maximum relative densities were attained in flowing air for YCC containing Ca=0.20 (98% TD) and for LSC with Sr=0.24 (93% TD).

Shrinkage during sintering was determined for YCC (Figure 2). Pressed pellets were heated in a vertical pushrod dilatometer at 100°/h. Samples with $x>0.12$ sintered rapidly between 1000 and 1100°C, with shrinkage proportional to calcium concentration. This rapid densification is attributed to liquid-phase sintering. At high temperatures, during combustion synthesis (1450°C) or during sintering (1550°C), the alkaline earths appeared to be completely soluble in the perovskite. Only single-phase perovskite chromites were evident after combustion or sintering, even at the highest dopant levels attempted. However, when the powders were heated at lower temperatures (e.g. 650°C), part of the Ca or Sr was exsoluted as $CaCrO_4$ or $SrCrO_4$, as found by XRD analysis of quenched samples. This occurred in the LSC above Sr=0.07 and in the YCC above Ca=0.12. These chromate compounds (or their solid decomposition products) melted near 1020°C for the YCC system and near 1250°C for the LSC system [4]. Near the maximum sintering temperature, the alkaline earths again substituted into the perovskite phase. Thus, these chromites produced a transient sintering aid, although remnants of the liquid have been detected in some samples.

Shrinkage during sintering was determined for a series of four LSCs (Figure 3). For Sr=0.0 the shrinkage rate increased smoothly as the temperature was increased, suggesting a simple sintering mechanism. For Sr=0.12, sintering began at lower temperatures. At higher Sr levels, Sr=0.24 and 0.27, the shrinkage exhibited three pronounced inflections, suggesting changes in sintering mechanisms during heating. Although high-temperature XRD analysis indicated that the inflections near 1250°C were probably due to melting of $SrCrO_4$ or its derivatives, the reactions associated with inflections near 1100°C and above 1400°C are unknown. Reactions at the highest temperatures appeared to be very sensitive to composition, occurring near 1450°C in the sample with Sr=0.24 but near 1550°C for Sr=0.27. A similar pair of composition-sensitive reactions were present in the YCC system (see Figure 2 for Ca=0.16 and Ca=0.20).

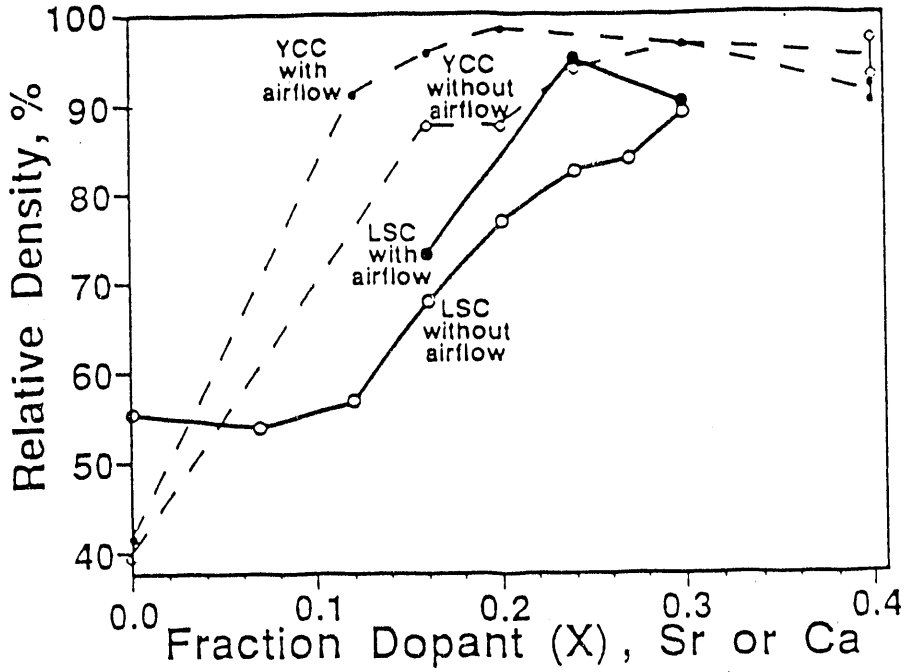

Figure 1. Relative sintered density as a function of alkaline earth substitution for $La_{1-x}Sr_xCrO_3$ and $Y_{1-x}Ca_xCrO_3$ sintered at 1550°C for 8 h in stagnant or 0.25 l/s air.

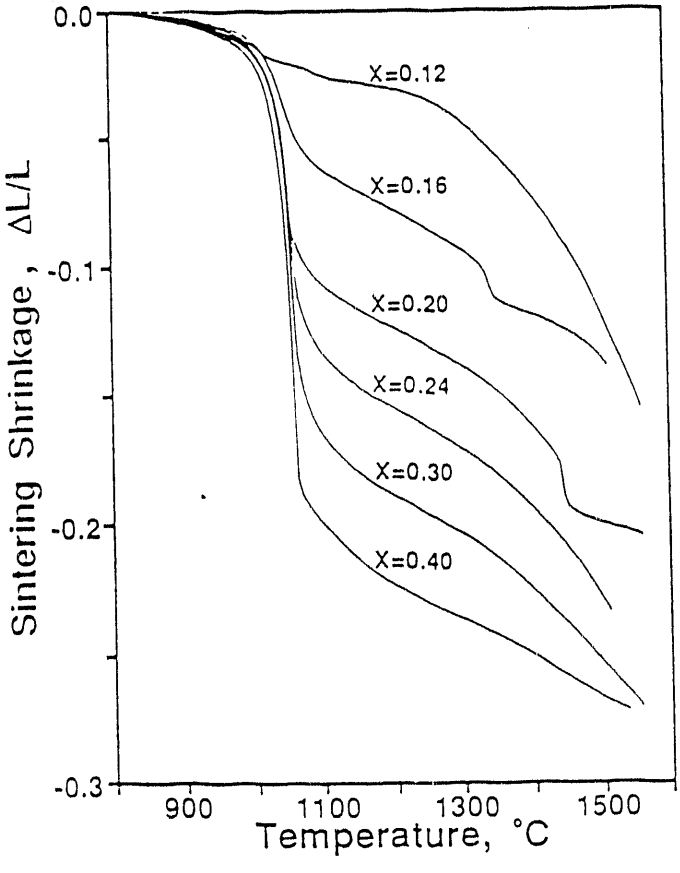

Figure 2.

Shrinkage during sintering of $Y_{1-x}Ca_xCrO_3$ measured by vertical pushrod dilatometer in stagnant air.

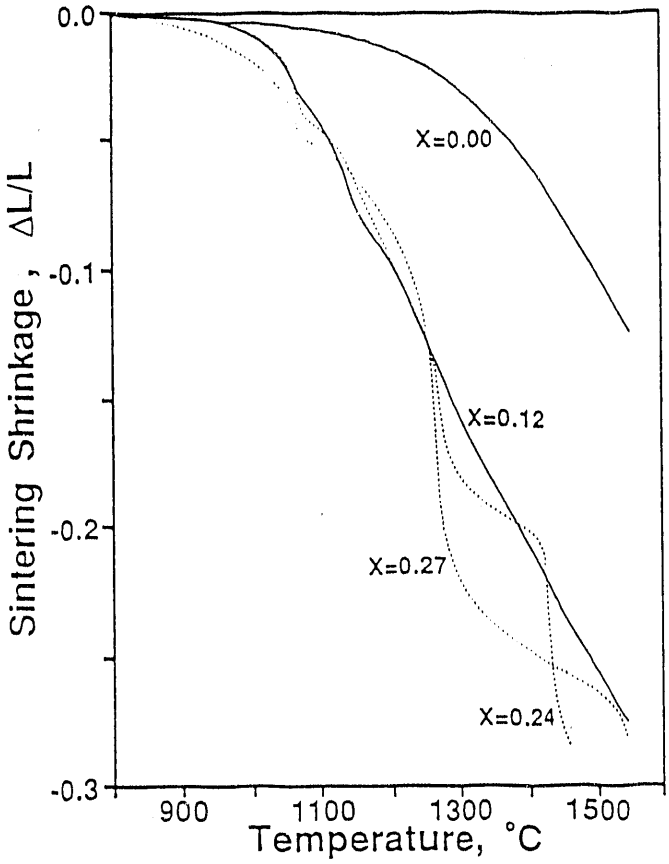

Figure 3.

Shrinkage during sintering of $La_{1-x}Sr_xCrO_3$ measured by vertical pushrod dilatometer in stagnant air.

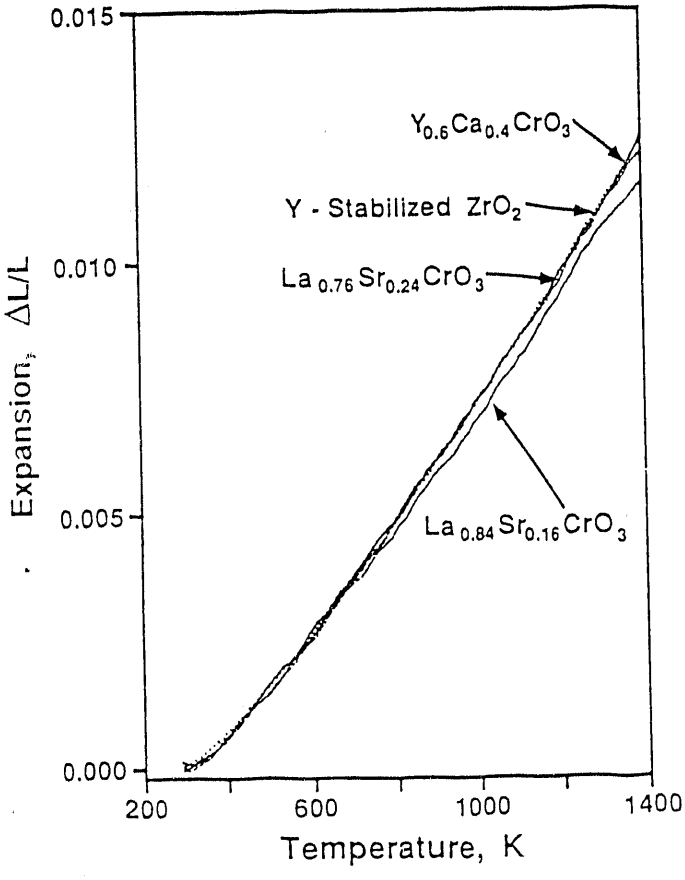

Figure 4.

Thermal expansion curves for two LSC and one YCC composition plotted with that for yttria stabilized zirconia.

Dilatometer studies showed that the thermal expansion of chromites increased with increased alkaline earth substitution. As shown in Figure 4, compositions with an optimum thermal expansion match to YSZ were $Y_{0.6}Ca_{0.4}CrO_3$ and $La_{0.76}Sr_{0.24}CrO_3$. For LSC, Sr=0.24 also gave a maximum relative density in flowing air (Figure 1). However, YCC with Ca=0.4 exceeded the optimum level for sinterability, although ≈95% TD was attained without airflow.

Sintered density versus peak temperature for $Y_{0.6}Ca_{0.4}CrO_3$ and $La_{0.76}Sr_{0.24}CrO_3$ are compared in Figure 5. Samples were heated at 300°/h to the desired temperature and quickly removed from the furnace. The higher densities shown at 1550°C were attained after 8 h at temperature. The LSC densified most rapidly above 1500°C whereas >50% of the YCC densification occurred between 1000 and 1100°C. The microstructures of quenched YCC samples in Figure 5 are shown in Figure 6. At 1100°C, the microstructure contained dense, irregular areas (white) that were apparently formed by localized liquid-phase sintering. The dense masses grew and coalesced on further sintering above 1100°C. Finally, at 1550°C, the voids coalesced into irregularly shaped pores. Further heating at 1550°C for 8 h removed the smallest pores.

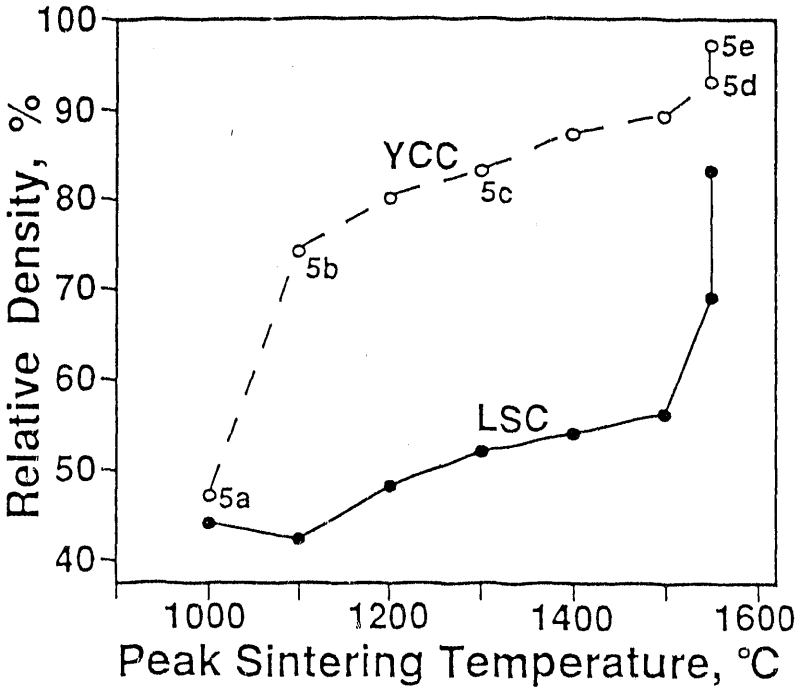

Figure 5. Relative sintered density as a function of peak sintering temperature for $Y_{0.6}Ca_{0.4}CrO_3$ and $La_{0.76}Sr_{0.24}CrO_3$ in stagnant air. The higher densities at 1550°C are after 8 h at temperature. Labels near data points are for microstructures in Figure 6.

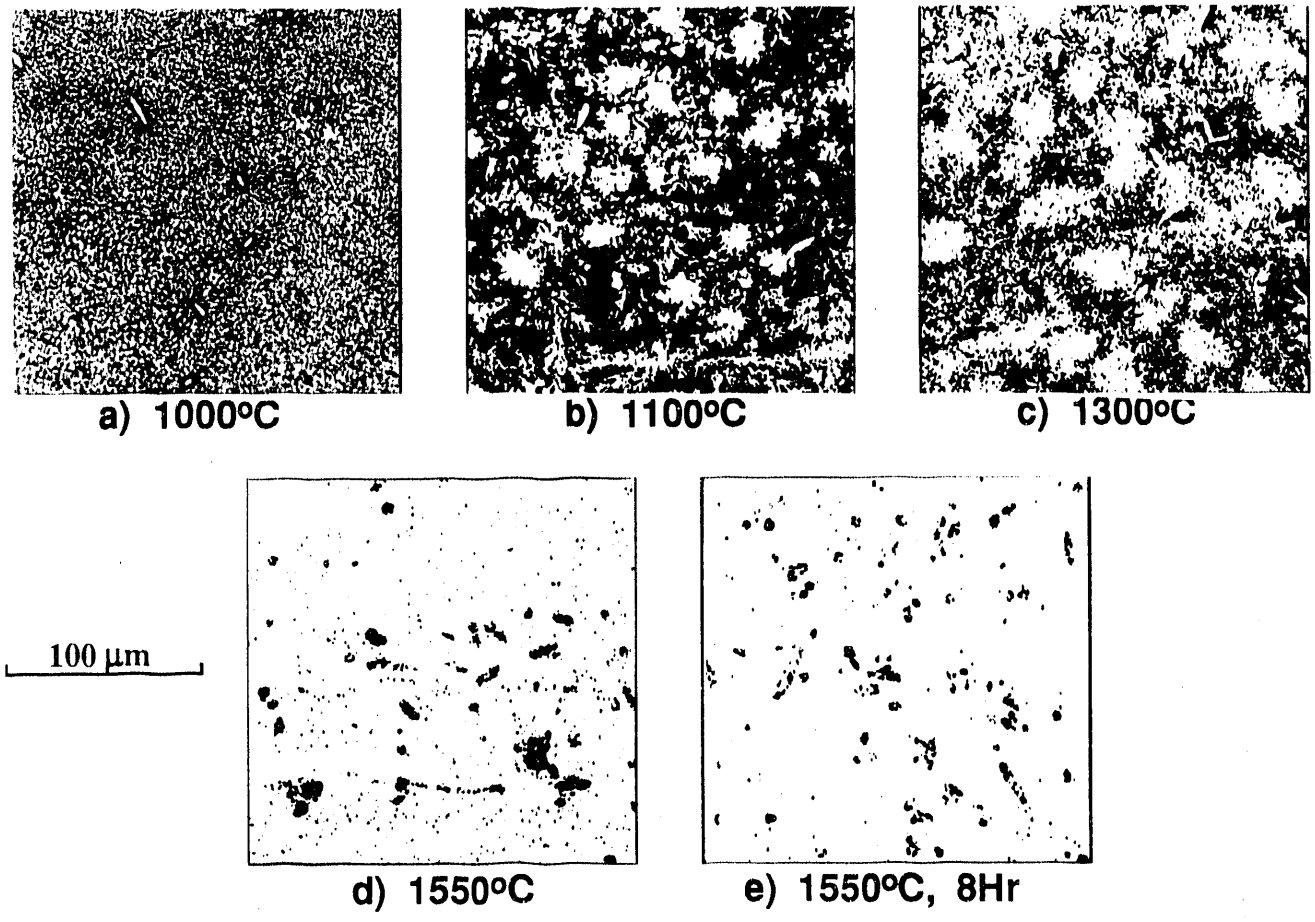

Figure 6. Microstructures at various temperatures during sintering for $Y_{0.6}Ca_{0.4}CrO_3$ from Figure 5 showing inhomogeneities induced by liquid-phase sintering.

A series of LSC samples from Figure 5 showed no discernable patterns of non-uniform densification as was typical of the YCC samples. Rather, scanning electron microscopy (SEM) revealed grain growth in the LSC, from about 20 nm at room temperature to about 500 nm by 1550°C. Therefore, although $SrCrO_4$ formation and subsequent melting at near 1250°C have been confirmed in LSC by high temperature XRD, the resulting liquid phase was apparently not as effective in causing densification as that in YCC. This implies that either grain boundary or bulk diffusion may account for densification of LSC, whereas vapor-phase transport probably accounts for much of the grain growth. This point is addressed further below.

Effects of Chromium Enrichment or Depletion

The effects of Cr depletion or enrichment were studied for $Y_{0.6}Ca_{0.4}CrO_3$ and $La_{0.76}Sr_{0.24}CrO_3$. Assuming that Ca and Sr substitute only on the "A" site in the perovskite lattice, then the ratios (La+Sr)/Cr and (Y+Ca)/Cr are the "A" site to "B" site cation ratios. When these ratios are less than unity, Cr is enriched, and the structure must either contain vacancies in the "A" site or a second, Cr-rich phase must appear. Conversely, when the ratios are greater than unity, Cr is depleted and the structure must either contain Cr (or "B" site) vacancies or a second phase that is rich in the "A" site cations. Another possibility is that vaporization of enriched species during sintering will bring the site populations back into balance.

The sintered densities in stagnant air are shown in Figure 7 as a function of cation ratio for $[Y_{0.6}Ca_{0.4}]_{(1-y)}Cr_{(1+y)}O_3$ and $La_{(0.76-y)}Sr_{(0.24)}Cr_{(1+y)}O_3$. The trends are similar, although the local minima are offset. This offset may be explained by partial substitution of Ca for the depleted Cr on the "B" site in YCC. Sakai et al. [5] reported similar local density minima for Ca variation within $(La_1\text{-}xCa_x)(Cr_1\text{-}yCa_y)O_3$, while Dokiya et al. [6] reported increased sintered density for Cr-deficient samples in the same system. For both the LSC and YCC systems, the highest densities were obtained for substantial Cr depletions. Weight losses during sintering (Figure 8), presumably due to volatility, are strongly dependent on Cr content for the LSC system, but only weakly so for the YCC system. Microstructures extending from sample surface to center for YCC samples in Figures 6 and 7 are shown in Figure 9. The samples, 9a through d, exhibited increased density as the amount of Cr enrichment was decreased. Small depletions in Cr, 9e and f, resulted in large changes in sintered morphology with a fully dense surface layer (100 to 200 μm) and an inhomogeneous, low-density interior. For the YCC with highest Cr depletion, 9g, the entire pellet was nearly fully dense, but the interior contained a second phase. Energy dispersive spectroscopy analyses showed that samples with enriched Cr, 9a, b and c, contained Cr-rich phase near the surface and within the interior in 9a. The low-density, Cr-depleted samples, 9e and d, exhibited a Ca-rich liquid-phase remnant near the surface and within the higher-density regions of the interior. The highest-density, Cr-depleted sample, 9g, appeared to consist of a single phase near the surface, but separated into two YCC phases in the interior, one of which was richer in Ca.

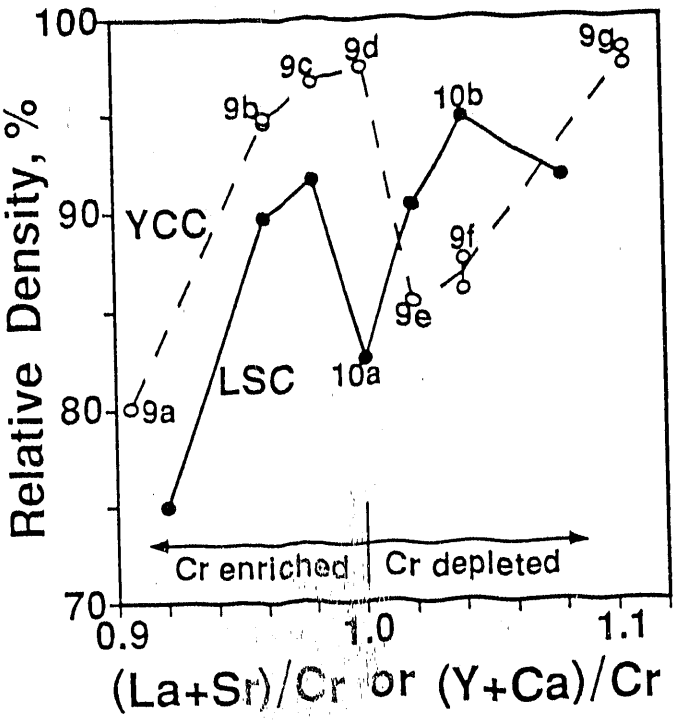

Figure 7. Relative sintered density as a function of chromium enrichment or depletion for $[Y_{0.6}Ca_{0.4}]_{(1-y)}Cr_{(1+y)}O_3$ and $La_{(0.76-y)}Sr_{(0.24)}Cr_{(1+y)}O_3$. Samples were sintered for 8 h at 1550°C in stagnant air. Labels near data points are for microstructures in Figures 8 and 9.

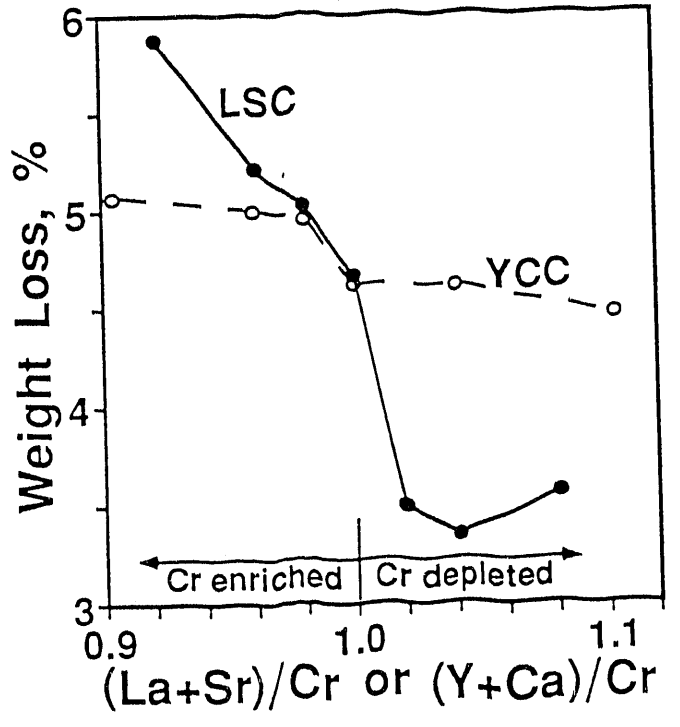

Figure 8. Weight lost during sintering for the samples in Figure 7.

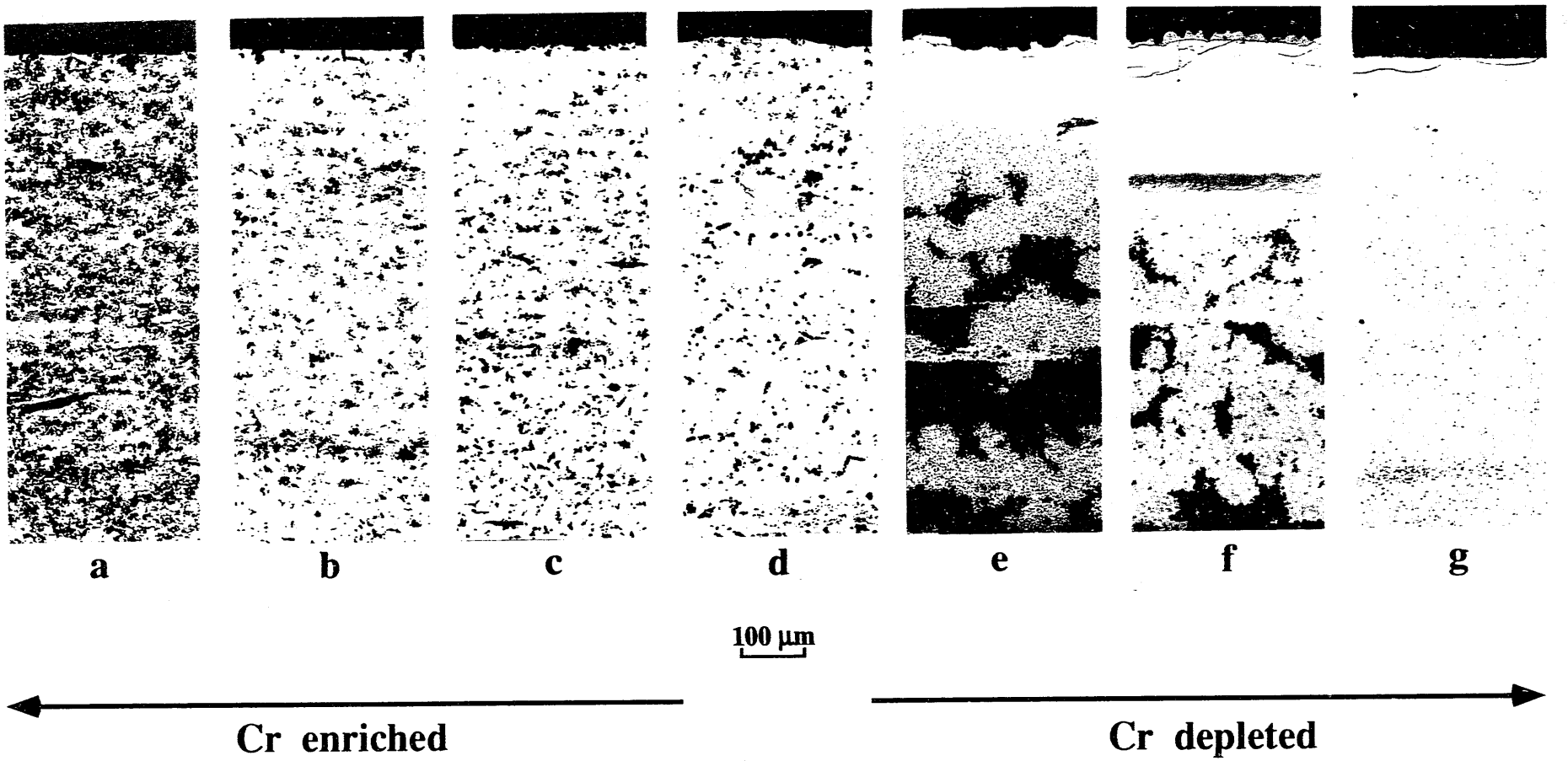

Figure 9. Microstructures at various levels of Cr content for the YCC samples labeled in Figure 7.

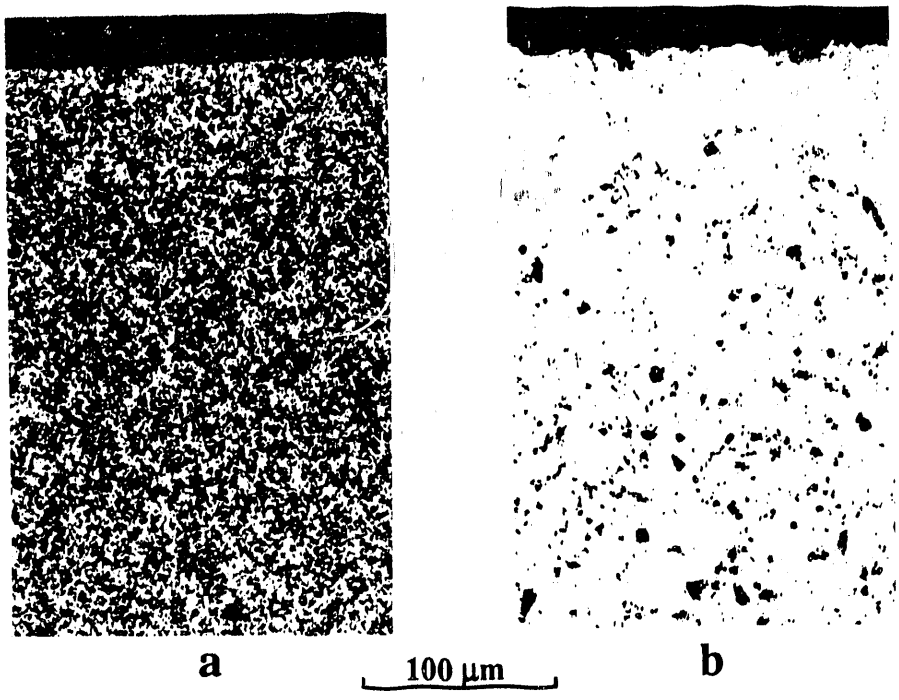

Figure 10. Microstructures for the two LSC samples labeled in Figure 7.

The microstructure of $La_{0.76}Sr_{0.24}CrO_3$ with (La+Sr)/Cr=1 is compared to that of Cr-depleted $La_{0.78}Sr_{0.24}Cr_{0.98}O_3$ in Figure 10, with (La+Sr)/Cr=1.04. The $La_{0.76}Sr_{0.24}CrO_3$, 9a, was homogeneous but of low density, while the Cr-depleted, 9b, had the highest density of any LSC sintered in air. The latter contained large crystals of La_2O_3, a phase susceptible to hydration, which causes cracking of the material.

In summary, the alteration of the A/B cation ratio caused secondary phase formation in both the YCC and the LSC systems. In LSC, volatility was apparently proportional to Cr enrichment. It is not known whether vacancies were induced on the relatively depleted sites. However it can be stated that the occurrence of secondary phase formation and enhanced volatility decreased (or perhaps eliminated) the concentration of vacancies that would be necessary to achieve site balance. Additionally, precipitous changes in density caused by small changes in Cr content (Figure 7) imply that good composition control is essential for the conduct of sintering studies on chromites. In this study, metal nitrate stock solution concentrations were determined by EDTA complexiometric titration to ±0.3% relative or better [2].

Volatility and Sintering Mechanisms

Ownby [8] showed that Cr_2O_3 could be sintered to full density at 1600°C when the $p(O_2)$ was maintained at the Cr/Cr_2O_3 equilibrium boundary (near 10^{-12} atm. $p(O_2)$ at 1600°C). This effect was confirmed for the LSC system in this study by immersing $La_{0.76}Sr_{0.24}CrO_3$ in a solid-solid buffer system, a mixture of Cr metal and Cr_2O_3 powders, which resulted in full density at 1550°C in 8 h.

However, oxides containing significant quantities of Cr are difficult (or impossible) to sinter to full density in air [7]. This was attributed to vapor phase transport due to volatility of Cr oxides, especially CrO_3 [8]. In the chromites, there may be other volatile species including SrO [9]. Readey [10] stated that vapor transport during the early stages of sintering results in particle growth, thereby decreasing the driving force for sintering (that is, a reduction in the surface area) without producing densification. Readey also maintained that rapid vapor transport during the final sintering stage will lead to improved pore mobility and increased final densities. Meadowcroft and Wimmer [9] found that enriched Cr content in LSC resulted in greatly enhanced volatility of Cr oxides. This is consistent with an observed trend of increased weight loss with Cr enrichment in LSC (Figure 8) and with a corresponding decrease in density (Figure 7). YCC may also be adversely affected by grain growth induced by excess Cr (Figure 9a-c).

For LSC and YCC, the role of vapor-phase transport can be complicated by secondary phase formation. The formation of the volatile Cr oxides, CrO_2 and CrO_3, and the formation of the liquid-phase-forming chromates, $SrCrO_4$ and $CaCrO_4$, require access to oxygen. Therefore, possible detrimental effects of vapor phase transport can be offset by liquid-phase sintering resulting from chromate formation and melting. The microstructures of Figures 9e and f suggest that oxygen access to the sample surface resulted in substantial, early liquid-phase formation and complete densification of the surface layer. This dense layer may have blocked access of oxygen to the interior. (These YCC compositions with slightly depleted Cr may be useful for those SOFC configurations in which the interconnect thickness is about 100 μm.) Additionally, two mechanisms can be postulated to explain the increase in sinterability in flowing air (Figure 1): 1) Cr oxide vapors may be removed before they can condense and cause grain growth, or 2) improved oxygen access may promote chromate formation, leading to more effective liquid-phase sintering.

In summary, although the roles of vapor-, liquid- and solid-phase transport in the chromites and their combined effects on densification are not yet fully understood, liquid-phase sintering appeares to be more pronounced for YCC than for LSC, particularly for YCC compositions with depleted Cr. The absence of an obvious liquid phase in LSC indicates that solid-phase sintering, involving either bulk or grain boundary diffusion, may be the predominating mechanism for densification. Therefore, LSC sintering appears to be dependent on the relative significance of vapor-phase versus solid-phase transport.

Effects of Chromium Enrichment or Depletion on B-Site Additives

The effects of A/B cation ratios on sintering were discussed above in connection with Figure 7. These results were for LSC and YCC compositions with no substitution on the B-site. Work conducted on a related program [supported by METC] has shown that changes in A/B cation ratios can significantly alter the effects of potential sintering aids that are added as B-site dopants. These results are reported here because of their relevance to this program. Figure 11 is a plot of percent of theoretical density as a

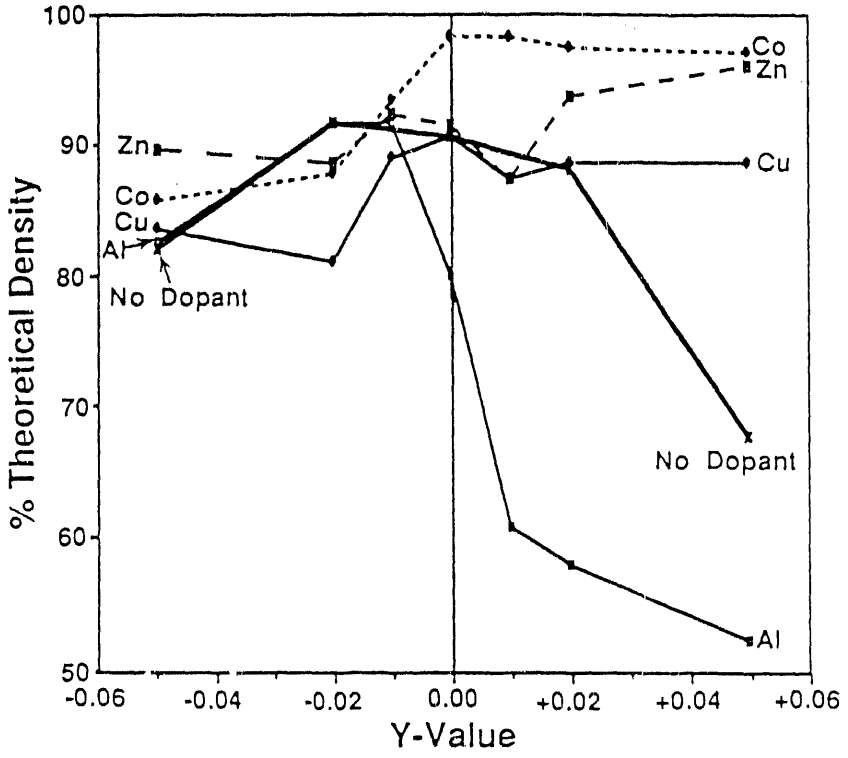

Figure 11. Percent of theoretical density attained during sintering at 1550°C for 8 h for $(La_{.76}Sr_{.24})_{(1-y)}(Cr_{.9}M"_{.1})_{(1+y)}O_3$, where M" is Al, Zn, Cu, or Co. The value of "y" controls the A/B cation ratio.

function of A/B ratio for chromites with the composition, $(La_{.76}Sr_{.24})_{(1-y)}(Cr_{.9}M"_{.1})_{(1+y)}O_3$, where M" is Al, Cu, Co, or Zn. Additives to the B-site gave only small effects on sintering rates when Cr was depleted (y<0). When Cr was enriched, however, sintering rates were quite sensitive to B-site substitution, although the effect could be either beneficial or detrimental. Cobalt appeared to have the most beneficial effect on sintering of LSC, although Zn was nearly as helpful for extreme Cr enrichment. It is clear that Al had a large detrimental effect when A/B ratio was unity (y=0), or when Cr was enriched.

Investigations are continuing to determine the mechanisms involved in sintering with these B-site dopants, however it is probable that these additives affect liquid phase formation (Co) and enhance or depress Cr vaporization.

Electrochemical Processes

The performance of high-temperature (T≥800°C) solid electrolyte systems often is dependent upon the electrochemical processes that occur at solid-solid-gas interfaces. Changes at these interfaces or in materials associated with these interfaces can alter reaction mechanisms and/or rates of reactions. This project seeks to understand these electrochemical processes and the influences that material properties and interfaces, electrical current and potential, temperature, gaseous environment and time exert on these processes.

In a SOFC, the performance of the air electrode-electrolyte interface is mainly governed by the net cathodic process:

$$1/2O_2(gas) + V_o^{\cdot\cdot}(electrolyte) \rightarrow O_o(electrolyte) + 2h^{\cdot} \qquad (1)$$

Oxygen gas adsorption onto a solid surface and subsequent dissociation into oxygen atoms is implied in Equation (1). These oxygen atoms, in turn, must migrate to a reaction site and exchange two electrons, whereupon they become oxygen ions and fill previously vacant oxygen lattice sites. Then, the oxygen ions must cross the interface between the air electrode and electrolyte. In the electrolyte, the oxygen ions conduct by a vacancy mechanism. In Equation (1), net oxygen conduction through the electrolyte is

represented in Kroger-Vink notation, while electron exchange is represented by two holes (2h) being created in the cathode material, which usually is a p-type (hole) conductor.

Cathodic performance can be improved by discovering the rate-limiting step and designing compositional or operational steps to enhance that particular reaction rate. Generally, the cathodic performance can be improved by reactions or processes that:

1) increase the rate at which the gas (O_2) molecules reach the interface,
2) increase the rate at which the oxygen molecules dissociate and acquire electrons to become oxygen ions at the surface of the cathode material, and/or
3) enhance the rate at which these oxygen ions diffuse and pass over into the electrolyte material.

Normally, the critically-important reaction zone is located at the physical triple phase boundary (tpb) between an electrically conducting, porous air electrode, the oxygen gas, and the oxygen ion-conducting electrolyte. The effective size of the reaction zone, and thus cell performance, can be enhanced if an air electrode exhibiting mixed electronic/ionic conduction is used. By increasing the size of the reaction zone, oxygen ions can now move through the air electrode into the electrolyte without having to be formed directly at the tpb. Through proper doping or by electrochemical means, the number of reaction sites within the reaction zone and the rate of charge transfer can be increased.

An experimental method has been designed to quantify the cathodic performance of a particular electrode material, which includes AC impedance and DC polarization measurements in conjunction with an unbonded interface cell (UIC) design. With this cell design, an effective reaction length (ERL), which is proportional to the size of the reaction zone, is measured for a particular electrode material/electrolyte interface [3]. The cathodic performance or net reaction rate can be improved by enlarging the effective size of the reaction zone and/or by lowering the reaction activation energy. The reaction activation energy can be determined using other cell designs, but the UIC design uniquely allows the simultaneous determination of activation energy and the ERL. This experimental method was used to compare the cathodic performance for two compositions of strontium-doped lanthanum manganite

electrode material, namely $La_{1-x}Sr_xMnO_3$ with x=0.1 and 0.3 [11, 12].

Unbonded Interface Cell (UIC)

An electrochemical cell using unbonded solid interfaces was developed to investigate high-temperature reactions at materials interfaces without influences of sample morphology, especially variations normally encountered when testing interfaces prepared by sintering of the electrode onto the electrolyte. Details of the UIC design are given elsewhere [11,12]. The important feature of the UIC design is the interface that consists of multiple "point" contacts with the surrounding gaseous atmosphere permeating between the unbonded (somewhat roughened) surfaces. Since the actual contact area between the electrode and electrolyte is relatively small, the contact resistance of the unbonded interface ($\approx$ 100 Ω at 900°C) dominates other cell resistances (a few ohms). Likewise, the interface polarization resistance (a few kΩ) is much larger than the polarization resistance of the porous platinum electrode on the electrolyte surface opposite the unbonded interface. For porous electrodes with a relatively large amount of tpb, the interface reaction rate frequently is limited by gaseous diffusion. In the UIC design with a relatively small amount of tpb, gaseous diffusion is not rate-limiting. Rather, reaction rates are determined by surface and interfacial properties of materials. Changes in the reaction rate or the polarization resistance therefore are primarily due to electrocatalytic effects when using the UIC design.

Two resistive-like parameters, R_B and R_p, are obtained from analysis of complex impedance spectra gathered using the UIC. These two parameters are correlated with electrocatalytic processes taking place in a reaction zone at the electrode-electrolyte interface.

The resistance parameter, R_B, is related to the size of the reaction zone through an expression derived by Newman [13].

$$R_B = \frac{1}{4\sigma r} \qquad (2)$$

Newman derived this expression for a conductor that makes a "point" contact of effective radius, r, with a semi-infinite electrolyte of conductivity, σ. Because of the non-uniform current flow lines in the electrolyte near the point contact, the net electrolyte resistance is R_B. Although derived for a single-point contact, Newman's formula should be applicable to multiple-point contacts at the interface in a UIC as long as the contacts are well separated. For such a case with radius r_i characteristic of each contact point and with numerous parallel interface resistances, $R_i = 1/(4\sigma r_i)$ via Newman's formula, the net resistance, R, is given by

$$\frac{1}{R} = \sum \frac{1}{R_i} = 4\sigma \sum r_i = \frac{2}{\pi}\sigma(2\pi r) \qquad (3)$$

In Equation (3), $r = \Sigma r_i$ and $2\pi r$ is the sum of the individual point contact perimeters called the effective reaction length, ERL. The specific ERL is obtained by dividing $2\pi r$ by the cross-sectional area of the electrode.

The DC polarization resistance $R_\eta = d\eta/dI$ at zero current, where η is the overpotential and I is the current. The resistance parameter, R_p, which was determined from small amplitude ac impedance analysis, was shown to be equal to R_η [2] and so it also is called the polarization resistance. The polarization resistance is inversely proportional to the oxygen reduction reaction rate at an electrode-electrolyte interface. Therefore for the UIC design, R_p^{-1} is a measure of the electrocatalytic activity of the particular electrode material.

Most of the experiments using the UIC design to date have examined the influence of operating variables such as temperature, $p(O_2)$, applied potential, and time as well as compositional variables on R_B and R_p. Since the UIC is a new design, it is important to confirm that the data analysis yields reproducible and meaningful results. The following experiments were performed to demonstrate that goal.

Experimental

Previously, the UIC system used two electrodes for both the AC impedance and DC polarization tests. Therefore, the overall cell impedance included the effects of a zirconia-porous Pt electrode as well as the zirconia-air

electrode, the electrode interface of interest. To remove the effects of the porous Pt electrode, a third electrode, a reference electrode, was added to the UIC test system as shown in Figure 12.

Referring to Figure 12, platinum paste (Engelhard #8026, non-fluxed) counter and reference electrodes were baked (20 min at 1100°C in air) onto a dense, 8.0 mole percent yttria-stabilized zirconia electrolyte disc. The disc was 1.26 cm in diameter by 0.94 mm thick. The centered porous platinum counter electrode was 0.64 cm in diameter. An 0.16-cm gap separated the counter electrode from an annular ring reference electrode. A small gap was cut through the annular reference electrode to allow more complete gas coverage of the interior counter electrode. Platinum mesh (52/inch) was cut to cover the same area as the reference and counter electrodes, and was backed by a spring-loaded solid platinum disc or ring connection. The platinum mesh ensured that gas coverage was uniform over the entire reference and counter electrode surfaces. The opposite face of the zirconia electrolyte disc was polished flat down to 1 μm diamond final polish. The previously used sample (LSM x=0.1 disc, 0.64 cm diameter by 1.42 mm thick) was remounted to check reproducibility of earlier results obtained with the original two electrode system. Before remounting, the surface of the LSM disc adjoining the bare and smooth zirconia surface was reground with 400 grit SiC paper in a 0-90° stroke pattern to provide numerous gaseous flow paths between the electrode-electrolyte interface.

A dramatic improvement in the signal-to-noise ratio was noticed in the data collected using the UIC system with a separate reference electrode. With the three-electrode system, we were able to collect data over a wider frequency range (100kHz to .01 Hz) and use a lower voltage amplitude (10mV rather than 50mV). Also, with these improvements the data collection sweep time was four times faster. By using a lower amplitude voltage signal, the equivalent circuit fit to the impedance data was improved by an order of magnitude, especially at the lower frequencies where the electrode reaction kinetics control the complex impedance.

The behavior of the effective reaction length (ERL) and the oxygen reduction reaction rate (R_p^{-1}) was re-examined for the LSM (x=0.1) sample. As before, AC impedance data were collected over a frequency range of 1-100kHz using a Solartron 1255 Frequency Response Analyzer, an EG&G PAR Model 273 Potentiostat, and an IBM PC for experimental control and data analysis. The

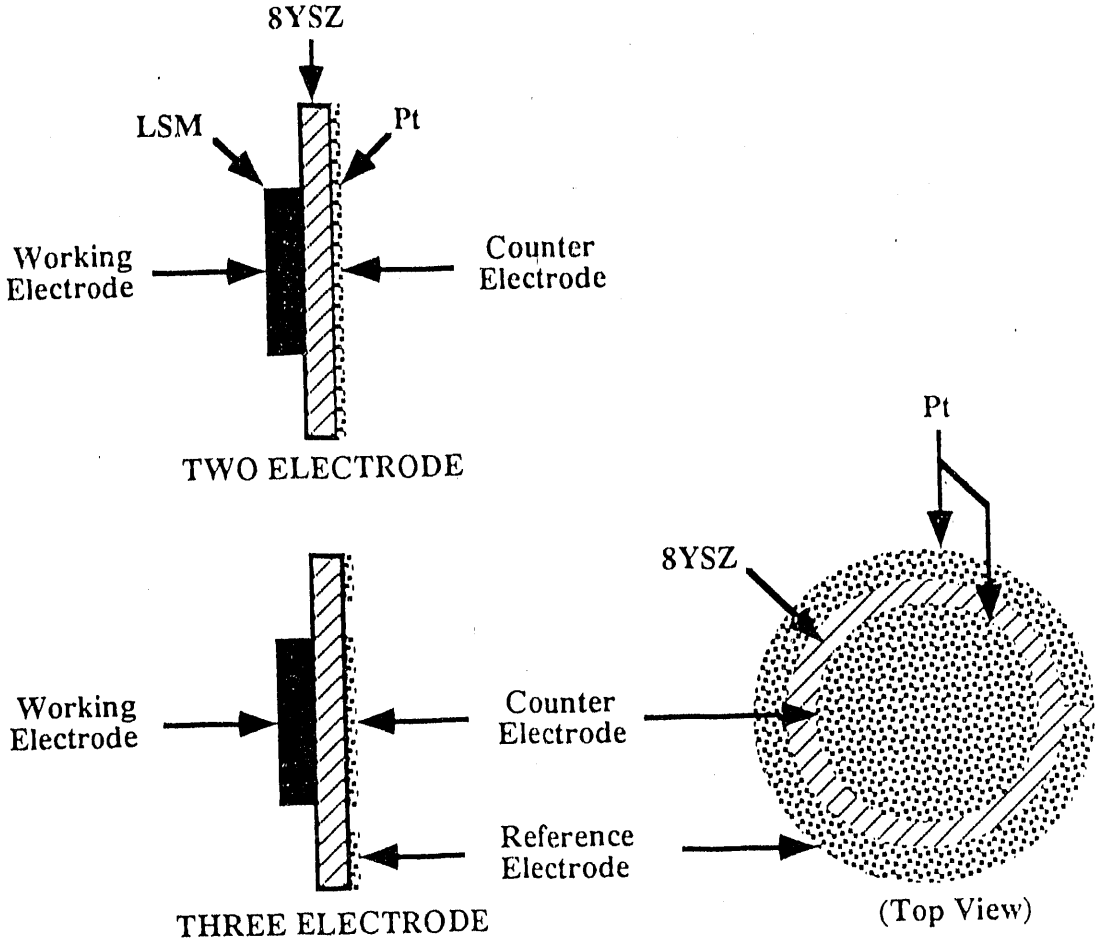

Figure 12. Arrangement of electrodes on the 8YSZ electrolyte for the two-electrode and three-electrode cell design.

temperature range was 973 to 1173K (700 to 900°C) and the oxygen partial pressure was varied from 0.2 atm to 10^{-5} atm by dilution of air with argon gas.

Electrocatalytic Performance of the $La_{0.9}Sr_{0.1}MnO_3$/8YSZ Interface

In Table 1, parameters that describe the electrocatalytic performance of the $La_{0.90}Sr_{0.10}MnO_3$/8YSZ interface are compared for the original two-electrode and the new three-electrode UIC systems. Pseudoeactivation energies are believed to reflect the activation energy for ionic conduction in the electrolyte, though other contributions may be present. Oxygen reduction activation energies and the reaction rate dependence on the partial pressure of oxygen are particularly important indicators of cathode performance and of the nature of the rate-determining step in the operation of the electrochemical cell. The ERL is related to that area in the vicinity of the gas/electrode/ electrolyte triple phase boundary where the rate-controlling electrochemical reactions take place. It is clear that the two experimental cell designs yielded indistinguishable results for reaction activation energies and the reaction rate dependence on the oxygen partial pressure. Differences in ERL may be attributed to the surface preparation of the electrolyte and electrode materials in the unbonded interface cell design.

Pseudoactivation Energies. Pseudoactivation energies for the two- and three-electrode UIC systems were identical within experimental error. This term is derived from Equation (4), a rearranged form of Equation (3):

$$\frac{T}{R_B} = 4r\sigma_o \exp[-E/kT] \qquad (4)$$

where $\sigma = \sigma_o T^{-1} \exp(-E/kT)$ has been substituted for the electrolyte conductivity. The slope of log (T/R_B) vs. 1000/T is called a pseudoactivation energy since it may include the influence of temperature dependence for the effective radius parameter, r. These pseudoactivation energies also were indistinguishable from the activation energy determined for ionic conduction in the 8YSZ electrolyte, previously measured to be 0.9eV over the 700 to 900°C temperature range [11].

Table 1. Comparison of Electrocatalytic Parameters for a $La_{0.90}Sr_{0.10}MnO_3$/8YSZ Interface Determined Using A Two- and Three-Electrode System

PARAMETER (700-900°C)	Two-Electrode[1]	Three-Electrode[2]
Pseudoactivation Energy for T/R_B (eV)	1.0±0.1	1.0±0.1
Oxygen Reduction Activation Energy in Air (eV)	2.1±0.2	1.9±0.2
Reaction Rate Dependence on $p(O_2)$ at 900°C	0.28±0.03	0.22±0.03
Specific ERL Values (cm/cm^2)	0.8 to 1.0	0.4 to 0.6

1 Both electrolyte and electrode surfaces roughened.
2 Electrolyte surface polished and electrode surface roughened.

The general agreement of the pseudoactivation energy with the electrolyte activation energy indicates that extending Newman's model [13] for a single- point contact to a multiple-point contact situation in the UIC design is probably valid. Furthermore, the interpretation of $2\pi r$ as an effective reaction length is justified. Also, previous measurements indicated that R_B was independent of the electrolyte thickness (from 0.5 to 2.0 mm). This would be expected since the electrolyte bulk resistance for uniform current flow would be only a few ohms, and R_B, which essentially is a contact resistance, was ≈100Ω at the 900°C measurement temperature.

Oxygen Reduction Activation Energies. Since the reciprocal polarization resistance (R_p^{-1}) is proportional to the reaction rate for oxygen reduction at the electrode-electrolyte interface, the slope of log (R_p^{-1}) vs. 1000/T yields the oxygen reduction activation energy. In air, this value was 1.9±0.2 eV when determined for the three-electrode UIC system and 2.1±0.2 eV for the two-electrode system. Both of these values are considerably greater than the 1.3 eV oxygen reduction activation energy determined previously for an unbonded platinum disc-8YSZ electrolyte interface in air [11]. For optimal cell performance, the activation energy for oxygen reduction should be as low as possible. While the Pt/YSZ interface yields a more desired activation energy, Pt is not a viable candidate material for SOFCs for reasons of cost and stability in a hostile fossil fuel environment. Preliminary evidence

suggests that the oxygen reduction activation energy may be decreased with increased Sr substitution. This relation is being further explored.

Reaction Rate Dependence on $p(O_2)$. The dependence of the rate of oxygen reduction on the partial pressure of oxygen is given by the empirical expression

$$R_p^{-1} = A\, p(O_2)^n \qquad (5)$$

here n is an empirical parameter related to the nature of the rate-controlling step in the interfacial reaction. An n value between ±1/4 is indicative of a rate-limiting step controlled by charge transfer, as shown by Wang and Nowick [14], where n=-1/4 when most of the reaction sites contain atomic oxygen and n=+1/4 when most of the reaction sites are empty. These limits are in good agreement with experimental values determined for the $La_{0.90}Sr_{0.10}MnO_{3-x}$/8YSZ interface. As summarized by Takeda et al. [15] , an n=1/2 dependence implies a rate limitation by the dissociative adsorption of oxygen, while an n=1 dependence implies rate control by the adsorption of molecular oxygen.

For the $La_{0.9}Sr_{0.1}MnO_3$/8YSZ interface, the oxygen reduction reaction rate (proportional to R_p^{-1}) appeared to depend upon changes in temperature and $p(O_2)$ in a manner similar to reaction rates determined for a solid platinum disc/8YSZ interface [11]. For the solid platinum electrode at 1174K, the $p(O_2)$ dependence of R_p^{-1} was characterized by an n index equal to 0.29. This value indicates reaction rates limited by charge transfer, where most of the surface sites along the tpb are uniccupied [14]. Furthermore, the dc polarization characteristics for the oxygen reduction reaction in air were similar in shape for both electrode materials.

Effective Reaction Lengths. The specific ERL values, determined for the original cell configuration with both electrolyte and electrode surfaces roughened, increased steadily from 0.8 to 1.0 cm/cm^2 as temperature increased from 700 to 900°C. For the remounted cell configuration, where the zirconia electrolyte surface was smooth opposite the roughened electrode surface, the specific ERL values ranged from 0.4 to 0.6 cm/cm^2 as the temperature increased. Thus, a reduction of the specific ERL by about a factor of two is observed for the cell configuration with a smooth surface opposite a rough surface when compared to a cell configuration with both surfaces roughened.

This design change was introduced to establish a reference for comparison to planned experiments using cells with porous electrodes sintered onto smooth electrolyte discs. The approximate factor of two in ERL values for the two UIC designs is believed to be due to a greater number of multiple contact points for mating rough surfaces compared with mating rough and smooth surfaces. Further measurements using different cross-sectional areas for the electrode are planned to confirm this interpretation.

Recently, Mizusaki et al. [16] estimated the length of tpb and the areas of actual contact for a porous (~35 to 40%) $La_{0.6}Ca_{0.4}MnO_3$/YSZ interface from SEM images. They found that both the tpb and contact area depended upon powder preparation procedures and sintering temperature, with both quantities generally increasing from 1000 to 1200°C. For the porous electrodes fired at 1200°C, the tpb was about $10^4 cm/cm^2$ and the contact area was about 0.5 cm^2/cm^2. The contact area coverage value agreed with the estimated 35 to 40% porosity value. Hence, the contact area and the tpb (or ERL) are reduced by a factor of 10^{-4} to 10^{-3} for the UIC design when compared to a normally sintered porous electrode-electrolyte interface. Accordingly, the polarization resistance for the UIC interface is a factor of 10^3 to 10^4 greater (a few kΩ compared to a few ohms) than for a sintered porous electrode-electrolyte interface, and is much more sensitive to electrochemical modification. Presumably, R_p also will be more sensitive to composition adjustments for the UIC design, although this assumption has not been tested yet. Finally, the UIC design allows one to estimate the ERL (the size of the reaction zone) from impedance measurements. This quantity, which depends upon composition, also is subject to electrochemical modification. In contrast, for a normally sintered porous electrode-electrolyte cell, R_B, determined by impedance spectroscopy, is just the bulk resistance of the electrolyte. In the latter case, R_B would include a contribution from any insulating reaction layers that may form at the interface. However, bulk R_B values would be insensitive to changes in the effective reaction zone size.

Electrocatalytic Performance of the $La_{0.7}Sr_{0.3}MnO_3$/8YSZ Interface

The principal conclusion drawn from these measurements and earlier studies [11, 12] is that the x=0.3 composition is more electrocatalytically active than the x=0.1 composition and, therefore, potentially would be a better air electrode material in a SOFC. Initial specific ERL values for the

x=0.3 electrode appeared to be slightly larger than for the x=0.1 electrode. A more significant observation for the x=0.3 composition was the sensitivity of both the specific ERL values and the oxygen reduction reaction rates to electrochemical modification induced by $p(O_2)$ or changes in applied potential. The reaction zone thus was subject to modification and apparently was extended beyond the physical triple-phase boundary. Preliminary measurements indicate factors of two and ten achievable for changes in ERL and R_p^{-1}, respectively, for x=0.3 electrode material. This sensitivity, presumably, comes about through a surface reduction model as described by Equation (1).

An increase in reaction kinetics of the x=0.3 material probably is due to an increased concentration of the electrocatalytically active species V_o and h in an extended reaction zone. These observations are consistent with a mechanism proposed by Hammouche et al [17] that for a relatively small cathodic overpotential (≈100mV for x=0.3), the surface of the air electrode material is partially reduced via the reaction:

$$2Mn_{Mn}^{\cdot} + O_o(LSM) + V_o^{\cdot\cdot}(Z8Y) \rightarrow 2Mn_{Mn} + V_o^{\cdot\cdot}(LSM) + O_o(8YSZ) + 2h^{\cdot} \quad (6)$$

In this reaction, a Mn^{4+} ion acquires an electron to become an additional Mn^{3+} ion on the surface of the LSM material. The surface Mn^{3+} ions are reaction sites whereby an oxygen gas molecule can be adsorbed, acquire two electrons, and dissociate. The dissociated oxygen atom is incorporated into the LSM lattice as a surface oxygen vacancy (V_o). Each time a surface Mn^{3+} ion loses an electron to an oxygen atom and becomes a Mn^{4+} ion, it must reacquire an electron from a bulk Mn^{3+} ion to repeat the process, thus serving as the reaction site to provide all the electrons necessary to reduce the oxygen gas atoms to bulk oxygen ions. Then the oxygen ion can diffuse through the bulk LSM to the electrolyte interface where it then simply transfers across the interface and conducts through the electrolyte by a vacancy mechanism. Improved kinetics and current generation are induced by having the proper mix of surface and bulk concentrations of oxygen vacancies, Mn^{3+}, and Mn^{4+} ions in the LSM electrode material.

Further measurements to examine the temperature and $p(O_2)$ dependence of R_B and R_p^{-1} are in progress using the UIC design with the x=0.3 electrode material. Hopefully, these measurements will support initial observations.

Recently, Hammouche, et al. [18], using DC sweep voltammetry and precise thermogravimetric measurements, reported on the electrocatalytic behavior of a series of $La_{1-x}Sr_xMnO_3$/8YSZ cells. The working electrode was a single "pin-shaped" sample of the perovskite composition under investigation. They ascribed the electrocatalytic properties of $La_{1-x}Sr_xMnO_3$ for oxygen reduction to the generation of oxide vacancies inside the material, which results in broadening of the electrode reaction zone. However, no measurements indicating the actual size of the reaction zone itself were reported in that study. Their conclusion was that the electrocatalytic process varies significantly with the Sr doping level. At the higher doping levels, the electrode material was more electrocatalytically active. This is in line with our conclusion reached using the UIC design and ac impedance analysis of $La_{1-x}Sr_xMnO_3$ with $x = 0.1$ and 0.3.

Preparation of Nanoparticles Using Microemulsions

Nickel sulfide and cobalt sulfide particles have been successfully prepared using microemulsions based on toluene and C12E4 and AOT surfactants. The principal application of these nanoparticles is as catalysts for the dehydrosulphurization and hydrogenation of asphaltenes, an important component of liquified coals. One of the remarkable features of these nanoparticles is their long-term stability (more than 3 weeks). Their stability crucially depends on the location of the microemulsion in the ternary phase diagram. The water/organic microemulsion phase boundary is highly susceptible to the type and the concentration of metal ions used. Preparation of water/organic microemulsions of asphaltene solubilized in toluene have also been initiated.

Catalytic nanoparticles stabilized in microemulsions will be potentially useful in the development of efficient and easily transportable active catalysts for dehydrosulphurization and hydrogenation of liquids derived from coal, and catalysis in general. If these microemulsions are thermodynamically stable, then it opens new avenues for the studies of nucleation phenomena in restricted geometries. Experimental methods developed as a part of this research will additionally be useful in the application of sols.

Stability and Structure of Nanoparticles

Nickel sulfide nanoparticles prepared in a microemulsion (CnEm/water/hexadecane) displayed two distinct size distributions, peaked at 2 to 4 nm and 50 to 60 nm, as determined using transmission electron microscopy (TEM). Nanoparticles in the latter size range may be an artifact associated with TEM sample preparation techniques. The process involves a slow evaporation of the hydrocarbon solvent, which may induce an aggregation of micelles. The metal sulfide particles within a 50-nm domain are only 0.8 to 1.0 nm in diameter, consistent with this interpretation. The largest fraction of the particles is, however, 2 to 4 nm in size, corresponding to inverse micelles containing nickel sulfide. Preliminary diffraction data do show lattice spacings in accordance with the nickel sulfide crystal structure.

In the next phase of this research, evolution of the bimodal size distribution with time will be investigated. These kinetic studies are crucial because, at this stage, it is not known whether the 50 nm diameter particles are artifacts of the sample preparation technique, or there exists a (meta)stable equilibrium between these two distinct size distributions.

A complementary x-ray scattering technique will be used to explore the changes in width associated with nickel sulphide lattice spacings (0.295 nm). The width of the x-ray diffraction peak depends on the size of the particle. Hence, the evolution of the diffraction peak profile can be monitored to study aggregation processes, if any. This study will provide an independent check on the TEM analysis.

During the course of this study, a major influence of the surfactant composition on the stability of nanoparticles was discovered. For example, nickel sulfide prepared in AOT/toluene/water-based microemulsions precipitated within a week. Nevertheless, an addition of C12E4 surfactant in this microemulsion appeared to enhance the stability dramatically. Therefore, the phase diagrams and the micellar structures in this mixed surfactant system requires further exploration. Such studies are important for the preparation of asphaltene microemulsions, which are described below.

Asphaltene Microemulsions

Asphaltenes are a class of compounds derived from coal liquids and heavy crude oil residues that exhibit preferential solubilization in aromatic solvents such as benzene, toluene, and xylenes.

Preliminary studies of toluene solutions of asphaltenes were conducted using a range of anionic and nonionic surfactants. Water in oil microemulsions can be prepared at very low water concentrations (less than 5 percent). At higher water concentrations, asphaltenes will precipitate. Thus, it appears that the coprecipitation of catalytically active mixtures of metal sulfides and asphaltenes is feasible. The precipitate may then be used in dehydrosulphurization and hydrogenation processes.

A systematic study of asphaltene microemulsions is planned. One aspect of this study will involve structural characterization of asphaltene microemulsions as a function of water concentration using small angle x-ray scattering (SAXS). Secondly, the chemical nature of asphaltenes depends on the geologic origin of the feed stock. Therefore, phase diagrams of asphaltenes from Syrian, Arabian (Unocal) and U. S. (Kerr McGee Corp.) crude oil sources will be constructed. X-ray powder diffraction patterns and TEM micrographs of the precipitated asphaltenes as a function of catalyst concentration will be analyzed. These studies will help to characterize the microheterogeneity and the catalyst distribution in the asphaltene matrix.

Organic Thin Films and Organized Assemblies as Templates for the Controlled Nucleation of Inorganic Particles

Organic interfaces of controlled chemical and physical properties have been proposed as appropriate model surfaces to control the heterogeneous nucleation of crystalline, inorganic particles suitable for use as catalysts. Self-assembled monolayers on solid substrates and Langmuir-Blodgett (L-B) films are being used as tailored interfaces to produce microenvironments suitable for nucleation events at surfaces.

Mineralization Schemes

Three approaches to creating organized, monomolecular, organic thin films as surfaces for heterogeneous nucleation have been explored. First, L-B multilayers of fatty acids and acidic phospholipids were formed by the transfer of ordered amphiphilic monolayers from the air-water interface. The necessity of maintaining an organized polar interface limited the durability, reliability, and handleability of these substrates in ambient environments. Collapse and structural disintegration of the traditional L-B films were

observed when exposed to ambient conditions. Therefore, supported monolayers, bilayers, and multilayers were produced on either hydrophobic or hydrophilic substrates using polymerizable amphiphiles (fatty acids and phospholipids). These polar interfacial materials could be either polymerized before or after transfer from the air-waster interface to the substrate simply by exposure to heat (<60°C) or ultraviolet light. Various modifications and studies of the properties of polymerizable L-B films on supports are being pursued. Ellipsometry, contact angle analysis, and x-ray photoelectron spectroscopy (XPS) are being applied to evaluate the properties of thin organic films produced by these techniques.

A second method for producing organized organic films is based on a technique using cast dispersions of lipid vesicles that produce organized multilayers of amphiphiles both before and after desiccation. Polymerizable and natural amphiphiles were used to create dry multilayer films on glass, Teflon, and other solid substrates. When cast together with soluble inorganic salts, these films were transformed into multilayer, mineralized precursors with the metal cations suspended within the aqueous interstices between each lamellae, associated closely with the acidic lipid polar regions. Gaseous reagents were perfused slowly into these films at controlled stoichiometry, creating the mineralized phase of interest within the organic layered structure.

This strategy has also been modified using soluble poly(ethylene oxide) together with inorganic salts in the aqueous dispersion. Poly (ethylene oxide) forms a helical structure in both solution and solid states, mimicking crown ethers in their ability to coordinate metal ions. This combination, when cast and dried as a film, is expected to create alternate organic layers containing high densities of inorganic salt, coordinated within the crystalline polymer. Coordination of the metal precursor creates a consistent microenvironment that chelates the metal cation, producing monocrystalline, inorganic material when gaseous reagents are diffused into the hybridized network.

A third method to produce inorganic crystalline particles via heterogeneous nucleation on organic interfaces utilizes aqueous dispersions of acidic amphiphiles that form lamellar or liquid crystalline lyotropic phases. Phase diagrams for many acidic amphiphiles in water are known. Negatively charged phospholipids and fatty acids have been utilized, for which the phase

diagrams demonstrate the existence of prominent lamellar phases across a wide range of concentrations. Amphiphiles dispersed in aqueous solutions of mineral salt precursors and/or poly(ethylene oxide) are prepared in quartz x-ray capillary tubes at known concentrations. Hydrated, lamellar phases are confirmed by low-angle x-ray analysis and then exposed to gaseous reagents to yield the crystalline inorganic phase desired. The lamellar nature of the lyotropic phase created alternate lamellae of hydrophobic (alkyl) and hydrophilic (polar, aqueous) regions for particle generation. This organic superstructure is expected to act as a layered, aqueous template to coordinate metal ions and to chelate them for crystallization into nanoparticles in reactions with the gaseous reagents of choice.

To date, cadmium chloride and hydrogen sulfide have been used as the soluble metal salt and gaseous reactive crystalline reagent, respectively. Crystalline cadmium sulfide particles have been produced using L-B films of cadmium-complexed fatty acids and water-cast vesicle dispersion film precursors, both with and without poly(ethylene oxide). These particles have been characterized by electron diffraction techniques and the crystalline phases determined. Dark field and bright field electron microscopy techniques are being used to assess relative effectiveness of each technique to produce homogeneous and high yields of crystalline phases.

Electrochemical Promotion Studies

Dramatic changes in the catalytic activity and product composition have been observed by Vayenas [19], who used one electrode of a fuel cell as a catalyst surface for gas phase reactions. In the conventional operation of a solid oxide fuel cell, platinum electrodes, deposited onto opposing surfaces of a material such as stabilized zirconia, are exposed to oxygen gas on one side and to fuel on the other. Oxide ions are transported from the oxygen side to the fuel side during galvanic operation. In the experiments reported by Vayenas et al., a mixture of oxygen and fuel (e. g., methane, ethane, ethylene, methanol, or carbon monoxide) was delivered to the fuel side and the potential or current through the cell was externally controlled. The significant observation was that the rate of the reaction could be increased by a factor of up to 55 by pumping oxide ions at a very low rate from the pure oxygen side to the reaction side. The ratio of increase of reaction rate to

pumping rate was reported to be as high as $3x10^5$. Further, the product composition, or catalyst selectivity, was also a function of the controlled pumping current. Solid state proton conductors have also been used in similar experiments by Demidov [20] and by Stoukides [21].

Vayenas [19] hypothesized that this electrochemical promotion effect, which he termed "non-faradaic electrochemical modification of catalytic activity (NEMCA)," was due to a decrease in work function of the metal catalyst that resulted from the increased activity of electrons at the triple-phase boundary of the zirconia electrolyte, platinum electrode, and gas reactant mixture. The change in work function caused a change in chemisorptive bond strength of reactants and/or intermediates. Although this hypothesis, which focuses on changes in work function, has merit and is also in conformity with current thinking of catalytic promoters, the report by Vayenas that reversal of the current applied to the cell also produces a NEMCA effect casts some doubt on the role of catalyst work function. Clearly, the work function increases when the current is reversed and, correspondingly, the chemisorptive bond strength changes in a direction related to the type of bond. Therefore, there is a need to confirm and further examine these exciting and promising results.

Experimental Approach and Results

From a thorough review of the literature on electrochemical promotion of gas phase reactions, it was concluded that the experimental information most needed would be an examination of catalyst surfaces using scanning electron microscopy and scanning tunneling microscopy and spectroscopy in various forms. Further, the triple-phase boundary must be subject to examination by using thin, evaporated platinum films rather than the rather crude deposits obtained by thermal decomposition of commercial pastes or paints. These requirements dictate that the cell be of a totally different design than previously so that the coated zirconia can be easily removed and replaced.

To this end, a cell was designed and constructed that utilized 13-mm-diameter disks of zirconia positioned between the ends of precision-ground quartz tubes and held in place with a sleeve of precision-bore quartz tubing. Electrical contact to the electrodes is through platinum foil pressed against the edges of the tubing. This assembly is then inserted into a tube furnace. Surfaces of the zirconia have been examined by optical and electron

microscopy. A polishing procedure has been developed to reduce the density of voids and surface imperfections. These disks can be used for either thermal decomposition of platinum paint or evaporation.

For the deposition of platinum (and other metal catalysts), a small electron beam evaporator was assembled. Using this technique provides easily controlled catalyst thicknesses and also ensures high purity of the deposit. Since it is desired to examine catalytic promotion as a function of metal thickness and of annealing treatment, a metal grid on the zirconia surface is necessary to provide good electrical contact. This was accomplished with conventional photolithography and a mask with a grid size of about 50 μm. Platinum was first deposited to a thickness of 1-3 μm with the mask in place. Then, the mask was removed and the catalytic layer was deposited. A blank experiment was used to determine the catalytic activity of the grid, which is generally very small. Agglomeration of platinum films on zirconia substrates was recently examined by Maskell, et al. [22]. These results are followed as a guide to determine appropriate annealing temperatures and times; the actual state of dispersion of the catalyst was, however, directly observed with the SEM. While this procedure for preparation of the catalytic electrodes is under development, platinum prepared from a commercial paint is being used to confirm the observations of Vayenas [19].

A gas delivery system was constructed so that known volumes of fuel and oxygen can be delivered into the cell at controlled rates. The outlet of the cell was connected to a gas chromatograph via a three-way valve and sample loop. The gas chromatograph columns found to be effective are molecular sieve 13A and Poropak QS. Thermal conductivity detectors are used, with a sensitivity of approximately 100 ppm for the gases of interest. A locally designed and constructed potentiostat/galvanostat completes the experimental set-up.

References

1. L. A. Chick, J. L. Bates, L.R. Pederson, and H.E. Kissinger in *Proceedings of the First International Symposium on Solid Oxide Fuel Cells* (ed. S.C. Singal) Electrochemical Society, Pennington, New Jersey, 1989, pp. 170-179.

2. L. A. Chick, L. R. Pederson, G. D. Maupin, J. L. Bates, L. E. Thomas, and G. J. Exarhos, *Materials Letters* 10: 1,2, 1990, pp. 6-12.

3. J. L. Bates, L. A. Chick, W. J. Weber, and G. E. Youngblood, *Proceedings of the Fourth Annual Conference on Fossil Energy Materials.* Oak Ridge, Tennessee, May 15-17, 1990.

4. W. F. Ford and J. White, Fig. 39 in: *Phase Diagrams for Ceramists* Vol. 1, American Ceramic Society, Columbus, OH, 1964.

5. N. Sakai, T. Kawada, H. Yokokawa, and M. Dokiya, presented at Japan AIST and U.S. D.O.E. Fuel Cell Subcommittee Meeting, Phoenix, Arizona, November, 1990.

6. M. Dokiya, N. Sakai, T. Kawada, H. Yokokawa, T. Iwata, and M. Mori in *Proceedings of the First International Symposium on Solid Oxide Fuel Cells* (ed. S.C. Singal) Electrochemical Society, Pennington, New Jersey, 1989, pp. 325-336.

7. H. U. Anderson in *Processing of Crystalline Ceramics* (eds. H. Palmour, R. F. Davis, and T. M. Hare) Plenum Press, New York, 1978, pp. 469-477.

8. P. D. Ownby in *Materials Science Research, 6*, 1973, pp. 431-437.

9. D. B. Meadowcroft and J.M. Wimmer, *American Ceramic Society Bull.*, 58: 6, 1979, pp. 610-615.

10. D. W. Readey in *Sintering of Advanced Ceramics*, Vol. 7, (eds. C. A. Handwerker, J. E. Blendell, and W. A. Kaysser) American Ceramic Society, Westerville, OH, 1990) 86-110.

11. J. L. Bates, L. A. Chick, W. J. Weber, and G. E. Youngblood, "Advanced Materials and Electrochemical Processes in High-Temperature Solid Electrolytes," in *Ar&TD Fossil Energy Material Program Semi-Annual Progress Report for the Period Ending Sept. 30*, ORNL/FMP/90/2, Oak Ridge National Laboratory, Oak Ridge, Tennessee, 1990.

12. G. E. Youngblood, W. J. Weber, and J. L. Bates, "Electrochemical Processes at Solid Electrode-Electrolyte-Gas Interfaces," *Proceedings of the Fifth Annual Conference on Fossil Energy Materials*, Oak Ridge, Tennessee, May 14-15, 1991 (in press).

13. J. Newman, "Resistance for Flow of Current to a Disk," *J. Electrochem. Soc. 113*, 1966, pp. 501-502.

14. D. Y. Wang and A. S. Nowick, "Cathodic and Anodic Polarization Phenomena at Platinum Electrodes with Doped CeO_2 as Electrolyte, I,"

J. Electrochem. Soc. 126:7, 1978, pp. 1155-1165.

15. Y. Takeda, R. Kamo, M. Noda, Y. Tomida, and O. Yamamoto, "Cathodic Polarization Phenomena of Perovskite Oxide Electrodes with Stabilized Zirconia," *J. Electrochem. Soc.* 134:11, 1987, pp. 2656-2661.

16. J. Mizusaki, H. Tagawa, K. Tsuneyoshi, and A. Sawata, "Reaction Kinetics and Microstructure of the Solid Oxide Fuel Cells Air Electrode $La_{0.6}Ca_{0.4}MnO_3$/YSZ," *J. Electrochem. Soc.* 138:7, 1991, pp. 1867-1873.

17. A. Hammouche, E. Siebert, M. Klietz, and A. Hammou, "Oxygen Reduction at the $La_{1-x}Sr_xMnO_3$/Zirconia Electrode," in *Proceedings of the First International Symposium on Solid Oxide Fuel Cells*, The Electrochemical Society, Inc., Vol. 89-11, 1989, pp. 265-276.

18. A. Hammouche, E. Siebert, A. Hammou, and M. Kleitz, "Electrocatalytic Properties and Nonstoichiometry of the High Temperature Air Electrode $La_{1-x}Sr_xMnO_3$," *J. Electrochem. Soc.* 138:5, 1991, pp. 1212-1216.

19. C. G. Vayenas, S. Bebelis, and S. Ladas, *Nature 343*, 1990, 625; C. G. Vayenas, S. Bebelis, S. Neophytides, and I. V. Yentekakis, *Appl. Phys. A 49*, 1989, 95 and references therein.

20. M. B. Demidov, E. N. Savinov, and V. N. Parmon, *React. Kinet. Cataly. Letters 38*, 1989, p. 255.

21. P.-H. Chaing, D. Eng, and M. Stoukides, *J. Electrochem. Soc. 138*, 1991, p. L11.

22. W. C. Maskell, N. M. Sammes, and B. C. H. Steele, *J. Phys. D: Appl. Phys. 20*, 1987, p. 99.

SNL-1-CERAMIC CATALYST MATERIALS: HYDROUS METAL OXIDE ION-EXCHANGE SUPPORTS FOR DIRECT COAL LIQUEFACTION

C. H. F. Peden

Interfacial Chemistry, Division 1841
Sandia National Laboratories
Albuquerque, NM 87185-5800

ABSTRACT

This semiannual report describes studies aimed at developing and optimizing the use of a unique catalyst support material, the hydrous titanium oxide ion-exchangers. In part, we seek to understand how the activity of a catalyst is related to the concentration and dispersion of active metals on the catalyst supports. Such information is critical to designing materials having optimum catalytic properties. We have developed synthetic techniques for controlling both the concentration and dispersion of nickel, molybdenum and rhodium on hydrous sodium titanate catalyst supports. The techniques were based on and required an understanding of the solution chemistry of both the support material and dissolved metal species. In addition, studies of the local molecular structure by Raman, XANES and solid-state ^{17}O NMR spectroscopies are being pursued because of the importance of the local structure in determining the ion-exchange properties of these materials. These were also critical to the development of appropriate catalyst preparation procedures. That these studies have impacted the development effort is demonstrated by the improved catalytic performance of more recently prepared materials. Currently, we have begun to explore alternate synthesis procedures for the preparation of the hydrous titanates. Recent work in this area will be described in forthcoming semiannual reports. Finally, we have also initiated studies of structure/activity relationships in the final catalyst materials in order to provide further guidance to the synthesis effort as to the most desirable physical properties. Some of this work is detailed here.

INTRODUCTION

Coal is our most abundant fossil fuel energy source. However, it requires extensive chemical treatment and processing to convert it from a hydrogen-poor "dirty" solid to a "clean" premium liquid fuel such as gasoline. One of the missions of the Department of Energy's AR&TD research is to permit expanded use of coal-based systems by providing a focus for the exploration of ideas pertaining to coal science, conversion and utilization. This project seeks to accomplish that mission by exploring the synthesis and evaluation of new ceramic catalytic materials for efficient, direct conversion of coal to clean liquid fuels. Because the recoverable U.S. supplies of coal are 50 to 100 times that of crude oil, development of new catalysts for efficient conversion of coal to environmentally acceptable liquid fuels would have an enormous impact on extending our usable energy reserves.

As an AR&TD project, the focus of this program is to conduct research and development on catalytic materials for fossil energy applications. In this way, we are obtaining a better understanding of these materials that will impact the long-term, generic needs of various fossil fuel technologies. However, sufficient testing of the hydrous metal oxide ion-exchange catalysts with coal and coal-derived feeds has been accomplished to demonstrate that they show great promise for end-use process applications.[1]

The specific materials under study in this AR&TD project are from a group of hydrous oxide ion-exchange compounds of Ti, Zr, Nb, and Ta developed at Sandia National Laboratories. The compounds have been used to prepare catalysts by a novel synthesis route involving the incorporation of active metals by ion exchange.[2] Hydrous oxide ion-exchange compounds were originally developed at Sandia for use in the decontamination of aqueous nuclear waste and as precursors for ceramic materials.[3] The use of these compounds as ceramic catalyst supports arises from the unique properties which these systems exhibit: 1) any metal or mixture of metals can be incorporated into the materials over a wide concentration range by a simple process; 2) the materials have high surface area; 3) they exhibit good chemical stability; 4) solution chemistry or more conventional high temperature reactions can be used to provide control of the active metal oxidation state; 5) acidity and basicity of the substrate can be modified by ion exchange; and 6) the catalysts can be prepared on transition metal-oxide supports (Ti, Nb, and Ta) known to undergo a so-called "strong metal support interaction" (SMSI).

The hydrous metal oxides investigated in this study belong to a group of inorganic ion-exchange compounds that can be represented by the empirical formula $M(M'_xO_yH_z)_n$, where M is an exchangable cation and M' is Ti, Nb, Zr, or Ta. When added to a solution of aqueous metal cations, these powdered materials will react to form amorphous precipitates containing the dissolved metal which has replaced the exchangable cation, M. Catalytic activity has been measured at Sandia for materials synthesized in this manner.[1,4] For example, catalysts prepared using the hydrous titania (HTO) ion exchangers are equally effective for conversion of coal to low molecular weight products as a commercial Ni-Mo/alumina catalyst containing 15% by weight active metals even at low (1%) active metal loadings.[1]

One possible reason for the improved performance of the catalysts prepared from the hydrous titanate materials may be that active metals are dispersed more completely via the ion-exchange process than when loaded by traditional incipient wetness techniques. As such, these materials offer a method to prepare greatly improved heterogeneous catalysts for many applications, provided we understand the important variables in the synthesis.

Our goal is to develop a fundamental understanding of the preparation and properties of these unique materials. Specifically, we have been investigating the following areas:

1) molecular and extended macroscopic structure of the hydrous titanate and how this relates to its other material properties;

2) determination of how the synthesis of the HTO powders affects its structure, and correspondingly its material properties;

3) mechanism of incorporation of catalytic metals;

4) catalytic and reactivity studies of the metal-loaded catalysts; and

5) development of structure/activity relationships for catalytic liquefaction reactions in order to determine the nature of optimum materials.

After developing this basic understanding, we envision being able to tailor catalyst properties for specific applications, as well as providing a foundation for further catalyst development. This report summarizes recent work on this project carried out in the last six months. Specifically, we describe studies in catagories 4 and 5 from the list above. Further background information, previous results, and experimental details are summarized in previous semiannual reports.[4]

DISCUSSION OF CURRENT ACTIVITIES

Results and Discussion

Preparation, Characterization and Reactivity Studies of Ni-Mo/HTO Catalysts

Our studies of the ion-exchange properties of the hydrous titanate (HTO) catalyst support materials, and the solution properties of cationic Ni have been documented in several previous semiannual reports (*e.g.*, see ref. 4f). These studies have led to the identification of optimum solution conditions for the loading of Ni onto the HTO supports that takes full advantage of the unique ion-exchange properties of these materials. The characterization and reactivity studies on this material have demonstrated the great utility of preparing catalysts on the HTO supports by ion exchange.

More recently, we have used optimum Ni loading conditions to prepare Ni/HTO supported catalysts which were subsequently contacted with solutions containing Mo anions. In this way bimetallic Ni-Mo/HTO supported catalysts have been prepared. In a very recent semiannual report,[4h] we described the preparation (and the rationale for the particular solution conditions used) and some preliminary characterization of these materials. In addition, we described some very promising results from the initial catalyst testing of the Ni-Mo/HTO catalysts in which pyrene hydrogenation was used as a model system to simulate reactions known

to be important in direct coal liquefaction.[1b] These catalytic tests were performed under the auspices of companion studies at Sandia funded by the D.O.E. Fossil Energy AR&TD Coal Liquefaction Program.

Fig. 1 shows the pseudo-first order rate constant for pyrene hydrogenation at 300 °C for the most active Ni-Mo/HTO catalyst that we have prepared to date. (The experimental apparatus and methodology used for the reactivity studies are described elsewhere.[1b]) Also contained in the figure for comparison purposes are rates obtained for pyrene hydrogenation on two commercial catalysts, Shell 324M and Amocat 1C,[1b] and a Ni-Mo/TiO_2 catalyst. The data point for each catalyst in Fig. 1 are rates normalized to the amount of active metal, Mo, in each catalyst. As can be seen in the figure, the reactivity of the hydrous titanate supported catalyst is almost a factor of 2 higher than the commercial catalysts and a factor of 4 higher than a material prepared by traditional methods on a commercial TiO_2 support.

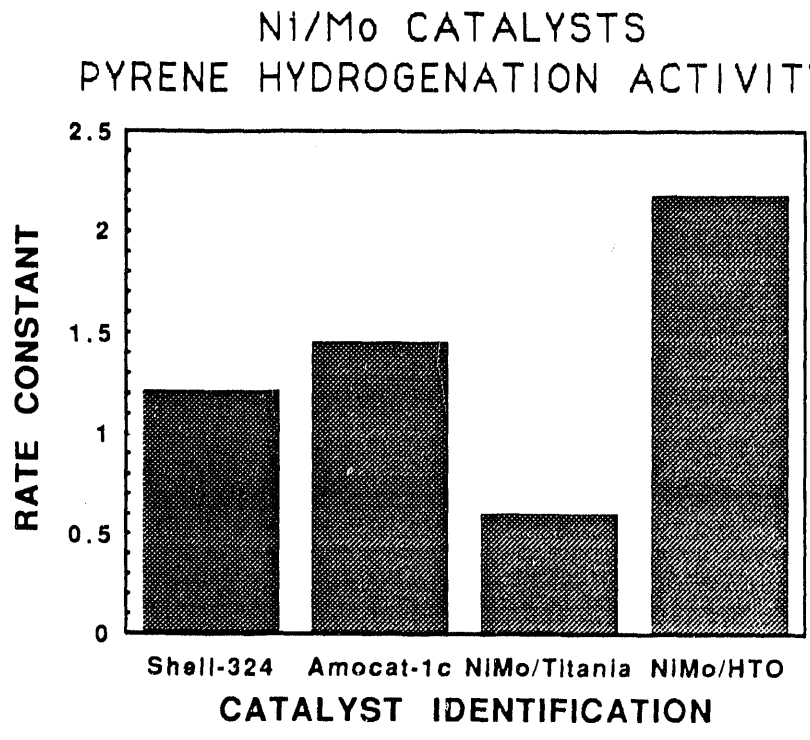

Figure 1: A comparison of pyrene hydrogenation activity for a recently prepared Ni-Mo/HTO supported catalyst. Also shown for comparison are rates obtained on a Ni-Mo/TiO_2 catalyst and two commercial catalysts, Shell 324 and Amocat 1C. Rates are normalized to the total amount of Mo in the catalysts.

TEM studies have also been carried out on the catalysts. The image shown in the Fig. 2 was obtained of the Ni-Mo/HT0 supported catalyst. The titanate support appears as crystalline TiO_2 particles approximately 10 nm in diameter. The darker lines are the catalytically active MoS_2 crystallites. The figure reveals that most of the MoS_2 particles in this very active Ni-Mo/HT0 supported catalyst are in the form of single layers. In fact, the commercial Shell 324M catalyst (supported on Al_2O_3) is largely composed of multiple layered MoS_2. This is strongly suggestive that the single-layer particles are a more optimum structure. Another important question concerning these active MoS_2 particles is their orientation relative to the oxide-support surface. Notably, it has been suggested that platelets of MoS_2 normal to the surface are more active than those oriented parallel to the surface due to the relative ease of access to the edges of the particles which are known to contain the active sites for catalytic hydrogenation.[5] We have focussed on the issue of the optimum structure of the active MoS_2 particles on an oxide support material and describe the results of these studies here.

MoS_2 supported on oxides such as alumina, and promoted with nickel or cobalt constitutes an active catalyst for reactions such as hydrogenation, hydrodesulfurization, and methanation.[6]

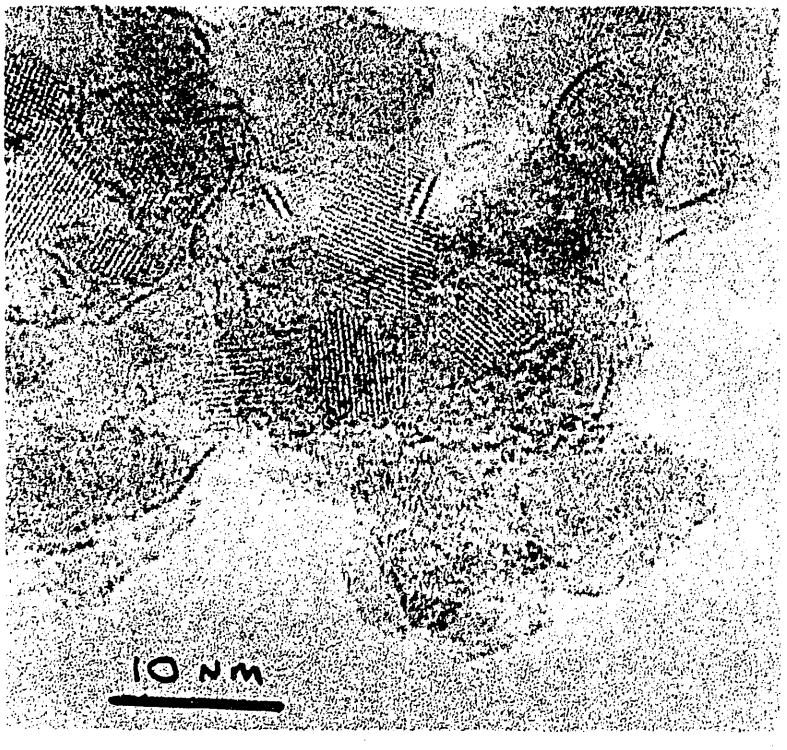

Figure 2: TEM images of a Ni-Mo/HT0 after calcining the materials in air at 500 °C for 1 hour and sulfiding in H_2S for 2 hours at 425 °C.

Recent work[7] shows that the support oxide has a marked effect on the specific activity of the sulfide catalysts and it has been suggested that these activity differences may be related to the morphology of the MoS_2 crystallites on the surface. MoS_2 is synthesized by sulfiding a supported MoO_3 in 10% H_2S/H_2 at 600K - 900K. It is now accepted that on alumina, after a standard calcination at 773 K and independent of the method of preparation, MoO_3 forms a 'monolayer' containing octahedral Mo^{+6} anchored to the surface with Mo-O-Al bonds.[8] Evidence for the dispersed molybdena comes from CO_2 chemisorption studies which show a decrease in exposed alumina, and from IR spectroscopy which shows a drop in the surface hydroxyl concentration with the addition of Mo to alumina.[8] When the concentration of molybdena exceeds that of a monolayer (≈5 Mo/nm^2), three-dimensional crystals of MoO_3 are also observed in addition to the 'monolayer' phase.[9]

During sulfiding of the MoO_3 in 10% H_2S/H_2 at temperatures in excess of 673 K, the MoO_3 transforms into MoS_2 and some of the hydroxyls on the alumina surface reappear. Based on these results, it was originally proposed that microcrystalline MoS_2 sheets are edge-bonded to the surface of the oxide support.[8] However, Zmierczak, *et al.*[9] have argued that the crystallization into MoS_2 should directly lead to a partial exposure of the alumina surface since the specific volume of the MoS_2 is considerably less than that of the dispersed MoO_3. Their calculations assume that the structure of the MoS_2 is very similar to that of bulk MoS_2, a conclusion supported by EXAFS spectroscopy.[8] Hence, an alternate model for the surface MoS_2 is that the the basal planes are located parallel to the oxide surface.

Direct experimental evidence for the morphology of the MoS_2 comes from transmission electron microscopy (TEM), which is particularly effective since the interplanar spacing of the basal planes of MoS_2 (hexagonal, space group $P6_3mm$) is large enough (0.613 nm) to be easily resolved. Thus, if a layer of MoS_2 were to lie with its basal plane parallel to the oxide surface, a dark line would be seen at the edge of the oxide support representing a monolayer of MoS_2. A three-dimensional MoS_2 crystallite would appear as an array of dark lines ≈0.6 nm apart corresponding to the (002) lattice planes. Indeed, on low surface area titania and zirconia supports, isolated dark lines suggestive of MoS_2 bonded to the oxide could be clearly seen[7] at the edge of the support when the coverage was below that of a monolayer. At a higher coverage of MoO_3, the dark lines completely covered the oxide surface and multilayers of MoS_2 were also observed. These results would be consistent with the formation of MoS_2 with its basal plane parallel to the oxide surface. On the other hand, on silica and alumina supports, there was no indication of similar dark lines at the edge of the oxide support.[7] Rather, the dark lines were always located in the interior of the oxide and it was suggested that the MoS_2 sheets were therefore oriented with their basal planes perpendicular to the oxide support.

Since the morphology of the MoO_3 precursor after calcination on TiO_2 and Al_2O_3 is very similar, it is remarkable that after sulfiding, the MoS_2 should adopt such different morphologies. Importantly as alluded to in a previous semiannual report[4h] and illustrated in Fig. 1, MoS_2 crystallites on the HTO supports are qualitatively similar to those observed on alumina-supported catalysts. Thus, it is crucial to resolve this apparent discrepancy in the literature concerning the morphology of MoS_2 on various oxide supports. Pratt et al.[7] suggested that differences in the hydroxyl groups may contribute to the observed morphology of the sulfide. The IR spectra of hydroxyls on these supports, however, do not reveal significant differences that may account for the altered morphology. There is, however, one significant difference between these supports; notably, their surface areas. Commercial TiO_2 is generally available as a low surface area powder (for example Degussa P-25 has 65 m^2/g) while γ-alumina and silica used commercially range in surface area from 100 - 300 m^2/g. The amorphous HTO powders show surface areas in this latter range.[1a] Commercial TiO_2 powders have larger primary particle sizes (as evident from XRD patterns) and electron micrographs reveal a smoother surface texture compared to the alumina, silica and HTO materials. The markedly different surface textures of the low and high surface area supports may constitute an important factor affecting the morphology of the dispersed MoS_2 that has been overlooked by previous investigators.

In order to study the role of surface texture and particle size, we have examined the morphology of MoS_2 on low surface area model alumina and silica powders and compared it with MoS_2 supported on both commercial and HTO materials. These model supports allow us to separate the role of surface area and morphology from that of oxide surface chemistry. The objective of the work is to document differences between the morphology of MoS_2 supported on silica, alumina and titania when powders of comparable surface area are used. Experimental details are provided in a forthcoming publication.[10]

Fig. 3 shows a micrograph of the sulfided MoO_3/TiO_2 sample. The presence of MoS_2 on the surface of titania can be clearly seen in the form of dark lines at the edge of the oxide support. These dark lines represent single sheets of MoS_2 lying flat on the surface of titania and the image is similar to that reported by Pratt, et al.[7] The concentration of MoO_3 in this sample was 3.1 wt%, as determined by ICP-AES (Table 1), which would be below the monolayer capacity of the titania. This is consistent with the presence only of patches of MoS_2 which do not completely cover the titania surface. Fig. 4 shows the sulfided sample of MoO_3/ALON C where the majority of the MoS_2 is seen in the interior of the particles, confirming the observations made by Pratt, et al.[7] However, closer examination does reveal a few areas where dark lines can be seen at the edge of the support, indicating that the morphology could be similar to that seen on the titania support.

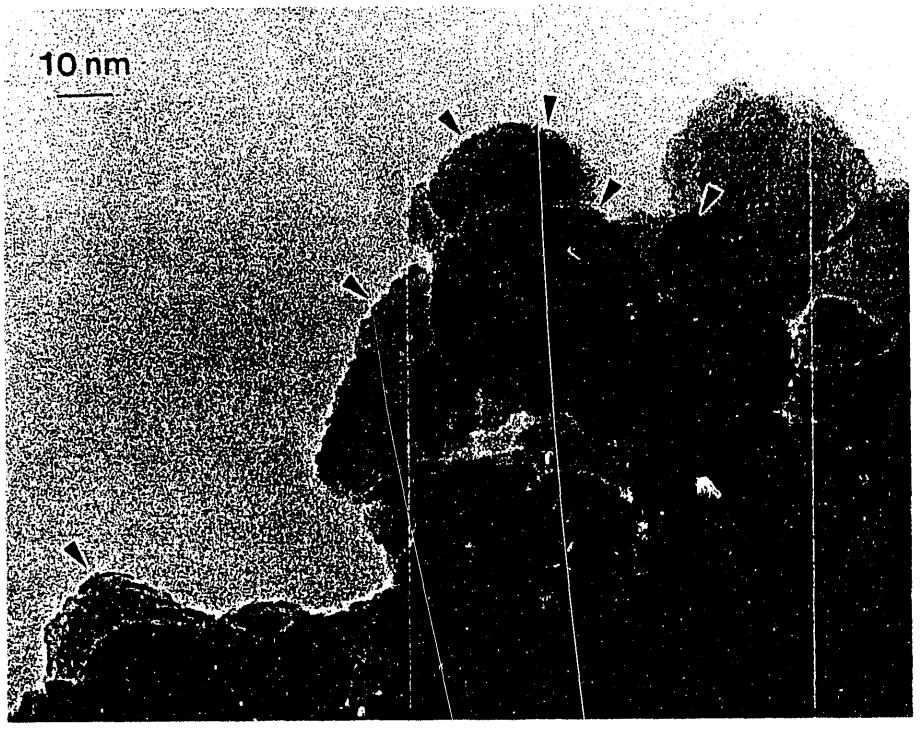

Figure 3: Micrograph of sulfided MoO_3 supported on Degussa P-25 TiO_2. Small crystals of MoS_2 are seen on the titania surface as indicated by the arrows.

Table 1

Sample Characterization

Support	Surface Area	Elemental	Analysis	by	ICP-AES
	m^2/gm	% Mo	%Al	%Ti	%Si
Alon C, Al_2O_3	100	2.6 ± 0.1	47.5 ± 0.4	-	-
Degussa P-25 TiO_2	65	3.13 ± 0.01	-	54.1 ± 0.1	-
HTO	120	3.35 ± 0.01	-	39.6 ± 0.3	-
Model alumina	50	20.0±0.1	37.3±0.3	-	-
Model silica	15	2.1±0.01	-	-	46.0±2.0

Figure 4: Micrograph of sulfided MoO_3 supported on Degussa ALON C alumina. Black lines from the basal planes of MoS_2 crystals are visible both on the surface of the alumina and in the interior. The dark lines within the interior appear to be associated with outgrowth on the alumina surface in a direction normal to the image plane.

The morphology of the MoS_2 seen on commercial titania and alumina will now be compared with that on several model, nonporous oxide samples having primary particles of controlled morphology. On the sulfided MoO_3/model alumina (as shown in Fig. 5), where the alumina particles started out as faceted single crystals, sheets as well as stacks of MoS_2 are seen on the alumina surface. The presence of stacks of MoS_2 is consistent with the higher molybdena loading on this sample (Table 1). Overall however, the morphology is very similar to that seen on titania and zirconia in previous work.[7] The nonporous nature of the model alumina provides unambiguous determination of the orientation of MoS_2 and shows clearly that the basal plane is parallel to the surface of the oxide. A similar morphology was also seen on the model silica

Figure 5: Sulfided MoO_3 supported on nonporous model alumina. The higher loading of Mo and the low surface area leads to the formation of large MoS_2 crystals imaged as dark lines at the surface of the oxide.

sample as shown in Fig. 6. On silica, small patches of MoS_2 coexist with three-dimensional islands of MoS_2. The high magnification view in Fig. 6a shows that the small patches of MoS_2 indicated by arrows are always located with their basal plane parallel to the oxide support. However, the large three dimensional island of MoO_3 has transformed into MoS_2 crystallites containing crystal planes randomly oriented with respect to the oxide support. If such a patch of MoS_2 were to be observed in a direction normal to the oxide surface, only the MoS_2 planes normal to the surface would be visible (since the others would not generate any contrast) and hence it would appear as if the MoS_2 sheets were standing up normal to the oxide surface. Fig. 6b shows that the MoS_2 multilayers also cause necking of the silica spheres.

The results of this study show clearly that MoS_2 particles in the sulfided and air-exposed samples always occur with their basal planes parallel to the oxide surface. We have found no evidence for MoS_2 'bookends' where the basal planes are stacked up perpendicular to the oxide surface on any of the supports used in this study. Thus, in contrast to observations reported previously,[7] we find no difference between the behavior of TiO_2, SiO_2 and Al_2O_3 when used as a support for MoS_2. By implication, there is no reason to expect that the morphology of MoS_2 would be different on the HTO supports either. The 'bookend' morphology of MoS_2 deduced by previous workers[7] was based on the absence of a dark line at the edge of the support particles. It

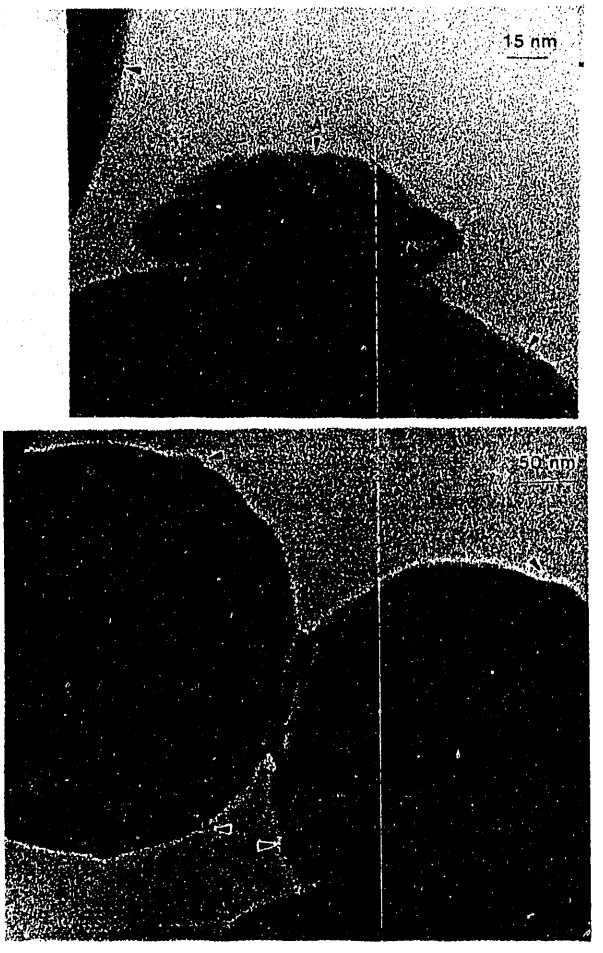

Figure 6: Sulfided MoO_3 supported on nonporous model silica: (a) a high magnification view showing small segments of dark lines corresponding to MoS_2 crystals (arrowed) and a large crystal of MoO_3 (marked A) which has also transformed into MoS_2; and (b) a low magnification view showing the necking of the silica spheres caused by the presence of MoS_2.

is important to recognize that the electron micrograph represents a projection of the three-dimensional sample along the beam direction. Thus, dark lines originating from the MoS_2 would typically be seen only when an MoS_2 sheet of sufficient size is oriented along the beam direction. If the primary oxide particles occur as thin plate-like or wedge-shaped crystals that lie flat on the carbon supporting film on the TEM grid, any MoS_2 at the edge would not be readily imaged. However, dark lines seen within the oxide support may well arise from a part of the oxide surface that is located parallel to the beam direction. The probability of detecting the MoS_2 on the surface would be enhanced considerably on a nonporous oxide particle and it is precisely from

such low surface area supports that the basal plane-bonded morphology of MoS_2 has been deduced.

In conclusion, we feel that the observed 'bookend' morphology on high surface area supports is an artifact of the electron microscopic examination of these materials since the images always represent a projected view of a three dimensional sample. It is evident that the surface texture of the support could play a major role in determining the morphology of the MoS_2. Supports such as alumina and the HTO's, that have microscopically rough surface textures, would tend to favor formation of numerous small crystals of MoS_2 while a low surface area support such as a commercial TiO_2, having a 'smooth' surface and fewer nucleation sites, would favor formation of fewer MoS_2 islands of larger size. Thus, on TiO_2 one would expect increasing Mo loading to lead to an increase in the size of MoS_2 islands and a corresponding lowering of the number of edge/basal plane sites. The data of Pratt, et al.[7] does indeed show a marked fall off in specific activity for thiophene HDS on Mo/TiO_2 with increasing Mo loading, but not on Mo/alumina. These results suggest that the surface texture of the oxide support may be an important factor affecting the morphology and, indirectly the reactivity, of the dispersed phase in a heterogeneous catalyst.

ACKNOWLEDGMENTS

Sandia National Laboratories is supported by the U. S. Dept. of Energy under contract No. DE-AC04-76DP00789. The author would especially like to thank Professor A. K. Datye and S. Srinivasan for collaboration on the TEM studies of MoS_2 on model oxide supports. In addition, coworkers at Sandia are acknowledged for participation in this work; notably, T. J. Headley for the TEM micrographs and E. P. Boespflug for the reactivity data obtained of the Ni-Mo/HTO catalyst.

REFERENCES

1. (a) R. G. Dosch, H. P. Stephens, F. V. Stohl, B. C. Bunker and C. H. F. Peden , "Hydrous Metal Oxide-Supported Catalysts: Part I. Preparation Chemistry and Physical and Chemical Properties," *Sandia Report* (SAND89-2399). (b) R. G. Dosch, H. P. Stephens and F. V. Stohl, "Hydrous Metal Oxide-Supported Catalysts: Part II . Catalytic Properties and Applications," *Sandia Report* (SAND89-2400).

2. H. P. Stephens, R. G. Dosch and F. V. Stohl, "Catalysis Using Hydrous Metal Oxide Ion Exchangers," *U. S. Patent* #4,511,455; April 16, 1985.

3. R. G. Dosch, T. J. Headley and P. Hlava, "Crystalline Titanate Ceramic Nuclear Waste Forms: Processing and Microstructure," *J. Am. Ceram. Soc.* **67** (1984) 354 .

4. (a) B. C. Bunker, C. H. F. Peden and S. L. Martinez, "Ceramic Catalyst Materials: Hydrous Metal Oxide Ion-Exchange Supports for Direct Coal Liquefaction," *AR&TD Materials Semiannual Report*, March - September, 1987; ORNL/FMP-87/2, p. 213. (b) C. H. F. Peden, B. C. Bunker and S. L. Martinez, ibid., October, 1987 - March, 1988; ORNL/FMP-88/1, p. 171. (c) C. H. F. Peden, B. C. Bunker and S. L. Martinez, ibid., April - September, 1988; ORNL/FMP-88/2, p. 207. (d) B. C. Bunker , C. H. F. Peden and S. L. Martinez , ibid., October, 1988 - March, 1989; ORNL/FMP-89/1, p. 183. (e) C. H. F. Peden, B. C. Bunker and S. L. Martinez, ibid., April - September, 1989; ORNL/FMP-89/2, p. 179. (f) C. H. F. Peden, B. C. Bunker, S. L. Martinez and D. H. Doughty, ibid., October, 1989 - March, 1990; ORNL/FMP-90/1, p. 171. (g) C. H. F. Peden, F. D. Hardcastle and K. B. Kidd, ibid., April - September, 1990; ORNL/FMP-90/2, p. 143. (h) C. H. F. Peden, ibid., October, 1990 - March, 1991; ORNL/FMP-91/1, p. 107.

5. R. R. Chianelli, "Fundamental Studies of Transition Metal Sulfide Hydrodesulfurization Catalysts," *Catal. Rev.-Sci. Eng.* **26** (1984) 361.

6. B. C. Gates, J. R. Katzer and G. C. A. Schuit, "Chemistry of Catalytic Processes", McGraw Hill, 1979.

7. K. C. Pratt, J. V. Sanders and V. Christov, "Morphology and Activity of MoS_2 on Various Supports: Genesis of the Active Phase," *J. Catal.* **124**, 416 (1990).

8. W. K. Hall, "Catalysis by Molybdena-Alumina and Related Oxide Systems," in *Chemistry and Physics of Solid Surfaces VI*", R. Vanselow and R. Howe, Eds., Springer-Verlag, 1986, p. 73.

9. W. Zmierczak, Q. Qader, and F. E. Massoth, "Studies on Molybdena-Alumina Catalysts: XII. MoS_2 Surface Coverage from CO_2 Adsorption," *J. Catal.***106**, 65 (1987).

10. S. Srinivasan, A. K. Datye and C. H. F. Peden, "The Morphology of Oxide-Supported MoS_2," *J. Catal.* submitted for publication.

VPI-I - INVESTIGATION OF PROPERTIES AND PERFORMANCE OF CERAMIC COMPOSITE COMPONENTS

K.L. Reifsnider, W.W. Stinchcomb, T.J. Dunyak

Materials Response Group
Engineering Science and Mechanics Department
Virginia Polytechnic Institute and State University
Blacksburg, Virginia 24061-0219

ABSTRACT

This report on properties and performance of ceramic composite components includes work performed during the period April 1, 1991 through September 30, 1991. The emphasis of this report is performance simulation of high temperature ceramic matrix composites.

INTRODUCTION

The anticipated use of ceramic composites in high temperature structural applications requires the technical community to make the transition from properties of materials to the performance of engineering components. Making this transition requires comprehensive characterization and understanding (i.e., philosophy and rigorous modeling) of long-term behavior. For example, information from quasi-static tests, modulus of rupture tests, and fracture toughness tests is not sufficient to design a complex component such as a heat exchanger tube fabricated from anisotropic, fiber-reinforced materials which may experience multiaxial stresses and elevated temperatures. The present research effort provides an experimental and analytical basis for the transition from properties to performance. In general, the program is a pioneering effort to make a first step beyond the limited characterization of small samples and coupons to the comprehensive mechanical characterization of complex engineering components such as ceramic composite tubes subjected to static and cyclic multiaxial loading and elevated temperature over various time periods.

OBJECTIVES AND APPROACH

The central objective of the present program is to develop an understanding of the mechanical behavior of advanced ceramic composites subjected to elevated temperature and dynamic (cyclic) loading, to develop a test system and test methods to obtain the properties and performance information required to design engineering components made from ceramic composite materials, and to provide critical and comprehensive evaluations of such materialsto material synthesizers and developers to support and enhance progress in ceramic composite material development. Specific objectives are given in Ref. 1.

The approach to the program is designed to meet the objectives of the program through a series of four coordinated and complimentary tasks outlined in Table 1. Specific details of each task are given in Ref. 1.

Table 1. Program Plan.

Task	1	2	3	4
Construction of Test Device	Purchase of Test Frame; Design of Test Chamber and Grips	Construction of Room Temperature Device; Design of High Temperature Equipment	Construction of High Temperature Device	Testing and Refinement
Quasi-static Room Temperature Characterization		Uniaxial Tension Tests	Monotonic Tensile Tests; Damage Analysis	Damage Analysis
Cyclic Room Temperature Characterization			Uniaxial Tension; Damage Analysis	Tension-Tension; Damage Analysis
High Temperature Characterization			Preliminary Tests; Quasi-static*	Uniaxial Cyclic Damage Analysis Multiaxial Cyclic Tests
Modeling	Literature Review	Identification of Failure Modes	Nondestructive Identification of Damage Modes	Formulations and Predictions
Planning of Investigations	Quasi-static Uniaxial Test Series	Uniaxial Cyclic Test Series	High Temperature Test Series	Verification Series; Future Work**

* All high temperature tests and multiaxial tests have been postponed because SiC/SiC specimens are not available.

** Future work will include multiaxial, high temperature tests if the program is continued into Phase II.

DISCUSSIONS OF PREVIOUS WORK

Tasks 1 and 2 and portions of Tasks 3 and 4 have been completed as of the reporting period ending September 30, 1991. These tasks included:

- design, construction, installation, and acceptance testing of an Instron computer-controlled high stiffness biaxial test frame with hydraulic grips,
- design, fabrication, and evaluation of chopped graphite fiber (Hercules HMU-PVA-3k) / glass matrix (Corning CGW-7070) composite tubes.
- extensive literature reviews in the areas of test methods, nondestructive evaluation, failure mechanisms, and modeling of ceramic composites,
- extensive literature reviews in the areas of test methods, nondestructive evaluation, failure mechanisms, and modeling of ceramic composites,
- investigation and application of nondestructive test methods to monitor the damage development process,
- completion of the room temperature, monotonic axial load test series, and planning of the room temperature, cyclic test series,
- development of a high temperature damage model based on the critical element concept,
- identification of future needs,
- design of a second ceramic composite tube configuration,
- selection of a second ceramic composite material system,
- completion of the room temperature, cyclic axial load test series,
- analysis of damage and failure modes in graphite fiber/borosilicate glass matrix tubular specimens,
- development and evaluation of a damage development model.

Each of these activities is discussed in detail in Refs. 1-8.

CURRENT ACTIVITIES

Current activities address the following topics:

- room temperature monotonic and cyclic load tests on a borosilicate glass tube,
- continued development and refinement of the MRLife performance simulation model.

This report describes the MRLife model and presents certain results applicable to the properties and performance program.

INTRODUCTION AND BACKGROUND

High temperature composite (HTC) material systems are widely regarded as the next major opportunity for major advancement in the performance, reliability, durability, and damage tolerance of engineering components which must operate under severe service conditions that include high temperatures and aggressive environments, especially when those environments are applied over long time periods. Examples of such important applications include fossil fuel heat exchanger and combustion devices, the High Speed Civil Transport, the Advanced Tactical Fighter aircraft, high performance jet engines, numerous missile components, and a wide array of other high temperature devices. In every one of these applications, HTC systems can provide not only significant increases in performance, but also (and perhaps most important) such material systems can provide major savings in cost through additional fuel efficiency, improved reliability and durability, and reduced maintenance costs.

Interest in this topic in the United States has been acute. Two recent studies by panels of the National Research Council have highlighted needs in this area[9,10]. (Dr. Reifsnider, one of the principal investigators on this program, served on both of those panels.) One panel was concerned with high temperature materials, especially the research needs associated with both classified and unclassified programs and directed efforts in the United States. Among other things, that panel identified a strong need for the integration of physics, chemistry, and mechanical behavior in efforts to represent the long-term performance of material systems which operate under severe thermal and chemical conditions. The panel devoted most of its time to the study of programs and activities associated with **high temperature composite systems** , in contrast to monolithic materials such as high temperature ceramics alone. The panel report makes it abundantly clear that the future of high temperature materials is defined by the future of high temperature composite material systems.

However, as the report shows, research in the area of high temperature materials is difficult, and research in the area of HTC systems is even more complex and demanding.

A second panel of the National Research Council addressed life prediction methods for composite materials. This panel, which addressed the application of composite materials in all temperature ranges, identified a variety of research needs and issues which are at the base of the slow rate of application of composite materials to high performance engineering components, especially those which operate under severe conditions. It was the position of the panel that this hesitancy has its basis in a lack of understanding of the fundamental nature of damage modes and failure modes associated with the use of composite materials under severe conditions, a lack of experience on the part of designers and engineers in the application of composite materials to primary structures, and a (severe) lack of predictive methodology which is mechanistically based and can be used to provide support for such applications. **The panel identified severe needs in the area of the determination of long-term high temperature properties; the characterization and modeling of remaining strength in terms of damage tolerance, durability, and reliability; and the need for life prediction methodologies which can be used to describe long-term behavior in the presence of mechanical, thermal, and chemical loading. The present effort on the subject program addresses this need.**

The Materials Response Group at Virginia Tech has suggested a mechanistic approach to the prediction of strength, remaining strength, and life of composite material systems, and has demonstrated the validity and utility of such models for the prediction of damage tolerance (remaining strength, remaining life, and reliability) in polymer composite systems, as well as promising results for similar predictions for ceramic composite materials at elevated temperatures. This simulation approach is the basis for the present effort, and will be described in more detail as it has been applied to the specific objectives of this program under the "Results" section, below. In the present section, we will briefly outline some of the salient aspects of the fundamentals behind our simulation method to provide a background for the subsequent discussion.

The first essential element of our "critical element approach" to life prediciton is a precise and comprehensive representation of micro-stress states in fiber-reinforced composite material systems, for continuous fibers and for short or broken fiber situations. This subject has received rather extensive attention in the literature, but is still inadequate for a complete description of the local processes which contribute to and control the damage and failure behavior of composite systems. The Materials Response Group has made major advances in this area. Indeed, three members of that group are in the process of preparing a manuscript which will be published as a monograph on the subject of "Micromechanics of Fibrous Composite Material Systems." This monograph should be a landmark in the effort to establish firm and precise representations of the local stress fields in fibrous composites which include broken/short fiber effects, the presence of material property variations as a function of position (a critical issue for high temperature composites),

interface and interphase regions, and thermal stress effects. It is expected that this book will be published, probably by Technomic Publishing Co., near the end of 1992.

The second essential element for our simulation approach is a micromechanical representation of strength, i.e., a mechanistic representation of the failure process that controls both initial and remaining strength in these systems under various loading conditions and environments. We claim that interpretive models must be based on precise definitions of damage accumulation and failure modes as determined from experimental observations. We assume that the damage associated with the properties and performance of interest in our composite material systems is widely distributed, and is contributed by a variety of damage modes acting in concert and interacting in a complex fashion. We further claim that this distribution allows us to define a "representative volume" which has "average properties" of the remaining material, such that the state of material and state of stress in that representative volume are typical of all other such elements. We further postulate that this representative volume can be divided into critical and subcritical domains (called "critical" and "subcritical" elements). The "critical element" remains intact and contiguous in the continuum sense until failure occurs at the global level, that is, the failure of the critical element defines the failure of the representative volume and the failure of our component.

We further assume that the remaining material in the representative volume consists of "subcritical elements" in the sense that their failure does not cause failure of the representative volume or of the engineering component. However, damage in the subcritical elements by such things as cracking, delamination, or other irreversible behavior does cause changes in the stress state in the critical element which are quite large and important. These stress states are addressed using the micromechanical stress analysis mentioned in a previous paragraph. In general, we will describe changes in "material state" using continuum constitutive information regarding the critical element, and changes in the stress state in the critical element by attempting to describe damage development in subcritical elements using our micromechanical treatments. It should be noted that our continuum assumption regarding the critical element does not exclude discrete events from occurring on a scale which is significantly smaller that the critical element dimension. Such events which do not directly control the final remaining strength and life of the critical element or the component are grouped into continuum descriptions; this has the important advantage of setting a "lower limit" on the scale at which mechanics must be done, and can have the effect of greatly simplifying the necessary complexity of our analysis, as we have shown in the literature. An example of this approach is provided by our recent development of the first comprehensive micromechanical model of tensile strength in fibrous composite materials[11,12].

The third and final essential element of our micromechanical approach is a predictive methodology for long-term behavior which includes the evolution of properties and performance, especially the evolution which is associated with variations in material state and stress state caused by high tem-

perature loading conditions. The approach developed by the Materials Response Group to handle this modeling challenge is a performance simulation scheme which is the basis for the MRLife code series, developed over the last 11 years and in its seventh issue. The performance simulation method that we have developed is based on the critical element concepts described above, and is thought to be the only mechanistic approach with reasonable generality that is presently available in the United States. This approach has garnered a great deal of attention from the technical community at the national and international levels. In the last three years, this approach has been the subject of an invited plenary lecture on life prediction methodology at the International Conference on Composite Materials in London[13]; the subject of an invited plenary lecture on performance simulation in polymer based composite systems at the International Colloquium on Durability of Polymer Based Composite Systems for Structural Applications in Brussels, Belgium[14], and the subject of an invited plenary lecture on performance simulation methods for the prediction of long-term behavior of composite material systems given at the Fifth Japan-U.S. Conference on Composite Materials in Tokyo, Japan[15]. These lectures were given by Ken Reifsnider, one of the principal investigators on this program. In addition, recently this mechanistic approach was the subject of a paper titled "Interpretation of Laboratory Test Information for Residual Strength and Life Prediction of Composite Systems," authored by Ken Reifsnider, which won the **Best Paper Award** at the ASTM Symposium on Cyclic Deformation, Fracture, and Nondestructive Evaluation of Advanced Materials, held in San Antonio, Texas[16]. It is clear that this approach and the results that it produces have been widely noticed and strongly embraced by the technical community at the national and international level.

RECENT RESULTS AND MODEL ENHANCEMENTS

In the context of our subsequent discussion of this effort, several elements of our approach must be briefly outlined. (Other details of the critical element approach as well as our supporting work in the area of micromechanics appears in references 17-19.

In general, advanced, high performance composite materials are really material systems in which the constituent materials and the interfacial / interphasal regions between them interact in such a way that their collective response is more than the linear sum of the response of the constituents. This fact provides the technical comunity with a remarkable opportunity to create composite material systems which are uniquely suited to perform specific engineering tasks. At the same time, the systems aspect of composite materials requires special attention when we attempt to discuss the mechanics related to properties such as stiffness and strength, and performance such as life.

If one wishes to consider the long term response of such materials under cyclic mechanical, chemical, and thermal loading, the systems aspect of the problem introduces interactions between

mechanical degradation, and any chemical or thermodynamic processes which may be occuring during the life of the component.

Achieving representations of such combined processes is a noble but challenging goal. One must begin with simple, fundamentally sound principles, and build an approach systematically (if not axiomatically). We will build the present discussion on the following principles.

1. In most of the material systems of interest, the damage or degradation processes that reduce stength and life are various, widely distributed, and highly interactive.
2. These processes cause changes in stress state and changes in material state, especially at the local level.
3. These changes define the remaining strength and life of the materials.

In the report which follows, we will discuss the changes in stress state and material state associated with damage development using micromechanical representations. We will then use the example of tensile failure under long term conditions to demonstrate how these micromechanical representations can be used in a performance simulation model to estimate the remaining strength and life of material systems which demonstrate complex damage and failure modes. A few demonstrative examples will be discussed to illustrate the advantages and limitations of the approach. Results from the present program as well as complementary programs we are conducting will be cited in order to bring the full description of our approach to the reader.

Changes in Stress States and Material States

During the long term service of composite materials, one can expect, in general, changes such as those suggested in Figure 1. Initial properties are altered by damage develpment (which causes changes in local geometry, and may change constitutive behavior); by chemical activity such as compound formation, molecular linking, etc.; or by thermodynamic events such as diffusion, phase changes, or morphological variations as a function of time. Most of these changes are brought about by local processes.

The X-ray radiograph shown in Figure 2 illustrates a typical complex array of widely distributed matrix cracks in a $[0/90_2]_3$ composite laminate made from glass epoxy material subjected to fully reversed cyclic loading at about 60% of the static ultimate strength of the laminate. The cracks in the 90 degree plies have formed a regular array, a saturated condition identified by the present investigators in the early 1970s, and called the "characteristic damage state for matrix cracking[20,21]. Since this condition is a well defined local arrangement which is repeated from point to point

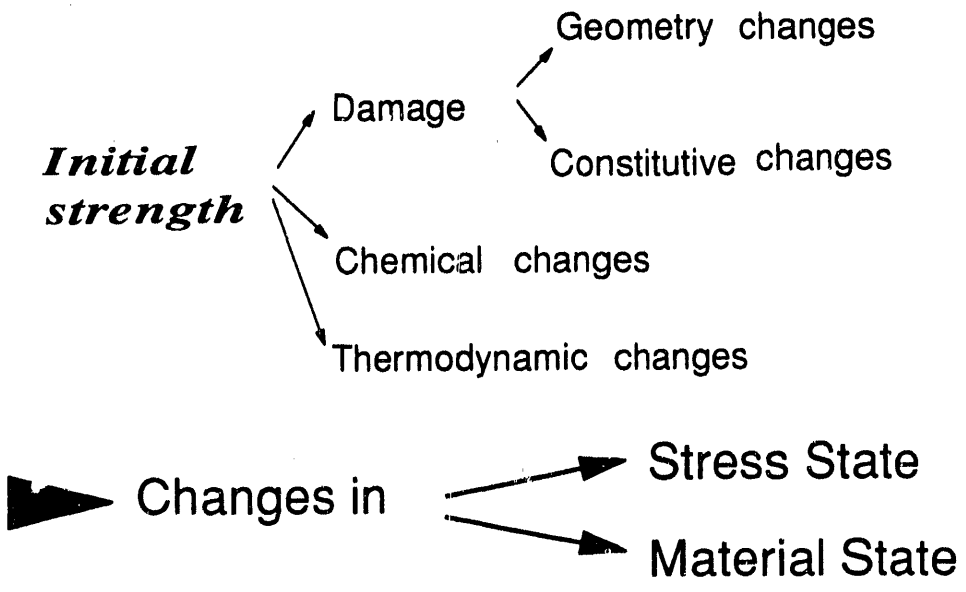

Figure 1. The evolution of properties and performance: Schematic diagram of the physical processes associated with the long-term response of material systems, and the conceptual approach to a representation of that complex process from the mechanics standpoint.

throughout the laminate, one could choose a "representative volume" for such a damage state that would include matrix cracks in off axis plies, matrix splitting in the ply that is oriented in the loading direction, a small delamination region on the plane between two plies which have matrix cracks that cross each other at the ply interfaces, and any attendent local fiber fracture.

The changes in local stress state brought about by such damage development is substantial. The local stress state in the "representative volume" described above can be determined, using the representative volume to properly set a three-dimensional mechanics analysis. Figure 3 on page 8

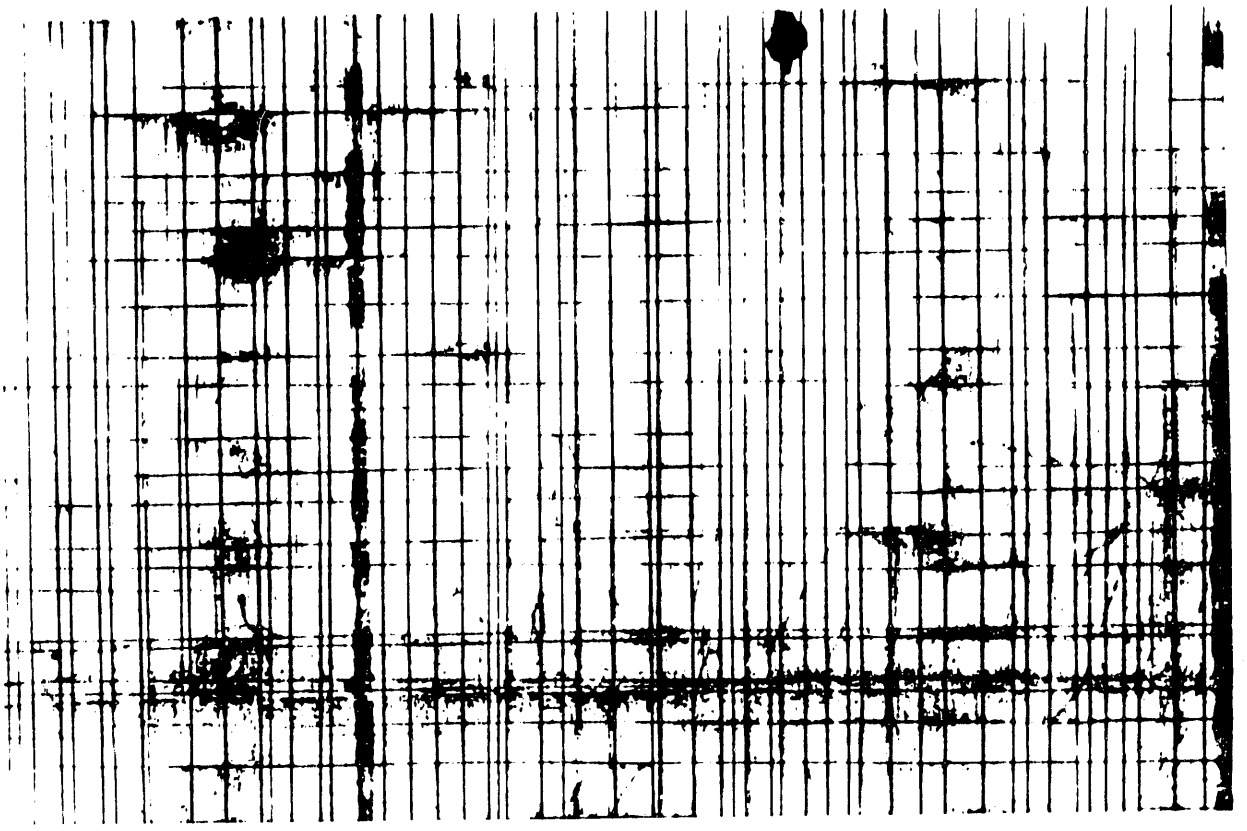

Figure 2. Distributed matrix cracking in a composite laminate.

shows an example of local interlaminar normal stress in the region in which the cracks cross. It can be seen that the interaction of the cracks causes a highly three dimensional stress state in that local region, and that this stress state involves an interlaminar component which will drive delamination. This type of delamination has been observed in the laboratory, and appears as the lightly shaded region in Figure 2 on page 8[22-25].

The resulting local stress states must be determined, not only to establish the stress state in which the unbroken material is operating and which drives subsequent damage development events, but also as a means to determine the effective stiffness with which the local region supports its share of the global stress field. This last requirement is especially important for global local schemes, or

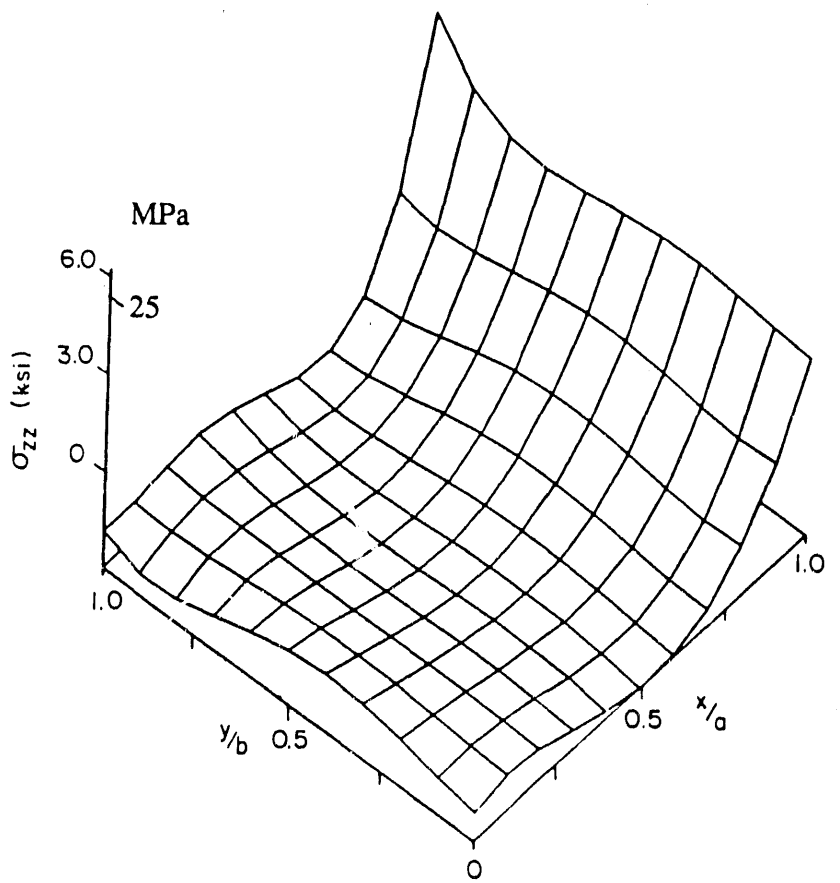

Figure 3. Three dimensional finite element analysis: Variation in the interlaminar normal stress between the 0 degree and 90 degree plies in the region near the position at which cracks cross in adjacent plies for a graphite epoxy laminate.

even for input into laminate analysis in the damaged condition. The effect of matrix cracking on the effective stiffness can be represented by various methods, including discount procedures in which the matrix-dominated ply-level stiffness valures are reduced in a laminate analysis. More exact representations are possible, of course. However, the most challenging part of this problem is associated with the effect of the fibers in typical composites, and the determination of the local stress state in the neighborhood of the fibers. This subject cannot be fully developed here, but a few points that are critical to our discussion will be made. In association with another research program, Carman has recently developed a hybrid three-dimensional short / long fiber composite

micromechanics model, using the following assumptions. Each material constituent is linear elastic; the embedded fibers are transversely isotropic and the surrounding matrix material is isotropic; the fiber/matrix interface is a perfect bond; the composite is a continuous material such that displacement fields can be generated which are representative of a constant average strain state existing in the continiuum; all fibers overlap in the same three dimentionsl space such that generation of curvature terms due to fiber-fiber interaction are neglected. End-to-end fiber-fiber interaction is allowed by the model[26,27]. The three-dimensional model generated utilizes the principle of superpositon in analyzing the point-wise local stress state, and incorporates transient solution concepts similar to those presented by Whitney and Drzal[28].

Figure 4 illustrates the capability of that model. (Berthelot studied the effect of fiber volume fraction on the axial stiffness of model short fiber composites; the short fibers embedded in composite were misaligned at plus or minus 10 degrees with the loading axis[29]. One can see that the predictions match reality well. A further validation of the analysis appears in Figure 5. The highly nonlinear dependence of he out-of-plane Poissons ratio on volume fraction is nicely represented by the model, and correlates with accepted approaches (which do not provide the correct local stress field). This modeling approach can be used to represent the effects of fiber fracture on the effective modulus of the remaining material, and to obtain good estimates of the local stress fields for subsequent damage analysis, as we will discuss below.

It should also be mentioned that, under NSF funding, we have been successful in including the effect of interphase regions with finite dimensions and nonuniform properties in representations of the local stress fields around the fibers[30]. This has particular importance for the application of performance prediction models to high temperature composite systems in which diffusion between the fiber and matrix phases, often through a fiber coating such as carbon, creates a finite region in which the properties depend on position. Such a representation is sometimes critical to the proper representation of the changes in local stress state during service.

Time dependent behavior can also change the local stress state. Figure 6 illustrates stiffness reduction in a composite material associated with viscoelastic creep. In an earlier paper, we have demonstrated that it is possible to reduce the creep compliance curve for lamina stiffness transverse to the fibers, shear stiffness, and matrix controled Poisson's ratio as a function of time (under the assumption of linear viscoelasticity) to a single master curve[28]. This representation, in Figure 6, can be used to specify the matrix-controlled compliance of each individual ply of a laminate as a function of time for epoxy matrix materials. The effect of temperature may be included as a shift factor which moves our creep compliance value along the abscissa according to the time-temperature equivalence principle. These reductions in matrix stiffness typically redistribute stress in the fiber

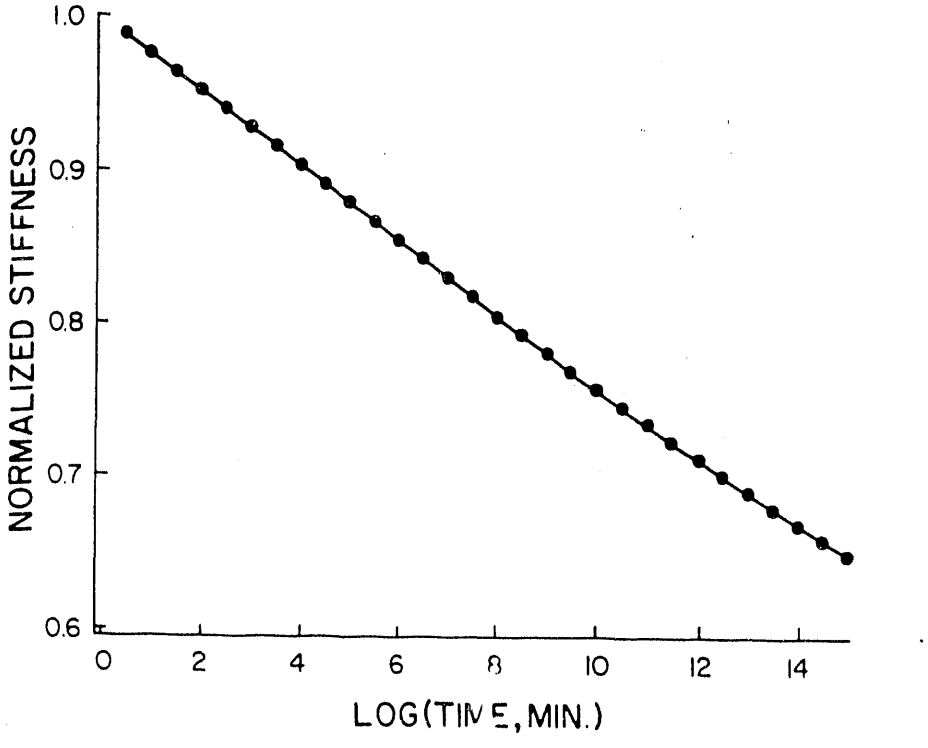

Figure 6. Viscoelastic stiffness reduction master curve.

$$REDUCTION\ IN\ STRENGTH = f(\frac{\bar{\sigma}}{\sigma_{ref}})g(\frac{t}{\tau_{ref}})\,\delta \tag{1}$$

where the functions f and g which scale the applied conditions to those for which data were measured must be determined from laboratory experiments or from representations of the thermodynamic processes which occur. In addition, such strength reductions must also be scaled for temperature.

A further example of a rate equation is the representation of the life of the critical element under current conditions of stress state and material state if those conditions were to remain constant. A particularly simple example of such a relationship is a representation of the S-N fatigue strength-life equation for constant amplitude fatigue such as the expression below.

$$S_a/S_u = A_n - B_n(\log N)^{P_n} \tag{2}$$

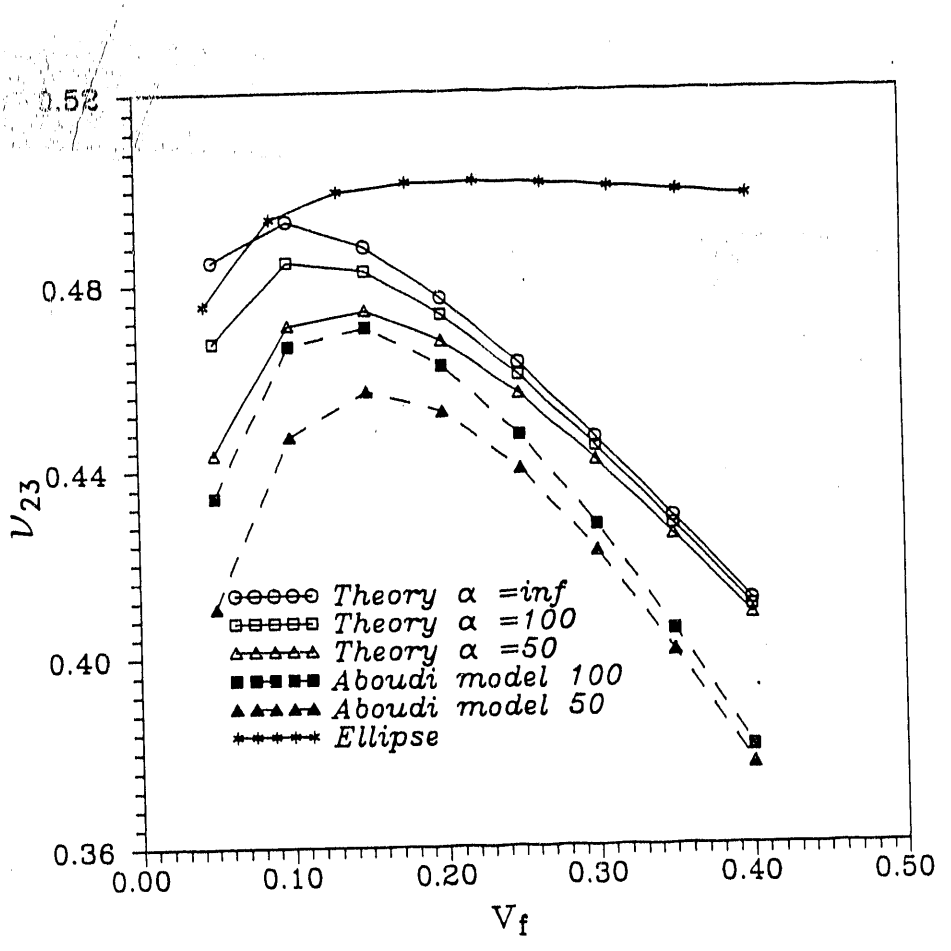

Figure 5. Micromechancal prediction of Poissons ratio: Comparison of predicted ν_{23} values for various theories in an epoxy/steel composite material.

Another rate equation that is essential for our micromechanical modeling is associated with a phenomenon generally called "creep rupture." In many instances this kind of behavior is a "misnomer" in the sense that chemical and thermodynamic processes such as oxidation and chemical attack may be the physical source of such rupture events rather than creep in the classical sense. For a measured strength reduction, δ , a reference time over which that reduction occurred, τ_{ref}, and a stress which was applied over that period of time, σ_{ref}, it is necessary to establish a relationship such as the one shown below.

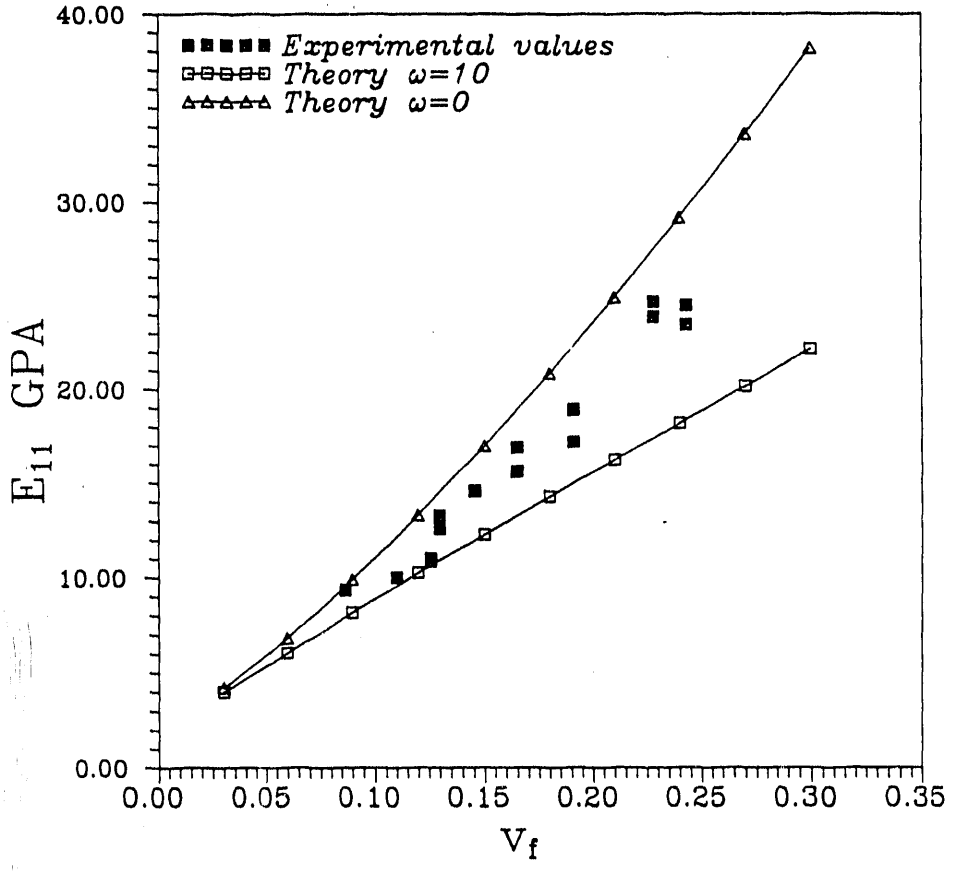

Figure 4. Micromechanical stiffness prediciton: Comparison of Berthelots experimental data with the predictions of Carman and Reifsnider.

direction, especially in plies which have orientations nearly parallel to a load axis. Hence, the stress redistribution associated with viscoelastic deformation may greatly influence the behavior of the critical elements and the performance of the material. Appropriate viscoelastic behavior representations for high temperature composite material systems must be identified. For the present effort, the form of the equations used for polymer matrix materials was maintained, and the associated constants were altered to fit the behavior of the ceramic matrix at elevated temperature. The linear viscoelastic results shown in Figure 6 on page 12 have been preliminarily modified with some success, as we will demonstrate below.

in which S_a is the function which specifies the local stress state, S_u is the corresponding function which specifies the local strength state in the critical element, and the constants A_n, B_n, and P_n are material constants which express the rate of degradation associated with the material under cyclic loading. Of course, the life of the critical element will not be constant because the state of stress, state of material, and possibly the material constants may be functions of the number of cycles of load application, generalized time, or environmental conditions such as temperature. Moreover, Eqn. 2 may be more appropriately replaced by life equations which are based on kinetic theory or those which are based on local slip in the case of high temperature composite material systems.

Performance Simulation

To illustrate how we carry this approach to completion, a very brief description of the performance simulation method we use is provided. As indicated earlier, we take the positon that life prediciton must be based on a clear and precise definition of damage accumulation mechanisms and failure modes as determined from experimental observations. The critical element aproach begins with the premise that life prediciton modeling should be concerned with representative volumes or units of material that control the ultimate failure process, defined by each distinct failure mode. We use a generalized expression for the normalized remaining strength in the critical element for a given failure mode

$$F_r = 1 - \int_1^0 \left(1 - \frac{S_a(\sigma_{ij}(n))}{S_u(X_{ij}(n))} \right) i \left(\frac{n}{N} \right)^{i-1} d\left(\frac{n}{N} \right) \tag{3}$$

It should be noted that in this expression, we have written the function which represents the local state of stress, S_a, in terms of its arguments, the tensor values of local stress, σ_{ij}, and that we have indicated that these local stress values are functions of the number of cycles, n. This recognizes the fact that the local stress state in the critical element may be changing as damage develops in the subcritical elements around it. For example, the stress in the fibers in will be altered greatly by the presence of matrix cracks in the off-axis plies and by matrix splitting in the axial plies. Further, the function which represents the local state of strength in the critical element S_u, is written in terms of the material strength tensor, X_{ij}, which is also a function of the number of applied cycles, since the strength in the critical element may be degraded due to processes such as oxidation, chemical degradation, or other degradation events. These details can be determined from experimental measurements.

We can simplify equation (3) by representing the ratio of the local state of stress to the local state of strength as a "normalized failure function," F_a, and write the expression

$$F_r = 1 - \int_1^0 (1 - F_a) i\left(\frac{n}{N}\right)^{i-1} d\left(\frac{n}{N}\right) \tag{4}$$

It should be noted that the total life of the critical element under current conditions, represented by N in equation (4), is also a function of the number of cycles, since the life will be altered by changes in both the local stress state and local material state. That fact will also be demonstrated in subsequent examples. Hence, we see from our expression that we need to determine the local state of stress in the critical element, the local state of strength in the critical element, the changes in that stress state and strength state as a function of applied cycles or generalized time, and the life of the critical element under specific conditions of stress and strength. The state of strength and state of stress of the material, represented by the generalized failure function, F_a, involves a criterion which is chosen to represent a specific failure mode. Indeed, equation (4) must be written for each failure mode independently. However, it should be noted that the interaction of failure modes is included in the single integral in equation (4) for a given failure mode in the sense that any stress state alteration or material state alteration associated with some damage event or other failure mode would be included in proper representations of the stress state and material state in the critical element, since our approach is a mechanistic one. Therefore, if a proper experimental investigation is conducted and the mechanics problem is properly set for a given failure mode, interactions will be included in a normal fashion and no artificial additions or interaction terms are required.

Figure 7 illustrates how these three essential elements of our approach can be combined in a mechanistic prediction of strength and remaining strength, and ultimately a prediction of life for high temperature materials. Figure 8 shows predicted S-N curves for a silicon-carbide-reinforced LAS glass composite, at elevated temperatures which cause oxidation and degradation of the composites. The results for 600° and 900° C represent the combined effect of the temperature degradation and the damage caused by cyclic mechanical loading. That figure shows a variety of predicted S-N curves for several temperatures above and below the 600 and 900° results, for which some data are available. The predicted results agree remarkably well with the available data (circles and triangles). Moreover, the other results allow the researcher and the engineer to anticipate behavior under a variety of other temperatures with some confidence. These data are very difficult (expensive and time consuming) to get. The present model, which is mechanistic, can provide guidance in the prediction of results under many such conditions, and can also provide guidance in the planning of tests to obtain data which may be critical for finalization of a design. Moreover, and most important, this method can provide guidance to material designers in the selection of constituents, their arrangement, their bonding and processing, manufacture, and final assembly into

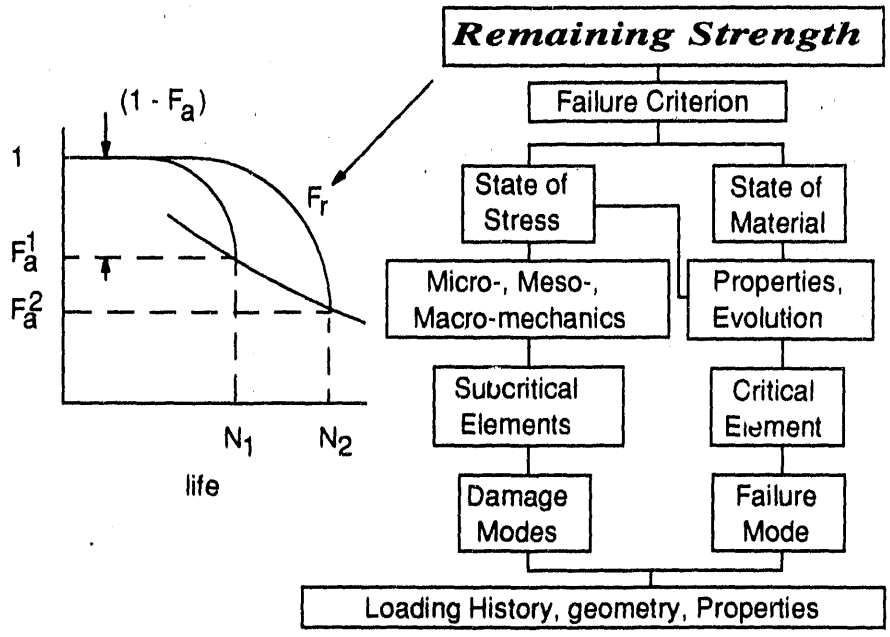

Figure 7. Critical element approach to remaining life prediction.

an engineering component to achieve specific performance characteristics under severe loading conditions such as long-term exposure to cyclic loading and high temperature environments.

SOME NEW DIRECTIONS

The manner in which mechanics should be used to describe strength is not firmly established for homogeneous materials, and is less well understood for composite materials. Moreover, if one wishes to describe the degradation of strength over long periods of time (say, during the engineering use of such materials) this fundamental weakness precludes definitive systematic use of mechanics for that purpose as well.

The use of various local mechanics approaches seems to offer hope of overcoming these limitations. Present efforts suggest that it is possible to describe the strength of composite materials using micromechanical representations of the failure modes that control the strength of those materials. In fact, it appears that it may be possible to construct such micromechanical models in such a way

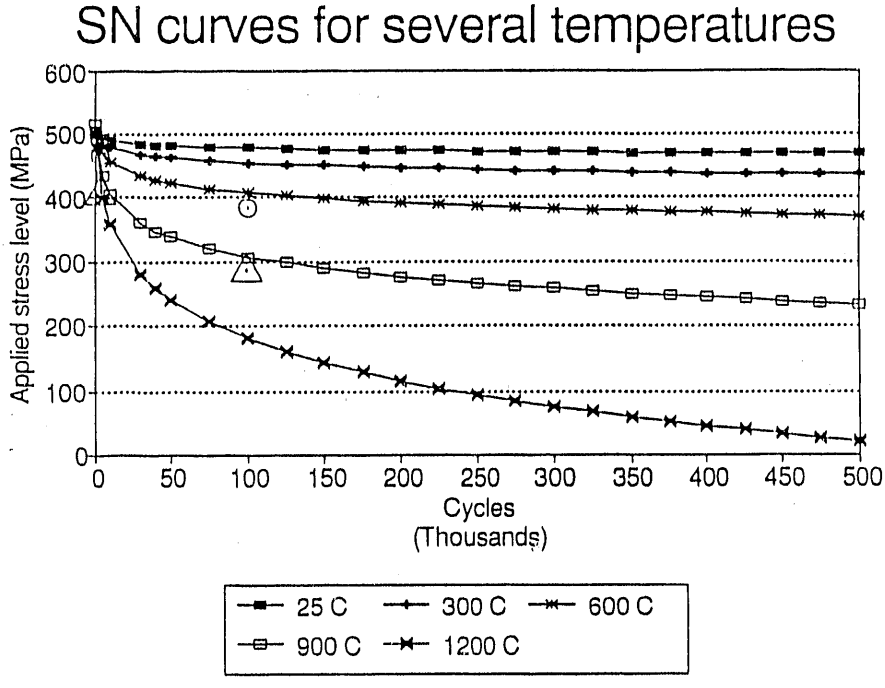

Figure 8. Predicted and observed fatigue life of LASII-glass ceramic composites: predicted results for several temperatures compared to available data for 600 deg. C (circles) and 900 deg. C (triangles).

that the changes in the parameters in those models during long-term loading can be measured and used to estimate the changes in the strength of the global composite. In addition, those parameters may be related, in many cases, to the manner in which the composites were synthesized and manufactured, so that a means of "designing" material systems for specific long-term performance may be provided by this approach.

Refinement of Mechanistic Models

One of the directions taken in our general approach is to develop a micromechanical representation of the tensile-strength-controlled remaining strength and life of fiber reinforced composite laminates with typical constituent properties. The sensitivity of the predicted results to various micro-parameters (including some statistical ones) is of special interest.

Reifsnider and Gao have postulated an approximate method of finding a relationship between the stress concentration in a fiber next to a broken one and the ineffective length under that condition, and have used stress concentrations from micromechanical relationships to determine ineffective lengths from the relationship

$$\Phi = \left[C + \frac{(1-C)}{(\delta\eta)} \right] [1 - \exp(-\delta\eta)] - \frac{(1-C)}{(\eta\delta)} [(\delta\eta + 1)\exp(-\delta\eta) - 1] \qquad (10)$$

When this approach is taken, **a maximum is predicted** in the specimen strength as a function, for example, of the ratio of the fiber stiffness to matrix stiffness[31]. Good agreement with experimental data was found.

Quite recently, Gao and Reifsnider have generated a new model which allows plastic deformation at the micro-level, and calculates the local stress concentration and the ineffective length as fibers break and the matrix yields. Although this model is still only one dimensional, much more information is obtained from the analysis[32]. For example, the predicted composite strength as a function of the interface or matrix strength, for two different fiber shape parameters shows a maximum in the strength which is very pronounced. To the right of the maximum, the local stress concentration controls strength (as it does for many ceramic composite materials, while to the left side of the peak in the curve, the length of the ineffective region around the break becomes large because the weak matrix or interface is yielding over a large region. It was also found that the ineffective length changes with the number of broken fibers (which is found by iteration by the nonlinear model). For low values of matrix strength, that length becomes quite large as the fibers break, while it grows slowly for high-stength (elastic) conditons. Changes in local stress concentration as a function of fiber fracture were also found for several values of matrix or interface strength. The stress concentration grows sharply for very strong material around the fibers (and causes failure), but the local yielding actually reduces the stress concentration for a large number of fiber fractures for very weak matrix materials. These results clearly show how the stress concentration controls in one case (for high strength matrix / interface materials) and the ineffective length controls the strength for the contrasting case of low matrix / interface strength. Moreover, the model identifies the micro-properties and behavior that controls this balance, and specifies the right combination for the material systems designer.

However, this type of micromechanical modeling does one other very critical thing, in the context of the present effort. The micromechanical models of strength can also be used in models of remaining strength and life in a special way. Since the parameters (such as constituent and interface or interphase properties, geometry, and arrangements) that define how a composite material system is made appear in those relationships, the variations in those parameters caused by mechanical damage, aging, chemical activity, or thermodynamic changes during long-term loading in mechan-

ical, thermal, or chemical environments can be used to **predict** the remaining strength and life of the composite materials and components in terms of those constituent changes. This is a powerful tool, since it offers the hope of providing a systematic and mechanistic method of designing material systems for known long-term performance. This is, in fact, the primary essence of our approach.

As described earlier, the Materials Response Group at Virginia Tech has provided leadership in the development of micromechanical strength models for fiber reinforced composite materials. In general, these models apply to ceramic composite materials to the extent that they include situations wherein the stress concentration in the fibers caused by other broken fibers dominates the strength, as it is known to do for many ceramic composite systems. However, many additions to the model are needed. A few are listed below:

- A representation of matrix-dominated crack propagation including the case when matrix cracks are bridged by other unbroken fibers under tensile loading is needed. This will require a corrected micromechanics analysis of local stresses in the presence of matrix cracks, some broken fibers, and some unbroken fibers. A recent model we have developed could be modified for this task .[31]

- The interphase region in ceramic composites usually includes a fiber coating (such as carbon) which has properties which are very different from the fiber and the matrix around it. Our current tension model does not include this region, but our local stress analysis is so constructed that it can represent such a region easily. Moreover, we have the only known solutions for such a region in the presence of spatial variations of properties from point to point through the thickness of the interphase region; it may be necessary to incorporate this model into the strength model[33].

- The present model addresses only failure modes which are precipitated by an overload of the fibers, either because the local stress field increases or the strength of the fibers decreases (due to oxidation, thermal weakening, etc.). If other failure modes dominate, entirely new models may have to be formulated.

In addition to the refinement of the local stress state representations to account for new damage and failure modes, refinements to the relationships used to represent material states and their evolution (as described by the appropriate rate equations) are needed. In an earlier section, we discussed several such rate equations. Presently, we have linear viscoelastic models for stiffness changes, and creep rupture equations which reduce the ply-level strength of the composite to account for such things as oxidation effects or other chemical degradation. Both of these representations are known to be inadequate for HTC systems in some cases.

Other New Directions

Our research indicates the presence of a distinct nonlinear creep rupture effect in certain ceramic composite systems at temperatures close to their upper limit use temperature. An example of such a systems is SiC reinforced CAS. The nonlinearity shows up as a applied stress level dependence on the rate of strength loss as a function of temperature and time, i.e., **the form of the degradation rate equation is different at different levels of applied static or cyclic loading.** This is an anomaly in a certain sense, and will be given special attention in our continuing work.

Another current direction (funded by the Virginia Institute for Material Systems) is the development and refinement of a model of cyclic loading as a forced vibration problem. This is an entirely new concept which we have pioneered, and it has given birth to an important new experimental method for monitoring the rate of damage development in specimens during high temperature testing. The approach considers the dynamic response of the test machine and the specimen together as a compound system. The forced vibration problem is posed with material nonlinearity so that the problem is nonlinear and becomes an initial value problem. In the laboratory, measurements are made by using the dynamic load and displacement signals used by the controller of the servohydraulic test machine to control the test. No attachments are made to the specimen. This is a very great advantage, since it is very difficult (essentially impossible) to fasten something to the specimen at very high temperature without interfering with the test results, and usually disturbing the uniformity of the temperature field. Moreover, the results are reproducible, and consistent to an extent that the data can be used to determine the percent of life left for a given specimen and a given test. This is a critical feature, since some method of this type must be used to terminate tests to recover comparable data from test to test.

Another direction of our research is the refinement of the models that we use to interpret measurements of interface / interphase strength using multifiber penetration methods for HTC systems [34]. This characterization, also conceived and developed in our laboratory under Air Force funding, has shown great promise as a method of measuring not only interfacial strength, but also for the measurement of compression strength and possibly for the measurement of shear strength. The approach involves a ball penetration in which a group of fibers are displaced with measured displacement and force to produce a force-displacement diagram as shown in Figure 9. The details of that record can be directly related, with our micromechanical models, to the interfacial strength. Figure 10 shows such data for three types of composite which have different levels of interfacial strength. The figure also shows measurements made by other means. We are concentrating on the development of this method for testing of properties at elevated temperatures, and on the modeling of such test data to make possible the interpretation in terms of interfacial strength. Special attention will be given to the question of how time-dependent behavior enters this characterization method, and how our models can be used to isolate this important effect in HTC systems.

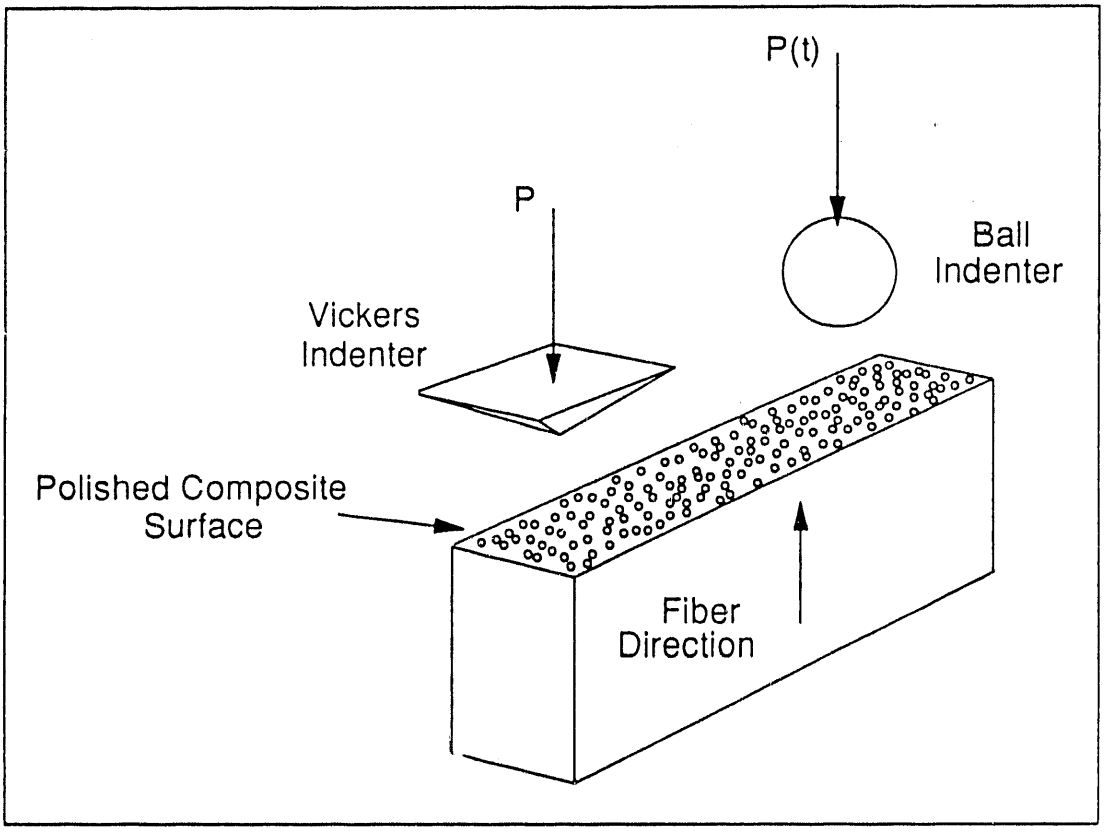

Figure 9. Multifiber penetration method: Method diagram of the multifiber penetration method of measuring interfacial strength, compression strength, and shear strength.

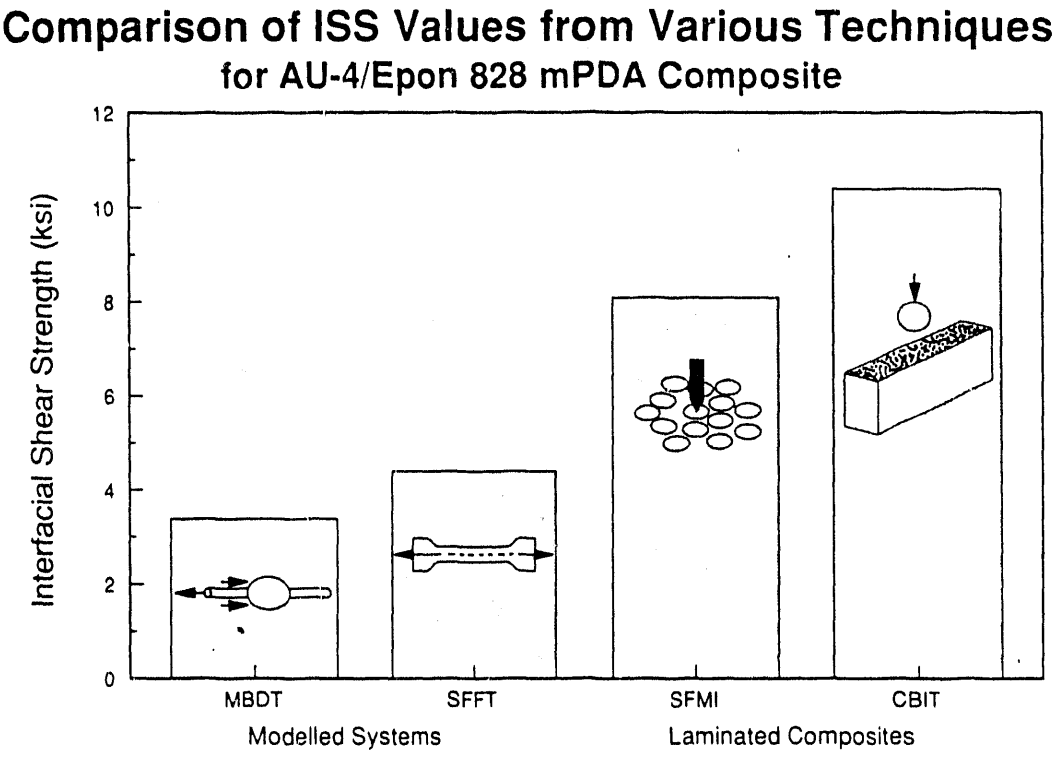

Figure 10. Comparative interfacial strength: Measurements of interfacial strength with microbead (MBDT), fragmentation (SFFT), nano-indentation (SFMI), and the present continuous ball indentation (CBIT) methods, for a polymer composite.

REFERENCES

1. K.L. Reifsnider, W.W. Stinchcomb and T.J. Dunyak, "VPI-1 - Investigation of Properties and Performance of Ceramic Composite Components," ORNL/FMP-88/1 AR&TD Fossil Energy Material Program Semiannual Progress Report for the Period Ending March 31, 1988.

2. T.J. Dunyak, K.L. Reifsnider and W.W. Stinchcomb, "Evaluation of NDE Methods as Applied to Ceramic Composite Tubes," ORNL/Sub/87-SA946/April 1990.

3. K.L. Reifsnider, W.W. Stinchcomb and T.J. Dunyak, "VPI-1 - Investigation of Properties and Performance of Ceramic Composite Components," ORNL/FMP-88/2 AR&TD Fossil Energy Material Program Semiannual Progress Report for the Period Ending September 30, 1988.

4. K.L. Reifsnider, W.W. Stinchcomb and T.J. Dunyak,"VPI-1 - Investigation of Properties and Performance of Ceramic Composite Components," ORNL/FMP-89/1 AR&TD Fossil Energy Material Program Semiannual Progress Report for the Period Ending March 31, 1989.

5. K.L. Reifsnider, W.W. Stinchcomb and T.J. Dunyak, "VPI-1 - Investigation of Properties and Performance of Ceramic Composite Components," ORNL/FMP-89/2 AR&TD Fossil Energy Material Program Semiannual Progress Report for the Period Ending September 30, 1989.

6. K.L. Reifsnider, W.W. Stinchcomb and T.J. Dunyak, "VPI-1 - Investigation of Properties and Performance of Ceramic Composite Components, ORNL/FMP-90/1 AR&TD Fossil Energy Material Program Semiannual Progress Report for the Period Ending March 31, 1990.

7. K.L. Reifsnider, W.W. Stinchcomb and T.J. Dunyak, "VPI-1 - Investigation of Properties and Performance of Ceramic Composite Components," ORNL/FMP-90/2 AR&TD Fossil Energy Material Program Semiannual Progress Report for the Period Ending September 30, 1990.

8. K.L. Reifsnider, W.W. Stinchcomb and T.J. Dunyak, "VPI- 1 -Investigation of Properties and Performance of Ceramic Composite Components," ORNL/FMP-91/1, Proc. of the Fifth Annual Conference on Fossil Energy Materials, September 1991.

9. "Life Prediction Methodologies for Composite Materials," Report of the Committee on Life Prediction Methodologies for Composite Materials, Nat. Matls. Advisory Board, Nat. Res. Council, NMAB-460, N. Ac. Press, 1990.

10. "High Temperature Materials for Advanced Technological Applications," Nat. Matls. Advis. Board, Nat. Res. Council, NMAB-450, N. Ac. Press, 1988.

11. Z. Gao and K.L. Reifsnider, "Micromechanics of Tensile Strength in Composite Systems," Proc. of Symposium on Composite Fatigue and Fracture, May 5-9, 1991, Indianapolis, IN, ASTM (in press).

12. S.B. Batdorf, "Tensile Strength of Unidirectionally Reinforced Composites - I," J. Reinforced Plastics and Composites, Vol. 1, 1982.

13. K.L. Reifsnider, "Life Prediction Analysis: Directions and Divagations," Proc. ICCM VI, London, 1987 (plenary lecture), Elsevier Applied Science, 1987, pp. 4.1-4.31. .K.L. Reifsnider, "Performance Simulation of Polymer Based Composite Systems," Proc. Int'l. Symp. on Durability of Polymer Based Composite Systems .us for Structural Applications, (invited plenary paper), Brussels, Belgium, Aug. 27-31, 1990 (in press).

14. K.L. Reifsnider, "Performance Simulation: A New Approach to the Prediction of the Long-Term Behavior of Composite Material Systems," (invited plenary paper), Fifth Japan-U.S. Conf. on Composite Materials, June 21-25, 1990, Tokyo, Japan (in press).

15. K.L. Reifsnider, "Interpretation of Laboratory Test Information for Residual Strength and Life Prediction of Composite Systems," ASTM Symp. on Cyclic Deformation, Fracture, and Nondestructive Evaluation of Advanced Materials, San Antonio, TX, Nov. 12-13, 1990 (in press).

16. K.L. Reifsnider, "Life Prediction Methods for Notched Composite Laminates," Proc. Fourth Japan-U.S. Conf. on Composite Materials, May 29, 1988.

17. J. Lesko, G. Carman, D. Dillard and K.L. Reifsnider, "Hardness Testing of Composite Materials as a Tool for Measuring Interfacial Quality," ASTM 4th Symposium on Composite Materials: Fatigue and Fracture, submitted 1991.

18. K.L. Reifsnider, "Life Prediction Methodology for Composite Material Systems," Proc. Indo-U.S. Conf. on Advanced Composite Materials for Aeronautical Applications, 23-25 July, 1990, (in press).

19. K.L. Reifsnider, "Some Fundamental Aspects of the Fatigue and Fracture Response of Composite Materials," Proc. 14th An. Meeting of the Society of Engineering Science, Lehigh Univ., 1977, pp. 373-384.

20. K.L. Reifsnider and A.L. Highsmith, "Characteristic Damge States: A New Aproach to Representing Fatigue Damage in Composite Laminates," Materials Experimentation and Design in Fatigue, Westbury House, Guildford, U.K., 1981, pp. 246-260.

21. A.L. Highsmith and K.L. Reifsnider, "On Delamination and the Damage Localization Process," Fracture of Fibrous Composites, AMD-Vol. 74, American Society of Mechanical Engineers, 1985, pp. 71-87.

22. K.L. Reifsnider and R.D. Jamison, "Fracture of Fatigue-Loaded Composite Laminates," Int'l. Journal of Fatigue, Vol. 4, 1982, pp. 187-198.

23. R.D. Jamison, A.L. Highsmith and K.L. Reifsnider, "Strain Field Response of 0 Degree Glass/Epoxy Composites under Tension," Composites Technology and Research, Vol. 3, 1981, pp. 158-159.

24. R.D. Jamison, "Damage Develpment and Failure of Fiber-Reinforced Composite Materials," PhD Dissertation, Dept. of Engineering Science and Mechanics, Virginia Polytechnic Institute and State University, Blacksburg, Virginia, 1982.

25. G.P. Carman and K.L. Reifsnider, "Micromechanics of Short Fiber Composites," Fiber Science and Technology, (in press).

26. G.L. Carman, "Micromechanics of Finite Length Fibers in Composite Materials," Dissertation, College of Engineering, Virginia Tech, 1991.

27. J.M. Whitney and L.T. Drzal, "Axisymmetric Stress Distribution Around an Isolated Fiber Fragment," ASTM STP 937, American Society for Testing and Materials, 1987, pp. 179-196.

28. J.M. Berthelot, "Effect of Fibre Misalignment on the Elastic Properties of Oriented Discontinuous Fibre Composites," Fibre Sci. and Tech., Vol. 17, 1982, pp. 25-39.

29. K. Jayaraman and K.L. Reifsnider, "Micromechanical Stress Analysis of Continuous-Fiber Composites with Local Material Property Gradients," Achievements in Composites in Japan and the United States, A. Kobayashi, Ed., Japan Society for Composite Materials, Tokyo, 1990, pp. 425-436.

30. Z. Gao and K.L. Reifsnider, "Micromechanics of Tensile Strength in Composite Systems," submitted to ASTM for publication, 1991.

31. Z. Gao and K.L. Reifsnider, "Composites with Different Interfacial Bonding," Proc. Sixth Technical Conference of the Am. Soc. for Composites, Technomic Press, Inc., October 15, 1991, pp. 742-750.

32. R. Swain, K.L. Reifsnider, K. Jayaraman and M. El-Zein, "Interface/Interphase Concepts in Composite Material Systems," Proc. of the Fourth Technical Conf. of the American Society for Composites, Technomic Press, 1989, pp. 377-386.

33. J. Lesko, G. Carman and K.L. Reifsnider, "Hardness Testing of Composite Materials as a Tool for Measuring Interfacial Quality," Proc. ASTM 4th Symposium on Composite Materials: Fatigue and Fracture, = = = = = Philadelphia, PA., submitted for publication, 1991.

PART III - NEW ALLOYS

CSM-2 - GRAIN GROWTH KINETICS OF IRON ALUMINIDE ALLOY FA-129

A. A. Fasching*, G. R. Edwards*, and S. A. David#

*Center for Welding and Joining Research
Department of Metallurgical and Materials Engineering
Colorado School of Mines
Golden, CO 80401

#Metals and Ceramic Division
Materials Joining Group
Oak Ridge National Laboratory
Oak Ridge, TN 37831

ABSTRACT

The grain growth behavior of iron aluminide (Fe_3Al) alloy FA-129 was studied as a function of time and temperature. Grain size in the temperature range 500-900°C was found to be very stable with respect to time, exhibiting an apparent activation energy of 23 kcal/mol (95.5 kJ/mol). At 1050°C abnormal grain growth was observed for times greater than 10 hours.

INTRODUCTION

Intermetallic ordered alloys are attractive engineering materials because they have good electrical, magnetic and corrosion resistant properties. Their inherent tendency to be brittle, however, limits their use as structural components. The recent development of ductile iron aluminides has necessitated research into the practicality of processing such materials using conventional means. In particular, welding is being investigated since it represents an important means of constructing engineering structures.

In welding, microstructural stability during the thermal cycles is very important. D.I. Ash et. al.[1] found that the microstructure of iron aluminide, FA-129, could be unstable during thermal cycling. The reasons for this were considered to be related to the thermomechanical history of the material. The understanding of the grain growth kinetics of these materials and how they relate to the prior processing history

has been limited to date. The purpose of this paper is to report the findings of an initial grain growth study conducted on alloy FA-129 Ht #D5-3966-1 and a follow-on study of a special heat (a heat number was not assigned) of the same.

EXPERIMENTAL PROCEDURES

An initial grain growth study was conducted on (HT #D5-3966-1) FA-129 iron aluminide sheet material received from Oak Ridge National Laboratories (ORNL). The nominal composition of alloy FA-129 is Fe-28AL-5Cr-0.5Nb-0.2C. The material had been stress relieved at 700°C for one hour, oil quenched and acid cleaned at ORNL. The sheet was sheared into 20mm x 20mm pieces (0.75mm thick) and annealed in a furnace with an argon back pressure. The samples were annealed for 20, 40, and 60 minutes at 650, 700, 750, 800, 850, 900, and 1000°C. Upon removal from the furnace, the samples were water quenched.

For the purpose of further characterizing the grain growth kinetics of iron aluminide, FA-129, a special ingot was cast at ORNL. The ingot was extruded and then hot rolled to a nominal thickness of 2.54mm. At that point the material was divided into thirds, each undergoing a separate thermomechanical processing sequence. Table 1 summarizes the three different processing conditions.

Table 1: Summary of the three thermomechanical conditions of FA-129

Rolling Condition Number 1	70% reduction at 650°C
Rolling Condition Number 2	57% reduction at 650°C 850°C for 1 hour 30% reduction at 650°C
Rolling Condition Number 3	57% reduction at 650°C 750°C for 1 hour 30% Cold Work

Each of these processing sequences resulted in 0.75mm-thick sheet. Samples of each of the three conditions were cut into 13mm x

10mm pieces, and encapsulated in quartz ampules which had been back-filled with argon (0.25 atm). Specimens from all three rolling conditions were annealed at the times and temperatures shown in Table 2. The test temperatures were chosen in relation to the known solid-state phase transformations of the iron-aluminum system. For consistency, all the samples with the same time and temperature parameters were exposed to the furnace environment simultaneously. After the samples were removed from the furnace, the ampule was broken open and the samples were quenched in ice water.

Table 2: Annealing Times and Temperatures for FA-129 Specimens.

	20 (min)	60 (min)	10 hours	50 hours	170 hrs
500°C	X	X	X	X	X
600°C	X	X	X	X	X
800°C	X	X	X	X	X
1050°C	X	X	X	X	X

The etchant used on all of the samples had the following composition: 60ml methanol, 20ml HCl, 40ml HNO_3. The shelf life of this etchant is about two hours. The etched sample was rinsed in hot water and swabbed for 10-20 seconds.

The grain size was measured using the intercept method (ASTM-E112). As-received samples were measured for comparison. The intercepts were counted using concentric circles of a total length of 300mm, over two fields. Grain size was calculated by determining the average number of intercepts per 1mm length; this value was multiplied by a conversion factor to determine the average grain size[2].

RESULTS

Grain size versus time was plotted for each temperature and the data were fit to a second order polynomial equation, indicating that these data exhibit ideal behavior, ($D^2 \sim kt$), as seen in Figure 1. An

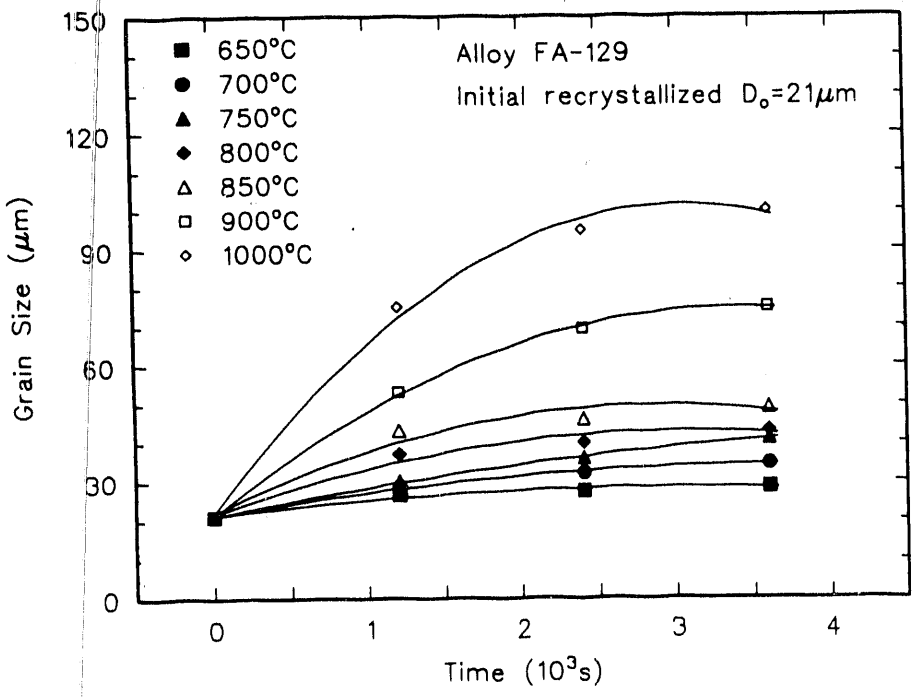

Figure 1. Grain size versus time for the initial grain growth study shown at the different annealing temperatures. Data were fit to a second order polynominal indicating ideal grain growth.

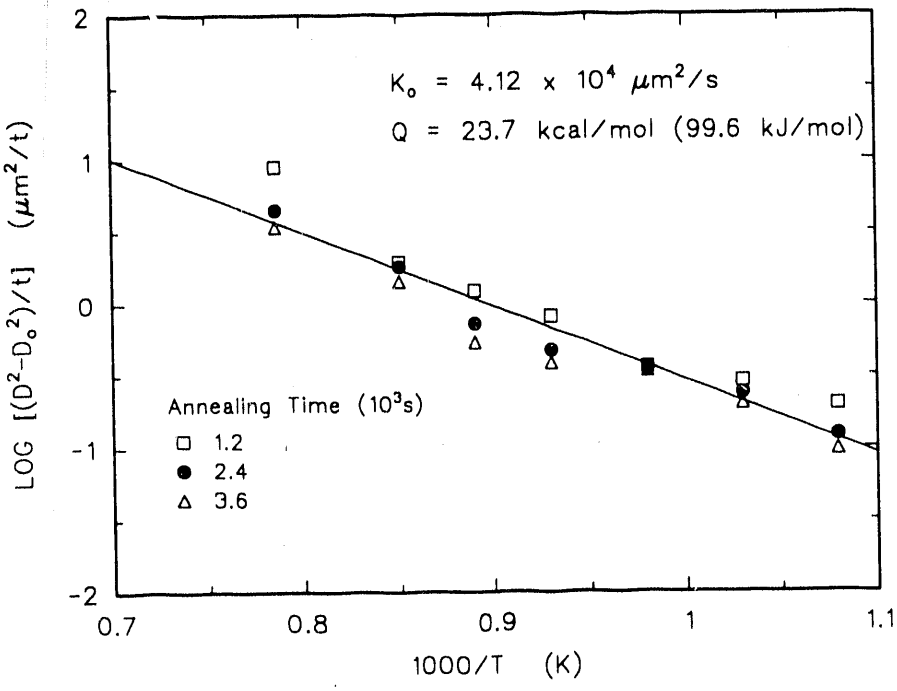

Figure 2. Linearization of the data from the initial grain growth study (LOG[D^2-D_o^2/t]) to determine K_o and Q.

apparent activation energy of 23.7 kcal/mol (99.6 kJ/mol) was also determined, as shown in Figure 2.

In the first rolling condition, the initial structure was unrecrystallized, highly elongated grains. The specimens representing the other two rolling conditions underwent recrystallization and, therefore, exhibited a recrystallized structure. The initial grain size of Rolling Condition Number 3 was slightly smaller than that of Rolling Condition Number 2. This result was expected since Rolling Condition Number 3 was recrystallized at a lower temperature than Rolling Condition Number 2.

The elongated grain structure observed for all of the samples annealed at 500 and 600°C was similar to that of the as-received sample. At 800°C, the microstructure recrystallized after 20 minutes in the furnace and the grains proceeded to grow. For those annealed at 1050°C, recrystallization and grain growth occurred, and after 10 hours of exposure, abnormal grain growth was observed.

Samples of the second rolling condition readily recrystallized, and normal grain growth was observed in all specimens annealed at 500, 600 and 800°C. At 1050°C normal grain growth occurred during the first 50 hours of annealing. At that point half of the specimens showed abnormal grain growth, while the other half exhibited normal grain growth. These results were repeated, verifying that this phenomena was not caused by temperature differences, such as those related to furnace position. For all times longer than 50 hours abnormal grain growth was observed.

Samples of the third rolling condition also readily recrystallized. As with Rolling Condition Number 2, all of the samples annealed at 500, 600 or 800°C showed normal grain growth. Again, for specimens annealed at 1050°C, normal grain growth was observed for times up to 50 hours. At 50 hours, half of the metallographic samples revealed normal grain growth behavior and the other half exhibited abnormal grain growth behavior. For times beyond 50 hours, abnormal grain growth was observed.

Grain size versus time was plotted for each rolling condition and temperature, as seen in Figures 3, 4, and 5. Using a power law fit, a best fit line of the form $D-D_o=Kt^n$ was plotted to characterize the time and temperature dependence of the change in grain size ($D-D_o$). If a normal thermally activated process for grain growth is assumed, the value K can be expressed as $K=K_oe^{-Q/RT}$; where K_o is a constant, R is the gas constant, T is temperature and Q is the apparent activation energy for grain growth.

In Figures 6 and 7 plots were made to determine Q and K_o for Rolling Conditions Numbers 2 and 3. Here, the slope of the line is equal to $-Q/2.3R$ and K_o is the y-intercept. In both cases, the 1050°C data were not considered in the fit but are shown on the graph.

DISCUSSION

The results of the initial grain growth study indicated that alloy FA-129 exhibited ideal grain growth. This study was conducted over a narrow range of times, and in the follow-on study this did not hold true. The apparent activation energy that was calculated for this initial grain growth study (99.6 kJ/mol) was the same as that calculated in the follow-on study.

Specimens of Rolling Condition Number 1 did not possess an initial recrystallized microstructure, and samples annealed at 500 or 600°C did not recrystallize. At 1050°C, recrystallization followed by abnormal grain growth rapidly occurred. Consequently, only the 800°C data could be plotted for this rolling condition. At 800°C for this condition, both recrystallization and normal grain growth occurred. The value for the initial grain size (D_o) therefore was assumed to be small compared to the final grain size (D), and the data were fit to an equation with the form $D=Kt^n$. This result is shown in Figure 3. One annealing temperature, however, does not provide sufficient data to determine Q or K_o for this rolling condition.

The major problem in analyzing the results for the recrystallized microstructures of Rolling Condition Number 2 and 3 was in determining

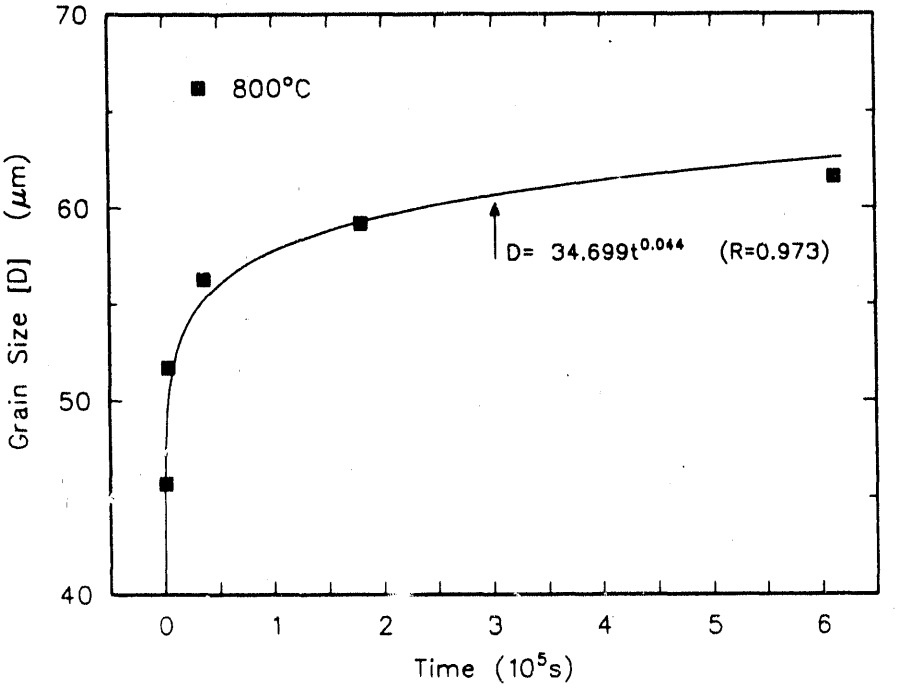

Figure 3. Grain size versus time for Rolling Condition Number 1 shown at 800°C.

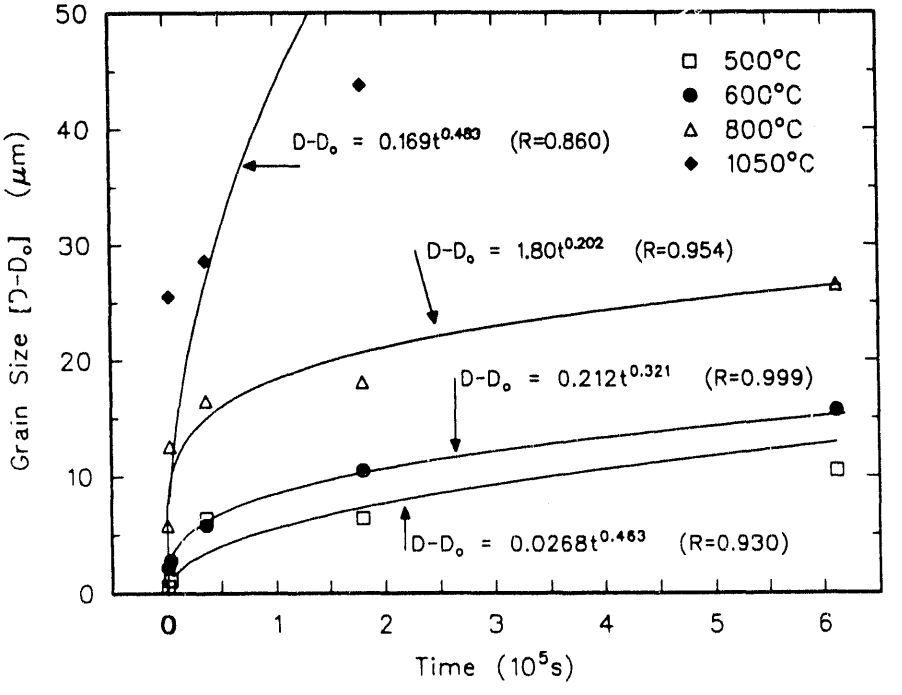

Figure 4. Grain size versus time for Rolling Condition Number 2 at the different annealing temperatures. Data were fit using a power law to the equation $D-D_o=Kt^n$.

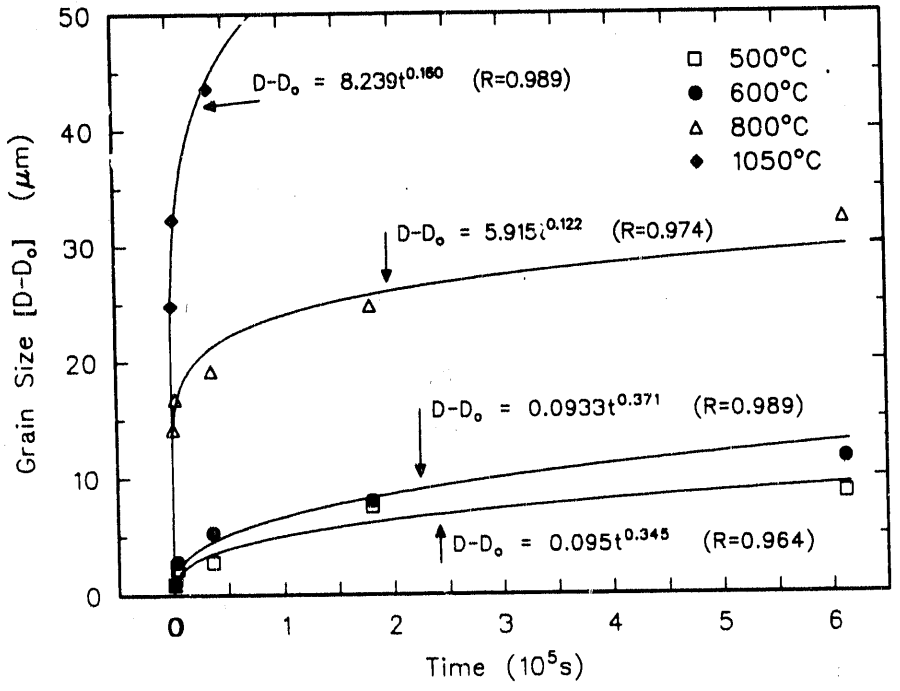

Figure 5. Grain size versus time for Rolling Condition Number 3 at the different annealing temperatures. Data were fit using a power law to the equation $D-D_o=Kt^n$.

an accurate way to represent n, the grain growth exponent. The data did not follow the ideal grain growth law, nor was the initial grain size insignificant as compared with the final grain size. Therefore, neglecting D_o, and fitting the data to the form $D = kt^n$, an approach commonly taken by other researchers[3], was not possible. The best solution was to characterize the change in grain size ($D-D_o$) with time using the power law ($D-D_o=Kt^n$); a time exponent (n) was determined for each temperature and rolling condition.

For Rolling Condition Number 2, the values of n varied from 0.20 to 0.48. Figure 4 shows these curves with their respective equations and the accuracy of the fit (R). Figure 5 shows the same for Rolling Condition Number 3 where n varied from 0.122 to 0.371. The grain growth exponent then appears to be quite dependent on temperature as well as thermomechanical processing. When the data were linearized to determine the activation energy (Figures 6 and 7) the points converged nicely, and a realistic activation energy (Q) was determined for both Rolling Conditions Numbers 2 and 3. For Rolling Condition Number 2, Q=22.98 kcal/mol (95.54 kJ/mol) and for Rolling Condition Number 3, Q=23.91 kcal/mol (99.41 kJ/mol). The data for 1050°C were not considered in the fit of the data for either rolling condition, due to the fact that abnormal grain growth occurred at this temperature. However, these data are shown in Figures 6 and 7 for comparison.

CONCLUSIONS

The results showed that the apparent activation energy of grain growth was consistent for all of the tests. The data in the initial study exhibited ideal grain growth kinetics ($D^2-D_o^2=kt$). The data from the follow-on study did not follow ideal grain growth. Since the initial grain size (D_o) was significant as compared to the final grain size (D) for Rolling Conditions Numbers 2 and 3, a modified analytical technique for describing the grain growth kinetics was required. The equation $D-D_o=Kt^n$ adequately characterized grain growth of alloy FA-129 in Rolling Condition Numbers 2 and 3. Samples of Rolling Condition

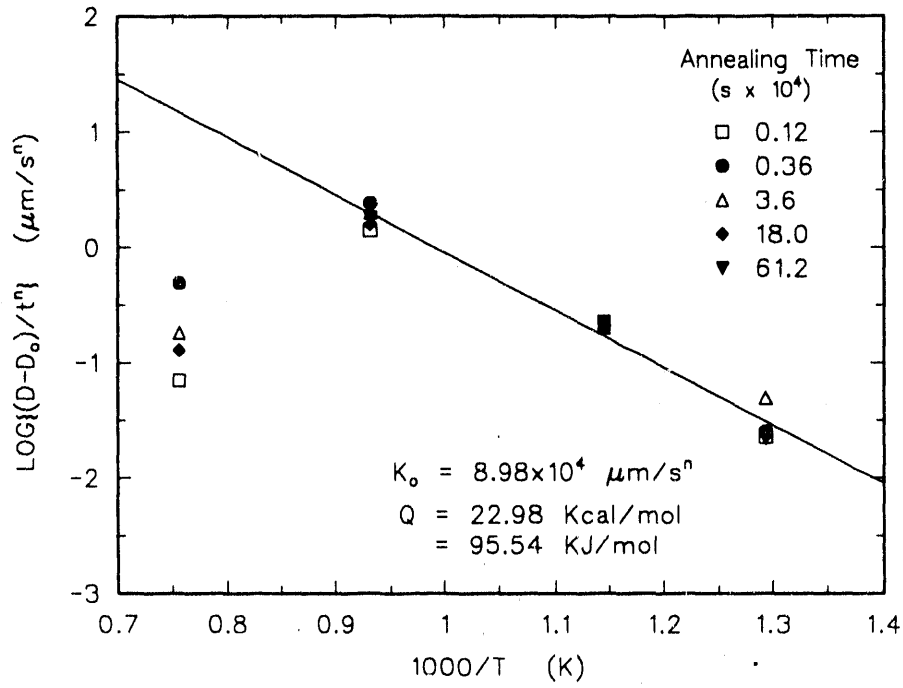

Figure 6. Linearization of the data from Rolling Condition Number 2 to determine K_o and Q. The 1050°C is shown on the plot but was not included in the fit because abnormal grain growth was observed at this temperature.

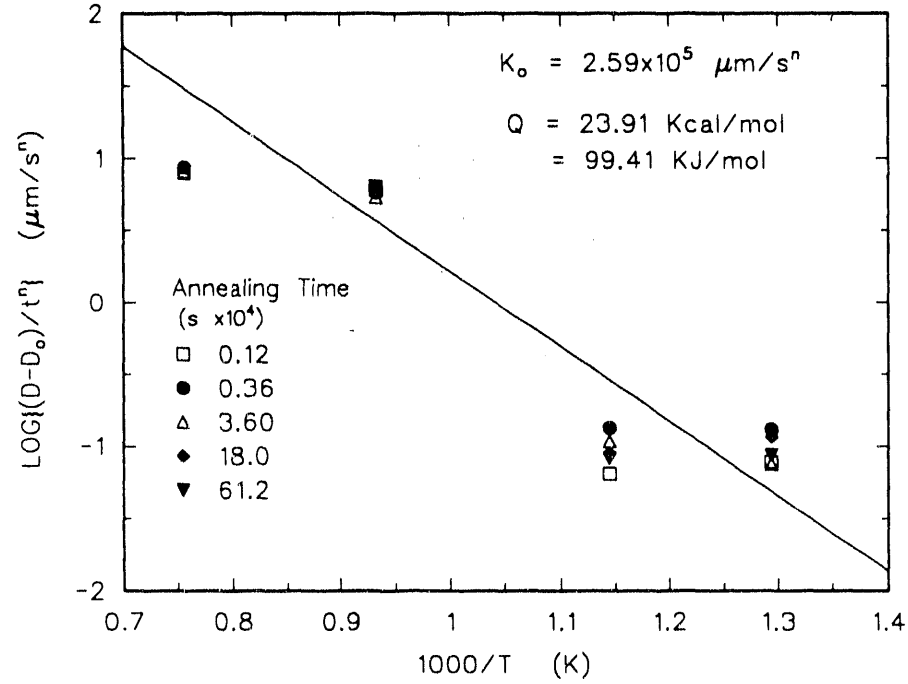

Figure 7. Linearization of the data from Rolling Condition Number 3 to determine K_o and Q. The 1050°C is shown on the plot but was not included in the fit because abnormal grain growth was observed at this temperature.

Number 1 did not recrystallize during the annealing cycles at 500 and 600°C, and exhibited abnormal grain growth at 1050°C. Thus, normal grain growth could be characterized only at 800°C for this condition. With the exception of the tests run at 1050°C, the grain size of alloy FA-129 was quite stable over exposure times up to 170 hours.

A relatively constant activation energy (95-99 kJ/mol) was observed for grain growth at all temperatures except 1050°C for Rolling Conditions Numbers 2 and 3. Prolonged exposure to temperatures above the B2 to disordered BCC transformation (~960°C) resulted in abnormal grain growth in these alloys.

REFERENCES

1. D. I. Ash, G. R. Edwards, and S. A. David, "Weldability and Hot Ductility of Iron Aluminides," ORNL/Sub/85-27421/04.

2. ASTM Handbook E112-84.

3. B. Ralph, "Grain Growth," Materials Science and Technology, vol.6, 1139-1142 (November 1990).

INEL-2-THE INFLUENCE OF THERMOMECHANICAL PROCESSING ON MICROSTRUCTURE AND MECHANICAL PROPERTIES OF Fe_3Al ALLOYS

J. R. Knibloe and R. N. Wright

Idaho National Engineering Laboratory
EG&G Idaho, Inc.
P.O. Box 1625
Idaho Falls, ID 83415-2218

INTRODUCTION

Alloys based on the intermetallic compound Fe_3Al have good resistance to oxidation and sulfidation as well as excellent resistance to abrasion and erosion.[1] Improved understanding of the effects of alloying and processing on controlling strength and ductility of these alloys has lead to interest in employing these materials at elevated temperature in aggressive environments in a number of systems.[2-5] It has been suggested that controlling the type of order in the alloys and establishing a high defect density through warm work result in the maximum room temperature ductility.[3] Alloying with chromium has been found to increase the ductility, while additions of niobium, molybdenum and silicon improve the elevated temperature strength, but significantly reduce the ductility.[5,6]

Alloys with compositions near 3:1 iron to aluminum have three possible crystal structures. Above about 900°C the equilibrium structure is a random bcc solid solution. Between 550 and 900°C the equilibrium phase is based on the B2 ordered structure. Below the critical temperature of 550°C, the DO_3 ordered structure is stable. The critical temperature can be altered significantly by the addition of substitutional alloying elements such as Mo and Si, although Cr additions have been found to have little effect[4]. In binary Fe_3Al it has been found that the B2 $\rightarrow$ DO_3 order transition occurs very rapidly and it is not possible to retain the B2 phase at room temperature through normal solid state quenching techniques.[7-9] Alloying with Cr appears to slow the ordering transformation on cooling and it is

relatively easy to form a predominantly B2 structure by quenching from above the critical temperature.[10]

The project objective is to examine the effect of thermomechanical processing on the structure and properties of iron aluminides. To date, most of the work has been on the 2 and 5% Cr alloys; however, emphasis is currently shifting to alloy FA-129 with Nb additions for improved elevated temperature strength. The role of substructure introduced by warm working in contributing to the properties of the material is being examined in some detail. The kinetics of recovery, recrystallization and grain growth and of the B2 to DO_3 order reaction are also being studied. The goal is to discern the individual effects of prior work, grain size, and order structure on the strength, ductility and toughness of these alloys.

DISCUSSION OF CURRENT ACTIVITIES

Effect of Prior Work

A study has been initiated on FA-129 to determine the effects of prior work on room temperature mechanical properties. The material was rolled at Oak Ridge National Laboratory (ORNL) to a thickness of 1.9 mm according to methods established by Sikka et al.[6] and then annealed at 1100°C for 1 h to eliminate dislocations. Pieces of this sheet were then rolled and annealed according to a schedule which resulted in six pieces of 0.8 mm thick sheet with 0, 15, 30, 45, and 60% reduction in thickness. Transmission electron microscopy (TEM) was used to verify that the pieces had increasing dislocation contents with increasing amount of work as shown in Figure 1 for samples with 15, 30 and 60% work. No dislocations were found in the 0% work sample which was annealed after the final reduction. Tensile specimens are currently being machined from this material, and additional characterization will be conducted after testing to verify other structural features, such as grain size and degree of order, are similar. Preliminary optical metallography indicates differences in grain size between some of the pieces.

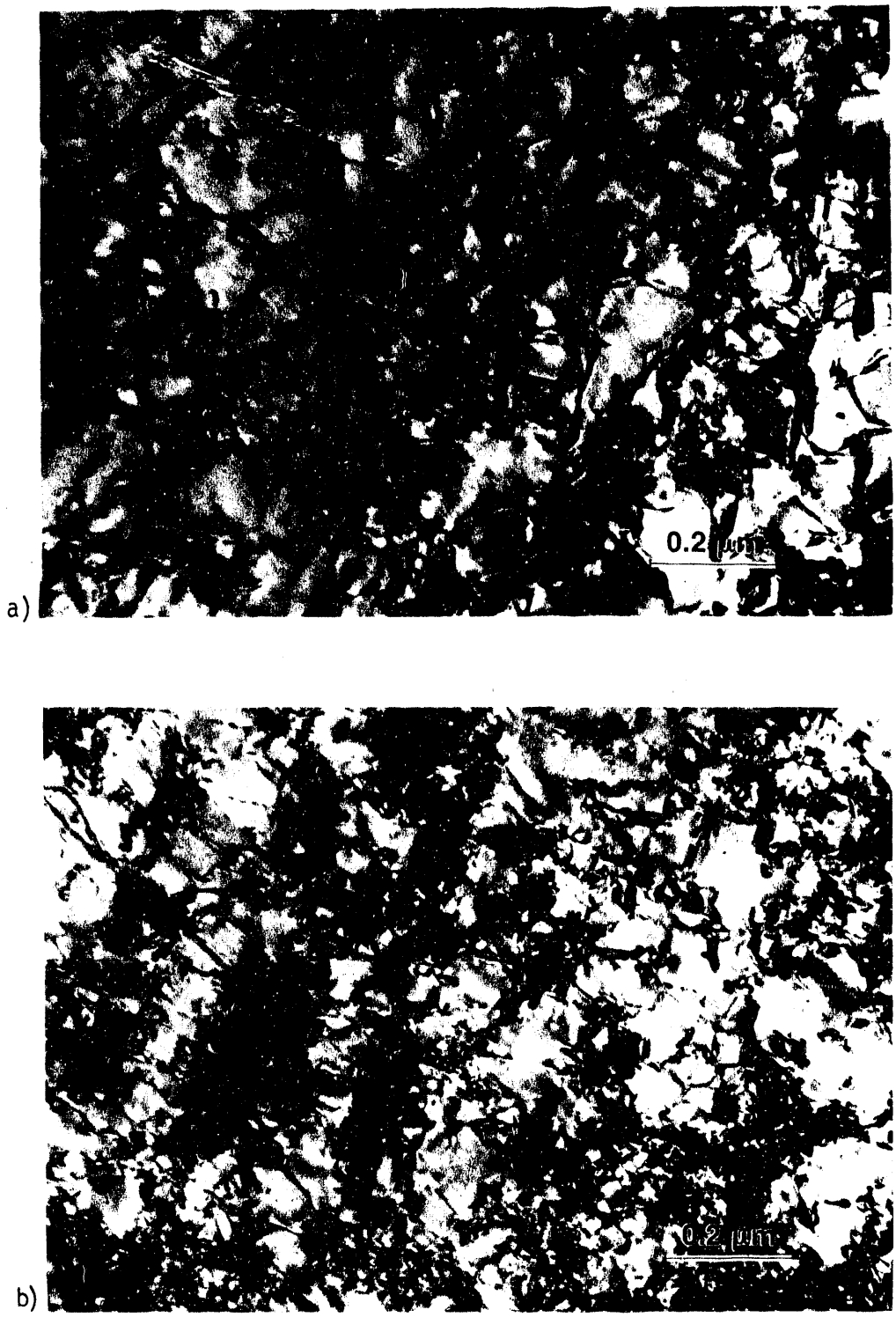

Fig. 1 - TEM photos illustrating qualitative difference in dislocation contents with increasing amount of work for samples with a) 15, b) 30, and c) 60% work.

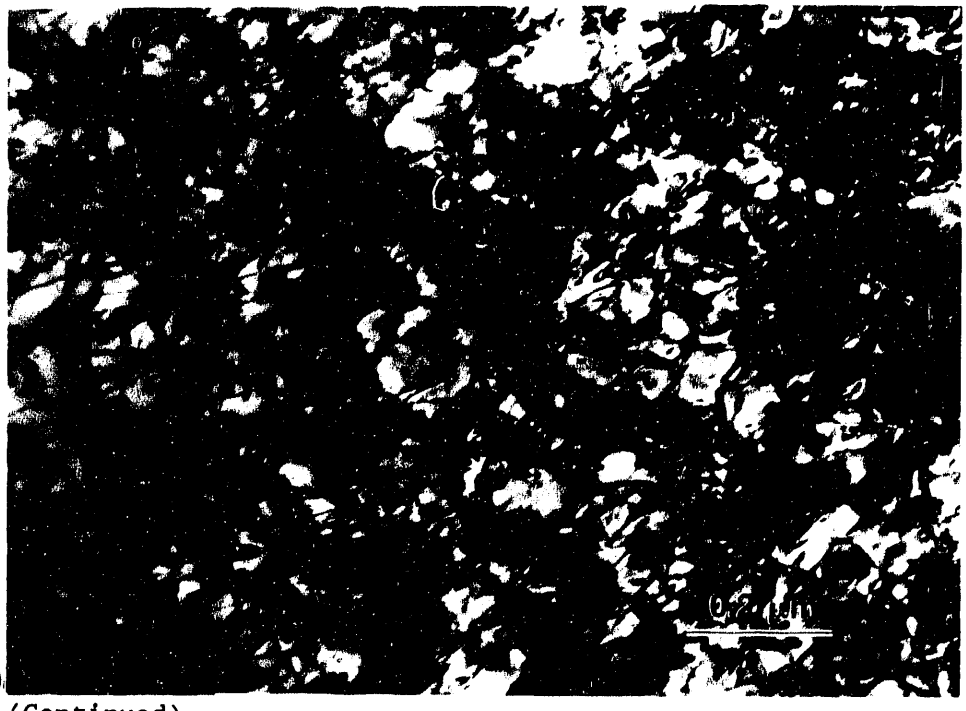

c)

Fig. 1 - (Continued).

Grain Growth, Recrystallization, Recovery

Optical metallography, microhardness and resistivity measurements are being used to determine the grain growth behavior as well as the occurrence of recovery and recrystallization in samples taken from 6 mm thick FA-129 plate after heat treating at various time/temperature combinations. Grain size and hardness results for two heat treatment temperatures are shown in Figure 2. The as-rolled plate had very elongated grains; however, 1 h at 750°C is sufficient to completely recrystallize the material. In contrast, samples heat treated for 100 h at 600°C are not recrystallized (and are consequently not shown on Figure 2). Note that while the grain size increases more dramatically as a function of time for samples heat treated at 1100°C than at 750°C, as expected; the hardness of samples heat treated at the higher temperature actually increases. This indicates that a phenomenon other than grain growth occurs at these high temperatures. Additional heat treatments are being done to determine the onset temperature of this hardening behavior and of recrystallization. The

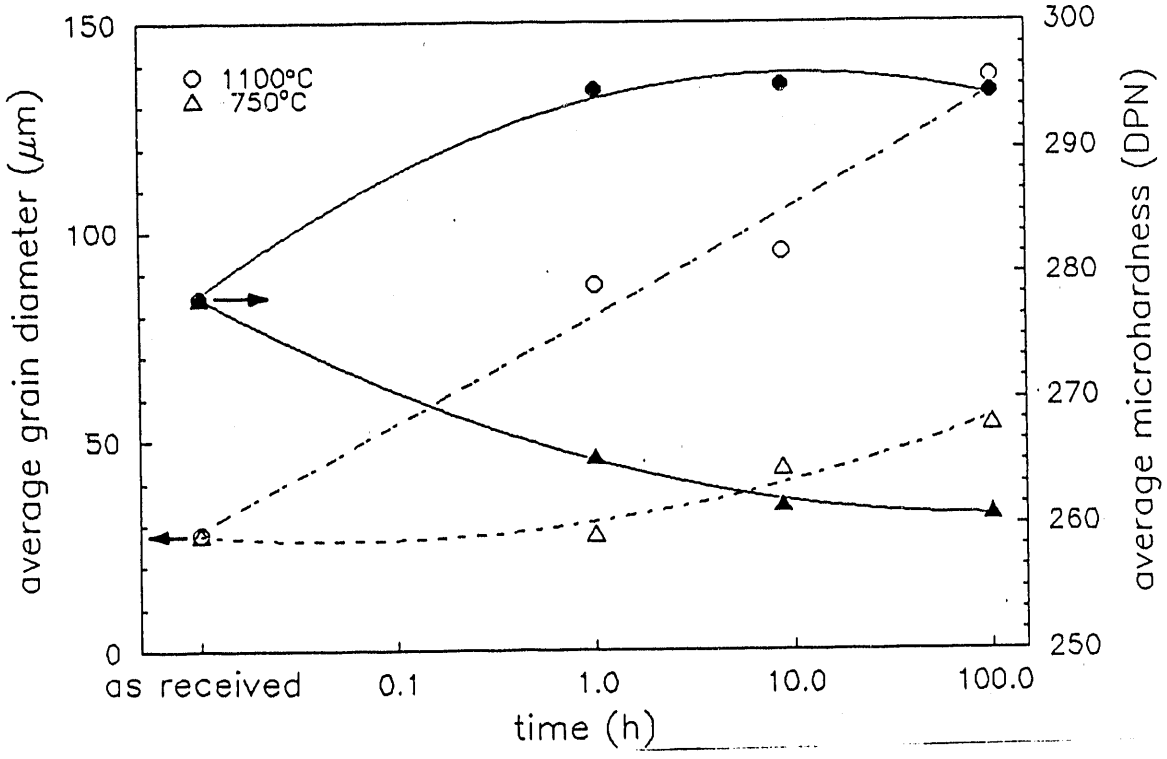

Fig. 2 - Grain size and hardness results for samples heat treated at 750 and 1100°C for approximately 1, 10 and 100 h.

mechanism responsible for this hardening behavior will be determined using TEM and x-ray diffraction.

Structure Characterization

Differential thermal analysis (DTA) indicates that the B2 ⇌ DO_3 order reaction in FA-129 occurs at approximately 550°C, the same transition temperature as binary Fe_3Al and alloys with 2 and 5%Cr[4]. Previous investigation of the 2 and 5% Cr alloys has shown that the B2 structure results in greater room temperature ductility. Studies are underway to determine if the kinetics of ordering for FA-129 are similar to those of the chrome containing alloys. X-ray diffraction of as-rolled FA-129 plate indicate the presence of NbC and both B2 and DO_3 order with strong preferred orientation. Scanning electron microscopy (SEM) with energy dispersive spectroscopy (EDS) confirms the presence

of Nb-rich angular precipitates but indicates about 0.3 at% Nb in the matrix in addition to about 4.4 at% Cr.

Wavy Flow

Both the 2 and 5% Cr alloys exhibited nonuniform plastic behavior that can best be described as wavy flow for a range of strain rates at elevated temperature.[11] Wavy flow was observed in both tension and compression. Similar nonuniform plastic flow has been observed in a wide range of alloys and is usually attributed to either dynamic recrystallization or dynamic strain aging from interstitial or substitutional impurities. The two possible causes for nonuniform flow are usually distinguished by metallographic evidence or through changes in the nature or magnitude of the stress undulations as the temperature or strain rate are changed. Depending on the origin of this phenomenon there may be processing paths that should be avoided in seeking to maximize properties in Fe_3Al. Dynamic recrystallization, for example, would tend to result in a microstructure with lower residual defect densities at room temperature and a resulting reduction in ductility.[10]

Baker et al. have reported dynamic recrystallization in FeAl based on metallographic observations of new strain-free grains formed in the gage section of tensile samples.[12] Although the B2 structure is stable at the temperatures where wavy flow has been observed, TEM of the Cr alloyed Fe_3Al compression samples show low angle boundaries, indicating recovery has occurred (see Figure 3). If recovery occurs during deformation, there is not enough remaining stored energy in the form of strain for dynamic recrystallization to occur. Furthermore, the flow curve cycles that can result from dynamic recrystallization tend to have wavelengths of 5-20% strain and generally damp out after two to eight cycles[13], unlike the small cycles observed up to the point of failure in this study.

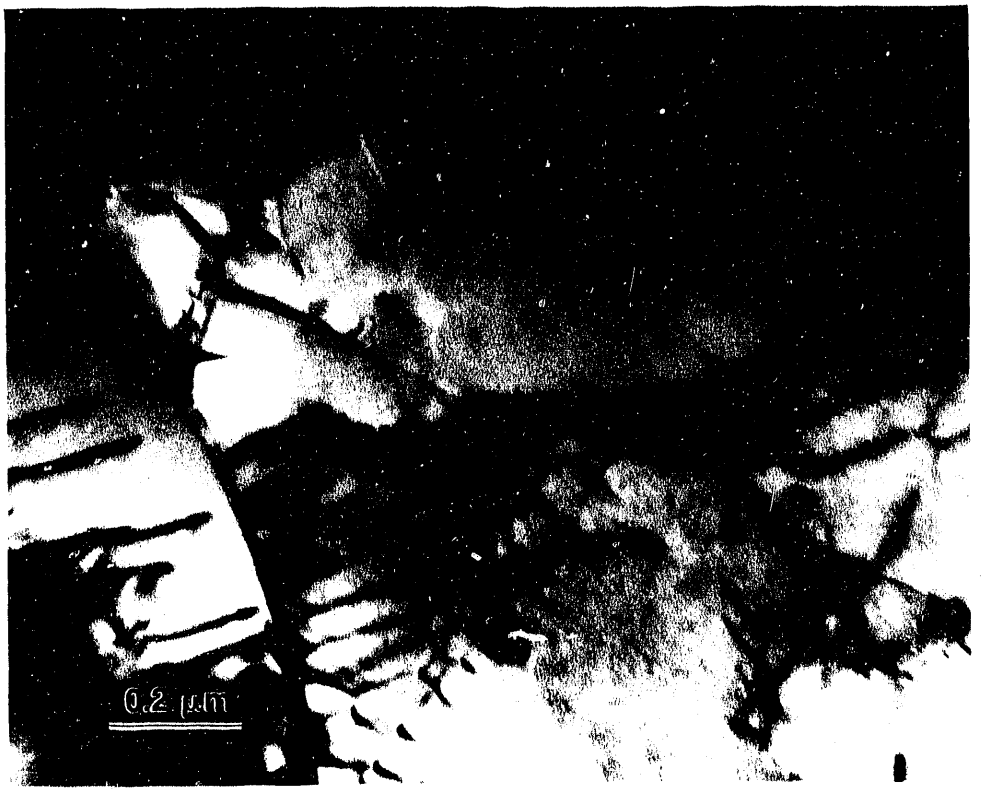

Fig. 3 - TEM micrograph showing low angle boundaries indicating recovery of 5% Cr Fe_3Al alloy sample during compression testing where wavy flow was observed.

Dynamic strain aging in substitutional solid solutions generally produces sharp, jerky serrations in the flow curve which usually occur only after some amount of smooth plastic flow.[14,15] The flow curves of both alloys tested at 300°C show sharp serrations, although serrations observed in the 500-900°C range are smooth, and in all cases serrations begin immediately upon yielding. Mulford and Kocks[14] have developed a theory requiring a negative strain rate sensitivity for the onset of jerky flow resulting from dynamic strain aging. Strain rate sensitivity experiments on the Cr alloyed Fe_3Al material, reported below, have shown that the strain rate sensitivity is positive in the temperature range of 500-900°C and for strain rates where wavy flow is observed. It should be noted that there are some questions of the validity of the assumptions used in deriving this theory and the underlying requirement for negative strain rate sensitivity.[16] Other

experiments, such as static aging at temperature during interrupted tensile tests, have yielded ambiguous results. Despite these discrepancies with previously observed behavior, the experimental results available to date indicate that the wavy flow in this study is probably the result of dynamic strain aging rather than dynamic recrystallization. These results were recently presented for discussion at the International Conference on High Temperature Aluminides and Intermetallics in San Diego, and it was suggested that oxygen from powder metallurgy processing may be a source of dislocation pinning.[17]

Strain Rate Sensitivity

The strength and ductility data for elevated temperatures suggest that the iron aluminides may exhibit superplastic behavior;[11] however, experiments described below indicate that this is not the case. The strain rate sensitivity indexes of both alloys, determined at temperatures from 500 to 900°C using strain rate jump tests, indicated maximum values generally less than about 0.2 for either alloy. The strain rate sensitivity of the 2% Cr alloy measured from continuous tests at 700°C with different strain rates ranged from 0.15 to 0.21, which agrees well with the 0.14 to 0.22 range measured from the jump test at that test temperature. It is usually found that a strain rate sensitivity of 0.5 is indicative of deformation by grain boundary sliding and is the minimum value for obtaining superplastic behavior. The other condition for true superplastic behavior is a fine (<10 μm) stable grain size. The iron aluminide materials in this study had a somewhat larger grain size of about 15 μm. In a separate study strain rate jump testing of combustion synthesized Fe_3Al with 5% Cr and an average grain size of about 3 μm[18] also produced strain rate sensitivity values less than 0.2. Thus the strain rate sensitivity results indicate that superplasticity is not likely for the single phase materials tested here. However, other researchers have reported superplastic deformation in a two phase 73Fe-25Al-2Nb alloy with a grain size of 5 μm.[19]

SUMMARY

Material has been processed with various amounts of stored work to determine the effect of dislocation density on room temperature mechanical properties of FA-129. The substructures have been characterized using TEM. Grain growth, recrystallization, recovery, and ordering studies have also been initiated for alloy FA-129. Wavy flow curves were observed for certain combinations of strain rate and test temperature for 2 and 5% Cr alloys tested in both tension and compression. The origin of this behavior is thought to be dynamic strain aging. Despite high elevated temperature ductilities, the maximum strain rate sensitivity values measured by either continuous or strain rate jump tests were about 0.2, even in very fine grained single phase material, indicating these alloys are not superplastic.

ACKNOWLEDGMENTS

The authors gratefully acknowledge the assistance of M. D. Harper, G. L. Fletcher, A. W. Erickson, V. L. Smith-Wackerle.

REFERENCES

1. M. Johnson, D. E. Mikkola, P. A. March, and R. N. Wright, "The Resistance of Nickel and Iron Aluminides to Cavitation Erosion and Abrasive Wear," Wear, 140, 1990, p. 279.

2. C. G. McKamey, J. A. Horton, and C. T. Liu, "Effect of Chromium on Properties of Fe_3Al," J. Mater. Res., 4, 1989, p. 1156.

3. R. S. Diehm, M. P. Kemppainen, and D. E. Mikkola, "Processing and Alloying of Modified Iron Aluminides," Mater. & Manufacturing Processes, 4, 1989, p. 61.

4. R. T. Fortnum and D. E. Mikkola, "Effects of Molybdenum, Titanium and Silicon Additions on the $DO_3 \rightleftharpoons B2$ Transition Temperature for Alloys near Fe_3Al," Mater. Sci. Eng., 91, 1987, p. 223.

5. R. S. Diehm and D. E. Mikkola, "Effects of Mo and Ti Additions on the High Temperature Compressive Properties of Iron Aluminides Near Fe_3Al," Mater. Res. Soc. Symp. Proc., 81, 1987, p. 329.

6 V. K. Sikka, C. G. McKamey, C. R. Howell, and R. H. Baldwin, "Fabrication and Mechanical Properties of Fe_3Al-Based Iron Aluminides", ORNL/TM-11465, 1990.

7. L. Anthony and B. Fultz, "Kinetic Paths of B2 and DO_3 Order Parameters: Experiment," J. Mater. Res., 4, 1989, p. 1140.

8. K. Oki, M. Hasaka and T. Eguchi, "Kinetics of Ordering in Fe-Al Alloys," Trans. JIM, 15, 1974, p. 143.

9. J. E. Krzanowski and S. M. Allen, "The Migration Kinetics of Antiphase Boundaries Wetted by a Second Phase," Acta Met., 31, 1983, p. 213.

10. J. R. Knibloe, R. N. Wright, C. L. Trybus, and V. K. Sikka, "Microstructure and Mechanical Properties of Fe_3Al Alloys with Chromium", submitted to J. Mater. Sci.

11. J. R. Knibloe, R. N. Wright, V. K. Sikka, R. H. Baldwin, and C. R. Howell, "Elevated Temperature Behavior of Fe_3Al with Cr Additions", accepted for publication by Mater. Sci. Eng.

12. I. Baker and D. J. Gaydosh, "Dynamic Recrystallization and Grain Boundary Migration in B2 FeAl", Metallography, 20, 1987, p. 347.

13. T. Sakai and J. J. Jonas, "Dynamic Recrystallization: Mechanical and Microstructural Considerations", Acta Metall., 32, 1984, p. 189.

14. R. A. Mulford and U. F. Kocks, "New Observations on the Mechanism of Dynamic Strain Aging and of Jerky Flow", Acta Metall., 27, 1979, p. 1125.

15. H. Fujita and T. Tabata, "Discontinuous Deformation in Al-Mg Alloys Under Various Conditions", Acta Metall., 25, 1977, p. 793.

16. C. Y. Li, personal communication.

17. C. T. Lui, personal communication.

18. B. H. Rabin and R. N. Wright, "Microstructure and Mechanical Properties of Fe_3Al Produced by SHS/HIP", in press Metall. Trans. A.

19. S. Ranganath, A. Dutta and J. Subrahmanyam, "On the Flow Behavior of Combustion Synthesized Fe-Al-Nb System", Scripta Metall., 25, 1991, p. 1593.

ORNL-2(B)-INVESTIGATION OF AUSTENITIC ALLOYS FOR ADVANCED HEAT RECOVERY AND HOT-GAS CLEANUP SYSTEMS*

R. W. Swindeman

Metals and Ceramics Division
Oak Ridge National Laboratory
Oak Ridge, Tennessee 37831

INTRODUCTION

The purpose of this activity is to evaluate austenitic alloys for the design, construction, and reliable operation of advanced steam cycle power plants, combined cycle power plants, and hot-gas cleanup systems for pressurized fluidized bed combustors and gasifiers. Depending upon the particulars, the performance requirements for structural materials vary significantly from one application to the next. Sometimes strength and fabricability are important. Other times corrosion resistance is most important. Advances in materials science relating composition and microstructure of austenitic alloys to their high-temperature mechanical properties, stability, and corrosion resistance have made it attractive to taylor alloys and combinations of alloys to meet specific missions. Applications of interest include superheater and reheater tubing for power boilers,[1] main steam line piping for higher efficiency steam plants,[2] very high temperature and pressure steam lines for topping cycles,[3] and materials of construction for hot-gas cleanup systems.[4] Under consideration are both new and old alloys. Research includes joining methods, high-temperature design methodology, and life prediction methods.[5] These are subjects of great concern in all applications. The investigations cover four categories of materials: lean stainless steels containing less than 20% chromium (which possess good strength), higher

* Research sponsored by the U.S. Department of Energy, Fossil Energy Advanced Research and Technology Development (AR&TD) Materials Program, DOE/FE AA 15 10 10 0, Work Breakdown Structure Element ORNL-2(B), DE-AC05-84OR21400 with Martin Marietta Energy Systems, Inc.

chromium iron base alloys (which possess good corrosion resistance), high chromium nickel base alloys (cladding alloys), and aluminum-bearing alloys (which possess excellent corrosion resistance).[5]

Lean Stainless Steels

To meet the requirements for tubing in an advanced boiler superheater, it was expected that a candidate alloy should possess nearly twice the creep strength of the best of the commercial 300 series austenitic stainless steels.[5] Steels meeting this criterion usually contain MC-forming elements such as titanium, niobium, and vanadium. Often nitrogen is added, as well. Several of these commercial, near-commercial, and developmental alloys were evaluated over a six year period; and the findings were reported in 1990. [6]

Most of the research on the lean stainless steels for superheater tubing has been completed. A few long-time tests remain in progress, and times have exceeded 50,000 h at 700°C. The steels continue to show excellent strength and ductility.

One limitation of the HT-UPS steels developed by Maziasz[7] was the need to cold or warm work the alloys in order to promote the strengthening mechanisms. This treatment also raised the yield strength so that advantage could be taken of the creep strength in setting design stresses for service below 650°C. An alternate method to increase the yield strength involves nitrogen additions,[6] hence the long time strength and ductility of nitrogen containing alloys is of interest. To this end, additional studies were undertaken in this reporting period to examine nitrogen-strengthened type 316 stainless steel.

Main steam line piping was obtained from the A. M. Williams plant . The material was type 316N stainless steel that had been in service for 96,000 h at 540°C. Stress-rupture testing was undertaken to examine strength and ductility. In Fig. 1(*a*), the rupture strength of the type 316N stainless steel base metal has been compared to type 316 stainless steel on the basis of the Larson Miller time-temperature parameter. Trends indicate that the type 316N stainless steel provide a strength advantage greater than 25% above steel not strengthened by nitrogen. Ductility of the type 316N stainless steel was excellent, as shown in Fig. 1(*b*). Values for elongation exceeded 20% and the reduction of area values exceeded 30%. The piping was removed from service because cracks were observed in

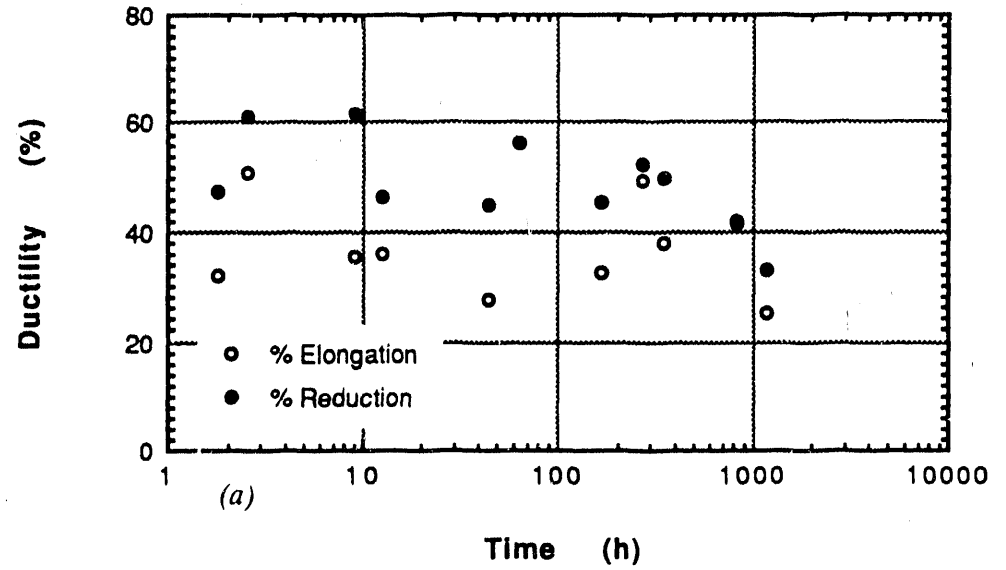

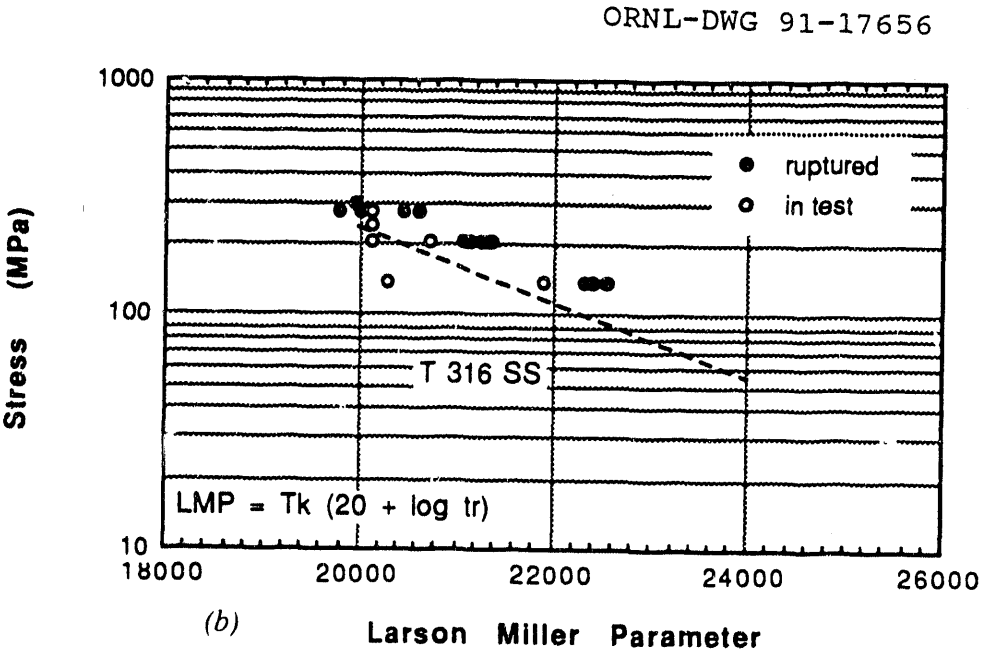

Fig. 1. Stress rupture data for type 316N stainless steel taken from a steam plant after 96,000 h at 540°C: (*a*) comparison of the rupture strength with the trend for type 316 stainless steel on the basis of the Larson-Miller time-temperature parameter; (*b*) ductility versus time of rupture.

welds. These were thought to arise from hot cracks produced in the original field welds. Some additional work is being performed to examine the use of the controlled resisidual element CRE 16-8-2 stainless steel filler metal for joining the type 316N stainless steel. evaluations are now in progress.

Testing of Weldments

The high-strength austenitic stainless steels have potential problems with regard to the performance of weldments in long-time, high-temperature service. Alloys that are balanced toward ferrite tend to have low-creep strength and embrittle due to sigma formation. Base metals and filler metals that are balanced toward austenite have good strength but are susceptible to hot-cracking.[8] Problems with alloys balanced toward austenite can be mitigated by reducing phosphorous and sulfur in the base metal and selecting the proper filler metal. Typical filler metals that have been examined in connection with the advanced austenitic alloys included Inconel 82®, 17-14 CuMo stainless steel, CRE 16-8-2 stainless steel, and Haynes alloy 556®. Performance of weldments to 10,000 h was reported previously.[6] Testing has been continued and times are approaching 20,000 h. The alloy 556 continues to offer the best strength at long times and high temperatures. No ruptures have been produced in this reporting period, so additional information on failure locations is not available.

Evaluation of Modified Alloy 800H

The high-chromium austenitic iron-base alloys are those that contain 20 to 30% chromium, and 20 to 35% nickel. Examples are type 310 stainless steel and alloy 800H. There are many modifications to the alloys, and new alloys of particular interest to the advanced austenitic alloy evaluation activity include Sumitomo HR3C®, which is a modified type 310 stainless steel,[9] and Nippon Steel NF709®, which is a modified 20Cr-25Ni steel.[10] In addition, modifications of alloy 800H were undertaken by Maziasz,[3] and this alloy has been produced as plate and tubing. An evaluation of the potential of these alloys for advanced steam service was completed in 1991 (ref. 11). Since then, interest in

the alloys for combined cycle applications at higher temperatures has developed, and the testing program on the materials has been expanded.

Much of the current research at Oak Ridge National Laboratory (ORNL) has focused on the modified alloy 800H tubing produced by Babcock & Wilcox Company.[12] Material that was initially examined had been cold finished and solution treated at a relatively low temperature (less than 1150°C). A new batch of tubing was received that had been solution treated at 1190°C and cold pilgered. Initial results indicated that the new fabrication route produced a material has twice the strength of alloy 800H at temperatures to 760°C. Testing times are relatively short, however, and the long time stability of the microstructure is an issue that has yet to be resolved.

Evaluation of weldments in modified alloy 800H continued. Again, alloy 556 has been used as a filler metal, and welds have been produced at ORNL and at the University of Tennessee. Times for in stress-rupture testing of transverse weldment specimens have exceeded 5,000 h for temperatures in the range 600 to 700°C. Included were samples that had been solution treated at 1200°C and welded either before or after cold working. In Fig. 2, the rupture data on transverse (cross) weldment specimens have been compared to

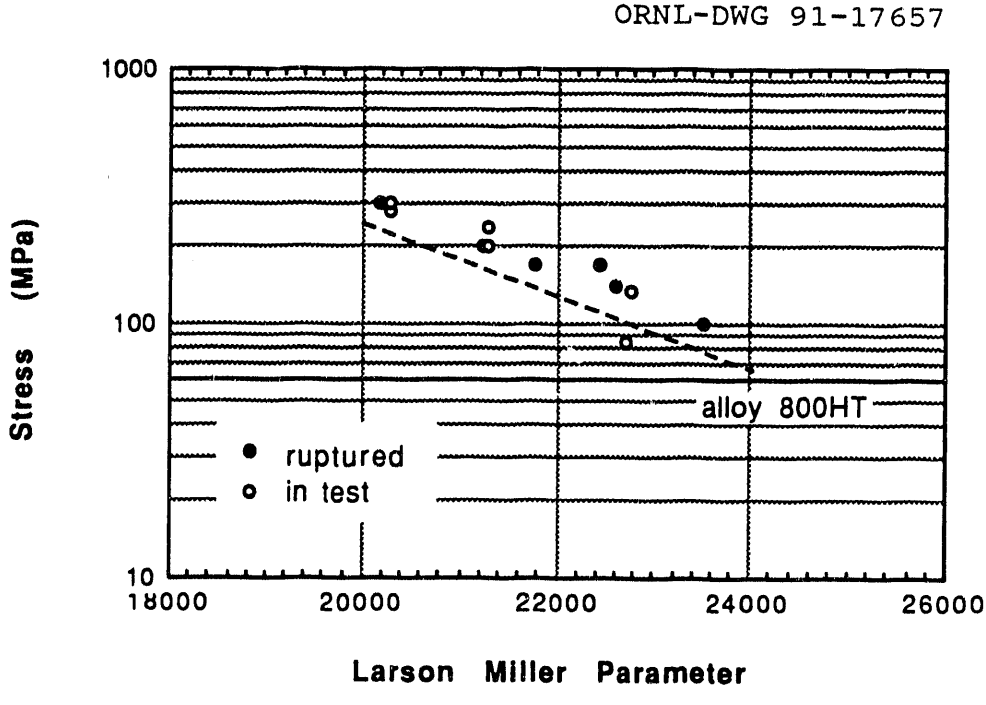

Fig. 2. Comparison of the rupture strength of transverse (cross) weldments of modified alloy 800H with the trend for alloy 800HT on the basis of the Larson Miller time-temperature parameter.

alloy 800HT on the basis of the Larson Miller time-temperature parameter. Trends suggest that the strength of weldments in the modified alloy 800 is approximately 25% greater than alloy 800HT base metal. In contrast to the lean stainless steels, which rupture in the alloy 556 filler metal, the modified alloy 800 weldments fail in the base metal of heat affect zone at short times. Long time testing is still in progress.

Several experimental modified alloy 800H heats were produced to evaluate the influence of minor element additions on oxidation resistance and weldability. A lower propensity for hot cracking was observed for these heats, while cyclic oxidation tests to 1000°C indicated that some heats were equivalent to standard alloy 800H.

Alloys for Hot-Gas Cleanup Applications

Hot-gas cleanup systems are being developed for pressurized fluidized bed combustors (PFBC). One cleanup concept involved the use of ceramic barrier filters that operate at temperatures in the range 800 to 900°C (ref. 4). Metallic materials will be used to support the filters and fabricate the blowback manifold systems that are required for filter cleaning. Although the gaseous environment is oxidizing, a potential for some sulfidation exists if sulfur-bearing particulates collect on metallic components in the dirty gas side of the cleanup vessel. High oxidation resistance, fabricability, and good thermal fatigue resistance are of primary concern in the selection of the structural components, and several alloys are being investigated to establish the potential for eventual use. Alloys of interest include RA333®, Haynes alloy 556®, Inconel 617®, HR160®, and the nickel-chromium-aluminides IC221 and IC396M. Research is being directed at producing the data needed for high-temperature component design, rather than optimization of chemistry or fabrication processes, and work underway includes creep-fatigue, thermal-mechanical fatigue, and the development of parameters needed in design evaluations.

Examination has been completed of RA333 and Haynes alloy 556 for use in the Tidd hot-gas clean vessel, and results have been reported elsewhere.[13,14] The nickel-chromium-aluminides offer an advantage over these two alloys for service under conditions of low primary stress and high-transient loadings because they possess high yield strengths and relatively poor creep strengths. This combination reduces the likelihood of plastic strains during transients and the rapid relaxation of any residual stresses that would produce creep

damage during steady-state operations. Research was undertaken on an electroslag casting of alloy IC396M. Most tensile, creep, and relaxation testing was completed, and a few fatigue tests and creep-fatigue tests have been undertaken on the material.

Summary

Long-time testing of HT-UPS austenitic stainless steel continued to indicate excellent strength and ductility in this type of steel.

Stress-rupture testing of transverse (cross) weldments in the HT-UPS steel joined with type 16-8-2 CRE and alloy 556 filler metals has extended to beyond 10,000 h. Both filler metals show good strength and ductility.

Creep-rupture testing of modified alloy 800H tubing in the cold-pilgered condition indicated excellent strength relative to alloy 800HT.

REFERENCES

1. P. L Rittenhouse, et al., *Assessment of Materials Needs for Advanced Steam Cycle Coal Fired Plants*, ORNL-6274, 1985.

2. S. Kjaer, "Elsam 400 MW Coal-Fired USC-Power Plant Investigation," paper presented at the *Third International Conference on Improved Coal-Fired Power Plants (ICPP)*, San Francisco, April 2-4, 1991.

3. P. E. Duffy and C. Knox, "Topping Systems for Repowering Coal Fueled Plants," paper presented at the *Third International Conference on Improved Coal-Fired Power Plants (ICPP)*, San Francisco, April 2-4, 1991.

4. Lippert, T. E., et al., *Performance Evaluation of a Ceramic Cross-Flow Filter on a Bench-Scale Coal Gasifier*, DOE/MC/21338-2749, Vol. 1 and 2, U.S. Department of Energy, Morgantown Energy Technology Center, Morgantown, W. Va. (September 1989).

5. R. W. Swindeman et al., *Alloy Design Criteria and Evaluation Methods for Advanced Austenitic Alloys in Steam Service*, ORNL-6274, May 1986.

6. R. W. Swindeman et al., *Evaluation of Advanced Austenitic Alloys Relative to Alloy Design Criteria for Steam Service- Part 1- Lean Stainless Steels*, ORNL-6629, May 1990.

7. P. J. Maziasz, "Developing an Austenitic Stainless Steel for Improved Performance in Fossil Power Facilities," *J. Met.* **41**, 14-20 (1989).

8. C. D. Lundin et al., *The Hot Ductility and Hot Cracking Behavior of Modified 316 Stainless Steels Designed for High Temperature Service*, University of Tennessee Report No. ORNL/Sub/88-07685/01 (1989).

9. Y. Sawaragi, H. Teranishi, K. and Yoshikawa, "The Development of Newly Steel with High Elevated Temperature Strength and High Corrosion Resistance for Boiler," pp. 238-44 in the *Proceedings, International Conference on Creep*, Japan Society of Mechanical Engineers, Tokyo, Japan, 1988.

10. T. Takahashi et al., "Development of a High Strength 25Ni-20Cr Steel for Tubes in Ultra Supercritical Power Boilers," paper 41-1 in *Second International Conference on Improved Coal Fired Power Plants*, EPRI publication GS-6422, 1989.

11. R. W. Swindeman et al., *Evaluation of Advanced Austenitic Alloys Relative to Alloy Design Criteria for Steam Service- Part 2 - 20 to 30% Chromium Alloys*, ORNL-6629 (May 1990).

12. M. Topolski, *Evaluation of the Fabricability of Advanced Austenitic Tubing*, Final Report CRD #1207, RDD:91:4500-01-01:01, Babcock & Wilcox Alliance Research Center, Alliance, Ohio, March 1991.

ORNL-2(F) - DEVELOPMENT OF IRON ALUMINIDES

C. G. McKamey, V. K. Sikka, T. Zacharia, and D. J. Alexander

Oak Ridge National Laboratory
P. O. Box 2008
Oak Ridge, TN 37831-6115

INTRODUCTION

Iron aluminides based on Fe_3Al have excellent oxidation and corrosion resistance.[1] However, until recently their potential use as structural material has been hindered by low room temperature ductility (<5%) and a drop in strength above 600°C.[2] Recent studies indicate that the poor ambient-temperature ductility observed in many aluminides is often caused by dynamic hydrogen embrittlement resulting from the dissociation of water molecules in the environment by aluminum atoms on the surface of the alloy.[3-6] This environmental embrittlement can be minimized through modification of alloy chemistry, microstructure, and surface condition.[5-8] Development efforts at this laboratory have indicated that by controlling alloy chemistry and thermomechanical processing, Fe_3Al-based alloys can achieve ambient temperature tensile ductilities of 10-20% and tensile yield strengths of as high as 500 MPa.[7,9]

Fe_3Al has been known for some time to have very poor creep resistance.[2] Preliminary studies of Fe_3Al-based ternary alloys have shown that additions of molybdenum or niobium result in improved creep rupture properties. At 593°C (1100°F) and 207 MPa (30 ksi), the binary lasted only 2-5 h, while the niobium-containing ternary alloy lasted over 300 h.[10] Although niobium and, to a lesser extent, molybdenum greatly improve the creep rupture resistance as ternary additives,[10,11] they do not necessarily provide room temperature ductility. With additions of other elements whose primary effect is to produce room-temperature ductility, synergistic effects become important. One purpose of the present phase of our alloy development program is to study such synergistic effects and separate the positive from negative synergisms, so that Fe_3Al-based alloys can be produced with improved creep rupture resistance to temperatures of 650-700°C, adequate room temperature tensile ductility (>10%), and still be weldable, fabricable, and maintain their excellent corrosion resistance.

Welding is a major area of concern for realizing the potential benefits of the unique properties of iron aluminides. The welding processes used must be capable of producing high

quality weldments under field and shop conditions which are free of defects and have good mechanical properties in comparison to the base metal. Initial work on the weldability of intermetallic alloys has identified some potential problems associated with these alloys.[12-14] These include a propensity for hot-cracking, a propensity for cold-cracking, and a possible degradation of the mechanical properties of the weldment in comparison to the base metal. The preliminary results of weldability studies of FA-129 indicate that this alloy may be welded by optimizing the welding process and parameters. However, those studies have also shown that iron aluminides are very sensitive to minor changes in composition of the base metal.[15]

Three categories of Fe_3Al alloys are under investigation at Oak Ridge National Laboratory (ORNL). The first composition has been optimized for sulfidation resistance and is designated as FAS. The second has been designed for maximum room temperature tensile ductility and is designated as FAL. The third is being designed for a combination of tensile ductility and high-temperature strength and is designated as FA-129. Its final designation will be FAH. Nominal compositions of these three alloys are given in Table I. Initially, mechanical property data was generated on experimental-size heats ranging from 0.5 to 7 kg.[7,16,17] The commercial melting, fabrication, and properties of 80- and 100-kg heats were described during the last reporting period.[18]

This report presents the current status of microalloying studies to produce an alloy with improved creep resistance and weldability, analytical electron microscopy to identify precipitates and correlate precipitate compositions with properties, weldability of recently-produced microalloyed alloys, and weldability of thick sections (0.5 in.) of FA-129 alloy. The commercial melting and properties of 2000- and 3000-kg heats of alloy FA-129 are also described.

Table I. Compositions of Ductile Fe_3Al-Based Alloys

Element	Alloy (wt%)		
	FAS[a]	FAL[b]	FA-129[c]
Al	15.9	15.9	15.9
Cr	2.2	5.5	5.5
B	0.01	0.01	--
Zr	--	0.15	--
Nb	--	--	1.0
C	--	--	0.05
Fe	Balance	Balance	Balance

[a]Maximum sulfidation resistance.
[b]Maximum room-temperature tensile ductility.
[c]High-temperature tensile strength with good room-temperature ductility.

DISCUSSION OF CURRENT ACTIVITIES

Alloy Development for Improved Creep Resistance

In terms of alloy development, this reporting period has been devoted to producing compositions which have an acceptable combination of several properties including tensile strength and ductility (both at room temperature and 600° C), creep-rupture resistance, and weldability. Alloy FA-129, which is currently being scaled-up to commercial-size castings for extensive study (see below), has good tensile properties at temperatures to approximately 650° C, with a room temperature ductility of 15-20%. It also has been shown that it can be welded using controlled pre- and post-weld heat treatments.[15] However, it has inadequate creep-rupture resistance (20-30 h life at 593° C and 207 MPa).[19] On the other hand, alloy FA-97 has very good creep-rupture resistance (400-500 h life at 593° C and 207 MPa),[19] but poor room temperature tensile ductility and poor weldability (see below). Several alloys with compositions which are compromises between these two alloys were therefore produced and tested during this reporting period in an effort to produce one alloy with an acceptable combination of properties.

The alloys were prepared by arc-melting and drop casting into chilled copper molds. Hot rolling to 0.76-mm-thick sheet was accomplished at either 1000-600° C or 1000-850° C, depending on composition. Flat tensile specimens (0.76 × 3.18 × 12.7 mm) were mechanically punched from the hot rolled sheet and were used for both tensile and creep-rupture tests. All heat treatments were performed in air, with quenching by either air or oil. For comparison between alloy compositions, tensile tests were performed at room temperature (RT) in air at a strain rate of 3.3×10^{-3}/s and creep rupture tests were performed in air at 593° C and 207 MPa.

Table II shows the compositions of alloys FA-97, -129 and several alloys produced during this reporting period. Table III compares their tensile and creep properties. Our studies in the past have suggested that a certain ratio of molybdenum, niobium, and zirconium is needed for creep resistance, but too much of any one can harden the alloy and lower the room temperature tensile ductility. Also, while carbon is detrimental to creep resistance, a certain level of carbon is desirable to promote weldability.[20] On the other hand, too much zirconium or boron results in reduced weldability. The properties of the new alloys (Table III) indicate that (1) levels of 0.03-0.05 at.% C are acceptable for both creep

Table II. Compositions of Iron Aluminides Under Study

Alloy Designation	Composition (at.%)							
	Al	Cr	Nb	Mo	Zr	C	B	Fe
FA-97	28	2.0	0.5	2.0	0.1		0.2	Bal.
FA-129	28	5.0	0.5			0.2		Bal.
FA-167	28	5.0	0.5	0.25	0.025	0.1	0.005	Bal.
FA-168	28	5.0	0.5	0.8	0.05	0.03	0.005	Bal.
FA-169	28	5.0	0.5	0.25	0.025	0.05		Bal.
FA-170	28	5.0	0.5	0.4	0.025	0.05		Bal.

Table III. Properties of Fe_3Al Alloys

Alloy	RT Tensile[a,b]			Creep rupture			Weldable?
	Yield (MPa)	Ultimate (MPa)	Elong. (%)	Life (h)	Elong. (%)	MCR (%/h)	
FA-129	384	930	16.9	22[c]	75	0.95	Y
FA-97	>690		<5.0	463[c]	47	0.04	N
FA-167	505(509)	723(822)	5.4(8.6)	84[a]	47	0.3	Y
FA-168	635(686)	744(773)	2.5(4.9)	391[a]	65	0.06	N
FA-169	(502)	(803)	(8.7)	40[d,a]	36	0.6	Y
FA-170	(474)	(680)	(5.5)	281[d,a]	32	0.04	Y

[a]Heat treated 1h/750°C air cooled.
[b]Values in parentheses were produced using grips designed to hold the specimen under the shoulders, not in the pinholes.
[c]Heat treated 1h/850°C+3-7d/500°C; tested at 593°C and 207 MPa.
[d]Hot rolled at 850°C; starting microstructure consisted of large recrystallized grains.

resistance and weldability, (2) boron is not necessary for creep resistance and may not be needed for ductility, but in any case, to promote weldability, should be kept at 0.005% or less, (3) for weldability, the zirconium level should be kept below 0.05 at.%, and (4) the molybdenum level needs to be near 0.4% for creep resistance. It is anticipated that, with optimization of fabrication techniques, alloys FA-169 and -170 will exhibit room temperature tensile ductilities of approximately 10%. These studies are promising and indicate that development of an alloy that will have a good combination of tensile and creep properties and weldability, as well as adequate corrosion resistance, may be possible in the near future.

Creep Mechanisms in Fe_3Al-Based Alloys

Along with efforts to improve creep resistance in Fe_3Al-based alloys through alloying, an effort has been underway to identify creep mechanisms in binary Fe_3Al and to determine how creep mechanisms are affected by alloying additions. Details of those studies can be found in the recent literature.[19,21,22] During this reporting period analytical electron microscopy (AEM) techniques [including x-ray energy dispersive spectroscopy (XEDS), selected-area diffraction (SAD), and convergent-beam electron diffraction (CBED)] were used to identify precipitates in Fe_3Al alloyed with 2% Mo or 1% Nb. AEM analysis of the precipitates in Fe_3Al+2%Mo extracted on a carbon replica film showed that they were Mo-rich (>95 at.% Mo) and had the hexagonal crystal structure characteristic of Mo_2C phase (Fig. 1).[21,22] The niobium-containing ternary alloy contained coarse and fine precipitates in the matrix and at grain boundaries which were identified as Nb- and/or Zr-

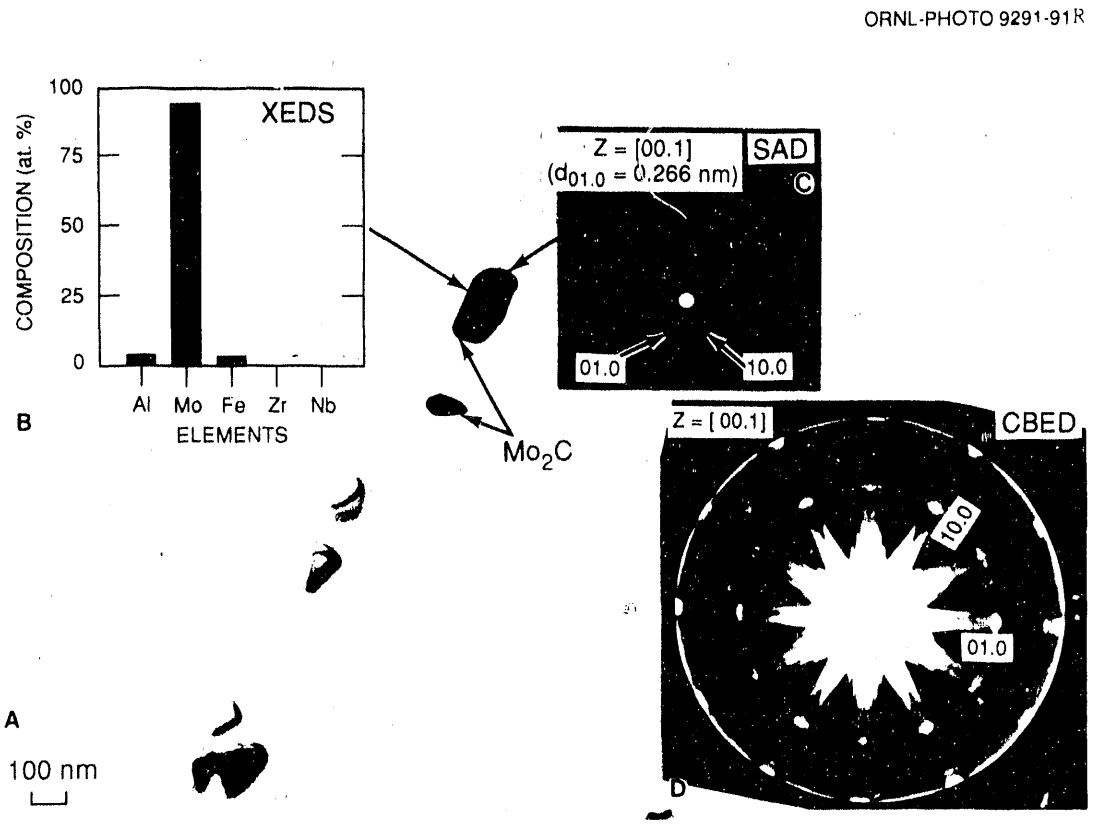

Fig. 1. AEM (a) of grain boundary precipitates in Fe_3Al+2Mo alloy creep tested at 650°C and 276 MPa. XEDS (b), SAD (c), and CBED (d) shows the precipitates are the hexagonal Mo_2C phase.

rich carbides.[21,22] The presence of zirconium in this alloy was not intentional, and was assumed to have been introduced during melting and casting. Many small (50-90 nm in size) Zr-rich MC particles (>70 at.% Zr) were dispersed uniformly throughout the matrix and were associated with dislocations (Fig. 2). Most likely the small matrix and grain boundary precipitates contributed to the low creep rate and high creep-rupture resistance observed in this specimen (300 h life at 650°C and 138 MPa compared to 0.6 h for Fe_3Al and 50 h for Fe_3Al+2Mo).

Weldability of Alloy FA-129

Initial work on the weldability of FA-129 based iron aluminides have shown that these alloys may be welded by controlling the welding process and parameters.[15] Crack-free welds were produced by preheating the base metal to 200°C and postweld heat treating at 700°C for one hour. Pre- and postweld-heat treating, in general, lowers the amount of

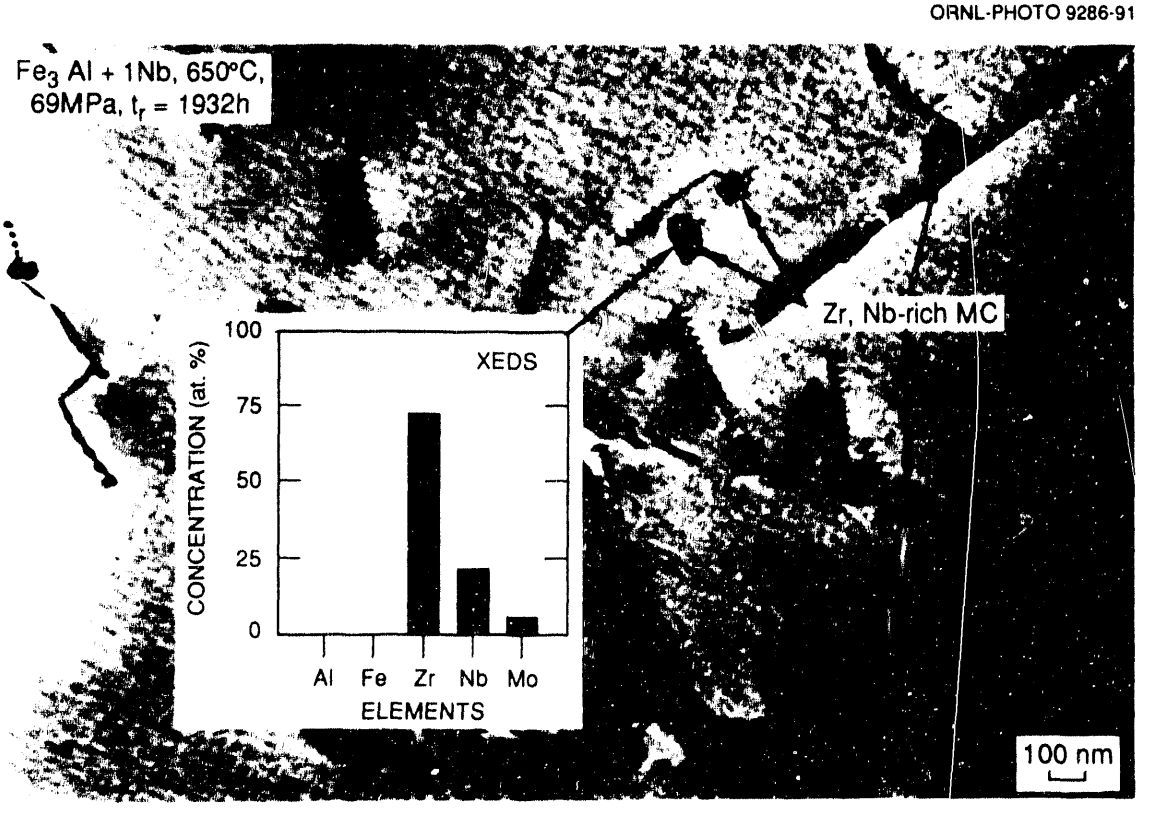

Fig. 2. TEM microstructure of a Fe_3Al+1Nb alloy creep tested at 650°C and 69 MPa showing pinning of dislocations by Zr-rich MC precipitates. XEDS shows presence of both Zr and Nb.

thermal stresses. In addition the slower cooling rate may provide an opportunity for any hydrogen that may be present in the weld metal to diffuse out without causing cracking. Following this, a systematic study was undertaken to evaluate the optimum pre- and postweld-heat treatment conditions. The results of the study indicate that successful welds can be made on laboratory specimens with a minimum preheat of 100°C and a postweld heat treatment of 400°C for one hour.

For the first time, welds have been made on 12.6 mm (0.5 in.) thick FA-129 material. The scaled-up alloy was obtained in the form of 6.3 mm (0.25 in.) and 12.6 mm (0.5 in.) plates. Welds were made on the plates using matching FA-129 filler metal deposited in a 90° included-angle V-groove with a 1.6 mm root opening. The welds were made using alternating current with argon shielding and backing gas. The filler wire was heat treated for 2 h at 300°C and the specimens were degreased and cleaned thoroughly prior to welding. The techniques developed for the 6.3 mm (0.25 in.) plates, including pre- and postweld-heat treatments, were successfully used to produce crack free welds in the thicker sections. Figure 3 shows the transverse section of the weld indicating very coarse grain structure in the fusion zone that may have an impact on its toughness.

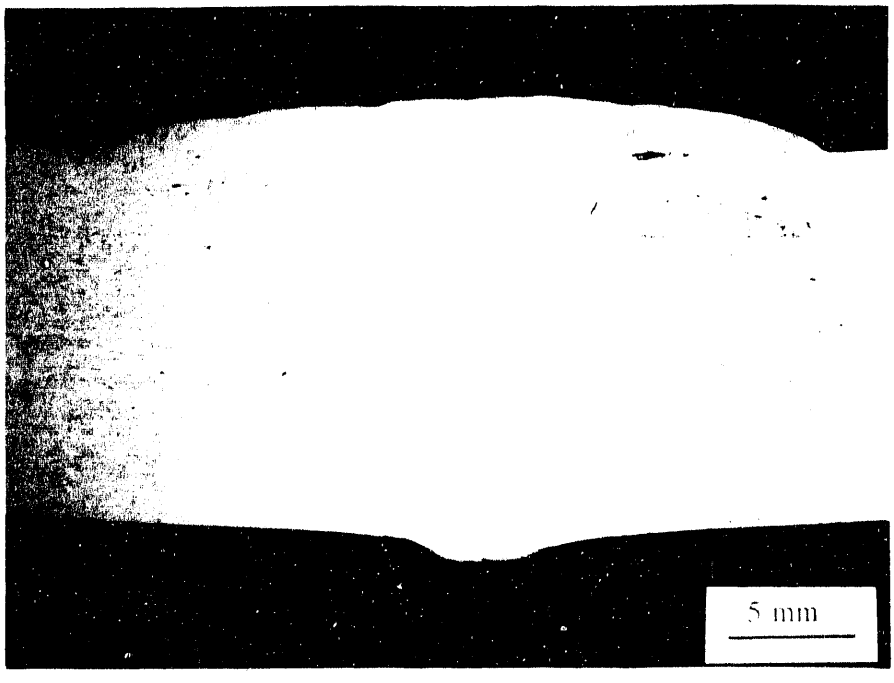

Fig. 3. Transverse section of 12.7-mm (0.5 in.) thick FA-129 plate showing coarse columnar structure in weld fusion zone.

Weldability of Micro-alloyed Iron Aluminides

Preliminary screening tests were performed on several new alloys. The compositions of these alloys are listed in Table II. These alloys were tested for hot-crack susceptibility using the Sigmajig test. The test has been used in the past to identify crack susceptibility of several iron-aluminide alloys including FA-129. The test uses a preapplied transverse stress during autogenous GTA welding of a 50 mm by 50 mm sheet specimen. The applied stress is sequentially increased until the specimen cracks. This test ranks materials based on the threshold stress above which cracking in the fusion zone occurs. The welds were characterized using optical microscopy of specimens etched with a solution containing 40 ml HNO_3, 60 ml CH_3COOH, and 20 ml HCl.

The preliminary results on the Sigmajig threshold cracking stress for the various alloys are presented in Table IV. Based on these results, several of these alloys indicate a potential for good weldability. The results clearly show that the weldability of iron aluminides are sensitive to changes in composition. Alloy FA-97 containing molybdenum and boron, which has excellent creep properties, showed very poor weldability. Although boron has been found to improve fabricability and grain boundary strength of iron aluminides, the results of the welding study suggest that boron is deleterious to weldability. Among alloys FA-167 to -170, all except alloy FA-168 exhibited promise of good weldability, the main difference between the alloys being the higher molybdenum and zirconium content in FA-168. Even though hot-cracking may not be a problem for these alloys, cold cracking remains a potential problem. Figure 4 shows transverse cold cracks in an alloy FA-167 weldment that developed several days after welding. However, it is expected that a combination of pre- and postweld heat treatments can be used to prevent cold cracking in these alloys.

Table IV. Sigmajig Threshold Cracking Stress

Alloy	Stress to cause hot-cracking [MPa(ksi)]
FA-97[a]	<<138(20)
FA-129[b]	=172(25)
FA-167[b]	=138(20)
FA-168[b]	<<138(20)
FA-169[a]	<103(15)
FA-170[a]	>>103(15), <138(20)

[a]Final processing done at 850° C.
[b]Final processing done at 600° C.

Preparation and Fabrication of Commercial-Size Ingots of Fe_3Al-Based Alloys

The commercial melting of 2000- and 3000-kg heats was limited to alloy FA-129 only. The scale-up effort is described below.

Melting

The scaleup of two heats of FA-129 alloy was conducted at Precision Rolled Products (PRP), Reno, Nevada. The first heat weighing 2000-kg was prepared by vacuum-induction melting (VIM) of the raw materials, was cast into a 330-mm-diam round electrode, and subsequently electroslag remelted (ESR) into a 406-mm-diam ingot. The ingot, shown in Fig. 5, was slow cooled after removing from the mold and stress relieved at 750° C for 8 h. The ingot's surface finish was similar to that observed for most commercial iron- and nickel-base alloys. The surface finish was such that the ingot can be processed without the need for any surface treatment.

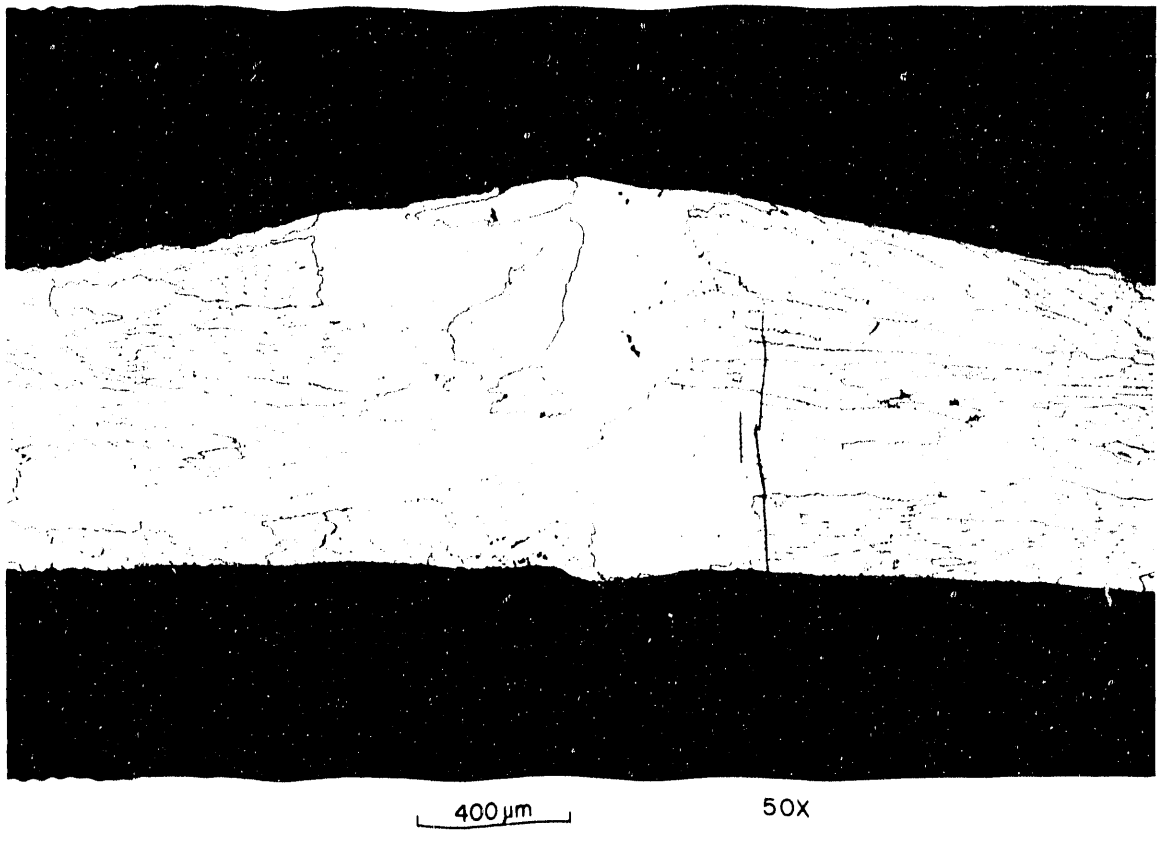

Fig. 4. Transverse section of FA-167 weldment showing delayed cold-cracking.

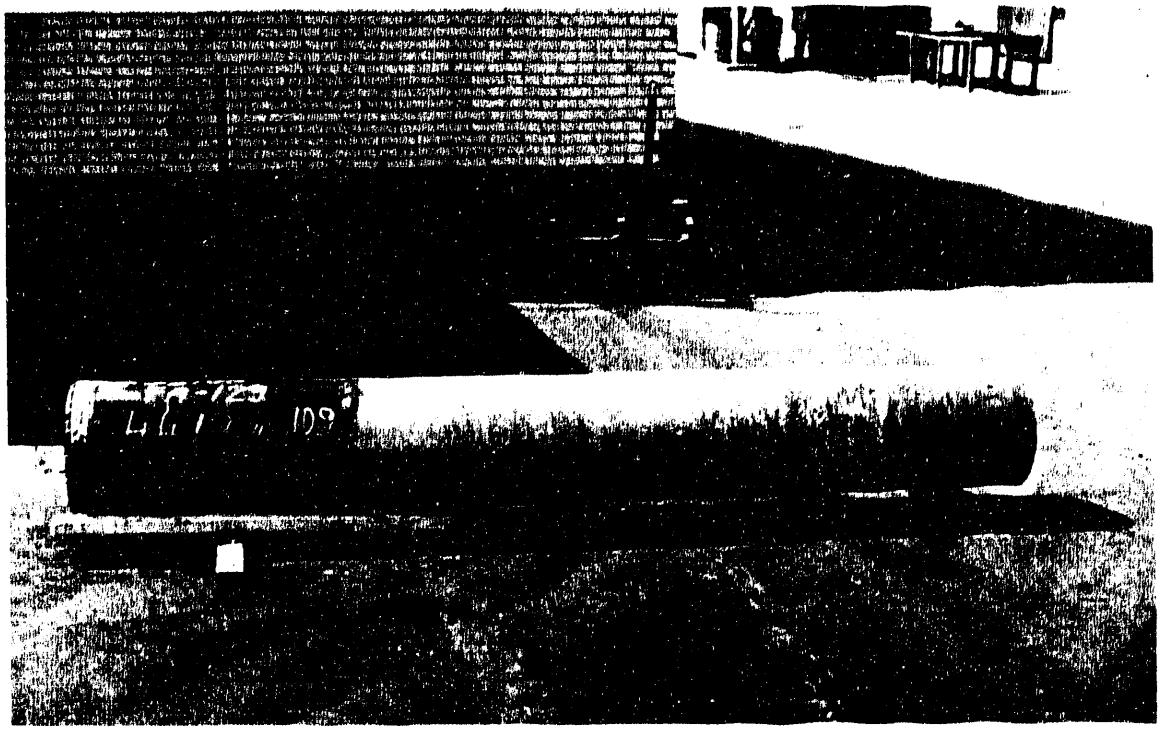

Fig. 5. A 406-mm-diam ingot of alloy FA-129. The alloy was prepared by VIM and ESR at Precision Rolled Products.

The second heat weighing 3000 kg was also processed by VIM. However, this heat was cast into a rectangular slab mold of 203 by 965 mm. The slab was removed from the mold, slow cooled, and stress relieved at 750°C for 8 h. The slab, shown in Fig. 6, will be processed in the as-cast condition. Compared to the ESR ingot, the surface quality of the VIM slab was not as good.

Chemical analysis of the large ingots are compared with the target composition in Table V. Note that the compositions of the large ingots are in good agreement with the target composition. PRP indicated that the melting of iron aluminide was no different than many commercial alloys, and that they would produce the alloy if customer requests were received.

Cutting

Because of its size, the VIM slab ingot has not been sectioned. However, prior to processing, the entire ESR ingot was sectioned to study its macrostructure and processing response. Because of very low ductility in the as-cast condition, ORNL recommended that

the ingot be cut by using a slow-speed band saw rather than a high-speed abrasive wheel, a common industry practice. PRP subcontracted the band-saw cutting to another vendor who found it to be extremely difficult to cut. In spite of the slow-cutting response, two slices were sectioned from near the top of the 406-mm-diam ESR ingot. The sectioned pieces showed evidence of cracks near the center of both slices. The cracking can be either from the solidification process or from the cutting process. Subsequent crack-free cutting of the slices at ORNL suggests that the cracks may be related to the solidification process. The macro- and microstructures of the ingot section are shown in Fig. 7. The macrostructure is very typical of that observed for the commercial alloys, and the microstructure is very similar to that observed for 102-mm-diam ingots of the same alloy (FA-129).[16]

Processing

A 28-mm-thick piece from the slice representing the top of the 406-mm-diam ESR ingot was processed into 0.76-mm-thick sheet. The processing steps, temperatures, and

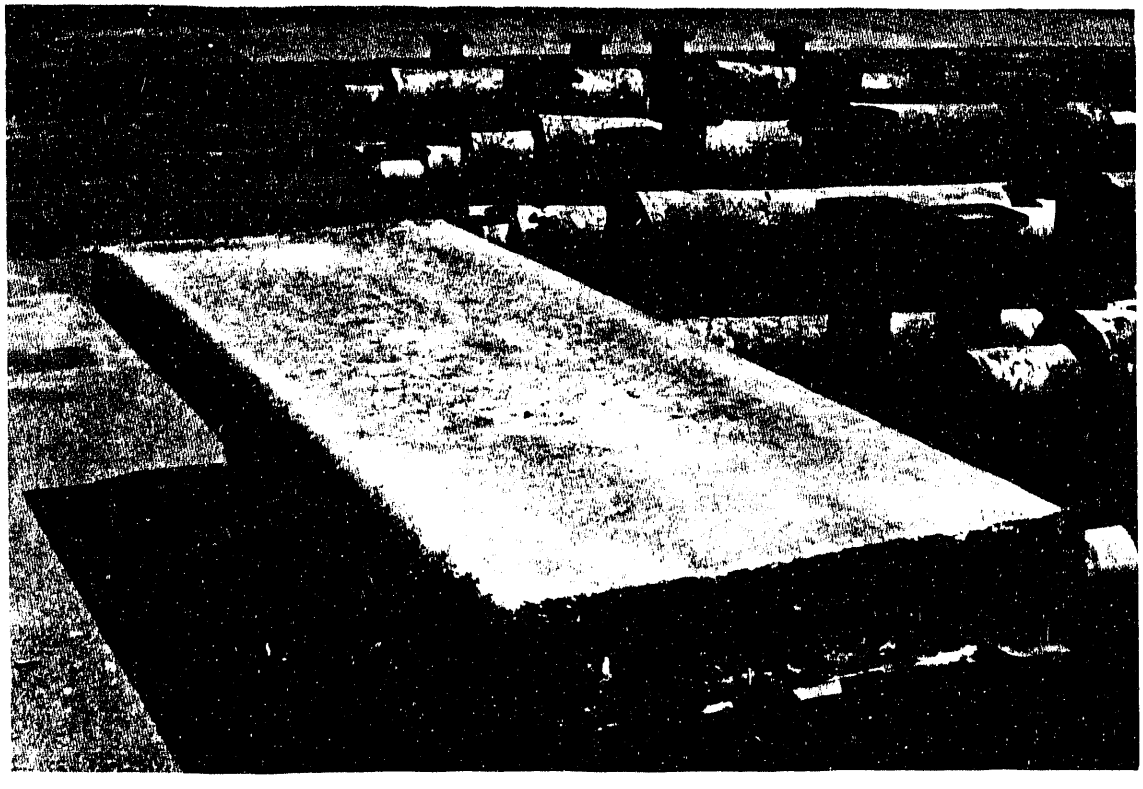

Fig. 6. A 203-mm by 965-mm slab of alloy FA-129 prepared by VIM at Precision Rolled Products. Note that, as opposed to the round ingot, this ingot was not electroslag remelted.

percent reductions are shown schematically in Fig. 8. The forging steps were at 1000° C, followed by rolling steps at 800 and 650° C, respectively. No problems were encountered in the preparation of the sheet. The processing steps used for the section from the 406-mm-diam ingot are the same as used previously for 102-mm-diam ingots.[16]

Mechanical Properties

The 0.76-mm-thick, as-rolled sheet was stress relieved at 700° C for 1 h, followed by oil quenching. The stress-relieved sheet was punched into specimens for tensile and creep testing. In order to remove the work from die punching, all of the specimens were given a final anneal of 700° C followed by oil quenching prior to testing. Optical microstructures of the sheet specimens prior to testing are shown in Fig. 9. Tensile tests on these specimens were conducted in the temperature range of room temperature to 800° C. Data from these tests are compared with similar data on 102-mm-diam ingots in Fig. 10, which shows that the

Table V. Composition of 406-mm-diam ESR Ingot of FA-129

Element	Composition (wt %)		
	Target composition	Check analysis[a]	
		Sample 1	Sample 2
Al	15.9	16.07	15.83
Cr	5.5	5.87	5.98
Nb	1.0	0.95	1.09
C	0.05	0.01	0.04
Fe	77.55	76.47	76.50
S	--	0.005	0.010
P	--	0.034	0.034
Ni	--	0.06	0.05
Mo	--	0.04	0.04
Mn	--	0.31	0.23
Si	--	0.09	0.08
V	--	0.01	0.01
Co	--	0.02	0.03
Cu	--	<0.01	<0.01
W	--	0.05	0.07
B	--	0.002	0.002

[a]Performed at MQS Inspection, Inc., Woodlawn, OH.

percent reductions are shown schematically in Fig. 8. The forging steps were at 1000° C, followed by rolling steps at 800 and 650° C, respectively. No problems were encountered in the preparation of the sheet. The processing steps used for the section from the 406-mm-diam ingot are the same as used previously for 102-mm-diam ingots.[16]

Mechanical Properties

The 0.76-mm-thick, as-rolled sheet was stress relieved at 700° C for 1 h, followed by oil quenching. The stress-relieved sheet was punched into specimens for tensile and creep testing. In order to remove the work from die punching, all of the specimens were given a final anneal of 700° C followed by oil quenching prior to testing. Optical microstructures of the sheet specimens prior to testing are shown in Fig. 9. Tensile tests on these specimens were conducted in the temperature range of room temperature to 800° C. Data from these tests are compared with similar data on 102-mm-diam ingots in Fig. 10, which shows that the

Table V. Composition of 406-mm-diam ESR Ingot of FA-129

Element	Composition (wt %)		
	Target composition	Check analysis[a]	
		Sample 1	Sample 2
Al	15.9	16.07	15.83
Cr	5.5	5.87	5.98
Nb	1.0	0.95	1.09
C	0.05	0.01	0.04
Fe	77.55	76.47	76.50
S	--	0.005	0.010
P	--	0.034	0.034
Ni	--	0.06	0.05
Mo	--	0.04	0.04
Mn	--	0.31	0.23
Si	--	0.09	0.08
V	--	0.01	0.01
Co	--	0.02	0.03
Cu	--	<0.01	<0.01
W	--	0.05	0.07
B	--	0.002	0.002

[a]Performed at MQS Inspection, Inc., Woodlawn, OH.

Fig. 7. Optical macrostructure (a) and microstructures (b,c) of a section taken from near the top of the 406-mm-diam ESR ingot of FA-129 showing (b) grain size and second-phase distribution at low magnification, and (c) eutectic and porosity at high magnification.

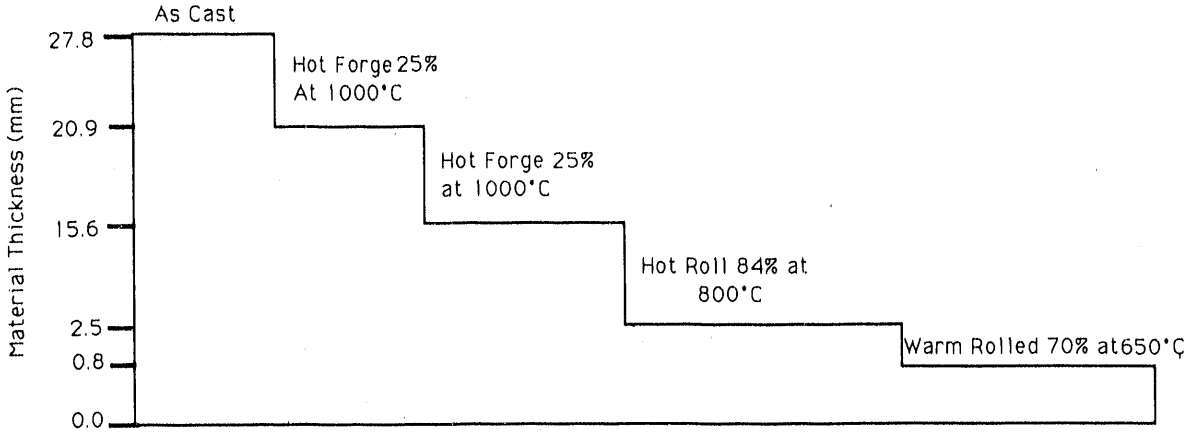

Fig. 8. Schematic showing the steps used for processing a section taken from near the top of the 406-mm-diam ESR ingot of FA-129.

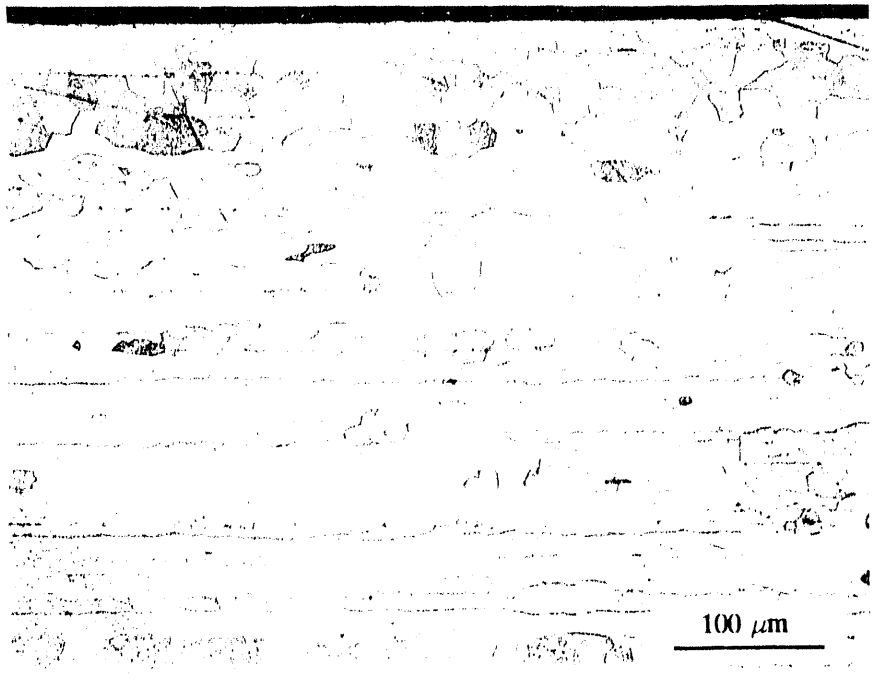

Fig. 9. Optical microstructure of 0.76-mm-thick sheet of alloy FA-129 prior to testing. The sheet was rolled from a section near the top of the 406-mm-diam ESR ingot produced at PRP.

a

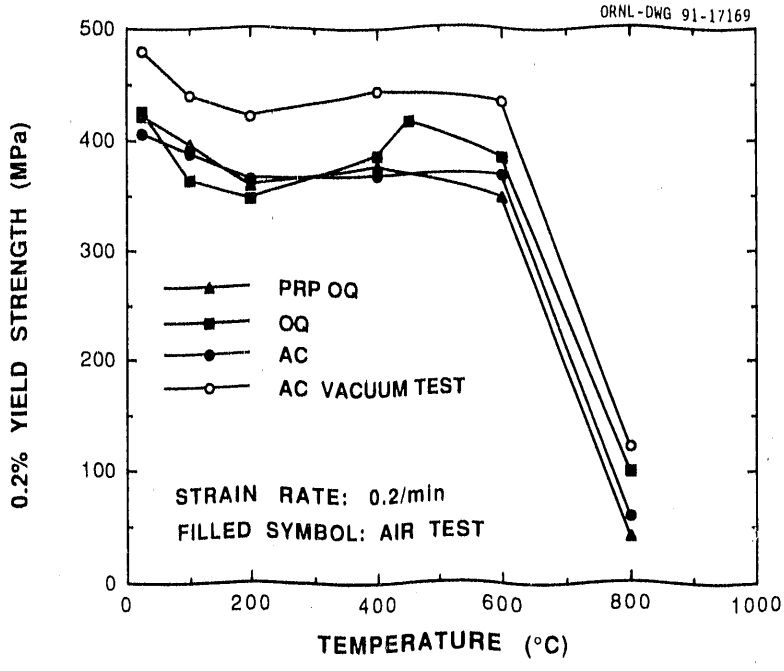

b

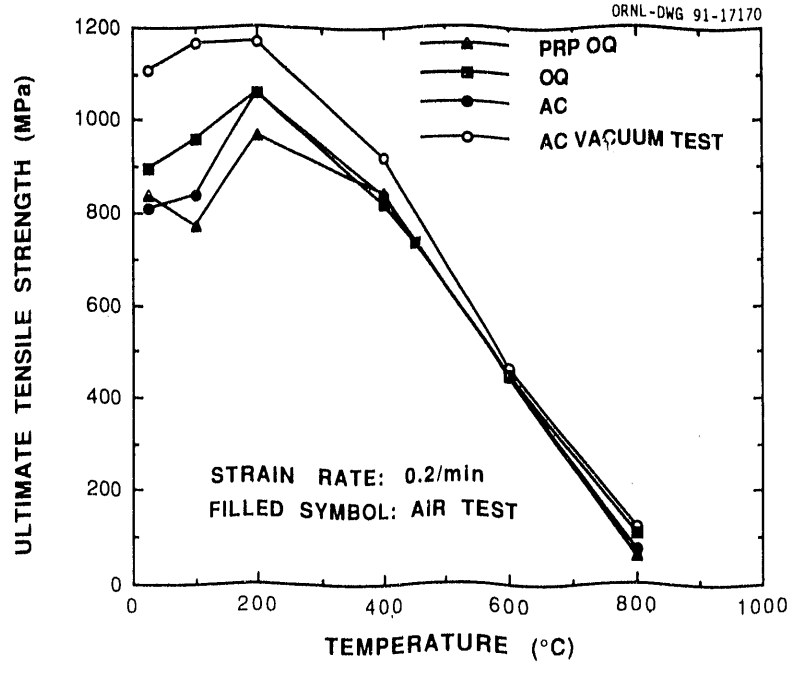

Fig. 10. Tensile properties of specimens from a 0.76-mm-thick sheet rolled from a section of the 406-mm-diam ESR ingot of alloy FA-129. Data on the 406-mm-diam ingot are compared with the previously developed data on a 102-mm-diam ingot of the same alloy. (a) yield strength, and (b) ultimate tensile strength.

c

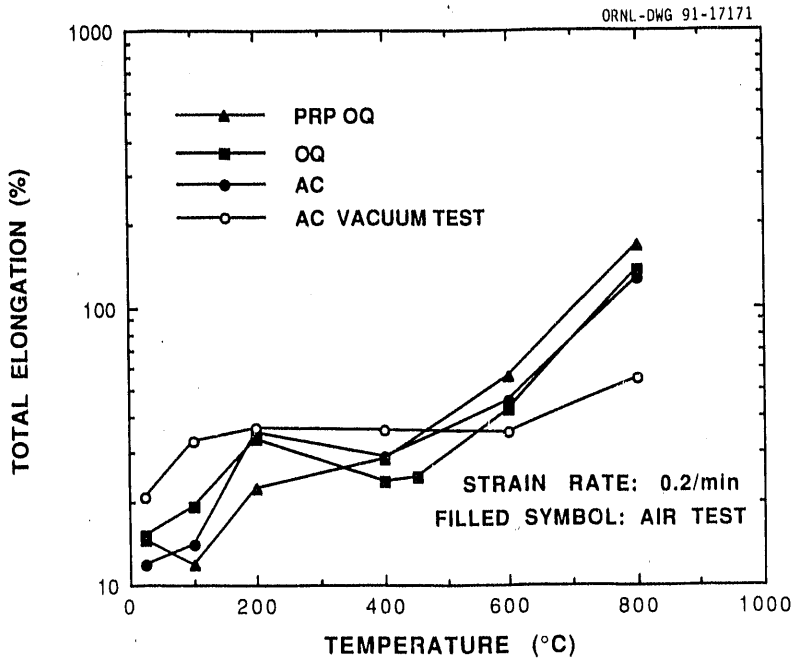

d

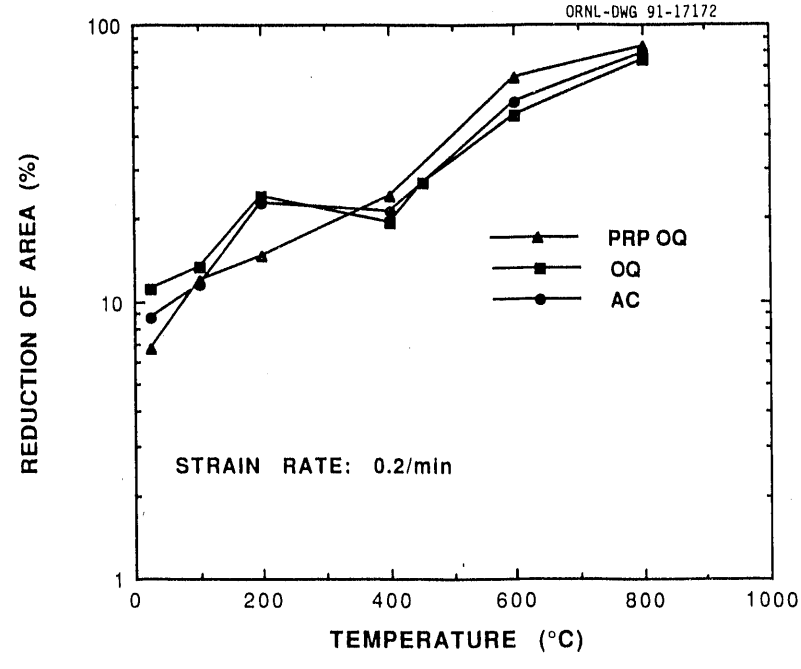

Fig. 10 (continued). Tensile properties of specimens from a 0.76-mm-thick sheet rolled from a section of the 406-mm-diam ESR ingot of alloy FA-129. Data on the 406-mm-diam ingot are compared with the previously developed data on a 102-mm-diam ingot of the same alloy. (c) total elongation, and (d) reduction of area.

sheet processed from the 406-mm-diam ingot has essentially the same strength and ductility properties as the sheet processed from the 102-mm-diam ingots. These results are very encouraging in that they suggest that the iron-aluminide alloy FA-129 and probably alloys of other compositions can be scaled up without sacrificing tensile properties.

Creep testing of specimens from the 406-mm-diam ESR ingot is in progress in the temperature range of 450 to 700° C. The results of these tests will be reported in the next semiannual.

SUMMARY AND CONCLUSIONS

Our efforts at alloying between alloy FA-129 (which has good tensile properties and weldability) and alloy FA-97 (which has good high-temperature creep properties) to produce a composition which has an acceptable combination of these properties have been encouraging. Alloy FA-170 shows good weldability and creep resistance, but initial tensile properties were not as good as expected. Further studies to optimize the fabrication schedule for this alloy are underway and are expected to result in improved tensile properties.

With the initiation in the past year of analytical electron microscopy studies on many of our alloys, we are beginning to develop an understanding of deformation mechanisms in the iron aluminides and a better understanding of the roll of alloying additions in promoting desirable properties. These studies will continue in the future.

For the first time, successful, crack-free welds were made on 12.6-mm (0.5 in.) thick plate material of FA-129 alloy. Optical metallography revealed a coarse, columnar grain structure that may be detrimental to the properties of the weldment. The preliminary weldability studies on the microalloyed iron aluminides are encouraging. Further weldability studies are essential to characterize the weldability of these materials.

The preparation of 2000- and 3000-kg heats of alloy FA-129 melted at Precision Rolled Products was described. This report also included the cutting and processing experience with one of the ingots. The macrostructure, microstructure, and tensile properties of the sheet rolled from the 406-mm-diam ESR ingot were presented. Tensile properties of the sheet from the 406-mm-diam ingot were compared with the sheet rolled from the 102-mm-diam ingot produced earlier. The following conclusions were reached from the results available: (1) No unusual problems were encountered in the preparation

of the 2000- and 3000-kg heats of alloy FA-129 at PRP. The surface quality of the 406-mm-diam ESR ingot was similar to that observed for other iron- and nickel-based alloys. (2) The sectioned slice from the ESR ingot showed some evidence of solidification-related cracking. (3) Small pieces from the sectioned slices were easily processable by a standard procedure developed for the laboratory-size heats. (4) Tensile properties of the sheet rolled from the 406-mm-diam ESR ingot are similar to those observed for sheet rolled from 102-mm-diam ingots. (5) The results presented in this study suggest that alloy FA-129 can be scaled up commercially without sacrificing tensile properties.

REFERENCES

1. J. H. DeVan, H. S. Hsu, and M. Howell, *Sulfidation/Oxidation Properties of Iron-Based Alloys Containing Niobium and Aluminum*, ORNL/TM-11176, (Oak Ridge National Laboratory, Oak Ridge, TN, May 1989).

2. C. G. McKamey, J. H. DeVan, P. F. Tortorelli, and V. K. Sikka, J. Mater. Res. 6(8), 1779 (1991).

3. C. T. Liu, E. H. Lee, and C. G. McKamey, Scripta Metal. 23, 875-880 (1989).

4. C. T. Liu, C. G. McKamey, and E. H. Lee, Scripta Metall. 24(2), 385 (1990).

5. C. T. Liu and C. G. McKamey, *High Temperature Aluminides and Intermetallics*, ed. by S. H. Whang, C. T. Liu, D. P. Pope, and J. O. Stiegler (TMS, Allentown, PA, 1990), p. 133.

6. C. G. McKamey and C. T. Liu, to be published in Proceedings of ADVMAT/91 Environmental Effects on Advanced Materials Symposium, 1991.

7. V. K. Sikka, C. G. McKamey, C. R. Howell, and R. H. Baldwin, *Fabrication and Mechanical Properties of Fe_3Al-Based Aluminides*, ORNL/TM-11465, (Oak Ridge National Laboratory, Oak Ridge, TN, March 1990).

8. C. G. McKamey and C. T. Liu, Scripta Metall. 24, 2119 (1990).

9. V. K. Sikka, SAMPE Quart. 22(4), 2 (1991).

10. C. G. McKamey, Proceedings of the Fourth Annual Conference on Fossil Energy Materials, Oak Ridge National Laboratory, ORNL/FMP-90/1, (U. S. Department of Energy, Oak Ridge, TN, August 1990), p. 197.

11. D. M. Dimiduk, M. G. Mendiratta, D. Banerjee, and H. A. Lipsitt, Acta Metall. 36, 2947 (1988).

12. S. A. David, W. A. Jemian, C. T. Liu, and J. A. Horton, Weld. J. 64(1), 22s (1985).

13. S. A. David, D. N. Braski, and C. T. Liu, Weld. J. 65(4), 93s (1986).

14. S. A. David, J. A. Horton, C. G. McKamey, T. Zacharia, and R. W. Reed, Weld. J. 68(9), 372s (1989).

15. T. Zacharia and S. A. David, Proceedings of the Fifth Annual Conference on Fossil Energy Materials, ORNL/FMP-91/1 (U. S. Department of Energy, Oak Ridge, TN, September 1991), p. 229.

16. V. K. Sikka, C. G. McKamey, C. R. Howell, and R. H. Baldwin, *Properties of Large Heats of Fe_3Al-Based Alloys*, ORNL/TM-11796 (Oak Ridge National Laboratory, Oak Ridge, TN, March 1991).

17. V. K. Sikka, Proceedings of the Fourth Annual Conference on Fossil Energy Materials, Oak Ridge National Laboratory, ORNL/FMP-90/1, (U. S. Department of Energy, Oak Ridge, TN, August 1990), p. 219.

18. V. K. Sikka, R. H. Baldwin, K. S. Blakely, E. C. Hatfield, C. R. Howell, and C. G. McKamey, Proceedings of the Fifth Annual Conference on Fossil Energy Materials, ORNL/FMP-91/1 (U. S. Department of Energy, Oak Ridge, TN, September 1991), p. 197.

19. C. G. McKamey and P. J. Maziasz, Proceedings of the Fifth Annual Conference on Fossil Energy Materials, ORNL/FMP-91/1 (U. S. Department of Energy, Oak Ridge, TN, September 1991), p. 175.

20. T. Zacharia, unpublished data.

21. P. J. Maziasz and C. G. McKamey, to be published in Proceedings of International Conference on High-Temperature Aluminides and Intermetallics, J. Mater. Sci. & Eng., 1992.

22. C. G. McKamey, P. J. Maziasz, and J. W. Jones, submitted to J. Mater. Res.

OSU-2 - PACK CEMENTATION DIFFUSION COATINGS FOR IRON-BASE ALLOYS: CODEPOSITION OF CHROMIUM AND SILICON

M.A. Harper, M. Zhu, and R.A. Rapp

Department of Materials Science & Engineering
The Ohio State University
Columbus, OH 43210

INTRODUCTION

The development of cost effective materials in corrosive high temperature environments, e.g. those experienced in the combustion of fossil fuels, has a major technological significance. In this study, a modified pack cementation process[1] has produced adherent corrosion-resistant diffusion coatings on various alloys used in fossil fuel burning power plants. The coating procedure and corrosion testing results have been published[2,3].

Cast irons containing 14-16wt% Si (Duriron, Fe_3Si) exhibit excellent acidic aqueous corrosion resistance[4]. This resistance is further enhanced by the presence of about 4wt% Cr. However, such high-Si Fe-base alloys are brittle and available only in the as-cast form. A study to produce diffusion coatings containing 14-16wt% Si (plus Cr) on a Fe-2.25Cr-1.0Mo-0.15C steel is currently being pursued.

In this report, new thermodynamic calculations for Cr+Si codeposition are presented. Preliminary work to identify the oxidation products and mechanism for coated plain carbon and low-alloy steels is discussed. Initial results on coating low-alloy steels with a high-Si diffusion coating are presented.

DISCUSSION OF CURRENT ACTIVITIES

A thermodynamic analysis and experimental results of the last six months are summarized here.

Thermodynamic Analysis

The use of a silica filler in the codeposition of Cr and Si has been recognized as an important factor in this laboratory for approximately three years. The reason for the significance of the silica filler has been identified through thermodynamic calculations that analyze packs containing the various Cr-Si masteralloys, a NaF and/or NaCl activator, and a silica or

alumina filler. Figure 1 plots the equilibrium vapor pressures as a function of the activity of silicon for a pack containing a NaF activator and an alumina filler at 1050°C. Figure 2 shows the result of an identical calculation except for the introduction of a silica filler instead of alumina. Upon comparing Figures 1 and 2, the calculated partial pressures of the Si and Cr fluorides are approximately two orders of magnitude higher for the silica filler. These increases in partial pressures for both the Si *and* Cr fluorides result from the stability of $Na_2Si_2O_5$ (*l*) at the process temperature. If $Na_2Si_2O_5$ (*l*) is not entered into the calculation for the pack containing the silica, the calculated partial pressures for the Si and Cr fluorides are virtually the same as for the alumina filler. However, the addition of $Na_2Si_2O_5$ (*l*) into the silica filler calculation produces the values shown in Figure 2. The explanation for this behavior is as follows. Sodium is consumed in the formation of $Na_2Si_2O_5$ (*l*). The only source of Na in the pack is NaF (*l*), and the reaction of silica to form $Na_2Si_2O_5$ (*l*) displaces Na from NaF (*l*), while the fluorine is released into the gas phase. Upon the release of fluorine, an increase in the fluorine activity in the pack occurs. Therefore, the vapor pressures of the Si- *and* Cr-fluoride species are increased. An amorphous glass phase develops on the inside of crucibles used for codepositing Cr and Si with a silica filler. This glassy phase has been analyzed using energy dispersive spectroscopy (EDS) and found to contain Na and Si.

Oxidation Mechanism

Chromized/Siliconized 1018 Steel. Figure 3 shows the low weight gain of a chromized/siliconized low alloy steel (surface concentration containing 34wt%Cr-3Si) cyclically oxidized in air at 700°C for over four months. The complete details of the coating process have been published previously[3]. Table 1 shows the qualitative results reported from companies that have tested similarly coated coupons. The low weight gain shown in Figure 3 and the excellent results reported in Table 1 are postulated to result from a very thin, slow growing, amorphous silica film at steady state. Preliminary efforts to identify this thin film are discussed next.

Figure 4 shows a spalled region of a sample isothermally oxidized in air at 700°C for 1100 hours. The spallation occurred during cooling to room temperature. The scale that is still attached to the substrate has been identified as Cr_2O_3 by x-ray diffraction and has a typical morphology of a chromia scale grown on a chromia-forming alloy. Figure 5 which is a higher magnification of the area shown in Figure 4 shows two distinct regions. Spot "a" appears to be smooth while spot "b" has a rough fracture surface appearance. Figures 6 and 7 show a spalled piece of oxide laying upside down to reveal the underside of the oxide. Of particular interest is the portion of the spalled oxide shown by the letter 'c'. This area has a smooth, finely faceted appearance and could possibly match

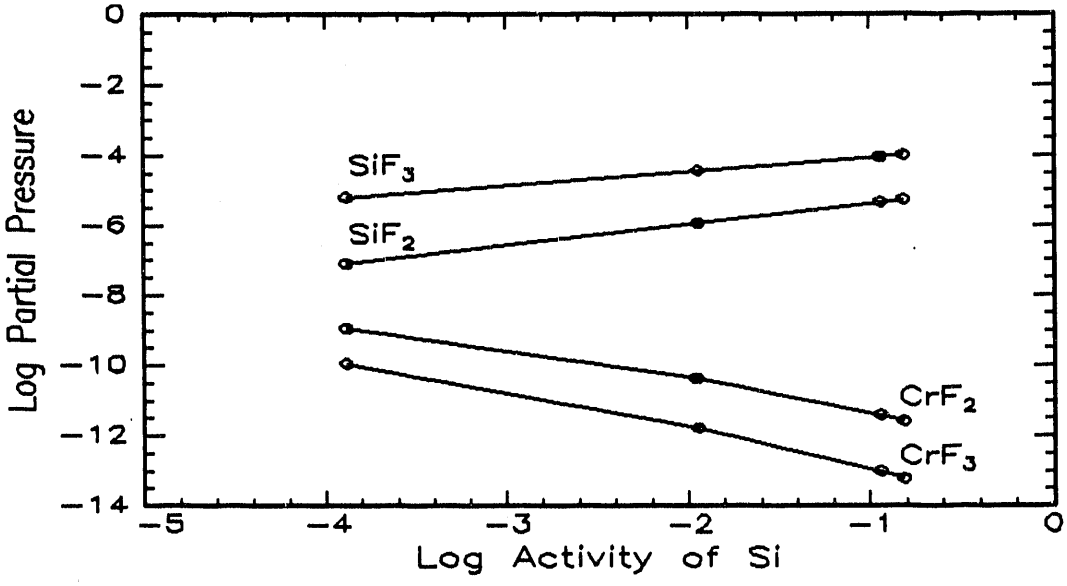

Figure 1. Equilibrium partial pressures of metallic halides in NaF activated packs containing Cr-Si masteralloys at 1050°C and Al_2O_3 filler.

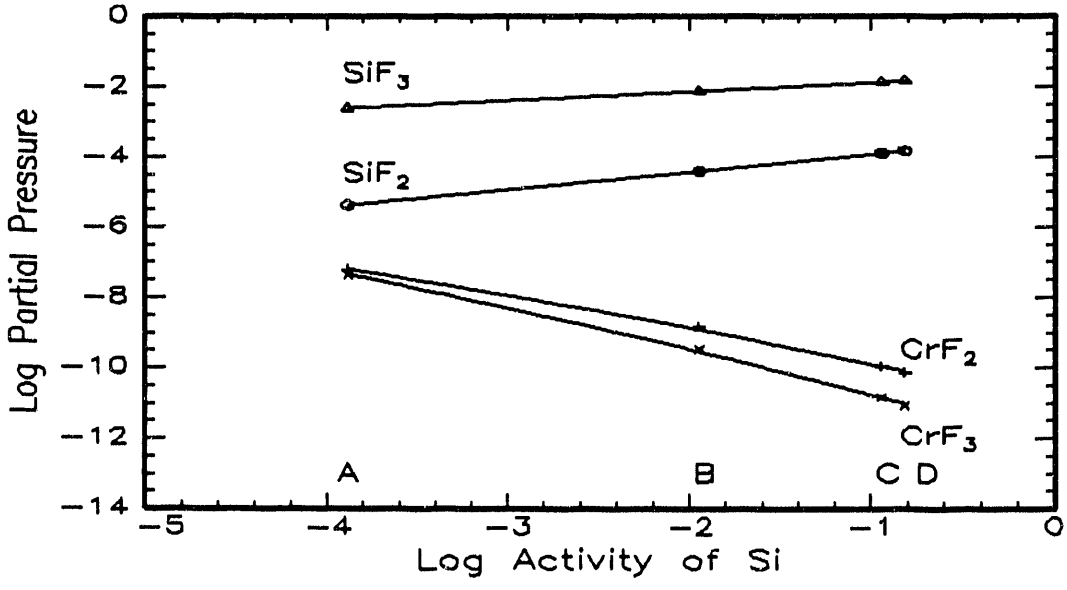

Figure 2. Equilibrium partial pressures of metallic halides in NaF activated packs containing Cr-Si masteralloys at 1050°C and SiO_2 filler.

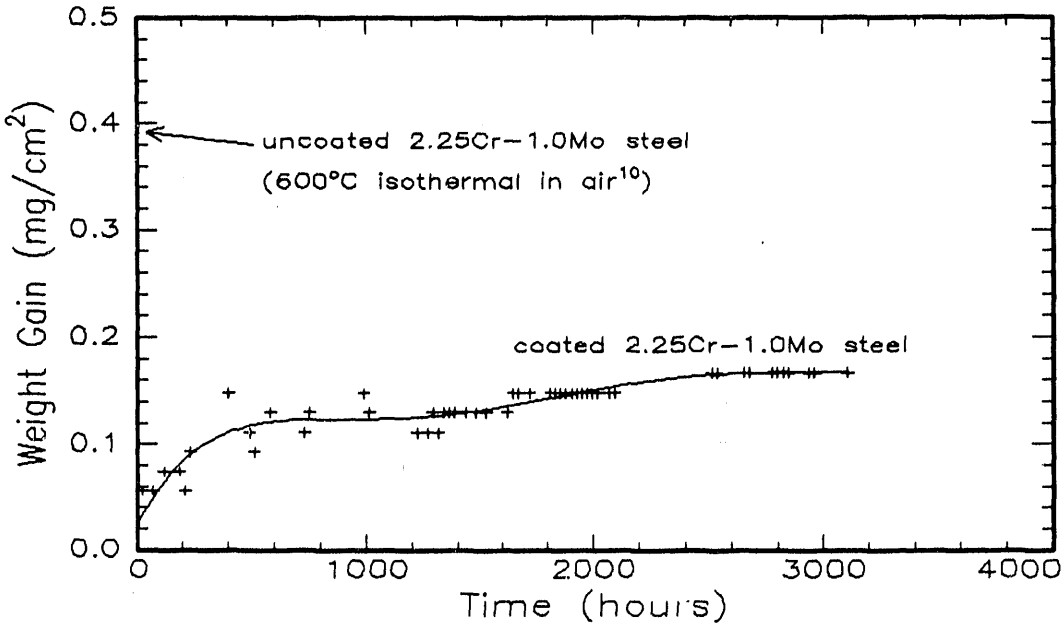

Figure 3. Plot of Weight-Gain versus Time for the Cyclic Oxidation in Air of Coated Sample with Surface Composition of 34Cr-3Si. Each Indicated Point Represents the Weight-Gain Measured After Cooling from 700°C to Room Temperature.

Table 1. Qualitative results from companies.

COMPANY	ATMOSPHERE	RESULTS
Shell Development	isothermal (400-700°C) reducing, S-containing gas (medium BTU fuel)	coatings performed better than typical heat-resistant austenitic alloys
Foster Wheeler	synthetic ash (containing 5wt% K_2SO_4, 5wt% Na_2SO_4, 30wt% Al_2O_3, 30wt% SiO_2, and 30wt% Fe_2O_3) plus 15.6% CO_2, 10.0% H_2O, 3.6% O_2, 1.0% SO_2, balance N_2 at 650°C and 700°C	- at 650°C (below melting temperature of sulfate in ash) coatings performed comparable to Incoloy 690 (Ni-29Cr-9Fe) - at 700°C (above melting temperature of sulfate in ash) coatings did not perform well
Babcock & Wilcox	isothermal (500-700°C) reducing, S-containing gas	chromized/siliconized coatings are performing comparable to or better than chromized coatings

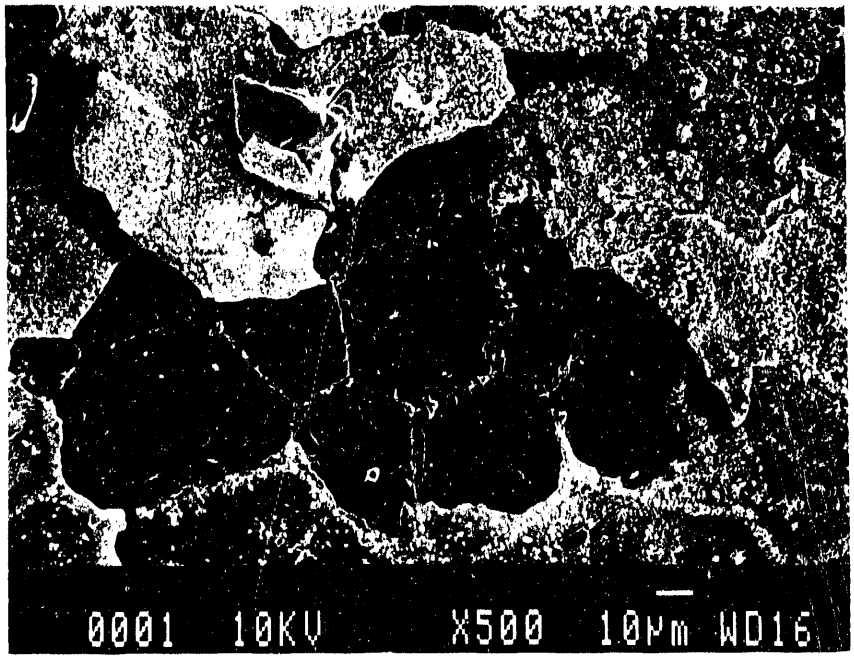

Figure 4. Secondary electron image of spalled region of coated 1018 steel coupon isothermally oxidized at 700°C for 1100 hours.

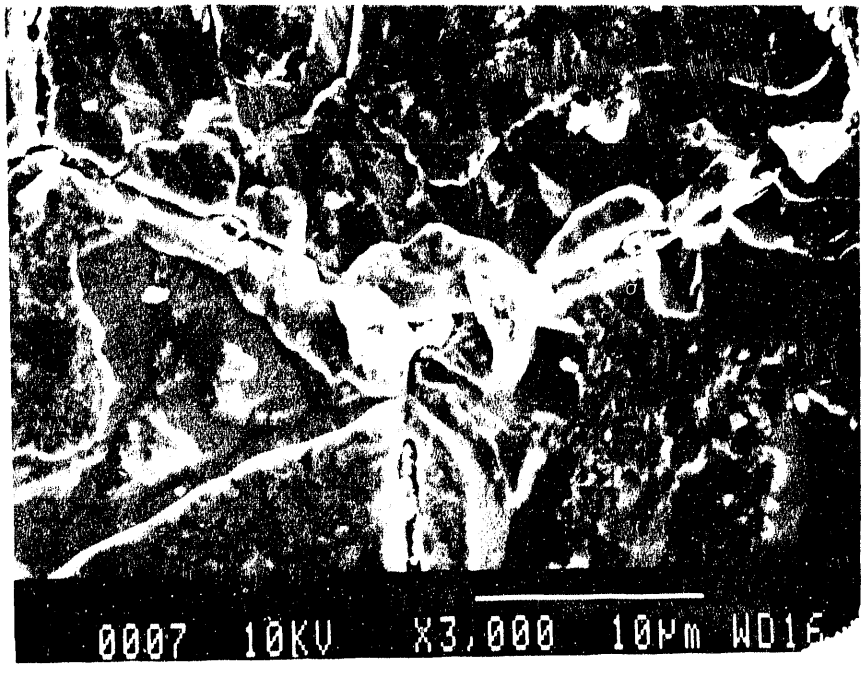

Figure 5. Higher magnification of spalled region in Figure 4 showing faceted regions "a" and rough regions "b".

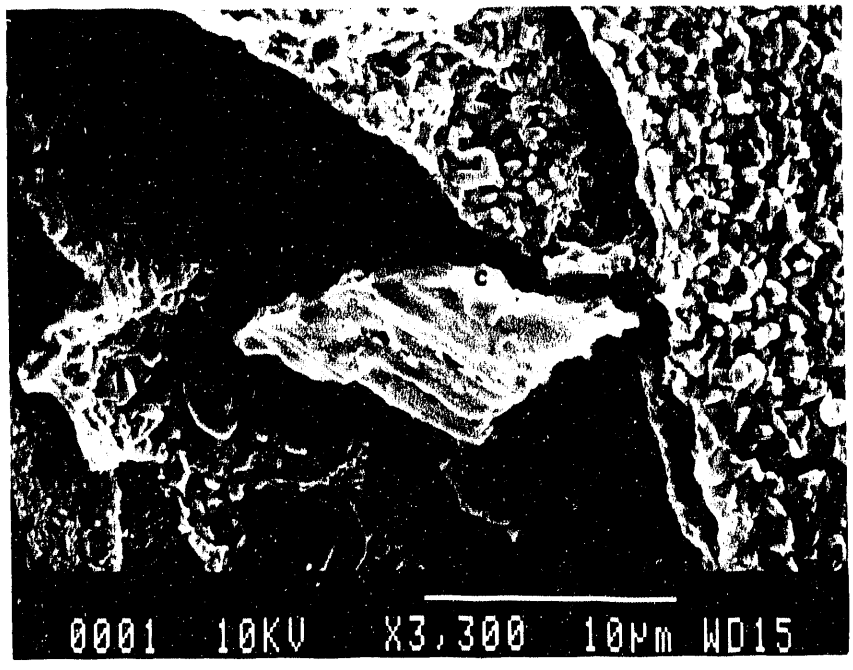

Figure 6. Secondary electron image of spalled oxide showing the underside of the oxide scale.

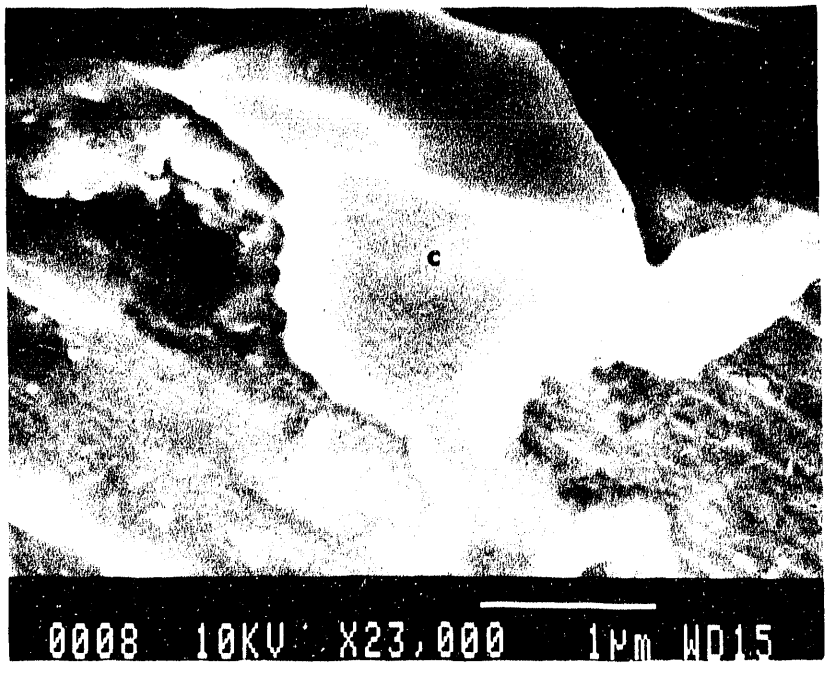

Figure 7. Higher magnification of spalled oxide shown in Figure 6.

the smooth areas shown in Figure 4. Whether area 'c' is amorphous silica has not been positively determined. However, surface compositional analysis of regions similar to 'a' and 'b' in Figure 5 using Auger Electron Microscopy will be conducted.

Coating Results

Efforts to produce a high silicon (Fe-14wt%Si) diffusion coating on three iron-base alloys (interstitial-free steel, AISI 1045 steel, and Fe-2.25Cr-1.0Mo-0.15C steel) are presently being pursued. Figure 8 shows the microstructure of a 2.25Cr-1.0Mo steel coated using a 60wt%Cr-40Si masteralloy, NaCl activator, and a SiO_2 filler diffused at 1050^{0}C for 20 hours. The composition of the coating, at a depth of 5 microns from the outer surface is Fe-9.2wt%Cr-7.2Si, as determined using energy dispersive spectroscopy. As shown on the micrograph in Figure 6, some porosity is observed in the 350 micron (14 mils) thick coating. These voids are probably closed Kirkendall voids resulting from Fe loss at the surface as $FeCl_2$ vapor. Experiments to increase the silicon content and eliminate the porosity using a different activator, and masteralloy are underway.

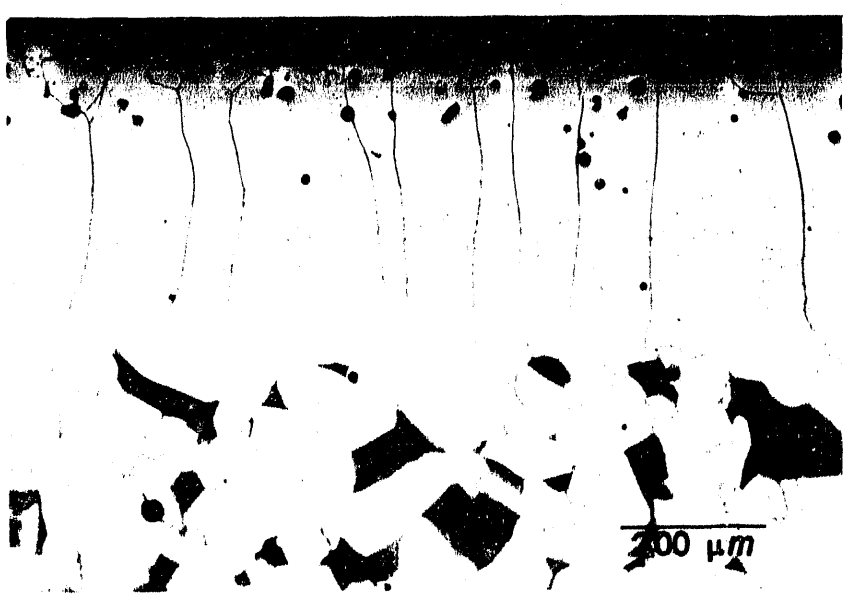

Figure 8. Optical micrograph of 2.25Cr-1.0Mo steel coated using 60wt%Cr-40Si masteralloy, NaCl activator, SiO_2 filler, diffused at 1050^{0}C for 20 hours.

CONCLUSIONS

A thermodynamic analysis of packs containing a silica filler versus an alumina filler explains the importance of using a silica filler to raise the fluorine activity during the codeposition of Cr and Si. A thin amorphous silica layer thought to form during the oxidation of codeposited diffusion coatings (containing approximately 20-30wt%Cr-3Si) has not yet been positively identified. Coatings containing 9.2wt%CR and 7.2wt%Si have been produced on 2.25Cr-1.0Mo substrates and experiments t increase the Si content and eliminate the coating porosity are presently underway.

REFERENCES

1. M.G. Hocking, V. Vasantasree and P.S. Sidky, Metallic and Ceramic Coatings, John Wiley & Sons, Inc., N.Y., 1989, p. 173.

2. M.A. Harper and R.A. Rapp, "Codeposition of Chromium and Silicon in Diffusion Coatings for Iron-Base Alloys Using Pack Cementation", in Fourth International Conference on Surface Modification Technologies, Paris, France, 1990, p. 415.

3. M.A. Harper and R.A. Rapp, "Chromized/Siliconized Pack Cementation diffusion Coatings for Heat Resistant Alloys", in First International Conference on Heat-Resistant Materials, ASM International, Fontana, WI, 1991.

4. M.G. Fontana, Corrosion Engineering, Third Edition, McGraw-Hill Book Company, N.Y., 1986, p. 322.

RPI-2 - INVESTIGATION OF MOISTURE - INDUCED EMBRITTLEMENT OF IRON ALUMINIDES

A. Castagna and N.S. Stoloff

Rensselaer Polytechnic Institute
Troy, NY 12180-3590

INTRODUCTION

The purpose of this investigation is to examine fatigue crack growth resistance and notched and unnotched tensile properties of the Fe_3Al type intermetallic compound, FA-129. The composition is 28.6 at.%Al, 4.8 at.%Cr, 0.21 at.%C, 0.5 at.%Nb, balance Fe. Tests have been performed in various environments and in the B2 and DO_3 ordered conditions.

DISCUSSION OF CURRENT ACTIVITIES

Fatigue Crack Growth

Fatigue crack growth tests were run following the ASTM E-647 procedures on compact tension specimens measuring 3.18 cm x 3.05 cm x 0.51 cm thick in the following environments: oxygen, vacuum, air, hydrogen gas, and air with hydrogen cathodically charged into the specimen. Tensile tests were run on cylindrical specimens with a gauge section 0.46 cm in diameter and 2.26 cm long. Notched tensile specimens had a notch cut around the gauge of depth .102 cm and radius 0.0089 cm. Notched and unnotched tensile specimens were run in oxygen and air. All tests were conducted on both the DO_3 and the B2 conditions.

Figs 1 and 2 show the da/dN curves generated for B2 and DO_3 material respectively. Table 1 lists the fracture mode for each test condition and summarizes the

slopes of the da/dN curves as well as the threshold and critical stress intensities. It should be noted that these critical stress intensities may not correspond to the ASTM defined ΔK_{IC} due to specimen size being smaller than required for valid ΔK_{IC} values.

Table 1

Condition	Fracture Surface	Striations	Stage II Slope	ΔK_{TH} (MPa$\sqrt{m}$)	ΔK_C (MPa$\sqrt{m}$)
B2 Oxygen	Dimpled	few	2.9	26	61
B2 Vacuum	TG	many	5.1	31	59
B2 Air	TG	many	9.4	30	44
B2 Charged	TG	few	6.8	23	44
B2 Gas	TG	few	8.6	22	41
DO_3	Dimpled + Cleavage	many	8.8	23	35
DO_3 Vacuum	TG	few	11.9	20	32
DO_3 Air	Mixed + Cleavage	few	22.8	19	24
DO_3 Charged	Mixed + Cleavage	none	9.1*	19	27
$D0_3$ Gas	Mixed + Cleavage	none	37.6	18	21

* - excessive crack branching observed

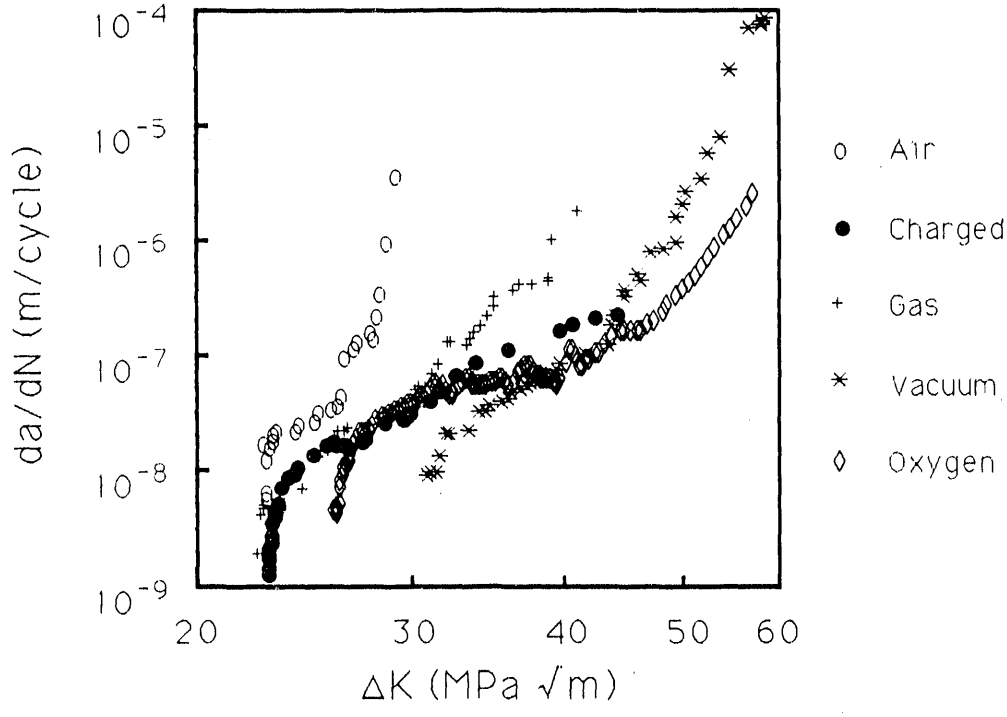

Fig. 1 - Fatigue Crack Growth in B2 Ordered FA-129

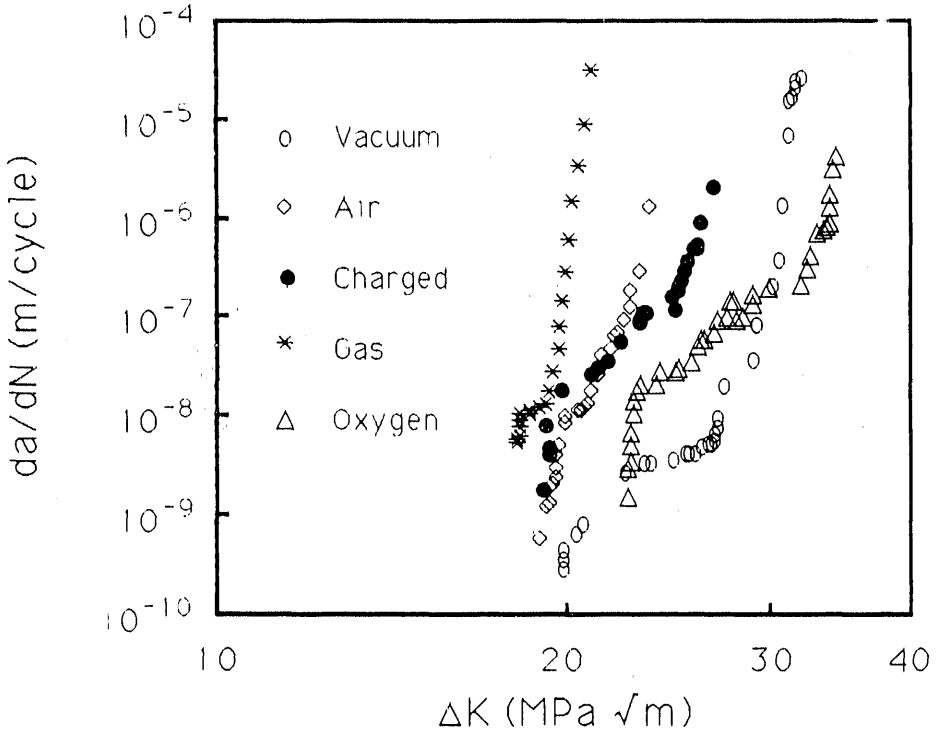

Fig. 2 - Fatigue Crack Growth in DO_3 Ordered FA-129

Several trends appear in the data. First is the effect of order. The threshold and critical stress intensities in the DO_3 state are approximately 40% lower than those in the B2 state. In addition to being shifted to the left on the ΔK axis, the da/dN curves for the DO_3 material exhibit a much steeper slope in the stage II region of crack propagation, or in some cases there was no well defined stage II region at all. The fracture surfaces in the two ordered states also are different. The B2 ordered specimens fail entirely transgranularly, with occasional fatigue striations, while the DO_3 ordered specimens demonstrate a shift from transgranular to mixed mode to predominantly intergranular with more aggressive environment.

The effect of environment is demonstrated by both a decrease of slope, ΔK_{TH} and ΔK_C of the da/dN curves, with hydrogen gas causing the poorest properties and oxygen

the best. The hydrogen charged curve flattens out and crosses over the air and vacuum curves. This is most likely due to excessive crack branching observed in the hydrogen charged specimens. Tests in oxygen and vacuum yield the greatest resistance to crack growth, with a decrease in toughness as the environment changes to air, hydrogen-charged, and hydrogen gas. Specimens of both ordered states showed a significant change in fracture surface in oxygen toward a dimpled appearance suggesting microvoid coalescence. In the B2 state all other environments resulted in predominantly transgranular failure.

The DO_3 ordered sample tested in vacuum exhibited cleavage failure with some striations present. In air it displayed intergranular regions as well as transgranular. Some striations also were visible. The fracture surface of the hydrogen charged specimen was similar to that in air, but showed no fatigue striations. The specimen tested in hydrogen gas showed more extensive regions of intergranular failure. In both the DO_3 and B2 states specimens tested in hydrogen gas showed a small amount of secondary cracking which appeared to be along cube planes.

The changes in ΔK_C shown in Table 1 clearly show the embrittling effect of hydrogen, whether it is present in the form of hydrogen gas or water vapor in air. Air and hydrogen gas have nearly the same effect on ΔK_C. This supports the theory that water vapor in air reacting with aluminum releases hydrogen at the crack tip[1]. The decrease in stage II slope between oxygen and vacuum also is consistent with this theory. Oxidation of aluminum occurs without H_2O vapor in the high oxygen environment, thus eliminating the release of hydrogen.

Notch Sensitivity

Tensile results are listed in Table 2. Comparison of unnotched data shows the expected embrittling effect of hydrogen on elongation (ε_f) and reduction of area (RA) in both ordered states. In the B2 state ε_f doubles when tested in oxygen, and in the DO_3 state there is a five-fold increase, with similar behavior for RA. As expected, ductility in the DO_3 state is lower than that in the partially ordered B2 material.

UTN-2 - INVESTIGATION OF JOINING TECHNIQUES FOR ADVANCED AUSTENITIC ALLOYS

C.D. Lundin, C.Y.P. Qiao and T. Kuroda

Materials Joining Research
Materials Science and Engineering Department
The University of Tennessee, Knoxville, TN 37996

INTRODUCTION

Modified 316 and 800H are members of a family of HT-UPS (high-temperature, ultrafine precipitate strengthened) austenitic alloys that have been developed by ORNL (Oak Ridge National Laboratory) for application in modern power generating systems [1]. Extensive weldability evaluations have been completed [2]. Like conventional nickel base alloys and fully austenitic stainless steels, the HT-UPS alloys also show some welding related problems (e.g. hot cracking and HAZ liquation cracking) during fabrication. Filler metal selection and proper welding procedures are significant factors in producing sound welded joints in addition to control of base material response. One heat of modified 316 and one heat of modified 800H tubing fabricated at Babcock and Wilcox were employed to conduct tube weld coupon fabrication using a state-of-art pipe welder. The welding procedures for the weld coupons are briefly described in this report.

HD 556 and Inconel 617 are potential filler alloys for HT-UPS materials. Successful GTA welding of modified 800H using HD 556 filler has been demonstrated by ORNL [3]. Hot cracking and hot ductility evaluations of HD 556 and Inconel 617 were conducted and reported previously [2]. The

metallographic and fractographic examinations on the hot ductility and hot cracking samples tested recently have been carried out. A summary of the preliminary fractographic examination results are included in this report.

DISCUSSION OF CURRENT ACTIVITIES

Welding Practices for Advanced Austenitic Alloy Tubing Coupons

An Astro-arc Model 3P-300-PE pipe welder was used for welding. A positioner was used to rotate the tubing in the horizontal (1G) position during welding. Figure 1 shows the tube welding fabrication system.

The modified 316 monolithic tubing is 2.02" OD, 1.32" ID. The modified 800H monolithic tubing is 2.02" OD, 1.01" ID. The welded coupons are composed of two 5" long pieces of tubing. A V groove preparation was applied for both modified 316 and modified 800H materials. Five weld beads were used to fill the groove for the modified 316 while seven weld beads were used for the modified 800H. Alloy 556 was used as the filler mater al. Suitable welds were obtained for both modified 316 and modified 800H.

Preliminary Weldability Evaluation Using Hot Ductility Testing of Haynes HD 556 and Inconel 617

The Gleeble hot ductility test has been used for evaluating weld HAZ properties since 1949. One of the important features of this testing is the ability to predict HAZ hot cracking propensity using hot ductility vs temperature behavior. The results of Varestraint hot

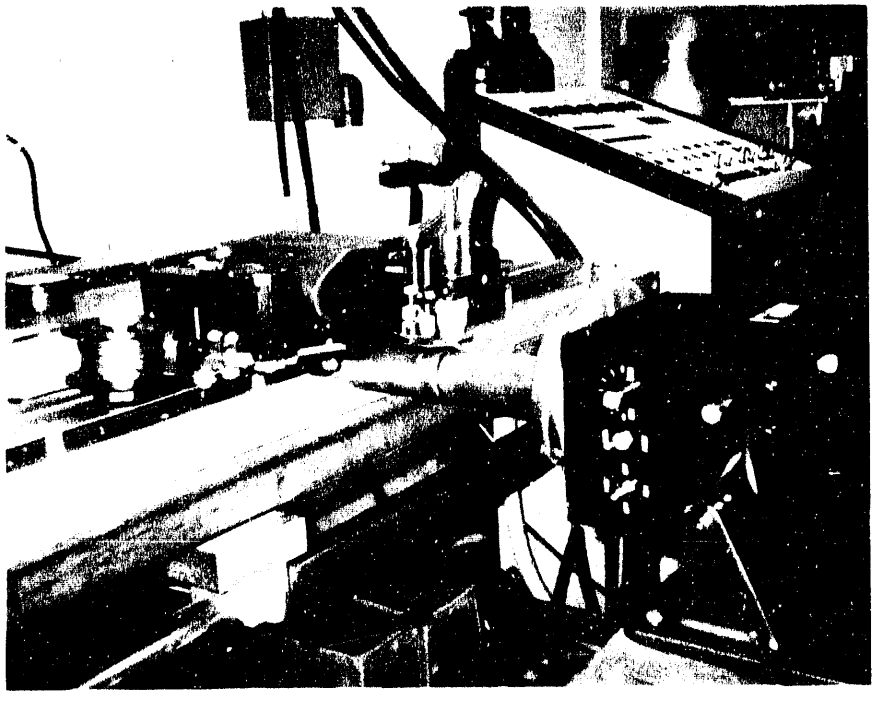

Figure 1. The tube welding fabrication system.

cracking test and Gleeble hot ductility test for HD 556 and Inconel 617 were presented in an earlier technical report [2]. It was shown that the Gleeble hot ductility test results agreed with the Varestraint hot cracking test (the most widely used hot cracking test method). Thus, this indicates that Gleeble hot ductility test can be reliably employed to assess HAZ hot cracking tendency. In order to reveal the metallurgical conditions related to the hot ductility behavior of HD 556 and Inconel 617 a fractographic examination was accomplished and the results are presented in this report. The chemical composition of Haynes HD 556 and Inconel 617 is tabulated in Table 1. The hot ductility curves for HD 556 and Inconel 617 are shown in Figure 2.

Table 1. Chemical Composition of Materials Studied

Material	C	Si	Mn	Ni	Cr	Nb	Mo	S	Al	W	Co	La	Fe
HD 556 855657305	0.11	0.49	1.20	19.44	31.39	0.76	2.72	<0.005	0.26	2.08	19.08	0.01	bal.
Inconel 617 XX14A6UK	0.06	0.18	0.02	55.31	21.74	-	8.91	0.002	1.11	-	12.32	-	0.53

The fractographic observations on hot ductility sample agreed with the ductility data obtained from hot ductility testing for both materials tested.

HD 556 Alloy

Figure 3 shows the fractographic morphology of a hot ductility test sample tested on-heating at 968°C. A typical dimple morphology fracture surface denotes that microviod coalescence is responsible for fracture at this temperature. The fracture surface morphology of the hot ductility specimen tested at on-heating 1262°C is shown in Figure 4. The intergranular type rupture is evident on this fracture surface. It is clear that grain size is small at this test temperature due to recrystallization. It should be noted

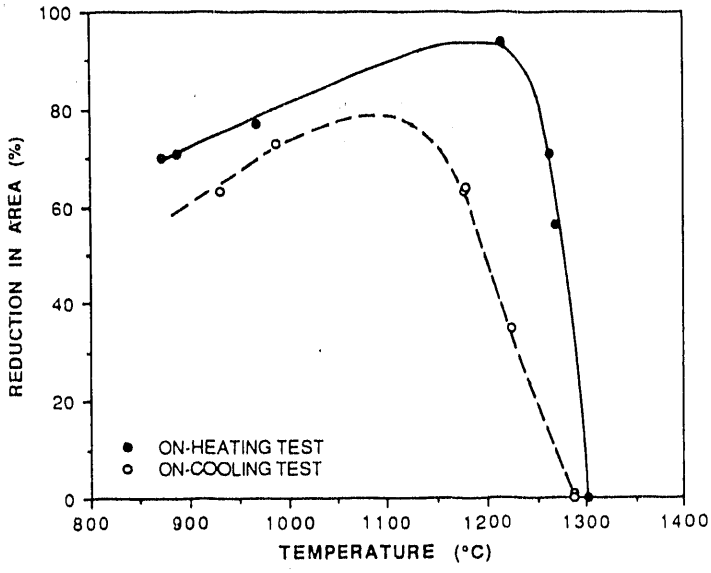

(a)

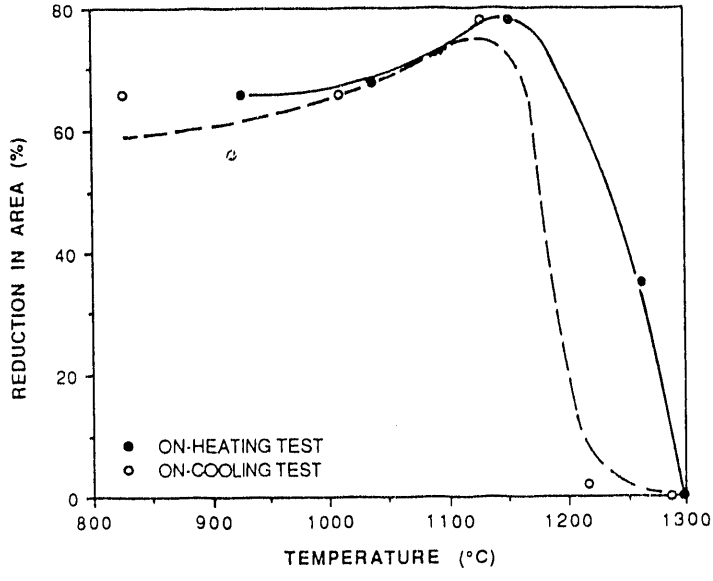

(b)

Figure 2. Hot ductility behavior of Haynes HD 556 (Ht. 855657305) and Inconel 617 (Ht. XX14A6UK). (a) Hot ductility behavior of HD 556; (b) Hot ductility behavior of Inconel 617.

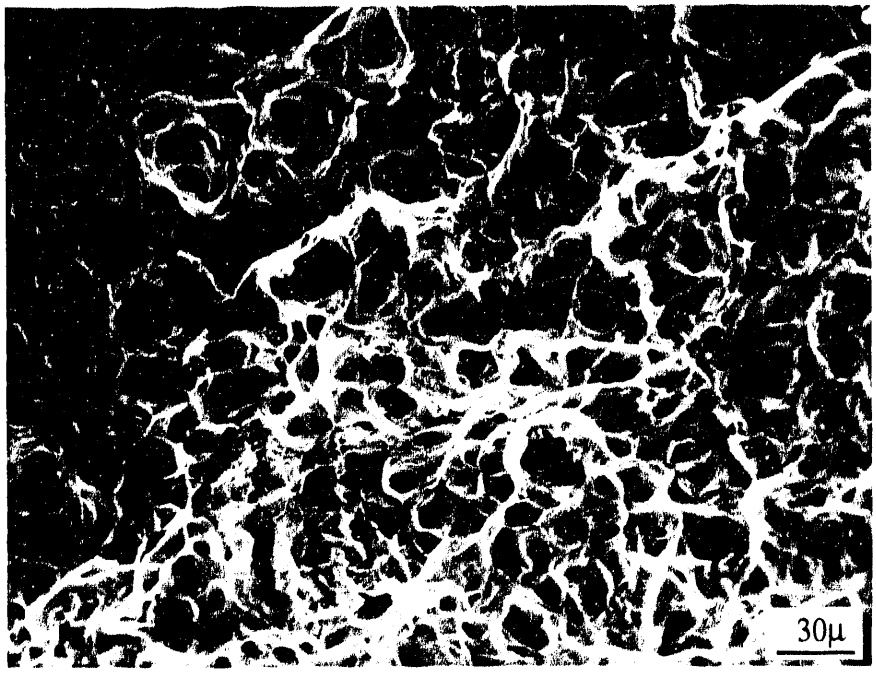

Figure 3. Fracture surface morphology of HD 556 hot ductility sample tested for on-heating at 968°C.

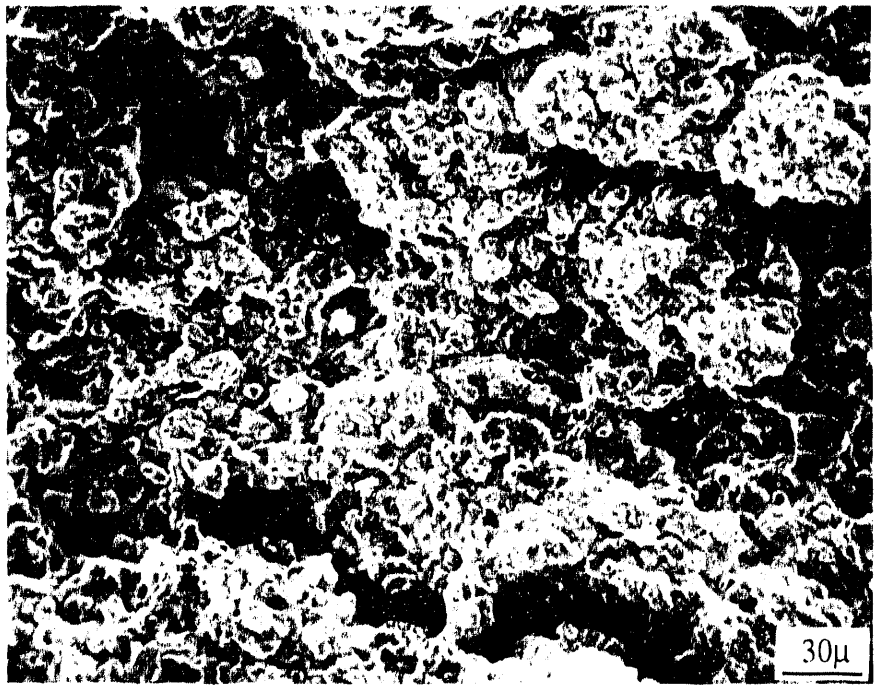

Figure 4. Fracture surface morphology of HD 556 hot ductility sample tested for on-heating at 1262°C.

that 1262°C is the temperature where hot ductility begins to decrease as the testing temperature increases during the on-heating tests. No clear evidence was obtained to show that liquation occurred during on-heating testing at this temperature. Figure 5 shows the fracture surface morphology of the sample tested at 1302°C (ZDT). Clear evidence is shown indicating that a "liquid" film covered the ruptured surface at the test temperature. The grain size at this temperature is greater than that at 1262°C due to grain growth.

The fracture surface morphology of the hot ductility sample tested at 1268°C on-cooling from ZDT is shown in Figure 6. It is characterized by a generally brittle morphology (intergranular) with a small amount of ductile rupture. The sample tested at 933°C during on-cooling shows a dimple morphology (see Figure 7). It is considered that the rupture at the lower temperature is intergranular along the prior melted and resolidified grain boundaries and this reflects the high temperature exposure.

Inconel 617 Material

The grain size of Inconel 617 is larger than that of HD 556. Figure 8 shows the fracture surface morphology of a hot ductility sample tested on-heating at 927°C. A clear dimple type surface fracture morphology with significant plastic deformation prior to rupture can be observed. As tested on-heating at 1204°C (hot ductility decrease temperature), the fracture surface shows typical intergranular rupture (see Figure 9). No clear evidence exists to show that liquid begin to form along the grain boundaries at this temperature. A sample tested at 1302°C (ZDT) on-heating possesses clear evidence of intergranular fracture surface covered with a "liquid" layer at elevated temperature (see Figure 10). Upon

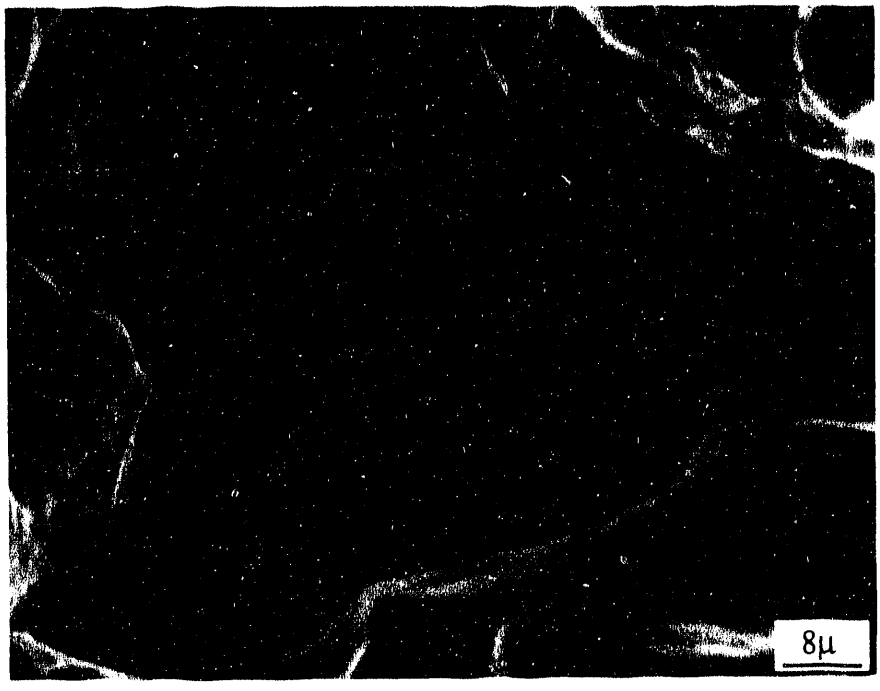

Figure 5. Fracture surface morphology of HD 556 hot ductility sample tested for on-heating at 1302°C (ZDT).

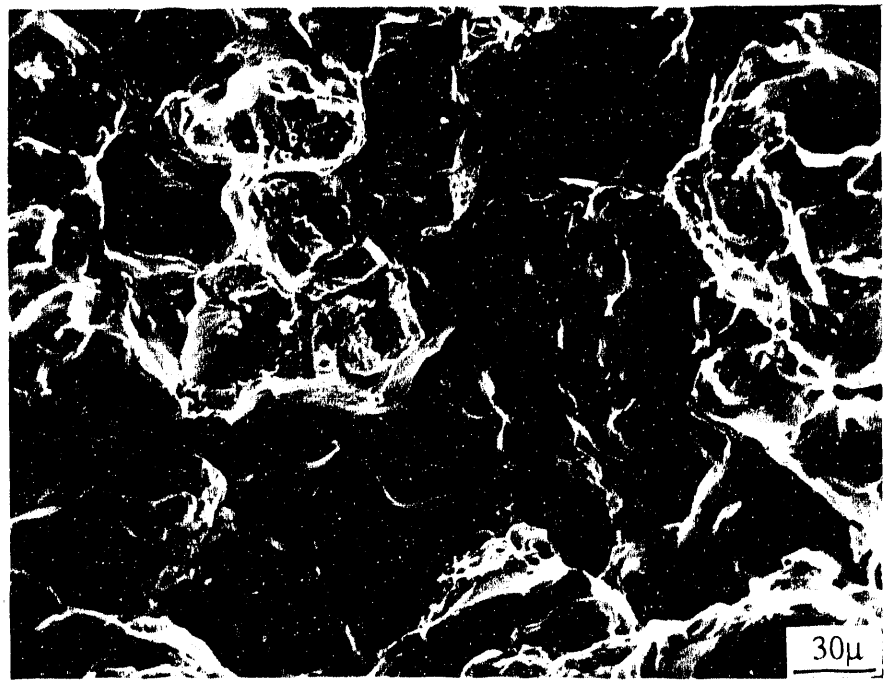

Figure 6. Fracture surface morphology of HD 556 hot ductility sample tested for on-cooling at 1268°C.

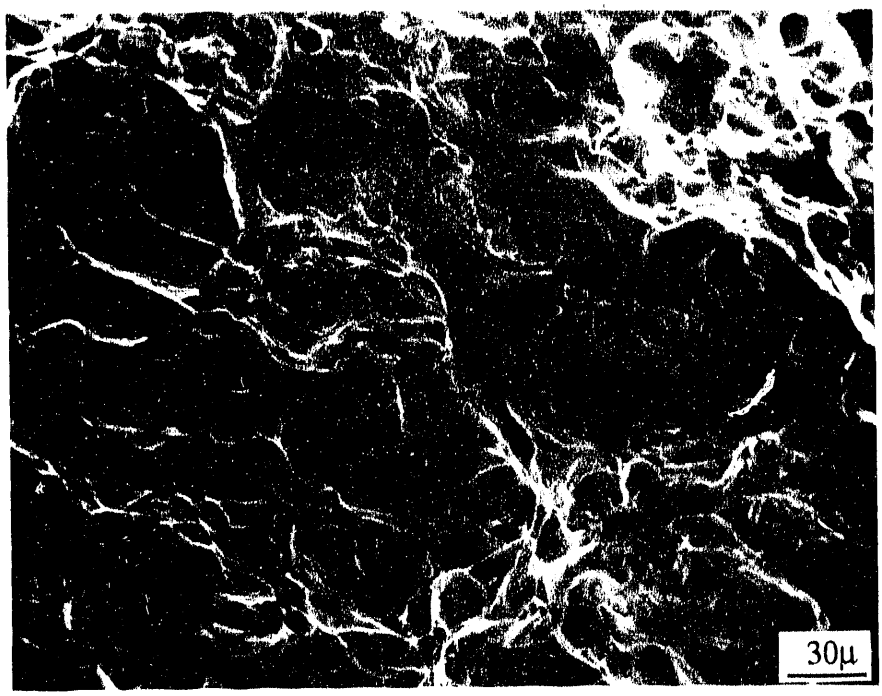

Figure 7. Fracture surface morphology of HD 556 hot ductility sample tested for on-cooling at 933°C.

Figure 8. Fracture surface morphology of Inconel 617 hot ductility sample tested for on-heating at 927°C.

Figure 9. Fracture surface morphology of Inconel 617 hot ductility sample tested for on-heating at 1204°C.

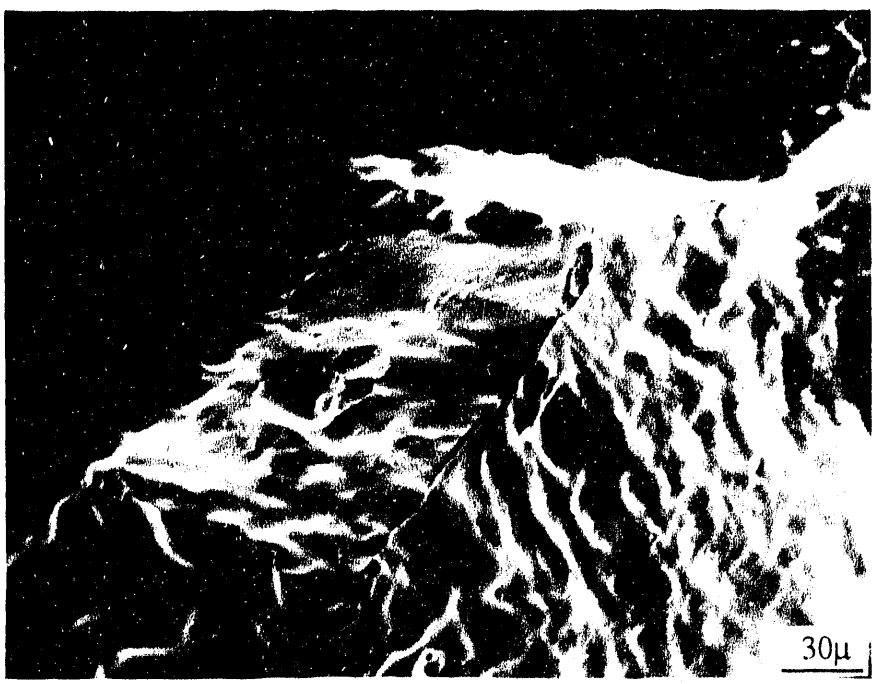

Figure 10. Fracture surface morphology of Inconel 617 hot ductility sample tested for on-heating at 1302°C (ZDT).

on-cooling testing at 1127°C, the fracture surface reveals intergranular type rupture along the prior melted and resolidified grain boundaries (see Figure 11). Figure 12 shows the fracture morphology of a hot ductility sample tested at 1010°C on-cooling. Larger size dimples dominate the fracture surface in this sample, however, the fracture is believed to occur along the prior melted and resolidified grain boundaries.

SUMMARY

1. Fabrication of welded coupons of modified 316 and modified 800H tubing using HD 556 filler metal has been completed.
2. Preliminary metallographic examinations of hot ductility test samples of alloys HD 556 and Inconel 617 were completed and the fractographic observations agree with hot ductility behavior for both HD 556 and Inconel 617.
3. Evidence for liquation related hot ductility mechanisms is clear in these alloys.
4. The hot ductility response of HD 556 and Inconel 617 is considered excellent and suggests a low cracking susceptibility.

FUTURE WORK

Metallographic examination of the welds on tubing coupons will be carried out in the near future. Microhardness measurements on the welds will also be conducted in order to evaluate HAZ softening behavior.

The Varestraint testing of eight small heats, with controlled additions of tungsten and nitrogen, of modified

Figure 11. Fracture surface morphology of Inconel 617 hot ductility sample tested for on-cooling at 1127°C.

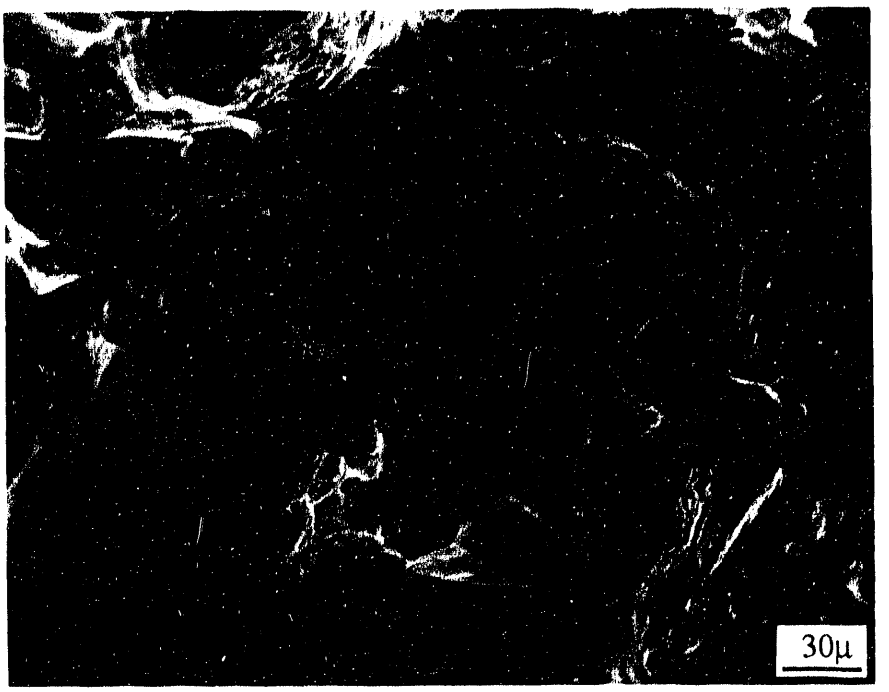

Figure 12. Fracture surface morphology of Inconel 617 hot ductility sample tested for on-heating at 1010°C.

800H will be undertaken for alloy modification investigations.

REFERENCES

1. Swindeman, R.W., Goodwin, G.M., Maziasz, P.J., Bolling, E., "Procurement and Screening Test Data for Advanced Austenitic Alloys for 650°C Steam Service (Part 1, 14Cr-16Ni Steels and 20Cr-30Ni-Fe Alloys)," ORNL/TM-10206/P1, April 1987.

2. Lundin, C.D., Qiao, C.Y.P., Kikuchi, Y., Shi, C., and Gill T.P.S., "Investigation of Joining Techniques for Advanced Austenitic Alloys," Final Report, ORNL/Sub/88-07585/02, May 1991.

3. Swindeman, R.W., and Maziasz, P.J., "Evaluation of Advanced Austenitic alloys Relative to Alloy Design Criteria for Steam Service - Part 2 - 20 to 30% Chromium Alloys," ORNL-6629/P2, June 1991.

WHC-2 - ELECTRO-SPARK DEPOSITED COATINGS FOR PROTECTION OF MATERIALS IN SULFIDIZING ATMOSPHERES

R. N. Johnson

Westinghouse Hanford Company
P. O. Box 1970, L6-39
Richland, WA 99352

INTRODUCTION

The objective of this program is to develop candidate coatings, using the Electro-Spark Deposition (ESD) process, for the protection of materials in sulfidizing atmospheres typical of fossil energy applications.

The ESD process contributes a new dimension to materials for fossil energy applications by allowing the investigation of surface compositions that are difficult or impractical to achieve by other processes. A wide range of both stable and meta-stable surface alloys and structures can be produced by the ESD alloying and by the rapid solidification inherent in the process. Not only can the standard corrosion-resistant alloys be formed or deposited, for example, but it is also possible to apply refractory metal alloy diffusion barriers on the surface or between the substrate and primary corrosion protection coatings.

Coatings of interest include single or multi-layer deposits of commercially available hardfacing alloys, as well as custom formulations of metal aluminides, chromium alloys, refractory metals, carbides, silicides, and borides. Materials to be protected include low alloy steels, Alloy 800, Type 310 stainless steel, and modified ("lean") stainless steels.

Background

Electro-spark deposition is a pulsed-arc micro-welding process that uses short-duration, high-current electrical pulses to weld a consumable

electrode material to a metallic substrate. The short duration of the electrical pulse allows an extremely rapid solidification of the deposited material and results in an extremely fine-grained, homogeneous coating that may be amorphous for some materials. The microstructures produced by ESD can provide exceptional corrosion-resistance and wear-resistance for many materials.

The ESD process is one of the few methods available by which a fused, metallurgically-bonded coating can be applied with such a low total heat input that the bulk substrate material remains at or near ambient temperatures. This eliminates thermal distortions or changes in metallurgical structure of the substrate. Since the coating is metallurgically bonded, it is inherently more resistant to damage and spalling than the mechanically-bonded coatings produced by most other low-heat-input processes such as detonation gun, plasma spray, electro-chemical plating, etc. Nearly any electrically-conductive metal, alloy or cermet can be applied by ESD to metallic substrates.

Further background information on the ESD process is provided in Reference 1.

Discussion of Prior Activities

Data collected so far indicate that ESD coatings tend to show lower corrosion rates in most environments than the same material would in either bulk form or as a coating applied by other processes. For example, ESD-applied coatings of chromium carbide-15% nickel exhibit significantly lower corrosion rates in aqueous and liquid metal environments than similar detonation-gun applied coatings.[2] The superior performance of the former is attributed to the extremely fine-grained, nearly amorphous structure inherent to the ESD coatings compared to the larger-grained, more heterogeneous detonation-gun coatings.

In tests at Argonne National Laboratory (ANL), this same ESD coating (chromium carbide-15% nickel) showed four times better sulfidation resistance than Type 310 stainless steel at 875°C.[3]

Normally, this composition would not be expected to perform that well because of the strong susceptibility of a nickel matrix to sulfidation attack. Again, the fine grain structure is believed to be a major factor in the corrosion resistance. This observation is in agreement with other Fossil Energy Materials Program work that indicates one mechanism of improving lifetimes of protective oxide films and scales is to maintain as fine a grain structure as possible.[4] Further improvement in corrosion resistance of the chromium carbide coating was achieved by alloying aluminum into the surface by a further ESD treatment.[5]

One of the most significant advances in ESD coatings for use in sulfidation environments has been the successful development of Fe_3Al as a coating material. Oak Ridge National Laboratory (ORNL) has demonstrated the exceptional corrosion properties of Fe_3Al in bulk form, but alloying the Fe_3Al to achieve acceptable mechanical properties so far appears to compromise the corrosion performance. As one alternate approach, ORNL supplied electrode materials to Westinghouse Hanford Company (WHC) for use in ESD coating development. (Using Fe_3Al as a coating material allows the selection of the substrate material for optimum mechanical properties and economy while retaining the corrosion resistance offered by the coating.) The coating results to date have been outstanding. The ESD parameters have been developed to the point that consistent, defect-free coatings over 100 μm thick can be applied relatively rapidly with good transfer efficiency. The Fe_3Al appears to produce some of the best coatings of all the materials evaluated for ESD application.

Further coating development is proving that the corrosion performance of the Fe_3Al coating can be significantly enhanced by the use of multi-layer ESD coating techniques. Sulfidation corrosion tests at ANL[5,6], for example, showed the beneficial effects of applying a Nb-1Zr diffusion barrier coating. The corrosion rate of an ESD coating of Fe_3Al was reduced by a factor of 2 in tests at 500°C when an intermediate ESD coating of Nb-1Zr was first applied to the steel, when compared to the same Fe_3Al coating applied directly to the steel.

DISCUSSION OF CURRENT ACTIVITIES

Improved Fe_3Al Coatings

Analyses of the Fe_3Al coatings with and without the Nb-1Zr diffusion barrier coating led to the conclusion that one of the principal reasons for the improved corrosion performance of the Fe_3Al coating over the Nb-1Zr layer was the higher aluminum content of the coating surface.[7] Scanning Electron Microprobe (SEM) analyses showed that the intermediate diffusion barrier reduced the dilution of substrate elements into the coating weld zone and resulted in about 50% more aluminum in the surface of the coating (15% vs. 9.5%).

An obvious next step in developing improved coatings is to further increase the aluminum content of the surface by ESD treatments and to explore the effects of various levels of aluminum in the composition. We used commercially pure aluminum electrodes to directly alloy aluminum into the Fe_3Al coating surface by ESD. The results so far have been disappointing. Although aluminum is successfully alloyed into the surface, the resulting alloy contains too many defects and cracks to be acceptable as a corrosion barrier coating. Further development of the ESD coating parameters has reduced, but so far not eliminated, the cracking tendencies. We believe the most likely method of producing an acceptable coating will include the use of a prealloyed electrode, such as the FeAl compositions in development at ORNL. We are awaiting the fabrication of the higher aluminum content materials into suitable electrode geometries.

Development efforts on another improved Fe_3Al-base coating candidate were more successful. The new coating consists of one layer of Nb-1Zr alloy diffusion barrier ESD coating applied to an iron-base alloy substrate, followed by a layer of Fe_3Al, which is then treated with a light alloying addition of platinum in the third layer. The benefits of the refractory metal diffusion barrier were discussed above, while experience in gas turbine coating applications has demonstrated that small alloying additions of Pt to aluminide coatings improves the

stability and life of the protective oxide film formation. (Such small amounts of Pt are used that these coatings can still be economically attractive.) The new coating is to be corrosion tested at ANL in FY 1992.

ESD Equipment Development

Development of an improved ESD welding power supply was completed. The new power supply increases the range and control of useable welding parameters with the result that we can now produce higher deposition rates while maintaining good coating uniformity and surface roughness control. Previous power supplies produced high deposition rates only at the expense of decreased coating uniformity or smoothness. While the new supply does not eliminate that general relationship, it does extend the useable range of deposition rates for a given surface structure desired. Further power supply improvement objectives have been identified for the next phase of development.

Fabrication of a prototype ESD applicator for coating the inside diameters of tubes and holes was completed. The applicator is designed to coat holes as small as 1.25 cm diameter x 15 cm deep. Holes 10 cm or larger can be coated up to 50 cm deep. An improved ID applicator capable of coating much longer lengths of tubing is being designed. Its ultimate capabilities will be determined by the availability of special geometry electronic components we are attempting to procure.

Technology Transfer Activities

We are involved in assisting in the start-up of a new business in Portland, OR, aimed at further commercialization of the ESD process. Activities have included training of personnel, recommendations for equipment and materials, and consulting on techniques and process parameters. Successful commercial applications of ESD now in production at the new organization include:

a) Wear resistant coatings on recreational and sports equipment. One example of a unique application was the coating service supplied to the 1991 U.S. Everest Expedition. Many of the light alloy (aluminum or titanium) climbing gear components, such as crampons, ice axes and various safety and rope handling tools were subjected to heavy wear and performance degradation during the course of the climb. Uncoated components were worn out, but those that were ESD coated with wear-resistant carbides were in near-new condition at the completion of the expedition. The coatings earned high praise from the successful U.S. team.

b) Knife and fish-hook sharpeners. ESD coated knife sharpeners are now appearing in specialty fishing gear catalogs. Customers report the ESD coated sharpeners cost less than diamond-impregnated sharpeners, but are equally effective and outlast the diamond sharpeners by several times.

c) Shredders in recycling plants. ESD coatings applied to paper and materials shredder teeth in a Portland recycling center increased the life of the shredder teeth by a factor of seven.

REFERENCES

1. R. N. Johnson, "Principles and Applications of Electro-Spark Deposition", *Surface Modification Technologies*, T. S. Sudarshan and D. G. Bhat, eds., The Metallurgical Society, January 1988, pp. 189-213.

2. R. N. Johnson, "Coatings for Fast Breeder Reactors", in *Metallurgical Coatings*, Elsevier Sequoia, S. A., New York, 1984, pp. 31-47.

3. K. Natesan and R. N. Johnson, "Corrosion Resistance of Chromium Carbide Coatings in Oxygen-Sulfur Environments", *Surface and Coatings Technology*, Vol, 33, 1987, pp. 341-351.

4. I. G. Wright and J. A. Colwell, "A Review of the Effects of Micro-Alloying Constituents on the Formation and Breakdown of Protective Oxide Scales on High Temperature Alloys at Temperatures Below 700°C", ORNL/Sub/86-57444/01, September 1989.

5. K. Natesan and R. N. Johnson, "Development of Coatings with Improved Corrosion Resistance in Sulfur-Containing Environments", presented at the International Conference on Metallurgical Coatings, San Diego, April 1990, published in *Surface and Coatings Technology*, Vol. 43/44, 1990, pp. 821-835.

6. R. N. Johnson, "Electro-Spark Deposited Coatings for Protection of Materials in Sulfidizing Environments", *Proceedings of the Fourth Annual Conference on Fossil Energy Materials*, ORNL/FMP-90/1, August 1990, pp. 321-329.

7. R. N. Johnson, "Electro-Spark Deposited Coatings for Protection of Materials in Sulfidizing Atmospheres", *Proceedings of the Fifth Annual Conference on Fossil Energy Materials*, ORNL/FMP-91/1, September 1991, pp. 281-288.

PART IV - CORROSION AND EROSION RESEARCH

ANL–3 – CORROSION AND MECHANICAL PROPERTIES OF ALLOYS IN FBC AND MIXED–GAS ENVIRONMENTS

K. Natesan and J. H. Park

Argonne National Laboratory
Materials and Components Technology Division
Argonne, IL 60439

INTRODUCTION

The purposes of this program are to (1) evaluate mechanisms of oxidation, sulfidation, and breakaway corrosion in chromia– and alumina–forming alloys and coatings exposed to mixed–gas atmospheres that span the wide range of oxygen and sulfur partial pressures typical of both combustion and gasification systems; (2) develop an understanding of the role of several microalloy constituents (e.g., Zr, Nb, Y, Ce) in oxidation/sulfidation processes; (3) characterize the physical, chemical, and mechanical properties of surface oxide scales that are resistant to sulfidation attack; and (4) evaluate the role of deposits, such as fluidized bed combustor sorbents containing sulfur and/or chlorine and ash constituents, in the corrosion behavior of metallic alloys and selected coatings.

DISCUSSION OF CURRENT ACTIVITIES

During the current reporting period, extensive oxidation experiments were conducted to evaluate the roles of reactive element additions in the oxidation kinetics and transport properties in the oxide scales. The corrosion resistance of structural alloys in high–temperature environments is achieved by the formation of a continuous chromium oxide (Cr_2O_3) scale. The scale can be treated principally as a rate–determining solid–state diffusion barrier between the environment and the alloy substrates. It is generally recognized that when the alloys are exposed to mixed–oxidant environments containing sulfur, the sulfur is the primary cause of the accelerated corrosion of these alloys.[1–3]

The generally accepted[4–7] defect reaction that is operative in nonstoichiometric Cr_2O_3 at high temperatures is

$$3/2\,O_2\,(g) \;=\; 2\,V_{Cr}^{'''} \;+\; 6\,Cr_{Cr}^{\cdot} \;+\; 3\,O_O^{x}, \qquad (1)$$

where $V_{Cr}^{'''}$, $Cr_{Cr}^{\cdot}$, and O_O^{x} represent, respectively, a triply ionized chromium vacancy, an electron hole trapped in a chromium site, and normal oxygen in the oxygen site. Based on extensive measurements of the electrical conductivity and electrochemical properties of thermally grown Cr_2O_3 scales in alloys without reactive element additions over a wide range of temperatures and oxygen partial pressures, several conclusions were drawn:[7]

1. Electrical conductivity data obtained on thermally grown specimens of $Cr_{2-\delta}O_3$ showed p-type behavior over a wide temperature range and over a wide range of oxygen partial pressures from that of air to that of the Cr/Cr_2O_3 equilibrium. At temperatures above 1000°C, chromium oxide exhibited predominantly intrinsic semiconductor behavior.

2. Good agreement was reported between the Cr oxidation rates measured by a thermogravimetric method with those determined from in situ measurement of electrical conductivity and electromotive force across the oxide layer.

3. The mobility of holes increased with an increase in temperature at fixed oxide compositions. The hole carrier concentration increased slightly with an increase in temperature at a fixed oxide composition.

Reactive element additions are made to structural alloys for the purpose of reducing the oxidation kinetics and to enhance the adhesion of the scale to the alloy substrate. When alloys contain so called "reactive elements" or "oxygen active elements," i.e, Y, La, and Ce, etc., the growth rate of the oxide layer is reduced and adhesion of the oxide layer to the base alloy is enhanced, especially at high temperatures.

The objective of the present work is to observe the overall schemes for the oxidation of the chromia-forming alloys of Fe-25Cr with and without additions of reactive elements (such as Ce, and Y) over a lower temperature range than previously studied. In addition, the beneficial effect, if any, of these elements in mixed oxidant environments that contain sulfur and/or chlorine species will be evaluated.

EXPERIMENTAL PROCEDURE

THERMOGRAVIMETRIC ANALYSIS OF Fe-25Cr OXIDATION- Oxidation studies were performed on samples of Fe-25Cr and Fe-25Cr-0.3Y with a CAHN electrobalance. Samples were suspended by a Pt wire, and a reaction gas was admitted from the bottom of the chamber. The samples were heated in the reaction gas to the desired temperature, and changes in sample weight were monitored continuously. Oxidation temperature was in the range of 700-1000°C and oxygen partial pressure (pO_2) was controlled by flowing oxygen, air, 1 vol.%CO-CO_2, and 18 vol.%CO-CO_2. After cooling, the oxidized samples were examined by a scanning electron microscopy (SEM): Both the surface and cross section of cold-mounted samples were evaluated. Other samples of Fe-25Cr (with as-received and enlarged grain size), Fe-25Cr-1Y, and Fe-25Cr-1Ce were oxidized at 1000°C in an O_2-N_2 gas mixture with a pO_2 of 10^{-4} atm.

ELECTRICAL RESISTIVITY OF OXIDIZED FOILS- Electrical resistivity of the oxidized samples of Fe-25Cr and Fe-25Cr-1Ce was measured by a standard four-probe method at a fixed DC current from a Keithley Calibrator/Source Model 263 over a range of 10-100 mA.

RESULTS AND DISCUSSION

OXIDATION OF Fe-25Cr AND Fe-25Cr-0.3Y- Figure 1 shows calculated equilibrium pO_2 for several gas mixtures and metal/metal oxides as a function of temperature. Figure 2 shows test data from thermogravimetric analysis (TGA) of the Fe-25Cr alloy oxidized in air, whereas Fig. 3 shows weight change versus time of oxidation of Fe-25Cr and Fe-25Cr-0.3Y alloys in gas mixtures of 1 vol.% CO-CO_2 and 18 vol.% CO-CO_2 at 1000°C. The rate of weight change of the Fe-25Cr alloy exposed to 1 vol.% CO-CO_2 is much higher than that of other alloys. This finding could be

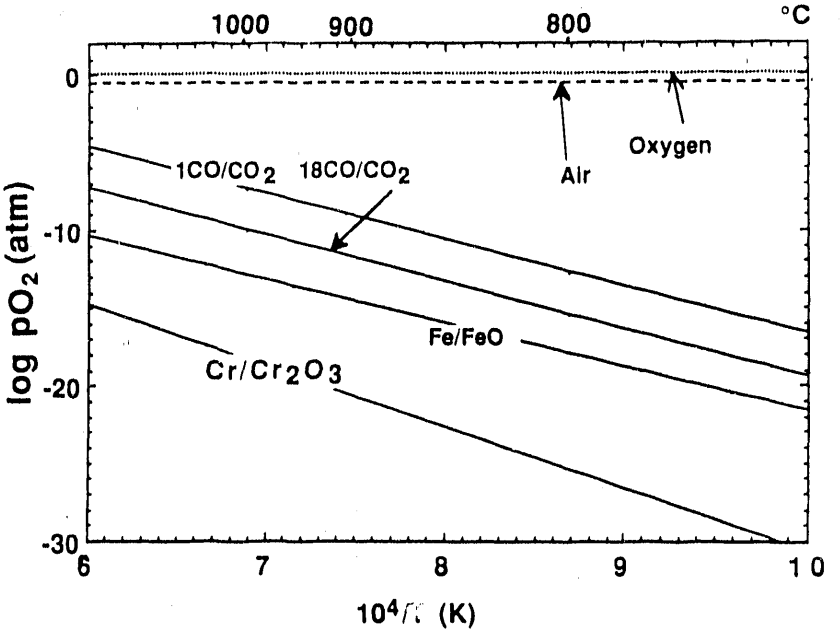

Fig. 1. Log pO2 versus inverse temperature for various gas mixtures and metal/oxide equilibria

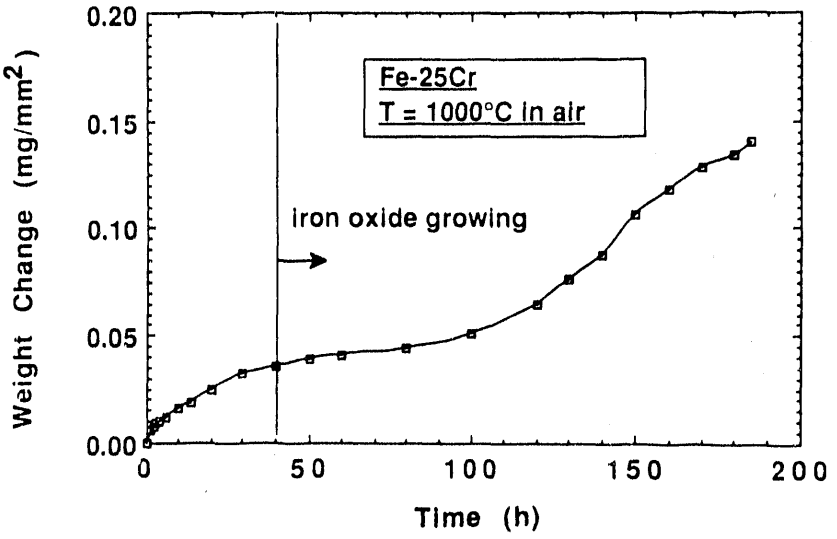

Fig. 2. Weight change versus time during oxidation of Fe–25Cr and Fe–25Cr–0.3Y alloys at low pO2

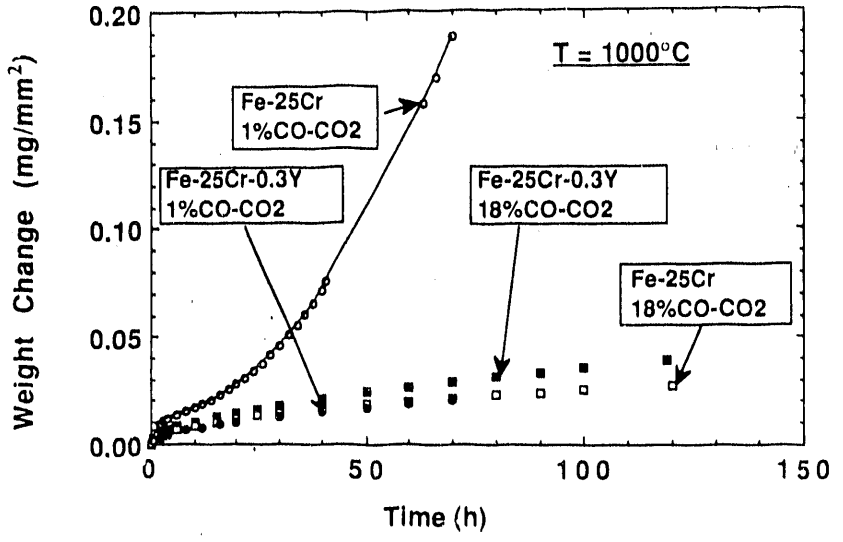

Fig. 3. Weight change versus time during oxidation of Fe–25Cr in air

explained by the composition of the growing scale, i.e., the outer surface of the sample was completely covered with an $Fe_{3-\delta}O_4$ scale; the inner surface with an $Fe_{1-\delta}O$ inner scale[8]. However, in the case of the 18 vol.% CO-CO_2 gas mixture, no iron oxide or large grain scale was observed on the sample surface, because the pO_2 values was not sufficient to form Fe oxides. At other temperatures and pO_2 value, tests did not show any significant difference in oxidation rates, even though TGA and visual observation of the cross sections of the oxidized scales showed a small amount of Fe. At high pO_2, the formation of hematite ($Fe_2O_{3-\delta}$) is expected. Hematite has the same crystal structure, i.e., corundum as chromium oxide, which would be expected to have diffusion properties similar to those of chromium oxide.

Oxide scales formed on alloys with small amount of Y contained no iron oxide over the wide range of temperature and pO_2 of the present investigation. The absence of iron oxide may be explained by the predominance of anion transport[9]. However, the values of the parabolic rate constant were similar for alloys with and without reactive elements, and the oxidation process seemed to be controlled by ionization of Cr at the scale/alloy interface. At 700°C and low oxygen partial pressures, calculated scale thickness from weight-change data by TGA exceeds the measured scale thickness

determined by SEM, which indicates that internal oxidation or solubility of some species occurs within the metal.

OXIDATION OF Fe-25Cr, Fe-25Cr-1Ce, AND Fe-25Cr-1Y AT 1000°C- After a 19-h oxidation and thermal quench of a Fe-25Cr specimen, the oxide scale separated from the substrate. At high magnification, 1-μm edge cracks were apparent in the 15-20 μm scale near the scale/alloy interface. Scale bending due to plasticity of the scale at elevated temperatures, and scale spallation due to thermal expansion mismatch between the scale and substrate alloy were also observed.[10] Analysis of the fracture surfaces of the spalled oxide scales by SEM and electron energy dispersive spectroscopy (EDS) showed that the scales were pore-free pure chromia. The presence of grinding/scratch marks remaining on the interface (i.e., scale/alloy interface of the spalled oxide) indicates that outward diffusion of cations through the oxide scale was dominant and similar to that observed in marker experiments.[11,12] Beneath the spalled scale, the alloy side of the scale/metal interface showed a number of small crystals. Analysis by EDS indicated that these crystals were Cr_2O_3. Crystal growth near the interface can be explained by

1. vapor phase transport of Cr at the reduced pO_2 present at the alloy/scale interface;
2. separation of alloy/scale interface at an earlier stage of the oxidation;
3. the gap between alloy substrate and scale could be wider than the crystal dimension which is, in this case ≈1 μm; and
4. the possibility of inward oxygen diffusion through the scale.

Grain-boundaries in the alloy substrate exhibited very fine grooving at the alloy surface, to a depth similar to the oxide grain size. This indicates good adhesion between scale and alloy substrate in the early stage of oxidation. No scale spallation was observed in the reoxidized sample after treatment by thermal quenching.

For longer oxidation times, weight-change versus time curves showed an abrupt increase in weight gain. A typical plot is shown in Fig. 2 for an Fe-25Cr specimen at 1000°C in high pO_2. Initially, a chromia scale formed. After ~100 h, the chromia scale became covered with fast-growing iron oxide. From sudden increase in

weight gain shown in Fig. 2, it is concluded that outward transport of Fe and subsequent oxidation are dominant features in long-term oxidation.[13] Typical chemical compositions of the scale layer after ~200 h of exposure are listed in Table 1. The scales and alloy substrates were observed visually before and after oxidation experiments. Enlarged alloy grains were seen in Fe-25Cr alloys after exposure. Since substantial grain growth was observed in alloy substrates, further studies focused on grain growth during oxidation of alloys with and without Y addition.[13]

According to the literature,[14] solid solubility of Y in Cr is 0.71 atomic percent; of Cr in Y is 0.70 atomic percent. However, the difference in the respective atomic radii of Cr and Y, as well as parametric data, suggests that the solid solubility of Y in Cr is < 0.005 atomic percent. In the Fe-Y phase diagram, a stable compound, Y_2Fe_{17}, with an hexagonal structure has been reported. In previous studies of the Fe-25Cr-0.87Y alloy, $Y_2(Fe, Cr)_{17}$ was identified in the alloy grain boundary.[15]

Samples of Fe-25Cr and the Y–containing alloy were oxidized, cold-mounted for SEM, and etched in slightly acidic solution to dissolve the alloy around the scale to examine the scale microstructure. The cross sections of the Fe-25Cr specimens showed large differences in grain size after oxidation at temperatures between 700 and 1000°C. However, in Fe-25Cr-1Y, no grain-growth was observed (Fig. 4). At temperatures below 800°C, no significant grain growth occurred in either of the alloys.

Table 1. Chemical compositions from EDS analysis, of scale on Fe-25Cr Alloy

Scale location	Cation composition
Outer scale	Fe
Thin scale (outer)	3Fe-97Cr
Outer middle scale	50Fe-50Cr
Inner middle scale	51Fe-49Cr
Thin scale (inner)	1Fe-99Cr

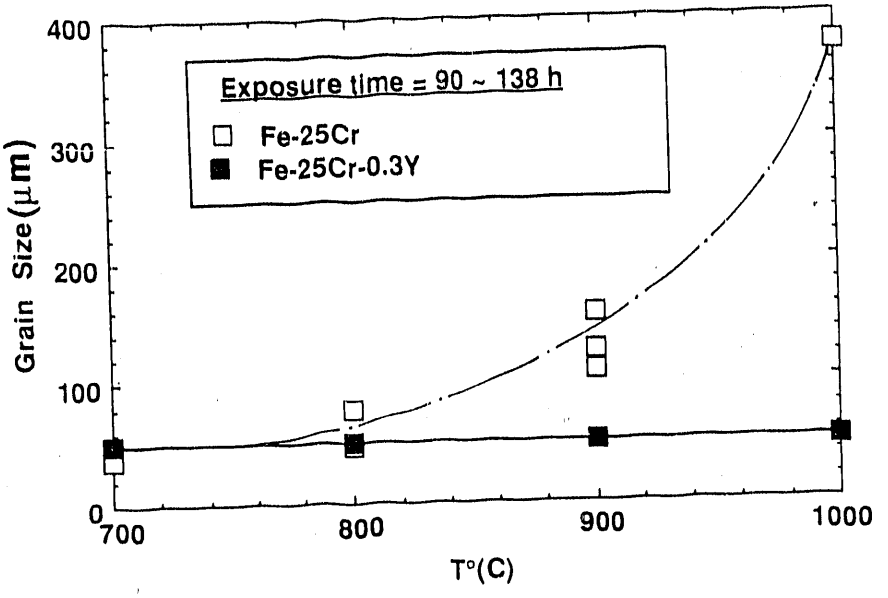

Fig. 4. Grain size of Fe–25Cr and Fe–25Cr–1Y alloys after oxidation at temperatures between 700 and 1000°C for 90 to 135 h

OXIDATION OF Fe-25Cr AFTER VACUUM ANNEAL AT 1000°C FOR 24 H- To investigate scale spallation in the Fe-25Cr alloy and the causes of grain growth during oxidation, alloy samples of Fe-25Cr were annealed in a vacuum at 1000°C for 24 h 40 min, and then oxidized for 20 h. Weight-change with time was compared with the oxidation of an as–received sample (1st run) and a spalled sample (2nd run). The oxidation behavior of the annealed sample, which had an enlarged grain size, was similar to that of the spalled sample (2nd run). No spallation was observed after thermal quenching of the annealed sample.

ELECTRICAL RESISTIVITY OF OXIDIZED FOILS- Figure 5 shows the log ohmic resistance versus reciprocal temperature for the oxide Fe-25Cr and Fe-25Cr-1Ce alloys. The ohmic resistance of the oxide scales that formed on the Ce-containing alloy was higher than that of the scale on the Fe-25Cr alloy. These results can be analyzed by the defect incorporation scheme described below. In the high-pO_2 region, the most stable valence state of Ce is +4. When cerium is incorporated into the cation sublattices at either the Cr (+3) or Fe (+3) site,

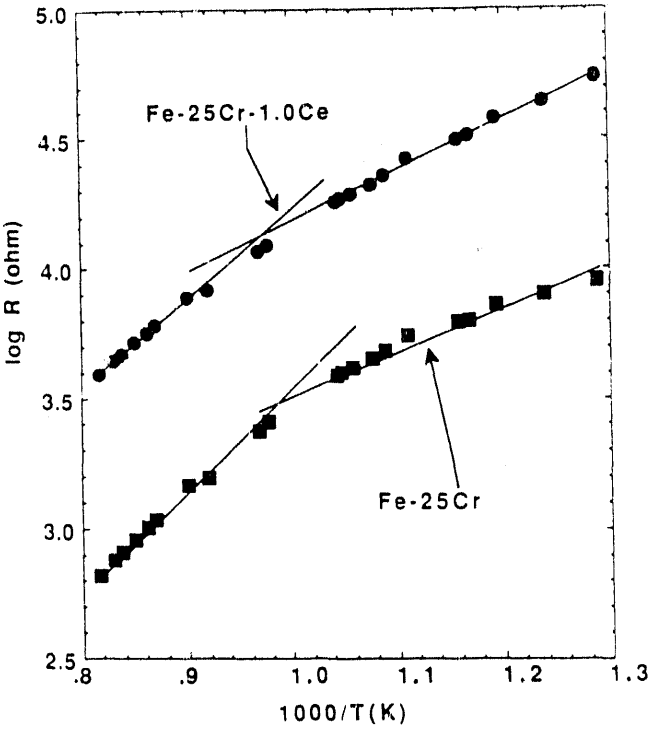

Fig. 5. Log (R, ohmic resistance) versus inverse temperature for oxidized foil samples of Fe–25Cr and Fe–25Cr–1Ce

$$CeO_2 = Ce^{\bullet}_{Cr\ (or\ Fe)} + 1/2\ O_2\ (g) + 3/2\ O^{x}_{o} + e'. \qquad (2)$$

Similarly, when we consider the cation interstitial as a point defect, incorporation of the Ce ion may be written as

$$CeO_2 = Ce^{\bullet}_{i} + 1/2\ O_2\ (g) + 3/2\ O^{x}_{o} + e'. \qquad (3)$$

In either case, electrons are produced as a charge-compensating defect. The electron holes are annihilated by recombination with electrons, i.e.,

$$nil = e' + h^{\bullet}. \qquad (4)$$

Consequently, the ohmic resistance increases, i.e., electrical conductivity decreases. Our studies indicate that Cr_2O_3 is predominantly a p-type semiconductor[7], as is the oxide developed on Fe-25Cr.

To observe the kinetics of cation mixing for Fe/Cr in the alloy oxide, the ohmic value was monitored as a function of time to obtain diffusion information. In the diffusion analysis, a thin-plate model was introduced with the condition of no oxygen chemical potential (μO_2) gradient across the sample. Results of the apparent and bulk diffusivity are plotted in Fig. 6. The apparent diffusivity is based on the overall thickness of the specimen, whereas, in calculating the bulk diffusivity, the oxide grain size was used. Oxygen diffusion data, obtained from literature, are also plotted.[16,17] The data indicate that at high temperatures, inward diffusion of anions becomes a possibility during the oxidation of Fe-25Cr when Fe becomes mixed in the scale. However, at lower temperatures, outward diffusion of cations is expected, based on the data in Fig. 6.

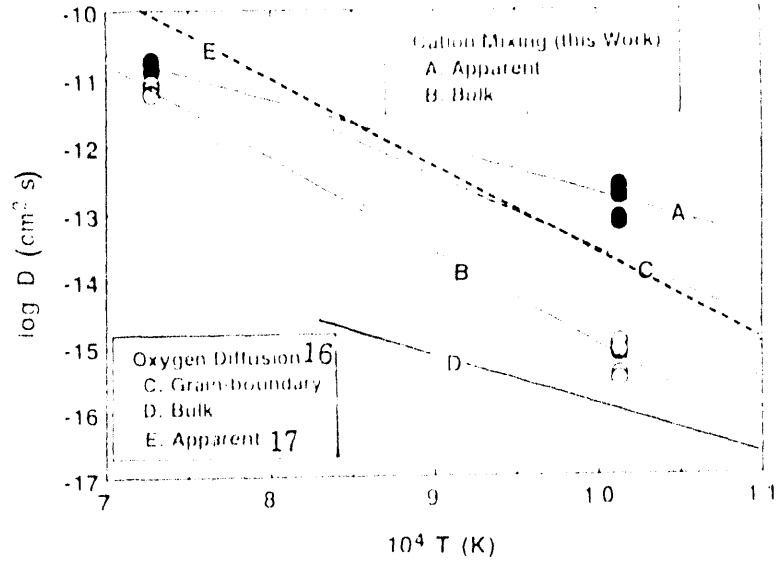

Fig. 6. Temperature dependence of cation and oxygen diffusion in thermally growing scales on Cr and Fe–25Cr alloys

SUMMARY

1. The major role of reactive elements in oxidation Fe-Cr alloys is to suppress Fe diffusion through the scale.

2. Reactive elements inhibit grain growth in the alloy. Consequently, no spallation of thermally grown scale was observed, even under thermal quenching conditions.

3. In alloys without reactive elements, scale spallation was minimized by large alloy grain size. However, outward diffusion of Fe occurred in a manner similar to that in alloys with normal grain size.

4. Alloy grain growth, in decreasing order is as follows:
   Fe-25Cr >> Fe-25Cr-1Ce > Fe-25Cr-1Y.

REFERENCES

1. T. C. Tiearney, Jr., and K. Natesan, "Sulfidation–Oxidation Behavior of Advanced Metallic Materials in Simulated Low–Btu Coal–Gasifier Environments," Oxid. Met., 17 (1982) 1.

2. K. Natesan, "Oxidation of Alloys in Bioxidants," Symposium on Oxidation of Metals and Associated Mass Transport, M. A. Dayananda, S. J. Rothman, and W. E. King (eds.), TMS–AIME, 1987, p. 161.

3. N. Birks and G. H. Meier, Introduction to High Temperature Oxidation of Metals (Edward Arnold, London, 1983).

4. T. F. Kassner, L. C. Waters, and R. E. Grace, Proc. Symp. Thermodynamics with Emphasis on Nucl. Mater. Atomic Transport in Solids, I.A.E.A., Vienna, 1966, p. 357.

5. K. Hoshino and N. L. Peterson, J.Am. Ceram. Soc., 1984, p.C112.

6. L. C. Walters, and R. E. Grace, J. Appl. Phys., 36(8), 1965, p. 2331.

7. J. –H. Park and K. Natesan, Oxid. Met., 33, 1990, p. 31 and Transport Properties of Thermally Grown Cr_2O_3, Argonne National Laboratory Report ANL/FE–89/5, 1989.

8. Dieckmann, R., "Proc. Symp. Metall. Soc. AIME and MSD-ASM Atomic Transport Activity," TMS-AIME Fall Meeting, Orlando, FL, Oct. 6-7 (1986): p. 7.

9. King, W. E. and J.-H. Park, Coll. De Phys. 51 C1-551-556 (1990)

10. Evans, A. G. and R. M. Cannon, "Proc. Symp. Metall. Soc. AIME and MSD-ASM Atomic Transport Activity, "TMS-AIME Fall Meeting, Orlando, FL, Oct. 6-7 (1986): p. 135

11. Giggings, C. S. and F. S. Pettit, Trans. Metall. Soc. AIME 245 2495 (1969)128. Kofstad, P. and A. Z. Hed, Werkst. Korros. 21 894 (1970)

12. P. Kofstad and A. Z. Hed, Werkst. Korros. 21 894 91970).

13. Park, J.-H. and K. Natesan, unpublished information

14. Hansen, M., "Constitution of Binary Alloys", McGraw-Hill Book Co., New York, (1958)

15. King, W. E., N. L Peterson, and J. F. Reddy, J. Physique 46 C4-423 (1985)

16. Graham, M. J., J. I. Eldridge, D. F. Mitchell, and R. J. Hussey, Mater. Sci. Forum 43 207 (1989)

17. Park, J.-H. and K. Natesan, "Transport Properties of Chromium and Fe-Cr Alloys Exposed to Oxygen/Sulfur Environments", Fourth Berkeley Conf. on Corrosion-Erosion-Wear of Materials at Elevated Temperatures, January 31 - February 2, 1990, Berkeley, California, to be published by NACE

LBL-3-WASTAGE OF STEELS IN THE EROSION-CORROSION (E-C) ENVIRONMENTS OF FLUIDIZED BED COMBUSTORS

A. V. Levy, B. Q. Wang, G. Q. Geng

Lawrence Berkeley Laboratory
University of California
Berkeley, California 94720

INTRODUCTION

The erosion of material surface by small particles carried in gas and liquid carriers is being investigated. The materials are tested over a range of conditions that simulate portions of the operating environment of containment surfaces in coal gasification, liquefaction and fluidized bed combustion processes. The effects of materials' properties, compositions and test temperature on their erosion behavior are determined. The effects of elevated temperature corrosion in combination with the erosion are studied to determine the mechanisms and rates of the combinesd surface degradation modes.

DISCUSSION OF CURRENT ACTIVITIES

3-2- Erosion-Corrosion Studies

The Relationship Between Erosion-Corrosion Metal Wastage and Temperature

The tests were carried out in an elevated temperature blast nozzle type of tester.[1] Air was utilized as the carrier gas for the particles, creating a generally oxidizing atmosphere. the target materials for the E-C tests were 1018, 2.25Cr1Mo and 2.5Cr0.55Mo1.4Si steels. The typical compositions of the steels tested are listed in Table 1. Tests were carried out at different temperatures: 150°, 250°, 350°, 450°, 500°, 550° and 650°C at V=2.5 m/s, using 180 μm angular Al_2O_3 particles. A test time of 100 hours was used at a particle loading of 7500 gm at an impact angle of 30°. The test conditions nearly simulated those experienced by in-bed FBC heat exchanger tubes.

TABLE 1

TYPICAL STEEL COMPOSITION (wt. %)

Steel	Fe	C	Cr	Mo	Mn	Si	S	P
1018	Bal	0.14-0.20	-	-	0.6-0.9	≤0.60	≤0.05	≤0.04
2.25Cr1Mo	Bal	0.15	2.0-2.5	0.9-1.1	0.3-0.6	≤0.5	≤0.03	≤0.03
2.5Cr0.55Mo1.4Si	Bal	0.1	2.5	0.55	0.45	1.4	≤0.02	≤0.03

The metal wastages of the specimens were determined by measuring the cross-sectional thickness of the sound metal after testing using an optical micrometer accurate to 0.1 μm to observe a cross section through the central part of the erosion zone and comparing it to the thickness of metal in the same area before test that was determined using a micrometer device accurate to 1 μm.

A summary of all of the test results is shown in Figure 1.

Thickness loss-Temperature Curve

It can be seen in Figure 1 that there are different relationships between E-C metal wastage and temperature for 1018 and 2.25Cr1Mo steels compared to 2.5Cr0.55CrMo1.4Si steel. The metal wastage of the 1018 and 2.25Cr1Mo steels increased with increasing temperature, reaching a maximum at 350°C and then decreased with further temperature increases, as reported in references (2-5). Above 500°C, the E-C metal wastage dramatically increased with increasing temperature, similar to behavior reported in previous work.[6] However, for the 2.5Cr0.55Mo1.4Si steel, below 450°C the metal wastage was relatively high and constant, having little dependence on the temperature. Above 450°C the metal wastage markedly decreased with test temperature. This behavior has been consistently observed on in-bed tubes in BFBC's [7][8], but until now has never been duplicated in laboratory tests.

1018 and 2.25Cr1Mo steels

For 1018 and 2.25Cr1Mo steels, the shape of the temperature-metal wastage curves indicates four different regimes. The first regime occurred at temperatures below 200°C where the E-C metal wastage was relatively low and had essentially no dependence on temperature. In the second regime, from about 200°C to a maximum value at 350°C the metal wastage sharply increased. In the third regime, above 350°C, the wastage decreased with temperature to 500°C. Above 500°C, in the fourth regime, the E-C metal wastage dramatically increased with temperature. In the low temperature regime, the low wastage was

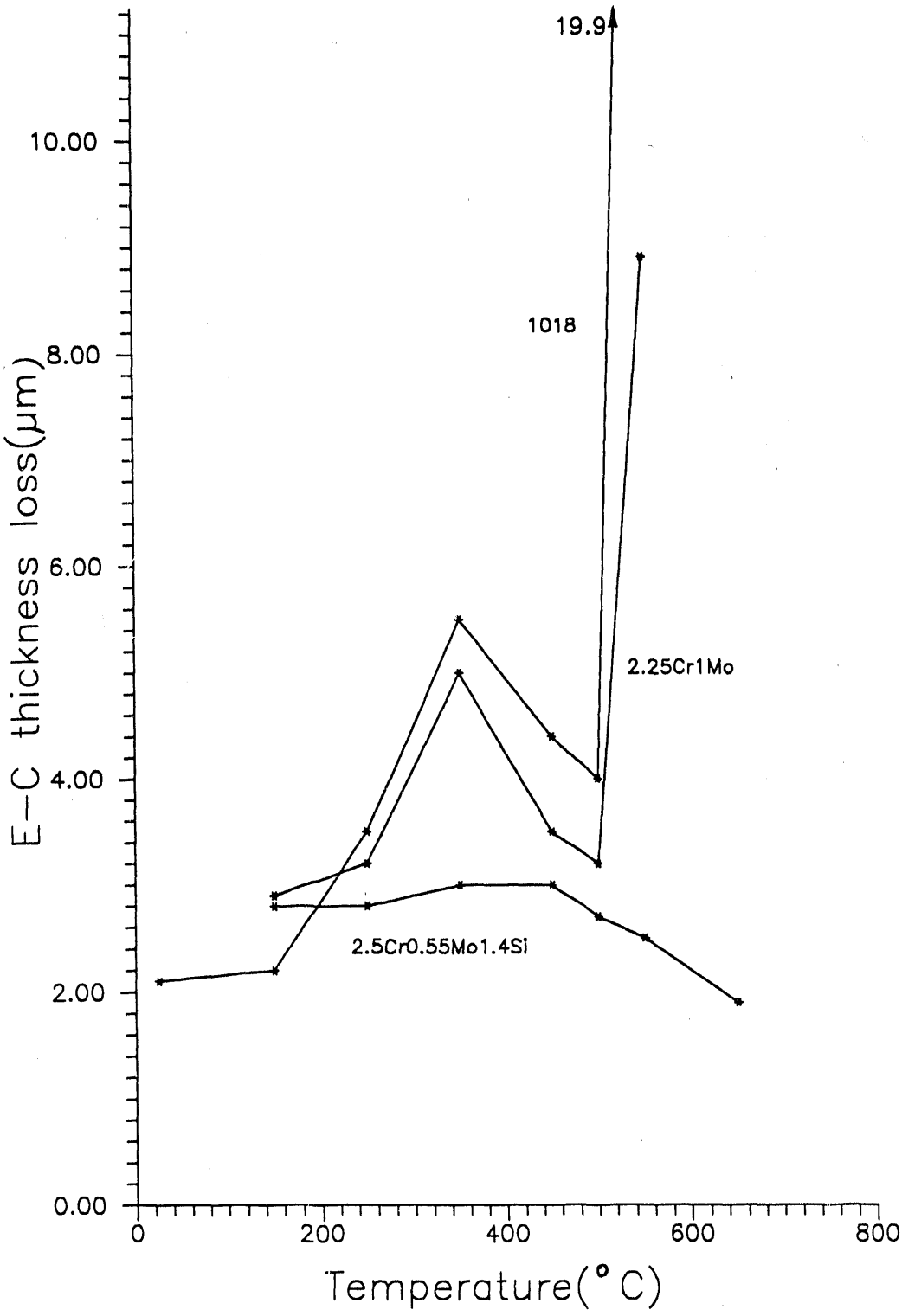

Figure 1. The plot of temperature vs. thickness loss of three steels, eroded-corroded at V=2.5m/s, α=30° by 180μm angular Al_2O_3 particles for an exposure time 100 hours.

due to mechanical wear by a process of erosion. In the second regime, where the wastage sharply increased, oxidation played a major role in the metal wastage with the rate of oxidation being greatly enchanced by the erodent particle impacts.[9] Increasing oxide plasticity and thickness were responsible for the wastage decrease with rising temperature in the third regime. The sharp increase in metal wastage at temperatures over 500°C is thought to be due to spalling of the thick scale that built up on the 1018 and 2.25Cr1Mo steels at temperatures above their free oxidation temperatures.

Figure 2 shows the plot of thickness loss versus temperature for 1018 steel eroded-corroded by 180μm angular Al_2O_3 at a higher particle velocity of 10m/s.[6] Comparing the curve in Figure 2 to that for 1018 steel in Figure 1, it is clear that particle velocity significantly influenced the relationship between metal wastage and test temperature. The presence of a wastage peak at V=2.5 m/s and none at V=10 m/s has also been observed by Stott,[10] who attributed the difference to the energy of the particles. [2] At the low particle velocity, the oxide scale, particle deposition layer developed at the higher temperature is better able to protect the surface. At the higher velocity, the particle energy is sufficient to cause a continuous material removal rate increase, even at the highest temperature studied.[10]

A possible reason for the influence of particle velocity on the relationship between E-C wastage and temperature has been discussed in previous work[6]. The particle velocity effect was attributed to the pseudoplasticity of the oxide scale at elevated temperature, which at certain elevated temperatures is related to the strain rate.[11] At low strain rates, e.g. V=2.5 m/s, the microcracking of the oxide scale essentially takes place simultaneously with crack healing to cause macroscopic plasticity of the oxide, i.e.,pseudoplasticity occurred.[11] Since plastic deformation can occur before cracking, the oxide scale can have a protective effect. However, at higher strain rates, e.g., V=10 m/s in this case, the crack healing could not take place, microcracks developed in the oxide and eventually cracking and chipping or spalling occurred. This explanation has correlated well with the observed morphologies of the affected surface and cross sections of the eroded-corroded specimens.[6]

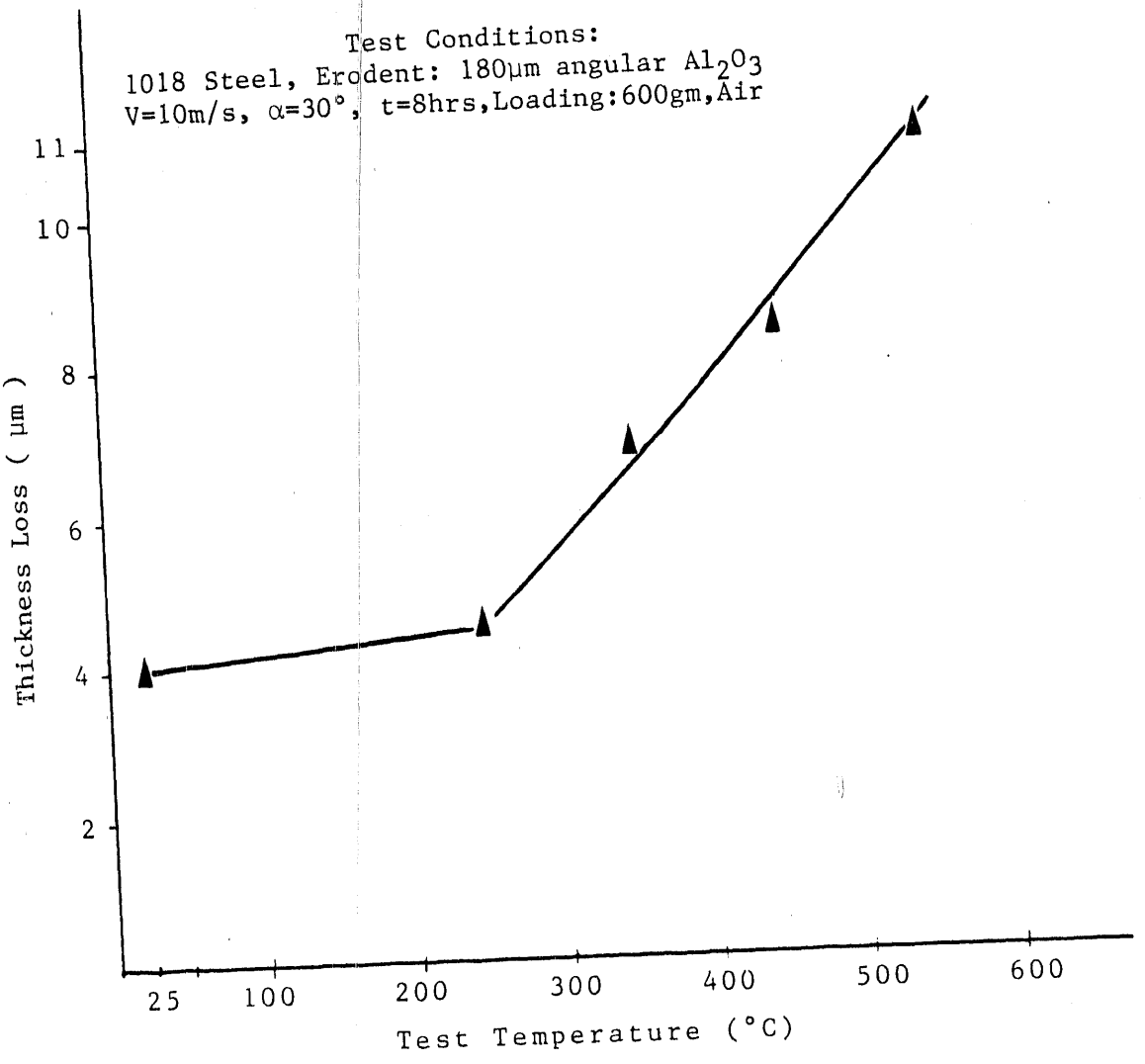

Figure 2. The plot of temperature vs. thickness loss for 1018 steel eroded-corroded by 180μm angular Al_2O_3 particles at V=10m/s, α=30°, t=8 hours.

In the present work the morphological evidence observed earlier[6] was seen again. Figure 3 shows the surfaces and cross sections of 2.25Cr1Mo steel specimens eroded-corroded at 350° and 450°C. It can be seen in (a) and (b) that at 350°C the scale is relative thin and appears to have not been ductile enough to cause plastic deformation before cracking. This resulted in crack formation and propagation with spalling also occurring, see upper left corner of (a). This corresponds to the highest E-C metal wastage. However, at 450°C, where metal loss was reduced, the oxide scale became thick and ductile enough to prevent cracks from forming, and the scale remained continuous without fracture, as the cross section shown in Figure 3d indicates. Some evidence of ductile material deformation(the presence of narrow, deep gouges, and flattened indentations,) can be seen in the surface morphology ,see Figure 3c.

Comparing the curve of 1018 steel in Figure 1 to that in Figure 2, it can be seen that when tested at V=2.5 m/s and 550°C the metal wastage had dramatically increased to 19.9μm, while when tested at a higher velocity, V=10m/s, at the same temperature, it had only increased to 11μm. This difference is primarily due to the difference in test times. The specimen tested at 2.5 m/s was exposed for 100 hours, while at 10m/s it was only exposed for 8 hours. At 550°C, which is above the free oxidation temperature of 1018 steel, the metal wastage was due to spalling of the thick scale. In this case corrosion (oxidation) played a dominant role, and the thick, brittle oxide scale broke off in relatively large pieces. Since this mechanism occurred over a much longer period in the V=2.5 m/s test, 100 hrs, than in the V=10 m/s test, 8 hrs, the metal wastage at 550°C, V=2.5 m/s was greater.

2.5Cr0.55Mo1.4Si Steel

Figure 4 is a curve of thickness loss vs test temperature of 2.5Cr0.55Mo1.4Si steel specimens along with cross section micrographs corresponding to the different test temperatures and thickness losses. It is evident that in the temperature regime below the transition temperature,[8] there is almost no scale on the surface, indicating that the oxide layer

Surface(T=350°C) 10μm

(a)

Cross section(T=350°C) 10μm

(b)

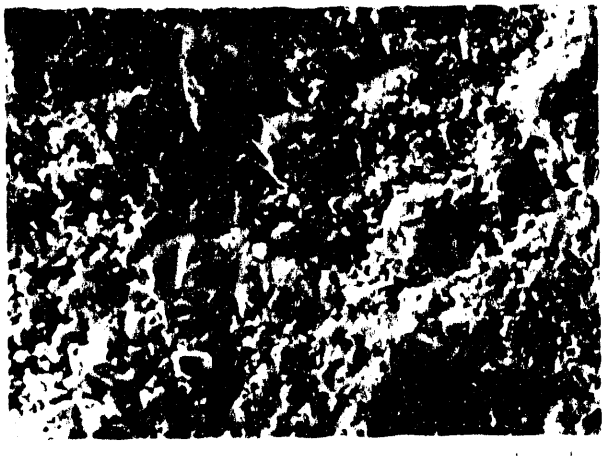

Surface(T=450°C) 10μm

(c)

Cross section(T=450°C) 10μm

(d)

2.25Cr1Mo steel
Nozzle Tester T=350°, 450°C
Corrosion-Erosion, α=30°
180 μm angular Al_2O_3 particles
t=100 hr (7500cm) Air, V=2.5m/s

XBB 9111-9153

Figure 3. The surfaces and cross sections of 2.25Cr1Mo steel specimens eroded-corroded by 180μm angular Al_2O_3 particles at V=2.5m/s, α=30°, t=100 hours at 350° and 450°C.

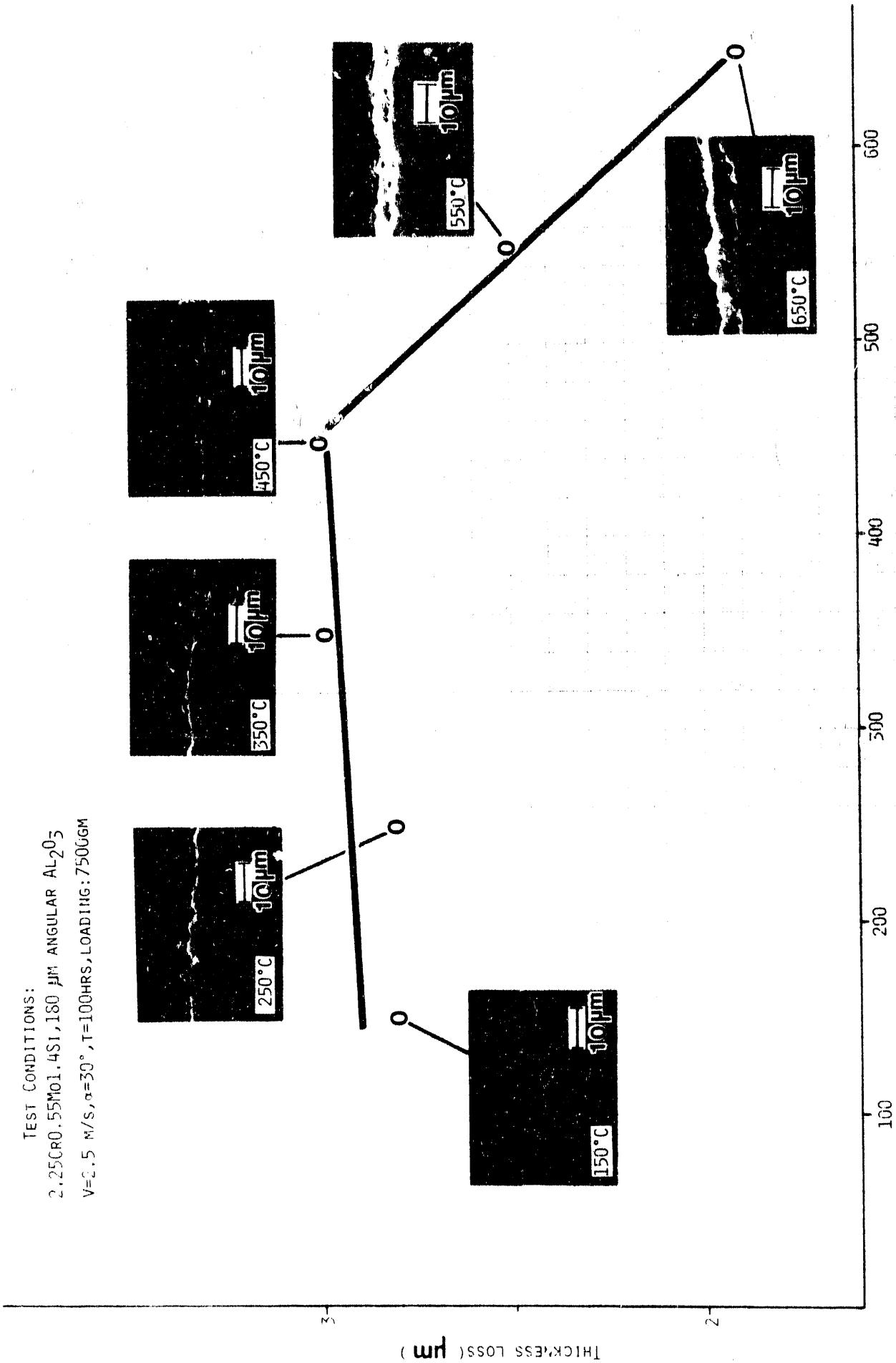

Figure 4. The cross sections of 2.5Cr0.55Mo1.4Si steel specimens corresponding to the different test temperature and thickness losses.

formed slowly and was not protective. This permitted the base metal to be directly eroded at a relatively high, more or less constant rate.[1] However, as Figure 4 shows, in the higher temperature regime, corresponding to the marked drop in thickness loss, the surfaces were covered with a thick, protective oxide layer. As the cross sections show, the oxide scale was continuous and dense without evidence of fracture, which indicated that during the tests the oxide scale formed in this temperature regime was more protective and ductile, i.e., pseudoplasticity occurred. This resulted in more deformation and retention; thereby protecting the surface. This occurrence is also indicated by the surface morphology of the 2.5Cr0.55Mo1.4Si steel specimens tested, which is shown in Figure 5. When combined with 450°C cross section in Figure 4, it can be seen that tested at 450°C the very thin scale on the surface of the specimen exhibited a brittle behavior with cracking and chipping, as evidenced by a fine surface texture consisting of many small craters and areas where bare metal was exposed. However, when tested at 650°C a very coarse surface texture occurred with large craters, indentations and gouges occurring in the continuous surface scale. This indicates the ductile, protective nature of the thick scale that was present on the specimen's surface.

The higher oxidation resistance of 2.5Cr0.55Mo1.4Si steel retarded scale formation at lower temperatures resulting in the exposure of base metal which eroded at a relatively high rate. When the temperature was high enough for oxidation to occur, the oxide that formed had a sufficient ductility to cause plastic deformation before cracking, and the wastage fell to a low level. Therefore, there was no increase in the slope of the curve for the 2.5Cr0.55Mo1.4Si steel, as occurred in the second regime for 1018 and 2.25Cr1Mo steels, see Figure 1. Also, the temperature range used in the present work is lower than the free oxidation temperature of 2.5Cr0.55Mo1.4Si steel.[12] Therefore, no spalling of thick scale occurred and there was no resulting dramatic increase in metal wastage, as occurred for the two normal Si content steels.

The difference in E-C behavior between the 2.25Cr1Mo and the 2.5Cr0.55Mo1.4Si steels, alloys whose only essential difference is 1 % more Si in the latter steel, provides important information to understanding the nature and role of the protective layer that can form

Surface(T=450°C)

10μm

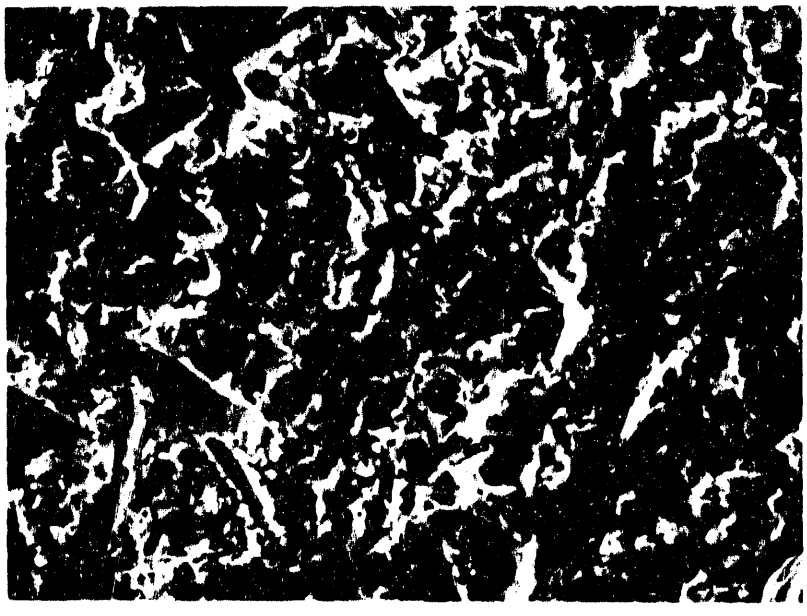

Surface(T=650°C)

10μm

2.5Cr0.55Mo1.4Si Steel
Nozzle Tester T=450°,650°C
Corrosion-Erosion, α=30°
180 μm angular Al_2O_3
t=100 hrs(7500gm) Air, V=2.5m/s

XBB 9111-9152

Figure 5. The surfaces of 2.5Cr0.55Mo1.4Si steel specimen, eroded-corroded at V=2.5 m/s, α=30°, t=100 hours by 180μm Al_2O_3 particles, at 450° and 650°C.

on steels during erosion-corrosion and markedly affect their material wastage rates. It is known[12] that the addition of small amounts of additional silicon to chromium steels increases their resistance to oxidation. In the current work, the increased resistance to the formation of an oxide layer of the 2.5Cr0.55Mo1.4Si steel prevented the formation of a protective scale at temperatures below the transition temperature of 450°C and a higher rate of material wastage of a bare metal surface occurred than above the transition temperature, see Figure 1 and 4. Below this temperature the normal Si content, 2.25Cr1Mo steel had a considerably different pattern of material loss that was related the nature of the oxide scale that formed on its surface, as was discussed above.

Above the transition temperature, where the normal Si content steel dropped to a low loss level and then almost catastrophically increased its material wastage, the additional silicon steel was forming a ductile, tenacious oxide scale that continued to increase its protective capability to the maximium test temperature, 650°C. This behavior difference can be related to the morphological differences in the scales shown in Figure 3 and 5.

Just what the exact differences in the protective nature of the scales on the essentially same chromium content steels are not known. But the significant differences in E-C behavior of the two, nearly identical steels is indicative of the major role that the protective layer can play and the sensitive nature of its formation.

In summary, there are two different relationships between E-C metal wastage and temperature. For 1018 and 2.25Cr1Mo steels a peak in the temperature-metal wastage curves occurred at 350°C. However, for 2.5Cr0.55Mo1.4Si steel below 450°C the metal wastage was relatively high and constant. Above 450°C the metal wastage markedly decreased with test temperature. This behavior has been observed on in-bed tubes in BFBC's but has never before been duplicated in laboratory tests. In addition to the particle velocity, the corrosion (oxidation) resistance of steels influence the relationship between metal wastage and test temperature, which is explained in terms of the ductility of the scale that occurred.

REFERENCES

1. A. V. Levy, J. Yan, J. Patterson, WEAR, 108 No.1, 1986, pp.43-60.

2. F. H. Stott, M. M. Stack, G. G. Wood, Proceedings of 4th Berkeley Conf. on Corrosion-Erosion-Wear of Materials at Elevated Temperatures, A. V. Levy (ed.), NACE, Houston, 1991, pp.12-1 to 12-16.

3. I. Hutchings, J. Little, A.Ninham, Proceedings of 4th Berkeley Conf. on Corrosion-Erosion-Wear of Materials at Elevated Temperatures, A. V. Levy (ed.), NACE, Houston, 1991, pp.14-1 to 14-17.

4. R. G. Cory, V. K. Sethi, NACE, Corrosion 87, paper No.10, San Francisco, March 1987.

5. I. G. Wright, M. A. Rocazella, V. Nagarajan, Proc. EPRI Workshop on Wastage of In-Bed Surfaces in FBCs, 5.5, Argonne (EPRI, Palo Alto, CA, 1987)

6. B. Q. Wang, G. Q. Geng, A. V. Levy, Proc. of 8th Int. Conf. on Wear of Materials, Orlando, Fl. April 7-11, 1991, K.C. Ludema, R. G. Bayer (eds.) ASME, New York, 1991, pp.703-707.

7. H. Tossaint, P. Rademakers, P. Van Norden, Conference paper, 7th Int. Conf. & Exhibition on Coal Technology & Coal Trade. Amsterdam, Holland, Nov. 21-13, 1988.

8. G. J. Holtzer, P. Rademakers, Proceedings of ASME 1991 FBC Conf., Montreal, Canada, April 21-24, 1991, pp.743-753.

9. V. K. Sethi, R. G. Corey, Proc. of 7th Int. Conf. Erosion by Liquid and Solid Impact. Paper 73, Cavendish Laboratory, Cambridge, England. 7-10 September, 1987.

10. F. H.Stott, S. W. Green, G. C. Wood, NACE, Corrosion '89, paper No.545, April 17-21, 1989, New Orleans, Louisiana.

11. M. Schutze, Materials Science and Technology, 6 (1), January 1990, pp 32-38.

12. G. Q. Geng, B. Q. Wang, F. Y. Hou, A. V. Levy, NACE Corrosion '90, Paper No.292, Las Vegas, Nevada, April 23-27, 1990. WEAR, 150 Nos. 1-2,1991, pp.89-105.

NIST-3-MECHANISMS OF GALLING AND ABRASIVE WEAR

L. K. Ives

National Institute of Standards and Technology
Building 220, Room A215
Gaithersburg, MD 20899

INTRODUCTION

The purpose of this investigation is to study wear processes that occur at the piston ring and cylinder wall contact of diesel engines that operate on pulverized coal-fuel. With conventional engine materials wear rates under coal-fuel operation may be 100 or more times greater than with No. 2 diesel oil fuel.[1] This markedly higher rate of wear is due to abrasion by hard particles which originate from mineral matter materials that are present in the coal-fuel. In previous reports in this series[2-7] results have been presented regarding the effects of a number of parameters and conditions on the wear process. A modified pin-on-disk test method was employed in carrying out the wear measurements. In the present report preliminary results are presented from experiments utilizing a reciprocating wear test method that more closely simulates the piston ring / cylinder wall contact configuration and sliding motion.

DISCUSSION OF CURRENT ACTIVITIES

The pin-on-disk method has a number of advantages. Among them are the simplicity of the test, flexibility with respect to control of test conditions, relative ease of specimen preparation, and precise measurement of wear losses. The contact geometry and specimen motion, however, are not a close approximation to that associated with the piston ring / cylinder wall assembly. Although this difference may not have an adverse effect on the determination of such important relationships as the influence of particle hardness and the relative wear rates of different contacting materials, some characteristics of

the wear process may not be adequately revealed without a closer simulation of the contact geometry and component motion. Of particular importance in this connection is the extent to which the contact geometry and sliding mode determines the number of particles that enter the contact. To study this and other effects preliminary experiments were conducted with a Falex #1* block-on-ring machine setup to operate in an oscillating mode by replacing the belt and pulley drive with a crank assembly that is provided as an accessory for that purpose. The rectangular contact area of the block-on-ring geometry with its relatively large length-to-width aspect ratio is a better representation of the piston ring / cylinder wall contact than is provided by the circular contact of the pin-on-disk arrangement. To obtain information on the influence of sliding motion while maintaining other conditions constant, additional block-on-ring tests were conducted with the Falex #1 machine in the unidirectional rotational sliding mode. The approach taken here is similar to that recently employed by Mehan et al.[8]

A second aspect of the current work was concerned with characterizing particles which exited the contact. These particles consisted of original abrasives, crushed abrasives, and wear debris from the block and ring specimen surfaces. Earlier studies[5,6,9] had indicated that the number and size of particles that successfully entered the contact constituted a critical factor controlling wear rate. Also, crushing and therefore particle strength was deemed to have an important influence on wear rate. Examination of the exiting particles is a means of studying this effect.

---

*Certain trade names and company products are identified in order to adequately specify the experimental procedure. In no case does such identification imply recommendation or endorsement by the National Institute of Standards and Technology, nor does it imply that these products are necessarily the best available for the purpose.

TEST CONDITIONS AND PROCEDURES

A schematic drawing of the test setup is shown in Fig. 1. Conventional LFW1 block and ring specimens[10] were employed in the experiments. Both specimens were of 52100 steel heat treated to a Knoop hardness of about 7.1 GPa. The initial roughness of the block and ring sliding surfaces was approximately 0.2 μm rms. Only wear of the block was measured. Profile traces across the scar were used to determine its average cross sectional area. The volume lost was given by the product of the area and length of the scar. All tests were conducted with an applied load of 225 N. The relative humidity during the tests was approximately 50%.

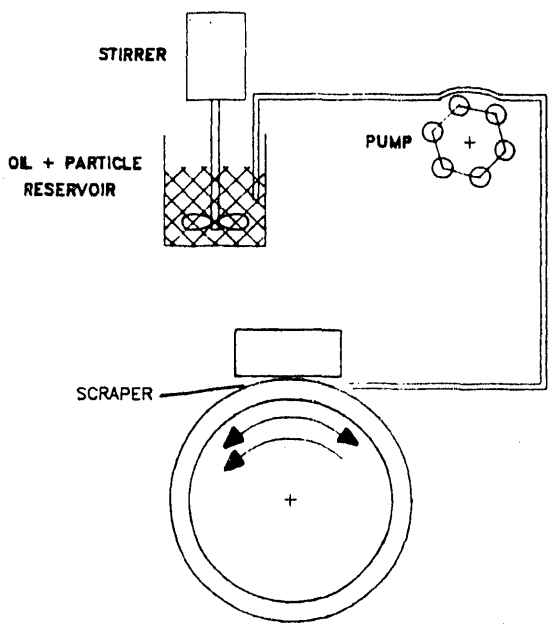

Fig. 1 - Schematic drawing of the block-on-ring test setup.

When setup to operate in the oscillating mode, the Falex #1 machine is not balanced with respect to inertial forces. Thus, machine vibration imposes a limit on the maximum allowable frequency of oscillation, depending on the amplitude of oscillation, which can be adjusted over the range 0 - 90 degrees. For these experiments an

oscillation amplitude of 90 degrees was used at a frequency of approximately 172 cycles/minute. At higher frequencies machine vibration was excessive. A test machine is currently under construction that will permit operation at substantially higher speeds, more consistent with that of an operating engine. For unidirectional tests a sliding speed of 0.16 m/s was employed, approximately equal to the average speed in the reciprocating mode. A fixed sliding distance of 495 m was used for each test.

The oil-particle mixture was delivered only to one side of the contact. The delivery system, shown schematically in Fig. 1, utilized a stirred reservoir to maintain the particles in suspension and a variable speed peristaltic pump to control the delivery rate. For these experiments a delivery rate of about 10 mg/min. was selected. Quartz particles of two different mean sizes were used: 2 μm and 10 μm. These particles were mixed at a concentration of 20 wt.% in white paraffinic mineral oil having a specified viscosity of 335-365 SUS at 40°C.

Particles were collected from the exit side of the contact by means of a thin scraper blade cut from cellulose acetate film that was pressed against the ring surface in the center of the wear track. The scraper blade was approximately 3 mm wide, about one half the width of the track. Only oil and particles that emerged from the contact were subject to collection. The scraper blade with its accumulation of oil and particles was placed in hexanes and ultrasonically agitated to assist in dissolving the oil and dispersing the accumulated particles. The solution with suspended particles was passed through a Nuclepore filter with a pore size of 0.05 μm and rinsed with additional hexanes to remove the mineral oil. The filter was coated with carbon and examined in a SEM. Compositional characterization of the particles was done with an energy dispersive x-ray analysis system attached to the SEM.

RESULTS AND DISCUSSION

Wear rate and Friction Effects

The wear rates for the reciprocating and unidirectional sliding modes with 2 μm and 10 μm quartz particles are shown in Fig. 2. Results are also included for tests without added particles. Each point in Fig. 2 corresponds to a single test. Although additional tests are needed to confirm the observed trends, these data indicate that the wear rate with 2 μm particles is higher during reciprocating sliding than it is for unidirectional sliding. This relationship also

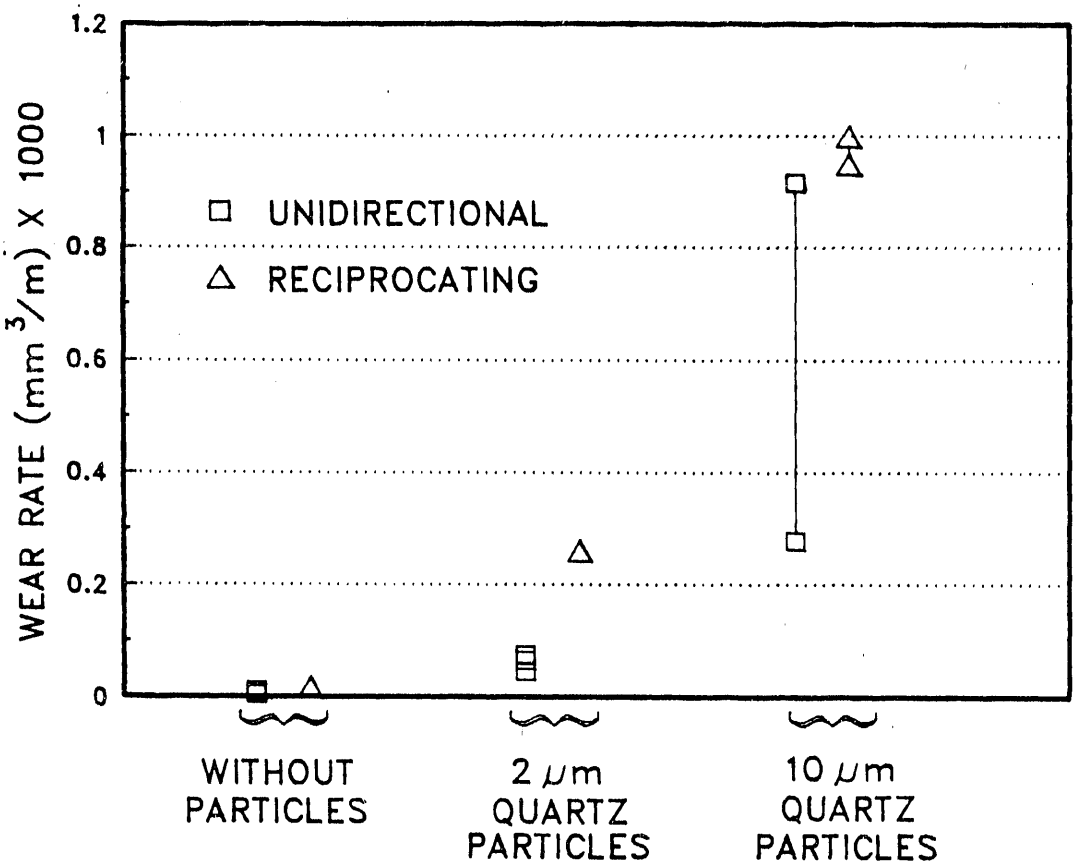

Fig. 2 - Wear rates in reciprocating and unidirectional sliding modes for 2 μm and 10 μm quartz particles in mineral oil and without added particles.

holds for 10 μm particles although the difference is much smaller. Mehan et al.[8] in their experiments concluded that there was no difference in wear rate between unidirectional and reciprocating sliding. However, the test conditions they employed differed from those used here in several respects, including the type of particles (2 μm Al_2O_3), the particle concentration (2 g/l), the specimen materials (principally tungsten carbide and other hard coatings), and in other details of the test setup as well. Apparently, it can not be concluded in general that one mode of sliding results in a higher wear rate than the other.

In Fig. 2 it is seen that the wear rate is significantly higher for 10 μm particles than for 2 μm particles. This is consistent with earlier results[5] obtained with the pin-on-disk method where it was found that the wear rate of 52100 steel increased exponentially with increasing particle size over this size range. These results disagree with those of Schwalb et al.[11] where it was found in reciprocating tests that small particles gave a higher wear rate than larger particles.

Values for the average coefficient of friction under each test condition are shown in Fig. 3. Addition of quartz particles to the oil is seen to result in an increase in the coefficient of friction, with larger values being obtained with 10 μm particles than with 2 μm particles. The increase in coefficient of friction can be attributed to the extra force required to overcome the scratching or plowing action of the particles. Sliding of the roughened block and ring surfaces may also have contributed to the increase. The higher wear rate associated with the 10 μm particles compared to 2 μm particles correlates with the higher observed coefficient of friction.

All coefficient of friction values lie in the range that is characteristic of a state of boundary lubrication rather than hydrodynamic lubrication. The variation in friction force over several cycles in the reciprocating mode with 10 μm particles is shown in Fig. 4. A decrease at the center of each stroke, where the

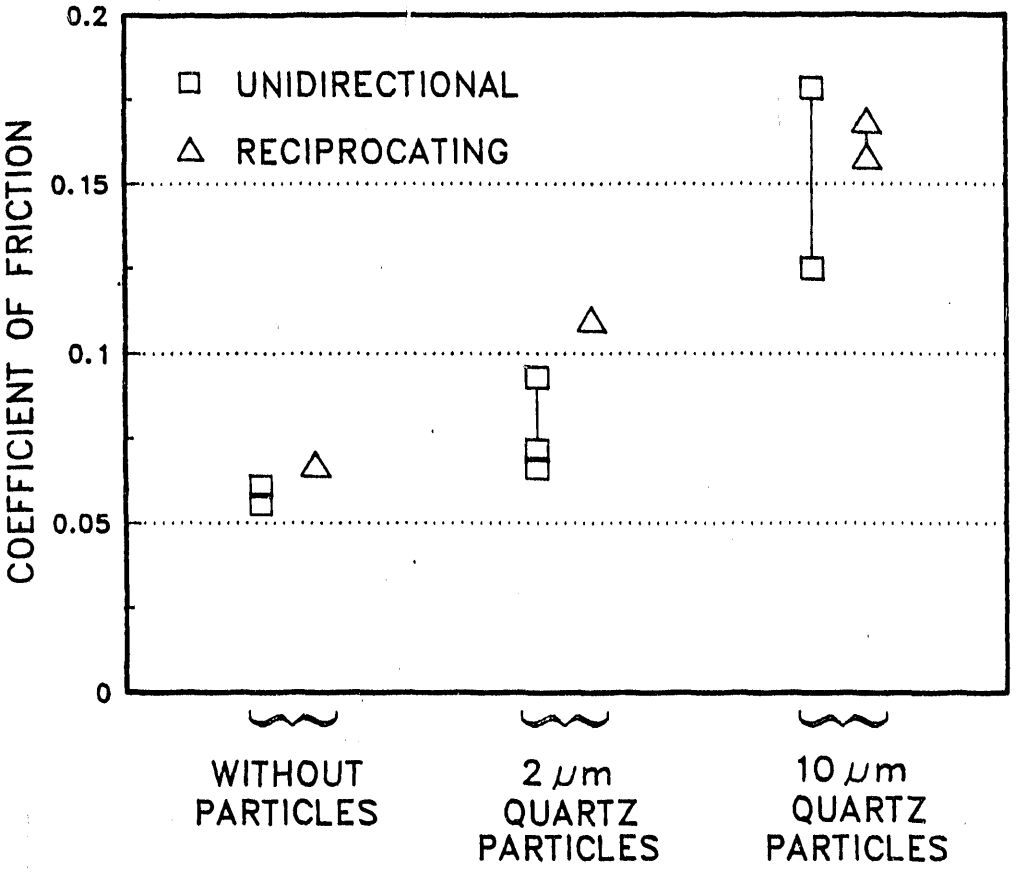

Fig. 3 - Coefficient of friction values for different test conditions.

velocity of sliding is greatest, is not observed that would indicate an increase in film thickness and transition to hydrodynamic lubrication. That is, a condition of boundary lubrication is sustained throughout the sliding cycle.

In an operating diesel engine the piston ring enters the boundary regime only during reversal. Throughout the remainder of the stroke hydrodynamic conditions prevail with an oil film that may reach several micrometers in thickness. This, in effect, would allow the entrapment of particles and exacerbate abrasion in the approach to and during boundary conditions. To obtain a similar state of lubrication with the present test arrangement would require a lower load (these experiments will be conducted in the future) or a higher sliding speed than is feasible with the Falex #1 machine in the oscillating mode (the machine under construction will address this limitation).

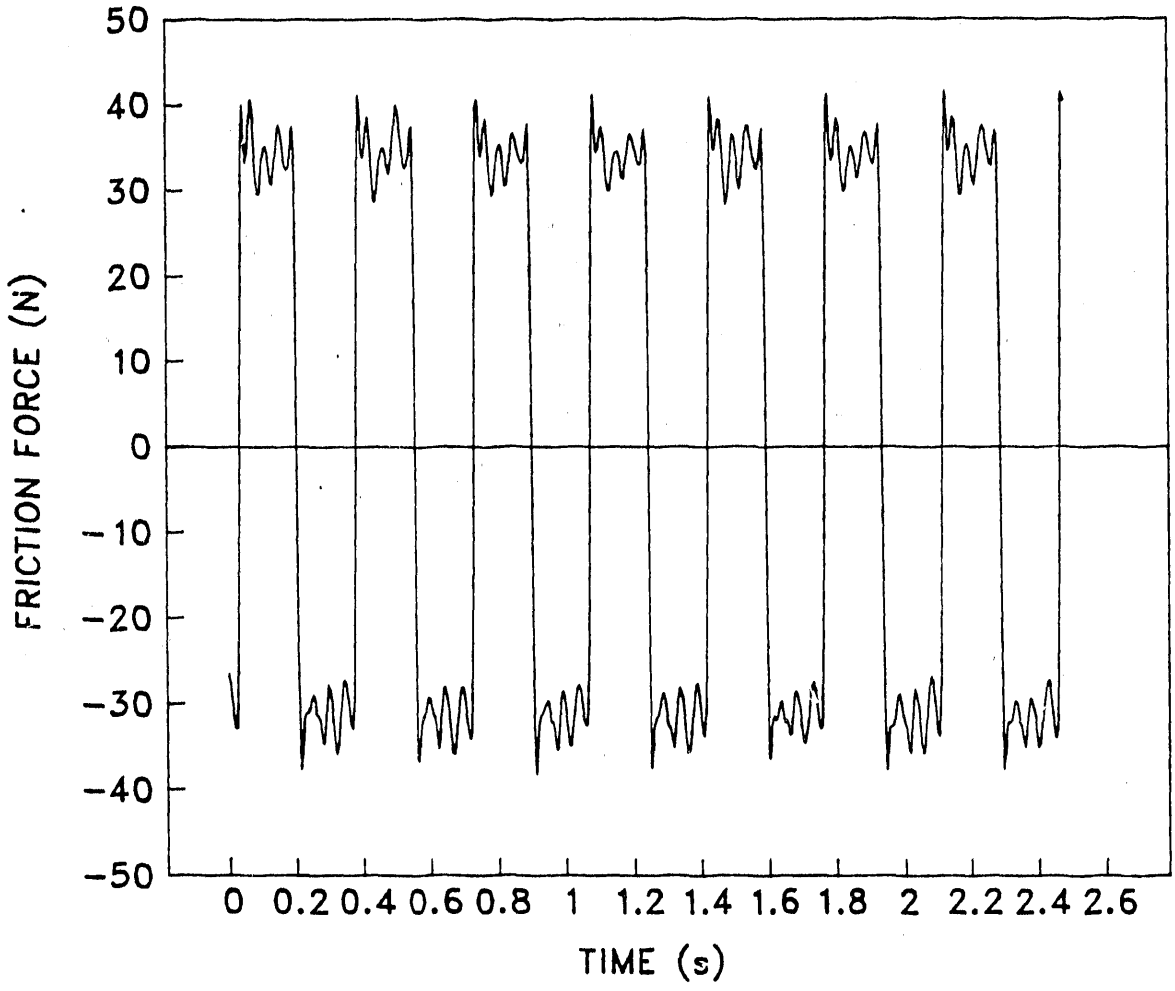

Fig. 4 - Friction force variation during reciprocating sliding with 10 μm particles in mineral oil.

An indication of the importance of a varying film thickness such as occurs in the diesel engine was provided in some experiments where misalignment between the ring and shaft, or an inaccurately ground ring, caused the ring to wobble excessively with respect to the block surface. As a result, a gap appeared first on one side of the contact and then on the other during rotation. When this occurred, wear was substantially greater at the ends of the scar than in the center. The

increased wear was attributed to the improved access of abrasive particles during the periodic opening of the gap at the sides of the block.

An example of a wear scar on a test block where this form of misalignment occurred is shown in Fig. 5. The scar is not only wider but appears rougher at the ends than in the center. Note the indentations along the inlet edge of the scar where particles were first engaged. Details of the surface topography at the end and center locations are shown in Fig. 6(a) and (b), respectively. In the end region, Fig. 6(a), the surface is covered by a profusion of indentations, apparently as a result of the entrapment of particles. In contrast, the surface at the center of the scar shown in Fig 6(b) is polished in appearance with a mixture of different size grooves ranging in width and depth from relatively large to very small.

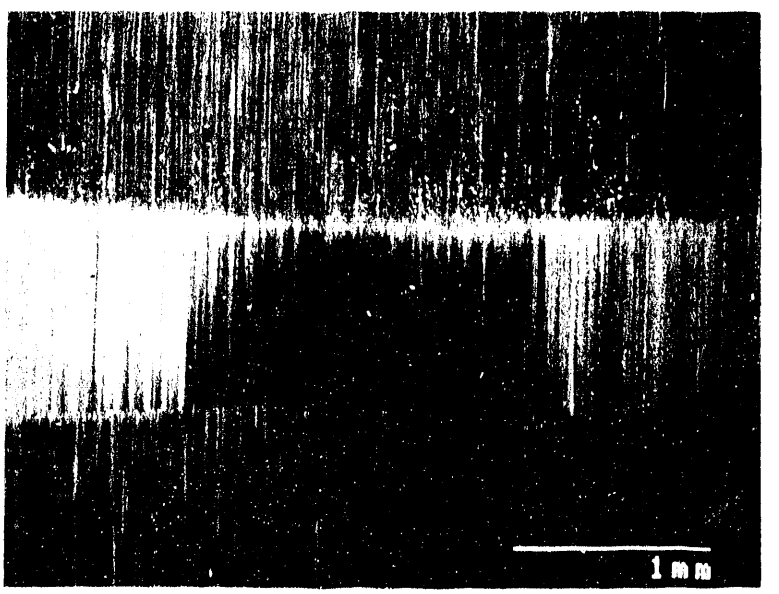

Fig. 5 - SEM micrograph of wear scar on block with misaligned ring surface after unidirectional sliding test with 2 μm quartz particles in mineral oil.

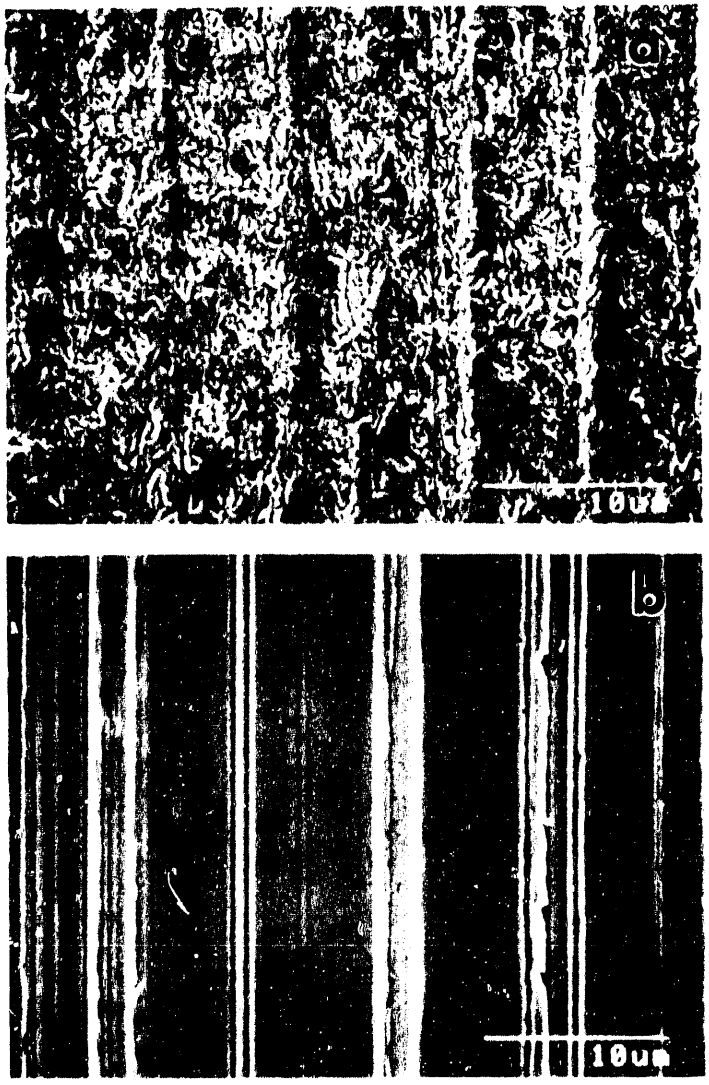

Fig. 6 - SEM micrographs of scar in Fig. 5 at higher magnification showing surface details in end region (a) and center region (b).

Particle Characterization

The oil-particle mixture delivery rate at the inlet side of the block (10 mg/min.) was substantially in excess of the amount that actually passed through the contact to the exit side. Most of the mixture flowed around the block and off the edges of the ring. At least 50 m of sliding distance was allowed before applying the scraper

to collect oil and particles at the exit side of the block and ring contact. The scraper was maintained in contact with the ring until a visible droplet of oil was collected. In tests without particles added to the oil, the edge of the scrapper was little more than wet with oil even though contact was maintained throughout most of the test. With particles added to the oil a droplet was collected fairly rapidly; the time required was much less for 10 μm particles than 2 μm particles. The increased volume of oil that passed through the contact was apparently due to roughening of the surfaces by particle abrasion. Also, the passage of particles themselves may, on average, have increased the space between the block and ring promoting a larger oil film thickness.

Particles collected from the exit side of the contact are compared with unused particles in Fig. 7 and 8. With both 2 μm particles shown in Fig. 6 and 10 μm particles in Fig. 7, the unused particles are substantially larger than the exit particles. The smaller size can be attributed to the fracture of particles in the contact and perhaps to the fact that smaller particles may enter the contact more easily than larger particles.

As might be expected, metal particles from the block and ring were also found in collected debris. Most of the observed particles were flake-like in shape and no larger than about 2 μm in diameter. A relatively large metal particle is shown in Fig. 9(a) together with its x-ray spectrum in Fig. 9(b). The small size of the particles suggests that quartz was not a very efficient abrasive with respect to 52100 steel. Consistent with the observation that the quartz particles were crushed in the contact, their limited strength also rendered them incapable of producing large chips. X-ray spectra from quartz particles sometimes showed the presence of iron. This is not unexpected since abraded metal often adheres to abrasive particles.

All the metal particles were not necessarily produced directly by abrasion. Sliding of the abrasion roughened block and ring surfaces may also have led to the production of debris.

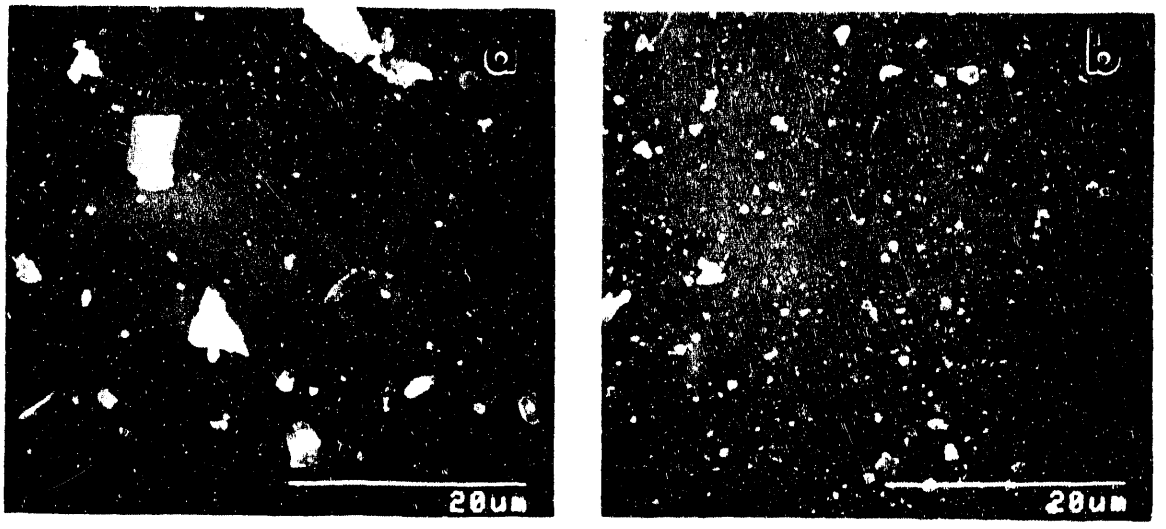

Fig. 7 - (a) Unused 2 μm quartz particles. (b) Particles collected from the exit side of the contact during unidirectional sliding test.

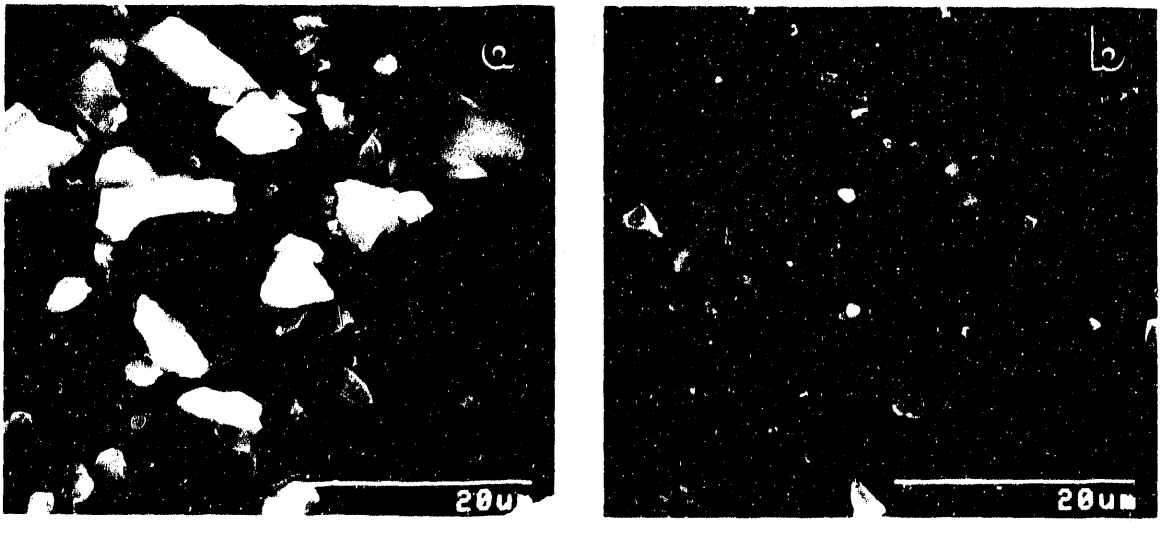

Fig. 8 - (a) Unused 10 μm particles. (b) Particles collected from the exit side of the contact during unidirectional sliding test.

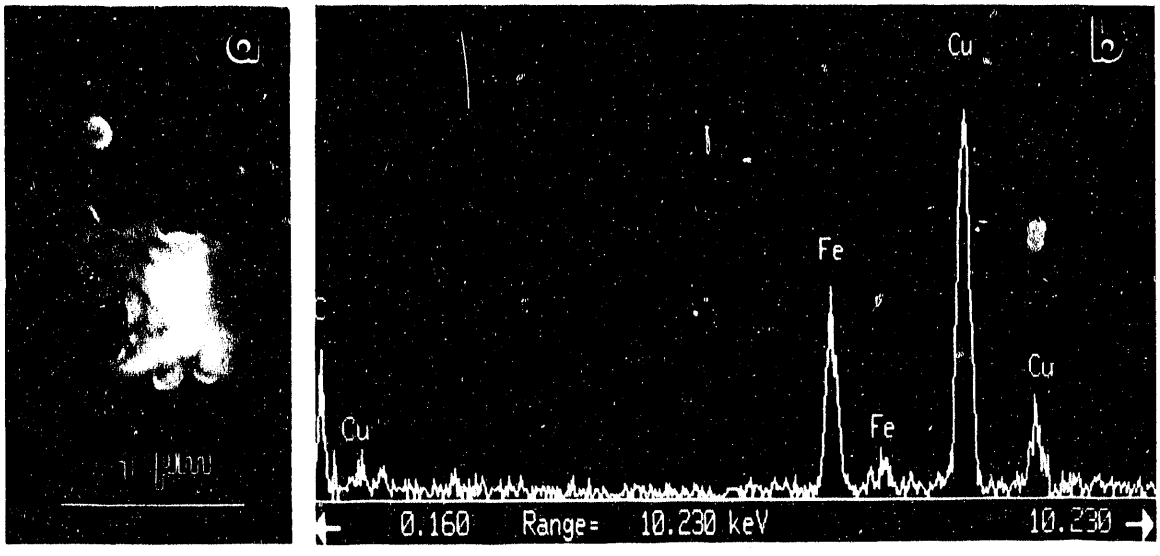

Fig. 9 - (a) Metal debris particle. (b) Energy dispersive x-ray spectrum from particle. The copper peak is from the support and the carbon peak is from the carbon coating.

SUMMARY AND CONCLUSIONS

Block-on-ring wear tests were conducted to compare the effect of two different sliding motions, reciprocating and unidirectional, on the wear of 52100 steel utilizing lubricant containing abrasive particles. The abrasives employed were 2 μm and 10 μm quartz particles at a concentration of 20 wt.% in mineral oil. Particles collected from the exit side of the contact were characterized to provide additional understanding of the wear process. Under the conditions of the experiments it was determined that:

1. The wear rate during reciprocating sliding is greater than during unidirectional sliding.

2. The wear rate for both unidirectional and reciprocating sliding modes is greater with 10 μm quartz particles than with 2 μm quartz particles.

3. Only a small fraction of the particles delivered to the inlet side of the contact actually enter the contact and the average exiting particle size is substantially less than the initial size.

REFERENCES

1. S. E. Nydick, F. Porchet, and H. A. Steiger, Continued Development of a Coal/Water Slurry-Fired Slow-Speed Diesel Engine: a Review of Recent Test Results, J. Engng. for Gas Turbines and Power, 109 (1987) pp. 465-476.

2. L. K. Ives, M. B. Peterson and E. P. Whitenton, "Mechanisms of Galling and Abrasive Wear," in AR&TD Fossil Energy Materials Program Semiannual Progress Report for the Period Ending September 30, 1988, ONRL/FMP-88/2, Oak Ridge National Laboratory, Oak Ridge, TN, January 1989, pp. 445-462.

3. L. K. Ives, M. B. Peterson and E. P. Whitenton, "Mechanisms of Galling and Abrasive Wear," in AR&TD Fossil Energy Materials Program Semiannual Progress Report for the Period Ending March 31, 1989, ONRL/FMP-89/1, Oak Ridge National Laboratory, Oak Ridge, TN, July, 1989, pp. 455-469.

4. L. K. Ives, M. B. Peterson and E. P. Whitenton, "Mechanisms of Galling and Abrasive Wear," in Fossil Energy Advanced Research and Technology Development Materials Program Semiannual Progress Report for the Period Ending September 30, 1989, ONRL/FMP-89/2, Oak Ridge National Laboratory, Oak Ridge, TN, January, 1990, pp. 447-465.

5. L. K. Ives, M. B. Peterson and E. P. Whitenton, "Mechanisms of Galling and Abrasive Wear," in Proceedings of the Fourth Annual Conference on Fossil Energy Materials, Oak Ridge National Laboratory, Oak Ridge, TN, August 1990, Conf. 900546, ONRL/FMP-90/1, pp. 417-426.

6. L. K. Ives, "Mechanisms of Galling and Abrasive Wear," in Fossil Energy Advanced Research and Technology Development Materials Program Semiannual Progress Report for the Period Ending September 30, 1990, ONRL/FMP-90/2, Oak Ridge National Laboratory, Oak Ridge, TN, December 1990, pp. 341-352.

7. L. K. Ives, "Wear by Coal-Fueled Diesel Engine Particles," in Proceedings of the Fifth Annual Conference on Fossil Energy Materials, Oak Ridge, TN, September 1991, Conf. 9105184, ORNL/FMP-91/1, pp. 367-376.

8. R. L. Mehan, P. L. Flynn and A. W. Giammarise, "Evaluation of Piston Ring Materials in Oil Containing an Abrasive Using a Ring-On-Block Test Machine," (to be published)

9. L. K. Ives, "Abrasive Wear by Coal-Fueled Engine Particles," Proceedings Corrosion-Erosion-Wear of Materials at Elevated Temperatures, A. V. Levy, ed., NACE, Houston, TX, 1991, pp. 29-1 thru 29-20.

10. "Practice for Ranking Resistance of Materials to Sliding Wear Using Block-On-Ring Wear Test," G77-91, 1991 Annual Book of ASTM Standards, Vol. 03.02, ASTM, Philadelphia, PA, 1991, pp. 306-317.

11. J. A. Schwalb, T. W. Ryan III, and M. Crane, "Wear Mechanism and Wear Prevention in Coal-Fueled Diesel Engines," Proceedings of the Seventh Annual Coal-Fueled Heat Engines and Gas Stream Cleanup Systems Contractors Review Meeting, Morgantown, WV, March 1990, DOE/METC-90/6110, pp. 329-338.

ORNL-2 (A) - ENVIRONMENTAL EFFECTS ON IRON ALUMINIDES

J. H. DeVan

Oak Ridge National Laboratory
Oak Ridge, TN 37871

INTRODUCTION

Alloys based on the long-range-ordered system Fe_3Al are under development at Oak Ridge National Laboratory in support of coal conversion and combustion materials requirements [see ORNL-2(F)]. Of particular interest is the performance of these alloys in coal gasifiers involving product gases with relatively low oxygen activities (10^{-20} atm) and high sulfur activities (10^{-8} atm). Using H_2S-H_2-H_2O gas mixtures, several experimental iron-aluminum alloys have been tested to assess the effects of aluminum concentration on corrosion behavior at 700 to 800°C in a simulated gasifier environment. Thermogravimetric analyses (TGA), together with metallographic and chemical analyses of the corrosion product scales, are performed to determine the role of respective metallic elements on oxidation and sulfidation processes. Additionally, the corrosion resistance of Fe_3Al alloys is being evaluated by exposures at 600 to 900°C in the gas-cooler section of an operating gasifier in the United Kingdom.

Studies of Fe_3Al-bases alloys are also being conducted in air at 800 to 1000°C to characterize the oxidation properties of the alloys in more oxidizing environments typical of coal-fired boilers and air preheaters. Mechanisms controlling the nucleation, growth, and exfoliation of oxide scales are characterized by TGA, electron microscopy, and secondary ion mass spectrometry. The latter technique is used in conjunction with ^{18}O labeling to determine the species and transport paths contributing to oxide growth.

DISCUSSION OF CURRENT ACTIVITIES

Air Oxidation Behavior of Fe_3Al alloys

Weight change data for Fe_3Al alloys tested in dry air were collected and analyzed to assess the effects of alloying additions on high temperature oxidation behavior. The data were obtained under isothermal conditions in slowly moving dry air for exposures up to 200 h. Test specimens were in the form of 16 x 76 x 1 mm coupons, and all surfaces were mechanically ground with 600-grit abrasive before exposure. Following exposure the coupons were visually checked for detachment of corrosion products scales, and selected specimens were then analyzed by optical imaging of a polished cross section and, in some cases, by scanning electron microscopy with associated energy dispersive x-ray analysis (EDX).

Weight change data from exposures of iron aluminides to 800°C air are shown in Fig. 1. Although all the measured weight gains were relatively small, the eight weight change curves of Fig. 1 tend to divide into two groupings. The lower grouping consists of the three Fe-28*Al coupons and one composed of Fe-28Al-2Cr, while the higher group includes two specimens of Fe-28Al-4Cr-0.1B and one each of Fe-28Al-6Cr and

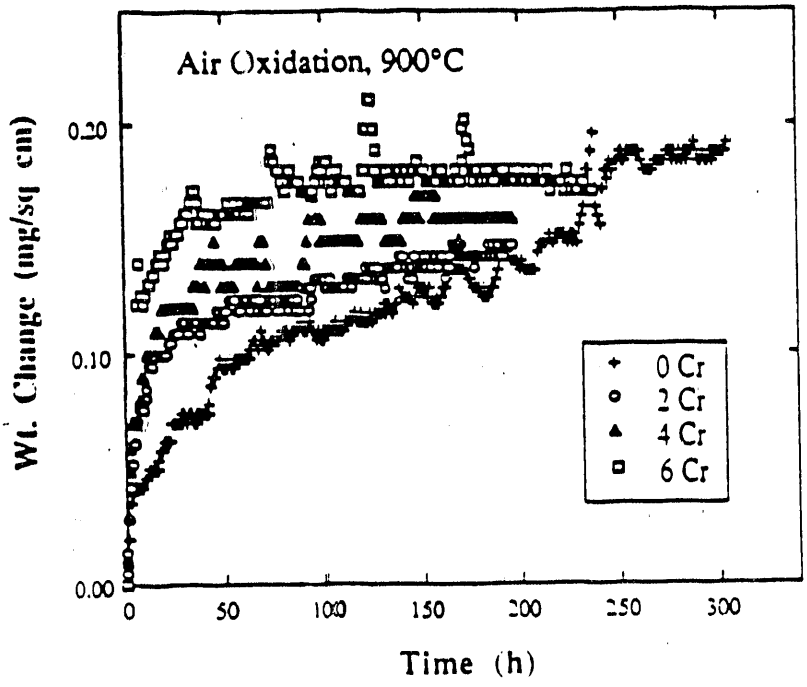

Fig. 1. Weight gains of Fe_3Al alloys (28 at.% Al) during exposure to dry air at 800°C. Cr concentrations are in at.%.

Fe-10Cr-0.1Zr-0.05B -0.5Nb-0.5Mo-0.02Y. The weight gains were not significantly affected by additions of minor alloying elements ($\leq$0.1 at.%) or variations between 4 and 10 at.% chromium. The chromium concentration also affected the measured parabolic rates constants, k_p as determined by the quotient $(\Delta w)^2/t$ where Δw is the change in weight per unit surface area after exposure for time t (see Table 1). The k_p values for the iron aluminides with $\geq$ 4 at.% chromium were approximately a factor of 10 greater than those for Fe-28Al-(0-2Cr). For comparison, the weight gains and parabolic rate constant of FeCrAl alloys (discussed in the next section) were also measured and found to be comparable to those of the Fe_3Al alloys with lower concentrations of chromium (see Table 1).

Table 1.
Parabolic rate constants determined for Fe_3Al alloys and FeCrSl in dry air at 800°C.

Alloys[a]	kp[b] ($mg^2/cm^4.h$)
28 Al	$2.3 - 1.1 \times 10^{-5}$
28 Al-2Cr	1.3×10^{-5}
28 Al-4Cr	$1.8 - 0.7 \times 10^{-4}$
28 Al-10Cr	2.0×10^{-4}
20 Cr-12Al	1.5×10^{-5}

At 900°C, the effect of chromium on the oxidation behavior of Fe_3Al in air was less pronounced than at 800°C. As shown in Fig. 2, increasing the chromium concentration of Fe_3Al alloys led to a more rapid weight gain during initial exposure. However, there was no significance influence on the oxidation rate after about 100 h. The parabolic rate constants (calculated from curve fits over the entire exposure range) fell within a range of 5-10 x 10^{-5} $mg^2/cm^4/h$ and did not vary monotonically with chromium concentration. The FeCrAl alloys showed weight changes similar to the Fe_3Al alloys at 900°C.

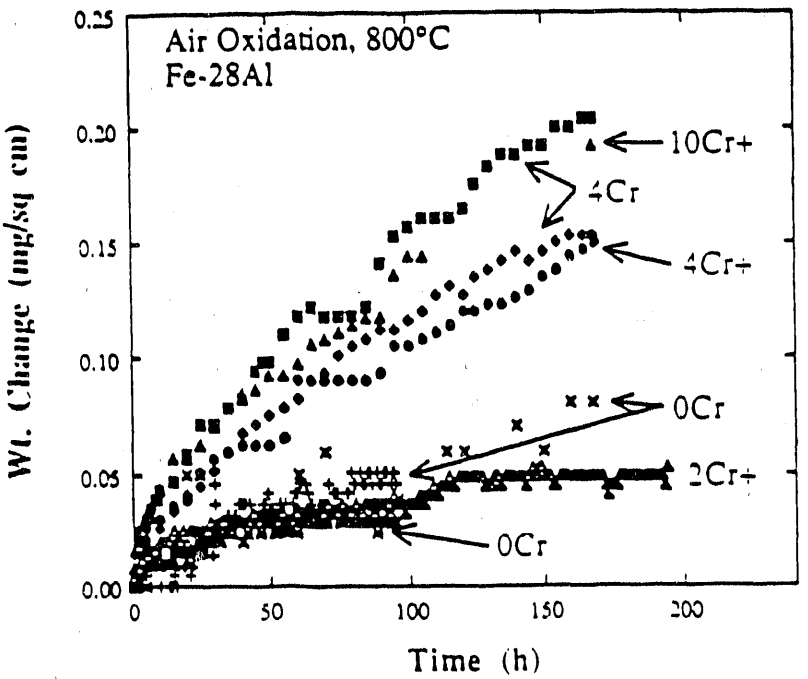

Fig. 2. Weight gains of Fe_3Al alloys (28 at.% Al) during exposure at dry air at 900°C. Cr concentrations are in at.%.

As expected from the small weight gains, the scales that formed on the oxidized Fe_3Al alloys were quite thin and difficult to image and characterize. Examination of polished cross sections of selected iron aluminides oxidized at 900°C and air-cooled revealed that only a fraction of an exposed surface retained pieces of the scale. EDX analysis of the thin, detached strip revealed only aluminum, which is consistent with the formation of an Al_2O_3 scale formed during high temperature exposure. (The x-ray system was not capable of detecting the oxygen in the scale.)

These results show that while chromium in Fe_3Al (up to 10 at.%) does not exert a large influence on air oxidation resistance there is a discernible effect at concentrations of 4% and above. At 800°C, this was manifested by faster oxygen uptake during the initial stages of exposure and overall higher parabolic rate constants (Fig.1). At 900°C, there was no apparent difference in rate constants for the Fe_3Al with various levels of chromium, but the amount of mass gain during the initial stages of oxidation was directly proportional to the chromium concentration (Fig. 2). Therefore, it appears that the presence of this element in

amounts greater than 2% leads to more rapid formation of an Al_2O_3 surface product. Under certain circumstances such an effect could prove beneficial if it acted to more quickly establish an external protective oxide layer prior to exposure to more aggressive or deleterious (hydrogen sulfide-containing) environments. Indeed, it has been hypothesized that the beneficial effect of chromium additions on room temperature ductility of iron aluminides[1] may relate to an oxidation effect during high temperature treatment such that the scale that forms then serves a a better barrier to hydrogen uptake by the alloy at ambient conditions[2].

Because FeCrAl is also an alumina-former under the oxidation conditions of this study, it is not unexpected that it shows comparable oxidation rates to that of Fe_3Al (see Table 1). However, the ability of FeCrAl alloys (containing about 7-12 at.% Al) to form Al_2O_3 critically depends on the presence of substantial amounts of chromium, which promotes the lateral growth of this surface product.[3,4] In the case of Fe_3Al alloys, the aluminum levels of the aluminide are well in excess of the critical concentration needed for external Al_2O_3 formation, even in the absence of chromium.

CORROSION IN H_2S-H_2-H_2O GAS MIXTURES

As shown in earlier reports[5,6] alloying with chromium (above 2%) significantly reduces the corrosion resistance of Fe_3Al-based alloys to high temperature H_2S-H_2-H_2O gas mixtures. To examine further the interplay between aluminum and chromium in mixed gas at relatively low oxygen pressures, it is of interest to compare the behavior of the FeCrAl (Fe-18 wt.% Cr-6 wt.% Al) alloy system with Fe_3Al alloys containing chromium. Three developmental FeCrAl alloys, whose compositions are listed in Table 2, were obtained from Harwell Laboratory and were exposed to a reference H_2S-H_2-H_2O gas mixture ($pO_2=10^{-21.6}$ atm and $pS_2=10^{-6}$) atm at 800°C, conditions that had been used previously to evaluate the effects of chromium on Fe_3Al alloys.

Weight changes for the respective alloys are shown in Fig. 3. Included for comparison are results for the largest chromium addition (10 at. %) that has made to the Fe_3Al alloy. The weight gain over a 24-h period is seen to exceed 30 mg/cm^2 in the case of the FeCrAl alloys compared to a gain of 3 mg/cm^2 for the Fe_3Al-based alloy.

Table 2.
Compositions of FeCrAl Alloys Supplied by Harwell Laboratory.

	Elemental Concentrations (atom %)					
Alloy	C	Si	Cr	Al	Mn	Ni
VB1852	0.074	0.41	20.3	9.11	0.38	0.24
VB1901	0.060	1.64	21.4	10.1	0.53	0.07
VB1902	0.085	4.09	21.7	9.47	0.53	0.08

(Weight gains for Fe_3Al alloys with 2% or less chromium are on the order of 0.2 mg/cm^2 over the same time period.) The resistance to sulfidation in "reducing" mixed gases gained by aluminum additions to iron-based alloys, as compared with chromium additions, served as the early impetus for the development of Fe_3Al-based alloys[7] The data in Fig. 3 again show the advantages of the higher aluminum concentrations afforded by Fe_3Al, even when chromium is also present. The beneficial effect of aluminum is even evident in comparisons of the FeCrAl alloys. Although corrosion rates are nearly the same for the three alloys tested, there is a consistent decrease in rate as the aluminum content increases. Furthermore, the addition of 4.1 at.% silicon to one of the alloys did not override this effect of aluminum.

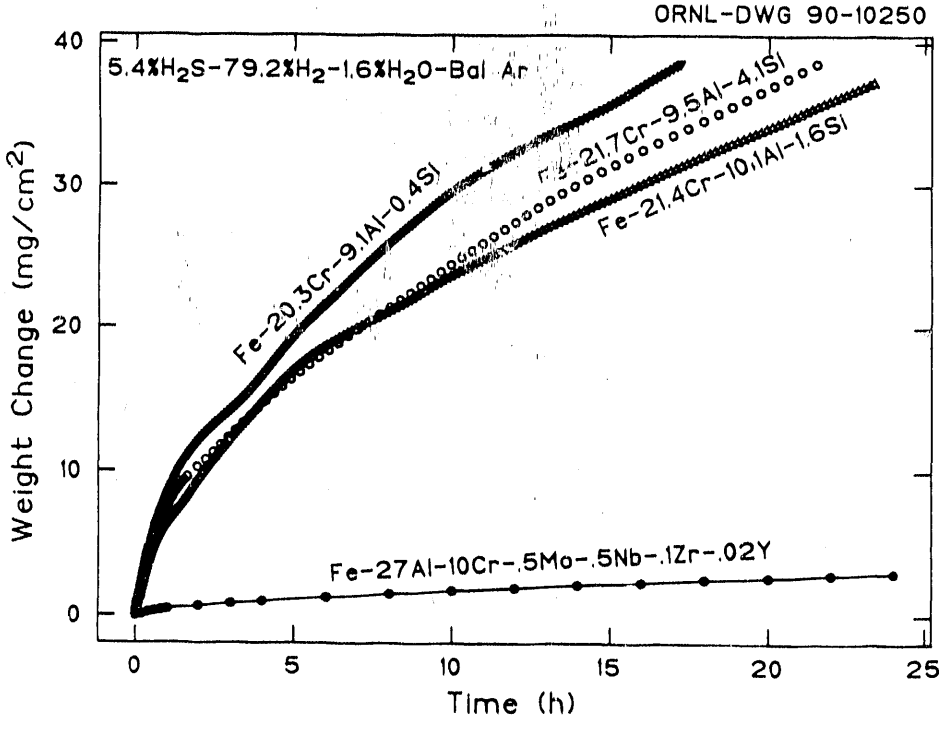

Fig. 3. Weight gains of FeCrAl alloys (upper curves) compared with Fe_3Al alloy containing 10 At.% Cr (lower curve) during exposure to H_2-H_2-H_2O gas mixture at 800°C.

Aqueous corrosion studies of Fe_3Al-based alloys have shown that the addition of 1 to 2 at.% Mo significantly increases the resistance of the alloy to attack in acid chloride solutions.[8] These same alloys have now been evaluated in high temperature H_2S-H_2-H_2O gas mixtures to determine the effect of the molybenum alloying addition on sulfidation/oxidation resistance. The alloys, containing 2 at.% molybdenum with 0 and 4 at.% Cr, respectively, were exposed at 800°C, and the weight change results, shown in Fig. 4

indicate significantly reduced corrosion rates compared with chromium-containing alloys with no molybdenum. Minor alloying additions of zirconium and zirconium plus yttrium also appear to improve the corrosion resistance of the chromium-containing alloy, but to a much lesser degree than the 2% Mo addition. In the absence of chromium, the 2% molybdenum alloy gained essentially the same weight after 168 h as Fe_3Al-based alloys containing 2% or less chromium (not shown in Fig. 4). Thus, the molybdenum addition is effective in suppressing the adverse effect of the 4% Cr addition but does not contribute to the innate corrosion resistance of Fe_3Al.

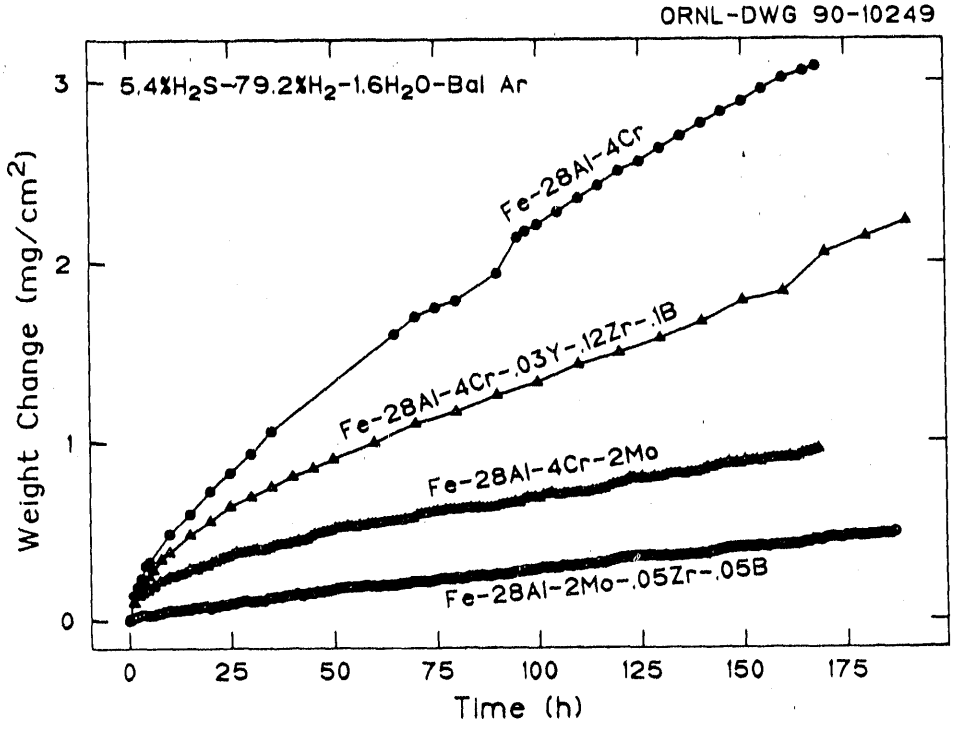

Fig. 4. Effect of Cr and Mo additions on weight gains of Fe_3Al alloys exposed to H_2S-H_2-H_2O gas mixture at 800°C.

References

1. C. G. McKamey, J. A. Horton, and C. T. Liu, J. Mater. Res., 4 (1989) 1156.

2. C. G. McKamey and C. T. Liu, Scripta Metall., 24 (1990) 2119.

3. W. C. Hagel, Corrosion, 21 (1965) 316.

4. G. H. Meier, in T. Grovstein and J. Doychak (eds.), Oxidation of High-Temperature Intrermetallics, TMS, Warrendale, PA, 1989, p.1.

5. J. H. DeVan, in T. Grobstein and J. Doychak (eds.), Oxidation of High-Temperature Intermetallics, TMS, Warrendale, PA, 1989, p. 107.

6. J. H. DeVan, Proceedings of the Fouth Annual Conference on Fossil Energy Materials, Confl 900546, U. S. Department of Energy, Oak Ridge, TN, Aug 1990, p. 299.

7. J. H. DeVan, H. S. Hsu, and M. Howell, Sulfidation/Oxidation Properties of Iron-Based Alloys Containing Niobium and Aluminum, ORNL/TM-11176,mg/cm^2 for Oak Ridge National Laboratory, Oak Ridge, TN, May 1989.

8. R. A. Buchanan and J. G. Kim, Aqueous Corrosion Charactoristics and Corrosion-Related Cracking Susceptibilities of Fe_3Al-Type Iron Aluminides, ORNL/Sub/88-07685CT92/01, University of Tennessee, Knoxville, TN., April 1991.

ORNL 3(B) - RESPONSES OF METALLIC AND OXIDE SURFACES TO DEFORMATION

M. Rao, J. R. Keiser, and P. F. Tortorelli

Oak Ridge National Laboratory
Oak Ridge, Tennessee 37831

Introduction

This project was divided into two tasks. The first, on erosion studies, addresses the deformation of metals and alloys during erosion and erosion-corrosion. The second task consists of a study of the mechanical properties of oxide scales formed on the surface of selected metals and alloys.

Erosion Studies

During the past six months, the results of a seven year experimental program to examine erosion mechanisms in metallic alloys (see, for example, refs. 1-7) were analyzed and the principal findings and conclusions are summarized here. These studies involved a fundamental approach to examining erosion mechanisms by experimentally modelling the process using realistically sized single particles as well as by examining material deformation and flow in multiple particle erosion tests. Spherical particles were used in all the tests in order to facilitate analysis by maintaining a simple impact geometry. Studies were conducted from the perspective of how material properties, and especially mechanical properties, control their response to particulate impacts. Results of the two types of experiments were compared and correlated.

Two gas guns were built and used for the single particle impact studies. The first gun, built at the program's initiation, is attached to a scanning electron microscope (SEM) and fires 343 μm spheres at velocities between 10-60 m/s.[1] The second gun, built in the sixth year of the program, fires sabots in air at velocities between 200-1000 m/s. The two guns were used to fire 343 μm diameter WC spheres at various targets oriented at 30° or 90° to the impacting particle.

Initial studies using the SEM gas gun showed that larger craters formed in softer alloys, but crater size could not be related to relative erosion rates. Mechanical properties microprobe (MPM) measurements showed work hardening due to impacts, but no thermal effects were evident for impacts at velocities around 30 m/s on a series of aluminum alloys. The depth of hardening was less in the stronger 7075-T6 alloy compared to 1100 Al. The significantly softer 1100 Al had shown superior erosion resistance in other studies, suggesting that the capacity to distribute the impact energy over large volumes improved a material's erosion resistance.

Detailed single impact studies over a wide range of velocities were conducted on targets of 1100 Al and a Fe_3Al-based ordered iron aluminide alloy, FA-129, in both heat treated and cold-worked conditions. For impacts at velocities around 60 m/s, craters were larger in the softer 1100 Al and the amount of material hardened by the impacts was less in the iron aluminide alloy, but the difference was less than expected based on the hardness differential between the two alloys. In some cases, at velocities of several hundred meters per second, the depth of hardening was greater in the iron aluminide alloy. Near-surface softening was observed in the cold-worked iron aluminide alloy, and possibly in annealed 1100 Al, at velocities around 60 m/s. Near-surface softening was observed in both alloys for impacts at velocities of several hundred meters per second, although the softening effects could be identified more clearly in the iron aluminide alloy. This softening was also observed due to moderately low velocity impacts on surfaces of previously eroded-corroded 2.25Cr1Mo steels, supporting the argument that greater softening occurred in more deformation resistant materials.

MPM measurements showed that for 30° incidence, more material was hardened in front of the impacting ball than vertically beneath the crater. Unlike at low velocities, significant differences were seen in the appearance of single impact craters at 30° incidence between 1100 Al and the iron aluminide alloy. Well developed extruded lips were formed in 1100 Al, with considerable deformation around the impact site but no material removal. In contrast, the extruded lip in the iron aluminide alloy fractured at the exit edge of the crater, perhaps due to low ductility in the material (around 15%) compared to annealed 1100 Al (35%). The velocity at which the extruded lips failed in the iron aluminide alloy was not well defined. In contrast, no difference was seen in the appearance of craters or extruded lips in annealed and cold-worked 1100 Al, even though the ductility was reduced from 35% to 6% upon cold-working.

To allow comparis on with the single particle impact studies, multiple particle erosion studies were conducted at a velocity of 45 m/s using steel shot either 600-700 μm in diameter (earlier studies) or 297-420 μm in diameter (later studies). The first study was conducted on 1100 Al and 7075-T6 Al, to examine the surface ripple structure that developed during erosion at 30° incidence. A work hardened layer was observed in both materials, with a maximum hardness greater than observed in single particle impact studies and no evidence of near-surface softening. Wave crests and valleys were identified and it was found that the depth of hardening under a wave crests extended to a distance equal to the height of the wave crest plus the depth of hardening beneath a valley. The depth of hardening beneath a valley was similar to that under single particle impacts.

The development of a ripple structure at 30° incidence and a hill-and-valley structure at 90° incidence was examined in detail for 1100 Al. It was found that the surface structures developed early in the erosion process and several overlapping impacts were necessary to achieve maximum strain hardening on the surface. The material continued to accumulate strain without fracture after the maximum flow stress was achieved. As in the earlier study, hardening extended to much greater depths under wave crests for erosion at 30°, supporting the view that strain hardened material was pushed up from the wave valleys into the crests. In contrast, for erosion at 90° incidence, the depth of hardening was approximately equal beneath hills and valleys. Significant embedment of erodent fragments, predominantly in the valleys, occurred for erosion at 90°. Deformation contours showed material being back-extruded from valleys into the hills, but most of this movement occurred near the surface rather than through the bulk of the material, leading to the observed hardness distribution. No near-surface softening was evident beneath the eroded surfaces of 1100 Al at either 30° or 90° incidence. However, there was some evidence for a constant hardness in the near-surface layers, especially at 90° incidence. Material removal was controlled by the attainment of a critical fracture strain and occurs due to overlapping impacts or by the fracture of lips of material extruded from wave crests.

The surface structure apparently initiated due to locally high concentrations of impacts leading to incipient hills or wave crests which persist because the impact energy is distributed over smaller volumes in the highly strain hardened material. The hills/crests grow since for 30° impacts, most of the hardened material is pushed in front of the impacting particle and for 90° impacts, a higher concentration of voids and fissures associated with particle embedment lead to greater deformation in valley regions. The peak hardness in valley regions were sometimes less than on hills/crests, perhaps due to recent

material movement out of the valleys. The structures continue to grow until material removal rates from hills/crests and valleys are balanced.

Surface structure is expected to be strongly influenced by target material strength and ductilities, developing to a greater extent on softer, more deformable materials. The spacings of the features are expected to be related to the range of deformation associated with an impact, and therefore to particle size (as has been observed) as well as to the impact velocity. Within the same family of alloys, the development of ripples or hills and valleys may contribute to increased erosion resistance due to longer incubation periods, greater absorption of the incident energy in material deformation and movement processes and possible shielding from impact of low lying areas by neighboring elevated regions.

Taper-sectioning was shown to be a powerful technique to examine the near-surface deformation of eroded surfaces. However, the technique has to be used judiciously and results analyzed carefully in order to avoid misinterpretation of the data.

The multiple particle erosion of the iron aluminide alloy FA-129 by steel shot was also examined in detail. It was found that erosion occurred even though most of the impacting particles were softer than the target material. Softer spherical particles appeared to merely form an impression on the target surface whereas harder particles formed extruded lips, especially under oblique impact. Two distinct erosion mechanisms were observed: extrusion and fracture of platelets by the impact of spherical particles and a cutting or gouging out of material by the impact of angular particles which were present in the shot as well as formed by fragmentation upon impact of an oxide scale covering many of the particles. The platelets and extrusions were relatively small and angular particles had more damage associated with each impact event. Both mechanisms were observed at 30° incidence but damage by angular particles and debris dominated at higher angles. The steady state erosion rates were roughly equal at 30° and 60° incidence with some indication that the steady state rate at 90° may also be similar, due to a complex balance of the extent of platelet formation and cutting at the various angles.

The alloy work hardened significantly under impacts at both 30° and 90° incidence. Unlike 1100 Al, the hardness dropped off in near-surface layers, and the thickness of this softened layer increased with erodent dose. Also unlike 1100 Al, the value of the peak subsurface hardness was similar to that under single particle impacts. The depth of overall work hardening as well as the thickness of the softened near-surface layer were both greater for

erosion at 90° because a greater fraction of the energy of impacting particles was transferred to the target. The angular dependance of the depth of hardening was less pronounced in 1100 Al, implying that in softer, more deformable materials, a larger fraction of the impact energy is expended in moving material and developing the surface topography.

The surface of the iron aluminide did not develop features observed on eroded 1100 aluminum, suggesting limited ductility under the erosion test conditions. The platelets and extrusions created by the impinging shot were also small, implying an inability of the material to sustain large plastic strains. However, there were no signs of cracks or delaminations that would indicate macroscopic brittle failure in the material. The near-surface layers of the iron aluminide alloy were found to be in a disordered state after erosion. However, the effect of this phase transformation on the erosion process was not clear. Data from available literature showed that the aluminides may have an erosion resistance comparable to other engineering alloys and the overall results indicate relatively good resistance of iron aluminides to solid particle erosion which may be improved by increasing the alloy's ductility.

In the case of the iron aluminide alloy, the maximum hardness reached was similar in single and multiple particle impact studies. However, in 1100 Al, the flow stress built up over several impacts. Increasing the velocity of the single impact caused near-surface softening before the maximum flow stress was achieved. This indicated possible thermal effects. Single particle impact studies at high velocities were found to correlate well with results from low velocity multiple particle erosion experiments. It was found that although a single impact can remove material at high velocities, the several overlapping impacts needed to remove material at relatively low velocities expend less overall energy due to strain localization effects in the extruded lips formed on impact. Single particle impacts will therefore tend to underestimate the erosion rate.

Relatively early material loss in the iron aluminide alloy in both single and multiple particle impact tests could be related to its lower ductility as well as its propensity to localize deformation due to its ordered nature. In contrast, the high dynamic recovery and stacking fault energy of 1100 Al allowed impact energy and deformation to be spread more uniformly, explaining the lack of brittle failure observations in cold-worked 1100 Al even though ductility was greatly reduced.

The mechanical properties of a material alone could not be consistently explain the observed deformation behavior and material removal under the various impact conditions. Contrary to what is generally assumed, the volume of deformed material due to an impact was significantly larger than the crater volume. It was shown that elastic-plastic contact mechanics did not accurately predict the similarity in hardening depths between the heat teated and cold-worked 1100 Al and iron aluminide alloys for impact around 60 m/s, and that influences other than pure mechanical properties effects were important at these velocities.

Residual stress effects explained the occurrence of near-surface softening in the iron aluminide alloy but could not satisfactorily explain the hardening behavior observed for single particle impacts at various velocities. Thermal effects could more completely explain the results based on the argument that at moderate velocities, strong dynamic recovery effects in 1100 Al promote the development of a constant flow stress whereas localization of deformation in the iron aluminide alloy promote dynamic recrystallization effects, leading to near-surface softening. At very high velocities, stronger thermal effects dominated over dynamic recovery effects in 1100 Al, leading to near-surface softening, probably due to recrystallization from residual heat. At low velocities, thermal effects no longer dominate and the impact response is controlled mainly by the mechanical properties of the alloy. Thermal effects may be expected to be significant over a significant portion of the velocity range for erosion applications. However, at any velocity, thermal effects will be less important for impacts with angular particles compared to spherical. Since thermal effects need not necessarily create a soft surface layer, erosion conditions have to be analyzed carefully to anticipate possible effects.

Thermal effects could explain lack of difference in hardening depths between the two alloys for moderately low velocity single impacts and the higher hardening depth in the iron aluminide alloy for high velocity single impacts. It was estimated that clear evidence of thermal effects in 1100 Al during multiple particle impact experiments would be seen under experimental conditions somewhat more severe than in the present study.

Potential areas for future work include erosion studies in iron aluminide alloys using angular particles, erosion induced order-disorder transformations in iron aluminide alloys, residual stress effects during erosion and high velocity single impact studies on various aluminum alloys or steels to study relative influence of mechanical properties and thermal effects on erosion.

Mechanical Properties of Oxide Scales

Introduction

The mechanical properties of protective oxide scales are being characterized based on the premise that properties such as hardness, modulus, etc., ultimately determine whether a chemically stable surface oxide will retain its integrity in corrosive, high-temperature environments and, thus, whether a particular high- temperature alloy is generally corrosion resistant. A mechanical properties microprobe (MPM) is being used to measure hardness, Young's modulus, and plasticity of alumina and chromia scales and bulk oxides by depth-sensing submicron indentation testing. During the current reporting period, emphasis was placed on the development of methodologies for measuring the mechanical properties of thin oxide scales by focusing on a greater in-depth analysis of the various MPM data sets.

Discussion Of Current Activities

It was previously shown[8] that while, in general, the MPM data did fall within the expected range and good precision was found, there was a significant variation among the moduli of four polycrystalline specimens of bulk alumina. Several of these values, as well as the measured moduli (E) and hardnesses (H) of sapphire, were higher than those reported in the literature.[8] Because the determinations of H and E strongly depend on the modeling of the indenter contact area, errors in the calculation due to surface roughness or the specific analytical approach to the estimation of the indenter tip shape have to be considered because they can lead to different results for the same material. However, this type of factor would not explain the specimen to specimen variation[8] because all the specimens had similar surface finishes and the same model was used for the properties determinations. Furthermore, recent calculations of the values of H/E^2, which does not depend on knowledge of indenter contact area,[9] showed that such estimation errors were not the cause of the scatter for a particular alumina specimen nor of the differences among them. Therefore, based on this finding and previous observations,[8] it is thought that the variability among different sets more likely arises from errors in the determination of the machine compliance, and/or other instrument changes.[10,11] Better control over some of these factors, as well as the use of standards for checking reproducibility over a period of time, may well reduce the specimen-to-specimen variation.

MPM results for chromia scales grown on chromium showed substantially greater scatter (in H and E) than those for other scales and bulk oxides.[8,12] It was therefore decided to reanalyze the data using the final unloading curves rather than the series of unloading curves gotten during the loading cycles.[13] The results (shown in Table 1) yielded a more realistic value of the elastic modulus (averaged over several successful indentations) and a smaller standard deviation. Further evaluation of the differences between the two analysis techniques will be required to determine the best measurement approach.

In FY 1992, the measurements of the mechanical properties of thin oxide scales will no longer be a separate task. Rather, such work will constitute one part of the overall characterization efforts being performed in support of the development of corrosion-resistant iron aluminides and ultrahigh strength high temperature intermetallics.

Table 1. Hardness, Young's Modulus, and Ratio of Plastic to Total Indentation Depth(PD/ID) As Determined Using The Mechanical Properties Microprobe

Type	H (GPa)	E (GPa)	PD/ID
Scale on Cr	30±9	318±52	0.68±0.04
Bulk Chromia	37±4	275±17	0.60±0.02
Unoxidized Cr	6±1	129±5	0.83±0.01

References

1. J. R. Keiser, Design, Construction and Initial Results for an Erosion-Corrosion Test System, *Oak Ridge National Laboratory, ORNL/TM-10049*, May 1986.

2. J. R. Keiser, p. 345 in *Proc. Conf. on Corrosion-Erosion-Wear of Materials at Elevated Temperatures*, A. V. Levy (ed.) National Association of Corrosion Engineers, Houston, TX, (1987) 345.

3. J. R. Keiser, R. C. Heidersbach, D. L. Dobbs, Jr., and W. C. Oliver, *Wear* **124** (1988) 105.

4. J. R. Keiser, R. C. Heidersbach, D. L. Dobbs, Jr., and W. C. Oliver, *J. Mater. Eng.*, **10** (1988) 273.

5. M. Rao, J. Keiser and D. Wilson, *Scripta Met.* **23** (1989) 1475.

6. J. R. Keiser, D. F. Wilson, J. N. Hines and A. V. Levy, *J. Mater. Eng.* **12** (1990) 245.

7. M. Rao, J. R. Keiser and D. F. Wilson, "Subsurface Hardening and Flow of Aluminum During the Incubation Period of Solid Particle Erosion, to be published in *Proc. 4th Berkeley Conf. on Corrosion-Erosion-Wear of Materials at Elevated Temperatures*, , National Association of Corrosion Engineers, Houston, TX,.

8. P. F. Tortorelli and J. R. Keiser, p. 377 in *Proc. 5th Annual Conf. Fossil Energy Materials*, N. C. Cole and R. R. Judkins (comp.), ORNL/FMP-91/1, September 1991

9. D. L. Joslin and W. C. Oliver, *J. Mater. Res.* **5** (1990) 123.

10. W. C. Oliver and G. M. Pharr, "An Improved Technique For Determining Hardness and Modulus Using Depth Sensing Microcontact Experiments," to be submitted for publication in *J. Mater. Res.*, 1991.

11. M. E. O'Hern, Nano Instruments, Inc., Knoxville, Tennessee, private communication, May 1991

12. P. F. Tortorelli, J. R. Keiser, K. R. Willson, and W. C. Oliver, p. 271 in *Microscopy of Oxidation*, M. J. Bennett and G. W. Lorimer (eds.), The Institute of Metals, London, United Kingdom, 1991.

13. W. D. Nix, *Metall. Trans. A* **20A** (1989) 2217-2245.

UCIN-3 - STUDY OF PARTICLE REBOUND CHARACTERISTICS AND MATERIAL EROSION AT HIGH TEMPERATURES

W. Tabakoff, A. Hamed and M. Metwally

Department of Aerospace Engineering and Engineering Mechanics
University of Cincinnati
Cincinnati, Ohio 45221-0070

INTRODUCTION

The objective of this research work is to investigate the basic erosion processes and fluid mechanics associated with material degradation in the components of various coal conversion and utilization systems. The understanding of erosion patterns and rates will be enhanced through a study of the rebound characteristics of particles impinging various surfaces and through the measurement of erosion rates of materials and coatings exposed to high temperatures. The overall goal is to develop a quantitative model, which will facilitate the prediction of erosion in systems operating in particulated environments.

DISCUSSION OF CURRENT ACTIVITIES

This program comprises an experimental investigation to study the ash particle rebound characteristics and the associated erosion behavior of superalloys and coatings subjected to particulate flows at elevated temperatures. A three-component LDV system was used to measure the restitution parameters of 15 micron mean diameter coal ash particles impacting some widely used superalloys and coatings at different angles. The experimental results were used to develop correlations for the restitution parameters for uncoated and coated superalloys. The erosion behaviors of superalloys and protective coatings have also been investigated experimentally at high temperatures using a specially designed erosion wind tunnel. The experimental results collected in the test program have been used to develop erosion models for the investigated materials. The proposed models have been used to predict the erosion behavior for FSX-414, IN-738, MAR-M246 and X40 alloys and N,

RT22 and RT22B coatings. The present results show comparison between predicted and measured erosion rates collected over wide ranges of test conditions. In addition, the developed models have been used to predict particle trajectories and blade erosion in a two-stage turbine for uncoated and coated blade surfaces. The predicted 3-D particle trajectories and spacial distribution of surface erosion over the blade pressure surfaces are presented.

Development of Erosion Model

For analyzing material erosion by solid particles, the material behavior is either "ductile" or "brittle". An ideally brittle material fractures after only plastic deformation, while ideally ductile material undergoes very large plastics strains before material removal. For ductile material erosion, further simplifications have been made by assuming two erosion mechanisms: one at low impingement angle and another at normal impact. At intermediate impingement angle, a combination of the two mechanisms was proposed. Following this approach, erosion models have been proposed for ductile erosion at oblique and normal impacts.

In the erosion process, the material removal depends on the crater volume formed by the particle. The crater volume depends on the maximum particle penetration normal to the surface and also on the particle displacement parallel to the surface. Since the crater shape is not critical parameter in material erosion, its geometry can be simplified. The simplified crater depth can be assumed constant. Although the proposed and actual crater shapes are different, their volumes can be assumed equal.

The normal penetration is a plastic deformation which depends on the normal force exerted by the particle upon impacting the target. This normal force depends on the change of momentum between the particle and the surface in the normal direction upon impact. The tangential displacement depends on the energy required to remove (or deform) the target material tangentially. This energy depends on the exchange of tangential kinetic energy between the particle and target upon impact.

Erosion Model at Low Impingement Angle

Considering a modified crater shape, the erosion process can be described in two steps as depicted in Fig. 1. First the particle penetrates the surface normally, then moves tangentially parallel to the undisturbed surface removing target material.

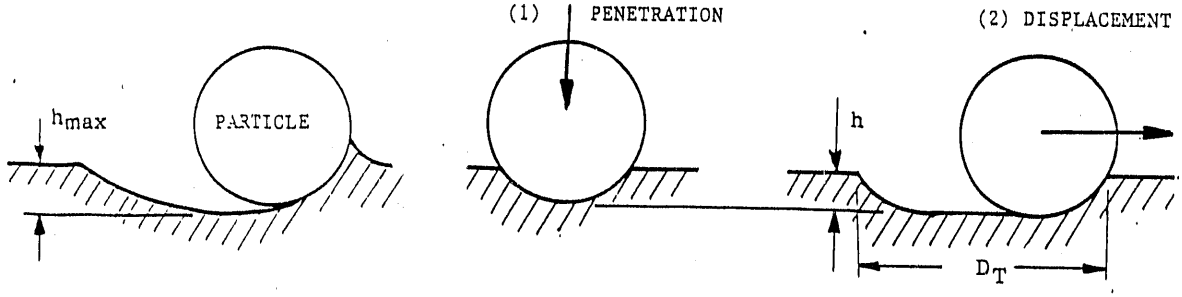

(a) Actual (b) Theoretical

FIG. 1. SCHEMATIC OF THEORETICAL AND ACTUAL EROSION PROCESS.

Based on the above discussion, the crater depth ,h, depends on the normal force exerted by the particle on the surface upon impact which is proportional to the particle momentum in the normal direction; i.e.:

$$h \propto M_P \, V_{N1} \tag{1}$$

where h: an average crater depth,

M_P: particle mass,

V_{N1}: normal component of the particle impact velocity.

The tangential particle displacement depends on the energy required for material removal which is proportional to kinetic energy exchange between the particle and the target tangentially upon impact.

$$D_T \propto M_P \, (V_{T1}^2 - V_{T2}^2)$$

$$\propto M_P \, V_{T1}^2 \, [1 - E_T^2] \tag{2}$$

where D_T: an average particle displacement in the tangential direction,

V_{T1}: tangential component of particle impact velocity,

V_{T2}: tangential component of particle rebound velocity,

E_T: tangential restitution ratio.

$$E_T = \frac{V_{T2}}{V_{T1}}$$

The volume of the material removed, (Vol.), depends on the depth, h, and displacement, D_T, i.e.

$$Vol \propto h \times D_T \tag{3}$$

where Vol: crater volume,

V_1: particle impact velocity,

β_1: particle impingement angle.

Using Eqs. (1) and (2), equation (3) can be written as:

$$\begin{aligned} Vol &\propto M_P V_{N1} \times M_P V_{T1}^2 (1 - E_T^2) \\ &\propto M_P^2 V_1^3 \sin\beta_1 \cos^2\beta_1 (1 - E_T^2) \end{aligned} \tag{4}$$

Consequently, material weight loss can be expressed as follows:

$$\begin{aligned} \Delta W &= \rho_t Vol \\ &= C_0 M_P^2 V_1^3 \sin\beta_1 \cos^2\beta_1 (1 - E_T^2) \end{aligned} \tag{5}$$

where C_0 : a constant depends on the target material,

ΔW : material weight loss,

ρ_t : material density.

Dividing Eq. (5) by the particle mass, M_P, the erosion mass rate can be expressed as follows:

$$\epsilon_c = C_0 M_P V_1^3 \sin\beta_1 \cos^2\beta_1 (1 - E_T^2) \quad (6)$$

where ϵ_c: material erosion per unit mass of particles. Since the particle mass can be assumed constant, equation (6) can be written

$$\epsilon_c = C_1 V_1^3 \sin\beta_1 \cos^2\beta_1 (1 - E_T^2) \quad (7)$$

where C_1: constant,

$= C_0 M_P$

In the above expression, the material erosion rate is proportional to particle velocity cube. This value of the velocity exponent agrees with the most velocity exponent values obtained experimentally.

Erosion Model at Normal Impact

The amount of material plastic deformation depends on the kinetic energy exchange between the particle and the target at normal impact. So that it can be assumed that material erosion is proportional to change of particle normal velocity kinetic energy. Therefore, the material erosion has been proposed as follows:

$$\Delta W_{90} = C_2 M_P (V_{N1}^2 - V_{N2}^2)$$

$$= C_2 M_P V_{N1}^2 (1 - E_N^2) \quad (8)$$

where ΔW_{90}: material removal at normal impacts,

V_{N1} : normal component of particle impact velocity,

V_{N2} : normal component of particle rebound velocity,

C_2 : empirical constant .

E_N: normal restitution ratio.

$$E_N = \frac{V_{N2}}{V_{N1}}$$

Dividing by particle mass, the material mass erosion can be express as follows:

$$\epsilon_{90} = C_2 V_{N1}^2 (1 - E_N^2)$$
$$= C_2 V_1^2 \sin^2\beta_1 (1 - E_N^2) \quad (9)$$

where ϵ_{90} : mass erosion per unit mass of particles at 90°.

Prediction of the Superalloy and Coating Erosion Rates

The total material erosion has been calculated at any angle by superimposing the two type of erosion described by Eqs. (7) and (9). The general relationship of the total erosion can be expressed as follows:

$$\epsilon = \epsilon_c + \epsilon_{90}$$
$$= C_1 V_1^3 \sin\beta_1 \cos^2\beta_1 (1 - E_T^2) + C_2 V_1^2 \sin^2\beta_1 (1 - E_N^2) \quad (10)$$

where ϵ is total mass erosion per unit mass of particles (mg/gm) and V_1 is impact velocity (m/s).

Although the experimental results showed that the velocity exponent is in the vicinity of three, the measured values were different for different materials. This might due to the effect of the other parameters effecting on the erosion rate which are not modeled in this analysis. Therefore the total mass erosion rate (Eq. (10)) has been modified to the following form.

$$\epsilon = C_1 V_1^{n1} \sin^{n2}\beta_1 (1 - E_T^2) + C_2 V_1^{n4} \sin^2\beta_1 (1 - E_N^2) \quad (11)$$

where the values of the exponents are empirically determined. In addition the erosion rate has been found to vary with target temperature. In this study, erosion rate was observed to change slightly with varying target temperature for most of the investigated materials. However, when the target temperature approached the level at which the yield strength begins to drop rapidly, the erosion rate increases abruptly. Therefore, the same approach used by Wakeman[5] has been employed to corporate the temperature effect on the erosion rate by using an empirical expression to match the data as follows:

$$\epsilon = F(T)\ \epsilon_{RT} \tag{12}$$

where:

$$F(T) = \left(\frac{Y_{RT}}{Y}\right)^{a} + \frac{Y}{Y_{RT}} - 1 \tag{13}$$

where ϵ : erosion rate at operating temperature,

ϵ_{RT} : erosion rate at reference temperature,

Y : material yield strength at operating temperature,

Y_{RT} : material yield strength at reference temperature,

a : empirical constant.

The ambient temperature has been taken as a reference temperature. Therefore, F(T) at ambient is equal to one and the erosion rate at ambient temperature can be expressed by Eq. (11).

Combining Eqs. (11), (12), and (13) gives:

$$\epsilon = F(T)\ [C_1(V_1/100)^{n1}\ \sin^{n2}\beta_1\ \cos^{n3}\beta_1\ (1 - E_T^2) + C_2(V_1/100)^{n4}\ \sin^{2}\beta_1(1 - E_N^2)] \tag{14}$$

The erosion rate model as described above gives the erosion rate as a function of material yield strength, particle impact velocity, impingement angle and particle velocity restitution ratios. The restitution ratios have been calculated using the equations developed experimentally. The constants C_1, and C_2 and the exponents, n's, are

determined empirically from the experimental data by using multiple regression analysis. $V_1/100$ is used in place of V_1 to control the magnitude of C_1 and C_2 in the correlation. Table 1 summarizes the values of the constants and exponents for the investigated alloys and coatings whose erosion behaviors are ductile.[1]

Table 1. Material Coefficients of Erosion Models

MATERIAL	a	C1	C2x10^2	n1	n2	n3	n4
FSX-414	1.05	1.18258	1.93233	2.90	0.50	2.40	3.13
IN-738	4.85	0.02173	2.61691	2.57	0.40	2.40	2.77
M-246	5.40	0.418612	2.73895	2.32	0.60	2.25	2.94
X-40	0.95	0.1888266	2.25033	3.18	1.15	2.25	2.63
N	--	0.0510006	0.11602	3.31	1.35	3.00	3.22
RT22	--	0.0562133	0.052228	2.72	0.65	4.75	2.75
RT22B	--	0.027657	0.01216	3.70	1.50	4.30	3.73

Using the semi-empirical equations the erosion rates have been calculated for the investigated superalloys and coatings for different velocities, impingement angles and temperatures. Figures 2 through 5 represent predicted erosion rates against measured erosion rates for INCO-738, FSX-414, M246 and X40 alloys. The material yield strength for the superalloys have been substituted into the temperature parameters, F(T). These terms have been plotted against target temperature in Fig. 6 for each material. The temperature parameters value have been used in the calculations involved with the erosion rate equations. Figures 7 through 9 show comparison between calculated and measured erosion rates for N, RT22 and RT22B coatings.[1] Due to lack of information about coatings yield strength, it was not possible to calculate its temperature parameters. The figures show that the calculated erosion

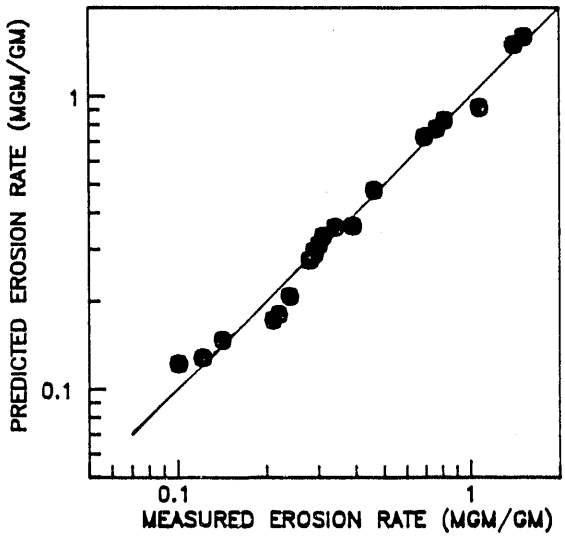

FIG. 2. COMPARISON BETWEEN MEASURED AND PREDICTED EROSION RATES FOR FSX-414 ALLOY

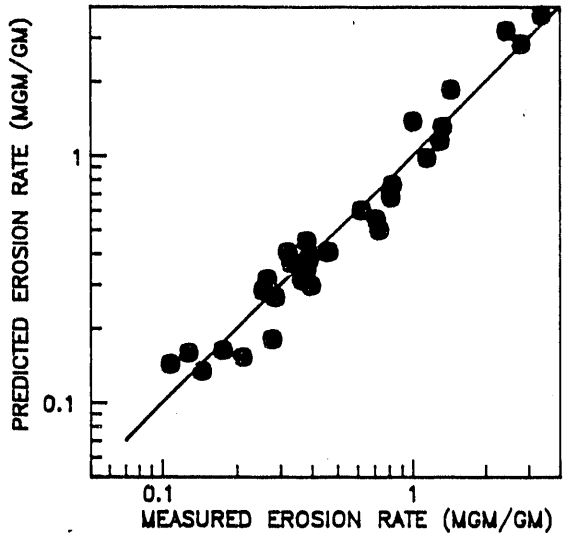

FIG. 4. COMPARISON BETWEEN MEASURED AND PREDICTED EROSION RATES FOR M246 ALLOY

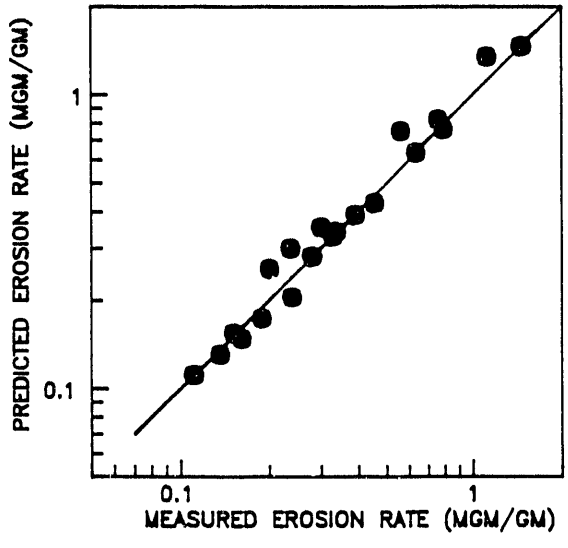

FIG. 3. COMPARISON BETWEEN MEASURED AND PREDICTED EROSION RATES FOR IN-738 ALLOY

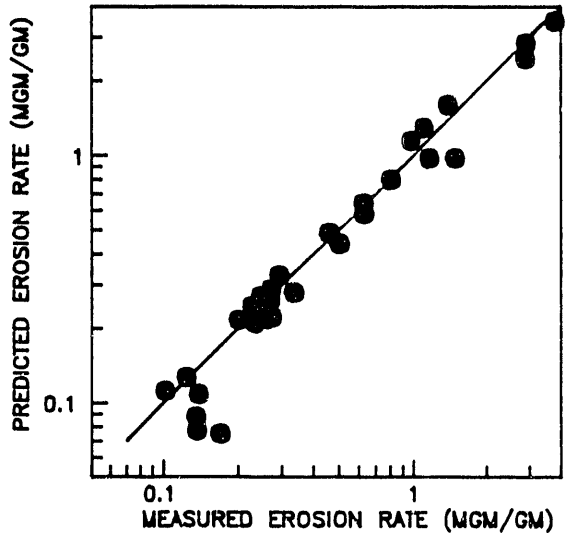

FIG. 5. COMPARISON BETWEEN MEASURED AND PREDICTED EROSION RATES FOR X40 ALLOY

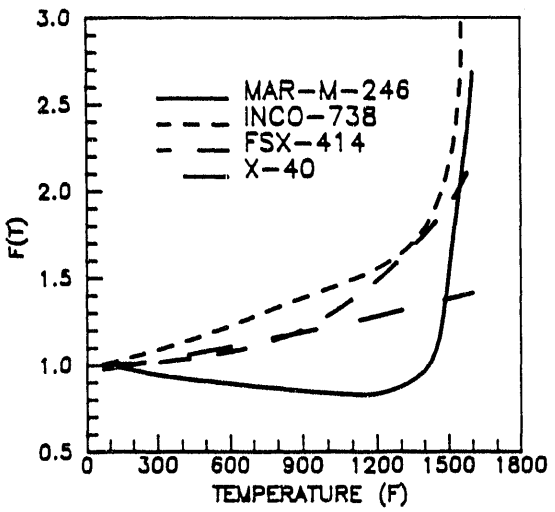

FIG. 6 VARIATION OF SUPERALLOY TEMPERATURE PARAMETERS WITH TEMPERATURE

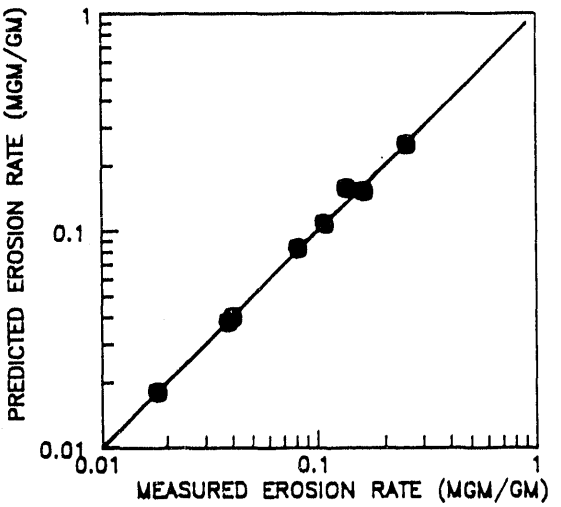

FIG. 8. COMPARISON BETWEEN MEASURED AND PREDICTED EROSION RATES FOR RT22 COATING

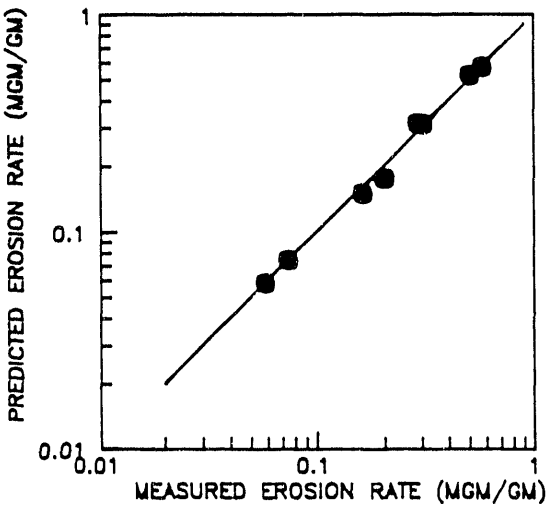

FIG. 7. COMPARISON BETWEEN MEASURED AND PREDICTED EROSION RATES FOR N COATING

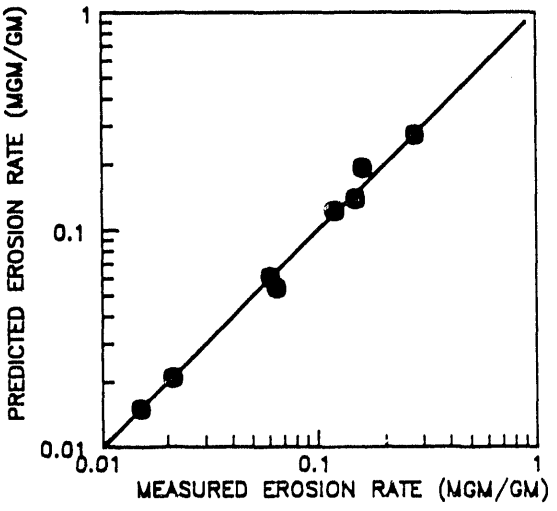

FIG. 9. COMPARISON BETWEEN MEASURED AND PREDICTED EROSION RATES FOR RT22B COATING

rates correlate well with measured erosion rates for both uncoated and coated surfaces.

Particle Trajectories and Blade Erosion in a Two-Stage Turbine Based on Rebound and Erosion Models

The proposed rebound and erosion models have been used to predict particle trajectories and blade erosion in a two stage axial flow gas turbine. The investigation involved three major modeling efforts, namely, (i) modeling the three dimensional flow field in each blade row, (ii) prediction of the three dimensional particle dynamics under the influence of the flow field aerodynamic forces and the interactions with blades, hub and shroud, and (iii) blade erosion computation based on particle impact data and erosion model of the blade material.

Particle Trajectories

Due to their higher inertia, the particle trajectories in turbomachines generally differ from the flow streamlines and particles tends to impact the blade surfaces, hub and tip walls. The particle trajectory calculation consists of numerical integration of the particle three dimensional equations of motion in the flow field, up to the point of blade, hub or casing impact. The magnitude and direction of particle rebound velocity after these impacts are predicted by using rebound model developed for the particle-material combination under consideration. Such computations have been conducted based on the proposed rebound model to investigate the trajectories in the flow passages of a two stage turbine for fly ash particles for uncoated and coated blade surfaces. The detailed description of computation technique and results can be found in ref. 2.

Figure 10 shows samples of particle trajectories projected in θ-z plane for 15 micron fly ash particles through a two stage turbine whose geometry can be found in ref. 3. The figure clearly indicate that the particle deviation from the streamlines. So that some of the particles tend to impact the pressure side of the first stator and some impacts the leading edges. At the first stator exit, the particle absolute velocities are lower than the gas velocity. Therefore, they enter the

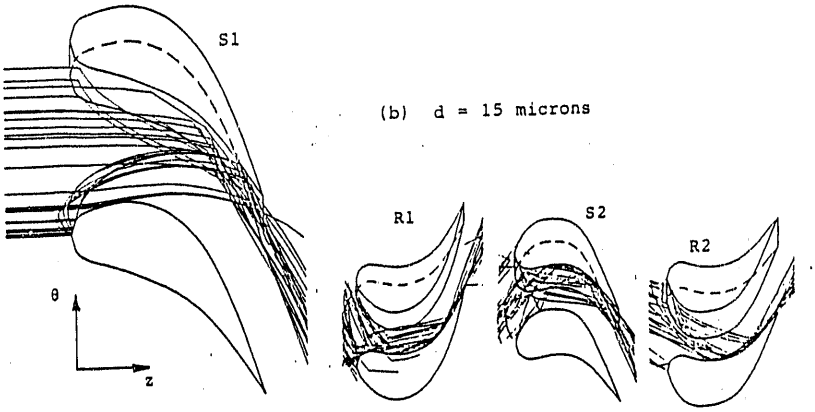

FIG. 10. PROJECTION OF PARTICLE TRAJECTORIES IN θ-z PLANE.

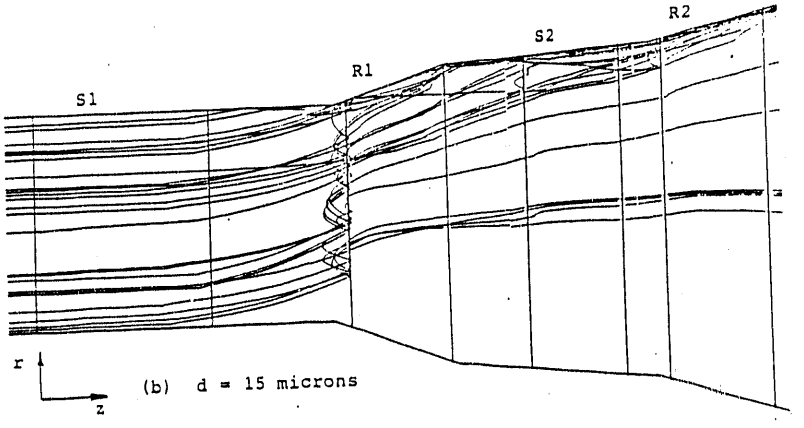

FIG. 11. PROJECTION OF PARTICLE TRAJECTORIES IN r-z PLANE.

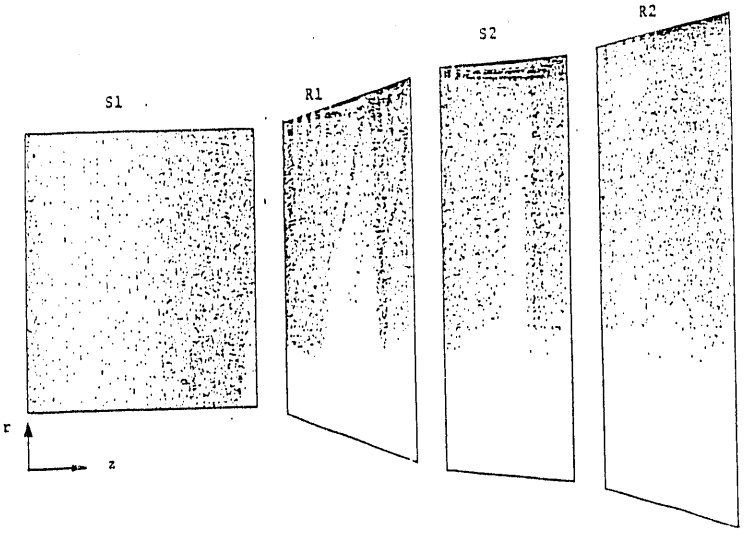

FIG. 12. IMPACT LOCATION FOR THE UNIFORM PARTICLES.

first rotor with higher incidence angles which causes the particles to impact the blade pressure surface near the rotor leading edge. After rebounding, they impact the rotor blade pressure surface near the trailing edge. In the second stage, similar behaviors can be observed.

The projection of particle trajectories in r-z plane is shown in Fig. 11. The results demonstrate the influence of blade impacts on the particles, which are centrifuged towards the tip after the blade impacts. This leads to high particle concentrations near the blade tips resulting in higher erosion damages at tip.

Particle trajectory computations provide, particle impact location coordinates, the impact velocity magnitude, and the impingement angle relative to the blade surface at each impact location. Figure 12 shows impact locations for 15 microns particles in a two stage turbine over the blade pressure surfaces. The effect of particle centrifugation are noticeable in the absence of impacts near the blade hubs. Figure 12 shows that particle migration towards the tip increases in downstream direction which leads to increased particle impacts towards the blade tips.

Blade Surface Erosion

The prediction of turbine blade erosion is based on the particle impact data as determined from the trajectories and erosion models developed for the particle-material combination. Based on the erosion models developed for M246 alloy and N and RT22 coating, the blade surface erosion have been predicted in a two stage turbine. The results are recently presented in the 5th International Symposium and Exposition on Gas Turbines in Cogeneration, Repowering and Peak-Load Power Generation in Budapest, 1991 (ref. 4). Some of these results are shown in Figs. 13 through 16. These figures present the spacial distribution of the erosion parameter (material weight loss per unit mass of particles per unit surface area) over the blade pressure surfaces in the two stage turbine for uncoated (M246 alloy) and coated surfaces (N and RT22 coatings). Although the coatings did not change the erosion pattern significantly over the blade surfaces, they remarkably reduced the blade erosion. Comparing the values of maximum erosion at the mid span of the trailing edge (Fig. 13) reveals that the uncoated blade

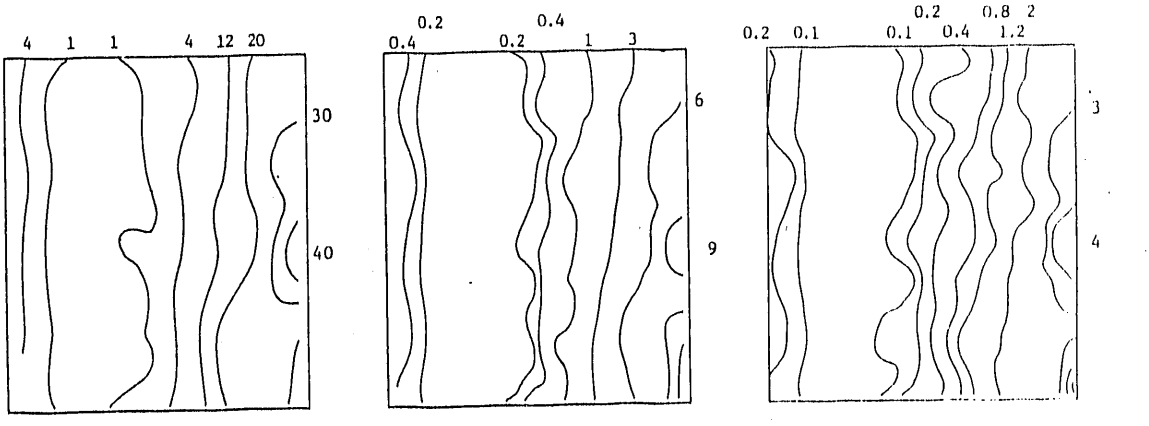

(a) M246 ALLOY
Nickel Base Alloy

(b) N COATING
Aluminide Coating
(Substrate M246)

(c) RT22 COATING
Platinum Aluminide Coating
(Substrate M246)

FIG. 13.
FIRST STATOR PRESSURE SURFACE EROSION RATE x 10^5 (mgm/gm/cm^2)

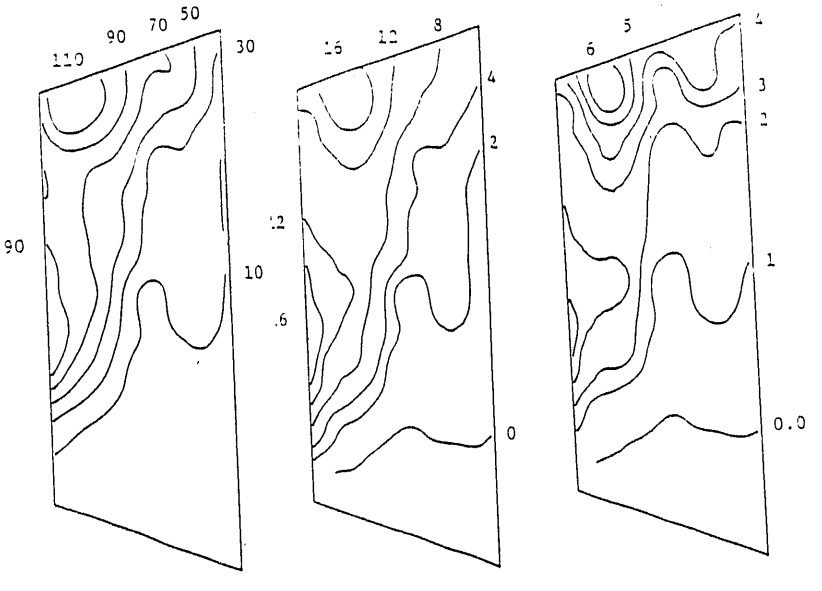

(a) M246 ALLOY (b) N COATING (c) RT22 COATING

FIG. 14.
FIRST ROTOR PRESSURE SURFACE EROSION RATE x 10^5 (mgm/gm/cm^2)

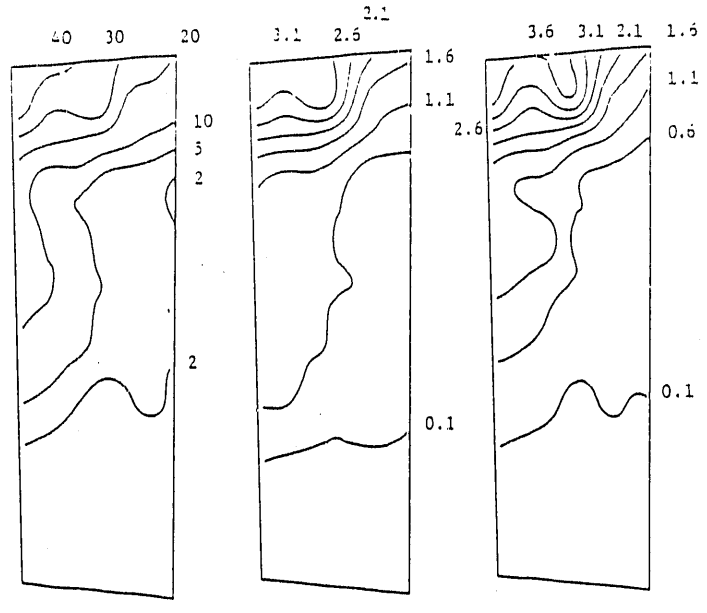

(a) M246 ALLOY (b) N COATING (c) RT22 COATING

FIG. 15
SECOND STATOR PRESSURE SURFACE EROSION RATE x 10^5 (mgm/gm/cm^2)

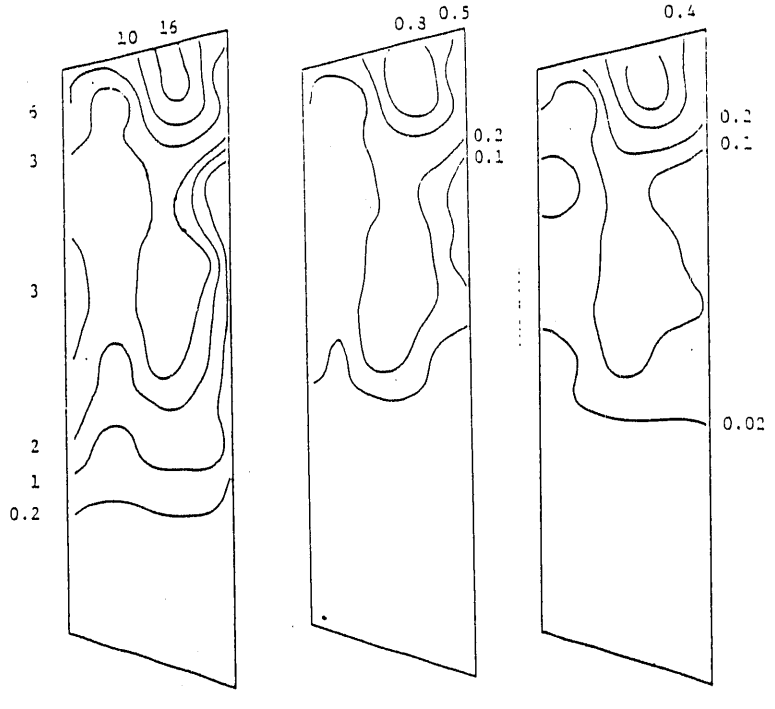

(a) M246 ALLOY (b) N COATING (c) RT22 COATING

FIG. 16.
SECOND ROTOR PRESSURE SURFACE EROSION RATE x 10^5 (mgm/gm/cm^2)

maximum erosion is one order of magnitude the maximum erosion of coated blade. Figure 14 shows that the reduction of the maximum erosion at the rotor tip leading edge is 70% for N coating and 95% for RT22 coating. This strong influence of the blade coating on the erosion can be clearly seen in Fig. 15 and 16 which show the erosion parameter of the second stage. This remarkable improvement of coated surface erosion prolongs greatly the blade life and reduces the blade material degradation due to particulated flows.

SUMMARY AND CONCLUSIONS

Erosion models have been developed for superalloys (MAR-M246, X40, FSX-414 and IN-738) and coatings (N, RT22 and RT22B) to predict the material erosion over a wide range of particulate flows. The predicted and measured erosion rates correlate well over a wide range of particle velocities, impingement angles, and target temperatures. Also, the models have been employed to predict fly ash particle trajectories and resulting blade erosion in a a two stage gas turbine for uncoated and coated surfaces. The results show that the blade pressure surfaces have much higher impacts than the suction surface. The results indicate that continuous particle centrifugation results in higher particle impacts towards the blade tips. The pressure surface erosion computations for uncoated and coated blades show that the coatings provide a very good protection and greatly prolong the blade life.

REFERENCES

1. Tabakoff, W., Hamed, A., Metwally, M., Yeuan, J., "Study of Particulate Rebound Material Erosion," ORNL Report FMP-90/2, September 1990, pp. 381-393.

2. Tabakoff, W., Hamed, A., Metwally, M., "Effect of Particle Size Distribution on Particle Dynamics Blade Erosion in Axial Flow Turbines," Journal of Engineering for Gas Turbines and Power, Vol. 113, No. 4, pp. 607-615, 1991.

3. Smith, J., Cargill, R.W., Strimbeck, D.C, Nabors, W.M. and McGee, J.P., "Bureau of Mines Coal-Fired Gas Turbine Research Project - Test of New Turbine Blade Design," RI 6920, U.S. Department of Interior, Bureau of Mines, 1967.

4. Tabakoff, W. and Metwally, M., "Coating Effect on Particle Trajectories and Turbine Blade Erosion," 5th International Symposium and Exposition on Gas Turbines in Cogeneration, Repowering and Peak-Load Power Generation, Budapest, September 3-5, 1991.

5. Wakeman, T., "Erosion Predictions and Measurements in High Temperature Particulate Flow Environments," Ph.D. Dissertation, Department of Aerospace Engineering and Engineering Mechanics, University of Cincinnati, 1982.

UND-3 - A STUDY OF EROSIVE PARTICLE REBOUND PARAMETERS

T.H. Kosel

Department of Materials Science and Engineering
University of Notre Dame
Notre Dame, IN 46556

INTRODUCTION

This research is designed to provide a systematic investigation of the effects of materials properties and experimental variables on the rebound directions and velocities of erodent particles. The general approach is to develop computer models for the impact of spherical and angular particles, and to compare the predictions with experimental measurements of both single and multiple impact rebound parameters. The project is also probing the question of the effects of various strengthening mechanisms on the dynamic flow stress of metals, which serves as the major material variable used as input for the computer rebound models. The project is primarily intended to develop computer models which can be used to predict the direction and velocity of rebound of a particle from a material, which is important in other programs aimed at computation of the flight path of particles through turbine engines. The rebound problem is also of interest from a purely scientific point of view, and because of the relationship between the energy lost and the amount of material removed by a particle during impact.

The computer models being developed take into account certain effects neglected in previous models, and are being used to concentrate primarily on the rebound problem. The project includes experiments in which rebound velocity measurements are made during both single and multiple-particle impact.

DISCUSSION OF CURRENT ACTIVITIES

Recent work has concentrated on preparation of the final report. Friction has been reintroduced into the angular particle model and improves the agreement with single impact experiments. In the area of dynamic hardness, a new experimental system has been designed and constructed, and initial data is in close agreement with previous data. The new system should permit measurements at higher velocities and with smaller particles, which will extend the range of temperature rise and strain rate. Separation of these variables with a simple model yields interesting results. An approximation used for crater volume in the Tabor model we have used for dynamic hardness was found to be inaccurate for higher velocities and soft materials, and has made it necessary to recompute all dynamic hardness data. No significant change was found in most data, and our previous conclusions are essentially unchanged.

Angular Particle Rebound Model

Following the modifications made to the angular particle rebound model (APM) described in the May, 1991 Fossil Energy Materials Program Conference,[1] friction has been reintroduced into the model. Figure 1 compares the rebound data for single impacts of 700 μm Al_2O_3 on 6061-T6 Al with the predictions of the APM with friction coefficients of $\mu = 0$ (no friction) and $\mu = 0.5$. Without friction, the model predictions are higher than the data at low angles of incidence, but are a reasonable fit at high angles of incidence. With $\mu = 0.5$ the predicted velocities are a much better fit. The direction of the frictional force depends on the direction of motion of each particle face relative to the target contact segment; these forces are added to the other forces on the particle. A more detailed description will be included in the final report.

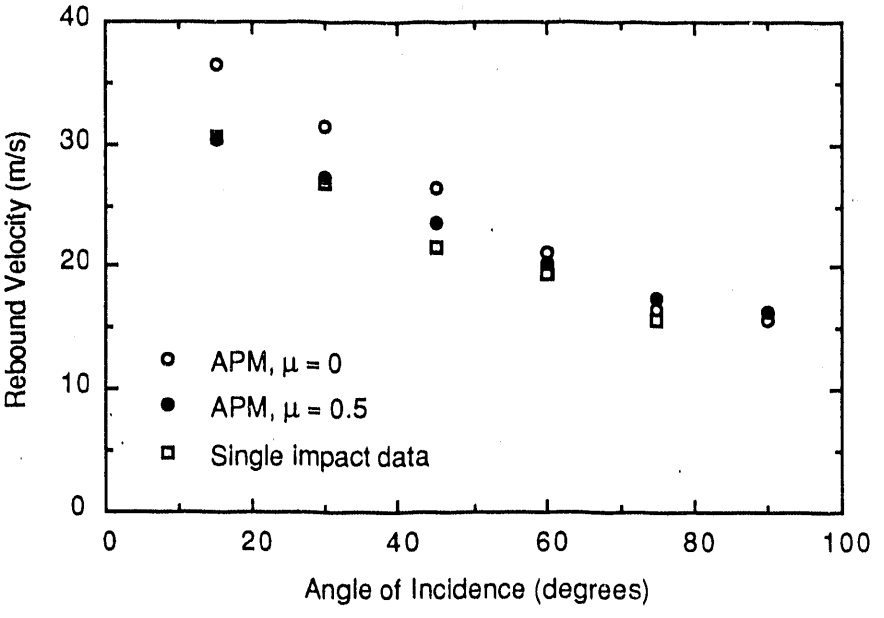

Figure 1. Effect of coefficient of friction μ on agreement of APM prediction of mean V_r vs α_1 (for all possible orientations of the realistic particle shape incident on 6061-T6 Al at 44.6 m/s) with data for single impacts of 700 μm Al_2O_3.

Dynamic Hardness

New Dynamic Hardness Test Apparatus

Additional experimental work on dynamic hardness is still in progress. This work is made possible by university support of one graduate student, and is beyond the original goals and expectations of the project. As discussed in a later section, by varying the diameter and velocity of spherical particles in the dynamic hardness method, it is possible to investigate the effects of temperature rise and strain rate on dynamic hardness. A new test apparatus has been constructed and tested which is designed to permit impacts at accurately predetermined velocities in vacuum. As discussed in earlier reports, the use of a pressurized gas pulse to accelerate particles toward the specimen produces a small deceleration of the rebounding particle. Although this effect has been measured and shown to be small, the desire to extend the tests to smaller particle diameters and a greater velocity range raised the issue of measuring this deceleration effect. It was decided to

avoid this problem by designing a system in which the specimen is mounted on the end of a rotating arm in vacuum, with particles being dropped in front of the arm. The impact velocity is then precisely known from the measured rotational rate of the arm. The particle rebounds through a pair of parallel 1 mm X 1 cm laser beams at a spacing of 1 cm to measure the velocity of the rebounding particle by means of photodiodes which detect the decrease of light intensity as the particle passes through the beams. During impact, the particle comes to rest in the specimen frame of reference before rebounding. It is therefore necessary to subtract the specimen velocity from the measured velocity of the rebounding particle to obtain the true rebound velocity, but since specimen velocity is accurately known this produces no significant error. The apparatus is shown schematically in Figure 2.

The particles are dropped one at a time in front of the specimen by placing them in small holes in a disc which is manually rotated to bring the hole over a drop tube. The probability of the particle hitting the specimen is quite close to unity due to the high speed of the specimen. This probability is increased by including a rebounding plate below the drop tube so that if a particle fails to strike the specimen, it bounces up and is struck on a subsequent pass of the specimen. The probability of the particles passing through the light beams is about 10 to 20%, but particles which do not strike the specimen are magnetically collected from the chamber. About 20 successful impacts can be made without breaking the vacuum system to change the specimen. To avoid striking an existing impact crater, the particle feeder is moved radially inwards slightly after each impact. The specimen arm is carefully balanced by means of a counterweight after the specimen is loaded, and velocities over 100 m/s have been reached without significant vibration. It is expected that higher velocities will be obtainable with a minor modification to the drive.

A second specimen is placed behind the light beams, and the particle then rebounds through the beams from this specimen. Since the incident and rebound velocities for the second specimen are measured from the light beams, dynamic hardness is obtained for two specimens with a single particle. Since the particle leaving the first specimen

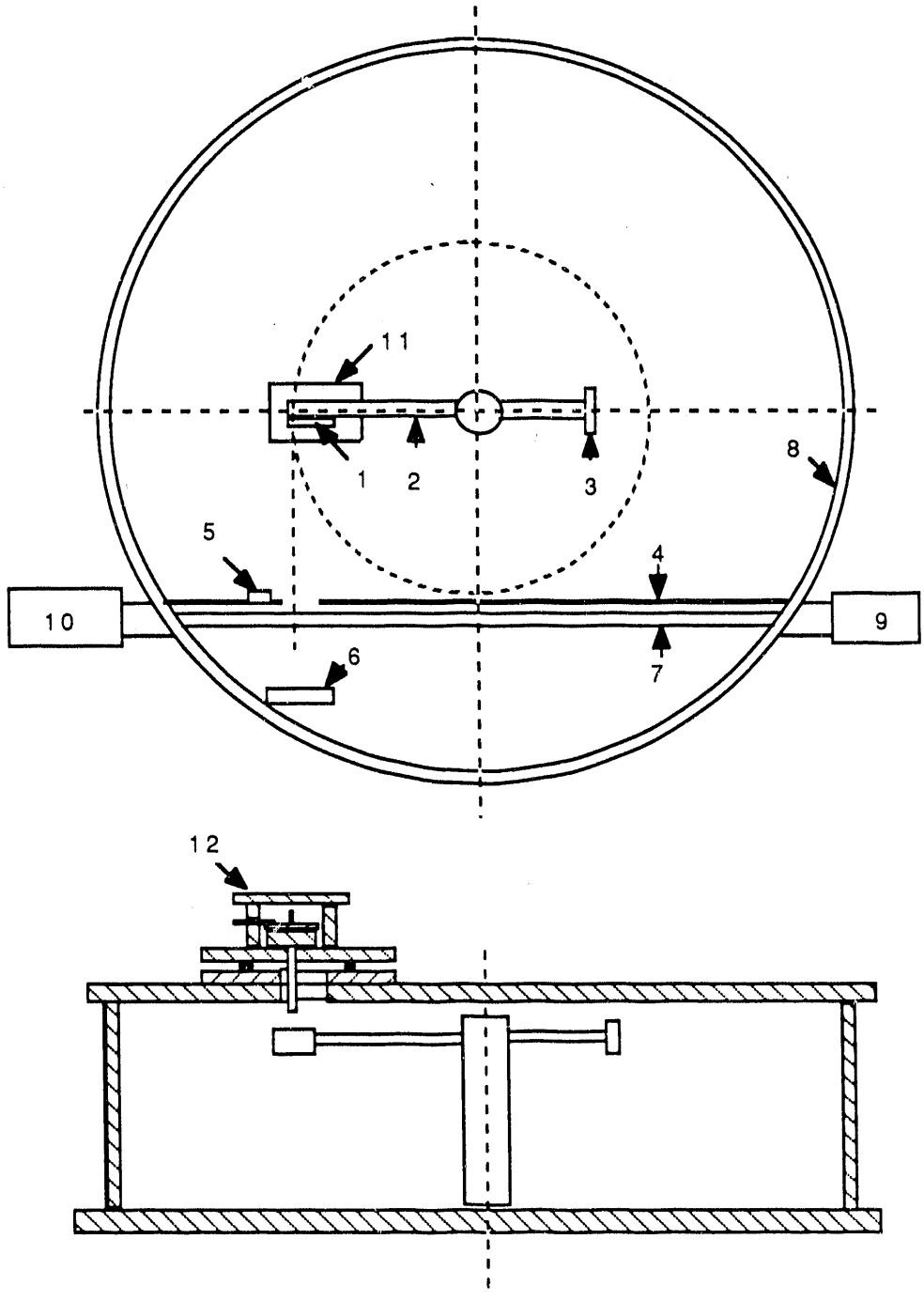

1. Specimen 1
2. Rotating Arm
3. Balance Weight
4. Shield Plate
5. Piezo Detector
6. Specimen 2
7. Laser Beams
8. Chamber
9. Photodiode Detector
10. Laser Source
11. Rebounding Plate
12. Ball Feeder

Figure 2. Schematic drawing of the new dynamic hardness apparatus.

has a higher velocity than the arm, incident velocities at the second specimen are higher. Using a very hard first specimen gives higher rebound velocities from specimen 1, and therefore increases the incident velocity at the second specimen, making it possible to reach higher incident velocities.

Figure 3 shows a comparison of dynamic hardness data obtained with the new and old test systems on 6061-T6 Al. As can be seen, there is an excellent correspondence between the data from the two systems.

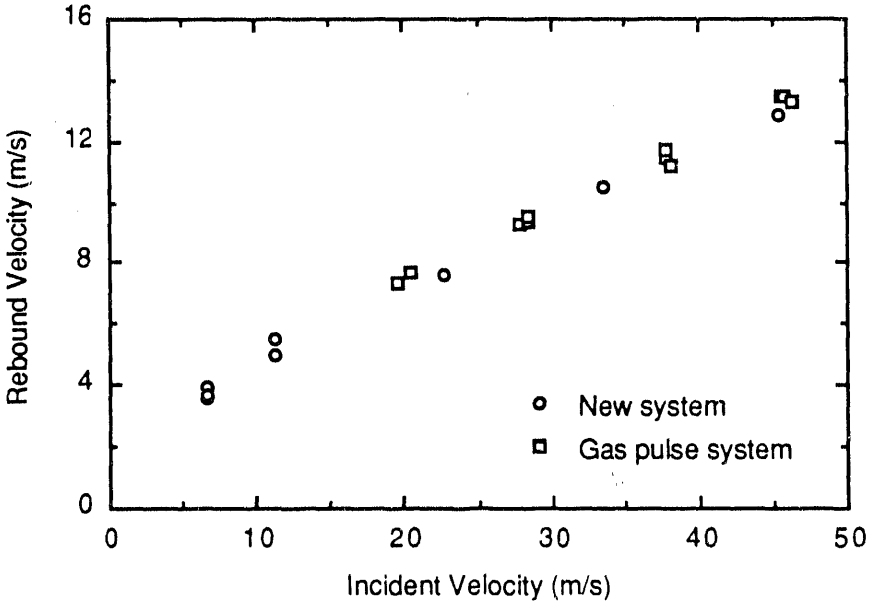

Figure 3. Comparison of rebound velocity data from the new vacuum dynamic hardness apparatus with that from the older gas pulse system.

Crater Volume Approximation

It was recently discovered that calculated values of crater radius sometimes actually exceeded the radius of the impacting sphere. This was traced to an approximation used in the Tabor formulation of dynamic hardness[2] in order to simplify the equations. Crater volume was approximated by

$$V = \pi a^4/4r \qquad (1)$$

where a is the crater radius and r is the sphere radius. The exact formula is

$$V = \pi h^2 (r - h/3) \qquad (2)$$

where h is the crater depth; this converges to the approximate expression in the limit of h = 0. The exact formula does not lend itself to simplification of the equations in the Tabor analysis, and we have therefore used an iterative computer solution to recalculate all dynamic hardness results. The results differ only by one to ten percent in most cases, since crater volumes are small. Significant differences occur only for the higher velocity tests on the softer alloys, particularly with dense WC-Co spheres. We previously reported the correlation of P calculated from the Tabor method (which requires only incident and rebound velocities) with P = $\Delta E/V$ (where ΔE is the energy lost by the sphere and V is the crater volume determined by profilometer measurements). This correlation is changed only very slightly.

Effects of Particle Size and Velocity

In a previous report,[3] we outlined a simplified analysis of the effects of velocity and particle diameter which permits separation of the effects of temperature rise ΔT and strain rate $\dot{\varepsilon}$) on dynamic hardness P. In addition, practical information is provided on input values of P for the rebound velocity models dealing with impacts of angular and spherical particles at oblique angles. Based on approximations for $\dot{\varepsilon}$ by Hutchings[4] and ΔT by Sundararajan,[5] we showed that particle diameter d_p should affect $\dot{\varepsilon}$ but not ΔT, while velocity should affect both $\dot{\varepsilon}$ and ΔT. $\dot{\varepsilon}$ can be calculated from our experimental data for incident and rebound velocity by using the Hutchings approximation to obtain the mean strain ε and the Tabor formulation of dynamic hardness to obtain the time of contact. In this way, we can obtain plots of P vs. $\dot{\varepsilon}$. The earlier report also included plots of P vs. velocity for pure Al, and annealed and quenched 1080 steel. We include here in Figures 4-6 plots of P vs. $\dot{\varepsilon}$ for these three materials. The data were calculated with the original Tabor formula rather than with the revised method which uses the exact crater volume, but it is expected that the revised method will not change the important trends in the information.

It is important to recognize that the increase of $\dot{\varepsilon}$ for each

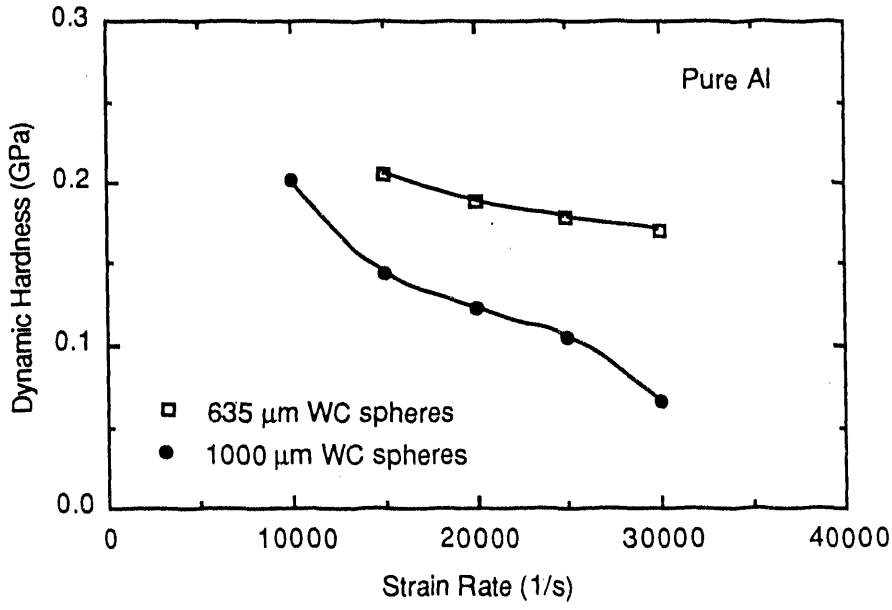

Figure 4. Effect of velocity on P for pure Al, plotted as P vs. $\dot{\varepsilon}$. (ΔT also increases with velocity.)

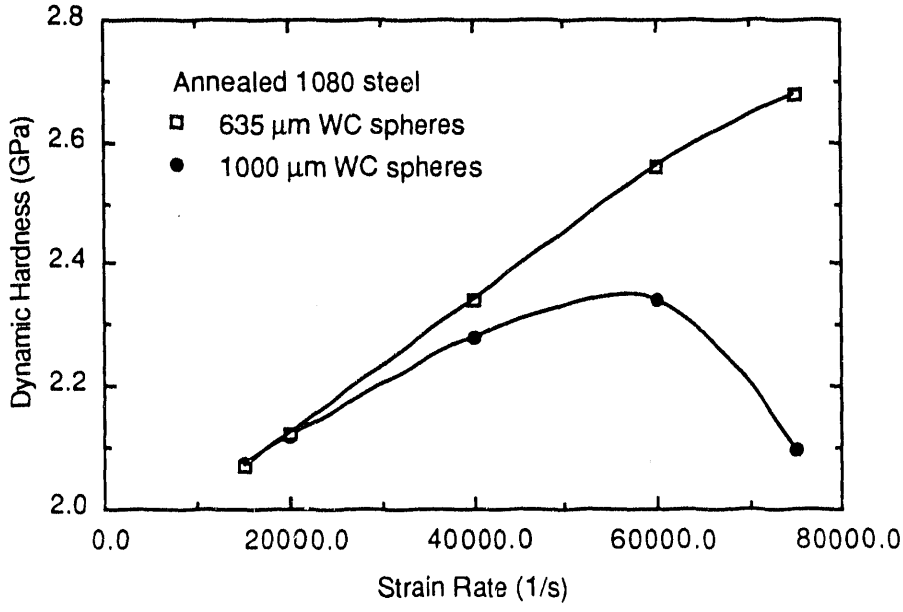

Figure 5. Effect of velocity on P for annealed 1080 steel, plotted as P vs. $\dot{\varepsilon}$.

particle size was accomplished by increasing velocity, which also increases ΔT. The plot can be thought of as essentially a plot of P vs. velocity with a revised velocity scale. Both $\dot{\varepsilon}$ and ΔT are proportional

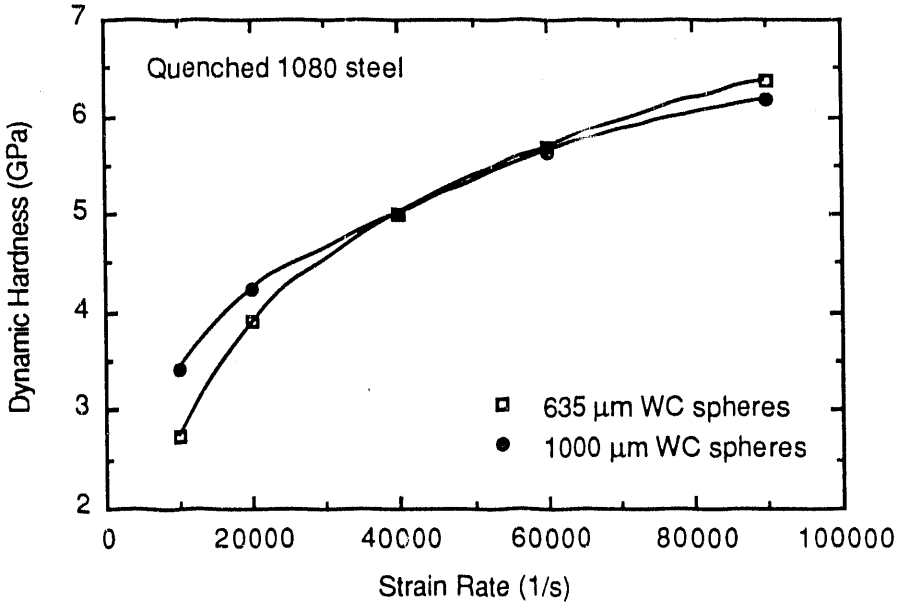

Figure 6. Effect of velocity on P for quenched 1080 steel, plotted as P vs. $\dot{\varepsilon}$.

to velocity within the approximations in our analysis. In the case of pure Al, we find a strong decrease of P with increasing $\dot{\varepsilon}$ and ΔT for the larger 1000 μm spheres, and a weaker decrease for the smaller 635 μm spheres. The literature on high strain rate deformation leads us to expect an increase of flow stress with $\dot{\varepsilon}$, while the temperature rise should decrease flow stress. This suggests that the decrease of P with $\dot{\varepsilon}$ should be attributed to a greater decrease of P due to increasing ΔT than the increase of P associated with the simultaneous increase of $\dot{\varepsilon}$.

Since the approximate analysis gives $\dot{\varepsilon}$ inversely proportional to particle diameter, the velocity necessary to obtain a given value of $\dot{\varepsilon}$ is smaller for the smaller spheres. Therefore, if we consider a given point on the curve for 1000 μm spheres, the point directly above it on the curve for 635 μm spheres has the same $\dot{\varepsilon}$, but a lower velocity and therefore a lower ΔT. The higher values of P for 635 μm spheres in Figure 4 (pure Al) is thus attributable to the lower ΔT alone, within the approximations of the simple model. This allows the effect of ΔT to be evaluated as a function of strain rate, and in fact would also allow a separate calculation of the effect of strain rate alone on P by taking the ΔT effect into account.

It is very interesting that there is a smaller negative slope of P vs. $\dot{\varepsilon}$ in Figure 4 (pure Al) for the 635 μm spheres. For the smaller sphere size, ΔT is smaller, so one would expect a smaller decrease of P associated with ΔT. By extrapolation, we would expect that if still smaller spheres are used, P would be higher, and the curve would become flat and then acquire a positive slope with decreasing d_p. If so, pure Al would approach the behavior observed for quenched 1080 steel (Figure 6), in which the positive slope is assumed to be due to the effect of strain rate being greater than that of temperature rise.

The case of annealed 1080 steel is intermediate between those of pure Al and quenched 1080 steel, with a positive slope for the smaller spheres and a maximum for larger spheres. For large spheres, the decrease of P past the maximum can, in our approximate treatment, be attributed to ΔT having a greater effect on P than $\dot{\varepsilon}$ for high velocities. The ΔT for smaller spheres is less, and one would therefore expect a higher velocity to be needed before ΔT began to have more influence than $\dot{\varepsilon}$. The continued rise of P with $\dot{\varepsilon}$ in Figure 5 is therefore consistent with our simple analysis, and there is even a suggestion that the 635 μm curve may be approaching a maximum at a higher velocity.

The low melting point of Al probably contributes to the fact that P decreases with increasing velocity, since less temperature rise is necessary to reach a given fraction of its absolute melting temperature. A study of the effect of melting temperature on the $\dot{\varepsilon}$ dependence of P for different pure metals would be of interest in evaluating this. However, according to Sundararajan's estimate of ΔT of

$$\Delta T = P\varepsilon/\rho C \qquad (3)$$

where ρ is density and C is heat capacity, ΔT will generally be larger for higher T_m metals due to the generally higher flow stress for higher T_m. Higher P also gives smaller ε, which tends to decrease the effect of T_m on P. Heat capacity will also play a role, and, since the impacts will not be perfectly adiabatic as assumed in the simple ΔT expression, thermal conductivity will also influence the results. Another complication is that different metals make the transition from thermally activated dislocation glide to phonon drag controlled glide at different

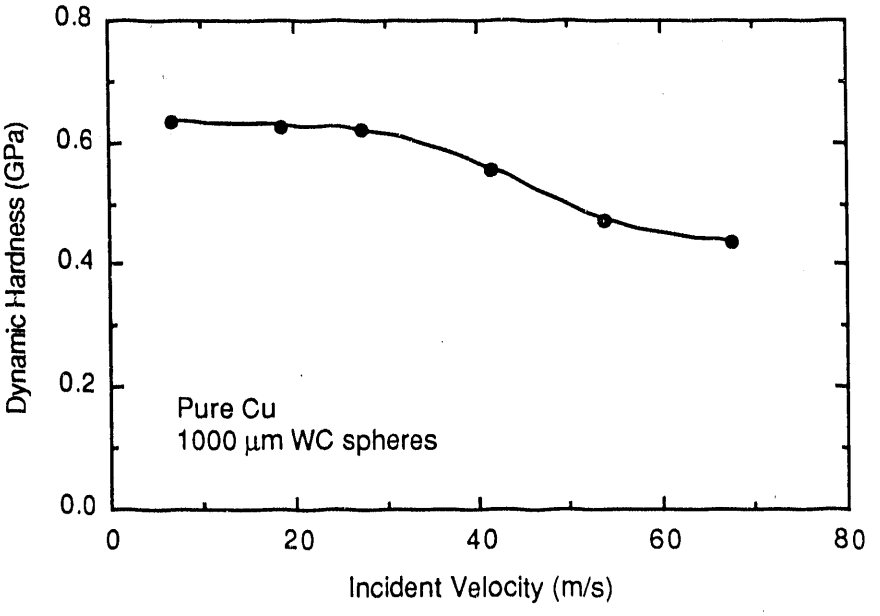

Figure 7. Effect of incident velocity on dynamic hardness for pure Cu, calculated with the original Tabor formula.

strain rates. We have obtained data for the dynamic hardness of pure Cu with 1000 and 635 μm spheres. Figure 7 shows the velocity dependence of P for 1000 μm spheres calculated with the Tabor method using the exact crater volume formulation. There is a small decrease of P with velocity, but it is much less than that for pure Al or the 6061 Al alloy in various microstructural conditions.

The difference in the behavior of quenched and annealed 1080 steel is complicated by a number of factors. The martensitic (quenched) steel has very high dislocation density and solution hardening due to carbon being trapped in solution, while the pearlitic annealed steel would have the constraint of cementite plates as a contribution to flow stress. It is not possible to provide a simple explanation of the different behavior of these two microstructures at this time.

Figures 8-10 show the effect of velocity on P for 6061 Al alloy in three conditions: i) O temper; annealed to give large precipitates in a matrix of low alloy content; ii) T4 temper; solution annealed condition, single phase with substantial solution hardening; and iii) T6 temper, precipitation hardened. The results are qualitatively similar to those presented earlier for pure Al, and do not show large differences in the

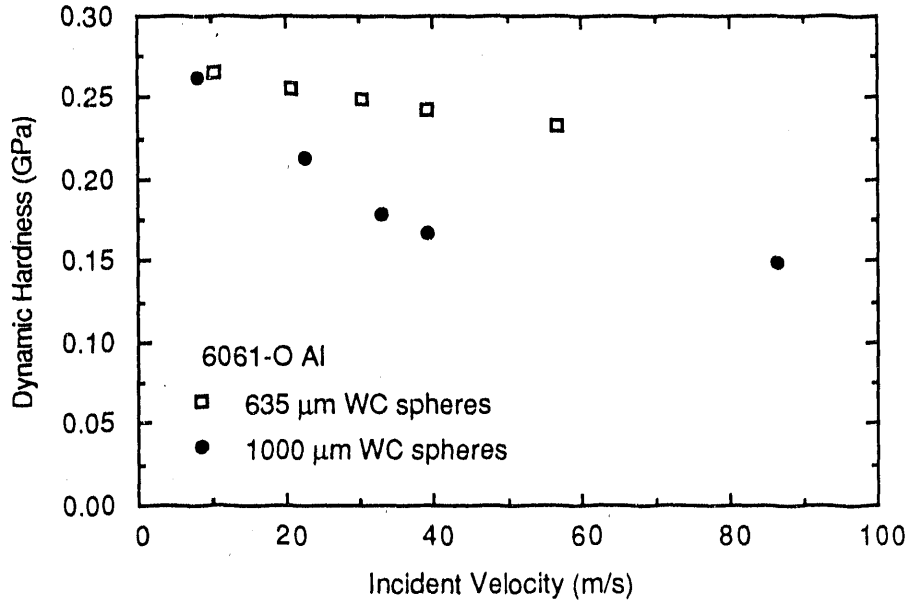

Figure 8. Effect of incident velocity on dynamic hardness for 6061-O Al, calculated with the original Tabor formula.

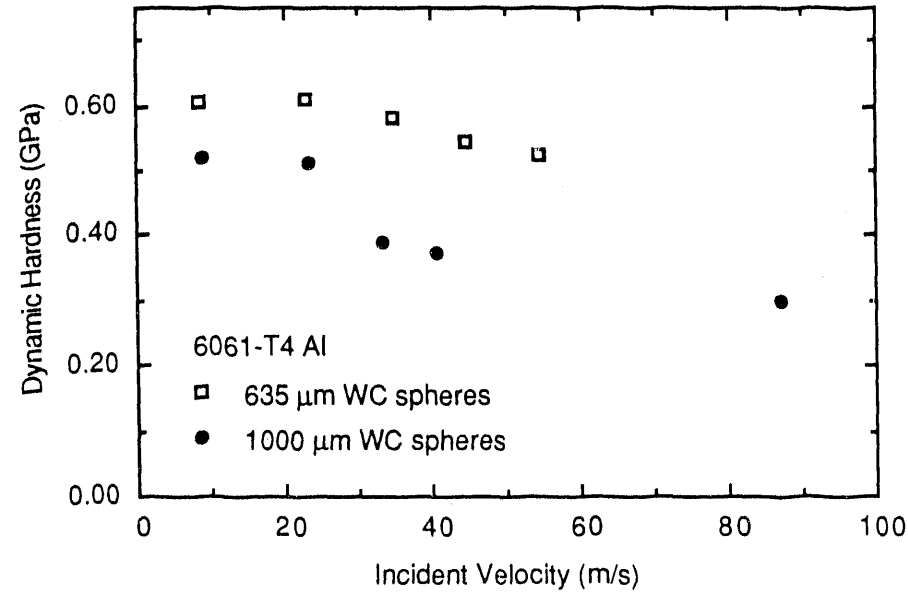

Figure 9. Effect of incident velocity on dynamic hardness for 6061-T4 Al, calculated with the original Tabor formula.

effect of sphere size or velocity on P for the different strengthening mechanisms. Further analysis of the results will be made to obtain P vs. $\dot{\varepsilon}$ plots as in Figures 8-10.

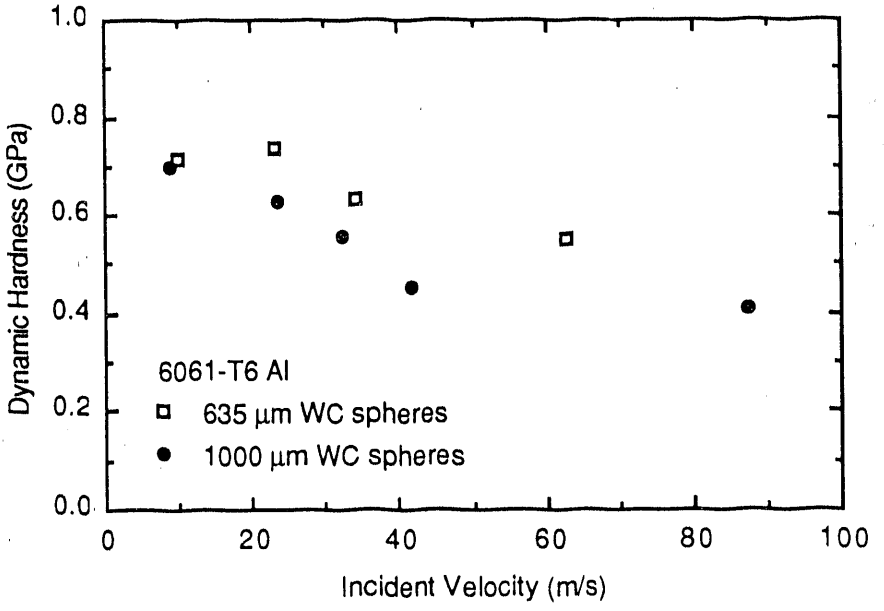

Figure 10. Effect of incident velocity on dynamic hardness for 6061-T6 Al, calculated with the original Tabor formula.

REFERENCES

1. U.S. D.O.E. Conference on Fossil Energy Materials, May 14-16, 1991, Oak Ridge, Tennessee

2. D. Tabor, The Hardness of Metals, Clarendon Press, Oxford, 1951

3. T.H. Kosel, "A Study of Erosive Particle Rebound Parameters," DOE-FEMP Semiannual Progress Report ORNL/FMP-90/2

4. I.M. Hutchings, "Strain Rate Effects in Microparticle Impact," J. Phys. D: Appl. Phys. 10 (1977) L179-L184

5. G. Sundararajan, Ph. D. dissertation, Ohio State Univ., 1981

UTN-3 - CORROSION OF IRON ALUMINIDES IN ACIDIC, BASIC AND CHLORIDE SOLUTIONS

R. A. Buchanan and J. G. Kim

Department of Materials Science and Engineering
The University of Tennessee
Knoxville, Tennessee 37996-2200

INTRODUCTION

The Fe_3Al-type iron aluminides have undergone continued development for enhancement of mechanical and corrosion properties over the past several years at the Oak Ridge National Laboratory. Improved alloys and thermo-mechanical processing methods have evolved. The overall purpose of this particular project is to evaluate the aqueous corrosion properties of the most recent alloy compositions in a wide range of possibly-aggressive solutions.

DISCUSSION OF CURRENT ACTIVITIES

The iron aluminides investigated during the time period of this progress report were FA-129 (Fe-28Al-5Cr-0.2C-1Nb, at.%) and FAL-Mo (Fe-28Al-5Cr-1Mo, at.%). As comparison or reference materials, the iron aluminide FA-84 (Fe-28Al-2Cr-0.05B, at.%) and annealed Type 304L stainless steel (SS) were also evaluated. The corrosion characteristics of these materials were determined in seven different electrolytes: 1N HCl, 1N H_2SO_4, 1N HNO_3, 1M NaOH, a mild acid-chloride solution (pH = 4 (H_2SO_4), 200 ppm Cl^-), 3.5 wt. % NaCl (pH ≈ 7), and synthetic seawater (Instant Ocean™, Aquarium Systems, Mentor, Ohio).

Three types of corrosion evaluations were performed to obtain complementary results. First, electrochemical cyclic anodic polarization measurements were made to determine active or passive behavior and relative stability within the various solutions. Second, electrochemical polarization resistance measurements were made to obtain corrosion current densities, from which average penetration rates in mils per year (mpy) were calculated by application of Faraday's Law. And third, three-week mass-loss immersion tests were conducted to substantiate the electrochemical results and to evaluate

any effects of time. The mass-loss values per unit area per unit time were converted to average penetration rates in mpy for comparison to the polarization resistance results.

After cutting the specimens to size for the various tests, the iron aluminides were heat treated for 1h at 750°C in air and then oil quenched. Next, for all materials, the specimens were ground to a 600-grit (SiC) surface finish. All corrosion tests were conducted at laboratory temperature (~25°C). In the electrochemical tests, the potential scan rate was 600 mV/h and the reversing current density for the polarization measurements was 10^3 $\mu A/cm^2$. Aeration was achieved by sparging with oxygen, which also resulted in a stirring action. In the immersion tests, oxygen sparging was not performed; the solutions were in a quiescent condition.

Before presenting the results of the cyclic anodic polarization measurements, a brief review of the typical forms of results and their physical interpretations will be given relative to the schematic curves in Figure 1. The anodic curve of Figure 1(a) represents active behavior only, i.e. as the potential is increased, the external anodic current density (i_{ex}) increases monotonically. Since i_{ex} is approximately equal to the true anodic current density (at potentials greater than about 50 mV above the open-circuit freely-corroding potential (E_{corr})), which in turn is directly proportional to the metal corrosion rate, this active behavior indicates that the metal corrosion rate continuously increases with increasing potential. The schematic curve of Figure 1(b) indicates that active corrosion is occurring at the freely-corroding potential (E_{corr}), but then as the potential is increased, the metal undergoes passivation to a low passive (P) current density (i_p). At higher potentials, breakdown of the passive film occurs resulting in high current densities. Upon reversal of the scan direction, no hysteresis (no H) occurs, which generally means that the metal is not susceptible to localized forms of corrosion (pitting and crevice corrosion) in this electrolyte. Thus, Figure 1(b) indicates active corrosion (A), followed by passivation (P), followed by breakdown of the passive film with no hysteresis (B (no H)). These tendencies are abbreviated as A-P-B (no H). The schematic curve of Figure 1(c) represents, for the most part, ideal behavior. The metal is passivated at the freely corroding potential, and finally undergoes breakdown at a significantly higher potential with no hysteresis, i.e. P-B (no H). The curve of Figure 1(d) indicates passivation at the freely corroding potential, and breakdown at a higher potential with hysteresis during the reverse scan, i.e. P-B (H). The breakdown potential (E_B) and the protection potential (E_P) are indicated in the figure, where

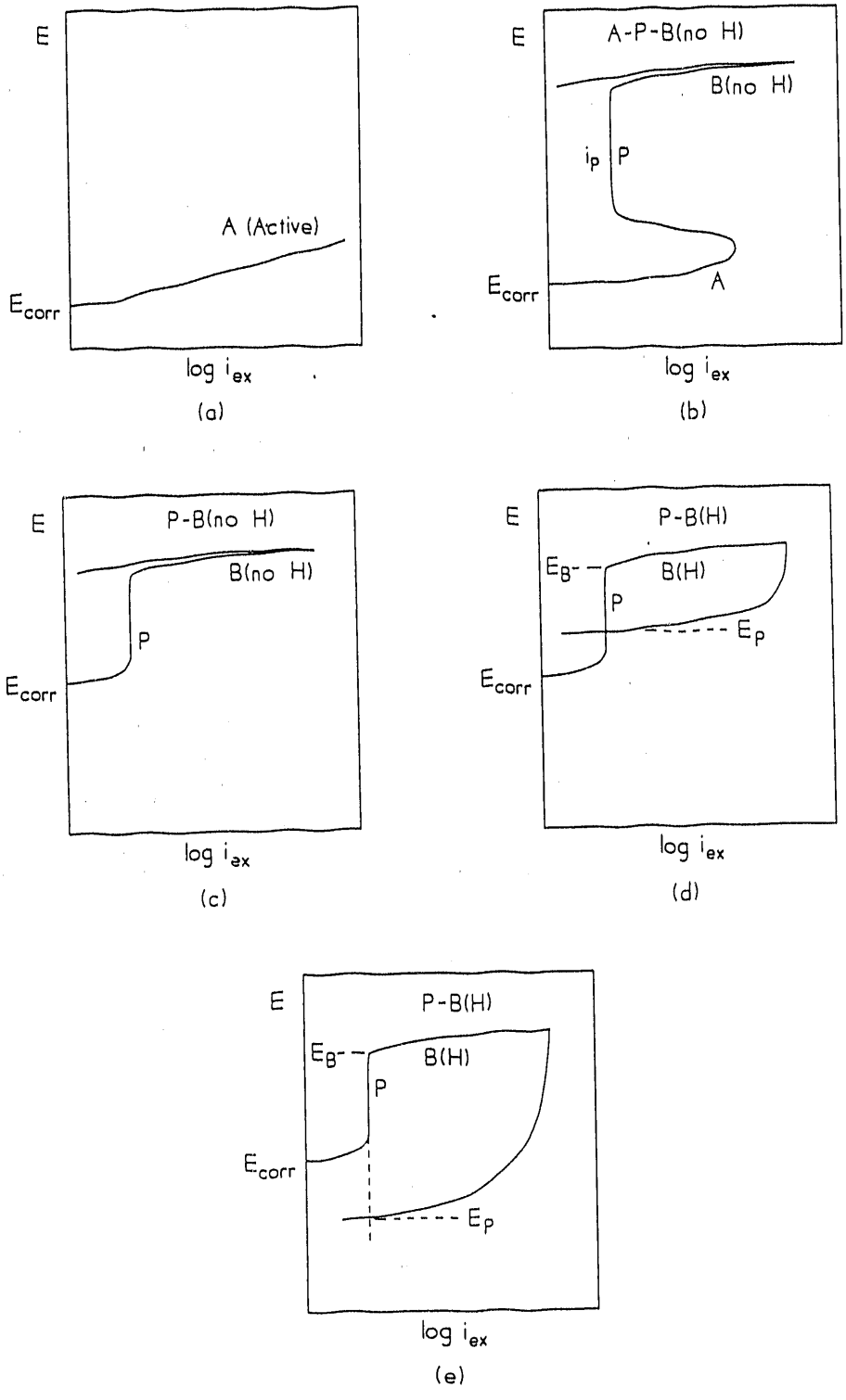

Fig. 1 - Schematic experimental cyclic anodic polarization curves.

E_P is the potential at which the reverse-scan curve intersects the forward-scan curve. The presence of the hysteresis loop indicates susceptibility to localized corrosion in this electrolyte. Although the metal is susceptible to localized corrosion, its relative resistance is proportional to (E_P - E_{corr}), i.e. greater resistance is afforded with higher values of E_P relative to E_{corr}. Finally, Figure 1(e) illustrates behavior similar to that of Figure 1(d) except that E_P is below E_{corr}, indicating less resistance to the onset of localized corrosion.

The results of the cyclic anodic polarization measurements for the four materials (FA-84, FA-129, FAL-Mo and 304L stainless steel (SS)) in the seven different electrolytes are presented in Figures 2-8. Table 1 summarizes these results in terms of the abbreviated notation previously described. In the 1N HCl acid, only active behavior was exhibited by all four materials. In both the 1N H_2SO_4 and 1N HNO_3 acids, at the freely-corroding potential (E_{corr}), corrosion was taking place in the active state for the three iron aluminides but in the passive state for the 304L SS. At higher potentials, the three aluminides underwent passivation. Upon breakdown, or apparent breakdown (oxygen evolution), no hysteresis was exhibited by any of the materials in these acids. In the highly basic 1M NaOH solution, all four materials were passivated at E_{corr}. No hysteresis was exhibited after breakdown (or apparent breakdown). Therefore, although widely differing behaviors were exhibited by the four materials in the three acidic solutions and the one basic solution, no material/electrolyte combination indicated susceptibility to localized pitting/crevice corrosion (i.e. no hysteresis loops were produced).

In the three chloride-containing solutions (mild acid-chloride, 3.5 wt.% NaCl and synthetic seawater), all materials were in the passive state at E_{corr}, and after breakdown of the passive film, all materials exhibited hysteresis behavior. Therefore, these material/electrolyte combinations exhibited susceptibility to localized corrosion. As previously discussed, a measure of the relative resistance to the onset of localized corrosion is the quantity (E_P - E_{corr}), with the resistance increasing as (E_P - E_{corr}) increases. This quantity is tabulated in Table 2 for the four materials in the chloride-containing solutions. Based on this electrochemical measurement, FAL-Mo and 304L SS were clearly superior to the other two materials in terms of resistance to chloride-induced localized corrosion.

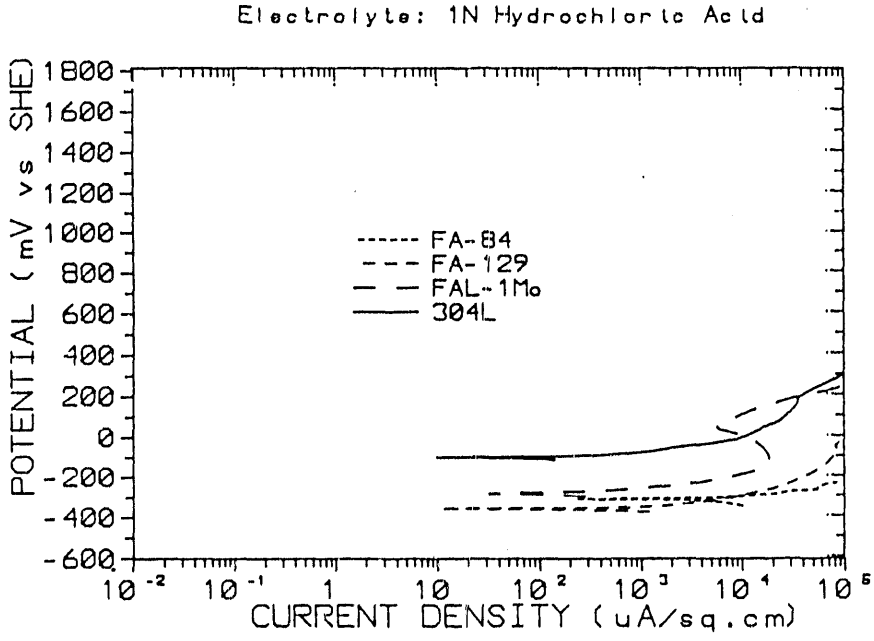

Fig. 2 - Cyclic anodic polarization results in 1N HCl.

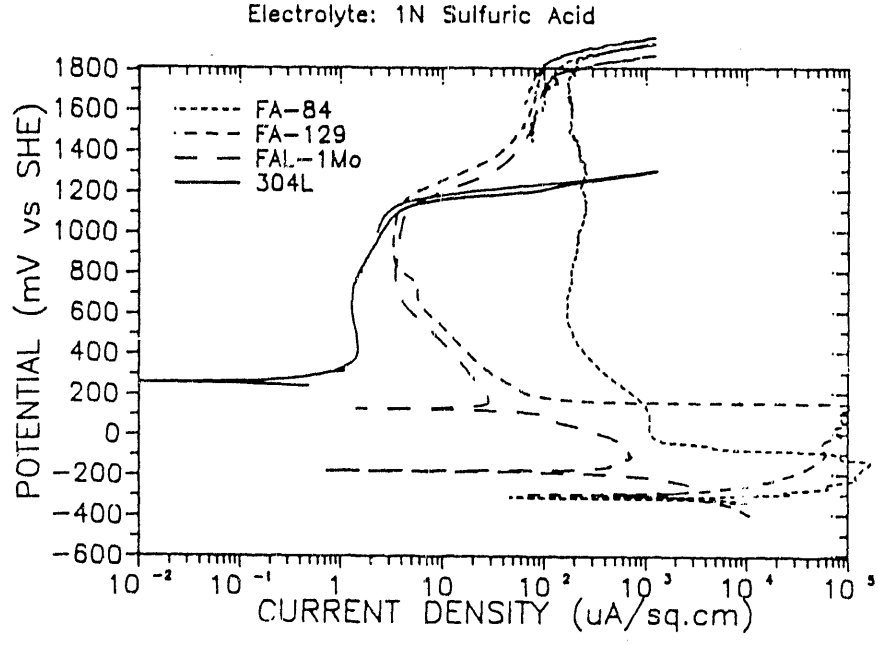

Fig. 3 - Cyclic anodic polarization results in 1N H_2SO_4.

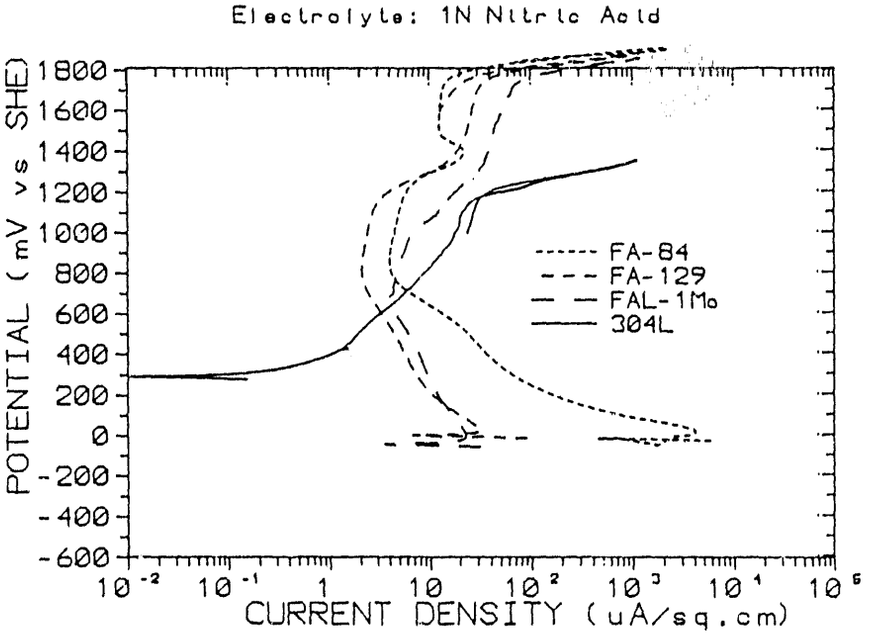

Fig. 4 - Cyclic anodic polarization results in 1N HNO_3.

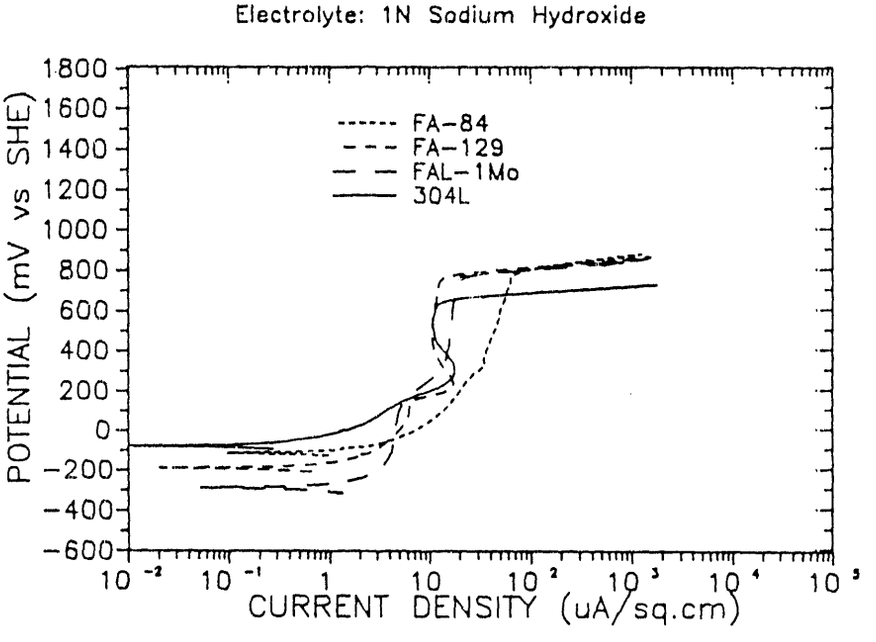

Fig. 5 - Cyclic anodic polarization results in 1M NaOH.

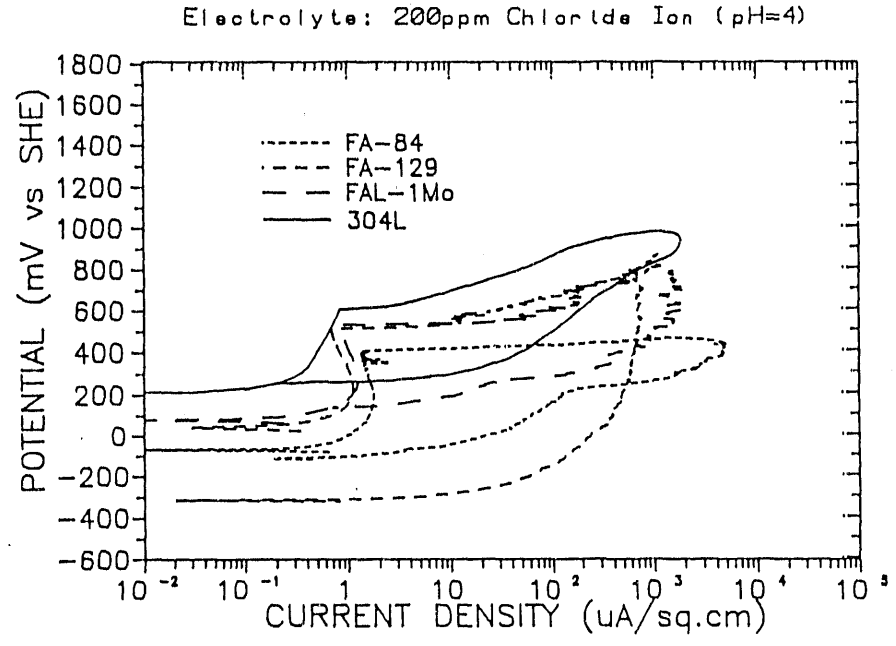

Fig. 6 - Cyclic anodic polarization results in mild acid-chloride solution (pH = 4, 200 ppm Cl^-).

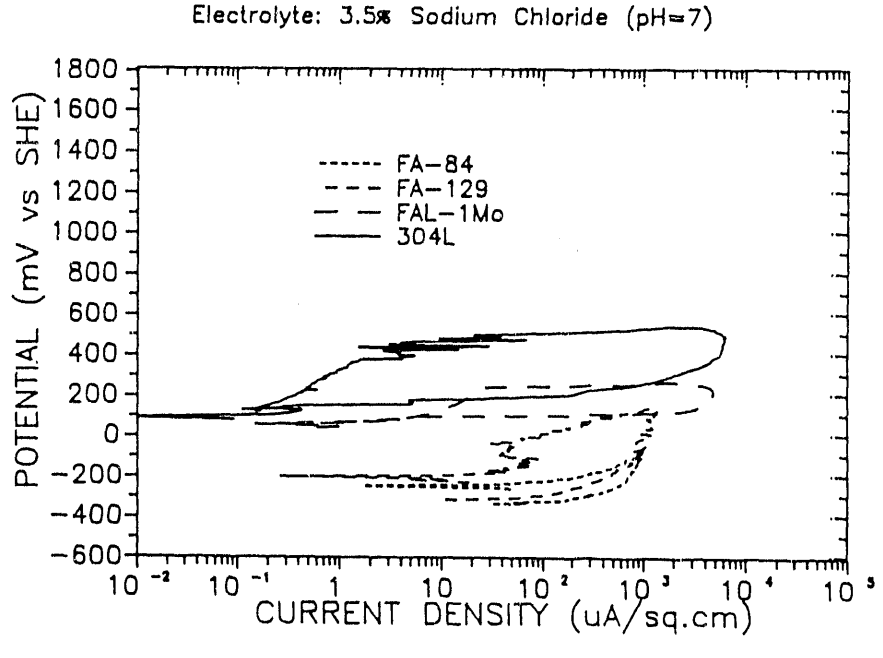

Fig. 7 - Cyclic anodic polarization results in 3.5 wt. % NaCl.

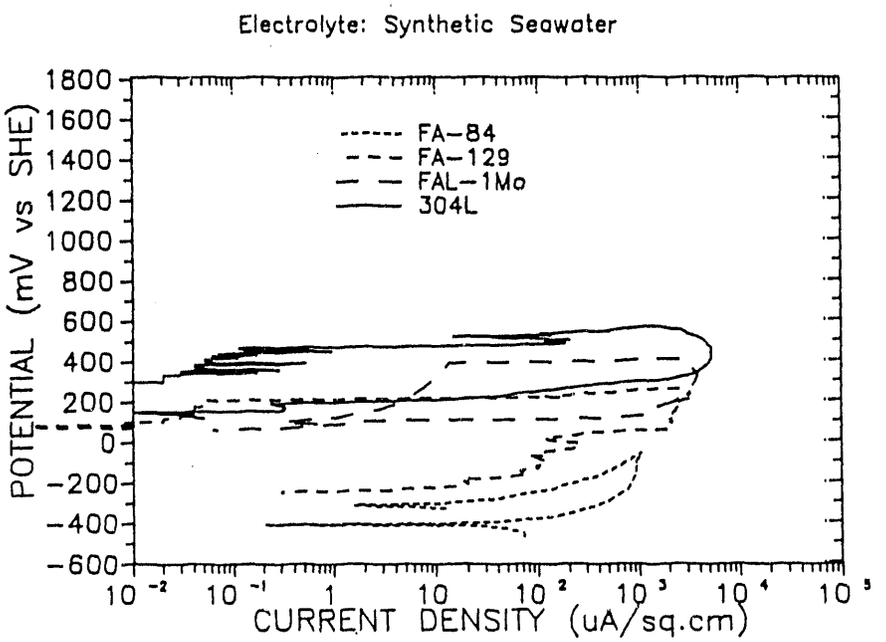

Fig.8 - Cyclic anodic polarization results in synthetic seawater.

Table 1. Summary of cyclic anodic polarization results.

Solutions		Materials			
		FA-84	FA-129	FAL-Mo	304L SS
Acids	1N HCl	A only	A only	A only	A only
	1N H_2SO_4	A-P-B (no H)	A-P-B (no H)	A-P-B (no H)	P-B (no H)
	1N HNO_3	A-P-B (no H)	A-P-B (no H)	A-P-B (no H)	P-B (no H)
Base	1M NaOH	P-B (no H)	P-B (no H)	P-B (no H)	P-B (no H)
Chlorides	Mild Acid-Chloride	P-B (H)	P-B (H)	P-B (H)	P-B (H)
	3.5 wt % NaOH	P-B (H)	P-B (H)	P-B (H)	P-B (H)
	Synthetic Seawater	P-B (H)	P-B (H)	P-B (H)	P-B (H)

Table 2. Electrochemical parameters in the chloride solutions.

Acid-Chloride Solution

Material	E_B mV (SHE)	i_{corr} $\mu A/cm^2$	E_P mV (SHE)	E_{corr} mV (SHE)	E_P-E_{corr} mV (SHE)
FA-84	420	1.04	-120	-70	-50
FA-129	500	0.44	-320	40	-360
FAL-Mo	540	0.3	140	80	60
304L	600	0.09	240	200	40

3.5% NaCl Solution

Material	E_B mV (SHE)	i_{corr} $\mu A/cm^2$	E_P mV (SHE)	E_{corr} mV (SHE)	E_P-E_{corr} mV (SHE)
FA-84	-240	78.2	-320	-240	-80
FA-129	-40	29.8, 0.2	-300	-200	-100
FAL-Mo	250	2.3	100	60	40
304L	490	0.15	120	100	20

Synthetic Seawater Solution

Material	E_B mV (SHE)	i_{corr} $\mu A/cm^2$	E_P mV (SHE)	E_{corr} mV (SHE)	E_P-E_{corr} mV (SHE)
FA-84	-300	18.27	-410	-300	-110
FA-129	200	26.73, 0.02	-260	70	-330
FAL-Mo	400	1.02	50	80	-30
304L	460	0.01	140	300	-160

The average penetration rates (mpy) at the freely-corroding potential (E_{corr}), as determined by polarization resistance measurements and Faraday's law, are given in Table 3. All four materials produced high corrosion rates in the 1N HCl. In the 1N H_2SO_4, the three iron aluminides produced high corrosion rates corresponding to active corrosion behavior, but the 304L SS exhibited a low passive corrosion rate. In the 1N HNO_3, the FA-84 iron aluminide showed a very high active corrosion rate; however, the FA-129 and FAL-Mo aluminides exhibited much lower active corrosion rates. Based on the polarization behaviors, these latter materials were corroding in an active state but very close to a state of passivation. Finally, in the 1N HNO_3 solution, the 304L SS showed a low passive corrosion rate. In the basic 1M NaOH solution, all four materials produced low passive corrosion rates. In the three chloride-containing solutions (mild acid-chloride, 3.5 wt. % NaCl and synthetic seawater), generally, low passive corrosion rates were exhibited by all materials. Within these solutions, the higher average penetration values (i.e. greater than about 1 mpy) could have been associated with small amounts of localized corrosion during the polarization-resistance measurements. Recall that all of these materials exhibited susceptibility to localized corrosion in these solutions by virtue of production of hysteresis loops within their cyclic anodic polarization curves.

Table 3. Results of polarization resistance measurements.

Solutions		Average Penetration Rates (mpy)			
		Materials			
		FA-84	FA-129	FAL-Mo	304L SS
Acids	1N HCl	6,220	740	200	140
	1N H_2SO_4	5,800	1,040	1,770	0.2
	1N HNO_3	2,240	50	20	0.1
Base	1M NaOH	0.6	0.3	0.8	0.1
Chlorides	Mild Acid-Chloride	0.4	0.2	0.1	0.04
	3.5 wt % NaCl	33	6.7	1.0	0.06
	Synthetic Seawater	7.7	6.0	0.5	0.007

The results of the three-week mass-loss immersion tests are presented in Table 4. These results are generally consistent with the polarization-resistance corrosion rates of Table 3. As shown in Table 4, the immersion tests indicated high corrosion rates for the iron aluminides in the 1N HCl and 1N H_2SO_4 acids. The corrosion rate for the 304L SS was much lower than the aluminides in both of these acids, with a very low corrosion rate (passivation) being indicated in the 1N H_2SO_4. In the 1N HNO_3, a very high corrosion rate was exhibited for FA-84, much lower corrosion rates for FA-129 and FAL-Mo (on the verge of passivation), and an extremely low corrosion rate for the 304L SS (passivation). In the highly-basic 1M NaOH, very low corrosion rates were produced by all four materials (passivation).

Table 4. Results of three-week mass-loss immersion tests.

Solutions		Average Penetration Rates (mpy)			
		Materials			
		FA-84	FA-129	FAL-Mo	304L SS
Acids	1N HCl	>8,020[1]	>3,150[2]	>637[3]	6.5
	1N H_2SO_4	>3,750[4]	>1,320[5]	>748[6]	<0.1
	1N HNO_3	>6,200[7]	0.25	7.0	<0.1
Base	1M NaOH	0.1	0.1	0.8	<0.1
Chlorides	Mild Acid-Chloride	2.3*	1.6*	0.9	<0.1
	3.5 wt % NaCl	2.7*	1.8*	1.0*	<0.1
	Synthetic Seawater	1.0*	1.0*	0.9	<0.1

1-7: Total dissolution within--1(12h), 2(36h), 3(192h), 4(24h), 5(72h), 6(213h), 7(12h).

* Localized corrosion initiated within 24h.

With regard to the chloride-containing solutions, as shown in Table 4, the mass-loss immersion results indicated low average corrosion rates for all of the materials. However, localized corrosion was observed to initiate for many of the material/electrolyte combinations over the three-week time period. Specifically, in all three chloride solutions, localized corrosion initiated on the FA-84 and FA-129 iron aluminides within 24 hours.

Also, localized corrosion initiated on the FAL-Mo aluminide within 24 hours in the 3.5 wt. % NaCl solution. Only the 304L SS in all three chloride solutions, and the FAL-Mo iron aluminide in the mild acid-chloride and the synthetic seawater solutions, remained completely passive (no localized corrosion) over the three-week time period.

One aspect of the procedures followed during preparation for the mass-loss tests may be important relative to the chloride-solution results for the iron aluminides. In the immersion tests, the samples were supported by glass racks: a hole was drilled in each specimen, then each specimen was supported vertically by a glass peg through the drilled hole. During the chloride tests of Table 4, when localized corrosion initiated, it tended to start at the periphery of the drilled hole. The point to be made here is that the holes were drilled after heat treatment. Therefore, cold-work effects could have influenced the initiation of localized corrosion. Consequently, these tests will be repeated with the drilling operation performed prior to heat treatment, such that the possible cold-work effects will be eliminated.

PART V - TECHNOLOGY DEVELOPMENT AND TRANSFER

BCL-4 - "MATERIALS AND COMPONENTS IN FOSSIL ENERGY APPLICATIONS", NEWSLETTER

I.G. Wright

Battelle
505 King Avenue
Columbus, Ohio 43201-2693

INTRODUCTION

The DOE Newsletter on Materials and Components in Fossil Energy Applications is intended as a vehicle to provide timely dissemination of information concerning developments in, or performance results of, materials and components in conventional or new processes for the utilization of coal, or for the conversion of coal to other energy forms. In recent years, emphasis has been placed on the direct utilization of coal as a fuel, rather than for providing a substitute for natural gas. Process efficiency and compliance with present and anticipated environmental regulations are two of the most important factors driving developments, and strongly influence not only new processes, but also existing systems.

The role of the newsletter has been to provide a guide to developing materials and components technology, and a forum for the presentation of the latest results and experiences.

DISCUSSION OF CURRENT ACTIVITIES

During this reporting period, three issues of the newsletter have been published. The articles in these editions were entitled:

Issue No. 92 (6/1/91)

- Control of Slagging in PC Boilers
- Update on Status of Tube Wastage in Fluidized-Bed Combustors
- Direct Casting of Nickel Aluminide

- Progress in the Development of a Nested-Fiber Filter for Hot-Gas Cleanup
- Industrial Developments

Issue No. 3 (8/1/91)

- Impact of Coal Switching on Performance of Boiler Materials and Components
- Factors Affecting Wear of Pump Valves in Fine Particle Slurries
- Cooperative Research Opportunities with DOE National Laboratories
- Update on Materials Experience in the Ratcliffe FGD Test Rig
- High-Temperature Self-Lubricating Composite Available for Commercialization
- Industrial Developments

Issue No. 94 (10/1/91)

- Application of Ceramics in Industrial Gas Turbines
- Report on a Workshop on Corrosion and Corrosion Protection in Flue Gas Desulfurization (FGD) Plants, held at DECHEMA, Frankfurt, Germany, January 1991.
- Deposits in Outlet Duct of Ratcliffe FGD Test Rig
- Performance of Vinyl Ester Linings in Ratcliffe FGD Test Rig
- State-of-the-Art Coal-Fired Plant
- Conceptual Design of a 150-MWe Coal-Fired MCFC Power Plant
- Development of Fuel Cells in Europe
- Industrial Developments

CARB-4 - ENGINEERING-SCALE DEVELOPMENT OF THE VAPOR-LIQUID-SOLID (VLS) PROCESS FOR THE PRODUCTION OF SILICON CARBIDE WHISKERS

William E. Hollar Jr. and J. Kim

The Carborundum Co.
Technology Division
P.O. Box 832
Niagara Falls, NY 14302

W. Mills

BP America
Warrensville, OH 44128

INTRODUCTION

The goal of this program is to develop the VLS SiC Whisker process to an engineering scale in order to establish a commercially viable process. Specifically, the program calls for obtaining reliable critical process design data for a reactor which is 12" wide x 40" long x 12" high, and which is capable of producing 200 - 500 gram/12 hour cycle.

Preliminary economic evaluation has identified a number of components of the VLS SiC whisker process concept which will require either improvement or further development in order to achieve reduced production costs and to reduce technical uncertainties associated with the process scaleup. Improvements in the growth process productivity, through increases in growth rate and yield of useful product, would reduce the production cost. The high cost of process gases necessitates the development of a process gas recycle system to reduce production costs. Finally, a cost-effective beneficiation process needs to be developed to process the raw or as-synthesized product into a form useful for composite reinforcement.

To achieve these goals, efforts are being focused in three key areas. Whisker growth experiments are being conducted in Carborundum's development reactor to achieve growth rate improvements and to develop critical scaleup data. A simulation model is under development for use in the design of the engineering scale reactor, using data obtained in the development reactor. Finally, a bench scale beneficiation process is under development to process SiC whiskers produced in this program.

DISCUSSION OF CURRENT ACTIVITIES

Whisker Growth

One of the key factors impacting the economics of SiC whisker growth is the productivity of the growth process, which historically has been low. Los Alamos National Laboratory (LANL) has implemented process improvements which have led to growth rates as high as 0.55 mg/cm^2 hour.[1] In order to lower production costs, further improvements in the growth rate to

1 mg/cm^2 hour have been targeted in the current program. To achieve increased growth rates, growth experiments are being performed in Carborundum's development reactor, which has an extended dimension in the vertical direction relative to the LANL process.[2] This extended vertical dimension allows for determination of reactor scaleup behavior in this direction. A number of process variables can impact growth rate, such as the supply of the reactants SiO and CH_4.[2] Growth experiments are being performed to define process conditions which maximize growth rates. In addition, kinetic data obtained during growth experiments will be added to the simulation model to improve its predictive ability.

SiO supply plays an important role in the VLS whisker process.[2] SiO formation rates have been evaluated by monitoring the evolution of CO in the exhaust gas by gas chromatography. Integrated CO evolution is used to correct SiO formation rates by taking into account SiC formation in the generator brick.[3] Corrected SiO formation rates have been evaluated for a number of different process conditions, including various input CO levels, temperature, and process gas flow rates. Trends in the SiO generation, SiC whisker formation and SiO utilization are summarized in Table 1. These results can be used to guide modifications in the SiO production to effect changes in the whisker growth process.

Table 1 - Trends in SiO Formation, SiO Utilization and SiC Formation as a Function of Process Conditions

Process Variable	Total SiO (moles)	Total SiC_w (moles)	SiO Utilization
Input CO (0% - 3%)	Increase	Increase	Increase
Input CO (3% - 6%)	Decrease	Increase	Increase
Temperature (1380 - 1450 °C)	Increase	Increase	Constant
Temperature (1450 - 1475 °C)	Constant	Decrease	Decrease
Flow Rate (100% - 200%)	Decrease	Increase	Increase
Flow Rate (200% - 300%)	Increase	Increase	Increase

The effect of temperature on SiO formation behavior is summarized in Table 2. Generator weight loss increases with increasing temperature. In the absence of side reactions such as SiC formation at the generator, the SiO formation rate would be proportional to the weight loss. CO evolution rates also increase rapidly with temperature. When the increased CO evolution is taken into account, the SiO formation rate increases more slowly with temperature than predicted by the weight loss, and peaks around 1450 °C. Thus, there are limits in using temperature changes to affect SiO formation rates.

Table 2 - Effect of Growth Temperature on SiO Formation

Temperature (°C)	Growth Period (min)	Generator Weight Loss (g)	Corrected SiO (g-moles)
1380	373	32.3	0.43
1400	444	56.9	0.47
1425	399	78.8	0.61
1450	442	93.3	0.86
1475	436	133.4	0.78

As mentioned in the earlier report[3], modification of the SiO generator geometry and process conditions relative to the LANL process concept[4] has been necessary to achieve acceptable growth rates in the upper portion of the reactor. Modifications included addition of more SiO generators, increased generator surface area/unit reactor volume, and higher process gas flow rates. Process modifications have allowed for improved growth rates in the upper portion of the reactor, along with more uniform substrate coverage and longer whisker product. A profile of growth rates as a function of height is shown in Figure 1. Note that specific growth rates in the bottom 2/3 of the reactor are higher than at the reactor top. Further modification of process conditions will be examined to improve growth uniformity.

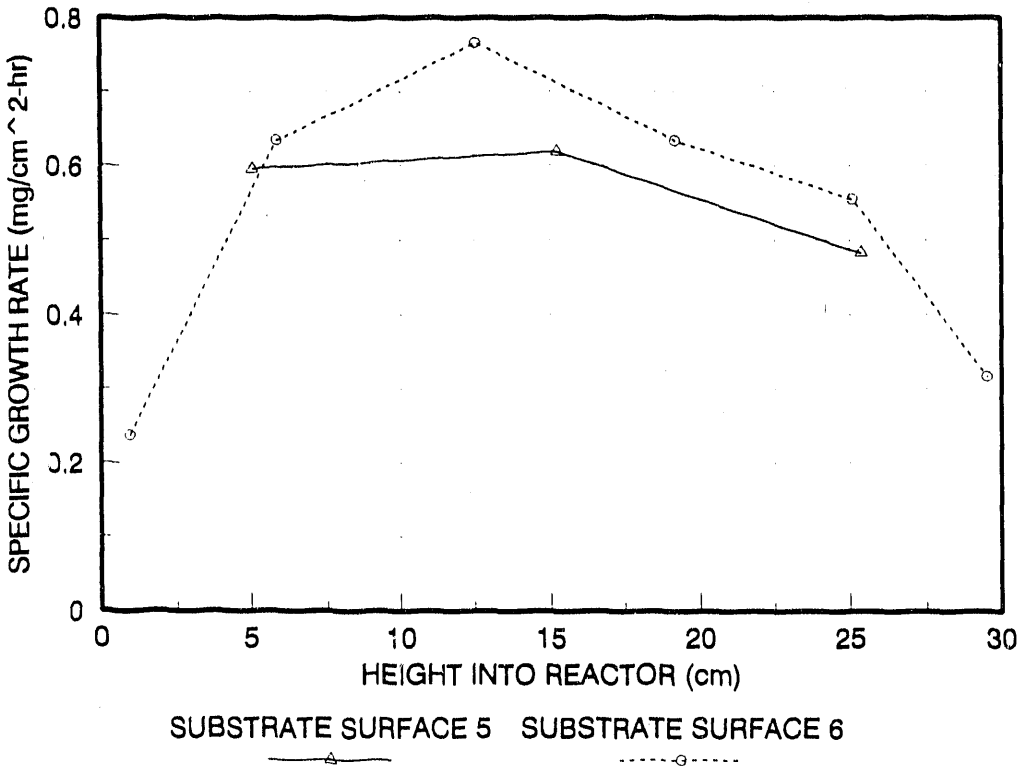

Fig. 1 - Specific Growth Rate as a Function of Position on the Substrate

Both the growth rate and product quality can be influenced by the catalyst. Evaluation of the influence of the catalyst application method on SiC whisker growth behavior is also underway. A Task 1 goal was to determine whether Carborundum's iron sol catalyst[5] could be modified to allow for increased catalyst site density. The proposed approach was a dual coating technique using multiple applications of catalyst precursor. Attempts at increasing site density using a dual coating technique were unsuccessful due to site interference between the first and second coating of catalyst precursor. Screening experiments comparing the sol catalyst to FeSi catalyst particles at fixed process conditions were also performed. The results are summarized in Table 3. Bulk growth rates were highest for the sol catalyst. Increasing the site density of the FeSi catalyst by increasing the slurry loading led to an increased mass of whiskers, but the total mass of whiskers remained lower than that produced with the sol catalyst. An effect of modifying the catalyst application technique has been to increase the length of whiskers grown on the central substrate. The product grown on the central substrate with the sol catalyst tends to be shorter than the growth on other substrates (1/8"), while use of the FeSi catalyst particles produced longer whiskers. The causes for this behavior will be evaluated. Microscopy of whisker product after beneficiation will be used to identify differences in product quality using the different catalysts.

Table 3 - Effect of Catalyst Application Technique on Total SiC_w Mass

Catalyst Application Method	Total SiC_w (g)
Iron sol	13.2
FeSi in acrylic resin (4.5%)	7.5
FeSi in acrylic resin (9.0%)	11.9

Modification of the process gas composition and improved utilization of catalyst sites are proposed to increase growth rates. Primary variables of concern are concentrations of CO, CH_4, SiO, N_2, and temperature. Initial growth experiments using a range of inlet CH_4 concentrations showed that the total mass of SiC whiskers increased approximately linearly with increasing methane supply. However, as methane is increased, there is an increase in whisker morphologies or growth formations typically associated with more carbon-rich growth environments (3D morphologies). These growths appear to make up a small proportion of the total whisker mass, and tend to grow at the catalyst end which may allow for physical separations from the desired whisker product. Increased carbon supply appears to be a potential method of achieving growth rate targets.

Table 4 - Effect of Input Methane on Total Mass of SiC Whiskers

Input CH_4 (%)	Total SiC_w (g)
0.4	13.2
0.6	21.2
0.8	26.2

Continued effort will be devoted towards improving the three key aspects of the whisker growth process: growth rate, product yield and product quality. Screening experiments defining key process variables will be completed to help define a statistical experimental design. These experiments will also be used to define rate controlling reactions. In addition, time series experiments will be performed to better define nucleation and growth kinetics for process improvements and for development of kinetic data for the simulation model.

Simulation Model Development

The goal of the simulation model development is to provide the basis for the design of a prototype scale reactor, including the evaluation of various design alternatives. Toward this end, kinetic data from the development reactor are being incorporated into a two dimensional model simulating a single channel of the development reactor.

The model simulates a single reactor channel from inlet to exhaust. The model is two dimensional and assumes isothermal behavior. Equations for the momentum and mass transfer of key species are included. The key reactions include SiO and CO formation along the surface of the SiO generator brick, and the disappearance of SiO and creation of CO along the substrate surfaces. Kinetic data have been obtained and incorporated into the model for the growth period following the nucleation or induction period. The effect of side product SiC formation at the generator is included. The model has been developed to allow for optimization of SiO and SiC formation rate constants through matching of experimental data.

Simulations have been performed with and without the presence of methane as a carbon source. Simulations assuming growth rate control by SiO supply alone incorrectly predict the trend of increasing whisker growth rates as a function of height, which is the opposite of the experimental trend of maximum growth rates in the bottom portion of the reactor. Inclusion of methane produces a growth rate profile similar to those observed in the development reactor. To achieve realistic growth rate profiles, the model requires the assumption of input methane supply rate less than the actual methane supply rate. These results indicate that the inclusion of a carbon source is necessary to simulate reactor behavior, and that it may be necessary to include alternative carbon sources (i.e. HCN) or side reactions involving the methane (i.e. carbonization) to predict experimental growth results accurately.

The plan is to continue development of the simulation model by improvements in the model boundary conditions and assumptions. Kinetic data generated in the development reactor will be added to the model as it is developed. The accuracy of model predictions will be evaluated. As the model's predictive ability improves, it will be used to help define experimental conditions for evaluation in the development reactor.

Harvesting and Beneficiation Process Development

VLS whiskers after harvesting contain a number of defects, such as catalyst balls and non-whisker debris, which potentially limit their effectiveness as a reinforcement phase. Some upgrade of the whisker product through removal of non-whisker or off-specification materials will be necessary to maximize its effectiveness as a composite reinforcement. The goal of this task is to develop a bench scale beneficiation process to upgrade long whisker product grown in the development reactor and to establish scaleup data for this process. Process research experiments to establish a preliminary process at a 1 - 2 g batch size have been completed.

The harvesting/beneficiation process and its relationship with the whisker production process are shown in Figure 2. The preliminary beneficiation process concept consists of dispersing harvested whisker product in ethylene glycol, followed by screening with a 20 mesh screen to separate long whiskers from short whiskers and non-whisker debris. Screened product is then leached in a mixture of HF and HNO_3 to remove residual catalyst balls.

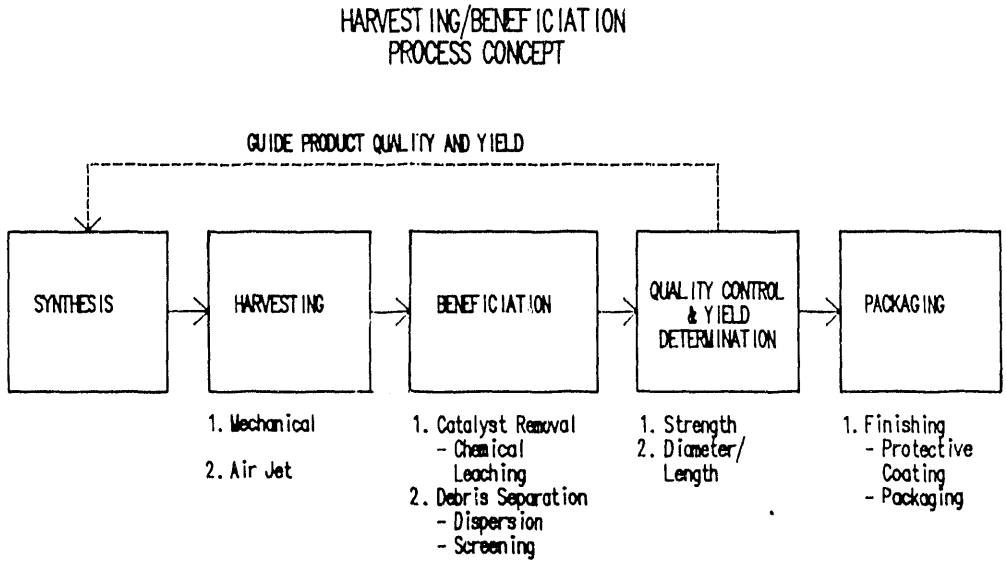

Fig. 2 - Process Concept for the Whisker Harvesting/Beneficiation Process

Current yields of +20 mesh whiskers after leaching are typically in the 40 - 50 % range. These yields are lower than the target of 90%. The causes for low yields are under evaluation. One problem area is that the dispersion process appears to be shortening the as-grown whiskers. Whiskers are currently dispersed using a magnetic stirrer. Alternative dispersion techniques which minimize the product size reduction need to be found. Detangling of whiskers prior to dispersion may reduce breakage. Less energetic dispersion techniques, such as use of air bubbles, may also improve this situation.[6] Air harvested materials may be easier to disperse.[6]

The plan is to scale up the beneficiation process to allow for processing of whisker product from the development reactor. The scaled-up process will allow for yield and quality evaluation of product grown under different process conditions and will be used to guide growth and beneficiation process improvements. Scaleup data will be obtained for future increases in the throughput of the beneficiation process.

Whisker Quality Evaluation

The purpose of this task is to: 1) define product quality, 2) guide improvements in product quality and 3) evaluate the impact of changes in the growth and beneficiation process. Quality evaluation efforts can be divided into three areas: physical, chemical and mechanical. In addition, bulk whisker product quality needs to be evaluated through composite fabrication.

Physical parameters to be characterized include diameter, length and the presence or absence of defects such as branching, bambooing and bent whisker sections. Diameter evaluation has been performed by split image microscopy on samples of thirty whiskers. Average diameter for the current baseline product is 7.5 microns, with a standard deviation of 4.5 microns; this distribution is wider than desired. SEM analysis of beneficiated product has been performed. An SEM photomicrograph of beneficiated whisker product is shown in Figure 3. Several types of defects are visible, including bent needle sections. Branching and bambooing of large diameter whiskers can also be seen. Evaluation of product in this manner will continue to help guide product quality improvements.

Chemical evaluation includes both bulk chemistry and trace element analysis. Total Si and C analysis of beneficiated product produced results of 69.5% Si and 29.3% C, which compares with the theoretical composition of stoichiometric SiC: 70% Si and 30% C. Other components which may be present include O and N,[7] which would explain the Si and C compositions slightly less than stoichiometric. Neutron activation analysis of trace impurities is being performed on both leached and unleached product to determine the effectiveness of the leaching step in removing catalyst balls and other impurities.

Preliminary mechanical property testing has been performed. Tensile tests on a single fiber test apparatus at Carborundum produced an average tensile strength of 400 - 500 ksi on a set of six samples. However, these may be lower than the true tensile strength due to testing difficulties associated with misalignment of the small diameter, high modulus fibers. Alternative methodologies for mechanical property testing will be examined.

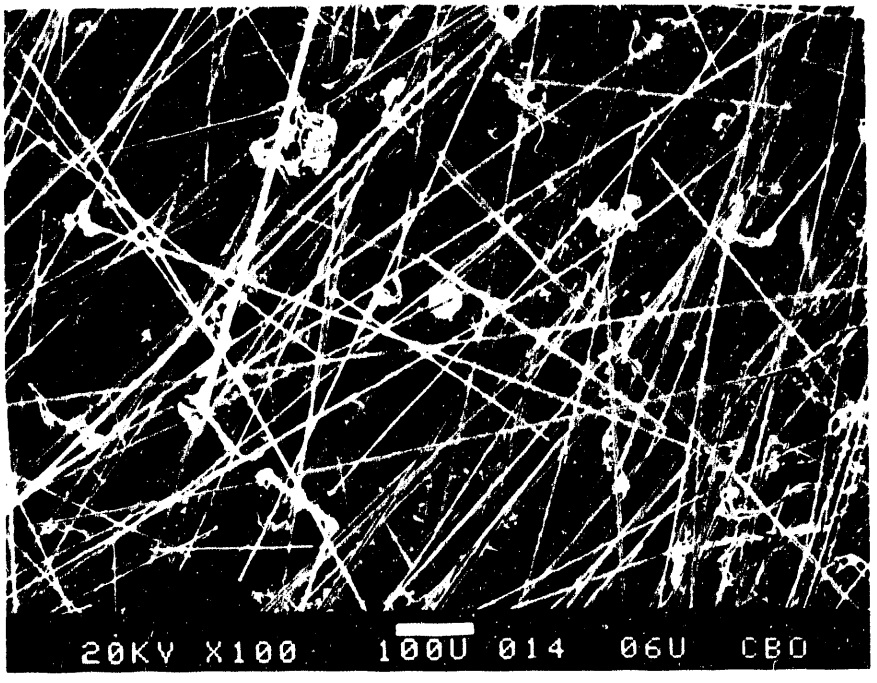

Fig. 3 - SEM Photomicrograph of Leached and Beneficiated Whisker Product (Low Magnification)

The true test of whisker quality is its effectiveness in enhancing the properties of composites. Composite fabrication and evaluation will be performed later in the contract.

The plan is to continue product quality evaluation. As growth conditions are modified to increase growth rates, product quality will need to be determined. In addition, product quality evaluation will be performed to determine attractive operating conditions from a quality standpoint.

Technology Transfer

A sub-task of the project has been to evaluate the feasibility of adapting MER's whisker growth technology to grow long, thick whiskers. This work has been divided into two tasks; the first involves identification of catalyst and substrate materials which lead to catalyst site size distributions with the potential to grow thicker whiskers. Task 2 will then use promising catalyst/substrate combinations to perform growth experiments. Task 1 was completed, with the identification of six candidate systems. Evaluation experiments designed to grow long whiskers > 3 microns in diameter have begun.

LANL-4-VAPOR-LIQUID-SOLID SIC WHISKER PROCESS DEVELOPMENT

J. D. Katz

Los Alamos National Laboratory
P.O. Box 1663
Los Alamos, NM 87545

ABSTRACT

The Los Alamos National Laboratory has developed a process for the synthesis of VLS SiC whiskers in small, laboratory-scale quantities. Through a long term research effort we have established the key processing factors important to successful fabrication of high quality VLS SiC whiskers in larger, scaled-up quantities. At this point in time, VLS SiC whiskers constitute the best form of whisker reinforcement for the manufacture of high fracture toughness ceramic composites and scaling-up the production of these whiskers is the crucial issue associated with the future development of whisker reinforced ceramic composites.

The Carborundum Company has been selected to pursue a scale-up demonstration of the VLS SiC whisker process. The purpose of this program is to assure the effective transfer of the expertise and information resident at Los Alamos to Carborundum through the interaction of the appropriate LANL personnel.

INTRODUCTION

Structural ceramic materials are of particular interest to the Fossil Energy Materials Program. Applications for which these materials can be considered include high temperature heat exchanger systems, coal gasification hardware, and engine components. SiC whisker-reinforced ceramic composites have been shown to be significantly tougher than their corresponding monolithic ceramic counterparts[1,2]. Thus, there is considerable interest in the development of such composites for structural applications.

SiC whiskers are of two generic types. The first type, termed Vapor-Solid (VS), consists of whiskers which are submicron in diameter and typically less than 100 microns in length. The second type, termed Vapor-Liquid-Solid (VLS), consists of whiskers averaging approximately 5 microns in diameter. Such whiskers have been grown to lengths as

long as 100 mm.

VLS SiC whiskers are much preferred over VS SiC whiskers for the reinforcement of ceramic composites. Because of their larger diameters, VLS SiC whiskers will produce significantly more toughening in a ceramic composite than will VS SiC whiskers[2]. Additionally, the mechanical properties of VLS SiC whiskers have been extensively characterized[3-5] while there is essentially no direct experimental information on the mechanical properties of VS SiC whiskers. Finally, there is a significant asbestos-like health and safety hazard associated with VS SiC whiskers due to their submicron diameter. However, it is expected that the 5 micron diameter VLS SiC whiskers will not produce such adverse health and safety effects.

The Los Alamos National Laboratory has developed a process for the synthesis of VLS SiC whiskers in small, laboratory-scale quantities. This work has established the key processing factors important to successful fabrication of high quality VLS SiC whiskers in larger, scale-up quantities.

DISCUSSION OF CURRENT ACTIVITIES

Interaction With Industrial Contractor

At the request of Carborundum Co. several experiments were performed at LANL the week of April 8th. Carborundum visited LANL during that week to observe the experiments. Two experiments were performed prior to Carborundum's arrival during the week of April 1st to check operation of the whisker growth facility, three experiments during their visit and two more experiments, the week after. Copies of all of the experimental data and parameters were provided to Carborundum.

Since the whisker growth facility had not operated for about a year it was necessary to made several anticipated repairs such as rebuilding the hot zone, replacing heating elements and re-calibrating the mass flow controllers. In addition, it was necessary to make several unanticipated repairs such as replacing defective circuit

boards in both the programmable furnace and the master mass flow controller. Other unanticipated repairs such as the need to use hydrogen and argon gas trailers instead of individual cylinders and the replacement of the existing hydrogen gas lines in the building were necessitated by more stringent safety requirements put in place over the past year. As a result the program was over spent by $ 18.9K and it was necessary to stop all work further work until receipt of FY92 operating funds.

AR&TD Topical Report

All work on the Summary Topical Report entitled "Scale-Up and Optimization of the VLS Growth Process for Beta-SiC Whiskers" has been completed except for the actual printing. The classification group at LANL has informed us that this report has been designated as *"Limited Access"* because it contains export control information. Since this program is currently overspent, all work was shutdown including printing of this report until receipt of FY92 operating funds.

REFERENCES

1. P.D.Shalek, J.J.Petrovic, G.F.Hurley and F.D.Gac, *"Hot-Pressed SiC Whisker/Si_3N_4 Matrix Composites"*, **Am. Ceram. Soc. Bull.**, **65**, 1986, pp. 351-356.

2. P.F.Becher, C-H Hsueh, P.Angelini and T.N.Tiegs, *"Toughening Behavior in Whisker-Reinforced Ceramic Matrix Composites"*, **J. Am. Ceram. Soc.**, **71**, 1988, pp. 1050-1061.

3. J.J.Petrovic, J.V.Milewski, D.L.Rohr and F.D.Gac, *"Tensile Mechanical Properties of SiC Whiskers"*, **J. Mat. Sci.**, **20**, 1985, pp. 1167-1177.

4. J.J.Petrovic and R.C.Hover, *"Tensile Fracture Behavior of Long SiC Whiskers"*, **J. Mat. Sci.**, **22**, 1987, pp. 517-522.

5. J.J.Petrovic and R.B.Roof, *"Fracture Toughness of a Beta-SiC Whisker"*, **J. Amer. Ceram. Soc.**, **67**, 1984, pp. C219-C220.

ORNL-4(B)-COAL CONVERSION AND UTILIZATION PLANT SUPPORT SERVICES

J. R. Keiser

Oak Ridge National Laboratory
P. O. Box 2008
Oak Ridge, TN 37831-6156

INTRODUCTION

During this period, support services were provided to several facilities. Assistance was provided to the staff of a coal gasification plant to help identify a means to eliminate corrosion in a distillation column. Corrosion samples were prepared for exposure in the reactor of a Japanese coal liquefaction facility, and samples provided by the Japanese were prepared for exposure in the two reactor vessels at the Wilsonville, Alabama, Coal Liquefaction Research and Development Facility.

DISCUSSION OF CURRENT ACTIVITIES

Coal Gasification

In May of this year, ORNL engineers were informed of a serious corrosion problem in a phenol distillation tower at the coal gasification plant located in Beulah, North Dakota. This facility was formerly known as the Great Plains Coal Gasification Plant, and is now operated by the Dakota Gasification Company.

The phenol distillation tower is part of the phenol separation facility which was constructed to permit separation of phenol (hydroxybenzene) and cresylic acids (generally defined as a mixture of multiply substituted hydroxybenzenes so that the boiling point is in the range 220-250°C), both of which can be sold commercially. The phenol separation facility began operation in December, 1990, and operated for a total of about 130 days. The phenol distillation tower along with the other two towers in the facility are constructed of 304L stainless steel; nevertheless, considerable thinning of column trays was detected and operation was discontinued.

An ORNL staff member twice visited the gasification plant to inspect the corroded vessel and to discuss investigation of the problem with plant engineers and chemists. To assist in

investigation of the corrosion problem, ORNL provided five racks of corrosion coupons which were exposed during a 24 day period in June and July when the phenol separation facility was operated. These racks of coupons were mounted on manway covers at five locations chosen to bracket the region where the most severe corrosion was expected. Corrosion rate calculations based on coupon weight changes are given in Tables 1-5. These results indicate that the most severe corrosion occurred between trays 40 and 60 and probably reached about 0.76 mm/y (30 mil/y) on 304L stainless steel. Based on the coupon studies, Carpenter 20Cb3 and Incoloy 825 were identified as materials that were very resistant to corrosion in the phenol tower environment. The high molybdenum content austenitic stainless steels showed good corrosion resistance, and, quite surprisingly, carbon steel consistently corroded at a lower rate than the chromium-molybdenum steels.

Results of extensive studies conducted by personnel of the gasification plant provided guidance as to means to remove the corrodent from the process streams. The corrosion coupons were returned to the plant for further exposure during a period when steps were taken to remove the corrodent.

Coal Liquefaction

An agreement between the U.S. Department of Energy (DOE) and the Japanese Agency for Industrial Science and Technology (AIST) calls for each country to provide corrosion samples for exposure in coal liquefaction plants operated by the other country. On behalf of AIST, two sets of samples were sent to ORNL where they were measured, weighed, and mounted on racks suitable for the two reactors vessel in the Wilsonville facility. These sample racks were delivered to Wilsonville in early September. Following exposure, the samples will be returned to ORNL for examination.

A set of samples was prepared by ORNL personnel for exposure in the Japanese coal liquefaction reactor. The compositions of these samples which were shipped to Japan in early September are listed in Table 6. Exposure of these samples is scheduled to begin in September, and they will be examined by the Japanese following exposure.

Material	Corrosion Rate mm/y	mil/y
Modified 9 Cr - 1 Mo	0.419	16.5
7 Cr - 1 Mo	0.271	10.6
2.25 Cr - 1 Mo	0.071	2.8
5 Cr - 1 Mo	0.063	2.5
Carbon Steel	0.016	0.6
Type 410 Stainless Steel	<0.003	<0.1
Type 321 Stainless Steel	<0.003	<0.1
Type 304L Stainless Steel	<0.003	<0.1
Carpenter 20Cb3	<0.003	<0.1
Incoloy 825	<0.003	<0.1
Type 316L Stainless Steel	<0.003	<0.1
Ferralium	<0.003	<0.1
Type 310 Stainless Steel	<0.003	<0.1
Type 317 Stainless Steel	<0.003	<0.1
Type 317LM Stainless Steel	<0.003	<0.1

Table 1. Calculated corrosion rates for coupons exposed 576 hours at the manway below tray 1 in the phenol distillation tower of the Dakota Gasification Company's Beulah, North Dakota plant.

Material	Corrosion Rate mm/y	mil/y
2.25 Cr - 1 Mo	1.706	67.1
5 Cr - 1 Mo	1.448	57.0
Modified 9 Cr - 1 Mo	1.385	54.5
7 Cr - 1 Mo	1.252	49.3
Type 410 Stainless Steel	0.469	18.4
Type 321 Stainless Steel	0.405	15.9
Carbon Steel	0.393	15.4
Type 304L Stainless Steel	0.218	8.6
Type 310 Stainless Steel	0.066	2.6
Type 316L Stainless Steel	0.062	2.4
Type 317 Stainless Steel	0.052	2.1
Ferralium	0.051	2.0
Type 317LM Stainless Steel	0.008	0.4
Carpenter 20Cb3	<0.003	<0.1
Incoloy 825	<0.003	<0.1

Table 2. Calculated corrosion rates for coupons exposed 576 hours at the manway located at tray 20 in the phenol distillation tower of the Dakota Gasification Company's Beulah, North Dakota plant.

Material	Corrosion Rate mm/y	mil/y
2.25 Cr - 1 Mo	3.349	131.
5 Cr - 1 Mo	2.830	111.
Modified 9 Cr - 1 Mo	2.690	105.
7 Cr - 1 Mo	2.645	104.
Type 410 Stainless Steel	0.755	29.7
Type 304L Stainless Steel	0.728	28.6
Type 321 Stainless Steel	0.715	28.1
Carbon Steel	0.504	19.8
Type 316L Stainless Steel	0.263	10.3
Ferralium	0.181	7.2
Type 310 Stainless Steel	0.155	6.1
Type 317 Stainless Steel	0.053	2.1
Carpenter 20Cb3	0.004	0.2
Type 317LM Stainless Steel	0.003	0.1
Incoloy 825	<0.003	<0.1

Table 3. Calculated corrosion rates for coupons exposed 576 hours at the manway located at tray 40 in the phenol distillation tower of the Dakota Gasification Company's Beulah, North Dakota plant.

Material	Corrosion Rate mm/y	mil/y
5 Cr - 1 Mo	2.652	104.
2.25 Cr - 1 Mo	2.305	90.7
Modified 9 Cr - 1 Mo	2.132	83.9
7 Cr - 1 Mo	1.875	73.8
Carbon Steel	0.827	32.5
Type 304L Stainless Steel	0.517	20.3
Type 321 Stainless Steel	0.446	17.5
Type 410 Stainless Steel	0.422	16.6
Type 316L Stainless Steel	0.250	9.9
Type 310 Stainless Steel	0.100	4.0
Ferralium	0.059	2.4
Type 317 Stainless Steel	<0.003	<0.1
Carpenter 20Cb3	<0.003	<0.1
Incoloy 825	<0.003	<0.1
Type 317LM Stainless Steel	<0.003	<0.1

Table 4. Calculated corrosion rates for coupons exposed 576 hours at the manway located at tray 60 in the phenol distillation tower of the Dakota Gasification Company's Beulah, North Dakota plant.

Material	Corrosion Rate mm/y	mil/y
Modified 9 Cr - 1 Mo	1.361	53.5
7 Cr - 1 Mo	1.339	52.7
5 Cr - 1 Mo	1.263	49.7
Type 410 Stainless Steel	0.980	38.6
Carbon Steel	0.546	21.4
Type 321	0.298	11.7
Type 304L	0.197	7.8
Type 310	0.051	2.0
Type 316L	0.041	1.6
Ferralium	0.004	0.2
Type 317	0.003	0.1
Carpenter 20Cb3	<0.003	<0.1
Type 317LM Stainless Steel	<0.003	<0.1

Table 5. Calculated corrosion rates for coupons exposed 576 hours at the manway located at tray 80 in the phenol distillation tower of the Dakota Gasification Company's Beulah, North Dakota plant.

Modified 9 Cr - 1 Mo (nominal)
8.5% Cr, 0.95% Mo, 0.40% Mn, 0.10% C, 0.21% V, 0.20% Si, 0.08% Nb, 0.05% N, Bal Fe

Type 347 Stainless Steel
17.98% Cr, 9.25% Ni, 0.28% Mo, 1.39% Mn, 0.047% C, 0.024% P, 0.022% S, 0.56% Si, 0.041% N, 0.71% Nb, Bal Fe

Type 304L Stainless Steel
18.27% Cr, 9.52% Ni, 0.20% Mo, 1.54% Mn, 0.015% C, 0.030% P, 0.022% S, 0.53% Si, 0.079% N, Bal Fe

Type 316L Stainless Steel
16.43% Cr, 10.95% Ni, 2.06% Mo, 1.58% Mn, 0.020% C, 0.021% P, 0.026% S, 0.50% Si, 0.073% N, Bal Fe

Ni_3Al (IC218)
8.40% Al, 7.84% Cr, 0.69% Zr, 0.02% B, Bal Ni

Fe_3Al (FA117)
15.7% Al, 2.2% Cr, 1.55% Nb, 1% Mo, 0.2% Zr, 0.01% B, 0.055% Y, Bal Fe

Fe_3Al (FA117)
15.85% Al, 5.45% Cr, 0.97% Nb, 0.05% C, Bal Fe

Table 6. Compositions of coupons supplied by ORNL to be exposed in the reactor of the Japanese Process Support Unit coal liquefaction facility.

ORNL/FMP-91/2

INTERNAL DISTRIBUTION

1. T. M. Besmann
2. P. J. Blau
3. R. A. Bradley
4. R. S. Carlsmith
5. P. T. Carlson
6. N. C. Cole
7. S. A. David
8. J. H. DeVan
9. B. Z. Egan
10. D. E. Fain
11. W. Fulkerson
12. M. A. Janney
13. D. R. Johnson
14. R. R. Judkins
15. J. R. Keiser
16. C. T. Liu
17. R. A. Lowden
18. D. J. McGuire
19. C. G. McKamey
20. V. K. Sikka
21. G. M. Slaughter
22. J. O. Stiegler
23. D. P. Stinton
24. R. W. Swindeman
25. V. J. Tennery
26. T. N. Tiegs
27. P. F. Tortorelli
28. J. R. Weir, Jr.
29. C. S. Yust
30-31. Central Research Library
32. Document Reference Section
33-34. ORNL Patent Section
35-36. Laboratory Records Department
37-38. M&C Records Office
39. Laboratory Records, ORNL-RC

EXTERNAL DISTRIBUTION

40. AIR PRODUCTS AND CHEMICALS, P.O. Box 538, Allentown, PA 18105

    S. C. Weiner

41. ALBERTA RESEARCH COUNCIL, Oil Sands Research Dept., P.O. Box 8330, Postal Station F, Edmonton, Alberta, Canada T6H5X2

    L. C. Gray

42. ALLIED-SIGNAL AEROSPACE COMPANY, 7550 Lucerne Drive, Suite 203, Middlesburg Heights, OH 44130

    S. D. Thompson

43-44. ALLISON GAS TURBINE OPERATIONS, P.O. Box 420, Indianapolis, IN 46206

P. Khandelwal, MS W-5
R. A. Wenglarz, MS W-16

45. AMAX RESEARCH AND DEVELOPMENT CENTER, 5950 McIntyre St., Golden, CO 80403

T. B. Cox

46-48. ARGONNE NATIONAL LABORATORY, 9700 S. Cass Ave., Argonne, IL 60439

W. A. Ellingson
K. Natesan
J. P. Singh

49. ARMCO, INCORPORATED, 705 Curtis St., Middletown, OH 45043

R. E. Hook

50. ATLANTIC RICHFIELD COMPANY, 8840 Iris Court, West Minister, CO 80020-4454

D. W. Bailey

51. AVCO RESEARCH LABORATORY, 2385 Revere Beach Parkway, Everett, MA 02149

R. J. Pollina

52-53. BABCOCK & WILCOX, 1562 Beeson St., Alliance, OH 44601

T. I. Johnson
M. J. Topolski

54. BABCOCK & WILCOX, Domestic Fossil Operations, 20 S. Van Buren Avenue, Barberton, OH 44203

M. Gold

55. BABCOCK & WILCOX, Lynchburg Research Center, P.O. Box 11165, Lynchburg, VA 24506

D. L. Hindman

56. BATTELLE COLUMBUS LABORATORIES, 505 King Avenue, Columbus, OH 43201

I. G. Wright

57. BERGBAU-FORSCHUNG GMBH, Postfach 130140, D-4300 Essen 13, Federal Republic of Germany

Gunter Fauth

58-59. BETHLEHEM STEEL CORPORATION, Homer Research Laboratory, Bethlehem, PA 18016

B. L. Bramfitt
J. M. Chilton

60. BRITISH GAS CORPORATION, Westfield Development Centre, Cardenden, Fife, Scotland KY50HP

J. E. Scott

61-62. CANADA CENTER FOR MINERAL AND ENERGY TECHNOLOGY, Physical Metallurgy Research Laboratories, 568 Booth Street, Ottawa, Ontario, Canada KlA OGI

R. Winston Revie
M. Sahoo

63. CASE WESTERN RESERVE UNIVERSITY, Department of Metallurgy and Materials Science, 10900 Euclid Avenue, Cleveland, OH 44106

K. M. Vedula

64. CENTER FOR APPLIED RESEARCH, 3572 Iron Works Pike, Lexington, KY 40511

R. E. Gonzalez

65. CENTRAL ELECTRIC RESEARCH LABORATORIES, Technology Planning and Research Division, Kelvin Avenue, Leatherhead, Surrey KT22 7SE, England

D. B. Meadowcroft

66. CERAMATEC, INC., 163 West 1700 South, Salt Lake City, UT 84115

D. W. Richerson

67. COLORADO SCHOOL OF MINES, Dept. of Metallurgical Engineering, Golden, CO 80401

G. R. Edwards

68-69. CONSOLIDATION COAL COMPANY, 4000 Brownsville Road, Library, PA 15129

F. P. Burke
S. Harding

70. CORNELL UNIVERSITY, Materials Sciences and Engineering Dept., Bard Hall, Ithaca, NY 14853

Che-Yu Li

71-72. DOW CHEMICAL COMPANY, Midland, MI 48674

P. A. Doty
G. S. Shier

73. DOW CORNING CORPORATION, 3901 South Saginaw Road, Midland, MI 48686-0995

W. H. Atwell

74. EC TECHNOLOGIES INC., 3614 Highpoint Dr., San Antonio, TX 78217

D. J. Kenton

75-78. EG&G IDAHO, INC., Idaho National Engineering Laboratory, P.O. Box 1625, Idaho Falls,ID 83415

D. W. Keefer
L. A. Lott
B. H. Rabin
R. N. Wright

79. EBASCO SERVICES, INC., P.O. Box 1002, Glen Rose, TX 76043

T. A. Flynn

80-84. ELECTRIC POWER RESEARCH INSTITUTE, P.O. Box 10412, 3412 Hillview Avenue, Palo Alto, CA 94303

S. B. Alpert
W. T. Bakker
C. J. Kulik
J. Stringer
R. H. Wolk

85. ENERGETICS, INC., 9210 Route 108, Columbia, MD 21045

C. C. Carey

86. EUROPEAN COMMUNITIES JOINT RESEARCH CENTRE, Petten Establishment, P.O. Box 2, 1755 ZG Petten, The Netherlands

M. Van de Voorde

87. EXXON RESEARCH AND ENGINEERING COMPANY, Clinton Township, Route 2 East, Annandale, NJ 08801

M. L. Gorbaty

88. FOSTER WHEELER DEVELOPMENT CORPORATION, Materials Technology Dept., John Blizard Research Center, 12 Peach Tree Hill Road, Livingston, NJ 07039

J. L. Blough

89. GAS RESEARCH INSTITUTE, 8600 West Bryn Mawr Avenue, Chicago, IL 60631

H. S. Meyer

90. GENERAL APPLIED SCIENCE LABS, 77 Raynor Avenue, Ronkonkoma, NY 11779
Martin Novack

91. GENERAL ATOMICS, INC., P.O. Box 85608, San Diego, CA 92138
T. D. Gulden

92. GEORGIA INSTITUTE OF TECHNOLOGY, Georgia Tech Research Institute, Atlanta, GA 30332
T. L. Starr

93. ILLINOIS INSTITUTE OF TECHNOLOGY, METM Dept., Perlstein Hall, Chicago, IL 60616
J. A. Todd Copley

94-95. INCO ALLOYS INTERNATIONAL, P. 0. Box 1958, Riverside Drive, Huntington, WV 25720
J. J. DeBarbadillo
S. Tassen

96. INSTITUTE OF GAS TECHNOLOGY, 3424 South State Street, Chicago, IL 60425
Robert Remick

97. THE JOHNS HOPKINS UNIVERSITY, Materials Science and Engineering, Maryland Hall, Baltimore, MD 21218
R. E. Green, Jr.

98. KENNAMETAL, INC., Philip McKenna Laboratory, 1011 Old Salem Rd., P.O. Box 639, Greensburg, PA 15601
B. North

99. LANXIDE CORPORATION, 1 Tralee Industrial Park, Newark, DE 19711
E. M. Anderson

100. LAVA CRUCIBLE-REFRACTORIES CO., P.O. Box 278, Zelienople, PA 16063
T. Mulholland

101. LAWRENCE BERKELEY LABORATORY, University of California, Berkeley, CA 94720
A. V. Levy

102. LAWRENCE LIVERMORE LABORATORY, P.O. Box 808, L-325, Livermore, CA 94550
W. A. Steele

103. LOS ALAMOS NATIONAL LABORATORY, P.O. Box 1663, Los Alamos, NM 87545
J. D. Katz

104. MASSACHUSETTS INSTITUTE OF TECHNOLOGY, Department of Civil Engineering, Room 1-280, 77 Massachusetts Avenue, Cambridge, MA 02139

O. Buyukozturk

105. THE MATERIALS PROPERTIES COUNCIL, INC., United Engineering Center, 345 East 47th Street, New York, NY 10017

M. Prager

106-108. NATIONAL INSTITUTE OF STANDARDS AND TECHNOLOGY, Materials Building, Gaithersburg, MD 20899

S. J. Dapkunas (Materials Bldg.)
E. R. Fuller (Bldg. 223, Rm. A-256)
L. K. Ives (Bldg. 220, Rm. A-215)

109. NATIONAL MATERIALS ADVISORY BOARD, National Research Council, 2101 Constitution Avenue, Washington, DC 20418

K. M. Zwilsky

110. NAVAL AIR SYSTEMS COMMAND, Propulsion and Power Division, AIR-536T, Washington, DC 20361-5360

L. E. Sloter

111. NEW ENERGY DEVELOPMENT ORGANIZATION, Sunshine 60 Bldg., P.O. Box 1151, 1-1 Higashi-Ikebukuro 3-Chrome, Toshima-Ku, Tokyo, 170, Japan

S. Ueda

112. NORTH CAROLINA A&T STATE UNIVERSITY, Department of Mechanical Engineering, Greensboro, NC 27411

J. Sankar

113. THE NORTON COMPANY, High Performance Ceramics Division, Goddard Road, Northboro, MA 01532-1545

N. Corbin

114. OHIO STATE UNIVERSITY, Department of Metallurgical Engineering, 116 W. 19th Avenue, Columbus, OH 43210

R. A Rapp

115. PACIFIC NORTHWEST LABORATORY, P.O. Box 999, Richland, WA 99352

J. L. Bates

116. PROMON ENGENHARIA S.A., Praia do Flamengo, 154-90 Andar, 22210 Rio de Janeiro, RJ Brazil

M. Saddy

117. RENSSELAER POLYTECHNIC INSTITUTE, Materials Engineering Department, Troy, NY 12180-3590

N. S. Stoloff

118. RISOE NATIONAL LABORATORY, P.O. Box 49, DK-4000, Roskilde, Denmark

Aksel Olsen

119. SANDIA NATIONAL LABORATORIES, Albuquerque, NM 87185

D. Doughty

120. SHELL DEVELOPMENT COMPANY, P.O. Box 1380, Houston, TX 77251-1380

L. W. R. Dicks

121. SORELL CONSULTING SERVICES, 49 Brookside Terrace, North Caldwell, NJ 07006

G. Sorell

122. SOUTHWEST RESEARCH INSTITUTE, 6620 Culebra Road, P.O. Drawer 28510, San Antonio, TX 78284

F. F. Lyle, Jr.

123. SRS TECHNOLOGIES, 990 Explorer Blvd., Huntsville, AL 35806

R. Bradford

124. SUPER FIBERS INC., 56 Finley Road, Princeton, NJ 08540

Dr. H. A. Huckins

125. TENNESSEE CENTER FOR RESEARCH AND DEVELOPMENT, P. 0. Box 23184, Knoxville, TN 37933-1184

A. H. von der Esch

126. TENNESSEE EASTMAN, P. 0. Box 511, Kingsport, TN 37662

L. M. Long

127. TENNESSEE VALLEY AUTHORITY, 3N66A Missionary Ridge Place, Chattanooga, TN 37402-2801

J. B. Brooks

128. TENNESSEE TECHNOLOGICAL UNIVERSITY, Manufacturing Center, P. 0. Box 5077, Cookeville, TN 38505

T. C. Ramaraz

129. TEXAS EASTERN TRANSMISSION CORPORATION, P.O. Box 2521, Houston, TX 77252

D. H. France

130. THE CARBORUNDUM COMPANY, P. O. Box 337, Niagara Falls, NY 14302

J. J. Kim

131. THE TORRINGTON COMPANY, Advanced Technology Center, 59 Field Street, Torrington, CT 06790

W. J. Chmura

132. 3M COMPANY, 3M Center, St. Paul, MN 55144

T. M. Kafka

133. UNION CARBIDE CORPORATION, Linde Division, P.O. Box 44,175 East Park Drive, Tonawanda, NY 14151-0044

H. Cheung

134-135. U. S. BUREAU OF MINES, Tuscaloosa, AL 35405

J. Bennett
T. Clancy

136. U.S. TREASURY, Office of Synthetic Fuels Projects, 806 15th Street NW, Suite 410, Washington, DC 20220

J. B. Beuton

137. UNITED TECHNOLOGIES RESEARCH CENTER, Silver Lane, MS 24, East Hartford, CT 06108

K. M. Prewo

138. UNIVERSAL ENERGY SYSTEMS, INC., 4401 Dayton-Zenia Road, Dayton, OH 45432

V. Srinivasan

139-140. UNIVERSITY OF CINCINNATI, Department of Aerospace Engineering and Applied Mechanics, Cincinnati, OH 45221

R. Y. Lin
W. Tabakoff

141. UNIVERSITY OF DELAWARE, Department of Chemical Engineering, Colburn Laboratory, Newark, DE 19716

W. A. Calkins

142. UNIVERSITY OF KENTUCKY, Mechanical Engineering Department, Lexington, KY 40506-0046

O. J. Hahn

143. UNIVERSITY OF NOTRE DAME, Department of Materials Science and Engineering, P.O. Box E, Notre Dame, IN 46556

T. H. Kosel

144-145. UNIVERSITY OF TENNESSEE, Materials Science and Engineering Department, Knoxville, TN 37996

R. A. Buchanan
C. D. Lundin

146. UNIVERSITY OF TENNESSEE SPACE INSTITUTE, Tullahoma, TN 37388

J. W. MuehIhauser

147. UNIVERSITY OF WASHINGTON, Department of Materials Science and Engineering, 101 Wilson, FB-10, Seattle, WA 98195

T. G. Stoebe

148-149. VIRGINIA POLYTECHNIC INSTITUTE AND STATE UNIVERSITY, Department of Materials Engineering, Blacksburg, VA 24061-0219

K. L. Reifsnider
W. W. Stinchcomb

150-151. WEST VIRGINIA UNIVERSITY, 617 Spruce St., P. 0. Box 6064, Morgantown, WV 26506-6064

C. I. Irwin
L. Wilson (Department of Physics)

152. WESTINGHOUSE HANFORD COMPANY, P.O. Box 1970, W/A-65, Richland, WA 99352

R. N. Johnson

153. DOE, IDAHO FIELD OFFICE, 785 DOE Place, Idaho Falls, ID 83402

R. B. Loop

154-160. DOE, MORGANTOWN ENERGY TECHNOLOGY CENTER, P.O. Box 880, Morgantown, WV 26505

R. A. Bajura
R. C. Bedick
F. W. Crouse, Jr.
N. Holcombe
W. J. Huber
J. E. Notestein
J. S. Wilson

161-162. DOE, OAK RIDGE FIELD OFFICE, P.O. Box 2008, Oak Ridge, TN 37831-6269

Manager, National Materials Program
E. E. Hoffman

163. DOE, OFFICE OF BASIC ENERGY SCIENCES, Materials Sciences Division, ER-131, GTN, Washington, DC 20585

J. B. Darby

164. DOE, OFFICE OF CONSERVATION AND RENEWABLE ENERGY, Energy Conversion and Utilization Technologies Division, CE-12, Forrestal Building, Washington, DC 20585

J. J. Eberhardt

165-166. DOE, OFFICE OF FOSSIL ENERGY, Washington, DC 20585

J. P. Carr, FE-14 (B-127/GTN)
T. B. Simpson, FE-231 (C-177/GTN)

167. DOE, OFFICE OF VEHICLE AND ENERGY R&D, CE-151, Forrestal Building, Washington, DC 20585

R. B. Schulz

168-173. DOE, PITTSBURGH ENERGY TECHNOLOGY CENTER, P.O. Box 10940, Pittsburgh, PA 15236

S. Akhtar
J. Hickerson
T. C. Rupel
R. Santore
T. M. Torkos
J. W. Wiggins

174. DOE, SBIR PROGRAM OFFICE, ER-16 GTN, Washington, DC 20545

S. J. Barish

175-176. DOE, OFFICE OF SCIENTIFIC AND TECHNICAL INFORMATION, P.O. Box 62, Oak Ridge, TN 37831

For distribution by microfiche as shown in DOE/TIC-4500, Distribution Category UC-114 (Coal Based Materials and Components)

END

DATE
FILMED
8/12/92